ESSAYS ON AERODYNAMICS

A COLLECTION OF SCIENTIFIC PAPERS AND SOME PERSONAL IMPRESSIONS

DEDICATED TO PROFESSOR J.A. STEKETEE

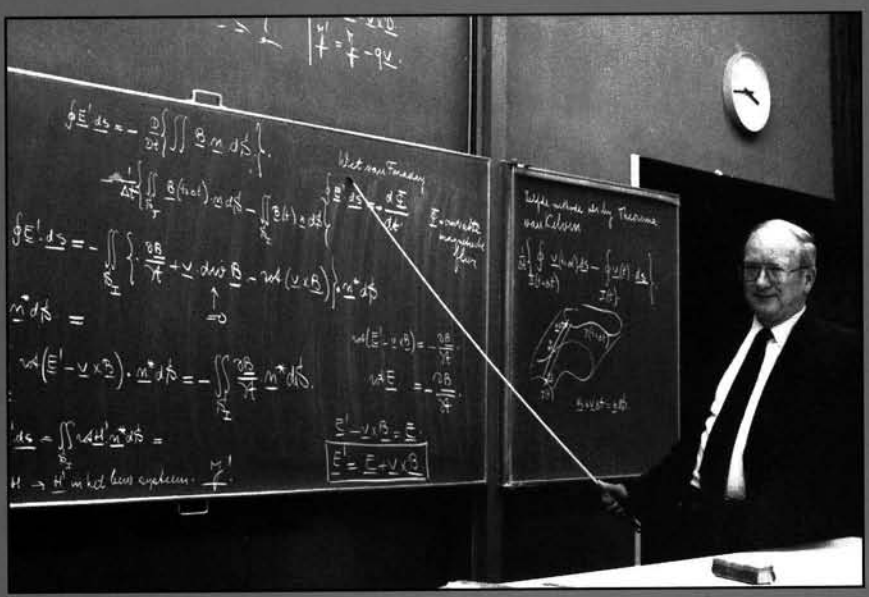

Edited by
P.G. Bakker, R. Coene and J.L. van Ingen
Department of Aerospace Engineering
Delft University of Technology

Essays on Aerodynamics

ESSAYS ON AERODYNAMICS

A COLLECTION OF SCIENTIFIC PAPERS
AND SOME PERSONAL IMPRESSIONS

DEDICATED TO PROFESSOR J.A. STEKETEE

Edited by
P.G. Bakker, R. Coene and J.L. van Ingen

Department of Aerospace Engineering
Delft University of Technology

Delft University Press / 1992

Published and Distributed by:

Delft University Press
Stevinweg 1
2628 CN Delft
The Netherlands

Telephone +31 15 783254
Fax +31 15 781661

by order of:

Department of Aerospace Engineering
Delft University of Technology
Kluyverweg 1
2629 HS Delft
The Netherlands

Telephone +31 15 785162
Fax +31 15 781822

ISBN 90 6275 763 4 / CIP

Typesetting : A/Z grafisch serviceburo, Den Haag
Print : Universiteitsdrukkerij, Delft

Contents

PART II – Personal memories and reflections

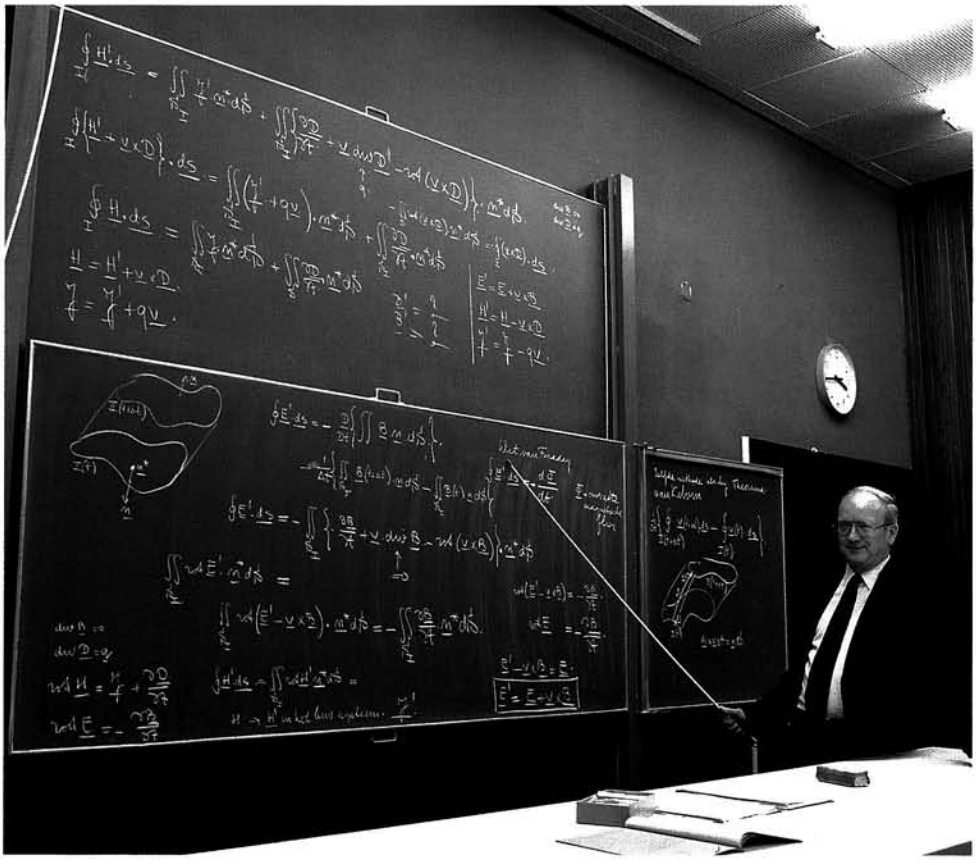

'Het is ook belangrijk dat het een beetje ordelijk op het bord komt'.

It makes all the difference how you do it on the blackboard.

Preface

This book is a collection of scientific papers and some personal impressions dedicated to Jacob Steketee on the occasion of his retirement as Professor in Theoretical Aerodynamics at the Department of Aerospace Engineering of Delft University of Technology. It was presented to him during the retirement ceremony on 18th March 1992.
Part I contains scientific contributions to fluid mechanics and its applications by a number of his former students and colleagues presently active in the field.
In Part II some personal recollections and impressions appear, together with a list of the names of his students and the titles of their master's or doctoral theses. The majority of the papers in Part I are in English, while in Part II most of the contributions are in Dutch. No efforts have been made by the editors to enforce either Dutch or English.

Jacob Abraham Steketee was born on 2nd January 1927 in Middelburg, the Netherlands. In 1944 he became a student in Mechanical Engineering at the Technische Hogeschool Delft, but in view of the war situation in the Netherlands his study actually began at a temporary dépendance in Eindhoven. In 1950 he graduated (with honours) under the supervision of prof. J.M. Burgers in theoretical fluid mechanics. From 1948 to 1950 he was a 'student-assistent' in the Laboratory for Aero- and Hydrodynamics in Delft. After graduation he was appointed lecturer in Applied Mechanics at the University of Toronto, Canada, (1950-1956) and then assistant professor in Applied Mechanics (1956-1960). At the same time he was Research Associate at the Institute of Aerophysics in Toronto.

During his time in Toronto, Professor Steketee became an expert in mathematical physics. His theoretical background enabled him to contribute to the theory of dislocations in the theory of elasticity, as well as to the field of fluid dynamics. He was always fascinated by the common mathematical foundations of different physical problems. He was very able and always willing to transfer his insight to colleagues and students. In 1955 he was awarded the degree of Doctor of Philosophy in Toronto for his thesis entitled: 'Some problems in boundary layer transition'. In 1958 Professor Steketee married Ruth Mildred Engledow (who even now retains her British passport). When, in 1960, the Department of Aeronautical Engineering at Delft felt the need to 'create a chair for theoretical aerodynamics in support of aeronautical engineering', Professor Steketee was the natural candidate for this chair.
From 1960 to the present time Professor Steketee has fulfilled this task admirably. Through his research and teaching more than one hundred graduates and a dozen Ph.D's have learned to appreciate the beauty of theoretical aerodynamics.

The benefit of his scholarly attitude extended not only to the universities but also to the aeronautical community at large (NLR, NIVR, Fokker) and to other industries and institutes such as the KNMI, TNO, Philips, Shell, etc. where most of his graduates and Ph.D's can be found. In his own research in Delft he concentrated mainly on two topics: unsteady gasdynamics and magnetohydrodynamics, and this work has led to a steady stream of publications. Moreover, he was deeply involved in the subject of the studies of his students and Ph.D candidates. A good impression of the diversity of these subjects is revealed by the list of master's and doctoral theses included in the present volume.
In addition to his research and teaching Professor Steketee was involved in various activities of an administrative nature which seem to be an unavoidable part of the life of a university professor. In the academic year 1970-1971 he spent a sabbatical at the University of Michigan.

Professor Steketee has participated in many other ways in national and international activities in the field of aerodynamics:
- by membership and subsequent chairmanship of the Sub-Committee for Aerodynamics of the National Aerospace Laboratory (NLR) and the Netherlands' Institute for Aircraft Development and Space Engineering (NIVR) and by membership of the Scientific Committee NLR-NIVR from 1962 to the present time.
- by membership, from 1965 to the present time, of the AGARD Fluid Dynamics Panel.
- by contributions to the FOM foundation advisory committee on Magneto Hydrodynamic Generators and Thermonuclear Research and Plasma Physics.

In addition to activities directly related to research and teaching in aerodynamics Professor Steketee was and is, in close cooperation with his wife Ruth, strongly involved with visitors from abroad through the International Neighbour Group Delft. Ruth has written a charming booklet 'Living in Delft, everyday life in Delft - some practical information'. The fifteenth edition appeared in 1991! No doubt Professor Steketee provided some of the basic research.

In conclusion it is mentioned that Professor Steketee has played the organ for the Mission to Seamen of the Anglican Church in Rotterdam virtually every week and that his expertise on organs and their architecture has been brought into play in the Organ Committee of the Dutch Reformed Church in Delft (the Old Church and the New Church).

The present volume is offered to Professor Steketee by his students and colleagues as a token of their appreciation.

Finally, we take the opportunity to acknowledge all help received in the preparation of this book. We wish to thank Marion Emons-van Gelderen for her secretarial efforts and for keeping the secret. The assistance given by all other secretarial staff of the Faculty of Aerospace Engineering is gratefully acknowledged.

Delft, March 1992

The Editors,
P.G. Bakker
R. Coene
J.L. van Ingen.

A mathematical model for 'open' separation in three-dimensional flow

By P.G. Bakker

Faculty of Aerospace Engineering, TU Delft

Abstract

This contribution to the 'Steketee boek' concerns the topology of separated flows in three dimensions. Topological aspects will be examined using local solutions of the Navier-Stokes equations. Emphasis is given to the so-called open separation structure. A theoretical model which describes local flow characteristics and the structural stability aspects is derived and discussed.

1. Introduction

Flow separation is a well-known interesting phenomena that may appear on bodies of various forms in three-dimensional fluid flow. Complicated separation structures can occur but in many cases they can be unwrapped so that a set of well organized basic separation forms can be recognized and identified. Two important examples of such a basic separation structure are the *bubble* type separation and the *free vortex layer-* or *open* separation, see Maskell (1955). Bubble type separation is typical for steady laminar flow; it can be identified as a closed region of recirculating fluid appearing in the main flow. The separated region fits on the body surface and is bounded by a streamsurface which intersects the body surface along the separation/attachment line. Inside the bubble the flow is more or less inactive since it circulates at a rather low energy and momentum level. The skin friction pattern on the wall surface shows some characteristic features. The separation/attachment curve is formed by two skin friction lines running between two saddle point singularities forming a closed region. Inside this region the skin friction pattern shows two sets of closed loops surrounding two center point singularities, see figure 1.

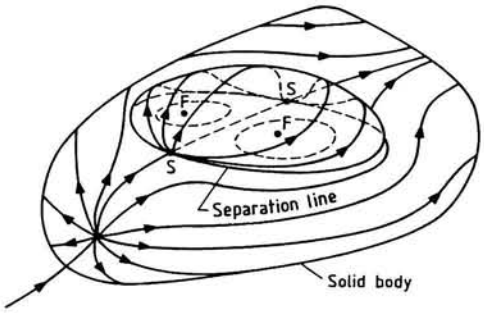

Fig. 1 Bubble type separation

Free vortex layer separation is another basic structure and not of closed form.
In fact there appear two basic types of free vortex layer separation.
At first one distinguishes the so-called Legendre-Werlé separation having a saddle-focus pair of singularities in the skin friction field. Some 3D topological features are depicted in figure 2a.
The second type of free vortex layer separation shows a strong convergence of skin friction lines somewhere on the body surface. see figure 2b. This strong convergence phenomena is accompanied with an apparently strong *divergence* of the flow away from the wall.

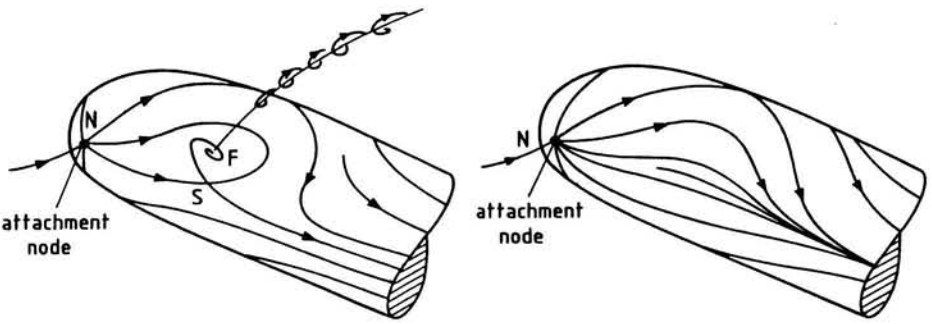

a Legendre-Werlé separation

b Free vortex layer separation with converging skin-friction lines

Fig. 2 Two basic types of open separation.

Since no closed curve in the skin friction pattern nor an isolated region of circulating fluid can be observed these two types of separation are frequently denoted as 'open' separations (Wang 1983).

The aforementioned basic types of three-dimensional separations have drawn much

attention in the fluiddynamic community. However, apart from several numerical attempts, a firm theoretical mathematical description of these separation structures is still lacking.
This essay attempts to develop a mathematical model for the 'open' separation flow structure. It will be based on the Navier-Stokes equations governing incompressible steady viscous flow. To obtain appropriate solutions of these equations, an indirect method is utilized. First a classification study of possible bifurcating solutions (unfoldings) of degenerate skin friction singularities is carried out. Careful examination of the topological properties of these solutions may lead to the identification of typical 'open' separation structures.

2. Trajectory pattern near singularities on the wall

The topology of three-dimensional separated flow structures is examined for steady incompressible viscous flows in the neighbourhood of a plane wall at rest. The flow is described in a Cartesian reference frame x,y,z and satisfies the no-slip and impermeability boundary condition on the wall surface, (y = 0): (u,v,w) = (0,0,0), $\forall x,z$.
u, v, w denote the velocity components in the x, y, z direction respectively.
The steady streamline pattern near the wall, which is studied in the upper half space $y \geqslant 0$ is represented by the trajectories of the third order autonomous dynamical system:

$$\begin{aligned} \frac{dx}{dt} &= u\,(x,y,z) \\ \frac{dy}{dt} &= v\,(x,y,z) \\ \frac{dz}{dt} &= w\,(x,y,z) \end{aligned} \qquad (1)$$

The topology of possible flow structures near the wall surface will be investigated by developing solutions of the Navier-Stokes equations. Solutions valid near the wall will be approximated by using Taylor expansions for the velocity components near an arbitrary point on the wall.
Recalling the no-slip boundary condition and the continuity equation one may propose

$$u = y\,\bar{u}(x,y,z),\quad v = y^2\,\bar{v}(x,y,z),\quad w = y\bar{w}\,(x,y,z).$$

Then it follows that $\frac{dx}{dt} = 0$, $\frac{dy}{dt} = 0$ and $\frac{dz}{dt} = 0$ in any point at y = 0; the plane y = 0 is a plane with singular points of system (1). Due to this singular behaviour no

trajectories of (1) can be identified on the wall surface. Since the trajectories of system (1) at $y \neq 0$ are identical with those of the equivalent system

$$\begin{aligned} \frac{dx}{dt} &= \bar{u}\,(x,y,z) \\ \frac{dy}{dt} &= y\bar{v}\,(x,y,z) \\ \frac{dz}{dt} &= \bar{w}\,(x,y,z) \end{aligned} \tag{2}$$

the singular character of the plane $y = 0$ can be removed by investigating (2) instead of (1).
The skin friction field on the wall surface is defined by the shear stress vector (τ,σ) with $\tau = \mu \frac{\partial u}{\partial y}(x,0,z)$, $\sigma = \mu \frac{\partial w}{\partial y}(x,0,z)$ and follows by integration of the system

$$\frac{dx}{dt} = \tau\,, \frac{dz}{dt} = \sigma.$$

Flows having interesting topological properties are found near singularities in the skin friction field on the wall surface. Singularities in the skin friction field occur where the shear stress components: τ and σ vanish simultaneously on the wall. If system (2) is expanded near a singularity on the wall it can be written in the form

$$\dot{\underline{X}} = A\,\underline{X} + f(\underline{X}) \tag{3}$$

where

$$\underline{X} = (x,y,z)^T$$

and

$$A = \frac{1}{\mu}\begin{pmatrix} \tau_x & \frac{1}{2}p_x & \tau_z \\ 0 & \frac{1}{2}p_y & 0 \\ \sigma_x & \frac{1}{2}p_z & \sigma_z \end{pmatrix}$$

A is the linear stress matrix evaluated in the singularity at the origin (0,0,0), $f(\underline{X})$ is a vector polynomial containing the higher order terms, see Bakker & De Winkel (1990).

Equation (3) has the form of a non-linear dynamical system which describes both streamlines in the flow as well as skin friction lines on the wall. The singularities of system (3) can be interpreted in two ways, those lying above the wall represent stagnation points in the flow, those located at the wall have a vanishing shear stress vector signalling either flow separation from the wall or flow attachment to the wall. Since we are particularly interested in the topology of separation and attachment structures this study is restricted to wall singularities. Applying the theorem of Hartman-Grobman, see Guckenheimer and Holmes (1983), the topological structure of a singularity is fully determined by the eigenvalues of the linear stress matrix, except if eigenvalues appear having real parts equal to zero, Re $(\lambda) = 0$.

Singularities are structurally stable if all eigenvalues satisfy Re $(\lambda) \neq 0$, these points are called *hyperbolic*. Otherwise singularities having Re $(\lambda) = 0$ are structurally unstable, they are called *non-hyperbolic* and higher-order nonlinear terms are necessary for a proper description of the topological structure of the singularity.
Non-hyperbolic points have a certain degree of degeneracy which make them sensitive to small disturbances so that they can bifurcate. The bifurcations of degenerate skin friction singularities are very interesting for separation studies, because via bifurcation new structurally stable flow patterns with a complicated topology can be found.

3. Jordan normal forms of skin friction singularities

Using system (3) hyperbolic and non-hyperbolic skin friction singularities can be classified. Writing Eq. (3) explicitely up to second order there follows

$$\frac{dx}{dt} = a_2x + a_3y + a_4z + a_5x^2 + a_6xy + a_7xz + a_8y^2 + a_9yz + a_{10}z^2 + 0(3)$$

$$\frac{dy}{dt} = y\,(b_1 + b_2x + b_3\,y + b_4\,z) + 0(3) \qquad (4)$$

$$\frac{dz}{dt} = c_2x + c_3y + c_4z + c_5x^2 + c_6xy + c_7xz + c_8y^2 + c_9yz + c_{10}z^2 + 0(3)$$

where a_i, b_j & c_k are constants. To fulfil the flow equations relations between a_i, b_j & c_k exist. For detals see De Winkel (1988).
The one which will be often used originates from the continuity equation and reads

$$a_2 + 2b_1 + c_4 = 0 \qquad (5)$$

The unknown coefficients occurring in (4) can be used for a proper embedding of a local flow structure into a surrounding main flow. The coefficients a_i, b_j and c_k can also be expressed in the physical quantities pressure p and shear stress components τ

and σ, to be evaluated in the origin (0,0,0).
The linear part of (4) is governed by the matrix A and yields the eigenvalues λ_i:

$$\lambda_{1,3}=\frac{1}{2}(\tau_x+\sigma_z)\mp\frac{1}{2}\sqrt{(\tau_x-\sigma_z)^2+4\tau_z\,\sigma_x}\ ,\ \lambda_2=\frac{1}{2}p_y \tag{6}$$

From continuity, Eq (5), follows

$$\lambda_1 + 2\,\lambda_2 + \lambda_3 = 0 \tag{7}$$

which is equivalent to the fundamental result

$$\frac{\partial\tau}{\partial x}+\frac{\partial p}{\partial y}+\frac{\partial\sigma}{\partial z}=0 \tag{8}$$

Since all eigenvalues can never have the same sign (Eq. (7)) it implies that a singularity on the wall can not occur as a source or as a sink of streamlines. It will always happen that if parts of the flow enter the singularity other parts exist which will leave the singularity.

The non-linear system $\dot{\underline{X}}= A\,\underline{X} + f(\underline{X})$ can be brought into the equivalent form

$$\dot{\underline{U}} = J\,\underline{U} + g(\underline{U}) \tag{9}$$

by performing the linear transformation $\underline{X} = T\underline{U}$ so that $J = T^{-1}\,AT$ and $g(\underline{U}) = T^{-1}\ f(T\underline{U})$.

All topologically different linear flow structures near a skin friction singularity are equivalently described by one of the Jordan normal forms represented by the various possibilities of J; they are listed in Figure 3.
These Jordan forms, involving both hyperbolic ($Re(\lambda_i) \neq 0, \forall i$) as well non- hyperbolic ($Re(\lambda_i) = 0$, for some i) singularities, satisfy the no-slip boundary conditions and can be obtained by transforming the original base to a base of the eigenvectors, see Reyn (1964).

Note that in the hyperbolic case three equal eigenvalues can not occur since in that case Eq (7) implies $\lambda_1 = \lambda_2 = \lambda_3 = 0$ so that the singularity is non-hyperbolic.
Similarly three real and two equal eigenvalues cannot occur in the non- hyperbolic case if Eq. (7) has to be satisfied.

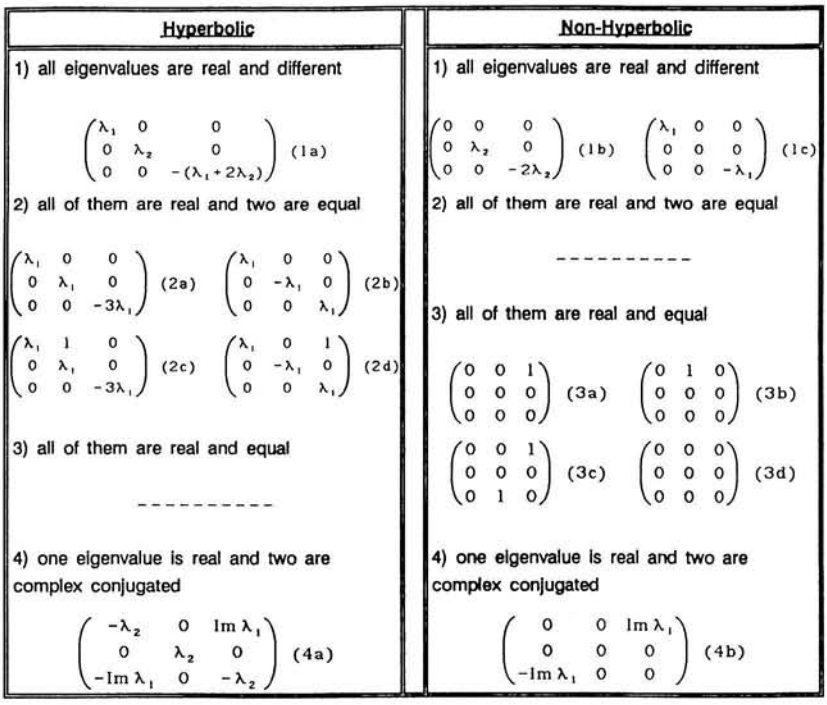

Fig.3 Jordan normal forms for hyperbolic and non-hyperbolic singularities

4. Elementary singularities, skin friction patterns

The possible types of 3D *elementary* singularities can now be classified using the Jordan normal forms for hyperbolic points as listed in Figure 3. Since λ_2 is related to the eigenvector e_2 in off-wall direction, it is appropriate to distinguish *attachment* points ($\lambda_2 < 0$) and *separation* points ($\lambda_2 > 0$).
A wall singularity is called an attachment point if a spatial streamline exists which terminates in the singularity; similarly separation points appear if a spatial streamline can be found which leaves the singularity.

Since sign (λ_2) = sign (p_y), Eq. (6), attachment points indicate a pressure decrease and separation points show a pressure increase when going in off -wall direction.
Three basically different skin friction patterns near an attachment point are observed: a *saddle* (τ_x and σ_z have different sign), an *unstable node* (τ_x and σ_z have the same sign) or an *unstable focus* $\{\tau_x - \sigma_z)^2 + 4\,\tau_z\,\sigma_x < 0\}$. Very similar patterns arise near a separation point, unless the node and the focus must be stable in that case, see Figure 4.

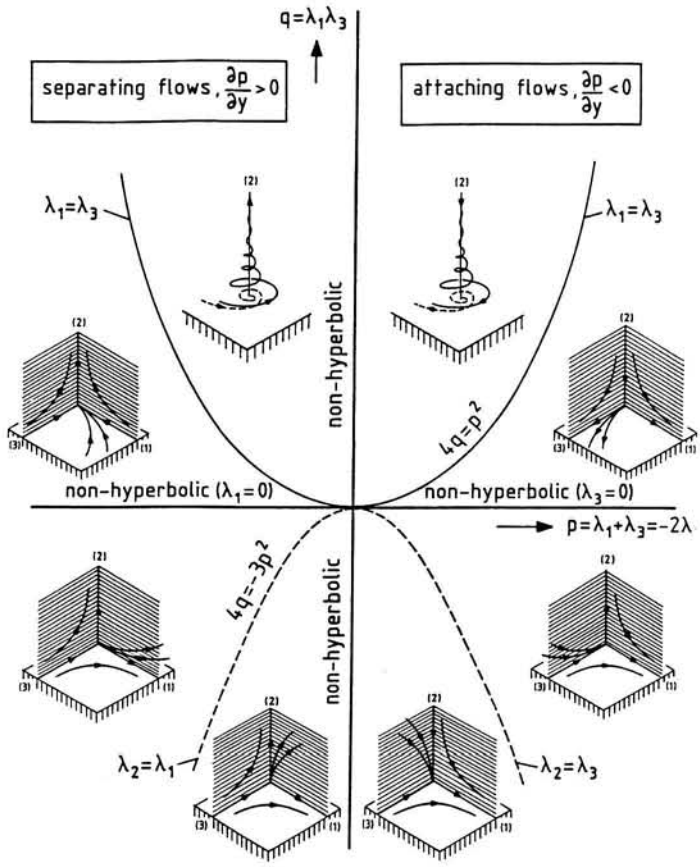

Fig. 4 Elementary singularities on a wall in 3D viscous flows

Some of these local flow structures can be recognized in Aerodynamics. The (general) node appears for instance on the surface of a body at the attachment point of the free stream. In case of a symmetrical body (for example a sphere) one might expect that a star node appears as an attachment point. The focus corresponds to a vortex standing on the surface of the body and saddles occur for example in flows with closed separation bubbles. The inflected node is not much familiar in aerodynamic applications because it appears as a transition pattern between node and focus.

5. Cusp singularity in the skin friction pattern (Jordan form J_{3c})

Flow structures derived from the Jordan normal form J_{3c} appear to be of particular interest for the open separation flow structure. As an example of a non-hyperbolic flow let us consider the flow associated with the Jordan form:

$$J_{3c}: \begin{pmatrix} 0 & 0 & 1 \\ 0 & 0 & 0 \\ 0 & 1 & 0 \end{pmatrix} \tag{10}$$

A proper determination of the local flow topology of this degenerate singularity in the skin friction field requires several non-linear terms added to the linear part. In fact these terms are already resident in Eq (4) but the question is raised whether some non-linear terms can be skipped without affecting the topological structure of the singularity. Using normal form theory (Guckenheimer & Holmes (1983)) the remaining essential terms may be found by the application of a near-identity transformation.

$$\underline{U} = \underline{Y} + P(\underline{Y}) \tag{11}$$

on system (9): $P(\underline{Y})$ is a vector polynomical of degree 2.
The normal form with linear part J_{3c} that satisfies the flow equations is obtained by Kooy & Bakker (1989) and can be written as

$$\begin{aligned} \frac{dx}{dt} &= z + x^2 - \frac{2}{3} y^2 + 0(3) \\ \frac{dy}{dt} &= -xy + 0(3) \\ \frac{dz}{dt} &= y + cx^2 - \frac{1}{3} cy^2 + 0(3) \end{aligned} \tag{12}$$

The coefficient c remains undetermined and can be identified with the local value of the stress derivative σ_{xx} at the singularity.

Flow patterns for $c > 0$ and $c < 0$ are shown in Figure 5.

Fig. 5 Local flow structures near a cusp singularity in the skin friction field

The skin friction pattern is given by the dotted lines. The non-hyperbolic case $c < 0$ implies $\sigma_{xx} < 0$; it represents a 3D degenerate flow structure with a cusp singularity

in the skin friction field. Above the wall there appear two special spatial trajectories, both passing through the origin. Near the singularity these trajectories form a parabola in the plane $-3y + 2cz = 0$. One trajectory is an attachment streamline whereas the other is a separation streamline; the wall surface is touched tangentially.
The case $c > 0$ implies $\sigma_{xx} > 0$ in the singularity. Again a cusp is formed in the skin friction pattern. The streamlines above the wall follow more or less the skin friction lines. There is no separation nor attachment in this particular structurally unstable flow situation. A numerical calculation of the skin friction field in the vicinity of the cusp shows a remarkable strong convergence of the skin friction lines to the separatrices of the cusp singularity; see Figure 6.

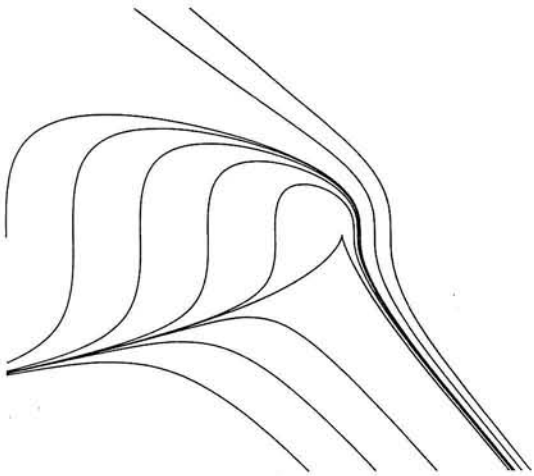

Fig. 6 Strong convergence of skin friction lines.

The separatrices show an attracting influence on neighbouring paths forming a river of converging skin friction lines. In aerodynamic applications the strong convergence phenomenon is mostly interpreted as a reliable indication for flow separation.
Furthermore note that the line of convergence can be identified as a particular skin friction line originating from the cusp singularity.

6. Bifurcation of system (12)

System (12) may be integrated to obtain the streamline pattern near a degenerate singularity displaying a cusp in the skin friction field on the wall surface.
Due to its degenerate state ($\mathrm{Re}(\lambda) = 0$) the corresponding flow pattern is structurally unstable, meaning that its topological structure can be disturbed when adding a linear term. To obtain all possible flow structures that can arise if linear terms are inserted in (12) we study the bifurcation or unfolding of system (12). Mather's theorem, see for example Shirer & Wells (1983) may be applied to obtain an unfolded system which contains the smallest number of perturbation terms without loosing an essen-

tial topologically different solution. According to this theorem the unfolded system satisfying the flow equations becomes

$$\begin{aligned} \frac{dx}{dt} &= \mu x + z + x^2 - \frac{2}{3}y^2 \\ \frac{dy}{dt} &= -\frac{1}{2}\mu y - xy \\ \frac{dz}{dt} &= \lambda + y + cx^2 - \frac{1}{3}cy^2 \end{aligned} \tag{13}$$

System (13) contains the bifurcation parameters μ and λ representing small perturbations of the shear stress quantities τ_x and σ respectively. These parameters may be chosen independently to obtain a complete set of possible topologically different flow structures. For $\mu = 0$, $\lambda = 0$ the original degenerate state reappears. If $c > 0$ this state has no typical streamlines which leave or approach the singularity. Therefore the case $c > 0$ seems of particular interest to investigate the open separation phenomenon.

Singularities of system (13) appearing after bifurcation may be found on the wall surface ($y = 0$) as well in the flow field. On the wall we observe them only if $\frac{\lambda}{c} \leq 0$ at:

$$x^{\pm} = \pm\sqrt{\frac{-\lambda}{c}}, \quad z^{\pm} = \pm\mu\sqrt{\frac{-\lambda}{c}} + \frac{\lambda}{c}$$

In the flow field only one singularity may be present which is located at:

$$x_s = -\frac{1}{2}\mu, \quad y_s = \lambda + c\frac{\mu^2}{4} + 0(\lambda^2, \lambda\mu^2, \mu^4), \quad z_s = \frac{\mu^2}{4} + 0(\lambda^2, \lambda\mu^2, \mu^4)$$

The bifurcation sets that appear are:

Hopf bifurcation (H) $\quad \frac{\lambda}{c} = -\frac{1}{4}\mu^2 \; (\mu > 0)$

Saddle-node (SN) $\quad \lambda = 0 \;\; \& \;\; \frac{\lambda}{c} = -\frac{1}{4}\mu^2 \; (\mu < 0)$

Homoclinic cycle (HC) $\quad \frac{\lambda}{c} = -(\frac{7}{10})^2\mu^2 + 0(\mu^3)$

Along, $\frac{\lambda}{c} = \frac{1}{64}\mu^4 (IN_1)$ and, $\frac{\lambda}{c} = -\frac{2}{9}\sqrt{3}\mu^{3/2} (IN_2)$ foci and nodal points transfer into each other by passing an inflected node.

Bifurcation sets and flow patterns are shown in Figure 7. Let us discuss them in some detail. Moving in the parameter plane (λ,μ) onto various domains, a sequence of 3D flow structures is encountered. The 'flow' on the wall, e.g. the skin friction lines are sketched by dashed curves. Spatial streamlines above the wall are depicted by full lines.

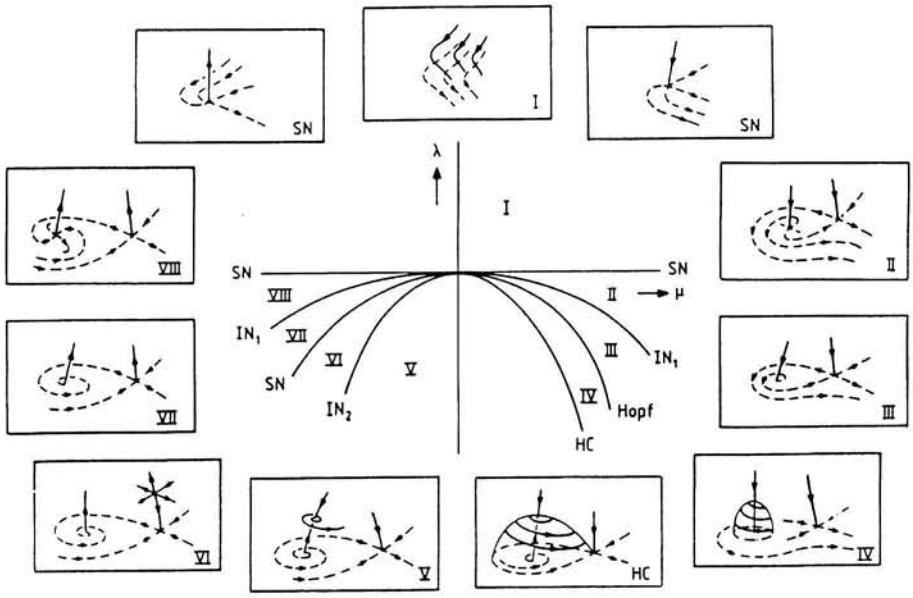

Fig. 7 Flow patterns of system (13) $c > 0$

If the degenerate state $\mu = 0$, $\lambda = 0$ is perturbed by taking $\lambda > 0$ a regular flow field results (I) meaning that the flow field has no singularities neither in the skin friction pattern on the wall nor in the flow region above the wall.

As we observe further the regular flow field can be disturbed by a saddle-node bifurcation causing two attachment singularities. One of them is always a saddle point S, the other can be either a nodal point N (II, VIII) or a focus F (III- VII). This focus can become structurally unstable so that via an unstable (in the Lyapunov sense) fine focus a Hopf bifurcation appears. The Hopf bifurcation creates a three-dimensional bubble-shape separation surface which forms a closed separation line on the wall (IV). Inside the bubble the fluid recirculates in a rotational movement; no singularities in the flow appear but a stable focus is formed in the skin friction pattern. A one-dimensional unstable manifold which originates from this focus transports the fluid on to the top of the bubble where it is spread out over the bubble surface. Then the fluid is conveyed by the closed separation surface again to the wall. The closed separation line on the wall appears as a limit cycle in the skin friction field. Via a global bifurcation (HC) the bubble dissolves into the main flow and the closed separation

line which has been grown into a saddle-loop breaks up resulting into the disappearance of a closed separation line and leaving the ordinary skin friction pattern with the well-known saddle-focus pattern (V-VII) (Legendre-Werlé) as observed by Legendre (1965). This pattern remains until the focus is transformed into a nodal point (VIII). Via a saddle-node bifurcation both singularities vanish and the regular flow field is obtained again.

7. 'Open' separation in three dimensional viscous flow

Careful examination of the flow patterns in Figure 7 show that this bifurcation has the very interesting property that a regular skin friction field is one of the bifurcation solutions (domain I). Such a regular skin friction field (absence of singularities) is of great value for the study of incipient separations occurring in these regular three-dimensional flow fields.
Within this aspect the skin friction field:

$$\frac{dx}{dt} = \mu x + z + x^2$$
$$\frac{dz}{dt} = \lambda + cx^2 \qquad (14)$$

is calculated numerically for the three cases

- regular flow (domain I, $\lambda = 1$, $\mu = 0$)
- saddle + node pattern (domain II, $\lambda = -1$, $\mu = -2$)
- saddle + focus pattern (domain III, $\lambda = -1.8$, $\mu = 1$)

The results are shown in Figure 8 for the case $c = 1$.

Note the strong convergence of skin friction lines in the case of a regular flow. Clearly the skin friction pattern froms a river of attracting paths along $z = -x^2$, $x > 0$. Following Lighthill (1963) and others, convergence of skin friction lines implies a divergence (upwash) of spatial streamlines from the wall surface. This upwash phenomenon is studied numerically from system (13) in Figure 9 which shows the time evolution of a stream tube starting at $z = -1$ with a slender rectangular cross section very near the wall in front of the domain of convergence. The calculations are carried out for $\lambda = 1$ $\mu = 0$. Figure 9 shows the deformation of the stream tube cross section in streamwise direction from $z = -1$ to $z = -6$.
It appears that the thin layer of fluid originally close to the wall lifts off from the wall and squeezes into a filament of fluid orientated more or less normal to the wall surface.

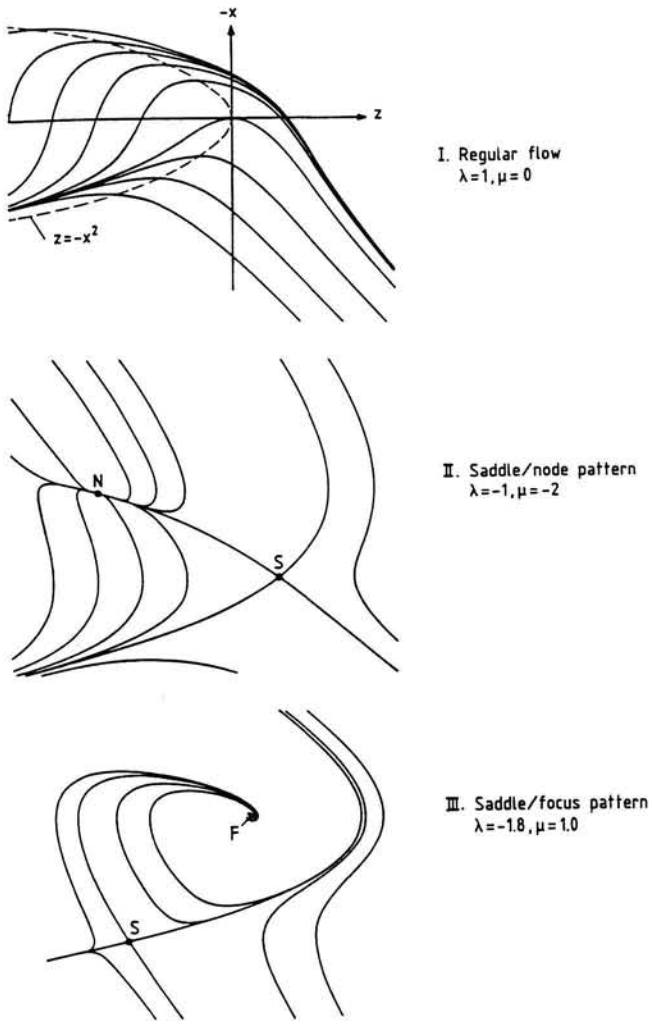

Fig. 8 Skin friction patterns generated from bifurcation of the cusp singularity

'Open' separation as modelled by system (13), domain I, shows no particular stream surfaces that originate from the wall and could act as a separation surface.
Furthermore no particular skin friction line can be identified as a typical separation line. The river $z = -x^2$, $x > 0$ shows itself as a typical line in the whole pattern however it is not a skin friction line. On the other hand skin friction lines are attracted by the river and all of them approach it only from one side, see Figure 8.

The successive skin friction patterns of system (13) depicted in Figure 8 draws the attention to another observation namely that 'open' separation (domain I) and

separation of Legendre-Werlé type (saddle-focus pattern domain III) can be changed into each other by a one parameter bifurcation.

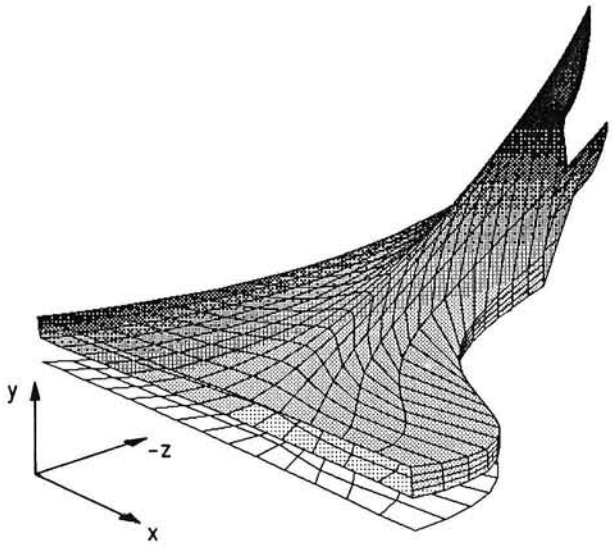

Fig. 9 Time evolution of near wall fluid in front of open separation

Via saddle-node bifurcation in the skin friction pattern (bifurcation set SN in Figure 7) and a saddle/node pair the saddle/focus pair can arise in an originally regular flow domain. A three-dimensional view of this bifurcation scenario is sketched in Figure 10. It may be concluded that the two basic types of free vortex layer separation as mentioned in the introduction are closely related separation structures. Both are described by the same mathematical model and can be generated by an appropriate unfolding of the cusp singularity.

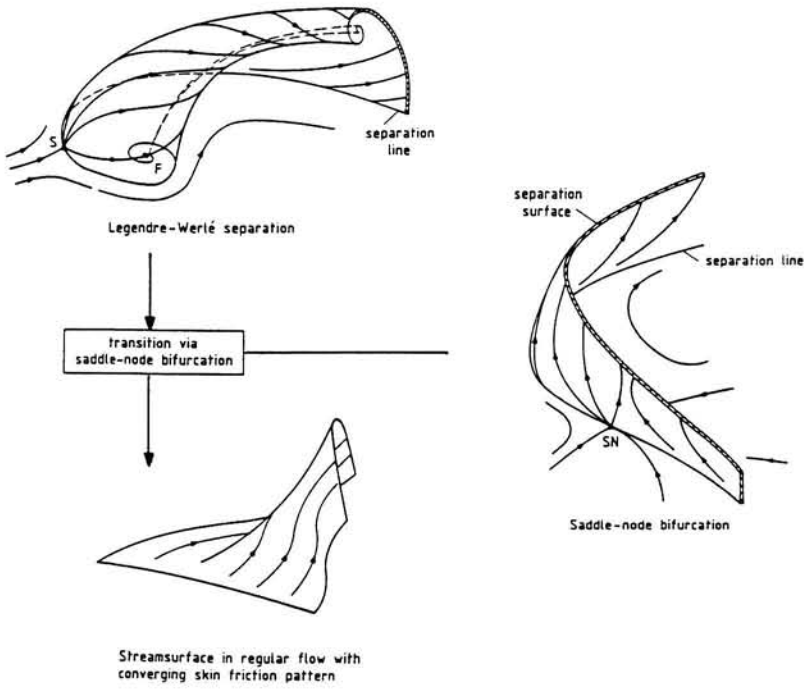

Fig. 10 Topological structure of basic types of free vortex layer separations

8. Conclusions

The topological structure of three-dimensional separations can be studied by unfolding degenerate singularities in the velocity vector field of a three- dimensional viscous flow.

A mathematical model for free vortex layer separation is presented. It appears that the two basic types of free vortex layer separation are closely related; both arise as an unfolding of a cusp singularity in the skin friction field.

Free vortex layer separation displaying no singularities in the skin friction pattern are identified by a strong convergence of skin friction lines. A typical separation line and corresponding separation surface can not be observed in this case.

Several topological aspects of free vortex layer separation such as the appearance of singularities, separation lines, topology of skin friction field and the three-dimensional streamline structure is modelled satisfactorily by a third order non-linear dynamical system containing at least terms of the second degree. Other aspects such as vorticity distribution and vortex formation may be a higher non-linear effect which has to be subject for further research.

9. References

Bakker, P.G. & De Winkel, M.E.M.	On the Topology of Three-Dimensional Separated Flow Structures and Local Solutions of the Navier- Stokes Equations, in Topological Fluid Mechanics. Ed. H.K. Moffatt and A. Tsinober, Cambridge University Press, 1990.
Guckenheimer, J. & & Holmes, P.J.	Non-linear oscillations, dynamical systems and bifurcation of vector fields. Springer, New York, Berlin, 1983.
Kooij, R.E. & Bakker, P.G.	Three-dimensional viscous flow structures from bifurcation of a degenerate singularity with three zero eigenvalues, Report LR-572, Delft University of Technology, 1989.
Legendre, R.	Lignes de courant d'un ecoulement continu, La Recherche Aerospatiale, 105. pp 3-9, 1965.
Lighthill, M.J.	Attachment and Separation in 3D Flow, in Laminar Boundary Layers, L. Rosenhead II (ed), Sec 2.6, pp 72-82, Oxford University Press, U.K., 1963.
Maskell, E.C.	Flow Separation in Three Dimensions, RAE Aero Rept. 2565, 1955.
Reyn, J.W.	Classification and description of the singular points of a system of three linear differential equations, ZAMP vol. 15, Fasc 5, pp 540-557, 1964.
Shirer, H.N. & Wells, R.	Mathematical structures of the singularities at the transitions between steady states in hydrodynamic systems, Lecture notes in physics, vol. 185, Springer, New York, 1983.
Wang, K.C.	On the disputes about open separation, AIAA-paper 83- 0296, 1983.

Experimental characteristics of vortex breakdown on a delta wing at high speeds

Faculty of Aerospace Engineering, TU Delft

By W.J. Bannink

Summary

The present paper deals with an experimental investigation of high subsonic and transonic flow at the leeward side of a sharp-edged planar delta wing with a leading edge sweep of 65°. The experiments were performed at Mach numbers from 0.7 to 0.9 and angles-of-attack up to 20°.

Surface pressure measurements, oil flow visualizations and schlieren visualizations have been made. Attention was paid to the presence of embedded shocks, vortex breakdown and the interaction between them.

Emphasis is given to the case with a free stream Mach number of 0.85, since that case attracted international interest because of computer code validation. At this Mach number and at angles-of-attack of 15° and higher, a shock was observed across the wing symmetry plane, with the shock terminating a local supersonic region. Beyond 19° angle-of-attack the shock was located at about 50% chord position and vortex breakdown occurred downstream of it. In this situation a strong expansion was generated immediately downstream of the shock. The expansion was neutralised by a second shock at 80% rootchord.

1. Introduction

The study of flow past delta wings in general has been a subject of particular interest in the past decades. The investigations concerned incompressible as well as compressible flow regimes and involved theoretical and experimental work. The flow field at the leeward side of a delta wing contains most complex phenomena ranging from attached flow to fully separated flow with the occurrence of vortices and, at high speeds where transonic and supersonic regimes are found, embedded shocks. The flow structure depends strongly on the free stream Mach number and the angle-of-attack, but also on the geometry of the wing: leading edge sweep and shape, and leading edge nose radius. It depends less on the fact whether the upper surface is curved or not (wing profile or flat surface), although it may have a quantitative effect on the results.

The reason for the growing interest in this subject may not only be found in the aerodynamics of fast manoeuvrable aircraft, but it may also be attributed to the capability to compute complex flow fields.
At high angles-of-attack the delta wing leeward flow shows a vortex system which induces locally high suction rates such as to increase the lift (vortex lift). At high free stream speeds it also gives rise to the appearance of embedded shocks. Even for relatively simple geometries like a planar triangular flat plate, the complexity of the flow structure is such that a reliable prediction by computational methods is difficult. Also experimentally it is not always possible to obtain a detailed insight into the flow structure, as shown for example by the results of the Joint US/European Vortex Flow Experiment (Ref. 1). The role of viscosity necessitates the application of Navier-Stokes codes for turbulent flow or, better, the use of experimental investigations. For compressible flows in the high subsonic and transonic speed regime experimental data are only moderately available (Refs. 1 through 6). With respect to vortex breakdown the problem becomes even more complex, since here the mechanism is not clear at all. This physical phenomenon has a strong unsteady viscous background; however, there are solutions from Euler codes that reveal phenomena similar to physical vortex breakdown. Imperfections in flow conditions and model conditions cause the vortex breakdown to be asymmetric, as the present results will show.
In this paper special attention is paid to the surface flow on the leeward side of a 65° swept back delta wing with sharp leading edges and a flat upper surface. The Mach number ranges from 0.6 to 0.9 and the angle-of-attack is taken from 10° to 20°.

2. Description of the flow field

2.1. Classification

The structure of the flow field at the leeward side of a delta wing depends on a number of parameters of which the free stream Mach number M_∞, the angle-of-attack α and the leading edge sweep angle Λ are the most significant.
Stanbrook and Squire (Ref. 3) proposed a diagram for the classification of possible flow types. In the diagram the above-mentioned parameters play a dominant role. The abscissa and ordinate are formed by M_N and α_N, respectively, being quantities based on the velocity component normal to the leading edge. In the course of a number of investigations (Ref. 7,8) the diagram developed into the one shown in Fig. 1.

It consists of 7 regions, each representing a particular flow type, depending on the set M_N ,α_N. The internal boundaries in the diagram are affected by other parameters such as the Reynolds number, nose radius, wing profile shape, taper ratio etc.
For the present investigations only region 1 is of significance.

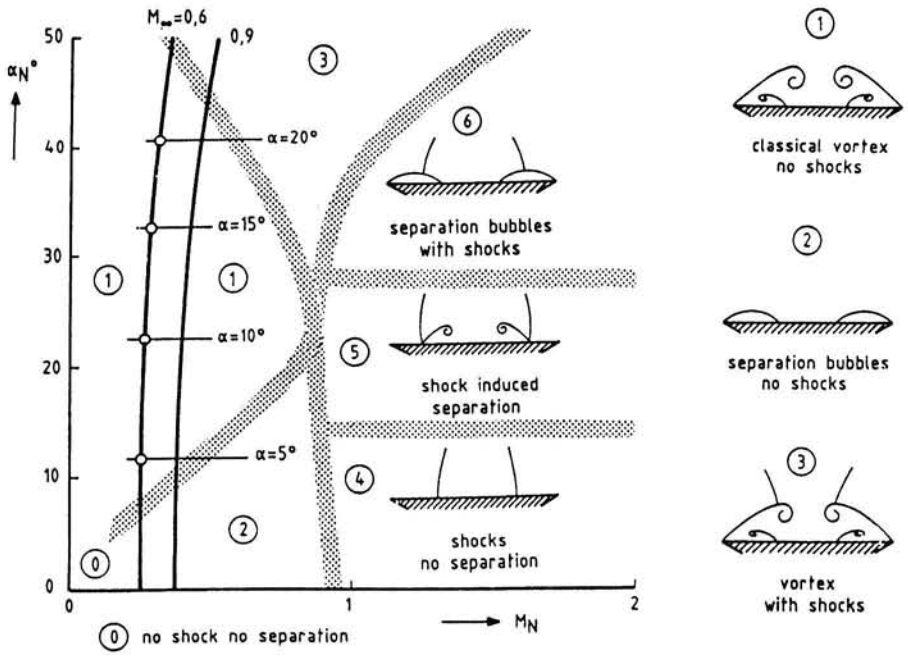

Fig. 1 Classification of delta wing leeward side flow patterns (Ref. 8)

2.2. Classical leading edge vortex separation

The classical leading edge vortex is normally found in region 1 of Fig. 1. Here, two strong and stable vortices emanate from the leading edges affecting the leeward side flow field to a large extent.

For moderate angles-of-attack we have the flow structure of Fig. 2a with a reattachment line A_1 and a region adjacent to the plane of symmetry where the surface streamlines are approximately parallel to the rootchord.

Outboard of A_1 a strong outward flow is created, which generally will separate due to a strong adverse pressure gradient. Then, a secondary vortex is formed counterrotating to the primary one. The surface flow separation exhibits a secondary separation line S_2 and, as a consequence, also a secondary reattachment line A_2, see Fig. 2b.

In a similar way tertiary vortices may be induced further outboard. When the angle-of-attack is further increased, the primary reattachment line A_1 moves towards the line of symmetry of the wing (rootchord) and eventually coincides with it; the latter situation is depicted in Fig. 2b. The separation and reattachment lines appear to a very good approximation as straight lines through the wing apex.

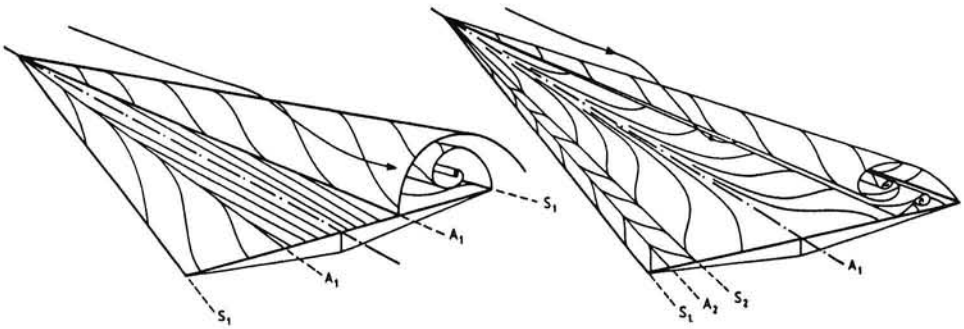

a. moderate angle-of-attack b. high angle-of-attack

Fig. 2 Vortical flow on a delta wing

2.3. Compressibility effects

At high subsonic speeds the overall features of the flow structure show a noticeable effect of compressibility. With increasing Mach number the vortex core moves closer to the wing surface and closer to the plane of symmetry; in addition, the vortex flattens out (Ref. 2). Experiments using a five-hole directional probe showed a considerable loss in total pressure, up to some 40% in the core of the vortex (Ref. 5). In addition to the low subsonic classical vortex flow concept we have to do with local embedded shocks, because, due to the acceleration of the flow in the rapidly swirling vortex areas, local supersonic regions may be present at free stream Mach numbers well below unity. Those regions may be found along the symmetry plane where they are terminated by a strong (normal) shock, see Ref. 1, as well as on top of the vortex and underneath it between vortex and wing surface (Ref. 4).

2.4. Vortex breakdown

At sufficiently high angle-of-attack vortex breakdown of the leading edge vortex is in aircraft aerodynamics usually defined if this phenomenon occurs above the wing. Thus the definition holds as soon as the angle-of-attack has arrived at that value where the breaking point of the vortex has reached the wing trailing edge from a downstream position. That particular angle-of-attack is called the critical angle. Its magnitude depends on a combination of parameters: leading edge sweep, leading edge shape (nose rounding, tip cropping), Mach number, Reynolds number.
An early experimental study on vortex breakdown was performed by Lambourne and Bryer, Ref. 9. In their experiments on sharp-edged delta wings in incompressible flow, a sudden deceleration of the flow in axial direction accompanied by an expansion around a stagnant core was observed. Downstream of the position where this occurred (the breakdown point) the flow was in an irregular turbulent motion. Similar observations were made in the supersonic speed regime, see Ref. 10.

In low subsonic flow the location of vortex breakdown occurs to be roughly independent of the Reynolds number and dependent on a combination of angle-of-attack and sweep angle. The location was found to move upstream for an adverse pressure gradient along the vortex axis.
In Ref. 9 it was suggested that vortex breakdown is associated with the pressure recovery coupled with the presence of the trailing edge. With respect to the angle-of-attack it appears that the critical angle for vortex breakdown increases with the sweep angle. This may be understood because the vortex strength increases with increasing sweep angle and consequently vortex breakdown is postponed to higher angles-of-attack. The Mach number is not a first order parameter in this respect. Increasing the angle-of-attack beyond the critical value causes the breakdown point to move rather smoothly upstream. As will be demonstrated by the present results, at transonic free stream conditions the breakdown position versus angle-of-attack is not a smooth curve; this has also been observed in Refs. 11, 12, 13.
Moreover, it was noticed that in the high speed regime vortex breakdown starts at lower angles-of-attack than at low speeds.

3. Experimental equipment and test program

The experiments have been performed in the TST-27 transonic -supersonic wind tunnel of the High Speed Laboratory, Department of Aerospace Engineering, University of Technology Delft. The wind tunnel is of a blow-down type with a test section of 27 cm x 26 cm. It can be equipped with different test sections. For the purpose of the present tests a slotted upper and lower wall section was used with a porosity of 7%.
Two identical delta wing models with a flat upper surface and a leading edge sweep of 65° have been tested. One is provided with pressure taps, the other one is used for oil flow visualization tests.
The tests have been made at free stream Mach numbers from 0.6 to 0.9, with emphasis on 0.85. The Reynolds number based on the rootchord was in the range from 3.0 to 3.6 million.
Pressure distributions were measured at angles-of-attack between 5° and 20°, mainly at a streamwise station of 70% rootchord and along the rootchord. Of all angles-of-attack surface oil flow pictures have been taken.

4. Discussion of results

4.1. Surface pressures

For the lower Mach numbers ($M_\infty < \sim 0.75$) the pressure distributions shown in Fig. 3 are typical for conditions without vortex breakdown or embedded shocks, even if the angle-of-attack is as high as 20°. The suction peak in the spanwise pressure distribution which is induced by the primary vortex increases with α and moves towards the wing symmetry line.

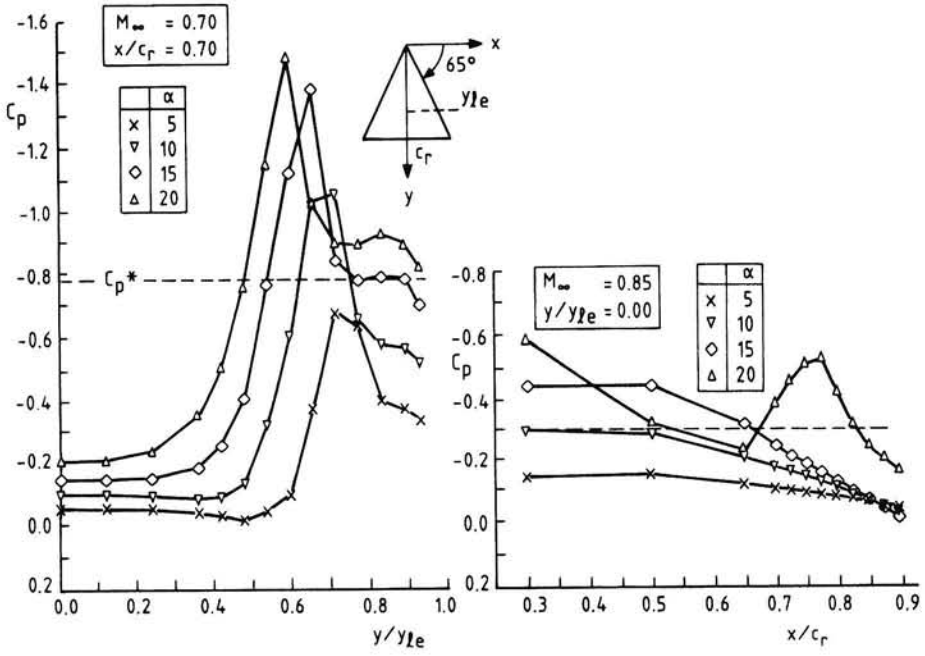

a. spanwise

b. along rootchord

Fig. 3 Pressure distributions at $M_\infty = 0.70$

Also the influence of the separating boundary layer is seen, in that for the higher values of α the secondary vortex induces a (less pronounced) suction outward of the primary one (Fig. 3a). The suction peak pressures appear well above the sonic value ($\alpha \geq 10°$) indicating that embedded supersonic zones may be present.
Along the rootchord the distributions show clearly that the flow is not conical, Fig. 3b, a continuous, almost linear, compression towards the trailing edge is measured at this Mach number.

At $M_\infty = 0.85$ the classical picture has disappeared for $\alpha = 20°$, as shows Fig. 4. The suction peak in the spanwise distribution has collapsed. The primary vortex which is burst now becomes disorganized and causes a much smaller degree of circular motion so that the flow adjacent to the wing surface is less accelerated outward. Fig. 4b illustrates that the rootchord pressure distribution has also changed drastically at $\alpha = 20°$.

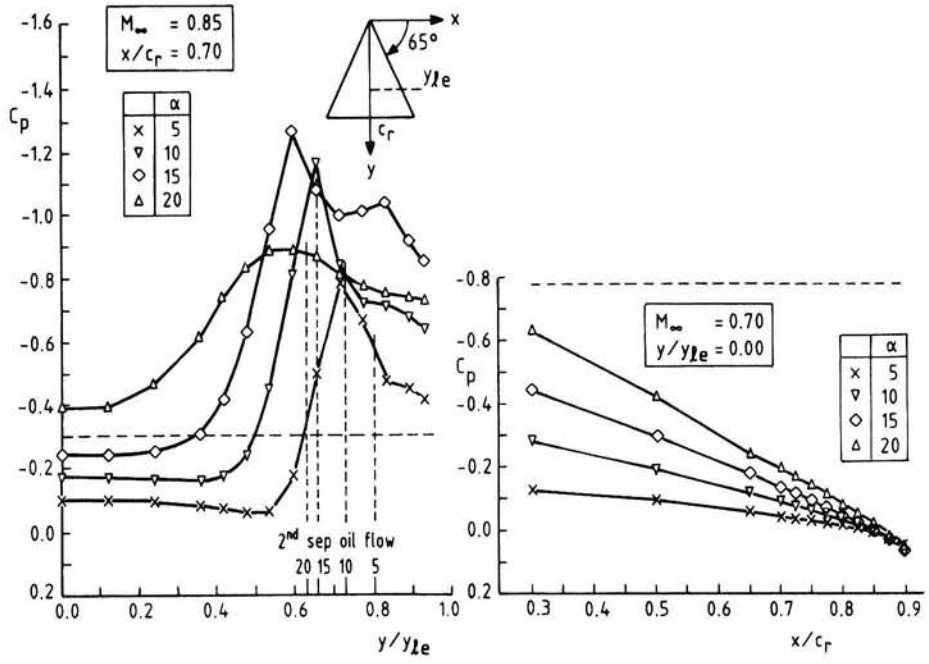

a. spanwise b. along rootchord

Fig. 4 Pressure distributions at $M_\infty = 0.85$

In order to analyse how pressure distributions are affected at angles-of-attack close to the critical value for breakdown the pressure distributions are plotted in two compilations: at $\alpha = 20°$ where vortex breakdown exists for different Mach numbers, Fig. 5, and at $M_\infty = 0.85$ for angles-of-attack around the critical value ($\alpha = 18.5$ in the present experiments), Fig. 6. In Fig. 5 the influence of the Mach number is demonstrated: for $M_\infty = 0.75$ and higher the existence of vortex breakdown is evident. Along the rootchord (Fig. 5b) we observe the upstream marching of the breakdown location point. In schlieren pictures a considerable expansion is distinguished downstream of 65% rootchord (for further details see Ref. 14). Due to the breakdown process the vortex increases in size with respect to its original dimensions so that near the symmetry plane a converging channel effect occurs, causing the subsonic flow to accelerate to supersonic speed again.

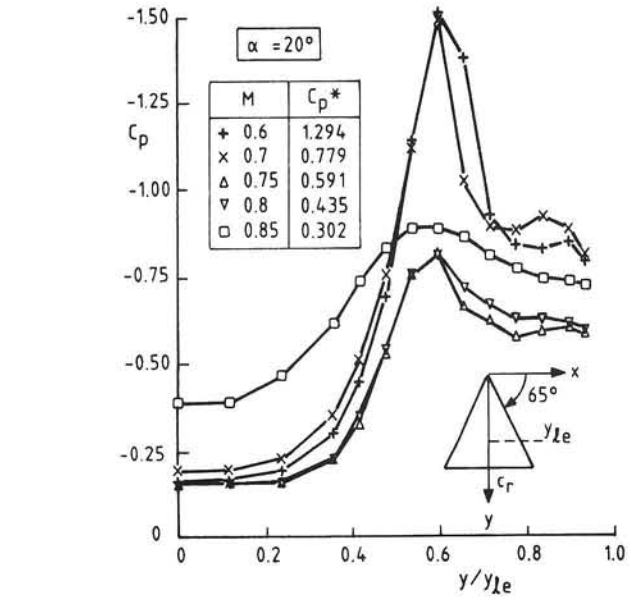

a. spanwise

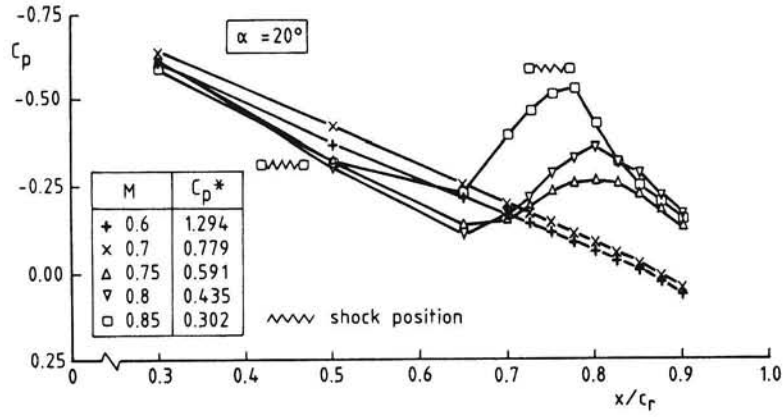

b. along rootchord

Fig. 5 Pressure distributions for $\alpha = 20°$ at various Mach numbers

The supersonic pocket is eventually terminated by a shock for the case where $M_\infty = 0.85$. The pressure distributions obtained at $M_\infty = 0.75$, 0.8 and 0.85 show a similar trend when vortex breakdown has occurred. However, at $M_\infty = 0.75$ and 0.8 two shocks were detected, at $x/c_r \approx 0.45$ and $x/c_r \approx 0.8$, with an expansion zone in between. The shock positions are indicated in fig. 5b.
A tentative conclusion could be that the second (rear) shock is generated by the burst vortex and not vice versa.

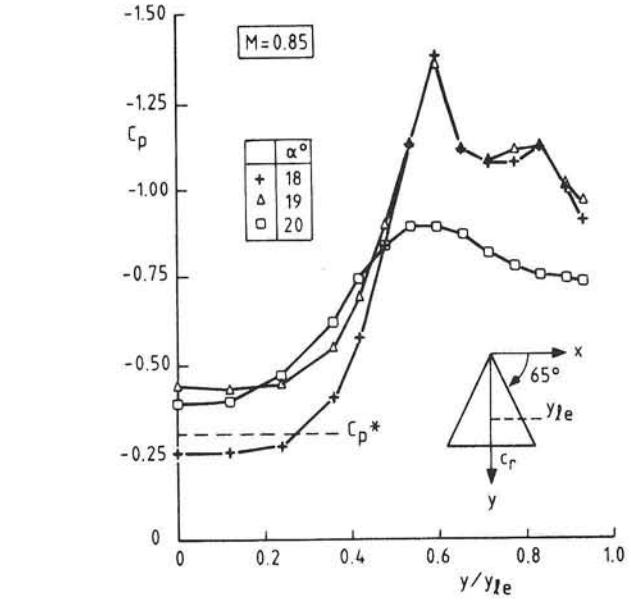

a. spanwise

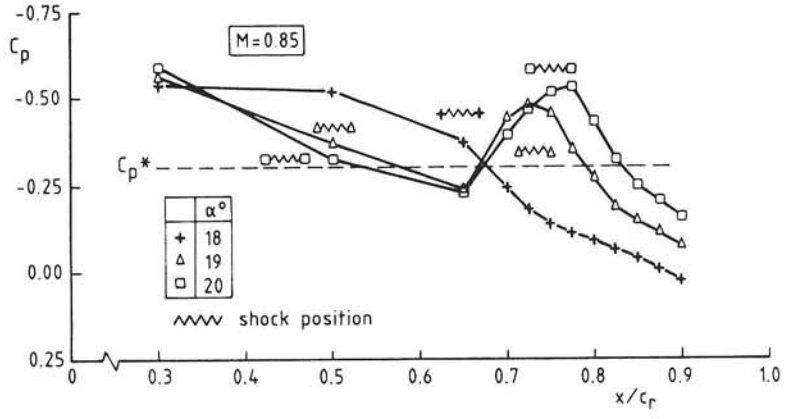

b. along rootchord

Fig. 6 Pressure distributions for $M_\infty = 0.85$ at various angles of attack

Apart from the existence of shocks another difference in the bursting process as compared to low speed results is the abrupt upstream motion of the burst location with increasing Mach number. In the narrow Mach number range from 0.7 to 0.75, the breakdown point moves from the trailing edge (or downstream of it) to about 65% rootchord to stay there at least up to $M_\infty = 0.85$.

From Fig. 6 it is evident that vortex breakdown occurs at an angle-of-attack between 18° and 20°. The rootchord pressures at $\alpha = 19°$ suggest vortex breakdown (Fig. 6a), although the spanwise distribution at $x/c_r = 0.70$ is not so clear at this point (Fig. 6b). The coinciding spanwise pressure distributions at $\alpha = 18°$ and 19° for spanwise positions $y/y_{le} > 0.50$ indicate, however, that breakdown has just reached the 70% rootchord position. It is evident that the flow changes drastically within a fraction of a degree. More details of the influence of vortex breakdown on the surface flow are given in Ref. 14.

4.2. Surface oilflow patterns

Results of the oilflow visualization study are shown in Figs. 7 to 11. Only the surface flow patterns at $M_\infty = 0.85$ are presented, for other Mach numbers the reader is referred to Ref. 14.

Fig. 7 is an illustration of a more or less classical flow pattern on delta wings such as this exists at angles-of-attack up to 18°, it is almost independent of the Mach number. The reattachment lines and separation lines, in particular the secondary separation line, show up rather straight suggesting a conical similarity in the flow field. This is in contrast to the pressure measurements, see the pressure distributions along the rootchord plotted in Fig. 3b.

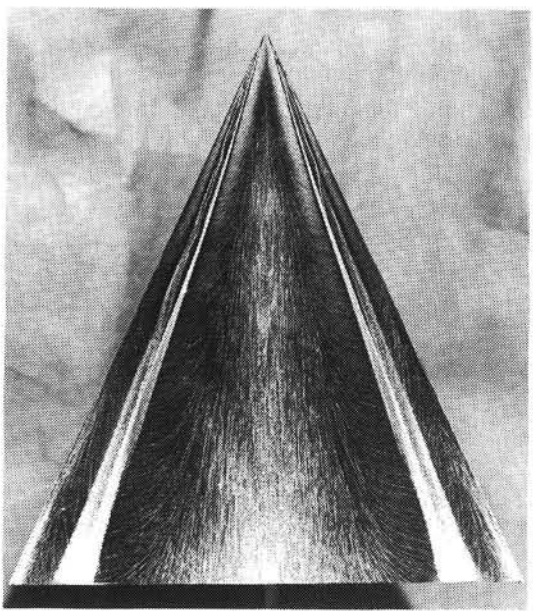

Fig. 7 Surface oil flow pattern $M_\infty = 0.85$, $\alpha = 10°$

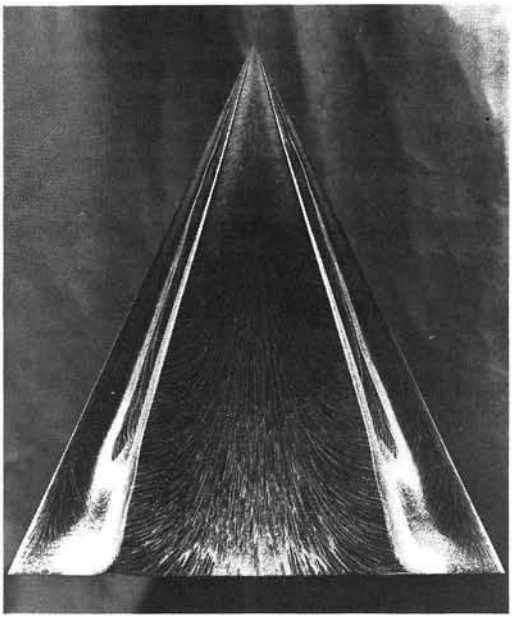

Fig. 8 Surface oil flow pattern; $M_\infty = 0.85$, $\alpha = 18°$

However, the spanwise variations of the pressure are much larger in the regions close to secondary separation (almost an order of magnitude) than those in streamwise direction (Ref. 14), and it is the spanwise pressure gradient that governs the secondary separation.
At higher angles-of-attack, when vortex breakdown is about to occur, the tertiary separation lines end up in a spiral (focus). Fig. 8 does not reveal this very convincingly because the surface oilflow is distorted due to the stopping process of the wind tunnel flow.
In order to close in the critical angle-of-attack a series of oil flow pictures have been made beyond $\alpha = 18°$. Fig. 9 shows a situation announcing that vortex breakdown is imminent; the secondary separation lines appear to have a 'gothic' shape. Increasing the angle-of-attack only very little to a value of 18.5° we observe that the starboard vortex has burst, see Fig. 10.

At the starboard side the secondary and tertiary separation lines merge and continue as a single line at an increased sweep angle. Since the oil streaklines converge into it, this continuation is a separation line as well. Asymmetric vortex breakdown, also observed in Refs. 11 and 12, is assumed to be generated by small imperfections in free stream flow conditions or by model irregularities. Asymmetry is not necessarily reproducible in cases which are nominally similar, see Ref. 14, breakdown may start on either side. Symmetry is restored for a slightly higher angle-of-attack, as shows Fig. 11.

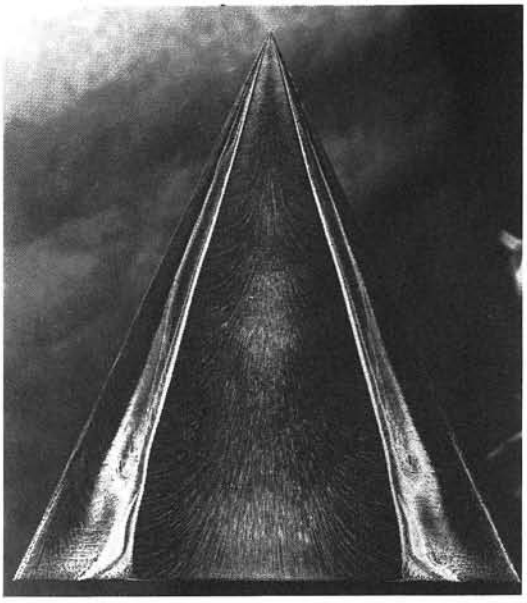

Fig. 9 Vortex breakdown imminent; $M_\infty = 0.85$, $\alpha = 18.3°$

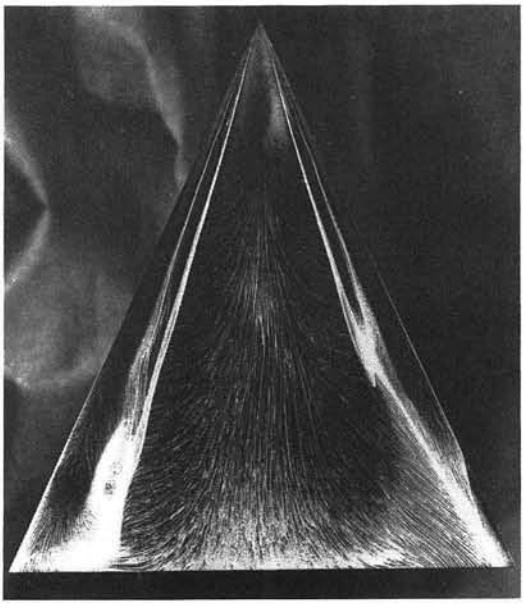

Fig. 10 Starboard vortex breakdown; $M_\infty = 0.85$, $\alpha = 18.5°$

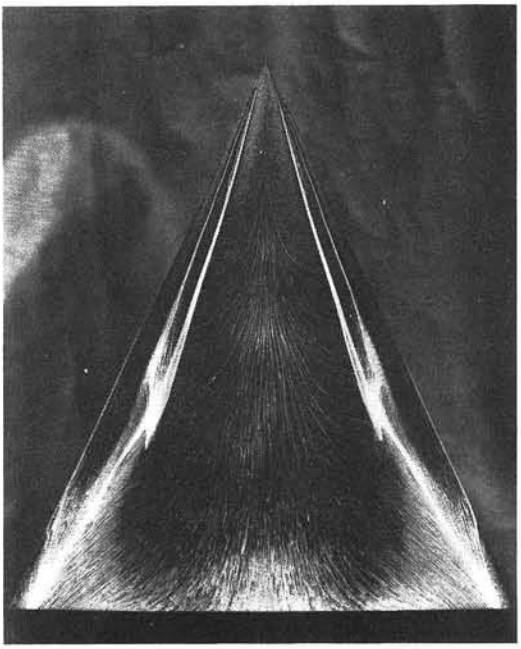

Fig. 11 Symmetric vortex breakdown; $M_\infty = 0.85$, $\alpha = 19°$

5. Conclusions

- Local supersonic flow regions terminated by shocks exist in the leeward flow field of a delta wing at high speed and at moderate to high angles-of-attack ($M_\infty > 0.75$, $\alpha > 10°$).
- At conditions where no shocks exist and no vortex breakdown occurs the pressure distribution along the rootchord shows an almost linear compression towards the trailing edge.
- Breakdown of the leading edge vortices was observed for angles of attack below 20° and free stream Mach numbers exceeding 0.7. The phenomena is associated with a collapse of the suction peak in the spanwise pressure distribution and with two strong compressions (shocks) separated by an expansion region in the root-chord pressure distribution. The first shock (upstream) existed before vortex breakdown occurred, therefore, a tentative conclusion may be that the second (rear) shock is generated by the burst vortex.
- Asymmetric vortex breakdown (either port or starboard vortex) was established.

References

1 Elsenaar, A. et al., The International Vortex Flow Experiment, AGARD CP-437, Vol. 1, Paper 10, 1988

2 Squire, L.C. et al., An Experimental Investigation of the Characteristics of Some Plane and Cambered 65 deg. Delta Wings at Mach Numbers from 0.7 to 2.0, ARC R&M No. 3305, 1961.

3 Stanbrook, A. and L.C. Squire, Possible Types of Flow at Swept Leading Edges, Aeron. Quart., Vol XV, February 1964, pp. 72-82.

4 Vorropoulos, G. and J.F. Wendt, Laser Velocimetry Study of Compressibility Effects on the Flow Field of a Delta Wing, AGARD CP-342, Paper 9, 1983.

5 Houtman, E.M. and W.J. Bannink, Experimental Investigations of the Transonic Flow at the Leeward Side of a Delta Wing at High Incidence, Delft University of Technology, Dept. of Aerospace Engineering, Report LR-518, 1987.

6 Schrader, K.F. et al., Effects of Mach Number and Reynolds Number on Leading-edge Vortices at High Angle-of-Attack, AIAA Paper 88-0172, 1988.

7 Szodruch, J.G. and D.J. Peake, Leeward Flow over Delta Wings at Supersonic Speeds, NASA TM 81187, 1980.

8 Miller, D.S. and R.M. Wood, Leeside Flows over Delta Wings at Supersonic Speeds, J. Aircraft, Vol. 21, No. 9, 1984 pp. 680-686.

9 Lambourne, N.C. and D.W. Bryer, The Bursting of Leading Edge Vortices - Some Observations and Discussion of the Phenomenon, ARC R&M No. 3282, 1962.

10 Monnerie, B. and H. Werlé, Etude de l'Ecoulement Supersonique et Hypersonique autour d'une Aile Elancée en Incidence, AGARD CP-30, Paper 23, 1968.

11 Wentz, W.H. and D.L. Kohlman, Wind Tunnel Investigation of Vortex Breakdown on Slender Sharp-Edged Wings, NASA CR 98731, 1968.

12 Muylaert, J.M., Effect of Compressibility on Vortex Bursting on Slender Wings, VKI PR 1980-21, 1980.

13 Skow, A.M. and G.E. Erickson, Modern Fighter Aircraft Design for High Angle-of-Attack Manoeuvring, AGARD LS-121, Paper 4, 1982.

14 Bannink, W.J. et al., Investigation of the Vortex Flow over a Sharp-edged Delta Wing in the Transonic Speed Regime, Delft University of Technology, Dept. of Aerospace Engineering, Report LR-594, 1989.

Conceptual design of a computer-code system for the calculation of flows around transport aircraft

By J.W. Boerstoel

National Aerospace Laboratory NLR, Amsterdam, The Netherlands

Summary

The design of a system of computer codes for the computation of three-dimensional flows around transport aircraft and other aerodynamic configurations is outlined. The topic is introduced with an example of a computational aerodynamic analysis. Hereby propeller-slipstream effects around a transport aircraft with two wing-mounted propellers in tractor position are analysed. Determining requirement for the design of the computer code system is: aerodynamic computational analyses of the effects of propulsion systems (propeller slipstreams, exhaust jets) on the flow around given aircraft should be possible, at acceptable costs, in acceptable turnaround times.
The design procedure consists of four major stages: 1) specification of aerodynamic and other design requirements for the computer code system, 2) mathematical-physical modelling of the aerodynamic computation problems, 3) numerical modelling of the problems, and design of a numerical solution algorithm, and 4) software design of the code implementing the numerical-solution algorithm, and design of codes for additional tasks in flow-computation work (like visualisation of computation results). Major advances can be reported in the special areas of surface modelling for Computational Fluid Dynamics problems, of multiblock grid generation, and of multiblock flow computation (block-interface handling with non-smooth grids over block faces).

1 Introduction

The design concepts of a system of computer codes for the computation of subsonic and transonic flows around aerodynamic configurations are presented [1-3]. This computer code system is able to handle complex aerodynamic configurations. Examples of complex configurations are: wing-winglet-fuselage and wing-nacelle-pylon configurations, complete transport aircraft, configurations in windtunnels. The codes also allow that the effects of propulsion systems (propeller slipstreams, exhaust jets) and ground effects on the flow around aircraft are taken into account. The system is made suitable for CFD analysis of questions that e.g. arise during aerodynamic

design of transport aircraft. The system is being extended to allow the computation of viscous and turbulent effects on wing lift, using the thin-layer Navier-Stokes flow equations, combined with standard modelling of turbulence.

The development started in about 1985 [4]. The computer code system is made operational on the computer network of the NLR. Today, this network contains a NEC SX3 supercomputer and various modern workstations of Silicon Graphics [5]. The computer code system is also kept operational on other computer networks, with other supercomputers.

The computer code system is also used for research and development work, to create a continuous flow of up-to-date scientific tests, extensions, improvements, and publications, see for example [6-12]. Such research and development work is required to bring and keep the performance of the system on an internationally competetive level.

A part of the testing of the computer codes occurs at the aerodynamic-design departments of aircraft industries [2,13]. This testing helps to define and to meet the requirements that the computer codes should satisfy in industrial aerodynamic-design environments. Which kind of use can be made of modern CFD codes in these departments has recently been discussed in e.g. [14].

The design of the computer code system is presented and discussed as follows.
- Section 2. Presentation of an introductory example of a flow computation around a complete transport aircraft. This example illustrates what kind of aerodynamic functional requirements must be satisfied by the computer code system. Further, the flow-computation procedure is outlined.
- Section 3. Outline of determining requirements for computer codes.
- Section 4. Mathematical-physical and numerical formulation of the aerodynamic computation problems, and outline of concept of numerical-solution algorithm.
- Section 5. Main layout of the computer-code-system design, including file interfaces.
- Section 6. Concluding summary.
- Section 7. References.

2. An example of a flow computation and outline of flow-computation procedure

The figures 2.1-2.6 below are an example of a flow computation around a transport aircraft. This example illustrates which main aerodynamic functional requirements must be satisfied by the computer codes, and which main tasks must be executed in a flow computation.

Figure 2.1 shows the aerodynamic surface of a transport aircraft used in the compu-

tations. This is a twin-engine high-wing transport aircraft for subsonic flight, with wing-mounted tractor propellers.

Figures 2.2-2.4 allow computational analysis of effects of the propeller-slipstream on the flow around the aircraft. Two computations were made, each at a free-stream Mach number 0.3, an incidence of 2 degrees, and a slip angle of 0 degrees. In one computation, the propeller is off, in the other computation the propeller (modelled as an actuator disk) generates a propeller slipstream having swirl and increased total pressure generated by the propeller disk. A few effects of this slipstream are shown in the figures 2.2-2.4.

- Figure 2.2 shows pressure distributions, in the form of isobars (lines of constant pressure), on aircraft-surface parts. Pressure-distribution differences are visible on the wing (upper and lower side), on the nacelle, and on the horizontal tailplane.
- Figure 2.3 (upper two subfigures) shows pressure-distribution differences in the flow, in the vertical symmetry plane of the nacelle. This plane cuts the horizontal tailplane. Further (bottom subfigure), the total-pressure distribution is shown, in the form of lines of constant total pressure. Theoretically, such lines coincide with streamlines. It may be observed, that the total pressure is (practically) constant in the whole flow domain (as it should be), except in the propeller slipstream. The total pressure on streamlines through the propeller disk is a measure for the amount of velocity-increasing effect of the propeller on the flow, and this is observable (upper two subfigures) as pressure-distribution differences. Further (bottom subfigure), it may be observed how the upper side of the slipstream hits the horizontal tailplane. This effect is sometimes desired, sometimes it is not.
- Figure 2.4 shows the pressure field in two surfaces in the flow, the vertical symmetry plane of the aircraft, and a surface between the fuselage and the nacelle, that is everywhere plane and vertical, except near the propeller disk where it is curved. In these surfaces, the computations did not reveal large propeller slipstream effects, so these effects are not shown here.
- However, figure 2.4 illustrates that the pressure field near the cockpit windows and above the fuselage near the wing can be analysed in detail, which could be useful for numerical aerodynamic analysis of cockpit-window designs and wing-fuselage-fairing designs.

Figures 2.5-2.6 show the grid in the aircraft surface and in a few vertical surfaces in the flow domain. The computations were made with a multiblock grid consisting of 1.2 million cells in the flow domain. Each cell has the shape of a small parallelepiped.
The development of methods for the construction of grids around complex aerodynamic configurations is, since about 1985, a major research item in CFD. For summaries of progress in this area, see [15]. Without modern grid-construction facilities, computation results like those presented in figures 2.2-2.4 cannot be produced.

Figure 2.7 illustrates how the complex flow-computation was decomposed in manageable subtasks.

- First, the initial mathematical representation the aerodynamic surface of the aircraft must be made available.
- Subsequently, a multiblock grid consisting of say about one million grid cells in the flow domain must be constructed. To make this subtask easier, this occurs in two steps.
- In the first step, the flow domain is subdivided in as small a number of blocks as possible, with each block having the shape of a large deformed cube in a part of the flow domain. Each block has thus 6 block faces, 12 block edges, and 8 block vertices, arranged with respect to each other as in a cube. In figures 2.1-2.6, the block edges in the aircraft surface and in the vertical surfaces in the flow are shown.
- In the second step, in each block, a mathematically smooth grid of cells with a well-ordered structure is generated. Grids should have these two properties if numerically accurate flow-computation results at low computation costs must be possible.
- Next, the flow is computed on a supercomputer, and the interesting part of the vast amount of numbers of the computation result (for about 1 million grid cells, about 12 million numbers) is extracted from the computation. This interesting part usually consists only of data on the aerodynamic configuration, and on a few grid surfaces in the flow.
- Finally, this part of the flow-computation result is analysed on a workstation.

Accurate computation of complex flows around complex aerodynamic surfaces -like that of a complete aircraft- requires careful planning. The flavour of the planning issues to be dealt with by the CFD engineer may be sketched as follows. The CFD engineer has to produce

- sufficiently accurate flow-computation results
- at acceptable costs
- in a sufficiently short turnaround time.

He obviously has thus to balance accuracy of computation results versus costs and turnaround times. Nowadays, the CFD engineer can do this, for a great deal, during block decomposition and grid generation, because here he has many possibilities to balance the above conflicting requirements. A few examples of the criteria he may apply here are given below.

Aerodynamic modelling criteria

- Reduce the complexity of the computation problem, by simplifying the aerodynamic aircraft surface, if this does not significantly affect the accuracy of the interesting parts of the total computation result. For example, when the flow around the wing is of interest, remove the tailplanes from the configuration, and simplify the fuselage shape at the cockpit windows, [16].

- Organise the modelling of desired flow conditions on e.g. the aircraft surface and elsewhere, by proper modelling the block-face shapes in the aircraft surface (propeller disks, inlets, outlets). (On each block face, one boundary condition can be specified.)
- Promote computation accuracy of wake surfaces and propeller-slipstream boundary surfaces, by placing block faces at expected positions of these boundary surfaces in three-dimensional space, so that grid lines will become approximately aligned with the streamlines in these surfaces.
- For thin-layer Navier Stokes computations in near future, reduce the complexity of the computation problem with zonal modelling, by only placing thin-layer Navier-Stokes blocks at expected positions of boundary layers and wakes, where their computation is significant, and place Euler blocks for the cheaper inviscid-flow computations everywhere else.

Numerical criteria

- Economize on grid resolution, by using large blocks where coarse grids are allowed (far-field uniform flow regions), and small blocks where grids should be fine (leading and trailing edges).
- Promote good numerical accuracy, by specifying, along block-edge curves in the three-dimensional flow domain, a smooth desired grid-size distribution along that edge, if the default distribution is unsatisfactory. Similarly, in block-face surfaces in three-dimensional space, specify a smooth desired grid, if the default distribution is unsatisfactory. In block volumes, up till now, default distributions were found to be nearly always acceptable.
- Economize on grid resolution, by applying grid-cell refinement or coarsening on a block-by-block basis.
- For thin-layer Navier Stokes computations in near future, optimize on numerical accuracy of computation results in each thin-layer Navier-Stokes block on an aerodynamic surface, by placing four block faces normal to that surface, and by placing the block-face surface opposite to the aerodynamic surface somewhat outside the expected thin boundary layer, and aligning it to the aerodynamic surface.

Computer efficiency

- Promote vector efficiency, by positioning and sizing each block such that, after grid generation, long arrays of grid cells are obtained in the three local-coordinate directions of the block, so that long vector lengths are obtained.

Post-processing convenience

- Make visualisation of flow-computation result in surfaces in the flow easy, by covering these surfaces with block faces. These surfaces become easily identifia-

ble grid surfaces. In practice, collections of block faces in plane surfaces are very handy.

Block subdivision must be done graphically and interactively, because it involves geometry manipulation in three-dimensional space. A modern graphical workstation with colour graphics is thus required, with a good amount of local computing power and memory. The tuning of the distribution of the cells in the blocks has also to occur interactively, and also requires such a modern workstation. However, the final computation of complete fine multiblock grids occurs in batch on supercomputers, because these grids are required on the supercomputer during execution of the flow computation codes.

The initial mathematical representation of an aerodynamic surface (e.g. a CAD/CAM definition) must be brought into forms that makes this representation suitable for the flow computations. During block subdivision of the flow domain, an induced block-face subdivision in the aircraft surface is created. The precise shape of this induced block-face subdivision in the aircraft surface is dictated by CFD requirements. Subsequently, during grid generation, the surface representation is further reduced from continuous mathematical forms to a dense set of grid points in the aerodynamic surface.

Accurate and reliable manipulation of aerodynamic surfaces is today based on transfinite multi-linear and multi-cubic polynomial Hermite interpolation, whereby non-linear algorithms ensure good curvature and twist behaviour of surface patches between given points on the surface [11]. The algorithms contain also mechanisms that prevent surface inconsistencies (e.g. overlaps and gaps) [11].

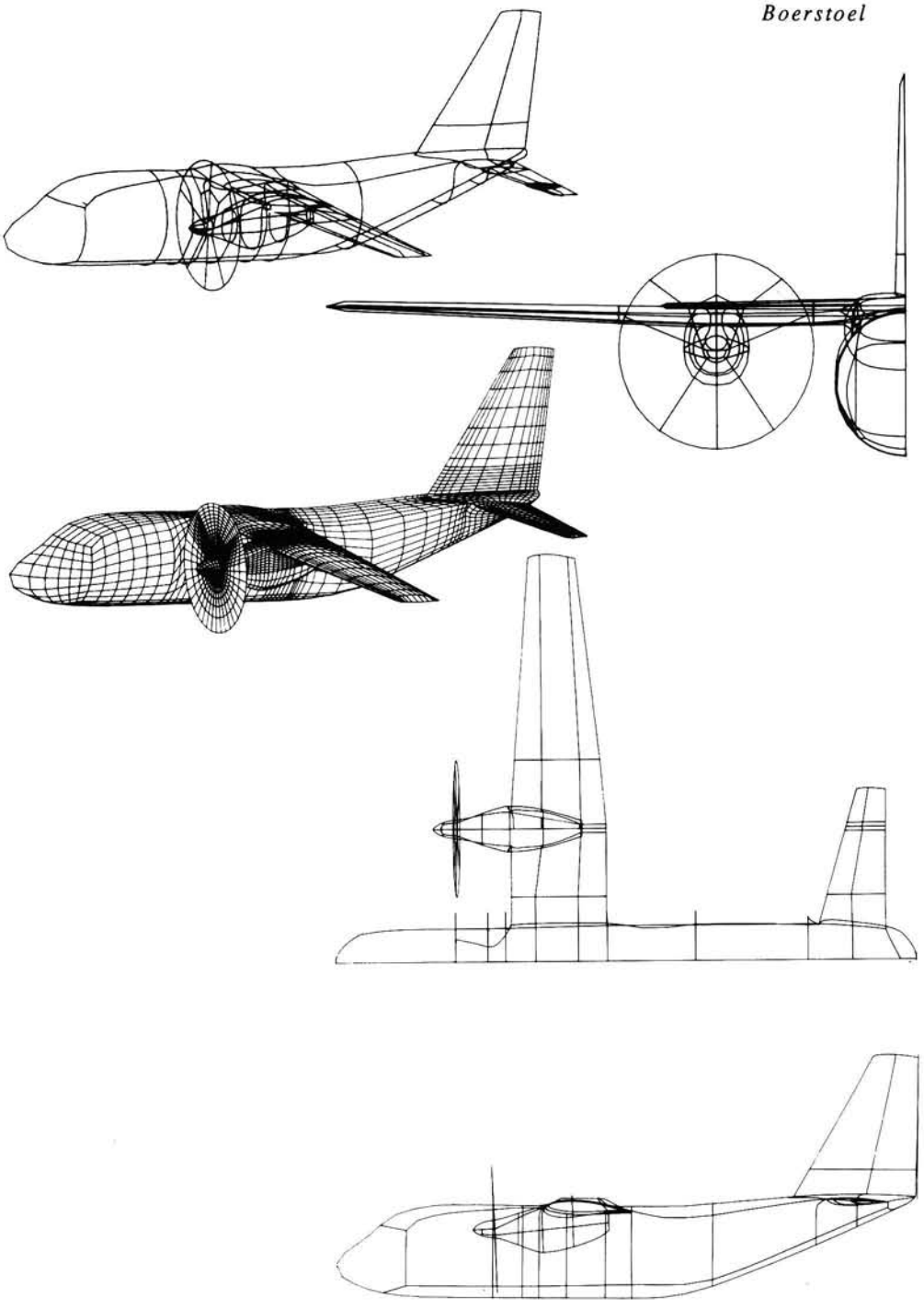

Fig. 2.1 Aerodynamic surface of ALENIA transport aircraft G222

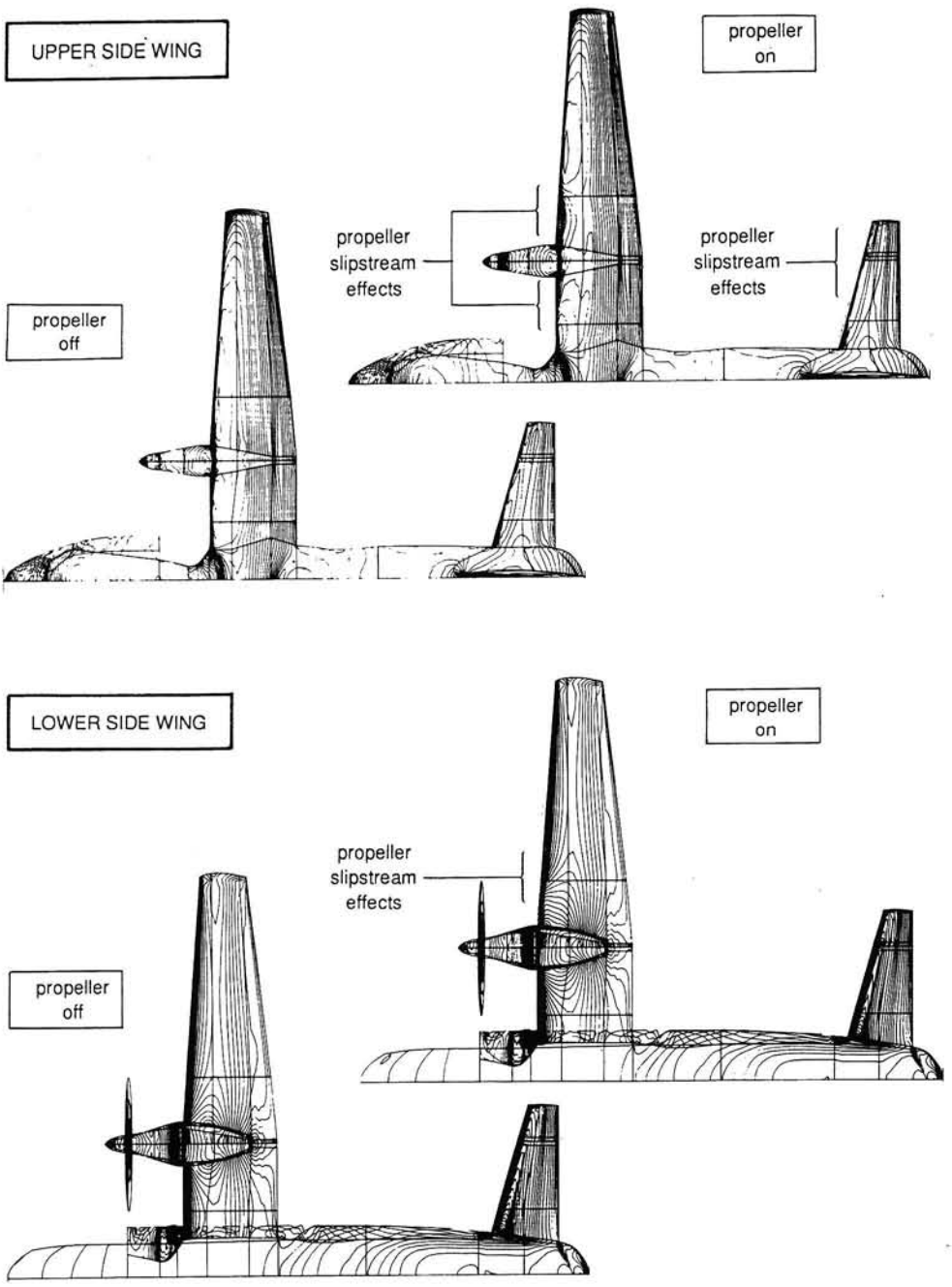

Fig. 2.2 Pressure distributions on upper and lower side of wing, propeller on (rhs) and off (lhs)

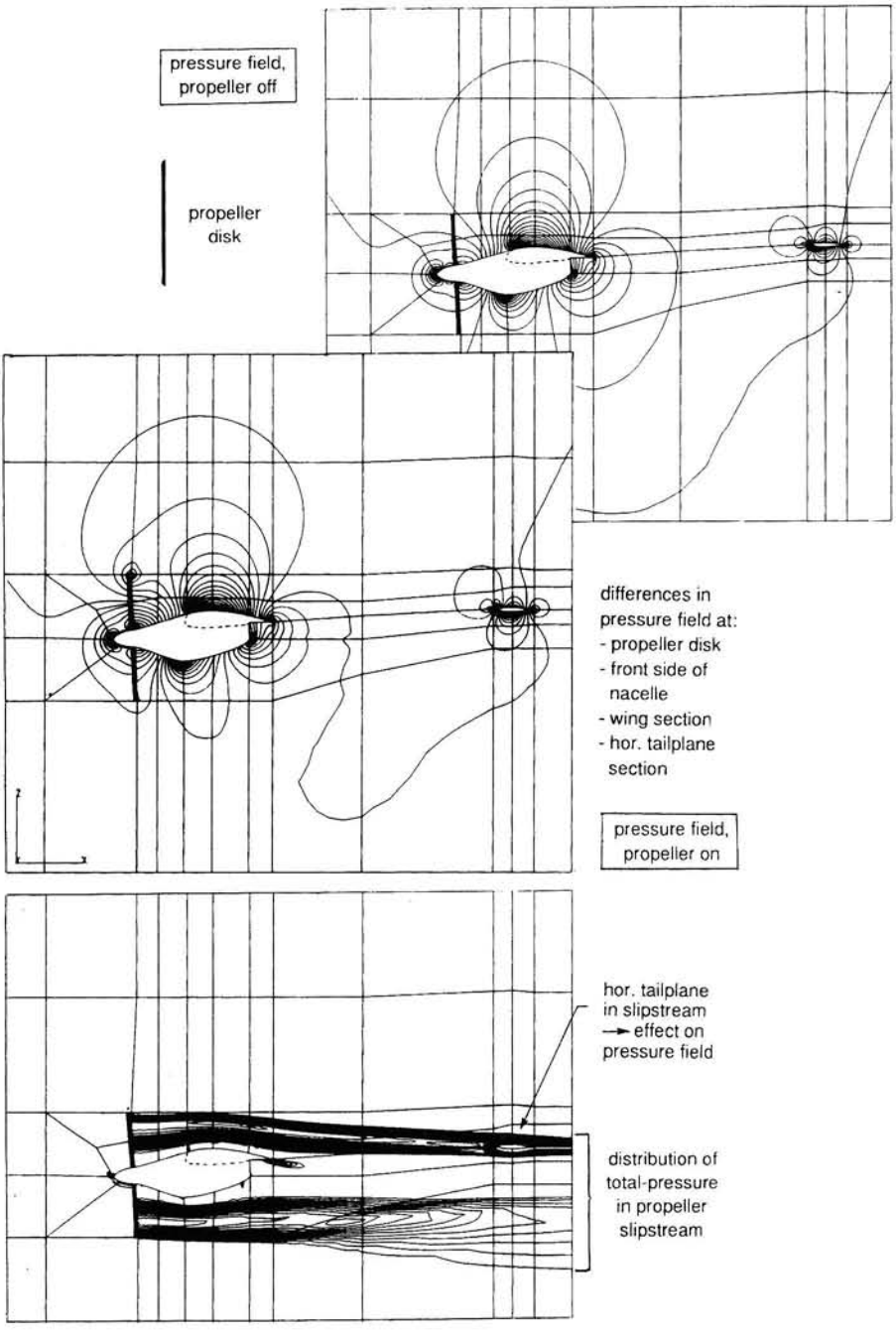

Fig. 2.3 Propeller slipstream effects in the flow, in vertical symmetry plane of the engine nacelle

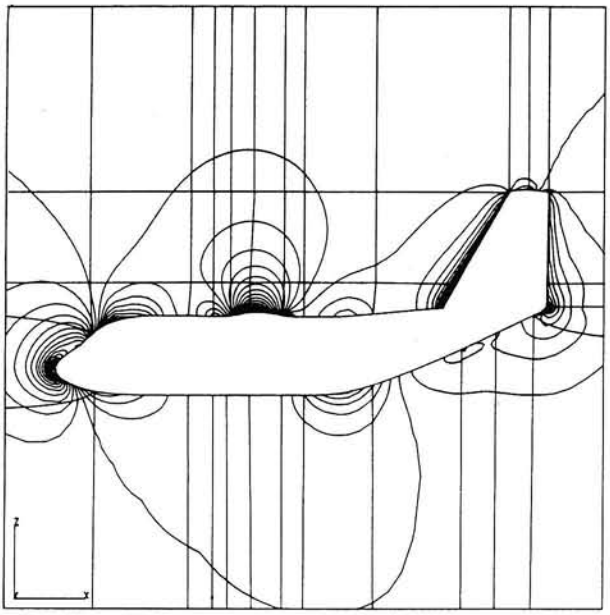

pressure field in flow, in vert. symmetry plane of aircraft

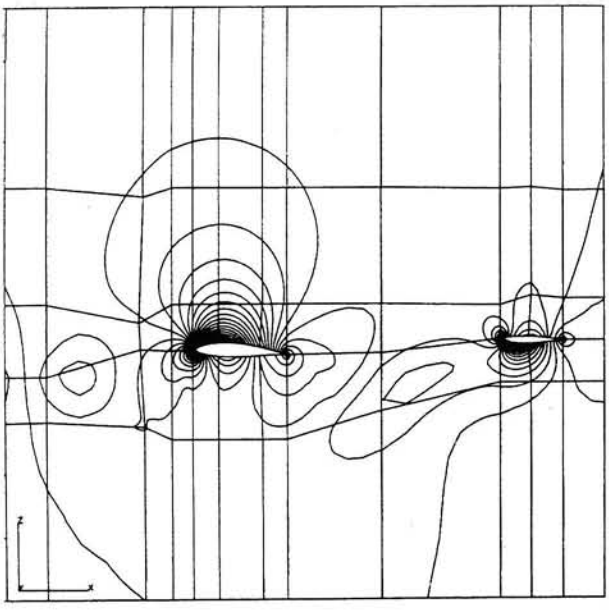

pressure field in flow, in vertical plane between fuselage and engine nacelle

observe sections with wing and with hor. tailplane

propeller off

Fig. 2.4 Pressure field in two vertical planes in flow

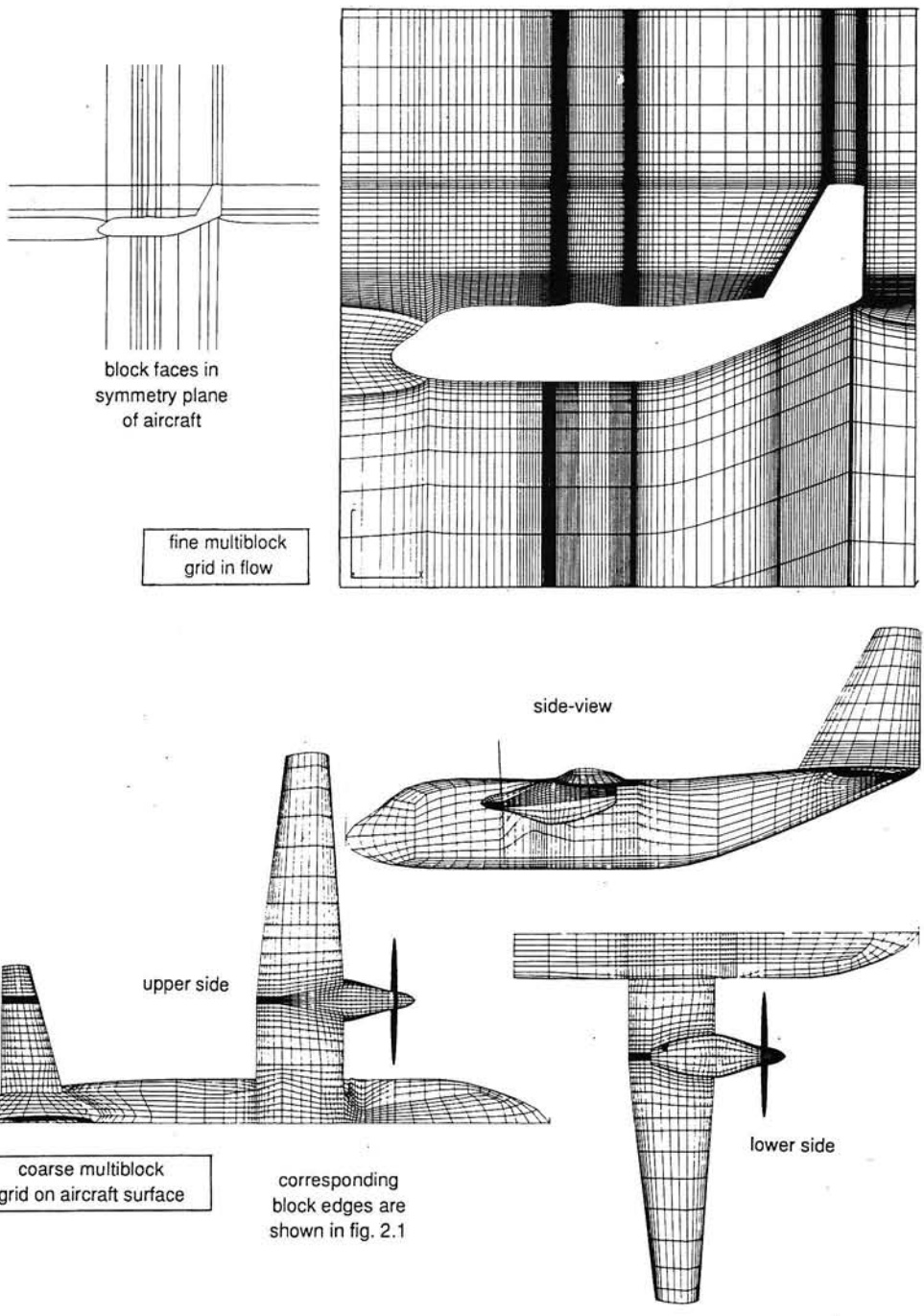

Fig. 2.5 Multiblock grid on aircraft surface and on vertical symmetry plane in flow

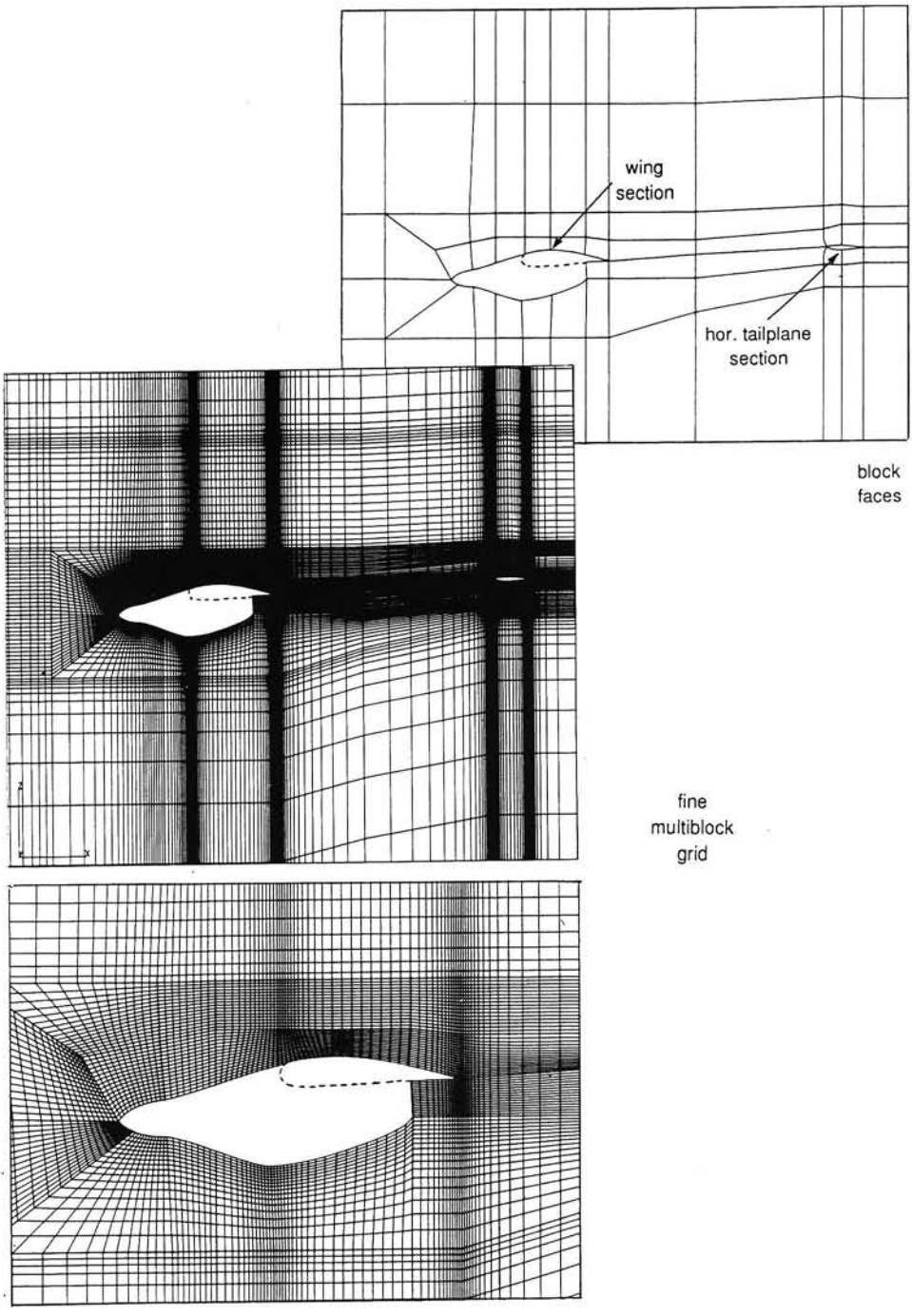

Fig. 2.6 Multiblock grid in flow, in vertical symmetry plane of engine nacelle

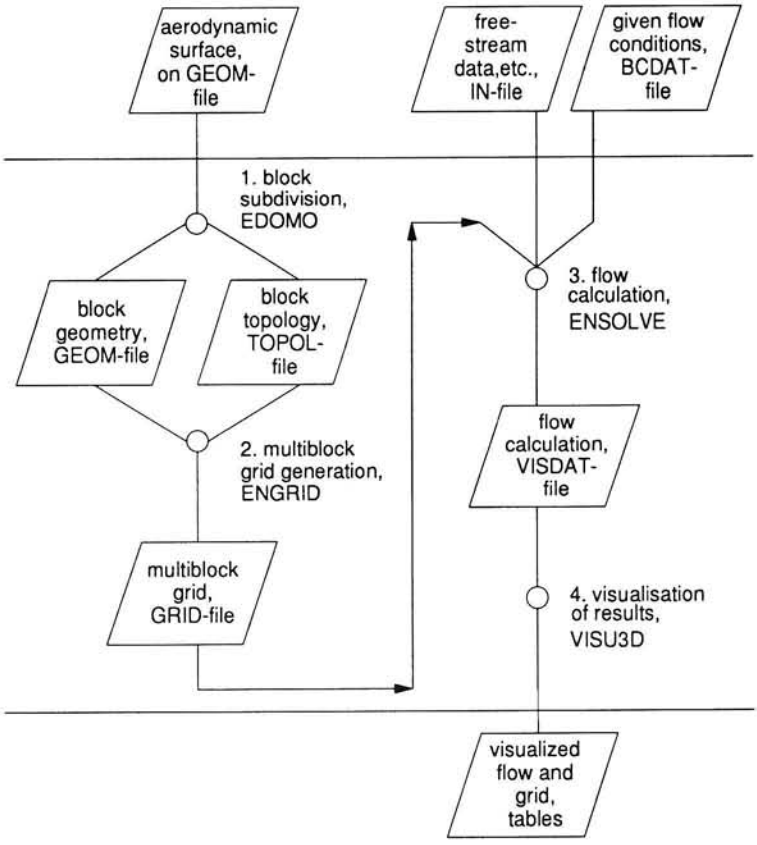

Fig. 2.7 Decomposition of flow-computation task in substasks

3. Determining design requirements for the computer code system

The design of the computer code system is based on a number of determining aerodynamic functional requirements. These are the following ones.

- Complex aerodynamic configurations should be allowed, in particular those encountered in propulsion-system/airframe-integration studies.
- The flows are subsonic or transonic, and steady.
- The following physical phenomena must be computable with sufficient accuracy:
  - shock waves,
  - time-averaged effects of propeller slipstreams and exhaust jets,
  - transport of vorticity and entropy, and spatial gradients in total enthalpy.

The effects of viscosty and turbulence were initially excluded. Then it is possible to satisfy the requirements with the Euler flow model. In future, viscosity and turbulence

effects will be accounted for using a thin-layer Navier-Stokes flow model, to capture their effect on wing lift, to begin with.

Further, operational and economical requirements must be satisfied. The determining requirements are the following ones.

- The turnaround times of computations must be short (for large complex computations, 1 day). In contrast to what sometimes is being thought, this is not only required for vast computation-production with the system during aerodynamic design, but also for research and development work.
- Computation results must have an accuracy that is acceptable for aerodynamic analysis work.
- The computation results must be produced at acceptable costs.

This package of conflicting determining design requirements is the starting point for the design of the computer code system. During detailed design of the computer codes, these determining overall requirements are the basis for derived detailed requirements.

4 Mathematical-psysical and numerical formulation of the airodynamic computation problems

The simplest mathematical-physical model of the flow conservation equations for the computation problems considered here is that of the Euler equations. These are a system of five PDEs (Partial Differential Equations) for the conservation of mass, momentum, and energy in the flow. In this model, the effects of viscosity and turbulence are neglected. The Euler equations have the form

$$U_t + F_x + G_y + H_z = 0 \text{ in } D, \tag{1}$$

where

$$U = [\rho,\rho u, \rho v, \rho w, E]^T,\ p = (\gamma - 1)E - \frac{1}{2}(\gamma - 1)(u^2 + v^2 + w^2),\ \underline{H} = E + p, \tag{2}$$

$$\begin{aligned} F &= [\rho u\ ,\ \rho u^2 + p\ ,\ \rho uv\ \ ,\ \rho uw\ \ ,\ u\underline{H}]^T\ , \\ G &= [\rho v\ ,\ \rho uv\ \ ,\ \rho v^2 + p\ ,\ \rho vw\ \ ,\ v\underline{H}]^T\ , \\ H &= [\rho w\ ,\ \rho uw\ \ ,\ \rho vw\ \ ,\ \rho w^2 + p\ ,\ w\underline{H}]^T\ , \end{aligned} \tag{3}$$

with D the flow domain around the aerodynamic configuration, $U = U(x,y,z,t)$ the flow-state vector, ρ the density, $[u,v,w]^T$ the velocity vector, E the total energy, F, G, and H the flux vectors in x, y, and z-direction, $\underline{H}$ the enthalpy, and p the pressure in the flow.

Althought the interest is in steady flows, so that solutions of the PDEs have the term $U_t = 0$ everywhere in the flow, the conservation equations are formulated in time-dependent form. This formulation is taken as basis for the construction of numerical-solution algorithms.

To obtain a well-posed mathematical-physical model of the aerodynamic computation problem, boundary conditions, initial conditions, and smoothness conditions must be also imposed.

- Boundary conditions have the form

$$B\{U(x,y,z,t)\}\,|_{\partial D} = 0 \tag{4}$$

  They specify, on the boundary ∂D of the flow domain D, relations between the elements of the flow-state vector U. The precise form of these relations must be modelled with characteristic theory for the PDEs (1-3), to achieve that on the boundary ∂D a form of the PDEs is satisfied that is consistent with equations (1-3) in the interior of the flow domain. Examples of boundary conditions are slip-flow conditions on solid surfaces, engine inlet- and outlet-plane conditions, and free-stream conditions on surfaces in (approximately) undisturbed flow. The NLR Euler-flow code handles about 10 different boundary conditions, so boundary conditions are in practice an important topic.
- Further, at an initial time $t = 0$, an initial flow-state vector $U_0(x,y,z)$ on D must be known, so that $U(x,y,z,t)$ can be constructed starting from this initial flow-state vector U_0,

$$U(x,y,z,0) = U_0(x,y,z) \text{ on D and on its boundary } \partial D \tag{5}$$

  A uniform flow, or a precomputed neighbouring flow is often used as initial solution.
- Finally, the differentiability properties of $U(x,y,z,t)$ should also be specified. Here it is assumed that $U(x,y,z,t)$ is continuous and piecewise twice differentiable with respect to (x,y,z) everywhere in the flow domain D, except over shock- and contact-discontinuity surfaces and at singular lines in boundaries, like sharp trailing edges. This condition eliminates mathematical solutions that are meaningless for the aerodynamic practice. Numerical smoothing is applied to satisfy this requirement.

Because, for the flow-computation problems considered here, the initial-boundary-value-problem formulations of the form (1-5) cannot be solved in useful closed forms, approximate solutions in numerical form are sought.
To obtain these, three numerical design steps are required.

The first step is to define, in the flow domain D, a grid G. This grid subdivides the flow domain D in small cells, and its boundary ∂D in small cell faces. The basic

shape of a cell is a parallelepiped (6 parallelogram faces) -and this usually leads to structured grids- or it is a tetrahedron (4 triangular faces) -and this leads to unstructured grids. At NLR, parallelepiped cells are preferred up till now, because then it is easy to construct grids G with good smoothness and regularity properties [6].
Good smoothness and regularity properties of grids are the basis of comparitively efficient (low operation counts, small data structures) and numerically accurate spatial approximations of the conservation equations and boundary conditions. On unstructured grids, comparable efficiency and numerical approximation accuracy cannot so easily be obtained. The majority of the CFD community opts for structured grids [15].

The second numerical design step is to convert mathematical-physical problem formulations of the form (1-5) to a semi-discretized form using space discretisation with the grid G.

- First, the unknown flow-state vector function $U(x,y,z,t)$ is replaced by a collection of time-dependent flow-state vectors $U_\alpha(t)$, with α a multi-index, that defines the location of the flow-state vector $U_\alpha(t)$ in the grid G. Two popular choices, that lead to about as many unknown flow-state vectors $U_\alpha(t)$ as there are cells, are as follows.
  - The multi-index counts along the centres (centroids) of the cells in the grid (cell-centred methods).
  - The multi-index counts along the vertices of the cells in the grid (cell-vertex methods).
- Subsequently, the equations (1-5) are discretized in space. This gives, for each cell centre or cell vertex in the flow, semi-discretized conservation equations of the form

$$dU_\alpha(t)/dt + D_\alpha = 0 \tag{6}$$

  Here D_α is the numerical approximation of the divergence expression $F_x + G_y + H_z$ in the conservation equations (1-3). The semi-discretized boundary conditions have the form

$$B_\alpha \{U_\alpha(t)\}_{\alpha \in \partial G} = 0 \tag{7}$$

  for each cell face or cell vertex on the grid boundary ∂G on the flow-domain boundary. The discretized initial conditions have the form

$$U_\alpha(0) = U_{0\alpha} \tag{8}$$

  with $U_{0\alpha}$ the restriction of the given initial flow-state condition to the grid points indicated by the multi-index α.
- The smoothness condition for $U(x,y,z,t)$ is satisfied by constructing numerical smoothing contributions to the divergence expression D_α. (This is often referred

to as avoiding odd-even decoupling.) It may be argued that these ensure that, in smooth parts of the flow, 2nd-order undivided differences of the flow-state vectors U_α are at most of the order of the numerical truncation errors already accepted above.

The computation results of chapter 2 were obtained with a fully-conservative, 2nd-order accurate, central-difference approximation of the spatial divergence expression $F_x + G_y + H_z$. In smooth parts of the flow, an explicit 4th-order numerical smoothing divergence was added to ensure the numerical equivalent of sufficient differentiability, and an explicit 2nd-order elliptic divergence was added that is designed to become important only in shocks, and creates steep numerical models of shock-discontinuity surfaces.
At block faces in the flow domain, special numerical procedures were applied to account for non-smooth behaviour of the grid over such block faces, so that the 2nd-order numerical accuracy is not impaired by such non-smoothness. Traces of grid lines, that are non-smooth (slope-discontinuous) over block faces, are visible at various locations in figures 2.5-2.6.

An equation system of the form (6-8) defines a semi-discretized initial-boundary-value problem for the collection of flow-state vectors $U_\alpha(t)$ on the grid G, $t > 0$. This collection of flow-state vectors approximates the unknown flow-state vector $U(x,y,z,t)$ on D, $t > 0$.

The third numerical design step is the specification of an algorithm that defines an approximate numerical solution of the semi-discretized initial-boundary-value problem (6-8) for $U_\alpha(t)$. Now the semi-discretized conservation equations (6) may be rewritten in the form $dU_\alpha(t)/dt = - D_\alpha$, and in practice this turns out to be a system of ordinary first-order differential equations for $U_\alpha(t)$, with the right-hand side depending also on the collection of $U_\alpha(t)$ vectors. This system may be numerically integrated in time with a suitable integrator. For Euler-flow computations, explicit Runge-Kutta-type integrators are popular. The end result of the specification of a numerical time-integrator is a recursion algorithm of the form

$$
\begin{aligned}
&U_\alpha^{\,0} = U_{0\alpha}, \\
&\text{for } n = 0 \text{ step } 1 \text{ until } N \text{ do:} \qquad (9) \\
&U_\alpha^{\,n+1} = U_\alpha^{\,n} - I_{\alpha\ \nu=n}^{\ n+1} \left(D_\alpha(\nu)\right)_{B_\alpha\{U_\alpha(\nu)\}=0} \Delta\nu.
\end{aligned}
$$

Here $U_\alpha^{\,n}$ is the grid function $U_\alpha(t)$ for the flow state at a time with time-step index n. In each step of the recursion, the grid function $U_\alpha^{\,n+1}$ at time step $n + 1$ is defined from $U_\alpha^{\,n}$ at time step n, using a discrete integrator operator

$$\int_{\nu=n}^{n+1} I_\alpha \; (.)\Delta\nu \tag{10}$$

that numerically integrates its argument (.) from time step $\nu = n$ to $\nu = n + 1$, whereby ν takes fractional values between n and n + 1, $\nu \in [n, n + 1]$. The argument

$$(D_\alpha(\nu))_{B_\alpha\{U_\alpha(\nu)\} = 0} \tag{11}$$

is the numerical divergence expression at a time step ν, and is evaluated such that all boundary conditions at that time step ν are also satisfied.

The detailed definition of the numerical integrator I(.) and of its argument (.) involves issues like:
- modelling of regions of influence and dependence, in accordance with physical principles obtained from characteristic theory,
- time-integration stability and maximum-time-step determination,
- numerical accuracy in time and in space.

The computation results of chapter 2 were obtained with a 4th-order explicit Runge-Kutta-type time integration algorithm. Local time stepping was applied to accelerate convergence to a steady state.

5. Main layout of computer-code system

The numerical-solution algorithm (9) may be worked out to a detail that it may be mapped in a flow-solver computer code, the core of the computer code system. This flow-solver code may be brought into execution on (super)computers, to produce numerical solutions. Input of the execution of a flow-solver is an actual grid G, output is a computed flow on that grid.
Other computer codes are required for the execution of auxiliary tasks around the flow computation (grid generation, flow visualisation). The codes are interfaced by standardized file interfaces. The decomposition of the total flow-computation task into subtasks has been discussed in section 2, in connection with figure 2.7.

The major codes and file interfaces are:

EDOMO : code for the subdivision of the flow domain in large blocks,
ENGRID : code for the design of multiblock grids in a blocked flow domain,
ENSOLVE : code for the computation of Euler (and in near future, thin-layer Navier-Stokes) flows,
VISU3D : code for the visualisation of flow-computation results,
GEOM-file : interface for point collections on aerodynamic surfaces and on block faces in the three-dimensional flow domain with a non-default shape,
TOPOL -file : interface for description of the topological structure of the point collections on the GEOM-file,

GRID -file : interface for multiblock-grid points,
VISDAT-file: interface for flow-computation results.

6. Concluding summary

The results presented may be summarized as follows.

The design of a system of computer codes for the computation of three-dimensional flows around transport aircraft and other aerodynamic configurations is reported. This system is made useful for computational aerodynamic-analysis work at aerodynamic-design departments in aircraft industries, in particular for analysis of the effect of propulsion systems on the flow around aircraft.

The topic is introduced with an example of a computational aerodynamic analysis (sect. 2). Hereby propeller-slipstream effects around a transport aircraft with two wing-mounted propellers in tractor position are analysed. The subtasks that must be executed to obtain such computation results are multiblock-grid generation, flow computation, and graphical-interactive analysis of computation results. Production of such computation results requires supercomputer computation power and top-of-the-line graphical workstations, available at e.g. NLR (sect. 1).

Starting from the determining aerodynamic and operational requirements for the design of the computer code system (sect. 3), the three steps of the conceptual design of the system are outlined.

1 The mathematical-physical model of the aerodynamic flow-computation problems is that of an initial-boundary-value problem for the unsteady Euler-flow equations in three-dimensional space, with complex aerodynamic surfaces bounding the three-dimensional flow domain (sect. 4).
2 The numerical-solution modelling of the problems is based on:
   a surface-modelling with transfinite multi-linear and multi-cubic polynomial Hermite interpolation (sect. 2),
   b modelling of multi-block structured grids (sect.s 2, 4),
   c semi-discretisation of Euler-flow conservation equations and boundary conditions with a cell-centered approach, with conservative central differencing, and explicit numerical smoothing to obtain smooth numerical solutions and high resolution of shock-discontinuity surfaces (sect. 4), and
   d numerical time integration with an explicit Runge-Kutta-type integrator, to define approximate numerical solutions of the aerodynamic flow-computation problems (sect. 4).
3 The conceptual design of the analysis work of computation results (surface modelling, grid modelling, inspection of flow-computation results) is based on the use of interactive graphical means on modern workstations (sect. 5).

7. References

1 Boerstoel, J.W., Spekreijse, S.P.: An information system for the numerical simulation of 3D Euler flows around aircraft, NLR TP 90264 L (1991), 2nd World Congress on Computational Mechanics, August 27-31, 1991, Stuttgart, Federal Republic of Germany, to be published in Comp. Methods in Applied Mechanics and Engineering (1991).

2 Amendola, A., Tognaccini, R., Boerstoel, J.W., Kassies, A.: Validation of a multiblock Euler flow solver with propeller slipstreams (1988), AGARD FDP Conf. Proc. 437, paper P1-1.

3 Boerstoel, J.W., Jacobs, J.M.J.W., Kassies, A., Amendola, A., Tognaccini, R., Vitagliano, P.L.: Design and testing of a multiblock grid generation procedure for aircraft design and research, NLR TP 89146 L (1989), AGARD FDP Conf. Appl. Mesh Gen. to Compl. 3D Conf.s, Loen, Norway, May 1989.

4 Boerstoel, J.W.: De ontwikkeling van een rekensysteem voor de numerieke simulatie van Euler stromingen (The development of a computer-program system for the numerical simulation of Euler flows, in Dutch), in: Supercomputer en technologie (Supercomputer and Technology, in Dutch), NLR PUB 8801, (April 1988) pag. 65-83.

5 Loeve, W.: CFD efforts in the Netherlands, NLR TP 91250 L (1991), 4th Int. Symp. on CFD, Sept. 1991, Davis, California, USA.

6 Boerstoel, J.W.: Numerical grid generation in 3D Euler-flow simulation, NLR MP 88013 U (1988), Conf. Num. Meth. for Fl. Dyn., Oxford, 1988.

7 Kassies, A., Tognaccini, R.: Boundary conditions for Euler equations at internal block faces of multi-block domains using local grid refinement, NLR TP 90134 L (1990), AIAA 21st Fl. Dyn. Conf., June 1990, Seattle, USA.

8 v.d. Berg, J.I., Boerstoel, J.W.: Development and validation of a characteristic boundary condition of a cell-centered Euler method, NLR TP 90144 L (1990), 17th ICAS congr., Sept. 1990, Stockholm.

9 Hoeijmakers, H.W.M., Van den Berg, J.I.: Application of an Euler-equation method to a sharp-edged delta-wing configuration with vortex flow, NLR TP 91306 L (1991), AIAA Paper 91-3310.

10 Hoeijmakers, H.W.M.: Modeling and numerical simulation of vortex flow in aerodynamics, NLR TP 91154 L (1991), AGARD Fluid Dynamics Symposium on 'Vortex Flow Dynamics', Oct. 1990, Scheveningen, The Netherlands.

11 Gerritsen, M.G.: Geometrical modelling of 3D aerodynamic configurations for numerical flow simulations, NLR TR 90045 L (1990) (student stage report).

12 Spekreijse, S.P., Boerstoel, J.W., Vitagliano, P.L.: New concepts for multiblock grid generation for flow domains around complex aerodynamic configurations, NLR TP 91046 L (1991), in: [15] pag.s 719-730.

13 Kuyvenhoven, J.L., Boerstoel, J.W.: 3D Euler flows around modern airplanes, NLR TR 89343 U (1989).

14 Obert, E.: The meaning of new developments in aerodynamics for the aerodynamic design (in Dutch), Symposium 'Recent Developments in Aerodynamics', Nederlandse Vereniging voor Luchtvaart techniek, Vliegtuigbouwkundige Studievereniging 'Leonardo da Vinci' (April 26, 1985).

15 Arcilla, A.S., Häuser, J., Eiseman, P.R., Thompson, F.J.: Numerical grid generation in computational fluid dynamics and related fields, Proceedings of the 3rd international conference on numerical grid generation in computational fluid dynamics and related fields, Barcelona, Spain, June 1991, North-Holland, Amsterdam (1991).

16 Kassies, A.: Informatics issues of large numerical flow simulations on the SX2 supercomputer, NLR MP 88037 U (1988) (in Dutch), NLR-WGS Symp. Computing on the NEC SX-2, June 1988.

Notes

[1] The result presented were obtained by the National Aerospace Laboratory NLR under contract 01604N with the Netherlands Agency for Aerospace Programs NIVR, under cooperation agreements with ALENIA (Napels, Italy) and with the Italian National Aerospace Laboratory CIRA (Capua, Italy)

Surface Tension Phenomena and Ventilation

By H.J. Bos,

Faculty of Aerospace Engineering, TU Delft

1. Introduction

The alveolar surface of the lungs is lined with a highly surface-active material. Under normal conditions the surfactant spreads as a monolayer at the air-liquid interface. By decreasing the surface tension surfactant protects the alveoli against collapse and facilitates the creation of a large surface area thus enhancing the gas exchange across the alveolar surface. Moreover the surfactant provides mechanical stability of the lung by preventing the growth of the larger alveoli at the expence of the smaller ones. Surfactant deficiency causes a disturbance of the alveolar gas exchange yielding several kinds of diseases. For instance lack of surfactant contributes in the clinical symptoms and signs of the neonatal respiratory distress syndrome, a major cause of neonatal death.

In this paper the role of surfactant in the mechanical behaviour of the lung is analyzed. Its influence on statical and dynamical equilibrium is emphasized. In particular the dynamical properties of the lung are of importance for its response to artificial ventilation.

During artificial ventilation the lung is activated by a forced alternating volume flow combined with the required alternating external pressure. The time history of the flow/pressure signal contains several characteristic parameters which need to be tuned in order to optimize the effect of ventilation. Important parameters are for instance ventilation volume and characteristic time scales like ventilation period and pressure rise time. In this paper a few important aspects of the role of surfactant in the ventilation process are analyzed.

2. Modeling

Considering the mechanical behaviour of the alveoli in a first approximation the alveoli are modeled as a set of spherical bubbles. Due to the structural details of the lung in reality deviations from the spherical shape will rather be a rule than an exception. For the analysis in this study the model is well suited, since the qualitative behaviour will only slightly be influenced by the structural details.

In addition to the geometrical approximation in this paper also compressibility effects of the air will be neglected.

3. Mechanical equilibrium

a Single alveolus

In a single alveolus (see figure 1) mechanical equilibrium of the spherical surface is established if the contribution made by the surface tension is balanced by a contribution made by the pressure difference across the interface, described by the socalled Laplace equation (1).

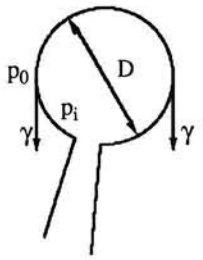

Figure 1 Static pressure and surface tension in an isolated alveolus

$$\Delta p * \frac{\pi}{4} * D^2 = \gamma * \pi * D \tag{1}$$

where: γ = surface tension between air and the alveolus lining
Δp = pressure difference across the alveolus wall
D = diameter of the alveolus

This relation may be simplified to:

$$\Delta p = \frac{4 * \gamma}{D} \tag{2}$$

A typical problem related to equation (2) is the nucleation problem. If D starts from zero the righthand side of (2) is infinitely large and an equally large pressure difference has to be applied to open the alveolus. However topology of the lung dictates a minimum size of the alveolus. Still it can be seen from equation (2) that a minimum pressure difference is needed to establish equilibrium between surface tension effects and pressure effect and that the required pressure difference is proportional to the surface tension. For instance for an air/water interface and a minimum alveolus diameter of 0.2 mm. the required pressure difference Δp is:

$$\Delta p = \frac{4 * (72 * 10^{-3})}{2 * 10^{-4}} \approx 15\ cm\ H_2O \tag{3}$$

being a relatively large pressure. Due to the presence of surfactant the surface tension is reduced and hence a reduction of the required pressure occurs. This aspect is not discussed in any detail in this paper only the equilibrium of the alveoli being considered.

b Multiple alveoli

The interaction of several alveoli is analyzed by considering two alveoli both connected to a common volume. (see figure 2). Mechanical equilibrium exists if:

$$\Delta p_1 = \Delta p_2 = p_l - p_{is.} = \Delta p_i = \frac{4 * \gamma_i}{D_i} \tag{4}$$

the subscripts 1, 2 and i refering to the 1st, 2nd and ith alveolus respectively.
p_l is the pressure in the alveolar space and $p_{i.s.}$ is the pressure in the intrathoracic space.

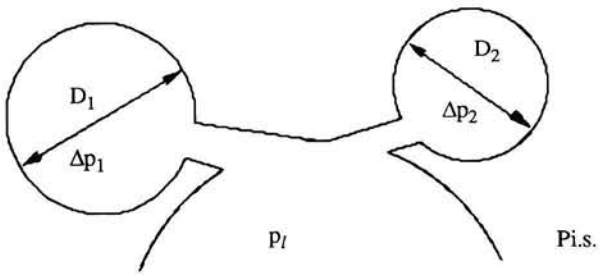

Figure 2 Connected alveoli

4. Stability of equilibrium

In the previous paragraph the equilibrium conditions have been derived for a single and multiple alveoli. However also the stability of equilibrium is of importance. Two aspects of stability will be treated in some detail in the following paragraphs:

a (quasi-)static aspect,
b dynamic aspect.

Static stability

The equilibrium of an alveolus is defined to be statically stable if a (pressure- or volume) disturbance from equilibrium generates a restoring effect.

a. Single alveolus

a.1. Isobaric alveolus

If a single alveolus with constant surface tension is connected to a volume at constant pressure (see figure 1) and by the addition of a small volume of air δV the alveolus diameter is disturbed by an amount δD the equilibrium pressure in the alveolus changes by an amount $\delta \Delta p$ given by:

$$\delta(\Delta p) = -\frac{4 * \gamma}{D^2} * \delta D \tag{5}$$

From (5) it follows that the equilibrium pressure in the alveolus decreases with an increasing diameter and an additional inflow of air into the alveolus is started which increases the diameter still further.
So *the mechanical equilibrium* of a single alveolus with constant surface tension connected to a volume of constant pressure is *unstable.*

However the lining of the alveolar wall is not a pure fluid but in general contains surface active components: the surfactant.
The first property of the presence of surfactant is a reduction of the equilibrium surface tension. Experimental results show (see ref. 1) that surface tension in equilibrium is reduced by the surfactant from a value for water/air: 72 mN/m to a typical value of 20 mN/m.
The surfactant forms a monolayer at the inside of the alveoli wall. The amount of surfactant per unit area decreases during expansion. Figure 3 shows a typical qualitative curve for the dependence of surface tension on concentration.(c.f. ref. 6)

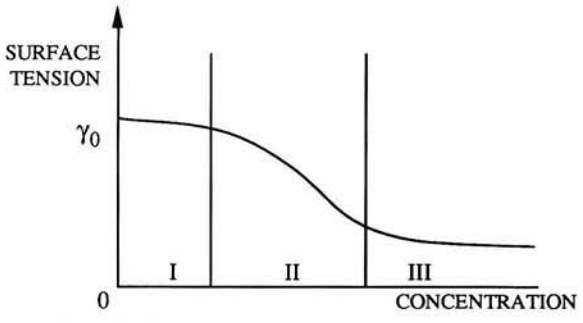

Figure 3 Surface tension versus surface concentration

The figure shows on the left hand side a zone with low concentrations where surfactant hardly influences the surface tension. And a zone on the right hand side where a saturation effect occurs. In between there is a transition region. In the transition region the actual surface tension is a function of the concentration of surfactant and hence in this case of the diameter of the alveolus. In the transition part of the figure in a first approximation the surface tension is supposed to be linearly proportional to the surfactant concentration, yielding:

$$\gamma(D) = \gamma_0 - \frac{C}{\pi * D^2} \tag{6}$$

where:

γ_0 = surface tension without surfactant (for water/air: 72 mN/m)
C = constant of proportionality, depending surfactant in monolayer.

Equation (6) is often written as a surface stiffness equation or a surface equivalent of Boyle's law:

$$\Pi * A = C \tag{7}$$

where:

Π = $\gamma_0 - \gamma(D)$ = surface pressure
A = $\pi * D^2$ = surface area
C = "stiffness coefficient"

It is noticed that the surface becomes **stiffer** if C increases i.e. if the **concentration** of **surfactant** becomes **larger**.

Once the influence of surfactant has been modelled again the diameter of the alveolus is varied and the resulting variation of the equilibrium pressure is determined:

$$\delta(\Delta p) = [\frac{4}{D} * \frac{d\gamma(D)}{dD} - \frac{4 * \gamma(D)}{D^2}] * \delta D \tag{8}$$

Static stability of a single alveolus now exists if:

$$\frac{d\gamma(D)}{dD} - \frac{\gamma(D)}{D} > 0 \tag{9}$$

For the surface tension model (6) the condition (9) reduces to:

$$\frac{2*C}{\pi*D^3} - \frac{\gamma_0}{D} + \frac{C}{\pi*D^3} > 0 \tag{10}$$

or upon rearrangement of terms:

$$\frac{C}{\pi*D^2} > \frac{\gamma_0}{3} \tag{11}$$

Comparing the condition (11) with the expression (6) it is noticed that static stability exists if the reduction of the surface tension produced by the surfactant is larger than one third of the surface tension for the pure fluid.
It has been indicated above that experimental results show that in the normal lung the surface tension is about 20 mN/m compared to 72 mN/m for pure water implying a reduction of 5/7. Hence under normal conditions with an properly functioning surfactant system the alveoli are stable if connected to a constant pressure volume confirming our daily experience.In order to make an estimate of the magnitude of the stiffness constant C a few numbers may be substituted in (6).

Taking:

γ_0 = 72 mN/m
$\gamma(D_0)$ = 20 mN/m
D_0 = 0.2 mm

for C is found:

$$C = (72 - 20) * 10^{-3} * \pi * (2 * 10^{-4})^2 \approx 65 * 10^{-10}\, Nm \tag{12}$$

It is also noticed from equation (11) that eventually with growing diameter D all alveoli become unstable. For instance for the value of C from equation (12) a maximum D for static stability is found. If the surface tension of 20 mN/m exists for an average diameter D_0 the maximum value of D for stability is 1.5 D_0. Based on this value for an individual alveolus the implication for the maximum total surface area is $A_{max} = 2.25 * A_0$ and for the total lungvolume $V_{max} = 3.4 * V_0$. So based on this simplified consideration one may conclude that if the lungvolume is driven by an oscillating pressure difference of limited amplitude the alveoli remain statically stable.

a.2. Isolated alveolus

On the other hand instead of connected to an isobaric volume if an alveolus is isolated completely and again the volume is increased in addition to the surface tension

effect there is an expansion effect of the contained amount of gas.
An isolated alveolus is stable if upon expansion the equilibrium pressure resulting from surface tension becomes larger than the gas pressure.
For a fixed amount of air Boyle's law applies:

$$(p_0 + \Delta p) * V = R * T \tag{13}$$

where:

p_0 = reference pressure
Δp = pressure difference across the alveolar wall
$V = \pi/6 * D^3$ = volume of the alveolus
R = applicable gas constant for air
T = applicable temperature.

Increasing the volume by an amount δV the resulting pressure disturbance from expansion of the gas is:

$$\delta(\Delta p) = -\frac{\delta V}{V^2} * R * T \tag{14}$$

Comparing this result with (8) the stability condition for the isolated alveolus becomes:

$$\frac{C}{\pi * D^2} > \frac{\gamma_0}{3} - \frac{3}{2} * \frac{R * T}{\pi * D^2} \tag{15}$$

The second term on the right hand side is a correction/reduction to (11) for an isolated alveolus.

b Multiple alveoli

Two alveoli are connected to a container with a fixed pressure (see figure 2). For both alveoli the equilibrium condition (4) applies with γ_i replaced by $\gamma_i(D_i)$:

$$\gamma_i(D_i) = \gamma_0 - \frac{C_i}{\pi * D_i^2} \tag{16}$$

If in all alveoli the surfactant concentration is equal the "stiffness coefficient" C_i is equal and all alveoli are equal in size and show the same stable or unstable behaviour.

If however there is a surfactant deficiency in one or more alveoli, the alveoli will be different in size and will have different stiffnesses. It should be noted that the alveoli with the surfactant deficiency will show a larger surface tension and hence will have a larger size (c.f. eq. (2)) and a smaller stability margin (c.f. eq. (11)).
Next an additional volume $\delta V = \delta V_1 + \delta V_2$ is applied to the two alveoli, the distribution of the volumina δV_1 and δV_2 follows from the condition:

$$\delta(\Delta p)_1 = \delta(\Delta p)_2 \tag{17}$$

By means of the equations:

$$\begin{aligned} \delta(\Delta p)_1 &= \left(\frac{d(\Delta p)}{dV}\right)_1 * \delta V_1 \\ \delta(\Delta p)_2 &= \left(\frac{d(\Delta p)}{dV}\right)_2 * \delta V_2 \end{aligned} \tag{18}$$

one finds:

$$\begin{aligned} \delta V_1 &= \frac{\left(\frac{d(\Delta p)}{dV}\right)_2}{\left(\frac{d(\Delta p)}{dV}\right)_2 + \left(\frac{d(\Delta p)}{dV}\right)_1} * \delta V \\ \delta V_2 &= \frac{\left(\frac{d(\Delta p)}{dV}\right)_1}{\left(\frac{d(\Delta p)}{dV}\right)_2 + \left(\frac{d(\Delta p)}{dV}\right)_1} * \delta V \end{aligned} \tag{19}$$

The values of $d(\Delta p)/dV$ follow from equation (8) and with the surface tension model (6) one finds:

$$\frac{d(\Delta p)}{dV} = \frac{24}{\pi * D^4} * \left[\frac{C}{\pi * D^2} - \frac{\gamma_0}{3}\right] \tag{20}$$

It has been indicated above that in our analysis the alveoli considered although some may show a surfactant deficiency are all supposed to be stable. The one with a surfactant deficiency possessing a smaller stability margin and a larger diameter. Hence for that particular alveolus both terms on the right hand side of equation (20) are smaller and therefore $d(\Delta p)/dV$ is smaller for the deficient alveolus. So from equation (19) it follows that the larger part of the additional volume ΔV is absorbed by the alveolus with the smaller $d(\Delta p)/dV$.

In conclusion for the (quasi)-static behaviour applies that if an alveolus shows a deficiency in surfactant it will show a low stiffness, a large diameter and during (artificial) ventilation it will grow stronger due to the smaller stiffness. Moreover since the increase in surface area is related to the volume increment by:

$$\delta A = \frac{4}{D} * \delta V \tag{21}$$

and since large surface areas enhance the gas exchange, the larger growth of the larger alveoli is also unfavourable from the viewpoint of ventilation efficiency.

5. Conclusion, effects on artificial ventilation

It has been indicated in the introduction that deficiency of surfactant contributes in the symptoms of neonatal respiratory distress syndrome. Patients with this disease often are artificially ventilated. One of the problems met during artificial ventilation at "normal" tidal volumes is that part of the alveoli (the part with the deficient surfactant as shown in this paper) is pushed over its stability limit and is blown up.
A solution to this problem is high frequncy low tidal volume ventilation. During this type of ventilation the lung is ventilated with a tidal volume smaller than the dead space of the airways and at frequncies ranging from 5-30 Hz. In spite of the small ventilation volume still gasexchange is maintained. This is due to enhancement of the diffusion/dispersion mechanism by the high frequency oscillating flow. A detailed description of this mechanism is beyond the scope of this paper.
Because in this technique tidal volume is small damage to the alveoli is reduced, however also dynamical effects may play a role. One may think of resonance phenomena of the alveoli. However an estimate of the lowest natural frequency of an alveolus shows that this cannot be the case. The lowest natural frequncy can be calculated from the generalized inertia and the generalized stiffness of an alveolus.
The generalized inertia is calculated from the kinetic energy of the alveolar interstitium during oscillation. The alveolar interstitium is a layer with a typical thickness of about 10 μm covering the alveolus on the outside. The inertia of this thin layer with respect to radial oscillations of an alveolus with a diameter D = $2 * 10^{-4}$ m. is:

$$m = \pi * D^2 * \delta * \rho_0 = \pi * (2 * 10^{-4})^2 * 10^{-5} * 10^3 = 1.25 * 10^{-9}\ kg \tag{22}$$

The generalized stiffness is calculated from the potential energy stored in surface tension during oscillation. Applying equation (6) the stiffness is calculated as:

$$k = 8 * \pi * \gamma_0 = 8 * \pi * 72 * 10^{-3} = 1.8\ \frac{N}{m} \tag{23}$$

and for the lowest natural frequency is found:

$$f_n = \frac{1}{2 * \pi} * \sqrt{\frac{k}{m}} \approx 6\ kHz \tag{24}$$

Apparently the lowest natural frequency is well above the excitation frequency hence a dynamical effect where inertia plays a role can be excluded.

However also a beneficial dynamical effect from surface tension exists. It is for instance demonstrated in experiments (see e.g. ref 6 and 7) that during expansion of a free surface with surfactant (at least if expansion is fast enough) the surface tension is higher than the equilibrium surface tension found during slow expansion.
The implication of this result for the alveoli during ventilation is that increasing the ventilation frequency or reducing the pressure risetime may increase the expansion velocity of the alveoli above a critical value thereby reducing the effect of surfactant and hence also reducing the imbalance between the various alveoli due to the deficiency of surfactant.

References

1 Hills, B.A. — The biology of surfactant, Cambridge University Press 1988

2 Nunn, J.F. — Applied Resperatory Physiology, Butterworth 1987

3 Fung, Y.C. — Biomechanics, Motion, Flow, Stress and Growth, Springer 1990

4 Goodrich, F.C. — Rheological properties of fluid interfaces, Proc. 52nd Colloid Surf. Symp. 1978/79

5 Van den Tempel — Surface Rheology, Journal of Non-Newtonian Fluid Mechanics, no 2 (1977) pp 205-219

6 Bergink-Martens D., Bos, H.J., Prins, A. Zuidberg, A.F. — Surface dilational behaviour of surfactant solutions. Colloids and Surfaces, 1992, to appear.

7 Bergink-Martens D., Bos, H.J., Prins, A. Schulte, B.C. — Surface dilation of Newtonian Liquids in an overflowing cylinder, Journal of Coll. and Int. Sciences, 138 (1990)

Flow excited resonance in a cavity covered by a grid: theory and experiment

By J.C. Bruggeman

TNO Institute of Applied Physics, TPD Delft

Abstract

Sound generation by flow past a cavity covered by a grid with louvers with rectangular cross section at 45° to the flow direction is analyzed. Simple models for the aero-acoustic source are presented for two cases: 1) grazing flow past the grid, and 2) grazing flow past the grid in combination with flow through the grid into the cavity. The source strength and the resonance conditions as predicted by the source models are compared to data from wind tunnel experiments. The use of ramps and arrays of roughness elements as suppression devices is evaluated.

Nomenclature

B	stagnation enthalpy (m^2/s^2)
c	velocity of sound (m/s)
f	frequency (1/s)
G	Green's function (m^2/s^2)
$H(t-\tau)$	Heaviside function
H	cavity width (m)
h	distance between louvers of the grid (m)
h'	height of ramp or height of array of roughness elements
$\underline{I}$	acoustic energy flux vector (N/(ms))
$k = 2\pi/\lambda$	acoustic wave number (1/m)
$\underline{i}, \underline{j}, \underline{k}$	unit direction vectors of x_1,x_2,x_3 coordinate system
l	louver thickness (m)
L	cavity depth (m)
$L_{eff} = L+\Delta L$	effective cavity depth (m)
$M = U_0/c$	Mach number
n	integer
p'	unsteady pressure (N/m^2)
p_n	mode of orthonormal set $\{p_n\}$

Q_{ls}	constant relating acoustic energy input from loudspeaker into cavity to p' (m^3/s)
S	boundary surface (m^2)
$Sr_x = fx/U_0$	Strouhal number based on length x, x = h, l or θ
t	time (s)
T	large time interval (s)
$\underline{U}$	steady flow velocity (m/s)
U_0	time averaged grazing flow velocity (m/s)
$\underline{U}_c$	convection velocity of vortex (m/s)
$\underline{u}$	acoustic velocity (m/s)
u'	x_1 component of unsteady velocity (m/s)
V	average steady flow velocity through grid (m/s)
V_{jet}	steady velocity of jet into cavity (m/s)
$\underline{v}$	local flow velocity (m/s)
v'	x_2 component of acoustic velocity (m/s)
$\underline{w} = \nabla \times \underline{v}$	local vorticity (1/s)
x_1, x_2, x_3	coordinates in Cartesian system, x_1-axis parallel to wall (m)
Γ	circulation (m^2/s)
ΔL	end correction (m)
$\epsilon = H/L_{eff}$	small parameter in low frequency approximation
ρ	density (kg/m^3)
θ	momentum thickness (m)
θ_s	initial shear layer momentum thickness (m)
λ	acoustic wavelength (m)
τ	time (s)
$\omega = 2\pi f$	angular frequency (1/s)

Indices:

c	convective
ls	caused by external loudspeaker
n	mode number
0	steady part

Superscripts:

'	unsteady part

1. Introduction

Open cavities in ship hulls exposed to flow are potential sources of noise and vibration [1,2]. The noise and vibration are caused by self excited flow oscillations in the cavity opening (see reviews [3,4,5]). While low frequency flow oscillations are successfully suppressed by placing a grid of bars or louvers in the cavity opening [5], the grid itself may in some cases cause higher frequency flow oscillations. In this paper, data are presented for sound generation by a grid with louvers of rectangular cross section at 45° to the flow direction (Fig. 1a). The grid generates sound for two different steady flow conditions: 1) grazing flow past the grid, and 2) grazing flow past the grid in combination with flow through the grid into the cavity. A better understanding of the self excited flow oscillations leads to design rules for suppression of this type of flow induced noise and vibration. A theoretical analysis (section 2) and experimental verification (section 3) are presented for a cavity with rigid walls, covered by a rigid grid. This description is appropriate for standard steel or aluminum constructions exposed to air flow. We expect that structural coupling is important in underwater applications. Therefore the influence of structural coupling is briefly discussed in section 4.

The main features of the phenomenon are illustrated with a wind tunnel experiment on the basic geometry of a grid with 6 louvers covering a cavity in a plane wall (Fig. 1a). The grid is exposed to a grazing flow with a velocity of 0 – 15 m/s. Flow through the grid into the cavity can be induced by a low noise fan (see section 3 for a description of the experimental setup). Provisions were made for testing of 2 dimensional ramps (Fig. 1b) and arrays of roughness elements (Fig. 1c) as suppression devices.

In a first experiment with zero flow through the grid into the cavity, a loud tone occurs for a range of grazing flow velocities (Fig. 2). The frequency f of the tone corresponds to an acoustic wavelength λ such that the effective depth L_{eff} of the cavity is equal to $\lambda/4$. The maximum amplitude of the sound pressure p' at the bottom of the cavity, $2p'/\rho U_0^2 = 0.08$, is found for a Strouhal number based on louver spacing h of $Sr_h = (fh)/U_0 = 0.54$. In a second experiment with a combination of grazing flow past the cavity and flow through the grid into the cavity, a similar flow induced tone appears. Again the wavelength of the tone is such that the effective depth of the cavity is equal to $\lambda/4$, but the maximum amplitude occurs at a lower grazing flow velocity, yielding $Sr_h = 1.47$ (Fig. 2). For nonzero flow through the grid, a Strouhal number Sr_l based on louver thickness l is more appropriate (section 2). This yields $Sr_l = 0.15$.

Visualization of the flow for a grazing flow of 9.5 m/s and zero flow through the grid shows that vortices are formed in the unstable shear layer above the grid. The unstable shear layer is an aero-acoustic source which drives the resonant acoustic field in the cavity. The acoustic field in turn controls the hydrodynamic (vortical) perturbations above the grid. This interaction takes place at points where the flow separates.

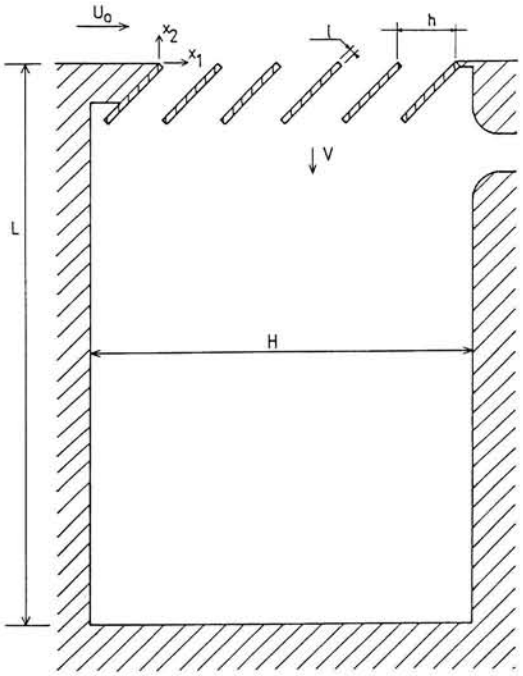

Fig. 1a Deep cavity in a plane wall covered by a grid with 45° louvers. H = 100 mm, L = 161 mm, h = 15.5 mm, l = 1.5 mm

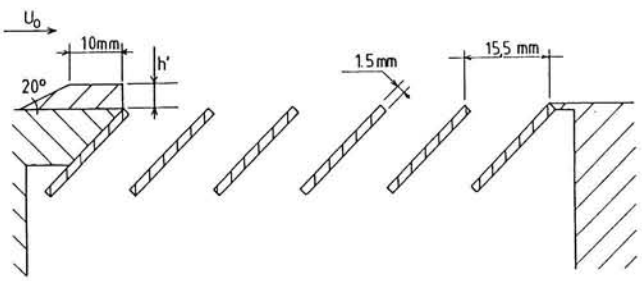

Fig. 1b Geometry of ramps tested as suppression device. h' = 1;2;5;10;20 mm

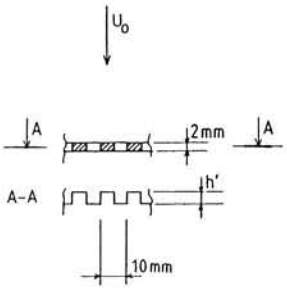

Fig. 1c Geometry of arrays of roughness elements tested as suppression device. h' = 2,5;5 mm

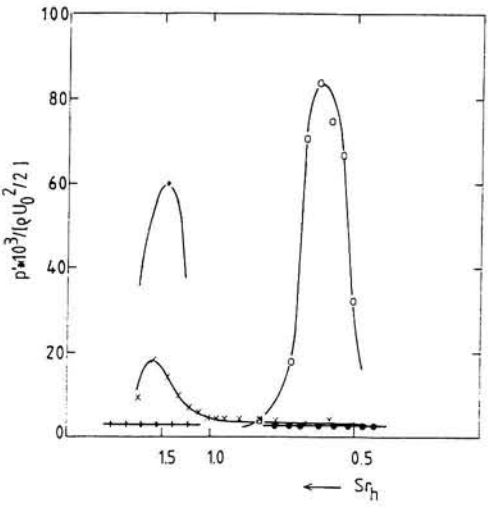

Fig. 2 Influence of grazing flow velocity U_0 on amplitude of flow induced tone, for zero flow (V = 0 m/s) and nonzero flow (V = 0.5 m/s) through the grid (see Fig. 1a). Frequency f = 340 Hz. o: V = 0.0 m/s, θ = 0.30 mm, • : V = 0.0 m/s, q = 0.73 mm, *: V = 0.5 m/s, q = 0.30 mm, ×: V = 0.5 m/s, 4 arrays of teeth, h' = 5mm upstream of grid, +: V = 0.5 m/s, 1 array of teeth, h' = 2.5 mm on top of each louver

In the case of zero flow through the grid the only separation point is the upstream edge of the grid. For nonzero flow through the grid, detailed hot wire velocity measurements (section 3) show that in that case the flow separates and a shear layer is formed at the edge of each louver.

The character of the flow past a cavity depends strongly on the ratio of unsteady to steady flow velocity at flow separation points [6]. For a deep cavity with opening area approximately equal to the cross sectional area of the cavity, as discussed in this paper, this ratio is $p'/\rho cU_0$, where p', ρ, c and U_0 are unsteady pressure at the bottom of the cavity, density, velocity of sound and steady flow velocity. For deep cavities covered by a lid with a small opening [7,8] or Helmholtz resonators [9], $p'/\rho cU_0$ should be replaced by the actual ratio of unsteady to steady flow velocity in the cavity opening. On the basis of the amplitude parameter $p'/\rho cU_0$, three cases can be distinguished. In the case of *small amplitudes* ($p'/\rho cU_0 < 10^{-3}$), the growth of the hydrodynamic velocity disturbances of the shear layer may be described with linearized stability theory up to a point one hydrodynamic wavelength downstream of the point where the shear layer is excited [10]. In the case of *moderate amplitudes* ($10^{-3} < p'/\rho cU_0 < 10^{-1}$), only the behavior of the first part of the shear layer may be described with linearized stability theory. In the large *amplitude case* ($p'/\rho cU_0 = O(1)$), the

behavior of the whole shear layer is nonlinear. Since the amplitude of self-sustained flow oscillations in the experiments discussed in this paper is in the moderate range, linearized stability theory provides a useful framework for the description of shear layer excitation at separation points. However, for the description of the dynamics of the larger part of the shear layer, linearized theory cannot be used. Therefore shear layer models are presented for the moderate amplitude case, based on the nonlinear concept of roll up of the shear layer into discrete vortices. These models are combined with the concept of vortex sound [11,12] for an aero-acoustic analysis.

2. Analysis

Shear Layer Instability and Vortex Shedding

Flow excited acoustic resonance is the result of a feedback interaction process which proceeds as follows [3,4,13]:

- The sound field excites the shear layer at the separation point,
- Instability of the shear layer results in the formation of coherent vortex structures,
- Interaction of the unsteady vorticity with the sound field results in a transfer of energy from the flow to the acoustic field,
- Acoustic properties of the cavity determine amplitude and phase of the feedback at the upstream edge.

For a thin shear layer ($f\theta/U_0 << 1$), the excitation of the shear layer by the acoustic field is described by an unsteady Kutta condition at the separation point. At high Reynolds numbers and small or moderate values of $p'/\rho cU_0$ this leads to the assumption of separation of the flow tangential to the wall upstream of a separation point [4]. This allows an estimate of the magnitude of the hydrodynamic perturbation of the shear layer at the separation point for a given acoustic field. For small amplitudes linearized stability theory for inviscid quasi parallel free shear layers may be used to estimate the influence of the steady flow velocity profile on the growth of the perturbation [8,10,14]. This theory predicts that growth will only occur when the Strouhal number based on initial momentum thickness of the shear layer θ and steady flow velocity U_0 satisfies the condition:

$$Sr_\theta = f\theta_s/U_0 < 0.04. \qquad (1)$$

An array of roughness elements or teeth placed upstream of the cavity increases θ_s. In the small amplitude case, condition (1) predicts a reduction of the flow induced cavity resonance when θ_s is increased, as observed experimentally by several investigators [3,4,15]. In the moderate amplitude case ($10^{-3} < p'/\rho cU_0 < 10^{-1}$), the shear layer vorticity soon concentrates into structures which can be described as discrete vortices. This saturation of the growth of shear layer disturbances is of course not described by linearized theory. In the case of large values of the ratio of unsteady to steady flow velocity ($p'/\rho cU_0 = O(1)$), condition (1) is expected to be of no use. Hence, for moderate and large amplitudes, $10^{-3} < p'/\rho cU_0$, it is questionable that self

sustained oscillations can always be suppressed by increasing θ_s to values such that $f\theta_s/U_0 > 0.04$. This is confirmed by the data of De Metz and Farabee [7] and Panton [9] who report self-sustained flow oscillations for cases where $f\theta_s/U_0 > 0.04$. It appears that these data relate to experiments where the ratio of unsteady to steady flow velocity is quite large.

Shear Layer Model for Moderate Amplitudes for the Case of Zero Flow Through the Grid into the Cavity

In the case of zero flow through the grid into the cavity, the grazing flow with steady velocity U_0 is separated from the stagnant medium in the cavity by a shear layer above the grid. When condition (1) is met, the shear layer will be unstable: small perturbations will grow and discrete vortices will be formed. This leads to a simple model for the shear layer (Fig. 3a). Similar to the modeling of the flute by Howe [12] and of the Helmholtz resonator by Nelson [16,17], we assume that a line vortex is shed periodically from the upstream edge. The path of the vortex is determined by the main flow, the acoustic velocity field above the grid, the images of the vortex in the walls and in the louvers of the grid and by the presence of other vortices. For the sake of simplicity we will assume that the line vortex travels at a constant velocity U_c parallel to the wall. U_c is proportional to U_0 and expected to be close to $U_0/2$. Following Nelson [17], we assume that the circulation of the vortex increases with a constant rate: $\Gamma = U_0^2\, t/2$, until it reaches the value corresponding to the concentrated circulation of one hydrodynamic wavelength of the shear layer disturbance: $\Gamma = U_0^2/2f$. At that moment a new vortex is shed from the upstream edge of the grid. The vortex formed in the previous period continues its path parallel to the grid with a constant circulation $\Gamma = U_0^2/2f$. It is assumed that the acoustic velocity field near the upstream edge of the grid triggers the formation of the new vortex. This leads to the assumption that a discrete vortex starts to develop at the moment when the direction of the acoustic velocity at the upstream edge changes from cavity outwards to cavity inwards. A similar model for the flow dynamics will be developed for the case of nonzero flow through the grid in the next paragraph.

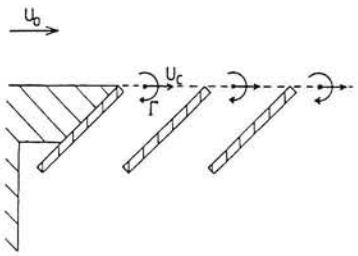

Fig. 3a Simple model of the shear layer for zero flow through the grid into the cavity

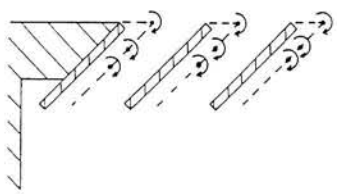

Fig. 3b Simple model of the shear layer for nonzero flow through the grid into the cavity

Shear Layer Model for Moderate Amplitudes for the Case of Nonzero Flow Through the Grid into the Cavity

Detailed flow velocity measurements (section 3) show that in the case of nonzero flow through the grid into the cavity, a dead water region and a jet directed into the cavity form behind each louver. The extent of the dead water region and the velocity gradient in the shear layer which forms the interface between dead water region and jet are determined by the grazing flow velocity U_0, the average flow velocity through the grid V and the boundary layer upstream of the grid. The velocity of the jet V_{jet} is approximately 1.7 times V [18]. The data (section 3) show that flow into the cavity causes a decrease of the momentum thickness θ_s of the shear layers at the louvers. Hence, even when $f\theta_s/U_0$ based on the momentum thickness upstream of the grid is larger than 0.04, condition (1) can still be met at the separation points on the louvers. In that case perturbations of the shear layers will grow and discrete vortices will be formed. For sufficiently large values of V/U_0 the vortices travel into the cavity. In that case the flow pictures behind different louvers of the grid show a large degree of similarity. This leads to a simple model for the shear layer behind a single louver of the grid (Fig. 3b). It is assumed that a line vortex starts to form at the edge of the louver at the moment when the acoustic velocity at the edge is zero and switches from cavity outwards to cavity inwards. The circulation of the vortex increases proportional to time: $\Gamma = U_{eff}^2\, t/2$, where U_{eff} is the total steady flow velocity at the edge, in principle determined by U_0 and V. The growth of the circulation of the line vortex saturates after 1 period, when $\Gamma = U_{eff}^2/2f$ and a new vortex is shed. The vortex path is simplified to 2 straight line segments. On the first segment the vortex travels parallel to the grazing flow velocity U_0. On the second segment the vortex travels parallel to the louvers. The length of the first segment of the simplified vortex path is equal to the width of the dead water region: approximately 0.4 times the louver spacing h [18]. Immediately after it is shed, when the vortex is close to the louver, U_c is expected to be smaller than $U_0/2$ due to the influence of its image in the louver: $U_c \approx U_0/4$. Further away from the louver $U_c \approx U_0/2$.

Sound Production by Vortex Shedding in a Cavity Covered by a Grid

Similar to the description of the acoustic field in pipe systems with side branches discussed in [6], the acoustic field in a cavity with compact vorticity inhomogeneities and a low Mach number homentropic and irrotational steady flow can be described with a convected wave equation:

$$\left\{\frac{1}{c_0^2}\left(\frac{\partial}{\partial t} + \underline{U}\cdot\nabla\right)^2 - \nabla^2 B'\right\} = \nabla\cdot\left(\underline{w}\times\underline{v}\right) \qquad (2)$$

where B' is the fluctuating part of the stagnation enthalpy:

$$B' = \frac{p'}{\rho} + \underline{U} \cdot \underline{u}, \tag{3}$$

and $\underline{U}$, $\underline{u}$ and w are irrotational steady flow velocity, acoustic velocity ($\underline{\nabla} \times \underline{u} = 0$) and vorticity, where $\underline{w} = \nabla \times \underline{v}$. The local velocity vector $\underline{v}$ is the sum of $\underline{U}$, $\underline{u}$ and the solenoidal unsteady velocity. When a low Mach number, nonuniform steady flow is present it is more convenient to use B' in combination with $\underline{u}$, rather than p' and $\underline{u}$ as acoustic variables [12]. $\underline{u}$ and B' are related by the momentum equation:

$$\partial \underline{u} / \partial t = \nabla B'. \tag{4}$$

The aero-acoustic source model for the moderate amplitude case, for zero flow through the grid (section 2.2) takes the form:

$$\nabla \cdot (\underline{w} \times \underline{v}) = \nabla \cdot \{-\underline{k} \times \underline{i}\} \, \delta(\underline{x} - \underline{i} U_c t)(U_0^2 t/2) U_c, \tag{5}$$

where U_c is expected to be close to $U_0/2$. The model for nonzero flow through the grid takes a form very similar to (5). During the first period, on the first part of the simplified vortex path it is described by:

$$\nabla \cdot (\underline{w} \times \underline{v}) = \nabla \cdot \{-\underline{k} \times \underline{i}\} \, \delta(\underline{x} - \underline{i} U_c t)(U_{eff}^2/2) U_c. \tag{6}$$

On the second part of the simplified vortex path the velocity of the vortex is parallel to the louvers instead of parallel to the wall and U_c is related to V_{jet} instead of U_0. Hence, for the proposed aero-acoustic source models, the source strength is determined by the steady flow velocity only and independent of the amplitude of the acoustic field.

For low frequencies, an approximate solution for the acoustic field in a deep cavity in a wall, to leading order in the ratio of cavity duct width to effective cavity depth, $\varepsilon = H/L_{eff} << 1$, can be obtained with the method of matched asymptotic expansions [19]. For low frequencies, $L_{eff} = O(\lambda/2\pi)$, H is smaller than $\lambda/2$. Hence only plane waves have to be considered in the cavity. To leading order in ε the acoustic velocity distribution in the open end of the cavity $\underline{u}$ can be described with an incompressible irrotational flow: div $\underline{u} = 0$ and rot $\underline{u} = 0$. Hence, the acoustic velocity in the cavity opening $\underline{u}$ is the gradient of a velocity potential which satisfies Laplace's equation [20]. For qualitative purposes, we replace the three dimensional acoustic velocity field in the opening by the acoustic velocity field in a two dimensional cavity opening which is connected to a two dimensional half space. This enables us to use conformal mapping [20] to estimate the acoustic velocity distribution close to the rectangular edges of the louvers. Later, we will check the accuracy of the two dimensional approximation with experimental data (3. Experiments). The external acoustic field is driven by the acoustic volume flux in the cavity opening, which we will approximate by a vibrating piston in a plane wall [21]. Matching of the one-

dimensional acoustic field inside the cavity, the incompressible acoustic velocity field in the cavity opening and the solution outside the cavity, yields a solution to leading order in ε. From now on B' and $\underline{u}$ denote the low frequency approximations of stagnation enthalpy and acoustic velocity.
A formal solution to Eq. (2) is obtained with Green's theorem:

$$B'(x,t) = \int_{-T}^{T} \int_{V} G \ \nabla \cdot (w \times v) \, dy \, dt + \int_{-T}^{T} \int_{S} (G \nabla B' - B' \nabla G) \cdot \underline{n} \, dS(\underline{y}) \, d\tau, \tag{7}$$

where G is the low frequency Green's function, obtained by mode expansion [6]:

$$G = \sum_{n} \frac{c_0^2 H(t-\tau) p_n(\underline{x}) p_n^*(\underline{y}) \sin[\omega_n(t-\tau)]}{\omega_n} \tag{8}$$

The low frequency modes $p_n(\underline{x}) \sin(\omega_n t)$ are free vibrations of the cavity for loss free boundary conditions. For a cavity with small or negligible radiation losses and for the aero-acoustic source in the present problem the solution to Eq. (7) will be a quasi periodic function of time. Hence, one can expand B' and $\underline{u}$ in the low frequency modes of the cavity:

$$B_n = \alpha_n \, p_n \sin \omega_n t, \tag{9a}$$

$$\underline{u}_n = \frac{\alpha_n}{\omega_n} \nabla p_n \{ \cos \omega_n t - \frac{\alpha_n}{\alpha_n \, \omega_n} \sin \omega_n t \}, \tag{9b}$$

and use the method of averaging [6] to find an approximate solution to Eq. (7):

$$\frac{\rho}{c_0^2} \alpha_n^* \dot{\alpha}_n = -\rho \int_V < (\underline{w} \times \underline{v}) \cdot \underline{u}_n > dy - \int_S < B_n^* \, \underline{u}_n > \cdot \underline{n} \, dS(\underline{y}), \tag{10}$$

where * and < > denote a complex adjoint and an average over the oscillation period respectively. Near resonance a single mode gives a reasonable description of the

acoustic field. Adding Eq. (10) to its complex adjoint yields an equation describing the balance of acoustic energy for mode n. For a stationary situation ($\alpha_n = 0$):

$$< P_n > = \int_S < \underline{I}_n > \cdot \underline{n}\, dS(\underline{y}), \tag{11}$$

where

$$P_n = -\rho \int_V \frac{1}{2} \left(\underline{u}_n + \underline{u}_n^*\right) \cdot \left(\underline{w} \times \underline{v}\right) d\underline{y}, \tag{12}$$

is the power delivered by the aero-acoustic source and

$$\int_S \underline{I}_n \cdot \underline{n} dS(\underline{y}) = \int_S \frac{1}{2} \{ B_n^* \underline{u}_n + B_n \underline{u}_n^* \} \cdot \underline{n} dS(\underline{y}), \tag{13}$$

denotes the flux of acoustic energy through the boundaries of the cavity. Since in our experiments the cavity resonates in its first mode, we will in the following approximate the acoustic field by this mode. Inserting one of the source models (Eq. 5) into Eq. (12) yields an expression for the acoustic power of the source averaged over 1 period:

$$< P > = \{\rho U_0^2 U_c S p'\} / \{2 f h \rho c\} F(Sr_h, \rho c \underline{u}/p'), \tag{14}$$

where S denotes the open area of the grid and $F(Sr_h, \rho c\underline{u}/p')$ is a nondimensional constant which depends on the acoustic velocity distribution in the source area and on the nondimensional frequency. It is convenient to write the acoustic power of the source averaged over 1 period as

$$< P > = < \{p'/(\rho c)\} \{\Delta p' S\} >, \tag{15}$$

where the aero-acoustic sound source is now represented by an unsteady pressure difference $\Delta p'$ acting on the open area S of the grid. From Eqs. (14,15) it is clear that for a given cavity opening geometry and fixed Strouhal number $\Delta p'$ is directly proportional to $\rho U_0^2/2$.

With the acoustic energy balance (Eq. 11) the source strength $\Delta p'$ can be determined from experimental data. An external loudspeaker tuned to the exact frequency of the aero-acoustic source is used to check the independence of the strength of the aero-acoustic source on the amplitude of the acoustic field. The energy input by the external loudspeaker into the cavity is proportional to the amplitude of the acoustic field:

$$\int_S < \underline{I} >_{ls} \cdot \underline{n}\, dS(y) = Q_{ls}\, p',$$

say. The radiation losses can be estimated using the low frequency impedance of a circular piston with diameter S in a plane wall [20]. This yields:

$$\int_S < \underline{I} > \cdot \underline{n}\, dS(\underline{y}) = {}^1/_8(k\sqrt{S})^2\, Sp'^2/(\rho c), \tag{16}$$

where k is the acoustic wave number $k = 2\pi/\lambda$. For the conditions in our experiments, losses due to friction and heat conduction can be neglected since they are much smaller than radiation losses. In combination with Eq. (15) this yields an acoustic energy balance for the experiment with aero-acoustic source and loudspeaker:

$${}^1/_8(k\sqrt{S})^2\, Sp'^2/(\rho c) = Q_{ls}p' + \Delta p'\{Sp'/(\rho c)\}. \tag{17}$$

Repeating the experiment without the aero-acoustic source but with the same current through the loudspeaker yields an amplitude p'_{ls}. Hence, $\Delta p'$ can be determined from:

$$\Delta p' = {}^1/_8(k\sqrt{S})^2\, (p' - p'_{ls}). \tag{18}$$

Resonance Conditions

Acoustic resonance condition. Optimum power transfer from the dipole sound source $\nabla \cdot (\underline{w} \times \underline{v})$ to the acoustic field occurs when the source is located in an acoustic pressure minimum. Since the source is located near the open end of a deep cavity, this condition is always met at the low frequency resonances of the cavity;

$$L_{eff} = (n + {}^1/_2)\, \lambda/2; \qquad n = 0,1,2,. \tag{19}$$

Hydrodynamic resonance condition for zero flow into the cavity. Since in this case vortices in the source model move in the x_1-direction, only the x_2 component of the acoustic velocity distribution along the path of the vortices is relevant for the acoustic power produced. The details of the exact distribution of the vertical component of acoustic velocity through the grid have a large effect on the acoustic power. Since we are interested in low frequencies ($\varepsilon = H/L_{eff} << 1$), the acoustic flow through the grid is to first order in ε an incompressible irrotational flow. Although this flow is three dimensional, the velocity field in the opening of a two-dimensional cavity, connected to a two-dimensional half space is sufficient for qualitative purposes. Using this two-dimensional acoustic velocity field, Eq. (12) and the source model of Eq. (5), a rough estimate of the source power can be made. We start with the case when the distance between 2 consecutive vortices is equal to the louver spacing h, hence for $fh/U_c = 1$. In that case the vortices shed in earlier periods each pass the edge of a louver at the moment when a new vortex is formed. In the first part of the next period for all vortices the phase relation between $\underline{u}$ and $(\underline{w} \times \underline{v})$ is such that acoustic energy is absorbed, hence P is negative. Half a period later $\underline{u}$ has changed sign and P becomes positive. For fh/U_c slightly larger than 1, each vortex passes through a region with a large amplitude of the vertical component of $\underline{u}$ (Fig. 4) at the moment when the phase

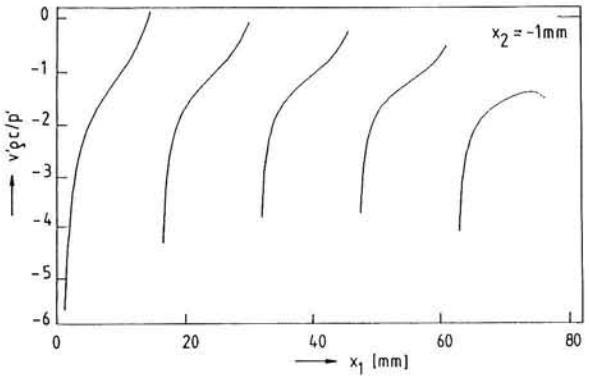

Fig. 4 Component in x_2 direction of two dimensional acoustic velocity distribution for grid geometry of Fig. 1a

relation between $\underline{u}$ and $(\underline{w} \times \underline{v})$ leads to positive acoustic power. Therefore, net acoustic energy production over a period is expected for fh/U_c slightly larger than 1. For very low frequencies $< P >$ is expected to be negative since the vortices have left the grid before $\underline{u}$ changes sign. The behavior of $< P >$ as a function of frequency is sketched in Fig. 5. For those values of fh/U_c where $< P > > 0$, acoustic energy losses due to friction and sound radiation are compensated and steady self sustained flow oscillations result. This situation is expected for fh/U_c slightly larger than 1, or, since U_c is assumed to be close to $U_0/2$, for:

$$Sr_h = fh/U_0 = 0.5, \text{ for } V = 0. \tag{20}$$

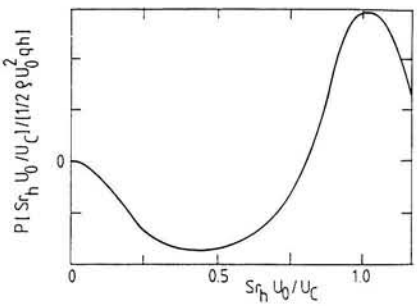

Fig. 5 Nondimensional source power as a function of nondimensional frequency for zero flow into the cavity

Hydrodynamic resonance condition for nonzero flow into the cavity

For this case the path of the vortex has been simplified to 2 straight line segments (section 2.3). The first is parallel to the x_1 direction and the second is parallel to the louvers. Since for $x_2 < 0$ the acoustic velocity is almost parallel to the louvers the contribution of the second segment of the vortex path to P can be neglected (Eq. (12)). Hence Eq. (12) is evaluated along the first segment, with a length of 0.4 h, parallel to the x_1 direction where only the vertical component of $\underline{u}$ is relevant. Again, in the first half of the period after a vortex is formed, P is negative. If the vortex passes through the region of maximum acoustic velocity at the downstream edge of the louver (Fig. 3b) during the first half of the period, the amount of acoustic energy absorption cannot be compensated in the second half, when the vortex passes through a region with much lower acoustic velocity (Fig. 4). Hence, in order to achieve net acoustic energy production over a period, the vortex has to reach the downstream edge of the louver ($x_1 = l/\sqrt{2}$) at $t \approx 1/(2f)$. When we assume that close to the louver $U_c \approx U_0/4$, this leads to:

$$Sr_1 = fl/U_0 = 0.18, \text{ for } V \neq 0. \tag{21}$$

Hence, for the grid geometry with louvers of rectangular cross section at 45° to the grazing flow, if vortices are sucked into the cavity, the rectangular edge of the louver plays an essential role in the mechanism of self sustained oscillations. In that case it is therefore more appropriate to base the Strouhal number on l instead of h. The mechanism is similar to Andersons "Pfeifenton" [22] and Hill and Greene's "whistler nozzle" [23], which were explained using the concept of vortex sound by Bruggeman [24] and Hirschberg [25].

3. Experiments

Experimental Setup

Experimental data were obtained in a wind tunnel with open test section. It has a 200 cm long plenum chamber of 100 × 100 cm^2 cross section with gauze screens, followed by a contraction to 10 × 20 cm^2. Maximum flow velocity is 36 m/s. Flow through the grid into the cavity is induced by a second fan which is connected via a 10 × 100 mm^2 slit in the downstream cavity wall, directly below the grid (Fig. 1a). Flow noise of the wind tunnel itself, measured outside the jet in the test room, is less than 70 dB re 2×10^{-5} Pa ($^1/_3$ octave, frequency range 63 Hz to 1 kHz) for a flow velocity of 20 m/s. A flat plate with a square opening is placed downstream of the contraction. A frame with 6 louvers is placed in the opening (Fig. 1a). The cavity below the grid has a cross section of 100 × 100 mm^2 and a depth of 160 mm. Since the frequency of the flow induced sound is well below the cutoff frequency for non-planar waves (1700 Hz), a single condenser microphone in the cavity bottom gives a non ambiguous measure of the acoustic field. A method was developed to measure

the strength of the aero-acoustic source, using this microphone and an external loudspeaker (section 2).

Steady flow and velocity fluctuations were measured with a constant temperature anemometer (CTA). The sensitive element is a 5 μm tungsten wire with a length of 2.5 mm. By using a standard DISA boundary layer probe, interference of the CTA probe with the shear layer disturbances and generation of spurious feedback signals were minimized. This was sufficient for experiments at $U_0 = 9.5$ m/s. For CTA measurements at $U_0 = 3.6$ m/s, directly above the grid or in the grid openings up to 1 mm below the plane of the wall, the external loudspeaker tuned to the frequency of the self sustained oscillations was used to raise the amplitude of the acoustic field $p'/\rho c$ from 2.5 mm/s without loudspeaker to 5 mm/s. This enhances the acoustic feedback in the shear layer-resonant cavity system so that probe interference is negligible. Horizontal and vertical traverses of the CTA probe were automated using stepper motors (accuracy 0.1 mm). A 4 volt reference voltage was subtracted from the CTA bridge voltage prior to AD conversion to improve the signal to noise ratio by 20 dB. After AD conversion the CTA signal was linearized, average velocity was determined and auto- and cross spectra were calculated from the velocity and acoustic pressure time series by standard FFT methods (0-2000 Hz, $\Delta f = 4$ Hz). The data were processed real time by a microcomputer with array processor.

Acoustic velocity distribution in the cavity opening

In order to check the modeling of the acoustic velocity in the cavity opening with a 2D incompressible flow, the x_1 component of unsteady velocity 1 mm above the grid was measured (Fig. 6a,b). The presence of a very slow steady grazing flow made it possible to take the data with a single wire CTA probe. The acoustic field was induced by an external loudspeaker. Agreement between the data and the 2D incompressible prediction is good. At the upstream and downstream edge of the opening 3D effects become important (Fig. 6a). In the prediction radiation losses are neglected, leading to a predicted phase difference between u' and p' of $\pm 90°$. Since in the experiment radiation losses are small but not zero, the argument of u'/p' is not exactly 90° (Fig. 6b). Overall, a 2D incompressible flow is an adequate model of the acoustic velocity distribution in the cavity opening.

Experiments with Zero Flow Through the Grid into the Cavity

In a first series of experiments the pressure p' was measured at the bottom of the cavity, as a function of steady flow velocity (Fig.2, see also 1. Introduction). The frequency of the flow induced sound (340 Hz) corresponds to a wavelength $\lambda = L_{eff}/4$, in agreement with the resonance condition for the acoustic field, Eq. (19). On the basis of the source model of section 2.2, Eq. (20) predicts $Sr_h = 0.5$ as the hydrodynamic condition for self sustained flow oscillations. In the experiments the maximum amplitude ($2p'/\rho U_0^2 = 0.08$ and $p'/\rho c U_0 = 0.0025$) occurs for $Sr_h = 0.54$. From CTA measurements it appears that the boundary layer at the separation point is laminar with a Blasius velocity profile with $\theta = 0.33$ mm. This yields $f\theta_s/U_0 = 0.012$. Hence,

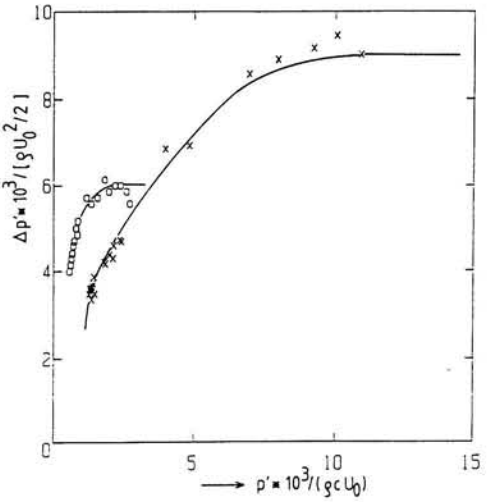

Fig. 6 Strength of aero-acoustic source, determined in experiments from $p' - p'_{ls}$, using Eq. ×: $U_0 = 9.5$ m/s, $V/U_0 = 0.00$, o : $U_0 = 3.6$ m/s, $V/U_0 = 0.14$

condition (1) is satisfied. Further downstream, after the third louver, a rapid change to a linear velocity profile is observed. This is a clear indication of roll up of the shear layer into vortices. Fluctuating velocity measurements 2 mm above the grid show a periodicity of 340 Hz, the frequency of the sound induced by the flow. At short distances downstream of the separation point the fluctuating velocity is a pure sine function of time. At first the amplitude increases exponentially as predicted by linearized theory. Further downstream saturation and harmonic distortion occur. The convection velocity of the shear layer disturbances, as determined from the phase behavior of the 340 Hz fluctuations is close to $U_0/2$.

From flow visualization experiments it appears that for small values of $p'/\rho_0 c U_0$ the shear layer develops instability waves which grow in amplitude until saturation occurs one hydrodynamic wavelength (approx. 15 mm) downstream of the separation point. This results in the formation of discrete vortices. At larger values of $p'/\rho_0 c U_0$, in the moderate amplitude range, vortex formation immediately at the separation point is observed. This leads to the source model developed in section 2, which states that in the moderate amplitude range the aero-acoustic source strength is insensitive to changes of $p'/\rho_0 c U_0$. The strength of the aero-acoustic source was determined experimentally with the method described in section 2, using the external loudspeaker. For different loudspeaker currents, p' at the bottom of the cavity was determined with flow (p') and without flow (p'_{ls}). For small values of $p'/\rho_0 c U_0$, $p' - p'_{ls}$ increases when $p'/\rho c U_0$ is increased, while for $p'/\rho c U_0 > 10^{-3}$, $\Delta p'$ determined from $p' - p'_{ls}$ with Eq. (18) is a constant: $\Delta p' = 0.009\ \rho U_0^2/2$ (Fig.7), independent of $p'/\rho c U_0$, as

predicted by the source model for the moderate amplitude case developed in section 2.

Raising the upstream edge of the cavity opening by means of a two-dimensional ramp has been suggested as a way to suppress flow induced noise [1,2]. In our experiments ramps of 2.5, 5, 10 and 20 mm were tested, for a cavity opening with a total length of 77.5 mm (Fig. 1b). We found that flow induced tones were still present after placing the 2.5 and 5 mm ramps, while noise was suppressed by the 10 and 20 mm ramps. Steady flow velocity measurements downstream of the 5 mm ramp show that the gradient length of the shear layer is equal to approximately 20% of the distance from the ramp, with the shear layer touching the louvers of the grid for the first time at a distance of 10 times the ramp height. This confirms Dunham's recommendation of a safe ramp height of 25% of the length of the cavity opening [1].

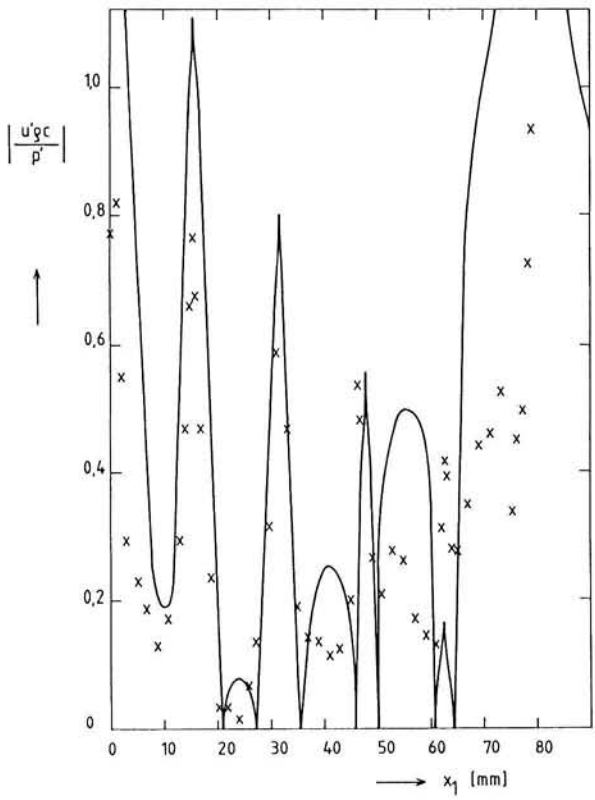

Fig. 7a Modulus of x_1 component of acoustic velocity for x_2 = 1mm (Fig. 1a).
——— : prediction with 2D incompressible flow,
× : experiment

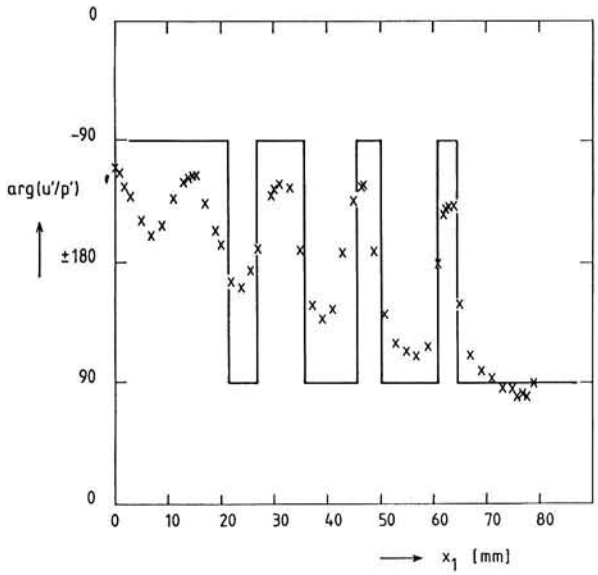

Fig. 7b Phase, relative to unsteady pressure at the bottom of the cavity of x_1 component of acoustic velocity for x_2 = 1mm (Fig. 1a). ——— : prediction with 2D incompressible flow, × : experiment

Finally, the effect of a single array of 2.5 mm teeth (Fig. 1c) 20 mm upstream of the grid was investigated. This array causes the boundary layer to become turbulent. The velocity profile closely resembles the $^1/_7{}^{th}$ power law, with θ = 0.73 mm and $f\theta_s/U_0 = 0.03$ for f = 340 Hz and U_0 = 9.5 m/s. Flow induced tones are now absent (Fig. 2). This is in agreement with data for open cavities reported by other authors [3,4,15]. The value $f\theta_s/U_0 = 0.03$ for suppression of flow induced tones is close to the value predicted by linearized theory (condition (1)). Hence, linearized theory gives an adequate description of the forcing of the shear layer at the separation point in the small to moderate amplitude range.

Experiments with Nonzero Flow Through the Grid into the Cavity

For nonzero flow through the grid, the maximum amplitude of flow induced sound occurs at a steady flow velocity U_0 = 3.6 m/s, a third of the value found in the case of zero flow through the grid (Fig. 2). The value of $Sr_1 = 0.15$ is close to the prediction in section 2 ($Sr_1 = 0.18$) for nonzero flow through the grid. The steady flow is characterized by a thin laminar boundary layer 20 mm upstream of the grid: θ_s = 0.33 mm and $f\theta_s/U_0 = 0.03$. Note that this value of $f\theta_s/U_0$ was sufficient to suppress flow induced tones in the case V = 0. The average steady flow velocity through the grid V affects the amplitude of the flow induced tone. The maximum amplitude of flow induced noise ($2p'/\rho U_0^2 = 0.059$ and $p'/\rho c U_0 = 3.14 \cdot 10^{-4}$) occurs for $V/U_0 = 0.14$. In order to clarify the behavior of the aero-acoustic source, steady and unsteady

velocity profiles in the first two slits of the grid were measured with the constant temperature anemometer for $U_0 = 3.6$ m/s and $V/U_0 = 0.14$. In both slits, the steady flow velocity data show a very thin shear layer separating stagnant air in the wake of the upstream louver from a wall jet that enters the cavity at the upstream side of the next louver. A scan of the fluctuating velocity 1 mm above the whole grid shows that velocity disturbances start to grow at the downstream side of each louver(Fig. 8). When a louver is approached from the upstream side the amplitude of the velocity fluctuations goes to zero. Apparently, vortices are shed at each louver and are convected into the cavity. This confirms the line vortex model for an individual aero-acoustic source downstream of each louver presented in section 2. A striking feature of Fig. 8 is the large amplitude of velocity fluctuations over the second slit, compared to the rest of the grid. Perhaps the different steady flow velocity profiles in the different slits cause this effect. The velocity profile in the second slit would then be the most unstable. In the experiments the convection velocity U_c of the vortices could only be determined some distance away from the louvers. A value of approximately $U_0/2$ was found, confirming the assumption in section 2.

The strength of the aero-acoustic source was determined using the method explained in section 2. For loudspeaker currents above the level where $p'/\rho c U_0 = 10^{-3}$, a source strength $\Delta p' = 0.006\ \rho U_0^2/2$ was found (Fig. 7). The independence of the source strength on $p'/\rho c U_0$ confirms the constant source strength model of section 2.
As for the case of zero flow through the grid, two-dimensional ramps of 2.5, 5, 10 and 20 mm height (Fig. 1b) and arrays of teeth (Fig. 1c) upstream of the cavity were investigated as means for suppression of the flow induced tones. For $V/U_0 = 0.14$ and $U_0 = 3.6$ m/s, flow induced noise is suppressed by the 20 mm ramp, but not by the 2,5, 5 and 10 mm ramps. Hence, flow through the grid reduces the effectiveness of the ramp. For the same flow conditions, a single array of teeth, height $h' = 2.5$ mm, placed 20 mm upstream of the grid has an insignificant effect on the amplitude of flow induced noise. Four arrays of teeth, height $h' = 5$ mm, (7% of the length of the cavity opening) placed upstream of the grid reduce the amplitude of flow induced noise to 35% of the original value (Fig. 2). Apparently, for nonzero flow through the grid this is not a successful strategy for suppression of flow induced noise. Since each louver has its own aero-acoustic source, it seems more appropriate to place an array of teeth, height $h' = 2.5$ mm (3.5% of the length of the cavity opening) on top of each louver. This completely suppresses all flow induced tones (20 dB reduction, see Fig. 2). Deleting rows of teeth on top of some of the louvers causes the flow induced tones to reappear.

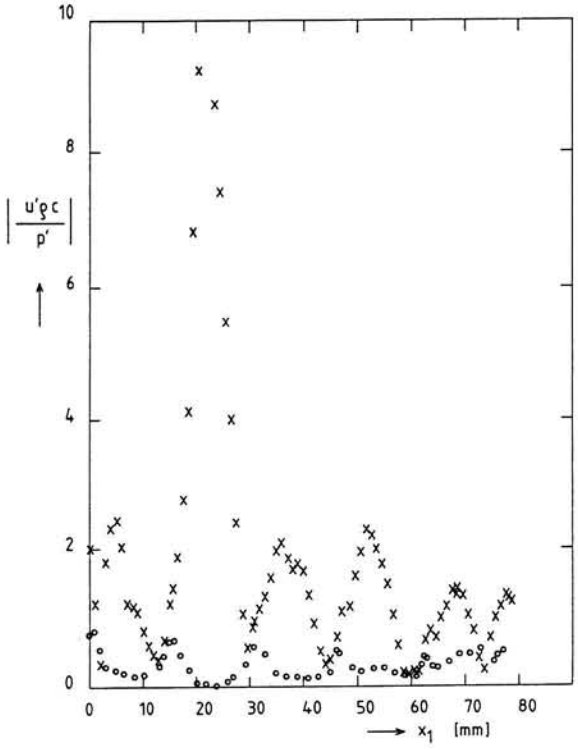

Fig. 8 Modulus of x_1 component of unsteady velocity for x_2 = 1mm (Fig. 1a).
× : U_0 = 3.6 m/s, V/U_0 = 0.14; o : acoustic field only (same data as Fig. 7a)

4. Scaling rules and influence of structural coupling

The theoretical analysis in section 2.4 provides the rules for scaling source strengths $\Delta p' \cdot S$ determined in wind tunnel experiments to different grid sizes, different flow velocities and different fluid densities. However, in underwater applications, the louvers of the grid can in general not be considered rigid. Moreover, bending wave resonances of the louvers can replace cavity resonances as the acoustic component in the feedback loop of self-sustained flow oscillations. In that case the source strength $\Delta p'S$ for moderate amplitudes, determined in a wind tunnel experiment with a rigid grid and a cavity tuned to the fluid loaded resonance frequency of the louvers, can be translated to an oscillatory exciting force for an individual louver. Next, the resonant amplitude of the fluid loaded louvers and the radiated sound can be estimated with the method described by Blake [26] for fluid loaded cylinders. Finally, the ratio of unsteady to steady flow velocity is calculated from the resonant amplitude of the louvers, to check if the moderate amplitude assumption is correct.

5. Conclusions

Aero-acoustic Source

A theoretical analysis, based on the concept of vortex sound by Powell and Howe[11,12], has been presented for the low frequency aero-acoustic behavior of a deep cavity in a plane wall, covered by a grid with louvers at an angle of 45° to the grazing flow. The analysis is limited to low Mach numbers and high Reynolds numbers and is based on the assumption of periodic shedding of line vortices at separation points of the steady flow. The character of the flow above the grid is determined by the ratio of unsteady to steady flow velocity: $p'/\rho cU_0$. For the experiments in the present paper this ratio is in the moderate amplitude range: $10^{-3} < p'/\rho cU_0 < 10^{-1}$. Source models have been developed for $p'/\rho cU_0$ in this range, for the case of grazing flow past the cavity opening and zero flow through the grid into the cavity, and for grazing flow past the cavity opening and nonzero flow through the grid into the cavity. In the first case an unstable shear layer is formed at a single separation point for the steady flow: at the upstream edge of the grid. In the second case the flow separates and unstable shear layers are formed downstream of each louver. Each unstable shear layer is modeled with a single vortex which is assumed to accumulate all the vorticity shed at its steady flow separation point. This leads to source models with source strengths which are independent of the amplitude of the acoustic field. For each case the power delivered by the aero-acoustic source is estimated using the acoustic energy balance for the cavity and a single mode, two dimensional, low frequency approximation of the acoustic velocity distribution in the cavity opening. Hydrodynamic conditions for resonance are derived from the requirement of positive net acoustic energy production by the aero-acoustic source over a period. The theoretical analysis provides the rules for scaling source strengths determined in wind tunnel experiments to different grid sizes, different steady flow velocities and different fluid densities.

Zero flow Through the Grid into the Cavity

Flow visualization and constant temperature anemometry experiments confirm the assumptions on vorticity shedding rate and vortex convection velocity used in the theoretical source model. The theoretical hydrodynamic condition for resonance $Sr_h = 0.5$ is confirmed by the experimental value $Sr_h = 0.54$. The theory explains why for a deep cavity flow induced sound often has a frequency corresponding to a wavelength λ such that $L_{eff} = (2n + 1)\lambda/4$, where L_{eff} is the effective depth of the cavity. An experimental method has been developed to determine the strength of the aero-acoustic source. The constant source strength, implied by the theoretical source model for moderate amplitudes is confirmed by the data.

Nonzero Flow Through the Grid into the Cavity

Measurements of steady and unsteady velocity distributions confirm the concept that vortices are shed at each louver and disappear into the cavity. Since vortices disappear into the cavity, the rectangular edge of the louvers plays an essential role

in the mechanism of self sustained oscillations. Therefore it is appropriate to use a Strouhal number based on louver thickness l instead of louver spacing h. The theoretical hydrodynamic condition for resonance $Sr_l = 0.18$ is reasonably well confirmed by the experimentally determined value $Sr_l = 0.15$. Again the constant source strength implied by the source model for moderate amplitudes is confirmed by the data.

Suppression of Flow Induced Tones

The results of Dunham [1] on the suppression of flow induced cavity resonance by raising the upstream edge with a ramp with a height of 25% of the total length of the cavity opening have been confirmed by the present data for the case of zero flow into the cavity. However, such a high ramp may be objectionable in practical cases. Moreover, the present data suggest that flow through the grid into the cavity reduces the effect of the ramp. In the case of zero flow through the grid into the cavity, the present data suggest that increasing the boundary layer thickness upstream of the cavity, as recommended by several authors [3,4,15] is an effective way to suppress flow induced tones. However, the present data clearly indicate that this strategy does not work for the case of nonzero flow through the grid into the cavity. In that case adding an array of teeth with a height of 15% of the louver spacing on top of each louver completely suppressed all flow induced tones. Deleting rows of teeth from some of the louvers caused the tones to reappear, confirming the concept of an individual aero-acoustic source for each louver.

Acknowledgements

The work described in this paper was carried out in close cooperation with J.C. Vellekoop, F.G.P. van der Knaap and P.J. Keuning.
This research is sponsored by the National Defense Division of the Netherlands Organization of Applied Scientific Research. The calculation of the two dimensional acoustic velocity distribution through the grid was carried out by C.A.F. de Jong. Technical support was provided in particular by A.W. Witvliet, H.M.A. Karreman and A. Huisman. The author wishes to express his appreciation to J.A. Steketee for his encouragements to use the powerful tool of theoretical analysis to solve problems in fluid dynamics.

References

[1] Dunham, W.H., "Flow Induced Cavity Resonance in Viscous Compressible and Incompressible Fluids," ONR Symposium 1963.

[2] Okamura, N., Sasajima, H., Tanida, K., "Vortex Induced Heavy Vibrations in Enclosed Hull Cavities," RINA, 1987.

[3] Rockwell, D., Naudascher, E., "Self Sustaining Oscillations of Flow Past Cavities," ASME J. of Fluids Engineering, Vol 100, pp. 152-165, 1978.

[4] Rockwell, D., "Oscillations of Impinging Shear Layers," AIAA Journal, Vol. 21, pp. 645-664, 1983.

[5] Blake, W.K., Mechanics of Flow Induced Sound and Vibration, Vol. I, pp. 130-218, Academic Press,1986.

[6] Bruggeman, J.C., "Flow Induced Pulsations in Pipe Systems," Thesis Eindhoven University of Technology, 1987.

[7] De Metz, F.C., Farabee, T.M., "Laminar and Turbulent Shear Flow Induced Cavity Resonance," AIAA paper 77-1293, AIAA 4th Aeroacoustics Conference, 1977.

[8] Elder, S.A., "Self Excited Depth Mode Resonance for a Wall Mounted Cavity in Turbulent Flow," J. Acoust. Soc. Am. Vol. 64(3), pp. 877-890, 1978.

[9] Panton, R.L., "Effect of Orifice Geometry on Helmholtz Resonator Excitation by Grazing Flow," AIAA Journal, Vol. 28(1), pp. 60-65, 1990.

[10] Michalke, A.On Spatially Growing Disturbances in an Inviscid Shear Layer," J. Fluid Mech., Vol. 23, pp. 521-544, 1965.

[11] Powell, A., "Theory of Vortex Sound," J. Acoust. Soc. Am., Vol. 36, pp. 177-195, 1964.

[12] Howe, M.S., "Contributions to the Theory of Aerodynamic Sound, with Application to Excess Jet Noise and the Theory of the Flute," J. Fluid Mech., Vol. 71, pp. 625-673, 1975

[13] Elder, S.A., "Forced Oscillations of a Separated Shear Layer with Application to Cavity Flow Tone Effects," J. Acoust. Soc. Am., Vol. 67(3), pp. 774-781, 1980.

[14] Michalke, A., "The Influence of the Vorticity Distribution on the Inviscid Instability of a Free Shear Layer," Fluid Dynamic Trans., Vol. 4, pp. 751-760, 1969.

[15] Shaw, L.L., "Suppression of Aerodynamically Induced Cavity Pressure Oscillations," J. Acoust. Soc. Am., Vol. 66, pp. 880-884, 1979.

[16] Nelson, P.A., Halliwell, N.A., Doak, P.E., "Fluid Dynamics of a Flow Excited Resonance, Part I: Experiment," J. of Sound and Vibration, Vol. 78, pp. 15-38, 1981.

[17] Nelson, P.A., Halliwell, N.A., Doak, P.E., "Fluid Dynamics of a Flow Excited Resonance, Part II: Flow Acoustic Interaction," J. of Sound and Vibration, Vol. 91, pp. 375-402, 1983.

[18] Dobbinga, E., "Preliminary Study of Suction Edges in the Two Dimensional Mini P Wind Tunnel," Internal Report LSW 80-15, Low Speed Wind Tunnel, Delft University of Technology, 1981.

[19] Lesser, M.B., Lewis, J.A., "Applications of Matched Asymptotic Expansion Methods to Acoustics. I. The Webster Horn Equation and the Stepped Duct," J. Acoust. Soc. Am., Vol. 51, pp. 1664-1669, 1972.

[20] Steketee, J.A., Lecture notes Aero 1, Delft University of Technology, Faculty of Aerospace Engineering, 1973.

[21] Morse, P.M., Ingard, K.U., "Theoretical Acoustics," McGraw-Hill, 1968.

[22] Anderson, A.B.C., "Dependence of the Primary Pfeifenton (Pipe Tone) Frequency on Pipe Orifice Geometry," J. Acoust. Soc. Am., Vol. 25, pp. 541-545, 1953.

[23] Hill, W.G.Jr., Greene, P.R., "Increased Turbulent Jet Mixing Rates Obtained by Self-Excited Acoustic Oscillations," Trans. ASME, J. Fluids Engineering, Vol. 99, pp. 520-525, 1977.

[24] Bruggeman, J.C., van Bakel, J.G., van der Knaap, F.G.P., Brackenhoff, H.E.A., "Noise Generation by Gas Flow in a Pipe with an Orifice Plate," Proceedings Internoise 89, pp. 99-102, 1989.

[25] Hirschberg, A., Bruggeman, J.C., Wijnands, A.P.J., Smits, N, "The Whistler Nozzle and Horn as Aero-Acoustic Sources in Pipe Systems," Acustica, Vol. 68, pp. 157-160, 1989.

[26] Blake, W.K., Mechanics of Flow Induced Sound and Vibration, Vol. I, pp. 342-346, Academic Press,1986.

The drift past an airfoil

By R. Coene

Faculty of Aerospace Engineering, TU Delft

1. Introduction

In a celebrated paper by Sir Charles Darwin (1953) it is shown that the 'hydrodynamic mass' (or 'added mass') of a body translating uniformly in an infinite expanse of perfect fluid is equal to the drift-volume multiplied by the density of the fluid. The **added mass** of a body in motion with respect to an infinite expanse of ideal fluid with constant density is a tensor relating the body's six linear and angular velocities to the kinetic energy, T, in the fluid.
For the case with only one linear velocity component, chosen in the x_1 direction and of magnitude U it amounts to m_{11}, given by

$$T = \frac{1}{2} m_{11} U^2. \tag{1.1}$$

One may imagine the flow to be started up impulsively by imparting an impulse I_1 in the x_1 direction with

$$I_1 = m_{11} U. \tag{1.2}$$

The linear momentum L_1, in the x_1 direction, of the fluid can be expressed as

$$L_1 = \rho \int_{V-V_0} u_1 dV, \tag{1.3}$$

where V_o is the displacement volume of the body. From a physical point of view it seems obvious to identify I_1 with L_1:

$$L_1 = I_1, \tag{1.4}$$

but it is well known that the volume integral appearing in (1.3) is only conditionally convergent. The proof of (1.4) depends on the ordering at infinity and involves some artifices of an almost metaphysical nature.

Darwin has defined the **drift-volume** D by considering "an infinite thin plane of fluid, at right angles to the motion, marked so as to be made recognizable, perhaps by means of some dye-stuff". He then goes on to investigate, "after the passage of the body, what is the form assumed by this infinite plane?" He then establishes the surprising fact that the part near where the body has been has drifted forwards in such a way that the volume of fluid, D, between the initial and final positions of the material surface, is equal to the added mass divided by the density ρ of the fluid: (in our notations).

$$D = \frac{m_{11}}{\rho}. \tag{1.5}$$

Obviously, Darwin's beautiful result is of great generality and provides us with an intriguing link between the Eulerian and Lagrangian realms.
Darwin treated the two dimensional case first and then went on to show that (1.5) is also true in the three dimensional case. It can be argued that if (1.5) is true in the three dimensional case it should be true also in the two dimensional case without circulation. As shown by Steketee in detail in Aero I the added mass for a sphere is equal to one half the mass of the fluid displaced by the sphere. In another example, for a two-dimensional case with an elliptic section with half axes a and b moving in the direction of the a axis, the added mass is, $\pi\rho b^2$ per unit length perpendicular to the plane of the section. It doesn't matter whether 2b is the minor or the major axis!

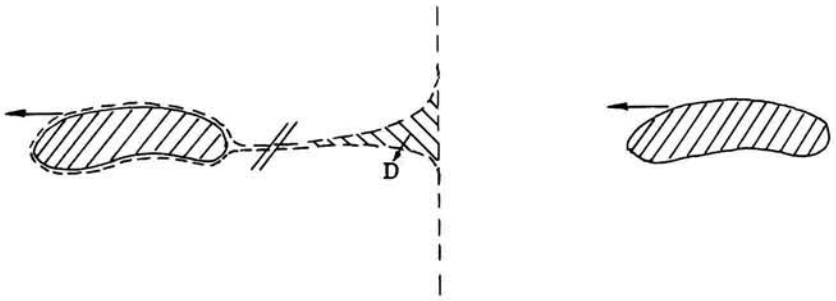

Fig. 1.1 The material surface before and after the passage of the body defines Darwin's drift-volume D

Following Darwin's suggestion to study the drift in classically investigated irrotational flows past bodies, Lighthill (1955) applied the notion of drift to the evaluation of secondary flows with vorticity. More recently Yih (1985) gave some new derivations of Darwin's theorem. Brooke Benjamin (1986) raised some mild objections to Yih's derivations and established some facts about drift which will be discussed in the next sections.

In what follows some new facts will be established about drift in the two dimensional case for airfoils with constant, non-zero, circulation (Γ), defined by

$$\Gamma = \oint \underline{v} \cdot \underline{ds}\,, \tag{1.6}$$

where the contour integral of the velocity $\underline{v}$ is taken around the airfoil. In view of the subtleties involved in the proof of Darwin's theorem it is by no means obvious that flows with $\Gamma \neq 0$ have the property (1.5). As the distantance r from the airfoil tends to infinity, the velocity field behaves like $\Gamma(2\pi r)^{-1}$. It dies out slowly and the difficulties related to the ordering at infinity are expected to be compounded. In de Jongh's master thesis (1987) the drift past various two dimensional contours has been calculated in the neighbourhood of these contours and some of his results will be used in the discussion that follows.

2. Some theorems in two dimensional potential flow

An airfoil which translates in the nullift direction carries no circulation ($\Gamma = 0$) and Darwin's theorem applies without further qualification. The usual definition of the nullift direction for an airfoil with a sharp trailing edge involves satisfying trivially (i.e. with $\Gamma = 0$) a Joukowski condition which ensures a smooth flow at the trailing edge. Dropping this condition for an airfoil which translates in a direction which differs from the nullift direction leads to a potential flow solution where the fluid does not separate from the sharp trailing edge. Such solutions are admissible in a strictly potential flow case and it will be clear that for all solutions with a cyclic constant Γ equal to zero, Darwin's theorem applies.

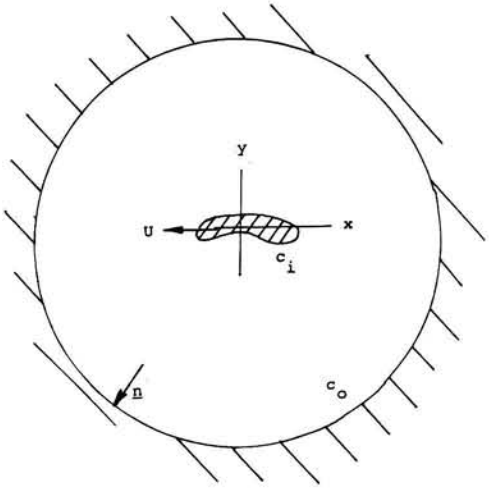

Fig. 2.1

We now consider the case where the airfoil moves to the left, along the (negative) x axis at speed U, carrying a constant circulation. In view of the considerations at the beginning of this section we decompose the velocity potential in two parts

$$\phi = \phi_1 + \phi_2, \tag{2.1}$$

where ϕ_1 is single valued and has the cyclic constant $\Gamma = 0$. Using Green's first identity

$$\iint u\Delta v dxdy + \iint (\frac{\partial u}{\partial x}\frac{\partial v}{\partial x} + \frac{\partial u}{\partial y}\frac{\partial v}{\partial y})dxdy = \oint u\frac{\partial v}{\partial n}\, ds, \tag{2.2}$$

one readily obtains various useful relations. Putting $u = \phi_1$ and $v = x$ one obtains

$$\iint \frac{\partial \phi_1}{\partial x}\, dxdy = \oint \phi_1 \frac{\partial x}{\partial n}\, ds = \oint \phi_1\, dy\,. \tag{2.3}$$

The surface integral is to be calculated over the entire fluid domain, enclosed by the outer and the inner contours C_o and C_i. Since ϕ_1 is 'regular at infinity' the contour integral over C_o vanishes when C_o recedes to infinity and for this limit the inner integral, over C_i, defines the added mass ρA of the airfoil moving in the (-)x direction, per unit length in the spanwise direction by

$$AU = \oint_{c_1} \phi_1 dy\,. \tag{2.4}$$

Putting $u = \phi_1$ and $v = \phi_1$ and $\Delta\phi_1 = 0$ we obtain from (2.2)

$$\iint [(\frac{\partial \phi_1}{\partial x})^2 + (\frac{\partial \phi_1}{\partial y})^2]\, dxdy = \oint \phi_1 \frac{\partial \phi_1}{\partial n}\, ds. \tag{2.5}$$

With the boundary condition

$$\frac{\partial \phi_1}{\partial n} = U n_x, \tag{2.6}$$

the right hand side of (2.5), using (2.4), is equal to U^2A. Then multiplying by $\frac{1}{2}\rho$ we obtain

$$\frac{1}{2}\rho\iint[(\frac{\partial\phi_1}{\partial x})^2+(\frac{\partial\phi_1}{\partial y})^2]\,dxdy=\frac{1}{2}\rho AU^2. \tag{2.7}$$

Now identifying ρA with m_{11} we see that (2.7) reproduces (1.1) and that the right hand side of (1.2) is equivalent to the right hand side of (2.4) multiplied by ρ.
The expression on the right hand side of (2.4) is convenient for the evaluation of the added mass of a given airfoil translating in an arbitrary direction.
In the far field ϕ_1 behaves like

$$\phi_1(x,y)=c_o+\frac{c_1x}{x^2+y^2}+\ldots. \tag{2.8}$$

Expressing c_1 as a contour integral over the airfoil yields

$$c_1=\frac{1}{2\pi}\oint(-x\frac{\partial\phi_1}{\partial n}+n_1\phi_1)\,dc. \tag{2.9}$$

The boundary condition on the airfoil contour is given by (2.6).

Since

$$\oint -xn_x\,dc=S, \tag{2.10}$$

where S is the surface area of the airfoil section and using (2.4) we have from (2.9)

$$c_1=\frac{U}{2\pi}(A+S). \tag{2.11}$$

Equation (2.11) shows that the strength of the dipole field far from the airfoil is proportional to the sum of the added mass and the mass of the fluid displaced by the airfoil per unit length in the spanwise direction.
We now choose the outer boundary of the flow field as a rigid circular cylinder with radius R much larger than the chord c of the airfoil and its centre in the airfoil. In order to satisfy the boundary condition at this cylinder:

$$\underline{v}\cdot\underline{n}=0, \tag{2.12}$$

we superimpose a solution

$$\phi_1^* = c_1 x R^{-2}, \tag{2.13}$$

which can be interpreted as the image of the inner dipole in the cylinder, which generates a uniform parallel flow within the cylinder with velocity $c_1 R^{-2}$ in the positive x direction which tends (rapidly) to zero with $R \to \infty$.
Since c_1 is given by (2.11) the reflux due to ϕ_1^* is proportional to (A + S).
At the dotted material surface in Fig. 2.1, one has, invariably and at every instant, by continuity,

$$\int \nabla\phi_1 \cdot \underline{n}\, ds = 0. \tag{2.14}$$

Since the contribution of ϕ_1^* to the driftvolume is A + S, Fig. 2.1 shows that we must have

$$A + S = D + S, \tag{2.15}$$

implying Darwin's theorem

$$A = D. \tag{2.16}$$

3. The acyclic case

In this section we assess the effect of the cyclic constant Γ given by (1.6)

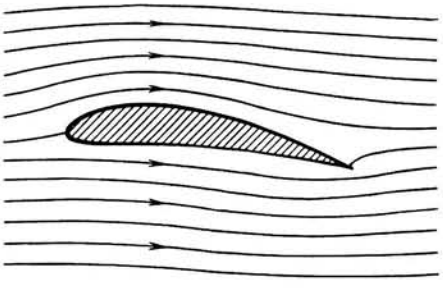

Fig. 3.1 The single valued case ϕ_1

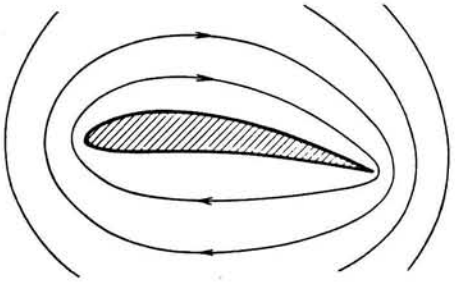

Fig. 3.2 The acyclic solution ϕ_2 with $\Gamma \neq 0$

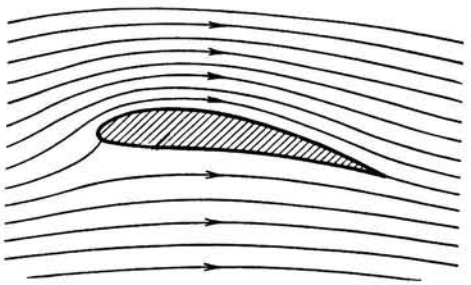

Fig. 3.3 Γ can be chosen to satisfy Joukowski's condition at a sharp trailing edge

It should be noted that the streamlines in Figs 3.1 to 3.3 are sketched for a coordinate system fixed to the airfoil so that the flow is steady for an airfoil translating at constant velocity $\underline{U}$. When passing to the coordinate system fixed to the air at rest far from the airfoil the flow is unsteady with ϕ (x + Ut,y) and, invariably,

$$\frac{\partial}{\partial t} = U\frac{\partial}{\partial x}. \tag{3.1}$$

In a potential flow one has

$$\nabla \cdot (\phi \nabla \phi) = \nabla \phi \cdot \nabla \phi. \tag{3.2}$$

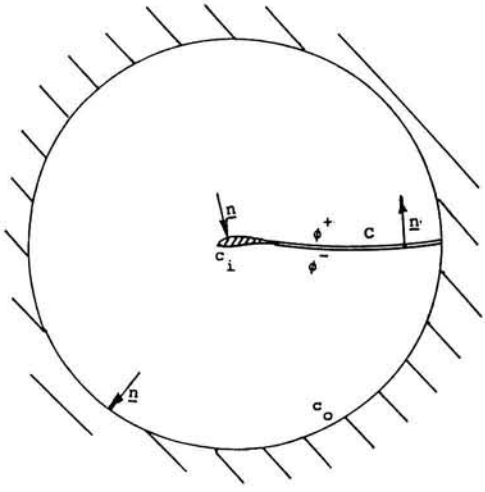

Fig. 3.4 In the doubly connected region a cut C is introduced with $\phi^+ - \phi^- = \Gamma$

Using the divergence theorem and (3.2) we obtain for the kinetic energy in the flow

$$\frac{1}{2}\rho\iint \nabla\phi \cdot \nabla\phi \, dxdy = \frac{1}{2}\rho \int_{c_i+c_o} \phi \, \frac{\partial\phi}{\partial n} dc - \frac{\rho\Gamma}{2}\int_C \frac{\partial\phi}{\partial n} dC. \tag{3.3}$$

Now using the decomposition

$$\phi = \phi_1 + \phi_2, \tag{2.1}$$

with the boundary conditions

$$\frac{\partial\phi_1}{\partial n} = Un_x, \frac{\partial\phi_2}{\partial n} = 0 \tag{3.4}$$

at the airfoil c_i. On the other hand, at the rigid outer boundary, c_o, one has

$$\frac{\partial\phi_1}{\partial n} = 0, \frac{\partial\phi_2}{\partial n} = 0, \tag{3.5}$$

Substituting ϕ_1 and ϕ_2 in (3.3) shows

$$\frac{1}{2}\rho\iint \nabla\phi_1 \cdot \nabla\phi_2 \, dxdy = 0 \tag{3.6}$$

and

$$\frac{1}{2}\rho\iint (\nabla\phi)^2 \, dxdy = \frac{1}{2}\rho\int_{c_i} \phi_1 \frac{\partial\phi_1}{\partial n} dc - \frac{1}{2}\rho\Gamma\int_C \frac{\partial\phi_2}{\partial n} dC. \tag{3.7}$$

From (3.6) it is clear that $\nabla\phi_1$ and $\nabla\phi_2$ are orthogonal in an integral sense and (3.7) shows that in order to start up the flow impulsively one needs two independent terms; one involving only ϕ_1 at the airfoil and another one proportional to the flux through C due to ϕ_2 only. Clearly, the latter term is independent of the position of C but will tend, logarithmically, to infinity when c_o is made to recede to infinity. For a concentrated vortex the kinetic energy is infinite anyway since the velocity field behaves like 1/r. In the airfoil case however, this difficulty does not arise in the near field since the vortex can be smeared out over the surface of the airfoil or within the airfoil. Of course the kinetic energy related to ϕ_2 remains infinite however, when c_o recedes to infinity.

It should be observed that in the decomposition (2.1) ϕ_1 does not represent the so called nullift solution, although ϕ_1 implies that there is no circulation and no lift. Since ϕ_2 is used to satisfy the Kutta-Joukowski condition, ϕ_1 is identical to the nul-lift solution only when this condition happens to be satisfied with $\phi_2 = 0$, i.e. when the airfoil translates in the nullift direction. One may say that here ϕ_1 represents the solution which leads to no lift for any direction of translation.

For convenience we assume that c_o is a circular cylinder with its center on the x-ais with x = 0 and supplement the bound vortex Γ within the contour with a vortex $-\Gamma$ at the image point $x = -r^2/a$ when the bound vortex is at $x = -a$. It is easily verified that this combination satisfies the boundary condition at c_o. Then with $d/dt(a) = -U$, the surface pressure at c_o yields the Kutta force

$$L = \rho U \Gamma, \tag{3.8}$$

perpendicular to the direction of motion. It is easily shown that (3.8) is exact if the vortex moves along a radius. For a vortex moving in a non radial direction however, (3.8) is true for $a/r \to 0$ only.

Now consider the (Eulerian) surface given by, say x = 0, which opens up when it is pierced by the passing airfoil like a diaphragm.We can now simply superimpose the momentaneous fluxes due to ϕ_1 and ϕ_2. The contribution due to ϕ_1 was discussed in section 2.
If the airfoil has moved from the far right to the far left through this surface, the global drift (A+S) to the right is balanced by a more local drift to the left (D+S), which by virtue of the continuity yields Darwin's theorem, A = D.

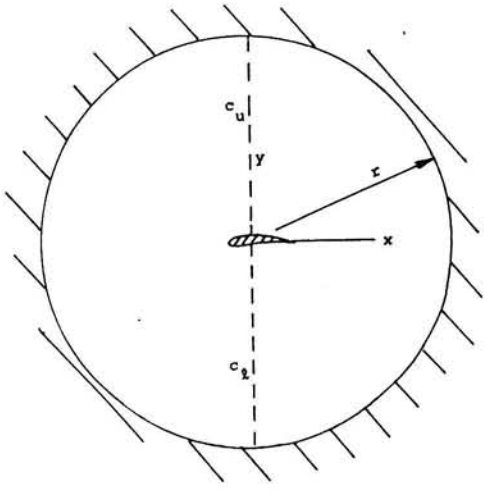

Fig. 3.5 The diaphragm $c_u + c_l$

By virtue of the fact that ϕ_2 gives contributions to the flux through c_u and c_l (see Fig 3.5), which balance at every moment, ϕ_2 does not contribute to the drift volume and Darwin's theorem remains valid.

It should be observed that although the drift volume appears to be unaffected by the presence of a cyclic constant (Γ) this conclusion depends on the assumptions made for the boundary conditions at infinity. Moreover, the details of the geometry of Darwin's material surface, after the passage of the airfoil, are obviously strongly affected by the circulation.

In the next section we calculate some properties of the deformation of Darwin's surface for cases with $\Gamma \neq 0$ which may be of some practical interest.

4. Some properties of the drift past an airfoil

Before proceeding to the case of an airfoil with $\Gamma \neq 0$ we consider an isolated vortex.

4.1. The flux of a moving vortex

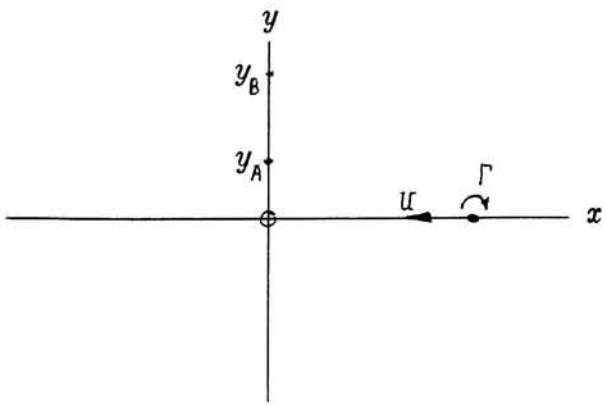

Fig. 4.1 A vortex moving along the x-axis

The complex velocity potential of a vortex with constant strength Γ moving at constant speed U along the x-axis, in the negative direction, can be expressed as

$$\chi(z,t) = \frac{i\Gamma}{2\pi} \ln(z - x_o + Ut). \tag{4.1}$$

It is seen from (4.1) that the vortex is at $z = x_o$ at $t = 0$. For $Ut = x_o$ the vortex passes through the origin. From (4.1) we obtain the velocity field (u,v) with

$$u = \frac{\Gamma}{2\pi} \frac{y}{(x - x_o + Ut)^2 + y^2}, \tag{4.2a}$$

$$v = \frac{\Gamma}{2\pi} \frac{-(x - x_o + Ut)}{(x - x_o + Ut)^2 + y^2}. \tag{4.2b}$$

The flux through the line, or any curve, connecting y_A and y_B is given by

$$F(y_A, y_B, t) = \int_{y_A}^{y_B} u\, dy = \frac{\Gamma}{2\pi} \int_{y_A}^{y_B} \frac{y\, dy}{(Ut - x_o)^2 + y^2} = \frac{\Gamma}{4\pi} \ln \frac{(Ut - x_o)^2 + y_B^2}{(Ut - x_o)^2 + y_A^2}. \tag{4.3}$$

Integrating with respect to time yields the contribution $D(y_A, y_B)$ to the drift volume:

$$D(y_A, y_B) = \frac{\Gamma}{4\pi} \lim_{x_o \to \infty} \int_o^{\infty} \ln \frac{(Ut - x_o)^2 + y_B^2}{(Ut - x_o)^2 + y_A^2}\, dt = \frac{\Gamma}{2U} (y_B - y_A). \tag{4.4}$$

We note that (4.4) depends only on the length of the line element and not on its position. We also observe that when the vortex has moved through the positive x-axis to the origin (i.e. to below the line (y_A, y_B)), the contribution to the drift volume is one half of the right hand side of (4.4). For a fixed value of Γ the contribution to the drift is inversely proportional to U. On the positive side of the y axis (4.4) is positive but it will be clear that the corresponding result for a line element on the negative part of the y-axis yields a negative contribution which precisely balances (4.4) whenever the elements have the same length.

4.2 The fluid entrained by a vortex and a vortex layer

It may be noted that the steady flow around a bound vortex (see Fig. 4.2), or equivalently, the flow seen by an observer moving steadily with the vortex at speed U through fluid at rest, is characterized by the fact that the part of the fluid enclosed by the streamline through the stagnation point, may be replaced by a (rigid) body with both A and S of $O(\Gamma/U)^2$.
This body, however, is speed dependent and the A and S which might be assigned are of a different nature than for a rigid body with A and S independent of the speed. In the limit with $U \to \infty$ this body would collapse.

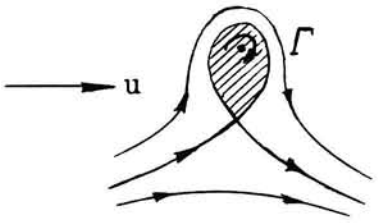

Fig. 4.2 The steady flow around a bound vortex

Obviously, with a vortex distribution at the surface of an airfoil the role of this body is played by the airfoil, and the effect of A and S is already accounted for by the solution ϕ_1 of section 2. Up to the limit of supercirculation (when the stagnation points at the airfoil would coalesce) the A and S need not be modified to account for the 'body' in Fig. 4.2
Moreover, from the fact that (4.4) depends only on the length $(y_B - y_A)$ and not on the distance of the element from the x-axis, we conclude that an airfoil moving along the x-axis contributes to (4.4) in proportion to the total amount of circulation it carries:

$$\Gamma = \oint \underline{v} \cdot \underline{ds} = \oint \nabla\phi_2 \cdot \underline{ds} = \oint \gamma_2 ds\,, \tag{4.5}$$

where γ_2 is the strength of the vortex layer at the airfoil contour which may be used to generate ϕ_2. It now becomes obvious that the vortex layer γ_1 at the airfoil contour which generates ϕ_1 and has strength $\gamma_1 = \partial\phi_1/\partial s$ and $\oint \gamma_1 ds = 0$ does not contribute to (4.4) in an infinite expanse.

We conclude that Darwin's drift volume can only stem from the flux through the smallest possible hole in the Eulerian surface through which the airfoil can pass.

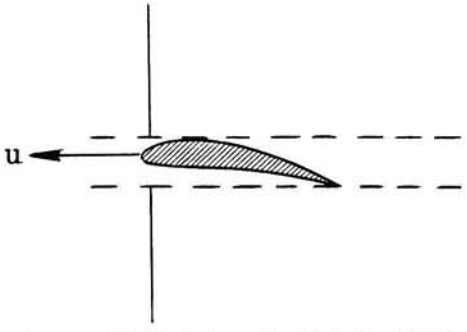

Fig. 4.3 The smallest possible hole through which the airfoil can pass

We thus obtain the result

$$D(y_A^+, y_B^+) + D(y_A^-, y_B^-) = 0, \tag{4.6}$$

for

$$y_B^+ - y_A^+ = y_A^- - y_B^-. \tag{4.7}$$

Equation (4.6) is similar to Brooke Benjamin's result for the cyclic case. The additional condition (4.7) permits the generalization to the acyclic case. For $y_B{}^+ \to \infty$ one may require $y_B{}^+ = -y_B{}^-$, equivalent to defining a principle value, in an infinite expanse.

5. Examples

In the classical case of a circular arc clearly explained in Aero II by Steketee, one readily establishes some properties of the drift.

At zero angle of incidence, the Joukowski condition at the trailing edge leads to a solution without leading edge suction. In this case the zero angle of attack is the 'ideal' angle of attack, but one has $\Gamma \neq 0$ for a finite radius of curvature. This may be shown by using a conformal mapping to the flow around a circular cylinder (see Fig. 5.1).

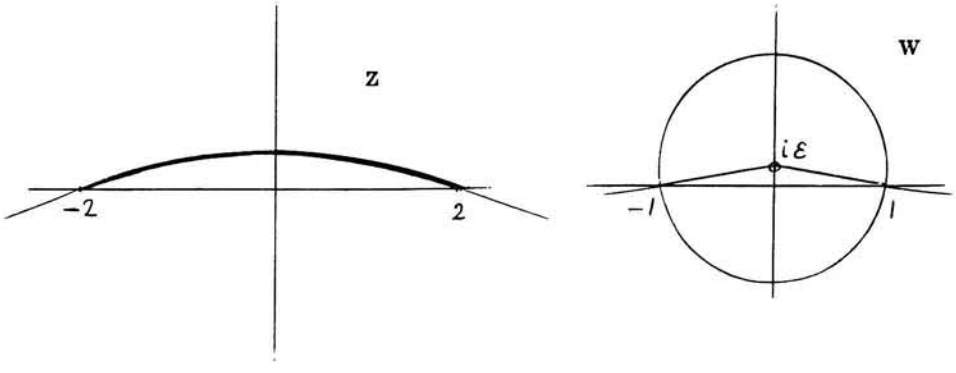

Fig. 5.1 A conformal mapping z=w+1/w for a circular arc

The complex potential in the w plane may be expressed as

$$\chi(w) = \chi_1(w) + \chi_2(w) = U\left(w + \frac{1+\varepsilon^2}{w - i\varepsilon}\right) + \frac{i\Gamma}{2\pi}\ln(w - i\varepsilon) + c. \qquad (5.1)$$

Requiring that w = 1 be a stagnation point (equivalent to requiring 'smooth flow' at z=2) yields

$$\Gamma = 4\pi U\varepsilon. \qquad (5.2)$$

We now calculate the time it takes for a fluid element just above and just below to pass along the circular arc for the case of small curvature ($\varepsilon << 1$).

For the upper side we have

$$t^+ = \int_{t_A^+}^{t_B^+} dt = \int_0^{S_B^+} \frac{ds}{\left\{(U+u^+)^2 + v^{+2}\right\}^{1/2}} = \int_{x_A^+}^{x_B^+} \frac{dx}{U+u^+} = \frac{x_B^+ - x_A^+}{U} - \frac{1}{U^2}\int_{x_A^+}^{x_B^+} u^+ dx + O(\varepsilon^2) \qquad (5.3)$$

And for the lower side:

$$t^- = \int_{t_A^-}^{t_B^-} dt = \frac{x_B^- - x_A^-}{U} - \frac{1}{U^2}\int_{x_A^-}^{x_B^-} u^- dx + O(\varepsilon^2). \qquad (5.4)$$

We thus find for the difference in time:

$$t^- - t^+ = + \frac{1}{U^2}\int_o^c (u^+ - u^-)\, dx = \frac{\Gamma}{U^2} + O(\varepsilon^2), \qquad (5.5)$$

where Γ is $O(\varepsilon)$ and given by (5.2).
In de Jongh's master thesis it has been shown that the exact value of the time difference for a circular arc is given by

$$t^- - t^+ = \frac{\Gamma}{U^2}(1 + \varepsilon^2)^{1/2}. \qquad (5.6)$$

It follows that the error in (5.5) is actually only $O(\varepsilon^3)$ as might have been expected by those who are familiar with linearized wing theory. On the other hand it should be observed that the integrals appearing in (5.3) are not invariant under conformal mapping. In fact it can be shown that the time difference for fluid elements passing

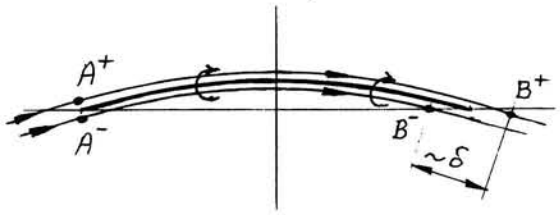

Fig. 5.2

along the upper and lower sides of a circular cylinder (Fig. 5.1) remains precisely equal to zero when the particles start in perfect opposition with respect to the stagnation streamline. A particle on the stagnation streamline never really gets to the stagnation point and a particle in the stagnation point never leaves it so one needs the artifice of a slight but symmetrical displacement in order to get finite values, of the same type as Cauchy principle values for an integral.
From (5.5) we conclude that for two particles which arrive in perfect opposition at the leading edge and are separated by the airfoil experience a dislocation δ given by

$$\delta = \frac{\Gamma}{U} + O(\varepsilon^2), \tag{5.7}$$

when they have arrived in the 'wake'. From the derivation of (5.5) it will be clear that (5.5) and (5.7) will remain valid for a large class of thin airfoils. It can also be verified that for a flat plate under incidence the errors in (5.5) and (5.7) are only $O(\alpha^3)$ when α is the angle of incidence.
The dislocation (5.7) is at variance with the bogus argument to explain the lift of an airfoil by assuming that twin particles, separated by the airfoil should meet again at the trailing edge.

Summarizing, we conclude to the qualitative evolution of Darwin's material surface for an airfoil as shown in Fig. 5.3

The results of section 4 explain that Darwin's material surface must look like the curve (a) when the airfoil has approached it to within a finite distance. The asymptotes are given by straight lines at a distance $\Gamma(4U)^{-1}$ from the reference surface. When the airfoil has pierced the reference surface, roughly speaking halfway, the surface is given by the curve (b). With the reference surface at the trailing edge the drift surface tends to be displaced twice as much in the near field as in the far field (i.e.$\Gamma(2U)^{-1}$ and $\Gamma(4U)^{-1}$). Far behind the airfoil, with $x>>c$, when c is the airfoil chord, we can distinguish two limits (see curve (d)), one with $|y|>>x$ and one with $|y|<<x$. With

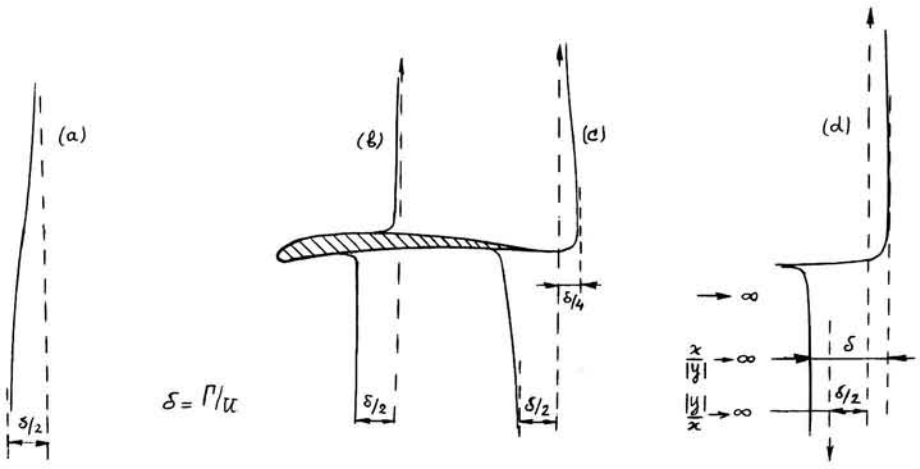

Fig. 5.3 Darwin's drift surface at various stages of evolution

$|y|>>x$ the asymptotes for the displacements with respect to the reference surface are given by $\Gamma(4U)^{-1}$). Approaching from the far field the curve for $y > 0$ tends to an asymptote $\Gamma(2U)^{-1}$) and then sharply bends back to the trailing edge. For $y < 0$ the curve tends to $\Gamma(2U)^{-1}$) and then also turns to the trailing edge. The sharply cusped deformation takes place over a distance $O(\varepsilon^2)$ in the y-direction while the deformation in the x-direction is O(1). By virtue of Darwin's theorem the volume within this strongly cusped region is only $O(\varepsilon^2)$.

6. Concluding remarks

The dislocation δ given by (5.7) is $O(\alpha)$ in the terminology of linearized airfoil theory. In fact, for an airfoil with a chord c at an angle of incidence α one has, for the leading term of $O(\alpha)$:

$$\frac{\delta}{c} = \frac{\Gamma}{Uc} = \pi\alpha = \frac{1}{2}C_L. \tag{6.1}$$

Obviously, the result (6.1) shows that the dislocation δ is not negligible with respect to the chord c for values of C_L of O(1). Two applications come to mind:

(i) The helical vortex layer in the wake of a propeller is distorted by a wing behind a propeller in approximately the way described in Fig. 5.3. This should lead to unsteady loadings on the wing and its flaps and ailerons which cannot be understood without the dislocation effect.

(ii) The response of an airfoil to turbulence is obviously affected by the type of dislocation effects described in this paper for reduced frequencies k = O(1) and larger.

We are now in a position to discuss some properties of the material surface (the dotted line) in Fig. 1.1 for the two-dimensional case. For a symmetrical body with $\Gamma = 0$ moving along the axis of symmetry, the x-axis, the drift surface will also be symmetrical with respect to the x-axis. All particles on the surface which were originally at the same distance from the x-axis will remain symmetrically disposed after the passage of the body. In the more general case without symmetry, but still with $\Gamma = 0$, this is not the case and two particles originally on the surface at the same distance from the x-axis will not end up symmetrically disposed. In a region close to the stagnation streamline leaving the body one also has dislocation which is of a much more local nature than the more global dislocation we found in sections 4 and 5 for cases with $\Gamma \neq 0$. For bodies with blunt leading edges and a finite radius of curvature in the region of the stagnation point, Darwin's surface folds around the body but there will be no cut or hole in it. In the case of a thin airfoil, such as a circular arc, at ideal angle of attack, Darwin's surface will be cut and the particles will spend finite times 'in contact' with the airfoil. Then Darwin's surface, after passage of the body will not exhibit the infinitely long cusp which is shown in Fig. 1.1, but the airfoil opens the curtain by an amount Γ/U.

These considerations make it clear that, although the particles may suffer displacements of strongly different orders of magnitude in the different cases this is irrelevant for the validity of Darwin's theorem which is only a statement on the drift volume. In the context of the airfoil case the drift volume remains $O(\varepsilon^2)$ but the extension of the drift volume and the drift surface in the direction of motion may be infinite, O(1), or $O(\varepsilon)$.

From the viewpoint of thin airfoil theory it would have been more natural to treat the $O(\varepsilon)$ drift which arises due to the circulation first, and the $O(\varepsilon^2)$ terms relevant to Darwin's theorem only in the second place as a correction to the first order results. In such an approach, however, one would probably have overlooked the more general integral properties which do not depend on orders of approximation. Generally speaking, however, it hardly deserves recommendation to construct $O(\varepsilon)$ corrections to an $O(\varepsilon^2)$ theory! I hope that my friend and teacher Professor Steketee, to whom this paper is dedicated, will forgive me this risky evolution.

References

Benjamin, T.B. 1980. Note on added mass and drift. J.Fluid Mech 169, 251-256.

Darwin, C. 1953. Note on hydrodynamics. Proc.Camb. Phil.Soc 49. 342-354.

Jongh, F.H.C. de 1987. Drift in 2D potentiaalstromingen. Master thesis TU Delft.

Lighthill, M.J. 1956. Drift. J.Fluid Mech 1, 31-53.

Steketee, J.A. 1973, 1975. Lecture notes Aero I, II.

Yih, C.S. 1985. New derivations of Darwin's theorem. J.Fluid Mech 152, 163-172.

The flamelet concept for turbulent combustion

By A.J.P.M. van Esch

Faculty of Aerospace Engineering, TU Delft

1. Introduction

Turbulent flows involving chemical reactions are found in many practical situations, for instance in burners in powerplants, jet engines, rocket engines, fires, car engines, wakes of bodies (re)-entering the atmosphere at high speeds. For various reasons calculation methods for turbulent reacting flows are becoming increasingly important. For instance from an environmental point of view it is important to know something about the formation of pollutants like NO_x, and with increasing fuel prices, a detailed knowledge of the processes occurring in engines and powerplants may contribute to the design of more fuel efficient devices.

Turbulent chemically reacting flows can be divided into two categories : premixed and non-premixed, depending on whether the reactants are mixed before chemical reaction or enter the reaction chamber in separated feeds. In the following we are mainly interested in non-premixed combustion, although a large part of the theory also applies to premixed combustion. For studying turbulent non-premixed flames (diffusion flames) a number of theoretical models has been developed. Each of them has its advantages and disadvantages. The simplest way to model a chemically reacting flow is the chemical equilibrium model, where it is assumed that chemical equilibrium is established in every point in the flowfield. It will be clear that in turbulent combustion where we have to deal with non-equilibrium effects like ignition and extinction, the chemical equilibrium model is not a good way of describing the reacting flowfield. Different models are developed when equilibrium is not assumed, then use is made of finite rate kinetics or the assumption is made that the reaction is very fast compared to the diffusion of the reactants. Modelling chemically reacting flows is greatly simplified if a conserved scalar formalism is employed. A conserved scalar is a variable (a scalar variable) which does not change under chemical reaction (e.g. the mass fraction of some element). In non-premixed combustion the reactants are initially separated. When the different feeds of reactants are brought together a reaction is possible. This reaction can only take place at the position where the reactants meet each other, and a flamesheet will be formed. If the chemical reaction is very fast compared to the diffusion this flamesheet will be very thin. In case of a laminar

flowfield, a laminar diffusion flame will exist. The case of a laminar diffusion flame has extensively been studied in the past by for instance Buckmaster and Ludford [1]. In practical cases however the flowfield will often be turbulent and the laminar diffusion flame model will lead to large errors when applied to turbulent combustion. There is however a way for including turbulence effects in the laminar diffusion flame model. This is done by weighting the instantaneous values of the laminar flame with a certain probability function. In that way averaged values of the variables can be obtained. This model is called the turbulent diffusion flame model. Although the turbulent diffusion flame model describes the turbulent combustion flow better than the equilibrium- and laminar diffusion flame model, it still lacks the modelling of the turbulence-combustion interaction. A model based on the laminar flamelet concept may bring us closer to the complete modelling of the turbulence-combustion interaction. What the laminar flamelet model exactly involves will be described in the next section.

2. The laminar flamelet concept

From experiments it is seen that at a microscopic level, a turbulent flame can be seen as a collection of laminar flames. Following this experiments Williams [2] introduced the concept of laminar diffusion flamelets. In the laminar diffusion flamelet concept the turbulent diffusion flame is thought to be an ensemble of laminar diffusion flamelets. A flamelet is a very thin layer embedded within the turbulent flow. In this flamelet the reaction takes place. Each flamelet has the structure of a laminar diffusion flame. The structure of the flamelet is influenced by the turbulent flowfield. Because of the velocity gradients present in a turbulent flow, the flamelet will be stretched. This stretching may result in extinction of the flamelet. If a flamelet (or a number of flamelets) is quenched, the reaction rate decrease because the number of burning flamelets is reduced. The main problem in the flamelet models is to determine whether a particular flamelet is burning or not. The implementation of the flamelet concept is based on the development of a library of flamelet profiles, each of which is characterized by the value of the stretching rate. The idea is then to determine the probability that a particular flamelet profile exists at a point in the turbulent flowfield.

3. Frequently used dimensionless coefficients in combustion

In flow problems the conservation equations can often be written in forms involving dimensionless ratios of transport coefficients. Some of the most important dimensionless coefficients frequently used in combustion flow equations are listed below.

The Lewis number, which is a measure of the ratio of the energy transported by conduction to that transported by diffusion, is defined as :

$$L_e = \frac{\lambda}{\rho c_p D} \tag{3.1}$$

The Prandtl number, which is a measure of the relative importance of the momentum transfer and the heat transfer, is defined as :

$$\sigma = \frac{c_p \mu}{\lambda} \tag{3.2}$$

The Schmidt number, which is a measure of the relative importance of the momentum transfer and the mass transfer, is defined as :

$$S_c = \frac{\nu}{D} \tag{3.3}$$

The Lewis- and the Schmidt number may be defined for each pair of species present in the multi component mixture.
In many situations the Lewis- Schmidt- and Prandtl number are close to one and so it is often allowed to assume the value one for these numbers.
Another dimensionless number used in combustion is the Damköhler number. The Damköhler number is defined as the ratio of a representative fluid time to the reaction time scale. When modelling diffusion flames, the Damköhler number is mostly defined as:

$$D_a = \frac{\textit{diffusion time scale}}{\textit{reaction time scale}} \tag{3.4}$$

4. Equations for a reactive gas flow

We consider a multi component gas mixture with N species and M elements. Then the system can be described by the following (conservation) equations [3]:

Conservation of mass:

$$\frac{\partial \rho}{\partial t} + \frac{\partial}{\partial x_k}(\rho u_k) = 0 \quad k = 1,2,3 \tag{4.1}$$

Conservation of momentum:

$$\frac{\partial \rho}{\partial t}(\rho u_i) + \frac{\partial}{\partial x_k}(\rho u_k u_i) = -\frac{\partial p}{\partial x_i} + g_i + \frac{\partial}{\partial x_k}\tau_{ik} \quad i,k = 1,2,3 \tag{4.2}$$

Where

$$\tau_{ik} = \mu[\frac{\partial u_i}{\partial x_k} + \frac{\partial u_k}{\partial x_i}] - (\frac{2}{3}\mu - \kappa)\frac{\partial u_i}{\partial x_i}\delta_{ik} \tag{4.3}$$

By making the following assumptions :

1 The Dufour and Soret effects are neglected.
2 The kinetic energy per unit mass compared to the mixture enthalpy per unit mass is neglected.
3 The viscous dissipation is neglected.
4 The radiant energy transfer is neglected.
5 The work associated with the action of body forces is neglected.

The equation for the conservation of energy can be written as

$$\frac{\partial}{\partial t}(\rho h) + \frac{\partial}{\partial x_k}(\rho u_k h) = \frac{\partial p}{\partial t} + \frac{\partial}{\partial x_k}[\frac{\mu}{\sigma}\frac{\partial h}{\partial x_k} + \mu[\frac{1}{S_c} - \frac{1}{\sigma}]\sum_{i=1}^{N} h_i \frac{\partial Y}{\partial x_k}] \tag{4.4}$$

Where h_i is the enthalpy of species i (considered to be a known function of T)
h is the mixture enthalpy:

$$h = \sum_{i=1}^{N} h_i Y_i \tag{4.5}$$

Y_i is the mass fraction of species i, defined as:

$$Y_i = \frac{m_i}{\sum_{j=1}^{N} m_j} \qquad with \sum_{i=1}^{N} Y_i = 1 \tag{4.6}$$

Conservation of species

$$\frac{\partial}{\partial t}(\rho Y_i) + \frac{\partial}{\partial x_k}(\rho u_k Y_i) - \frac{\partial}{\partial x_k}(\rho D \frac{\partial Y_i}{\partial x_k}) = W_i \qquad i = 1..N \tag{4.7}$$

Where W_i is the rate at which species i is produced by the chemical reaction.

From the definition of the enthalpy it follows :

$$dh = c_p dT + \sum_{i=1}^{N} h_i dY_i \tag{4.8}$$

Where

$$c_p = \sum_{i=1}^{N} c_{p_i} Y_i \tag{4.9}$$

By substituting equation (4.8) in the energy equation (4.4), we obtain:

$$\frac{\partial}{\partial t}(\rho T) + \frac{\partial}{\partial x_k}(\rho u_k T) - \frac{\partial}{\partial x_k}\left(\frac{\lambda}{c_p}\frac{\partial T}{\partial x_k}\right) = \frac{1}{c_p}\frac{\partial p}{\partial t} - \sum_{i=1}^{N}\frac{h_i}{c_p}W_i + \sum_{i=1}^{N}\frac{\lambda c_{p_i}}{c_p^2}\frac{\partial T}{\partial x_k}\frac{\partial Y_i}{\partial x_k} \tag{4.10}$$

In (4.10) the assumption $S_c = \sigma = 1$ (this means that $L_e = 1$) is used. The first and last term of the righthand side of (4.10) can normally be neglected.

We now introduce the element mass fraction in the analysis. The element mass fraction of element i, Z_i, is defined as:

$$Z_i = \sum_{j=1}^{N} \alpha_{ij} Y_j \qquad i = 1..M \tag{4.11}$$

Where α_{ij} is the number of grams of element i in species j. Because no atoms are formed nor destroyed, it follows:

$$\sum_{j=1}^{N} \alpha_{ij} W_i = 0 \qquad i = 1..M \tag{4.12}$$

Upon multiplication of equation (4.7) with α_{ij} and summation we find:

$$\frac{\partial}{\partial t}(\rho Z_i) + \frac{\partial}{\partial x_k}(\rho u_k Z_i) - \frac{\partial}{\partial x_k}(\rho D \frac{\partial Z_i}{\partial x_k}) = 0 \qquad i = 1..M \tag{4.13}$$

Since no source term is present in the right hand side of (5.10), the element mass fraction is a so called conserved scalar.

5. The flamelet formulation

We consider a combustion problem where pure fuel is mixed with an oxidizer stream containing no fuel, a so called two feed combustion problem. The element mass fractions can be normalized yielding:

$$Z = \frac{Z_i - Z_{i2}}{Z_{i1} - Z_{i2}} \tag{5.1}$$

where Z_i is the element mass fraction of element i.
Z_{i1} is the element mass fraction of element i in stream 1.
Z_{i2} is the element mass fraction of element i in stream 2.
Z is the normalized mass fraction which will be called the mixture fraction.

From equation (5.1) it follows that Z = 1 in feed 1 and Z = 0 in feed 2. Substituting equation (5.1) in (4.13) yields:

$$\frac{\partial}{\partial t}(\rho Z) + \frac{\partial}{\partial x_k}(\rho u_k Z) \frac{\partial}{\partial x_k}(\rho D \frac{\partial Z}{\partial x_k}) = 0 \tag{5.2}$$

Now equation (5.2) can be solved if the velocity field is known. The surface of stoichiometric mixture can then be determined from:

$$Z(\boldsymbol{x}, t) = Z_{st} \tag{5.3}$$

where **x** is the position vector of a point on the surface of stoichiometric mixture.
It is convenient to introduce a coördinate transformation of the Crocco type [4]. We

express the scalars T and Y as functions of Z. The new coördinates are chosen:

$$z_1 = Z, \quad z_2 = x_2, \quad z_3 = x_3, \quad \tau = t \qquad (5.4)$$

Where the coördinate x_1 is replaced by Z.
With (5.4) we find the following transformation rules:

$$\begin{aligned} \frac{\partial}{\partial t} &= \frac{\partial}{\partial \tau} + \frac{\partial Z}{\partial t}\frac{\partial}{\partial Z} \\ \partial x_1 &= \frac{\partial Z}{\partial x_1}\frac{\partial}{\partial Z} \\ \frac{\partial}{\partial x_k} &= \frac{\partial}{\partial z_k} + \frac{\partial Z}{\partial z_k}\frac{\partial}{\partial Z} \end{aligned} \qquad (5.5)$$

In terms of the new coördinate system (the flame attached system) the equations (4.7) and (4.10) take the form:

$$\begin{aligned} \rho\frac{\partial Y_i}{\partial \tau} - \rho D\left(\frac{\partial Z}{\partial x_k}\right)^2\frac{\partial^2 Y_i}{\partial Z^2} &= W_i - L(Y_i) \\ \rho\frac{\partial T}{\partial \tau} - \rho D\left(\frac{\partial Z}{\partial x_k}\right)^2\frac{\partial^2 T}{\partial Z^2} &= -\sum_{i=1}^{N}\frac{h_i}{c_p}W_i - L(T) \end{aligned} \qquad (5.6)$$

Where

$$\begin{aligned} L = \rho\left[\frac{\partial}{\partial \tau} + u_2\frac{\partial}{\partial z_2} + u_3\frac{\partial}{\partial z_3}\right] - \frac{\partial(\rho D)}{\partial x_2}\frac{\partial}{\partial z_2} - \frac{\partial(\rho D)}{\partial x_3}\frac{\partial}{\partial z_3} \\ -\rho D\sum_{k=2}^{3}\left[2\frac{\partial Z}{\partial x_k}\frac{\partial^2}{\partial Z \partial z_k} + \frac{\partial^2}{\partial z_k^2}\right] \end{aligned} \qquad (5.7)$$

In order to analyze the behavior of T and Y in the neighbourhood of the flame sheet

a coördinate stretching is introduced. Upon introduction of :

$$\eta = \frac{Z - Z_{st}}{\varepsilon}, \quad t^* = \frac{t}{\varepsilon^2} \tag{5.8}$$

where ε is a small expansion parameter,it can be shown [5] that in the reaction layer,the operator L is of higher order in ε. Equations (5.6) then take the form :

$$\begin{aligned} \frac{\partial Y_i}{\partial t} - \frac{1}{2}\chi \frac{\partial^2 Y_i}{\partial Z^2} &= W_i \\ \frac{\partial T}{\partial t} - \frac{1}{2}\chi \frac{\partial^2 T}{\partial Z^2} &= -\sum_{i=1}^{N} \frac{h_i W_i}{C_p \rho} \end{aligned} \tag{5.9}$$

where

$$\chi = 2D\left[\left(\frac{\partial Z}{\partial x_1}\right)^2 + \left(\frac{\partial Z}{\partial x_2}\right)^2 + \left(\frac{\partial Z}{\partial x_3}\right)^2\right] \tag{5.10}$$

χ is called the instantaneous scalar dissipation rate. Equations (5.9) are a set of N+1 nonlinear partial differential equations that describe the structure of the flamelet normal to the surface of stoichiometric mixture. They can be solved either via asymptotics or numerically.
χ represents the influence of the flowfield on the combustion system. χ is decreased by diffusion and increased by stretching. If the heat conduction out of the flamelet is larger than the heat formed by the chemical reaction, the flamelet will be quenched.
After a chemistry model has been chosen, equations (5.9) enable us to calculate the flamelet structure for a certain fixed value of χ. By doing this for a number of different values of χ, we obtain a set of flamelet profiles characterized by the value of χ. Combining this with a probabilistic description of the turbulent flowfield it is then possible to calculate the mean value of any scalar quantity in the turbulent flowfield.

6. The different states of a flamelet

According to [4] there are five different states of the flamelet:

1 The steady non-reacting mixture
2 The unsteady transition after ignition
3 The quasi steady burning state
4 The unsteady transition after quenching
5 The unsteady transition after reïgnition

The unsteady transition states are supposed to occur not very frequently, so their contribution to the flamelet will not be taken into account. For the statistical description the flamelet consist only of the steady initial state and the burning state. The steady unreacted initial state depends on Z only, while the burning state depends on both Z and χ. In order to describe the burning state, it is necessary to know the joint probability density function of Z and χ. The theory of probability density functions is very well described by Pope in [6].

7. Quenching of flamelets

The parameter χ describes the interaction between the turbulent flowfield and the combustion. When χ becomes too large, the diffusion of heat away from the reaction zone is no longer balanced by the production of heat by chemical reaction. This results in a reduction of the temperature in the reaction zone. The decrease of temperature in its turn results in a decrease of the chemical reaction rate, and so the flamelet will be quenched. This implies that there exists a critical value of χ. For values of χ larger then the critical value χ_q there is no burning state of the flamelet possible. Numerical values for χ_q can be found from asymptotic analysis. In [5], χ_q is derived for a one-step irreversible reaction in the limit of large activation energy:

$$\chi_q = \frac{4Z_{st}(1 - Z_{st})^2 \nu_{O_2} B\rho}{\beta^3(1 + a(1 - Z_{st}))M_F} e^{-(1+\frac{E}{T_{st}})} \tag{7.1}$$

In (7.1), β and a are parameters depending on the activation energy, E and the adiabatic flame temperature T_{st}. Unless the frequency factor, B and the activation energy, E are known, it is not possible to calculate χ_q directly from (7.1). In [7] it is shown that for a counterflow diffusion flame χ_q can be related to the velocity gradient a_q at extinction:

$$\chi_q = \frac{a_q}{\pi} e^{-2(\text{erfc}^{-1}(2Z_{st}))^2} \tag{7.2}$$

where erfc^{-1} means the inverse of the erfc function. a_q can be found from extinction experiments.
Equation (7.1) and (7.2) can be used to predict the chemical rate parameters E and B. The values deduced by this method are valid only in the range where the combustion can be modelled by a one-step irreversible reaction. This is true if the flame temperature is such that dissociation can be neglected. The effect of dissociation must be included at higher flame temperature. If dissociation is included, the criteria for extinction can be substantially different than stated in (7.1) and (7.2) [8].

8. Statistical modelling of the turbulent flow

During recent years intensive research has been done on modelling turbulent reacting flows. This is mainly because of the demand for better combustors and environmental motivations (pollutant emission).
Because of the closure problem in modelling turbulent flows (more unknowns than equations), a number of ways has been developed to model turbulent flows. Three classes of models can be distinguished:

1 Moment methods, which use correlations and spectral methods.

2 Probability Density Function methods, which use a statistical description of the turbulent flow.

3 Mixed methods, which use the moment method for the fluid dynamic quantities and use the p.d.f method for the species mass fractions and enthalpy.

The moment method is not often used in turbulent reacting flows. This is related to the problems that arise when applying the moment method. For a simple three reactant problem A+B $\rightarrow$C, thirteen moments have to be modelled!
In the following section a description of the use of the p.d.f. method for the flamelet model is explained. For a more detailed description of p.d.f. methods the reader is referred to the literature [6].

8.1. The p.d.f. method and the flamelet formulation

If the assumptions as mentioned earlier are valid (and they are in many practical situations), the structure of a flamelet depends only on the mixture fraction Z and the scalar dissipation χ. In a turbulent flow, these quantities are statistical l_y distributed. So it is necessary to predict the joint probability density function of Z and χ.
The joint probability density function of Z and χ can be written as:

$$\widetilde{P}_{z_\chi}(Z,\chi) = \widetilde{P}_z(Z)\widetilde{P}_\chi(\chi\,|Z) \tag{8.1}$$

where:

$$\widetilde{P}_Z(Z) = \int_0^\infty \widetilde{P}_{z_\chi}(Z,\chi)\,d\chi \tag{8.2}$$

is the marginal distribution. The tilde denotes a favre average.
$\widetilde{P}_\chi(\chi\,|\,Z)$is the conditioned p.d.f. of χ at a fixed Z.

If Z and χ are statistically independent, then (8.1) would take the form:

$$\widetilde{P}_{Z\chi}(Z,\chi) = \widetilde{P}_Z(Z)\widetilde{P}_\chi(\chi) \tag{8.3}$$

where:

$$\widetilde{P}_\chi(\chi) = \int_0^1 \widetilde{P}_{Z\chi}(Z,\chi)dZ \tag{8.4}$$

is the marginal distribution.
The assumption of statistical independence of Z and χ is often applied although its validity is questionable. Calculations by Ashurst et. al [9] show a strong dependence between Z and χ. Bilger [10] however argues in favour for such an assumption.

With the information as given above, the favre average of any scalar quantity f in the turbulent flow can be calculated from:

$$\tilde{f} = \int_0^\infty \int_0^1 f\widetilde{P}_{Z\chi}(Z,\chi)dZd\chi \tag{8.5}$$

if the p.d.f.'s of Z and χ are known.

The form of the p.d.f. will depend on the flow conditions and the chemical heat release rates. Although this may seem to limit the application of the conserved scalar formulation in reacting flows, it is found that the actual shape of the p.d.f. has little effect on the calculated mean and variance quantities.

8.2 The conserved scalar p.d.f.

The probability density function for the conserved scalar can be obtained for measurements in reacting flows. The problem with this approach is that there are very little measurements available in turbulent reacting flows.
Another way of determining the conserved scalar p.d.f. is solving a transport equation for the p.d.f. Because of the very large computational costs this is not often done.
The most widely used way of determining the p.d.f. is to assume an n-parameter function for the p.d.f. Several functions have been proposed by different authors. Spalding [11] uses a sinusoidal function. A 'clipped Gaussian' function is used by Lockwood [12]. Richardson et. al [13] were the first to use the so called β function p.d.f. The β function p.d.f. is defined as:

$$\widetilde{P}(Z) = \frac{Z^{\alpha-1}(1-Z)^{\beta-1}}{\int_0^1 Z^{\alpha-1}(1-Z)^{\beta-1}dZ} \tag{8.6}$$

where:

$$\alpha = \widetilde{Z}\left(\frac{\widetilde{Z}(1-\widetilde{Z})}{\widetilde{Z}''^2} - 1\right) \tag{8.7}$$

$$\beta = \frac{(1-\widetilde{Z})\,\alpha}{\widetilde{Z}} \tag{8.8}$$

So the conserved scalar p.d.f. can be determined if the mean and variance of the conserved scalar are known. The mean and variance are found from solving their balance equations.

8.3 The scalar dissipation p.d.f

The p.d.f. of the scalar dissipation is mostly assumed to be log-normally distributed. This is found from Kolmogorov's third hypothesis which says that the p.d.f. for the viscous dissipation rate, averaged over a volume of characteristic dimension r is log-normally distributed. When extended to the scalar dissipation rate the same result is found.

The log-normally distribution of the scalar dissipation rate p.d.f. is confirmed by experiments (Masseillo [14], Sreenivasan et. al [15]) and calculations (Kerstein and Ashurst [16]).

The scalar dissipation rate p.d.f. is thus defined as:

$$\widetilde{P}(\chi) = \frac{1}{\chi\sigma\sqrt{2\pi}} e^{-\frac{1}{2\sigma^2}(\ln\chi-\mu)^2} \tag{8.9}$$

where μ and σ are found from the mean and variance of χ

$$\widetilde{\chi} = e^{(\mu+\frac{1}{2}\sigma^2)} \tag{8.10}$$

$$\widetilde{\chi}''^2 = \widetilde{\chi}^2 e^{\sigma^2} - 1 \tag{8.11}$$

Closing remarks

In this paper a review of the theory describing the flamelet concept was given. The theory can be implemented in a computer program. To achieve this its is necessary to choose a reaction model (one-step, reduced mechanism or full mechanism). After the reaction mechanism is chosen one can construct the flamelet library by calculating the flamelet structure for different values of the scalar dissipation. This library can be used by the computer code that solves for the mean values of the flow quantities.

References

[1] Buckmaster J.D., Ludford G.S. — Theory of laminar flames.

[2] Williams F.A. — Recent advances in theoretical descriptions of turbulent diffusion flames. in: Turbulent mixing in non-reactive and reactive flows. pp 189 1975

[3] Kuo K.K. — Principles of combustion

[4] Peters N. — Prog. Energy Combust. Sci. vol 10 pp 319 1984

[5] Peters N. — Combustion Science and Technology vol 30 pp 1 1983

[6] Pope S.B. — Prog. Energy Combust. Sci. vol 11 pp 119 1985

[7] Donnerhack S., Peters N. — Combustion Science and Technology vol 41 pp 101 1984

[8] Peters N., Williams F.A. — Proceedings of the 9th ICODERS 1984.

[9] Ashurst — 4th symposium on turbulent shear flows. Karlsruhe, 1983.

[10] Bilger R.W. — in Turbulent reacting flows. (Libby P.A. & Williams F.A. eds)

[11] Spalding D.B. — Chem. Eng. Sci. vol 26 pp 95 1971

[12] Lockwood F.C., Naguib A.S. — Combustion and flame vol 24 pp 109 1975.

[13] Richardson J., Howard H.C. — 4th symposium (Int) on combustion 1953.

[14] Masseillo P.J. — Intermittency of the fine structure of turbulent velocity and temperature fields measured at high Reynolds number. Ph.D. thesis University of California San Diego 1974

[15] Sreenivasan K., Antonio R.A., Danh H.Q. — Physics of fluids vol 20 pp 1800 1977

[16] Kerstein A.R., Ashurst W.T. Lognormality of gradients of diffusive scalars in homogeneous, two dimensional mixing layers. Sandia National Laboratories.

Symbols

a	parameter depending on initial temperature of the two feeds and the adiabatic flame temperature
a_q	velocity of counterflow flame gradient at extinction
β	parameter in eq (7.1) depending on adiabatic flame temperature and activation energy
B	frequency factor in Arrhenius law
c_p	specific heat at constant pressure of mixture
c_{pi}	specific heat at constant pressure of species i
D	diffusion coëfficient
D_a	Damköhler number
$\tilde{f}$	favre average of quantity f
F	symbol for fuel
g_i	body force
h	mixture enthalpy
h_i	enthalpy of species i
L_e	Lewis number
m_i	mass of species i
M_F	mol mass of fuel
M_O	mol mass of oxidizer
p	pressure
$\tilde{P}_{Z\chi}(Z,\chi)$	joint probability density function of Z and χ
S_c	Schmidt number
t^*	'stretched' time
T	temperature
T_f	frozen flow temperature
T_{st}	adiabatic flame temperature
u_k	velocity component in k-direction
W_i	chemical production rate of species i
x_1,x_2,x_3,t	cartesian coördinate system
Y_i	mass fraction of species i
Z	mixture fraction
Z_i	element mass fraction of element i
Z_{i1}	element mass fraction of element i in stream 1
Z_{i2}	element mass fraction of element i in stream 2
Z_{st}	stoichiometric values of mixture fraction
z_1,z_2,z_3,τ	flame attached coördinate system
α_{ij}	number of grams of element i in species j
δ_{ij}	Kronecker delta
ε	small expansion parameter
η	stretched coördinate
κ	bulk viscosity
λ	thermal conductivity
μ	dynamic viscosity
ν	kinematic viscosity
ν_F	stoichiometric coëfficient of fuel

ν_O	stoichiometric coëfficient of oxidizer
ρ	density
σ	Prandtl number
τ_{ik}	stress tensor
χ	scalar dissipation rate
χ_q	scalar dissipation rate at extinction

Numerical simulation of leading-edge vortex flow

By H.W.M. Hoeijmakers

Theoretical Aerodynamics
National Aerospace Laboratory
NLR Amsterdam

Faculty of Applied Physics
TU Eindhoven

Summary

An analysis is presented of results of a computational method to simulate the steady compressible vortical type of flow around a 65-deg sharp-edged cropped delta wing. The discussion emphasizes some more fundamental aspects of the numerical simulation such as the separation of the flow, the structure of the leading-edge vortex core and the flow inside the free shear layer. For the vortex core in isolation as well as for the free shear layer closed-form solutions are presented which might assist in the analysis of the numerical results.

Introduction

In aircraft aerodynamics vortex flows play an important role, especially if they involve the strong interaction of the free shear (vortex) layers and vortex cores with the flow about the aircraft. (Küchemann, Ref. 1). Well-known are the favourable effects induced by the leading-edge vortices on highly swept wing and strake-wing configurations at high incidence, resulting in a substantial increase of their lift capability. This is of great practical importance for configurations employing these wings with their, according to classical wing theory, relatively small lift slope.

At the high Reynolds numbers relevant to aircraft aerodynamics free shear layers form whenever the flow encounters a sharp edge and is forced to separate from the surface. The properties of such a (thin) shear layer are determined by the conditions that at the edge (a geometrical singularity) the velocity remains finite and that vorticity is convected away from it, i.e. within the framework of inviscid flow theory by the Kutta condition. It should be realized that, in the three-dimensional high-Reynolds-number flow of interest here, the vorticity contents of the free shear layer is primarily determined by the shear of the velocity vector (i.e. magnitude of the discontinuity in its direction) at the separation line, not by the vorticity contained within the viscous layers meeting at the separation line (Hirschel, Ref. 2).

Away from the edge usually the free shear layer rolls up into one or more vortex cores which remain linked up with the shear layer and are continuously fed with vorticity from the shear layer. Still further along the shear layer most of the vorticity generated at the edge will be concentrated in the cores, i.e. in regions with distributed vorticity. This vortical flow structure is often well-ordered, steady and persistent.On an aircraft or missile configuration the flow may break away from the surface and form a free shear layer before a sharp edge is reached, i.e. at a smooth portion of the surface. In contrast to the separation at a sharp edge the location of the smooth-surface separation line depends on Mach number, incidence, Reynolds number, state of the boundary layer, etc. and is not known a priori. In three-dimensional flow this type of separation (i.e. specifically the so-called 'open' type of separation) may result in another well-defined and steady vortical flow structure. In the present paper the emphasis is on the vortex flow associated with separation from a sharp edge, i.e. leading-edge vortex flow.

Increasing the incidence of a sharp-edged delta wing leads to an increase in the strength of the leading-edge vortex. It has been observed in experiments that above a critical value of the incidence the internal structure of the vortex changes dramatically, resulting in an abrupt increase in the cross-sectional size of the vortex core. Downstream of the region where the phenomenon of vortex breakdown (burst) occurs the flow might recover, but usually the flow becomes unsteady and loses its well-ordered structure. Vortex breakdown marks the end of the favourable effects induced by leading-edge vortex flow and for example determines the maximum attainable lift coefficient. Therefore, understanding the mechanisms involved in the onset of vortex breakdown is of foremost practical interest.

Usually leading-edge vortex breakdown starts in the wake, where the vortex is strongest and where there is a rapid increase of the static pressure along the vortex core, progressing forward with increasing incidence. A possible cause of the burst of the vortex is the low total pressure at the center of the vortex core, due to viscous-flow losses within the vortex core. It has been suggested, in analogy with boundary-layer separation, that the pressure rise at the trailing-edge or in the near wake can easily bring the flow within the vortex core to stagnation, leading to a so-called bubble-type of breakdown. A possible alternative explanation proposed is that instabilities within the outer (inviscid) part of the vortex core cause the onset of vortex breakdown.

Vortical flow due to separation from moderately- to highly-swept aerodynamically-sharp leading edges plays an particularly prominent role in the aerodynamics of high-performance fighter aircraft and missiles operating in the high-angle-of-attack flight regime. An accurate numerical simulation of the detailed flow field, often involving along with vortices shocks and the mutual interaction of vortices and shocks, is of paramount importance to advance the understanding and eventually the utilization of these complex highly non-linear types of flow.
The present paper addresses the numerical simulation of the flow about a cropped

sharp-edged 65-deg delta wing which may be considered as a configuration generic for configurations with complex vortex flow.

Flow models

The formation of the leading-edge vortex above the upper surface of the wing, as a result of the rolling-up of the free shear layer which forms at the sharp leading edge, as well as the influence of the vortex on the flow over the upper surface of the wing, appears to be only slightly dependent on Reynolds number, at least within the range of Reynolds numbers relevant here. This implies that this type of flow can be simulated by inviscid flow models.

Potential-flow methods have been applied with some success to the sub-critical flow about delta-like wing configurations, e.g. Ref. 3. In these methods the vortical flow is modelled by 'fitting' vortex sheets and vortex filaments within the potential flow field. Although both the strength and the position of these vortex sheets and filaments are determined as part of the solution, the general structure of the flow must be well-defined and known in advance.

The mathematical inviscid-flow model based on the Euler equations allows for rotational flow everywhere in the flow field. Furthermore it describes the convection and stretching of vorticity as well as the generation of vorticity through shocks of varying strength and through intersecting shocks. Computational methods based on this flow model 'capture' vortical flow regions along with (strong) shocks as integral part of the discrete flow solution. This renders computational methods based on the Euler equations rather attractive for cases with a complex vortical flow structure of an a priori unknown topology. This is even more true for transonic flow with both vortices and shocks and the interaction of these two non-linear flow phenomena. The latter type of highly non-linear flow occurs on the moderately-swept wing configuration considered in the present paper. Fig. 1, taken from Ref. 4, provides an overview in the M_∞-α plane of the experimentally found main flow features for a configuration from which the 65-deg cropped delta wing considered here was derived.

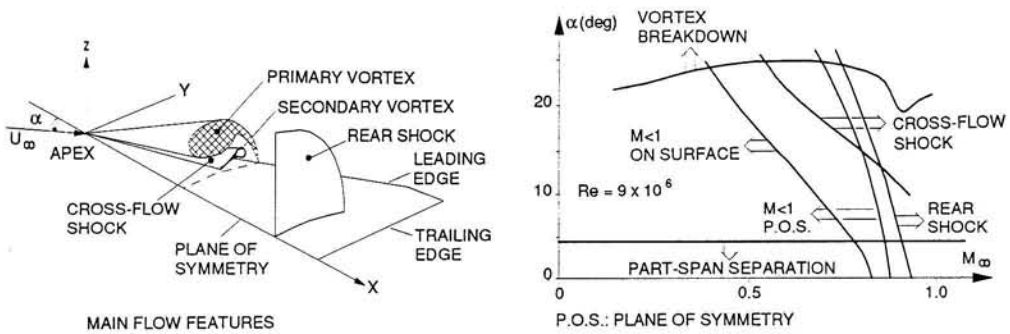

Fig. 1 Summary of flow features in (M_∞,α) plane, 65-deg sharp-edged cropped delta wing configuration (Ref.4)

In the flow model based on the Euler equations viscous effects are neglected altogether. Thus at the sharp edges such as the trailing and the leading-edge a Kutta-type of condition should be prescribed to invoke flow separation. However, as follows from several earlier investigations into the numerical simulation of steady-state, vortex-dominated flows, it is well accepted now that finite-volume time-stepping Euler methods capture separation from sharp trailing and leading edges. In these methods numerical dissipation is instrumental in mimicking the effects of the true viscous flow at and near the sharp edge, forcing the flow to separate rather than to round the edge. The separation of the flow at a line on a smooth portion of the geometry of the configuration is not captured automatically by the method and has to be accommodated in some more elaborate way.

The phenomenon of vortex breakdown above delta-like wings has first been identified in experiments, e.g. Refs. 10 and 11 for some early observations. It has been studied in detail in more recent experimental work as well as in computational investigations using Euler methods (e.g. Refs. 7 and 8) and Navier-Stokes methods (e.g. Ref. 12). Until now the precise mechanisms leading to vortex breakdown are still unclear.

In the wind-tunnel investigation for the present configuration vortex breakdown occurs at incidences above 20 deg. Therefore in the present investigation computations have been pursued for incidences of 20 deg and higher. In this way the highest, 'critical', incidence has been determined for which the numerical procedure produces a converged (steady-state) solution. It also provides the opportunity to identify possibly new features within the numerical solution at the critical incidence and whether or not these features resemble those observed in experiments.

Outline of computational method used

In inviscid flow the five equations for the conservation of mass, momentum in each of the three space directions and energy are expressed, in integral form, as follows:

$$\frac{\partial}{\partial t}\iiint_V U\,dV + \iint_{\partial V} \vec{F} \cdot \vec{n}\,dS = 0 \tag{1a}$$

which is applied to any closed control volume V. In Eq. (1a) U is the column vector containing the flow variables, which can be expressed as:

$$U = [\rho, \rho u, \rho v, \rho w, \rho E]^T \tag{1b}$$

In Eq. (1a) $\vec{F}$ is the inviscid flux vector, which has F, G, and H as components in each of the three Cartesian coordinate directions, respectively. In terms of the Cartesian coordinate system these components are:

$$F = [\rho u,\ \rho u^2 + p,\ \rho uv,\ \rho uw,\ \rho uh]^T \quad (1c)$$
$$G = [\rho v,\ \rho uv,\ \rho v^2 + p,\ \rho vw,\ \rho vh]^T \quad (1d)$$
$$H = [\rho w,\ \rho uw,\ \rho vw,\ \rho w^2 + p,\ \rho wh]^T \quad (1e)$$

In above expressions ρ denotes the mass density, p the static pressure, $\vec{u} = (u,v,w)^T$ the velocity vector, $E = \{e + (u^2 + v^2 + w^2)/2\}$ the total energy per unit mass and $h = E + p/\rho$ the total enthalpy per unit mass.

The above system of equations is supplemented by the equations of state. For the present type of flows the gas may be assumed to be an ideal perfect gas for which:

$$p = \rho RT \quad (1f)$$
$$e = c_v T \quad (1g)$$

where T is the static temperature and $R = c_p - c_v$. Here c_p and c_v are the specific heats which may be assumed to be constant.

The Euler method as developed at NLR (Ref. 13), solves the time-dependent Euler equations employing the fully conservative scheme of Jameson et al. (Ref. 14). The above five equations for the conservation of mass, momentum in each of the three space directions and energy are applied to a large number of patched volumes V. In the method each control volume V consists of one cell of the computational grid and Eq. (1a) is spatially discretized using a cell-centered central-difference scheme. To provide stability second- and fourth-difference artificial dissipation terms are added to the discretized equations. The fourth-difference term is required to provide the background dissipation for suppressing the tendency for the numerical solution to decouple at odd and even points. In regions with large gradients, specifically near shocks, the second-difference dissipative term is required to damp oscillations.

To obtain a steady-state solution, integration in time is carried out by a four-stage Runge-Kutta scheme in which the artificial dissipative terms are evaluated at the first stage only. Convergence to steady state is accelerated by using local time-stepping, enthalpy damping and implicit residual averaging.
At the surface of the wing the flux vector is evaluated employing the boundary condition of zero normal velocity, combined with a second-order accurate extrapolation of the pressure towards the solid wall. At the outer boundary of the computational domain the boundary conditions are based on one-dimensional Riemann invariants.

Geometry and grid

The geometry considered is the 65-deg sharp-edged cropped delta wing of the configuration considered in the experimental investigation of Ref. 4. The wing has a taper ratio of 0.15. The chordwise airfoil section is the NACA 64A005 airfoil, which

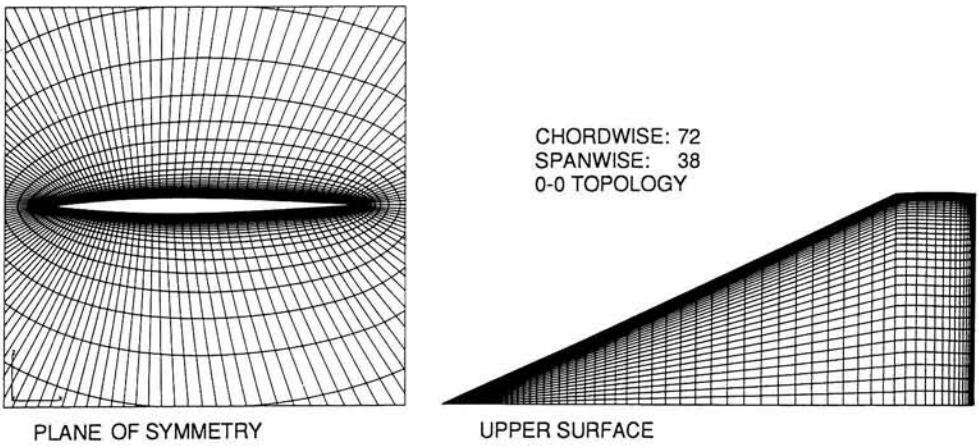

Fig. 2 Details of medium grid

upstream of its point of maximum thickness (0.4c) is smoothly blended into a biconvex shape. For this configuration, with an under-wing body, an extensive body of detailed experimental data is available (e.g. Ref. 4). It is presumed that the presence of the under-wing body has only a small effect on the flow field on and above the upper surface of the wing, so that here the computational results for the wing-alone configuration can be compared quantitatively with the measured data for the complete configuration.

For the wing a grid with O-O topology is used to discretize the starboard half of the computational domain. The grid has two levels of grid-point density, namely:

(i) A 'fine' grid, which has grid dimensions $288 \times 76 \times 56$ (1,225,728 cells), that is in chordwise direction 144 cells on both the wing upper and lower surface, in spanwise direction 76 cells and in normal direction 56 cells between the wing surface and the outer boundary of the computational domain.

(ii) A 'medium' grid, obtained by combining groups of eight cells of the 'fine' grid. This still relatively fine grid has dimensions $144 \times 38 \times 28$ (153,216 cells).

The grid is symmetric with respect to the horizontal plane of symmetry of the wing. On the forward portion of the wing surface the grid is 'conical' as is shown in Fig. 2, which presents details of the medium grid. The quasi-conical arrangement of the grid preserves the grid resolution near the apex. On the wing surface the grid lines are clustered near the apex, near the leading edge and near the trailing edge. Adjacent to the surface of the wing, where large gradients in the flow quantities are expected, the cell stretching ratio in the direction normal to the surface remains close to unity. The grid contains a singular line which starts at the apex and runs along the x-axis in upstream direction.

The outer boundary of the computational domain is formed by the surface of a sphere

with a radius of 5 root chords c_R, which has proven to be sufficient for the present applications.

Influence of grid-point density on the flow solution

For a free-stream Mach number of 0.5 computational results have been obtained for the wing at 20 deg incidence. In order to assess the influence of the grid-point density on the numerical solution the solution has been computed on the medium as well as on the fine grid.
For the calculation on the medium grid the second-difference dissipative term was not used. The calculation on the fine grid was carried out utilizing both the second- and the fourth-difference dissipative terms.

Isobar pattern on the upper wing surface

The isobar patterns obtained from the computed results on the medium and fine grid are shown in Fig. 3. For both grids the low-pressure region on the wing upper surface, forming the footprint of the leading-edge vortex, indicates that flow separation from the sharp leading-edge starts very close to the apex. The lowest values of the surface pressure coefficient are found near the apex underneath the vortex, which is typical for subsonic flow cases where there is a relatively large effect of the singularity at the apex as well as a relatively strong upstream influence of the trailing edge. For higher free-stream Mach numbers the region with lowest pressures moves to a more aft position on the wing.

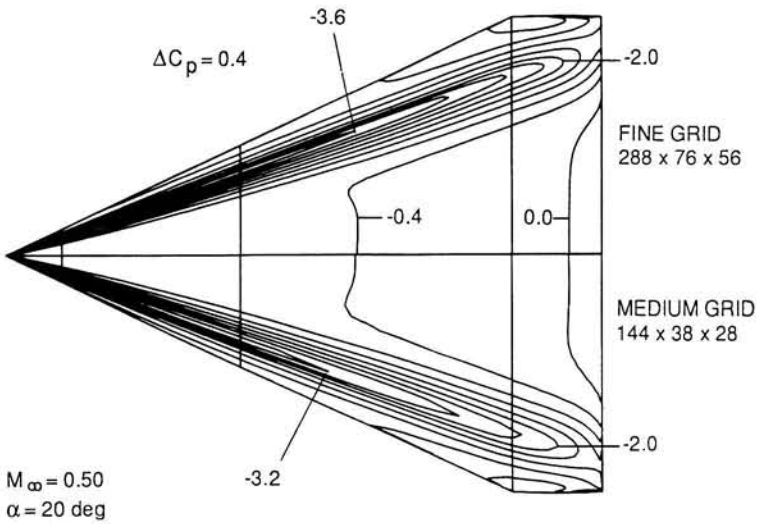

Fig. 3 Upper-surface isobar pattern for $\alpha = 20$ deg

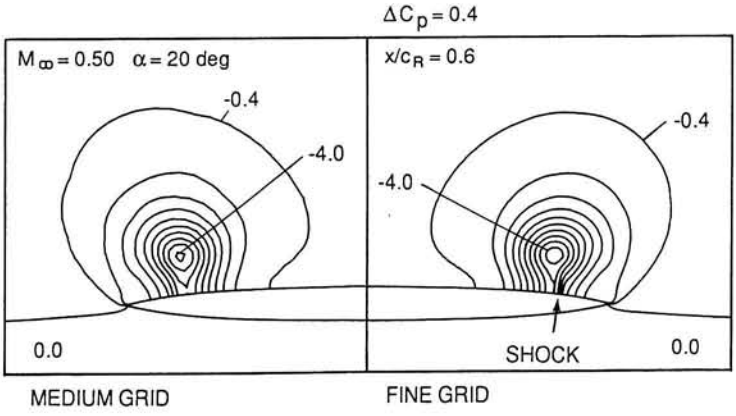

Fig. 4 Cross-flow-plane isobar pattern in plane $x/c_R = 0.6$

Comparison of the two patterns in Fig. 3 shows that the Euler solution on the medium grid and the one on the fine grid do not differ much in essence. However, on the fine grid the pressures in the suction peak are substantially lower than those found in the result on the medium grid. Since the 'critical' value of the pressure coefficient is −2.13 it is seen that the flow on the upper wing surface is supersonic in the low-pressure region, reaching Mach numbers above 1.5 on the fine grid.

Isobar pattern in the cross-flow plane

In Fig. 4 the isobar pattern in the plane $x/c_R = 0.6$ is presented. It shows the comparison of the pattern obtained from the solution on the medium grid with the one obtained on the fine grid. The cross-flow-plane isobar pattern clearly reveals the presence of the leading-edge vortex above the wing upper surface. The minimum value of the pressure, attained at the center of the vortex core, is somewhat lower for the solution on the fine grid than it is for the one on the medium grid. The position at which the static pressure attains its minimum, i.e. the position of the center of the vortex core, is almost the same for the two solutions. As indicated by the clustering of isobars, the solution on the fine grid features a weak 'cross-flow shock', situated underneath the vortex just outboard of its center, which is not present in the solution on the medium grid.

Spanwise pressure distribution

In Fig. 5 the spanwise pressure distribution for the station $x/c_R = 0.6$ as computed on the medium and the fine grid are compared with each other and with experimental data from Ref. 4. Comparison of the solution on the fine grid with the one on the medium grid shows that, when the grid is refined, the spanwise surface pressure

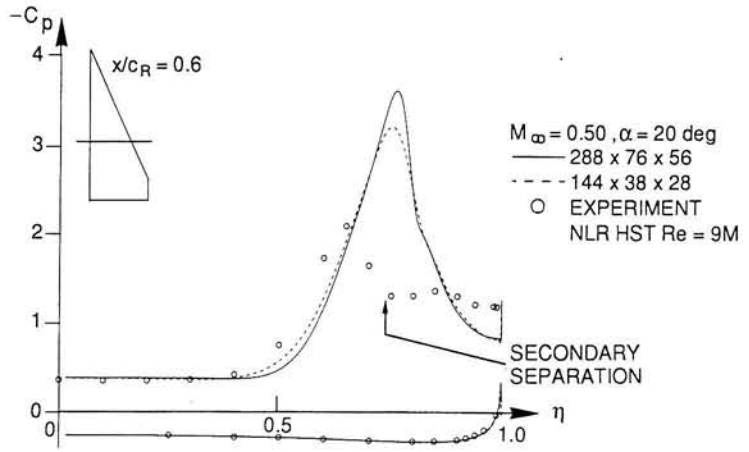

Fig. 5 Spanwise surface pressure distribution for section at $x/c_R = 0.6$

distribution remains the same everywhere except in the region around the upper-surface suction peak. The latter becomes steeper and higher while its position shifts slightly in outboard direction. The location of the cross-flow shock, in the fine grid result just outboard of the suction peak, is recognized as the location where the spanwise pressure distribution steepens up.

Comparison of the computed results with experimental data shows that for the lower wing surface the agreement is quite satisfactory. However, on the upper wing surface the Euler method grossly over-predicts the suction peak, also resulting in an over-prediction of the lift coefficient by about 15 percent. This is primarily due to the circumstance that the Euler method lacks the ability to simulate flow separation from a smooth part of the surface, which here occurs when the flow encounters the steep adverse pressure gradient just outboard of the suction peak. This so-called secondary separation, which primarily affects the pressure distribution underneath the leading-edge vortex, is not captured by the Euler method without explicitly incorporating some kind of a model for the viscosity dominated phenomenon of smooth-surface separation.

It might be expected that seen in the light of the findings of a study carried out within the framework of potential-flow theory (see Ref. 3), also within the framework of an Euler method the inclusion of a model for smooth-surface separation will result in an improved correlation of predicted and measured surface pressure distributions.

Cross-flow plane contours of equal total-pressure loss

Fig. 6 shows the total pressure loss in the cross-flow plane at the station $x/c_R = 0.6$,

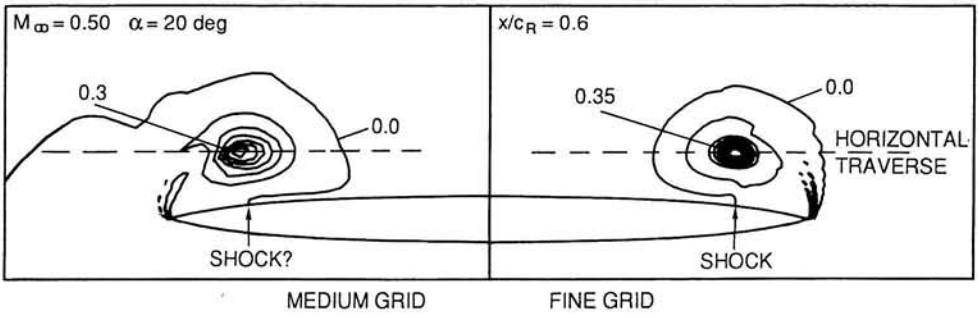

Fig. 6 Cross-flow-plane total-pressure distribution in plane $x/c_R = 0.6$

both for the medium- and the fine-grid solution. The pattern as well as the magnitude of the total-pressure losses do not vary very much in chordwise direction and Fig. 6 can be considered as representative for any station on the wing.
For inviscid flows without shocks the total pressure should be constant, equal to its free-stream value. In Euler methods errors are caused by the artificial dissipation introduced by the numerics.
Primarily due to a high grid resolution in the direction normal to the wing, the error in total pressure is negligible in most part of the computational domain. For instance on the major part of the upper wing surface the error is small (less than 0.5% gain) for the solution obtained on both grids, with the fine-grid solution having the smallest error. The error on the lower wing surface is due to the smaller gradients in the solution an order of magnitude smaller.In the solution obtained on the medium grid as well as in the solution on the fine grid one observes that on the upper surface, at about 75% local semi-span, there is a sudden increase in total-pressure loss, to about 1% and 2% on the medium and fine grid, respectively. This increase is due to the occurrence of the (weak) cross-flow shock discussed above, which is strongest on the finer grid. Right at the leading edge, where the flow separates, without explicitly prescribing separation, the total-pressure loss increases rather abruptly to values of about 10% of the free-stream value.

Fig. 6 clearly illustrates that in the leading-edge vortex above the wing upper surface the total-pressure loss becomes largest, attaining values of 30 to 35% of the free-stream value. The total-pressure loss at the center of the vortex core in the fine grid solution is higher than in the medium grid solution. However, on the fine grid the area in which there are significant total-pressure losses is smaller, i.e. it is more confined around the center of the vortex core. Apparently for the present subsonic case the reductions due to grid refinement of the errors in total pressure cause the area in which they occur to be reduced, but at the center of the core the reduction of the errors due to grid refinement cannot balance the increase in the errors associated with the improved resolution of steeper gradients.

Solution within leading-edge vortex core

In the following the solution within the leading-edge vortex core is considered in more detail. Fig. 7 presents medium- and fine-grid results along a horizontal traverse through the center of the vortex core. The traverse is located in the plane $x/c_R = 0.6$ and is indicated in Fig. 6. The two top plots in Fig. 7 show the distribution along the traverse of the static pressure and the total-pressure loss. The effect of refining the grid is clearly evident: not much effect on the static pressure distribution while the total-pressure loss decreases everywhere except near the center of the vortex core and in the leading-edge shear layer. In the fine-grid solution two passages of the layer through the traverse can be detected.
The middle two plots in Fig. 7 show the distribution of the chordwise and vertical (circumferential) component of the velocity vector. At the center of the vortex core the chordwise component reaches values of about 2.2 times the free-stream value on the fine grid and a 10% lower value on the medium grid. The intersections of the traverse with the leading-edge shear layer appear as the steeper parts in the u/U_∞ distribution along the traverse, while in the w/U_∞ distribution the passage through the layer also shows up clearly. These results demonstrate that refining the grid results in an improved resolution of steep gradients, i.e. the change in the direction of the velocity vector across the leading-edge shear layer is better represented on the fine grid.

Directly related to the chordwise velocity component is the cross-flow-plane component of the vorticity vector $\vec{\omega}$, while the cross-flow-plane component of the velocity is directly related to the chordwise component of the vorticity, e.g. Ref. 3. The bottom two plots of Fig. 7 present the distribution along the horizontal traverse of the vertical (circumferential), $(\vec{\omega} \cdot \vec{e}_z)c_R/U_\infty$, and chordwise component of the vorticity $(\vec{\omega} \cdot \vec{e}_x)c_R/U_\infty$. The chordwise component reaches high values in the core of the vortex and in the leading-edge shear layer. The cross-flow-plane component attains its maximum near the edge of the vortex core and near the edges of the leading-edge shear layer. The influence of refining the grid is again clearly illustrated.

It may be concluded that the computational results on the two grids are qualitatively the same, i.e. both solutions feature the same flow phenomena, warranting the conclusion that the result on the medium grid is sufficiently accurate for engineering purposes. Quantitatively there are some differences, but these can be understood in terms of differences in grid density. As far as the surface pressure distribution is concerned the differences between the results on the two grids are considerably smaller than the differences between computational results and experimental data.
The latter differences are due to the inviscid flow method being unable to capture the secondary separation. Differences similar to the ones shown here for the Euler method have also been found for potential-flow methods, which usually only include the leading-edge vortex sheet (e.g. Ref. 3).

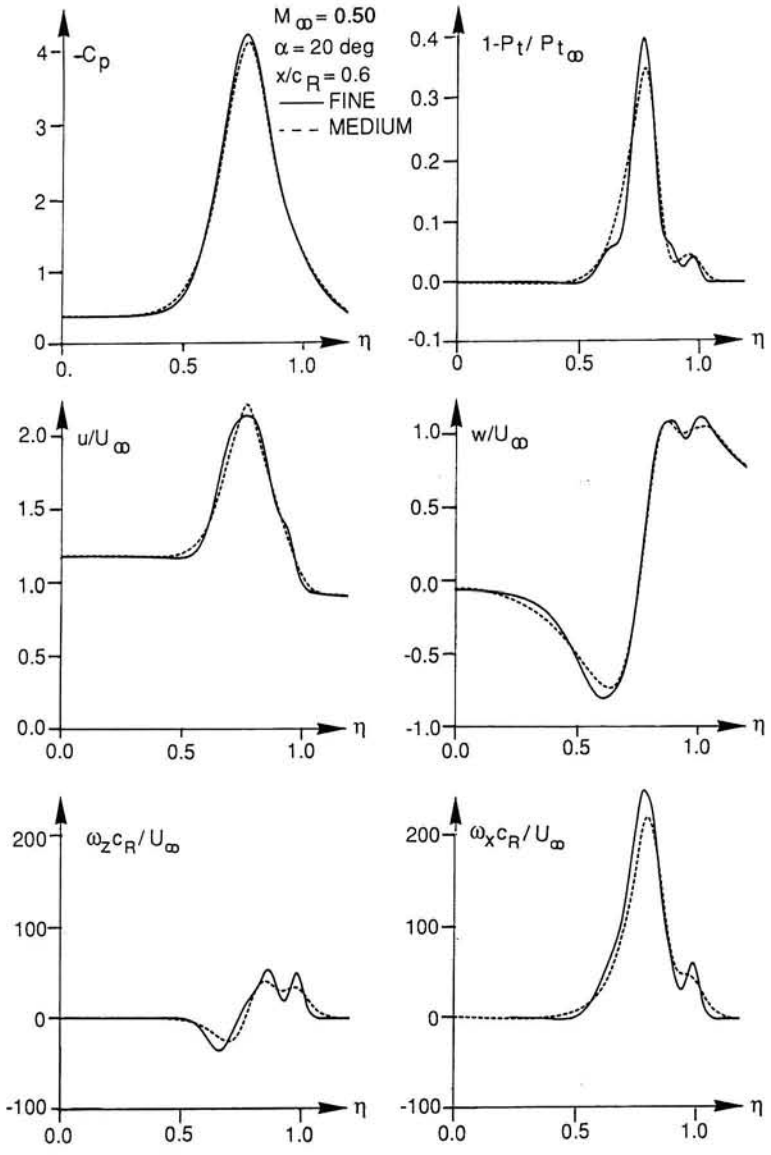

Fig. 7 Flow-field quantities along horizontal traverse through the vortex center in plane $x/c_R = 0.6$

Total-pressure losses in euler solutions

Total-pressure losses within the free shear layer

As far as the total-pressure losses in the numerical solution is concerned it will be clear that they are largest in regions with the largest gradients in the flow field, such as occur in regions where vorticity is or becomes concentrated. For the present application these regions are the center of the vortex core and the part of the leading-edge shear layer where it is strongest, which is close to the leading edge . It has been conjectured by amongst others Hirschel (Ref. 2) and Powell (Ref. 15) that simulating numerically a shear layer employing an Euler method as the one used above has total-pressure losses inextricably associated with it. Here it will be shown that this is not necessarily the case. Starting from Crocco's relation

$$\frac{\partial \vec{u}}{\partial t} + \vec{\nabla} h = T\vec{\nabla} S + \vec{u} \times \vec{\omega} \tag{2a}$$

where h is the total enthalpy ($h = E + p/\rho$), $\vec{\omega}$ is the vorticity vector ($\vec{\omega} = \vec{\nabla} \times \vec{u}$) and S is the entropy. The latter can be related to the total pressure p_t through

$$p_t/p_{t\infty} = \exp[-(S-S_\infty)/R] \tag{2b}$$

For steady inviscid flow it follows from the equation for the conservation of energy (see Eq. 1) that h is constant. So one finds from Eqs. (2a) and (2b) that in case $\vec{u}$ and $\vec{\omega}$ are parallel (which is the case in so-called Beltrami flow) the total pressure will not change across the layer. It can be shown that there are distributions of $\vec{u}$ and $\vec{\omega}$ that indeed satisfy these conditions. Assuming that the shear layer consists of parallel stream surfaces the velocity vector within the shear layer can be decomposed in terms of its component along the average of the velocity at the upper and the lower edge of the layer and its component normal to this direction (see Fig. 8), as:

$$\vec{u} = U_o\{\, a(z)\vec{e}_1 + b(z)\vec{e}_2\}, \tag{2c}$$

it then follows from the definition of the vorticity that:

$$\vec{\omega} = U_o\{-b'(z)\vec{e}_1 + a'(z)\vec{e}_2\} \tag{2d}$$

where $z \in [-\delta,\delta]$, i.e. within the layer. Setting then $\vec{u} \times \vec{\omega} = \vec{0}$ yields:

$$a(z) = 1/\cosh f(z) \tag{2e}$$
$$b(z) = \tanh f(z) \tag{2f}$$

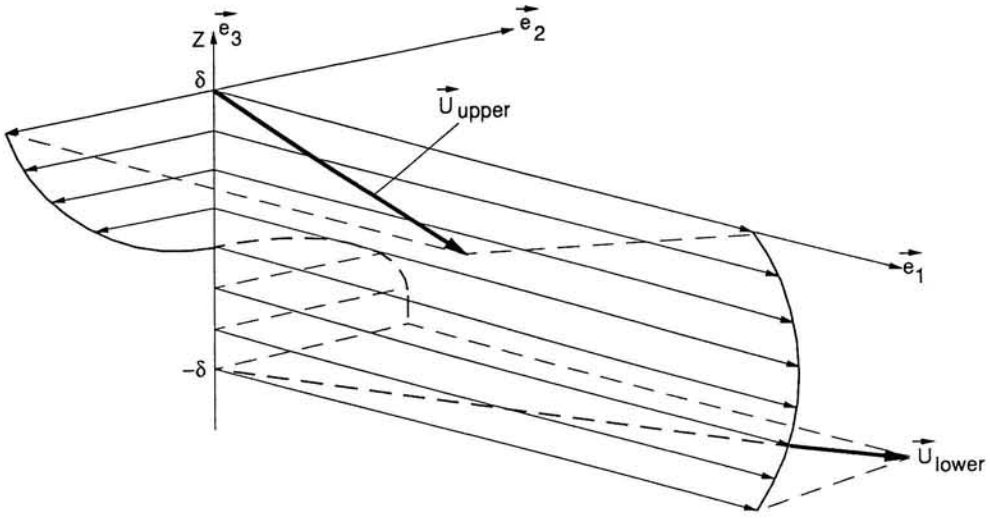

Fig. 8 Constant-total-pressure velocity distribution through shear layer

where $f(-\delta) = -f(\delta)$. It may be expected that these types of total-pressure conserving velocity profiles can be supported by a discrete Euler solution as long as locally the thickness of the layer is of the order of 3-5 cells of the grid. This is confirmed by the cross-flow-plane iso-contour plots of the total pressure, such as Fig. 6, where the total-pressure losses in the leading-edge shear layer rapidly diminish with distance from the leading edge, i.e. in the region where the vorticity is not as high and the numerical diffusion has spread the layer to a sufficient degree.
Above kinematical arguments are quite similar to the ones used by Hirschel (Ref. 2) and Powell (Ref. 15), but with the principal difference that in above analysis the component of the velocity along the average direction ($\vec{e}_1$) is allowed to vary through the shear layer while it was held constant by Hirschel and Powell.

An additional important question to be posed is whether the total-pressure losses invoked by the numerics (i.e. errors due to the numerical method used to solve the inviscid flow equations) in the insufficiently resolved thin shear layer near the leading edge remain local *or* convect somehow, subject to some diffusion, along the vortex layer towards the center of the vortex core. The present (subsonic) results strongly suggest that the errors have a local implication only, i.e. that the numerical total-pressure losses behave differently from the total-pressure losses encountered in the real viscous flow.

Total-pressure losses within the vortex core

As far as the vortex core is concerned it can be remarked that Hall (Ref. 16) derived a constant-total-pressure Euler solution for the case of an isolated axially-symmetric, slender, conical vortex core in incompressible flow. The inviscid solution is valid up to the axis of the core where a (logarithmic) singularity is present. By matching a viscous solution, for the region very close to the core axis (the viscous subcore), to the inviscid solution for the outer parts of the core, Stewartson & Hall (Ref. 17) could remove the inviscid flow singularity. In this model total-pressure losses occur in the viscous subcore only, the outer region of the vortical flow region is without total-pressure losses. Although in the real vortex the whole vortical flow region exhibits total-pressure losses it is demonstrated that the velocity and pressure distribution through the core agree satisfactorily with experimental data. Brown (Ref. 18) considered the case of an isolated slender conical vortex core in inviscid compressible flow and also found an inviscid constant-total-pressure solution.

In the above two inviscid, in an approximate framework derived but analytical, solutions a singularity appears at the center of the core. The large gradients associated with the singularity will not be resolvable on a finite grid on which a discrete Euler solution is sought, leading to total-pressure losses in the solution in the vortex core. However, as the mesh is refined more and more the total-pressure losses in the numerical Euler solution should become confined to a region near the sharp leading edge and a region around the center of the vortex core and Beltrami flow will prevail everywhere else. The grid refinement study discussed above tends to confirm this.

Some investigators have emphasized that the level of the total-pressure loss at the center as produced by Euler methods appears to agree with experimental data. However, it must be concluded from the discussion presented here that this must be fortuitous: the occurrence of total-pressure losses at the center of the core, as well as in the rest of the core, in the numerical results produced by Euler methods is a purely spurious numerical artifact.

On the other hand it can be observed, similar to what has been observed for the potential-flow solutions, that the position of the vortex core, its vorticity contents (circulation), as well as the flow outside the core appear to be influenced only very little by exactly what happens within the vortex core itself. However, it is to be expected that some vortex core characteristics, such as the onset of vortex breakdown, might be affected by the numerically induced total-pressure losses within Euler solutions.

Solution at higher incidence

Solution breakdown

For the same Mach number of 0.5 computations have been carried out for a series of incidences, starting at 20 deg and increasing the incidence in small increments, keeping all the other parameters identical. All computational results discussed here have been obtained on the medium grid. It turned out that fully converged solutions could be obtained for incidences up to 21.25 deg, although the number of iterations required increased significantly with incidence. For $\alpha = 22.5$ deg the numerical procedure neither really diverged nor converged. Monitoring the development in (pseudo-)time of the solution variables it was observed that a feature termed 'solution breakdown' occurred. This phenomenon results in the situation in which the solution in the region above the forward part of the wing appears to have reached its final state, while above the aft part of the wing the solution persists in changing substantially during the iteration process without reaching something like a final state. Some of the results of this investigation have been reported in Ref. 19. In the following the solution for 21.25 deg will be analyzed in some more detail.

Analysis of the solution close to the critical incidence

Fig. 9 compares the upper surface isobar pattern for the incidence of 20 deg (see also Fig. 3) and the one for 21.25 deg. It shows that for the incidence of 21.25 deg, the isobar pattern on the aft part of the wing indicates that the low pressure region does

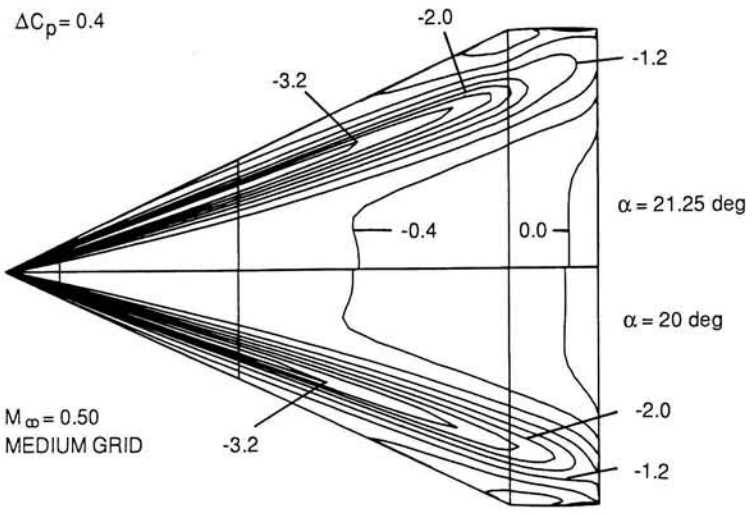

Fig. 9 Upper-surface isobar pattern for $\alpha = 20$ and 21.25 deg

not extend so far aft as for $\alpha = 20$ deg. This means that while with increasing incidence the pressure drops further on the forward part of the wing, it has started to increase on the aft part.

For the cross-flow plane $x/c_R = 0.95$ Figs. 10 and 11 show for $\alpha = 20$ and 21.25 deg the contours of equal static pressure and total-pressure loss, respectively. Fig. 12 presents the distribution of flow-field quantities along a horizontal traverse through the center of the vortex core, situated in the same cross-flow plane.
At this section close to the trailing edge the solution experiences a dramatic change in structure when the incidence is increased from 20 to 21.25 deg. While at $\alpha = 20$ deg the flow at $x/c_R = 0.95$ strongly resembles the one at $x/c_R = 0.6$ (see Figs. 4, 6 and 7) and is jet-like, the flow at $\alpha = 21.25$ deg is completely different. As indicated in Fig. 12 the flow within the vortex core is now wake-like, i.e. while the circumferential velocity distribution has not changed very much the chordwise velocity has decreased significantly, it even has reversed its direction. This corresponds with a significant increase of the minimum pressure coefficient from $C_p = -3.6$ for $\alpha = 20$ deg to $C_p = -1.8$ for $\alpha = 21.25$ deg.

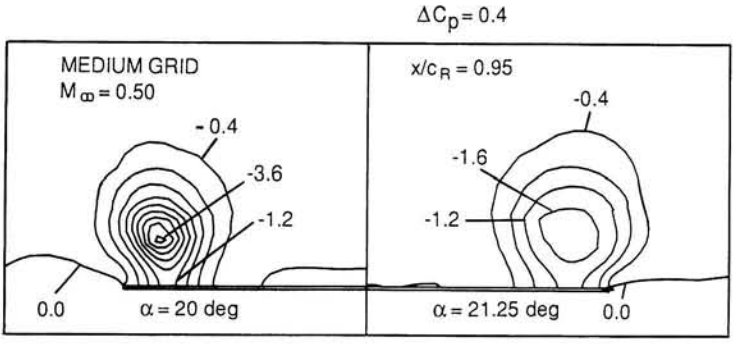

Fig. 10 Cross-flow-plane isobar pattern in plane $x/c_R = 0.95$

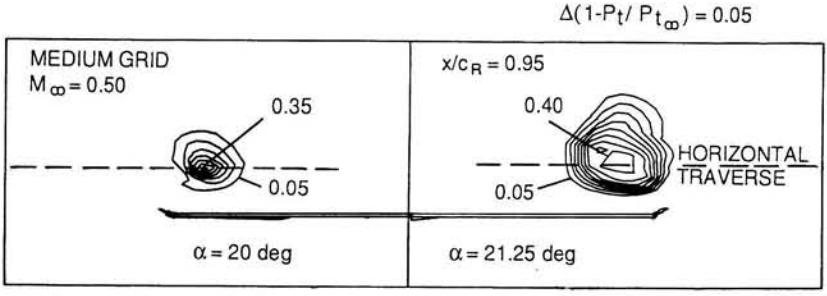

Fig. 11 Cross-flow-plane total-pressure distribution in plane $x/c_R = 0.95$

In the cross-flow-plane isobar plot (Fig. 10) the isoline of -1.2 surrounds a comparable cross-sectional area for both incidences, indicating that primarily the internal structure of the vortex core is affected by the phenomenon. Fig. 11 indicates that during the process of change in structure, the maximum loss in total-pressure remains at the same level but the cross-sectional area in which the largest losses occur increases significantly. The latter is thought to be due to the high gradients in the velocity field now occurring both near the center and near the outer edge of the vortex core.

For $\alpha = 20$ deg the cross-flow-plane vorticity vector, directly related to the distribution of the chordwise velocity component, turns around the center of the vortex core in the same direction as the sense of the circulation of the core. For $\alpha = 21.25$ deg this is also the case for that part of the vortex which is above the forward part of the wing. For that part of the vortex which is above the aft part of the wing Fig. 12 reveals that, at $x/c_R = 0.95$, within the vortex core the circumferential vorticity component has switched sign. The latter immediately explains why near the center of the core the chordwise velocity component has reduced significantly and becomes even negative.

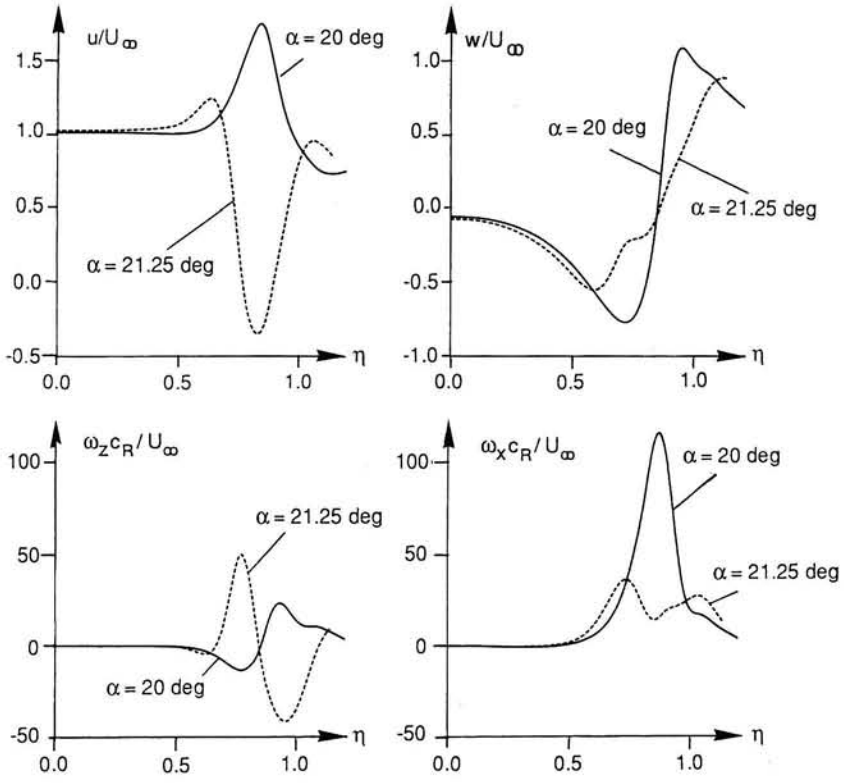

Fig. 12 Flow-field quantities along horizontal traverse through the vortex center in plane $x/c_R = 0.95$

The results further indicate that the chordwise vorticity component undergoes a change in that the peak at the center, found for $\alpha = 20$ deg, disappears and for $\alpha = 21.25$ deg a peak at the edge of the vortex core appears. Directly associated with the distribution of this vorticity component is the distribution of the circumferential velocity component, which at the higher incidence has a smaller gradient at the center of the vortex core.

Crocco's relation, Eq. (2a), states that, in steady inviscid flow and in absence of total-pressure variation, the vorticity vector and the velocity vector are aligned. For the present solutions apparently the angle between the two vectors is zero everywhere, except in the reversed-flow region where it is 180 deg. The mechanism for the change-over in the direction of the cross-flow-plane vorticity vector is not known. However, this phenomenon may greatly affect the stability of the vortex, possibly leading to solution breakdown at a slightly higher incidence.

Aspects of slender, narrow vortex cores

In order to gain some insight in the possibility of multiple states of vortex cores an analysis has been carried out on a core in isolation. The vortex cores encountered in the present context are vortex cores of a cross-sectional dimension which is small relative to a typical length scale along the axis of the vortex core, i.e. vortex cores that may be characterized as slender (slowly varying in axial direction, quasi-cylindrical) and narrow. This forms the starting point for the analysis described below.

Governing equations

Consider the slender, narrow region with rotational flow depicted in Fig. 13. The geometry and the flow are assumed to be *axially symmetric*. For the case of incompressible flow considered here the continuity and Euler equations for axi-symmetric flow in cylindrical coordinates follow from Eq. (1) as:

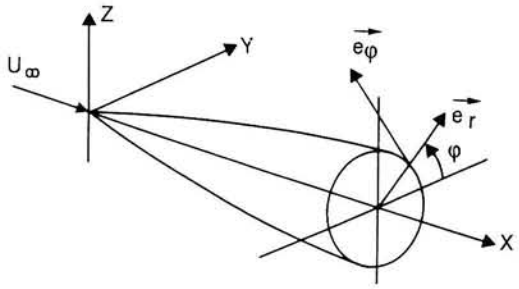

Fig. 13 Isolated slender, narrow vortex core

$$\frac{\partial}{\partial x}u_x + \frac{1}{r}u_r + \frac{\partial}{\partial r}u_r = 0 \tag{3a}$$

and

$$u_x\frac{\partial}{\partial x}u_x + u_r\frac{\partial}{\partial r}u_x + \frac{1}{\rho}\frac{\partial}{\partial x}p = 0 \tag{3b}$$

$$u_x\frac{\partial}{\partial x}u_r + u_r\frac{\partial}{\partial r}u_r - \frac{1}{r}u_\varphi^2 + \frac{1}{\rho}\frac{\partial}{\partial r}p = 0 \tag{3c}$$

$$u_x\frac{\partial}{\partial x}u_\varphi + u_r\frac{\partial}{\partial r}u_\varphi + \frac{1}{r}u_r u_\varphi = 0 \tag{3d}$$

respectively. Denoting the radius of the cross-section of the core in the plane x = constant by $r_e(x)$, the velocity and pressure can be expressed as functions of $\theta = r/r_e(x)$ and x. The first derivative with respect to r of any function $f = f(\theta,x)$ is found from:

$$\frac{\partial f}{\partial r} = \frac{1}{r_e}\frac{\partial f}{\partial \theta} \qquad \text{while} \qquad \frac{\partial f}{\partial x} = -\theta\frac{\dot{r_e}}{r_e}\frac{\partial f}{\partial \theta} + \frac{\partial f}{\partial x}$$

is the derivative with respect to x of $f(\theta,x)$. Eqs. (3a-d) then become:

$$-\theta\frac{\partial F}{\partial \theta} + \frac{2}{\theta}u_r + r_e\frac{\partial}{\partial x}u_x = 0 \tag{4a}$$

$$-\theta F\frac{\partial}{\partial \theta}u_x - \dot{r_e}\frac{\theta}{\rho}\frac{\partial p}{\partial \theta} + r_e\left(u_x\frac{\partial}{\partial x}u_x + \frac{1}{\rho}\frac{\partial p}{\partial x}\right) = 0 \tag{4b}$$

$$-\theta F\frac{\partial}{\partial \theta}u_x - \dot{r_e}\frac{\theta}{\rho}\frac{\partial p}{\partial \theta} + r_e\left(u_x\frac{\partial}{\partial x}u_x + \frac{1}{\rho}\frac{\partial p}{\partial x}\right) = 0 \tag{4c}$$

$$-\theta F\frac{\partial}{\partial\theta}u_\varphi + \frac{1}{\theta}u_r u_\varphi + r_e u_x\frac{\partial}{\partial x}u_\varphi = 0 \tag{4d}$$

where $F = r_e' u_x - \frac{1}{\theta}u_r$

These equations are subject to the boundary conditions that at the axis of the core the radial velocity component vanishes, i.e.

$$u_r = 0 \quad \text{for} \quad \theta = 0 \tag{5a}$$

and that at the edge of the vortex core the axial and circumferential component of the velocity and the pressure are given, i.e. follow from the matching with the outer flow. Here we specify

$$u_x = U_e(x), \quad u_\varphi = V_e(x), \quad p = P_e(x), \quad \text{for } \theta = 1 \tag{5b}$$

The solution of Eqs. (4a-d), subject to the above boundary conditions, can be found in closed form if it is assumed that the product of the core radius r_e with the variation in x-direction of u_x, u_r, u_φ and p may be neglected, i.e. with the last term in each of the Eqs. (4a-d) omitted. This assumption is always met for the case of the *conical* flow inside a *conical* vortex core where the velocity components and the pressure are constant in x-direction and depend on θ only. For *non-conical* flows inside *conical* vortex cores as well as for *non-conical* vortex cores the solution will be valid for slender, narrow vortex cores.

Closed-form solutions

For the case of a *slender conical* vortex core, for which $r_e = Kx$, with $K << 1$, an analytical solution has been derived by Hall (Refs. 16 and 17). Based on this analysis a more general closed-form solution has been derived in Ref. 3, which reduces to Hall's solution upon expansion for small $r_e' = K$. Triggered by the numerical results discussed above a further closed-form solution satisfying the same boundary conditions has been discovered. The two solutions can be expressed in the following form:

$$\frac{u_x}{U_e} = 1 - a\ln\frac{G(\theta)}{G(1)} \tag{6a}$$

$$\frac{u_r}{U_e} = - aG(\theta) \tag{6b}$$

$$\frac{u_\varphi}{U_e} = S\left[1 - \frac{a^2}{S^2}\{\ln\frac{G(\theta)}{G(1)} - \frac{G(\theta)}{\theta r_e'} + \frac{G(1)}{r_e'}\}\right]^{1/2} \tag{6c}$$

$$\frac{p - p_e}{\rho U_e^2} = a\left[(1 + \frac{a}{2})\ln\frac{G(\theta)}{G(1)} - \frac{a}{2}\{(\ln\frac{G(\theta)}{G(1)})^2 - \frac{G(\theta)}{\theta r_e'} + \frac{G(1)}{r_e'}\}\right] \tag{6d}$$

where S is the swirl ratio $S = V_e/U_e$,

$$G(\theta) = [(1 + \theta^2 r_e'^2)^{1/2} - 1]/\theta r_e' \tag{6e}$$

and with $T = \pm 1$

$$a = [T(1 + 4\frac{G(1)}{r_e'} S^2)^{1/2} - 1]/2\frac{G(1)}{r_e'} \tag{6f}$$

The solution derived in Ref. 3 is the solution for T = 1. The second solution is the solution for T = −1. It can be shown that indeed for both solutions the total enthalpy is constant throughout the vortex core.
The stability of the two solutions has not been investigated.

The full expressions for the vorticity vector can be derived directly by taking the curl of the velocity vector given in Eqs. (6a-c). However, here the expressions will be given for the velocity and vorticity components for small r_e', accurate to $O(r_e'^2)$. For the velocity one finds:

$$\frac{u_x}{U_e} = 1 - a\ln\theta \tag{7a}$$

$$\frac{u_r}{U_e} = -\frac{a}{2} r'_e \theta \tag{7b}$$

$$\frac{u_\varphi}{U_e} = S\,[1 - \frac{a^2}{S^2} 1n\theta\,]^{1/2} \tag{7c}$$

where now $a = T(1 + 2S^2)^{1/2} - 1$. For $T = 1$ these are the expressions given in Refs. 16 and 17. The vorticity components then follow as:

$$\frac{\omega_x r_e}{V_e} = \frac{a}{\theta S^2}(1 - a1n\theta) / [\,1 - \frac{a^2}{S^2} 1n\theta\,]^{1/2} \tag{8a}$$

$$\frac{\omega_r r_e}{V_e} = -\frac{r'_e a^2}{2S^2} / [\,1 - \frac{a^2}{S^2} 1n\theta\,]^{1/2} \tag{8b}$$

$$\frac{\omega_\varphi r_e}{V_e} = \frac{a}{\theta S} \tag{8c}$$

It can be verified directly that the present solution satisfies $\vec{u} \times \vec{\omega} = \vec{0}$, not only for the first-order terms given here, but also for the more general expressions, showing that the flow is a Beltrami flow, i.e. that the vorticity vector and the velocity vector are parallel. The principal difference between the two solutions is that in case $T = 1$ the velocity vector and the vorticity vector are pointing in the same direction, while for $T = -1$ the two vectors are in opposing directions.

Discussion of the two solutions

In the solution for the flow inside the axi-symmetric slender and narrow core with distributed vorticity, given in Eqs. (6) and (7), there are two parameters on which the solution depends: the 'swirl parameter' $S = V_e/U_e$ and the (local) slope of the core r'_e. Note that the latter only occurs in the radial velocity component, the radial velocity component going linearly to zero for $r'_e \to 0$.

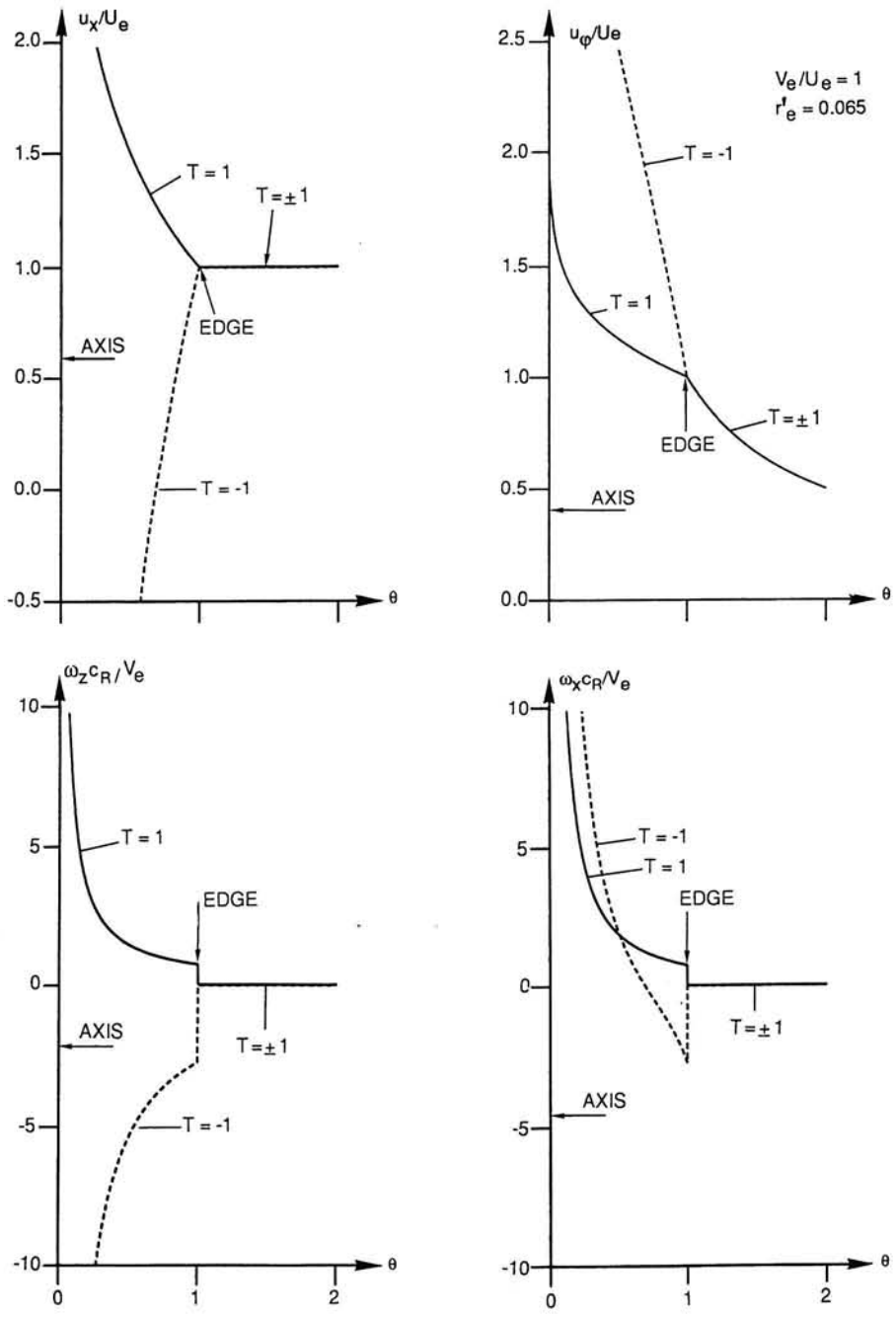

Fig. 14 Flow-field quantities along traverse through isolated vortex core

In Fig. 14 the above expressions are presented for the case of unit swirl ratio and $r_e' = 0.065$. These values correspond, qualitatively, with the values for the case of the numerical solution discussed above (see Fig. 12). The results are given for both solutions, i.e. for T = 1 and −1.
Aside from the inviscid-flow singularity at the axis, which is neither physically meaningful nor resolved in the Euler solution on a finite grid, the figure shows the same type of behaviour as observed in the numerical solution. For T = 1 the regular, jet-like, vortex core emerges with the flow circulating in the direction of the circulation of the core, an increase in the axial velocity component, while the circumferential vorticity component co-rotates with the circumferential velocity component. For T = −1 the wake-like vortex core is found with in the core the flow also circulating in the same direction as the circulation but now with a large deficit in the axial component of the velocity while the circumferential component of the vorticity counter-rotates with respect to the circumferential velocity component. Also note that near the edge of the core the axial component of the vorticity becomes negative though, because of the boundary conditions at the edge, the circulation at a given station along the vortex axis is identical for both solutions. The radial component of the velocity, which is an order of magnitude smaller than the other two components, is negative for T = 1 and positive for T = −1.

Fig. 15 shows two views of the streamline which intersects the edge of the vortex core at $(x, y, z) = (1, 0, r_e')$. For T = 1 the streamline originates from upstream, enters the vortex core and continues in downstream direction spiralling around the core axis, closing in onto the axis by gradually spiralling towards the axis and decreasing the axial spacing of the spiral.
For T = −1 the situation is completely different: the streamline starts at infinity downstream close to the axis and runs in upstream direction, spiralling around the axis now gradually moving towards the edge rather than towards the axis of the core. In upstream direction the axial spacing of the spiral decreases as the streamline moves towards the edge of the core where the axial velocity has a smaller deficit. At a certain point the axial component of the velocity becomes positive and the spiralling streamline starts to run in downstream direction again, reaching the edge of the core at the prescribed location, leaving the vortex core and continuing, spiralling, in downstream direction in the flow field outside the core.
For both solutions the vortex lines are parallel to the streamlines. Since for T = 1 the vorticity vector points in the same, and for T = −1 in the opposite, direction as the velocity vector, in both cases vortex lines feed into the vortex core and ultimately run in downstream direction spiralling towards the vortex axis. This corresponds with the boundary conditions on the edge of the core, which imply, for the present conical geometry, that the circulation increases linearly in axial direction.

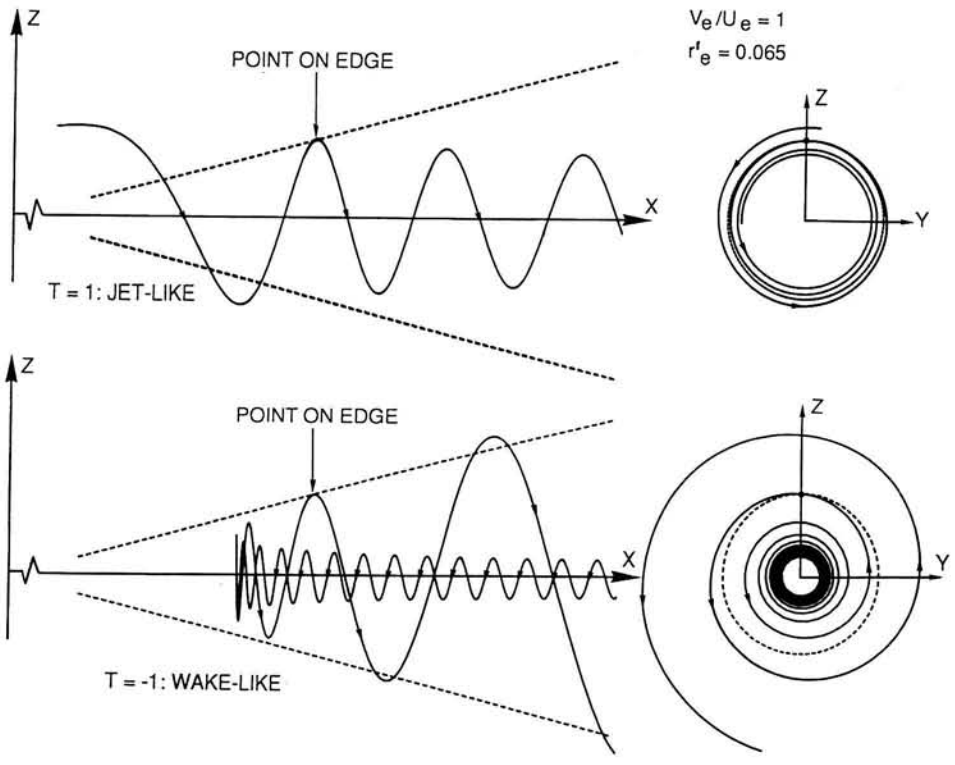

Fig. 15 Streamline related to the two isolated-vortex-core solutions

The features of the above two analytical isolated-core solutions have a remarkable resemblance with the features found in the Euler solution for the flow about the wing at $\alpha = 21.25$ deg. On the forward part of the wing the vortex core is jet-like ($T = 1$) and on the aft part of the wing the core is wake-like ($T = -1$). However, the mechanism responsible for the switch in the flow state from one to the other is still unclear.

Concluding remarks

(i) Solutions obtained with an Euler method for the steady flow about a 65-deg cropped sharp-edged delta wing at $M_\infty = 0.5$ have been analyzed. The analysis included an investigation into the effects of grid refinement for the solution at $\alpha = 20$ deg and a study into the flow solution at $\alpha = 21.25$ deg, which is close to the incidence at which 'solution breakdown' occurs.

(ii) The results of the grid refinement study indicate that the most important flow features are already resolved on the medium grid. The effect of grid refinement on the total-pressure losses has been illustrated. The investigation into the occurrence of total-pressure losses in the numerical solution has led to some more insight in what may be expected from Euler methods as far as free shear layers and vortex cores is concerned.

(iii) The analysis of the solution at $\alpha = 21.25$ deg showed that above the aft part of the wing the leading-edge vortex core experiences a striking change in its internal structure, resulting in a switch from jet-like to wake-like flow. It is shown that associated with this phenomenon is a reversal in the direction of the cross-flow-plane vorticity vector. As a result the vorticity vector and the velocity vector, though still parallel, point now in opposite directions.

(iv) The features of the wake-like type of, second, closed-form Euler solution for the isolated vortex core, derived in the present investigation, show a remarkable resemblance with the features observed in the numerical Euler solution for the flow about the delta wing at $\alpha = 21.25$ deg.

Acknowledgement

It is much appreciated that Prof. Steketee has persistently encouraged further analysis of fundamental aspects of vortical flow through his vivid interest in the topic, as for instance surfaced during the discussion of reports, on NLR work on modeling and numerical simulation of vortical flow, proposed for publication to the NIVR/NLR Scientific Committee.

References

1 Küchemann, D.: The Aerodynamic Design of Aircraft. Pergamon Press (1978).

2 Hirschel, E.H., Rizzi, A.: The Mechanism of Vorticity Creation in Euler Solutions for Lifting Wings. In: Proceedings of Symposium on 'International Vortex Flow Experiment on Euler Code Validation', ed. by A. Elsenaar and G. Eriksson. FFA, Stockholm, October 1-3 1986, pp. 127-161 (1986).

3 Hoeijmakers, H.W.M.: Computational Aerodynamics of Ordered Vortex Flows. NLR TR 88088 U (1989).

4 Elsenaar, A., Hoeijmakers, H.W.M.: An Experimental Study of the Flow Over a Sharp-Edged Delta Wing at Subsonic and Transonic Speeds. AGARD CP-494, Paper 15 (1991).

5 Murman, E.M., Rizzi, A.: Applications of Euler Equations to Sharp-Edged Delta Wings with Leading Edge Vortices. AGARD CP412, Paper 15 (1986).

6 Longo, J.M.A.: The Role of the Numerical Dissipation on the Computational Euler-Equations-Solutions for Vortical Flows. AIAA Paper 89-2232 (1989).

7 Hitzel, S.M.: Wing Vortex-Flows up into Vortex Breakdown. A Numerical Simulation. AIAA Paper 89-2232 (1989).

8 O'Neill, P.J., Barnett, R.M., Louie, C.M.: Numerical Simulation of Leading-Edge Vortex Breakdown using an Euler Code. AIAA Paper 89-2189 (1989).

9 Raj, P., Sikora, J.S., Keen, J.M.: Free-Vortex Flow Simulation using a Three-Dimensional Euler Aerodynamic Method. J. of Aircraft, Vol. 25, No. 2, pp. 128-134 (1988).

10 Peckham, P.D., Atkinson, S.A.: Preliminary Results of Low Speed Wind Tunnel Tests on a Gothic Wing of Aspect Ratio 1.0, ARC Rep. CP-508 (1957).

11 Elle, B.J.: An Investigation at Low Speed of the Flow near the Apex of Thin Delta Wings with Sharp Leading Edges. ARC Rep. R&M. No. 3176 (1958).

12 Ekaterinaris, J.A., Schiff, L.B.: Numerical Simulation of the Effects of Variation of Angle of Attack and Sweep Angle on Vortex Breakdown over Delta Wings. AIAA-90-3000-CP (1990).

13 Boerstoel, J.W.: Progress Report of the Development of a System for the Numerical Simulation of Euler flows, with Results of Preliminary 3D Propeller-Slipstream/Exhaust-Jet Calculations. NLR TR 88008 U (1988).

14 Jameson, A., Schmidt, W., Turkel, E.: Numerical Solution of Euler Equations by Finite Volume Methods Using Runge-Kutta Time-Stepping Scheme. AIAA Paper 81-1259 (1981).

15 Powell, K.G., Murman, E.M., Perez, E.S., Baron, J.S.: Total Pressure Loss in Vortical Solutions of the Conical Euler Equations. AIAA Paper 85-1701 (1985). See also AIAA J., Vol. 25, No. 3, pp. 360-368 (1987).

16 Hall, M.G.: A Theory for the Core of a Leading-Edge Vortex. JFM, Vol. 11, pp. 209-227 (1961).

17 Stewartson, K., Hall, M.G.: The Inner Viscous Solution for the Core of a Leading-Edge Vortex. JFM, Vol. 15, pp. 306-318 (1963).

18 Brown, S.: The Compressible Inviscid Leading-Edge Vortex. JFM, Vol. 22, pp. 17-32 (1965).

19 Berg, J.I. van den, Hoeijmakers, H.W.M., Sytsma, H.A.: Study into the Limits of an Euler-Equation Method Applied to Leading-Edge Vortex Flow. 9th GAMM Conf. Num. Meth. Fl. Mech., Lausanne, Sept. 1991, (1991).

Note

This work is partly based on results obtained in investigations carried out under contract with the Netherlands Agency for Aerospace Programs (NIVR) for the Netherlands Ministry of Defence.

Falkner-Skan and Hartree revisited in the phase plane

By J.L. van Ingen

Faculty of Aerospace Engineering TU Delft

Summary

This note discusses the advantage which may be obtained in the numerical solution of the similar and non-similar laminar boundary layer equations by discussing these solutions in the 'phase plane'. In the phase plane representation shear stress τ is plotted versus the velocity component u, in contrast with the usual presentation of u vs wall distance y. The phase plane was introduced 25 years ago by the author while working on his Ph.D thesis [2] under the guidance of professor Steketee. This earlier work is briefly reviewed first and after that it is shown that numerical solution procedures can benefit from the phase plane description.

Notation

Notation is as usual in boundary layer theory; most symbols are defined in the text where they first occur.

1. Introduction

It is well known that solutions of the Falkner-Skan equation for similar laminar boundary layer flows show a remarkably different behaviour for adverse and favourable pressure gradients. The solution for the adverse pressure gradient case is not unique unless the so-called 'Hartree condition' is introduced (chapter 2).

A special similar boundary layer is that for the flow between non-parallel plane walls. It was shown by the present author [1,2,3] that this special case can be used to explain the relevance of the Hartree condition. It appeared advantageous to discuss this flow in the'phase plane' where shear stress τ is plotted versus the velocity component u parallel to the wall. In this way it was easy to explain why in the case for outflow between non-parallel plane walls a solution with boundary layer character is not possible unless a sufficient amount of suction is applied at the wall. To make these solutions unique it was also necessary to introduce the Hartree condition, which however in this case followed naturally from the phase plane description (chapter 3). It appears that numerical solutions of the Falkner-Skan equation show an analogous

behaviour when plotted in the phase plane. Furthermore it follows that numerical solutions can be obtained much quicker in the phaseplane than in the usual way where u is plotted vs wall distance y (chapter 4). It should be observed that non-similar boundary layers can be calculated by solving a partial differential equation which resembles the (ordinary) Falkner-Skan equation. Therefore the phase plane description is also a promising approach for the numerical calculation of non-similar boundary layers (chapter 5).

2. The Falkner-Skan equation for similar boundary layers

In the present chapter we will derive the Falkner-Skan equation by investigating whether there are pressure-distributions for which similar boundary layers can be obtained. More detailed discussions can be found in Schlichting [4] and Rosenhead [5], the original treatment of the subject is mainly due to Mangler [6], Falkner-Skan [7] and Hartree [8]. We start from the boundary layer equations:

$$u\frac{\partial u}{\partial x} + v\frac{\partial u}{\partial y} = U\frac{dU}{dx} + \nu\frac{\partial^2 u}{\partial y^2} \tag{1}$$

$$\frac{\partial u}{\partial x} + \frac{\partial v}{\partial y} = 0 \tag{2}$$

With the boundary conditions:

$$y = 0 \qquad u = 0 \qquad v = 0 \tag{3}$$

$$y \to \infty \qquad u \to U(x) \tag{4}$$

The boundary condition (3) states that we will not discuss the possibility of using suction ($v_0 < 0$) or blowing ($v_0 > 0$) at the wall to obtain similarity.
We satisfy the continuity equation (2) by introducing the stream function ψ with

$$u = \frac{\partial \psi}{\partial y}; \qquad v = -\frac{\partial \psi}{\partial x} \tag{5}$$

Furthermore we introduce a characteristic length L, and velocity U_∞ and the Reynoldsnumber $R = \frac{U_\infty L}{\nu}$. To be able to introduce a proper scaling for the y-coordinate which depends on x in such a way that similarity is obtained, we introduce a function

g(x). The non-dimensional x and y then can be defined by

$$\xi = \frac{x}{L}; \qquad \eta = \frac{\frac{y}{L}\sqrt{R}}{g(x)} \tag{6}$$

where L and R ensure independence of the resulting equation of the Reynoldsnumber and g(x) should ensure similarity. For the streamfunction we then can write:

$$\psi = \int_0^y u\,dy = \frac{U(x)L}{\sqrt{R}}\, g(x) \int_0^y \frac{u}{U}\, d\left(\frac{\frac{y}{L}\sqrt{R}}{g(x)}\right) \tag{7}$$

or

$$\psi = \frac{U(x)L\, g(x)}{\sqrt{R}} \int_0^\eta \frac{u}{U}\, d\eta \tag{8}$$

In general the integral in (8) will be a function of ξ and η: say $f(\xi,\eta)$. It is our aim in this chapter to find out whether functions U(x) and g(x) exist for which f can be reduced to a function of η only. Note that from (8) it follows that at the wall ($\eta = 0$) we obtain ψ = constant = 0; hence the wall is a streamline. This reflects our neglect of suction and blowing at the wall.
Using (5) and (8) we can show that (primes' denote differentiation with respect to η)

$$\frac{u}{U(x)} = f'(\xi, \eta) \tag{9}$$

and that the boundary layer equation is reduced to the following partial differential equation for the non-dimensional stream function f.

$$f''' + \alpha(x)\, ff'' + \beta(x)\{1 - (f')^2\} = \frac{U(x)}{U_\infty}\, g^2 \left\{f' \frac{\partial f'}{\partial \xi} - f'' \frac{\partial f}{\partial \xi}\right\} \tag{10}$$

where α and β stand for:

$$\alpha(x) = \frac{L\, g}{U_\infty} \frac{d}{dx}(Ug) \tag{11}$$

$$\beta(x) = \frac{L}{U_\infty} g^2 \frac{dU}{dx} \tag{12}$$

The boundary conditions (3) and (4) and equation (9) lead to:

$$\eta = 0 \qquad f = 0 \qquad f' = 0 \tag{13}$$

$$\eta \to \infty \qquad f' \to 1 \tag{14}$$

We will now look for functions U(x) and g(x) which allow f to be a function of η only. This requires that the right hand side of (10) disappears and that α and β are constants.
Then (10) reduces to:

$$f''' + \alpha f f'' + \beta \{1 - (f')^2\} = 0 \tag{15}$$

With α and β constants, independent of x, (11) and (12) provide us with the following simultaneous ordinary differential equations for U(x) and g(x):

$$\frac{L g}{U_\infty} \frac{d}{dx} (Ug) = \alpha \ (= \text{constant}) \tag{16}$$

$$\frac{L g^2}{U_\infty} \frac{dU}{dx} = \beta \quad (= \text{constant}) \tag{17}$$

Solutions for U and g are found to be (see Schlichting chapter [7])

$$g(x) = \sqrt{(2\alpha - \beta)\frac{x}{L}} \left(\frac{U}{U_\infty}\right)^{-\frac{1}{2}} \tag{18}$$

$$\frac{U}{U_\infty} = \text{constant} * \left[(2\alpha - \beta)\frac{x}{L}\right]^{\frac{\beta}{2\alpha - \beta}} \tag{19}$$

In the derivation of (19) the case $2\alpha - \beta = 0$ has been excluded.
The equations (18) and (19) are the main results of our analysis. They show that similarity is possible when

$$U = u_1 x^m \tag{20}$$

where u_1 and m are constants. To see the similarity also expressed in the mathematical sense, that means that we obtain an ordinary differential equation for the stream function, we have to introduce the scaling factor g according to (18).
We can now consider 3 cases.

Case 1: $\alpha \neq 0$
If $\alpha \neq 0$ we can, without loss of generality, take $\alpha = 1$ because $\alpha \neq 1$ would just mean rescaling g with a constant.
With

$$\frac{\beta}{2-\beta} = m \qquad \text{or} \qquad \beta = \frac{2m}{m+1} \tag{21}$$

$$U = u_1 x^m \tag{22}$$

$$g = \sqrt{\frac{2}{m+1}\,\frac{x}{L}\,\frac{U_\infty}{U}} \tag{23}$$

$$\eta = y\sqrt{\frac{m+1}{2}\,\frac{U}{\nu x}} \tag{24}$$

$$\psi(x, y) = \sqrt{\frac{2}{m+1}\,\upsilon\, u_1}\; x^{\frac{m+1}{2}}\, f(\eta) \tag{25}$$

$$f''' + f f'' + \beta\,\{1 - (f')^2\} = 0 \tag{26}$$

Boundary conditions for (26) are

$$\eta = 0 \qquad u = 0 \qquad v = 0 \qquad f = 0 \qquad f' = 0 \tag{27}$$

$$\eta \to \infty \qquad f' = \frac{u}{U} = \bar{u} \to 1 \tag{28}$$

Equation (26) is known as the Falkner-Skan equation. Solutions for various values of β correspond to the flow on a wedge with angle $\pi\beta$; hence $\beta = 1$ represents the stagnation point flow, $\beta = 0$ produces the Blasius flat plate boundary layer.
Because the boundary conditions (27) and (28) are given on both ends of an (infinitely long) integration interval, a special procedure is necessary to find numerical

solutions of equation (26). Very often the'shooting method' is used where a value for f '' at $\eta = 0$ is guessed and the integration is performed to a sufficiently large value of η to check whether the boundary condition (28) is satisfied. If not, the guess for f ''(0) is modified in an appropriate way, etc.
It was shown by Hartree [8] that the character of the trial solutions is different, depending on whether β is positive, zero or negative (fig. 1).
For $\beta \geqslant 0$ there is only one value of the starting value f ''(0) for which the boundary condition at $\eta \rightarrow \infty$ is satisfied.
For $-.198838 \leqslant \beta < 0$ there is for each value of β an infinite number of solutions satisfying the boundary condition for $\eta \rightarrow \infty$. Hartree introduced an extra condition to arrive at a unique solution for each β. This 'Hartree condition' states that the relevant solution is that one which reaches f ' = 1 as soon as possible without making an overshoot (f ' > 1). It turns out that this choice makes the non-dimensional skin friction f ''(0) as a function of β continuous at $\beta = 0$ (fig. 2). Some velocity profiles according to the Hartree solutions are shown in fig. 3. In 1954 it was shown by Stewartson [9] that for $-.198838 \leqslant \beta < 0$ there are so-called 'second branch solutions' to the Falker-Skan equation which satisfy the Hartree condition with a region of backflow near the wall.
These reversed flow solutions are often used to model laminar separation bubbles, they will not be further discussed here.

Case 2: $\alpha = 0$
If we take $\alpha = 0$ then the corresponding external velocity distribution is found to follow from

$$U = \frac{\text{constant}}{x} \tag{29}$$

This solution is also found from (26) for $\beta \rightarrow \infty$.
We will discuss this case in detail in chapter 3.

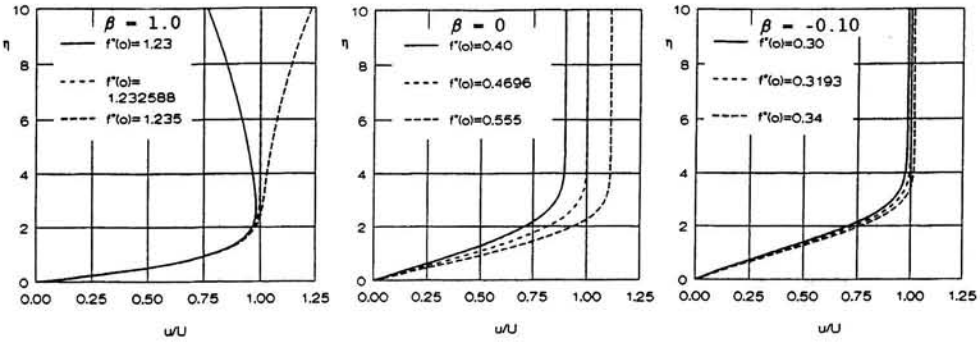

Fig. 1 Characteristic behaviour of trial solutions of the Falkner-Skan equation for various values of β

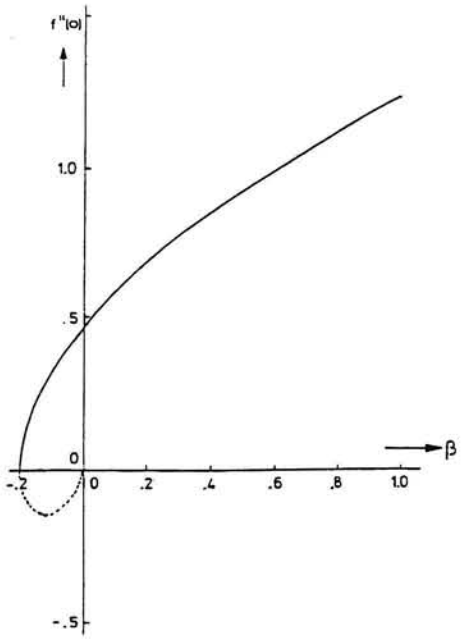

Fig. 2 Non-dimensional skin friction f "(0) as a function of β

Case 3: $2\alpha - \beta = 0$
The case $2\alpha - \beta = 0$ was excluded when deriving equations (18) and (19). This can be shown to lead to

$$U = p\, e^{qx} \tag{30}$$

with p and q constant. This case is of not much practical importance and will not be further discussed here.

3. The flow between non-parallel plane walls

In chapter 2 we mentioned as one of the possible U(x) distributions for which a similarity solution exists

$$U = \frac{u_1}{x} \quad \text{with } u_1 = \text{constant} \tag{31}$$

This resulted from the case $\alpha = 0$, which on further analysis can be shown to be equivalent to $\beta \to \infty$. Because this special case allows a simple treatment we will discuss it here separately.

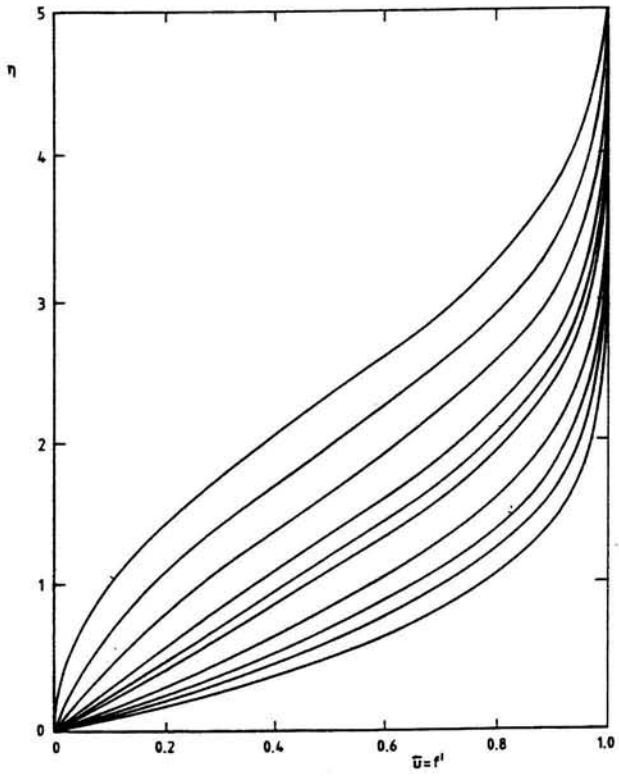

Fig. 3 Hartree solution of the Falker-Skan equation for various values of β (from top to bottom: $\beta = -0.198838; -0.19; -0.16; -0.10; -0.05; 0.0; 0.2; 0.4; 0.6; 1.0$)

The inviscid flow (31) corresponds to the flow between non-parallel plane walls. For $u_1 > 0$ we have outflow, generated by a source at $x = 0$; for $u_1 < 0$ we have inflow generated by a sink (fig. 4).
For η and ψ we can write here

$$\eta = \frac{y}{x}\sqrt{\frac{|u_1|}{\nu}} = \frac{y}{x}\sqrt{\frac{|U|x}{\nu}} \tag{32}$$

$$v = \sqrt{\nu|u_1|}\, f(\eta) = \sqrt{\nu x|U|}\, f(\eta) \tag{33}$$

This transforms the boundary layer equation into

$$f''' + (f')^2 - 1 = 0 \tag{34}$$

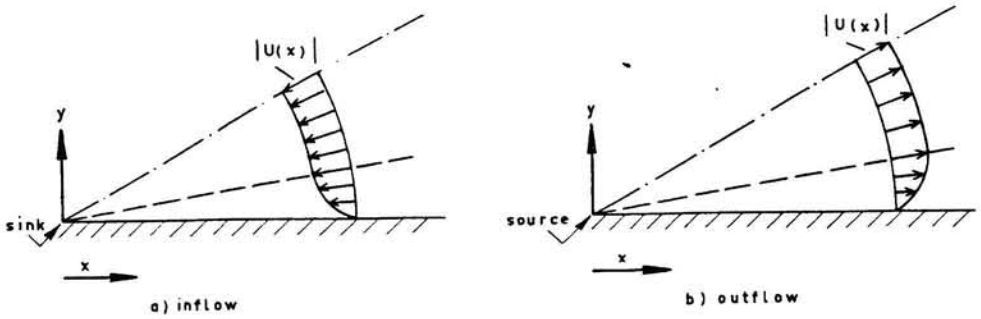

Fig. 4 The flow between non-parallel plane walls

We are now in the pleasant circumstance that f does not appear in (34); therefore we can reduce the order of this differential equation by introducing:

$$f'(\eta) = \frac{u}{|U|} = \bar{u} \tag{35}$$

We then obtain the following second order non-linear ordinary differential equation for $\bar{u}$:

$$\bar{u}'' + \bar{u}^2 - 1 = 0 \tag{36}$$

With boundary conditions

$$\bar{u} = 0 \quad \text{for} \quad \eta = 0$$

$$\bar{u} \to +1 \qquad \text{for} \qquad \eta \to \infty \quad \text{when } u_1 > 0 \text{ (outflow)}$$

$$\bar{u} \to -1 \qquad \text{for} \qquad \eta \to \infty \quad \text{when } u_1 < 0 \text{ (inflow)} \tag{37}$$

for the solution to show a 'boundary layer behaviour' we should find $\bar{u}' \to 0$ for $\eta \to \infty$.

Equation (36) is one of the rare occasions in which a boundary layer solution can be obtained in a closed form. After multiplying (36) with $2\bar{u}'$ we can integrate the equation to give

$$(u')^2 + \frac{2}{3}\,\bar{u}^3 - 2\bar{u} = \text{constant, say A} \tag{38}$$

For inflow ($u_1 < 0$) the boundary conditions (37) for $\eta \to \infty$ require $A = \frac{4}{3}$. Then at $\eta = 0$ we obtain

$$\{u'(0)\}^2 = \frac{4}{3} \tag{39}$$

or

$$u'(0) = \pm \sqrt{\frac{4}{3}} = \pm \frac{2}{\sqrt{3}} \tag{40}$$

Of course we have to use the –sign in (40); hence

$$\bar{u}'(0) = -\frac{2}{\sqrt{3}} \tag{41}$$

With $A = \frac{4}{3}$ we obtain from (38):

$$\bar{u}' = \frac{d\bar{u}}{d\eta} = -\sqrt{\frac{4}{3} + 2\bar{u} - \frac{2}{3}(\bar{u})^3} \tag{42}$$

or

$$\eta = -\int_0^{\bar{u}} \frac{d\bar{u}}{\sqrt{\frac{4}{3} + 2\bar{u} - \frac{2}{3}\bar{u}^3}} \tag{43}$$

The integral (43) can be reduced to

$$-\bar{u} = 3\ \mathrm{tgh}^2\ \{\frac{\eta}{\sqrt{2}} + 1.146216\} - 2 \tag{44}$$

For outflow ($u_1 > 0$) we find in a similar way

$$A = -\frac{4}{3} \qquad \text{and} \qquad \{\bar{u}'(0)\}^2 = -\frac{4}{3} \tag{45}$$

Hence there is no real value for the wall shear stress in the case of outflow, if we impose the last of the conditions (37), that is if we require the solution to show a boundary layer behaviour.
It was shown by van Ingen [1,2,3], that this character of the solution can easily be explained by discussing the solution in a 'phase plane' where shear stress is plotted versus $\bar{u}$. In [1] it was shown that a similar treatment is possible for the full Navier-Stokes solution for this case, including the effects of suction and blowing at the wall. For the present purpose it is sufficient only to discuss the boundary layer flow.
We start again from equation (36); where

$$\bar{u}' = \frac{d\bar{u}}{d\eta} = \text{non-dimensional shear stress} = \text{say } \bar{\tau} \tag{46}$$

Then

$$\bar{u}'' = \frac{d\bar{u}'}{d\eta} = \frac{d\bar{\tau}}{d\eta} \tag{47}$$

and (36) can be written as

$$\frac{d\bar{\tau}}{d\eta} = 1 - \bar{u}^2 \tag{48}$$

Eliminating η from (46) and (48) gives

$$\frac{d\bar{\tau}}{d\bar{\eta}} = \frac{1 - \bar{u}^2}{\bar{\tau}} \tag{49}$$

We now try to discuss possible solutions of (49). One could sketch possible solutions in a $\bar{\tau}$ vs $\bar{u}$ plane by calculating $\frac{d\bar{\tau}}{d\bar{u}}$ in a great number of points and drawing short line- elements through these points, having the direction which follows from $\frac{d\bar{\tau}}{d\bar{u}}$. It will be clear that difficulties will arise in singular points ($\bar{u}$, $\bar{\tau}$) where both the numerator and denominator of (49) become zero, leaving the undetermined form 0/0. Apparently these are the points $\bar{u} = \pm 1$, $\bar{\tau} = 0$ which correspond to the edge of the boundary layer for inflow and outflow respectively. If we shift the origin of t he 'phase plane' to such a singular point we obtain an equation which is of the form

$$\frac{dy}{dx} = \frac{P(x, y)}{Q(x, y)} \tag{50}$$

with $P = Q = 0$ for $x = 0$, $y = 0$.
This type of equation is discussed in many books; a good introduction to the subject may be found in Stoker [10]. It is found that the character of the solution in the neighbourhood of the singular point can be found from the linear terms in P and Q. This means that equations are studied of the form

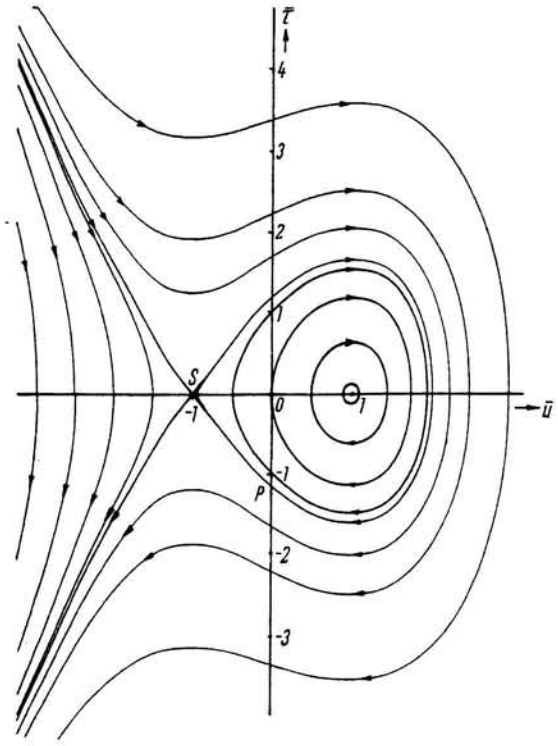

Fig. 5 Phase plane portrait for the boundary layer flow between non-porous non-parallel plane walls

$$\frac{dy}{dx} = \frac{ax + by}{cx + dy} \tag{51}$$

The character of the solution near the origin can then be found from certain discriminants, formed from a, b, c and d. In the present case the singular points are found at $\bar{u} = \pm 1$, $\bar{\tau} = 0$. Shifting the origin to these points in turn and applying the discriminants it is found that (-1, 0) is a so called 'saddle-point' and that (+1, 0) is a 'centre'. Once this is known it is not difficult to make a qualitative sketch of all possible solutions. Of course these solutions can also be calculated accurately. Fig. 5 shows a collection of solution curves according to such a calculation. A solution which fulfils the boundary conditions (37) should start at the wall, that is in a point of the vertical axis and should end in one of the singular points corresponding to the edge of the boundary layer. It is obvious from fig. 5 that this is only possible for inflow; the solution is given by

$$\bar{\tau}^2 = \frac{4}{3} + 2\bar{u} - \frac{2}{3}\bar{u}^3 \tag{52}$$

This solution corresponds to (44) and is represented by PS in fig. 5. If we choose as a starting point for the solution in the phase plane a point on the vertical axis, a little bit away from P_1, we obtain velocity profiles as sketched in fig. 6. These solutions show the same behaviour as those of the Falkner-Skan equation for $\beta > 0$ (see fig. 1) when applying the shooting method.
In [1,2,3], it was shown by van Ingen that also for outflow solutions with boundary layer character can be obtained if only a sufficient amount of suction is applied at the wall. In order to maintain similarity also in the case of porous walls, the normal velocity at the wall (v_o), should be inversely proportional to x. A non-dimensional suction or blowing coefficient λ can then be defined by

$$v_o = \frac{\lambda}{x}\sqrt{\nu\,|u_1|} \tag{53}$$

Blowing occurs for $\lambda > 0$ and suction for $\lambda < 0$.
The boundary layer equation is in this case reduced to

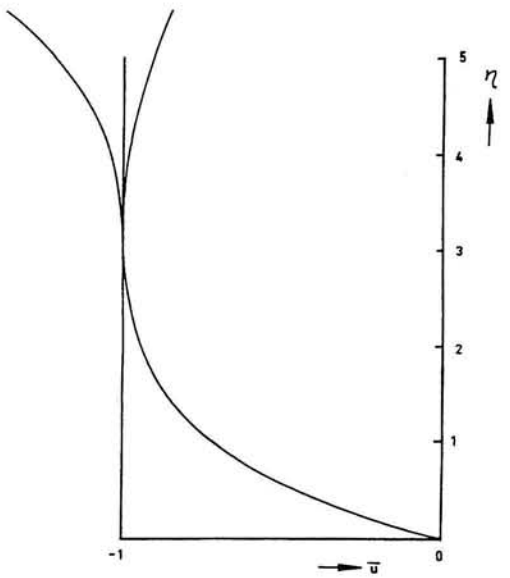

Fig. 6 Velocity profiles corresponding to the saddle point (–1,0) in fig. 5.

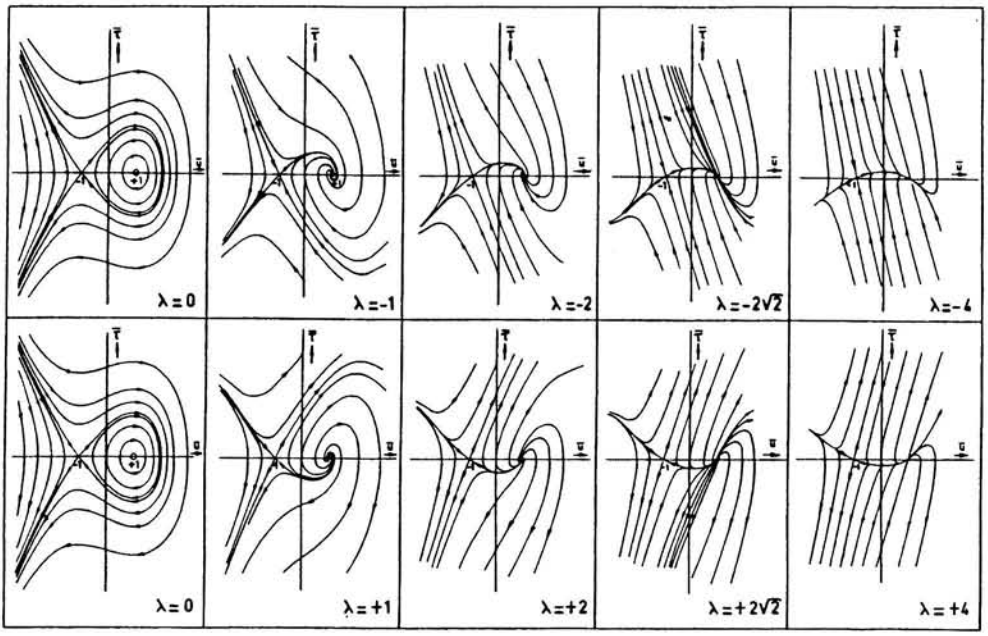

Fig. 7 Phase plane portraits for the boundary layer flow between porous, non-parallel plane walls ($\lambda < 0$: suction; $\lambda > 0$: blowing).

$$f''' - \lambda f'' + (f')^2 - 1 = 0 \tag{54}$$

In the phase plane we obtain [3]

$$\frac{d\bar{\tau}}{d\bar{u}} = \frac{\lambda\bar{\tau} + 1 - \bar{u}^2}{\bar{\tau}} \tag{55}$$

Also in this case the singular points are given by $\bar{u} = \pm 1$, $\bar{\tau} = 0$ and correspond to the edge of the boundary layer (fig. 7). The singularity at (-1,0) remains a saddle point, irrespective of the (positive or negative) value of λ. This always leads to a unique boundary layer solution for inflow between non-parallel walls, irrespective of the value of λ. For the case of outflow, only when there is relatively strong suction ($\lambda \leq -2\sqrt{2}$) the center at (+1,0) is transformed via a stable spiral into a stable node, making it possible to obtain realistic boundary layer type solutions (fig. 8). Such a node (fig. 9) leads to an infinite number of solutions which all satisfy the boundary condition at the edge of the boundary layer. It was shown in [1,2,3] that the steep main branch of the node leads to the relevant solution, which at the same time is found to satisfy the Hartree condition (producing the fastest approach of $\bar{u} = 1$ without making an overshoot). For further arguments the reader is referred to [1,2,3].

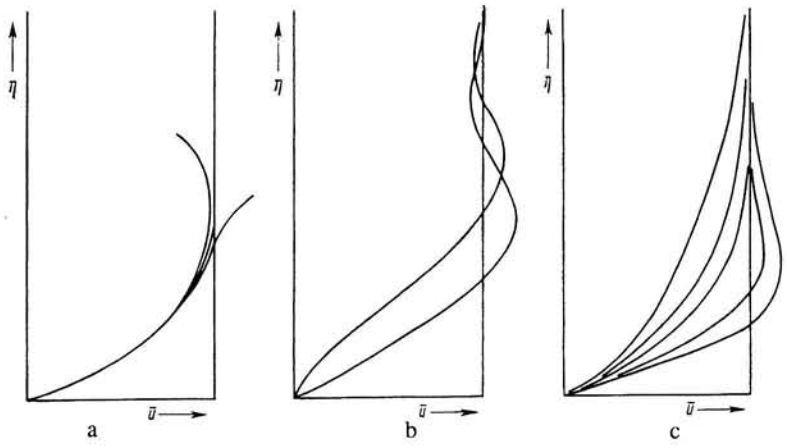

Fig. 8 Velocity profiles for:
(a) saddle point: inflow,
(b) stable spiral:, outflow with modest suction,
(c) stable node: outflow with strong suction

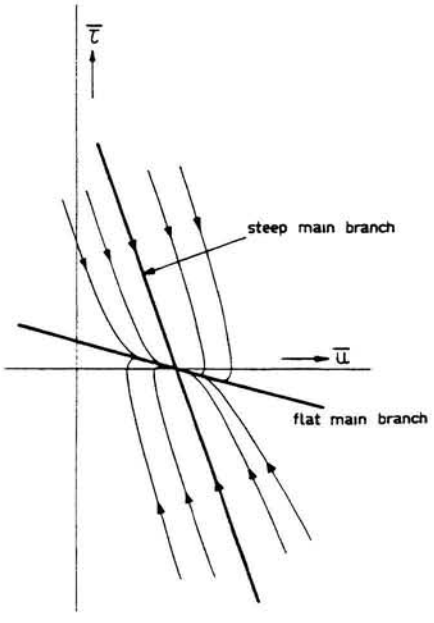

Fig. 9 Characteristics of a stable node

4. The phase plane description of the solutions of the Falkner-Skan equation

It was mentioned in chapter 2 that the Falkner-Skan equation for $\beta \to \infty$ is in fact equivalent to equation (34) describing the flow between non-parallel plane walls. The latter case allowed a simple description in a two-dimensional phase plane because the equation did not contain f and hence could be reduced to a second order equation. The full Falkner-Skan equation is a third order equation and hence requires a three-dimensional phase space to plot the results. In the following discussion we will plot solutions in the f "– f ' plane, hence these are the projections on the f " – f ' plane of the three-dimensional curves. It will follow that this gives a good insight into the behaviour of the solutions and will allow a fast numerical computation. To begin with, fig. 10 shows a number of solutions of the Falkner-Skan equation (26) for the correct values of f "(0). It should be noted that the separation solution for β = -0.198838 shows a square-root behaviour at f' = 0. This was the reason that van Ingen based his further phase plane discussion on plots of $(f'')^2$. (see fig. 11). In the present discussion we will emphasize the behaviour for f ' $\to$ 1 and hence can stick to f" as the dependent variable.

Fig. 12 shows a number of trial solutions for various values of β and f "(0), plotted as f " vs f '; only the region near f ' = 1, f " = 0 is shown.

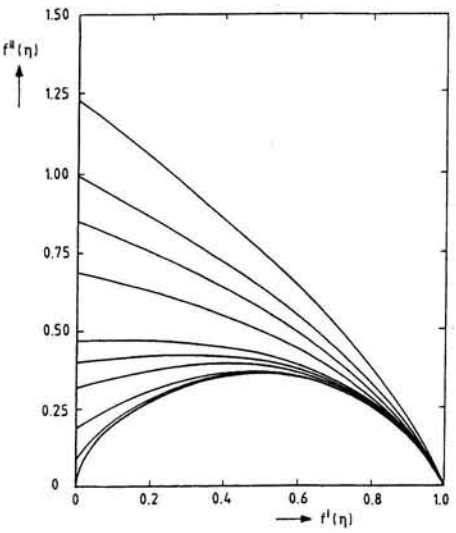

Fig. 10

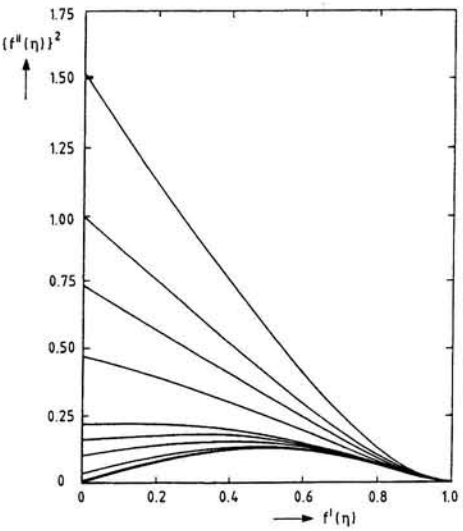

Fig. 11

Figs. 10 and 11 show f "(η) and $\{f''(\eta)\}^2$ respectively as a function of f '(η) = $\bar{u}$ for solutions of the Falkner-Skan equation. The curves (from top to bottom) are for β = 1.0; 0.6; 0.4; 0.2; 0.0; –0.05; –0.10; –0.16; –.019 and –0.198838. Note that in fig. 11 the last two curves more or less collapsed.

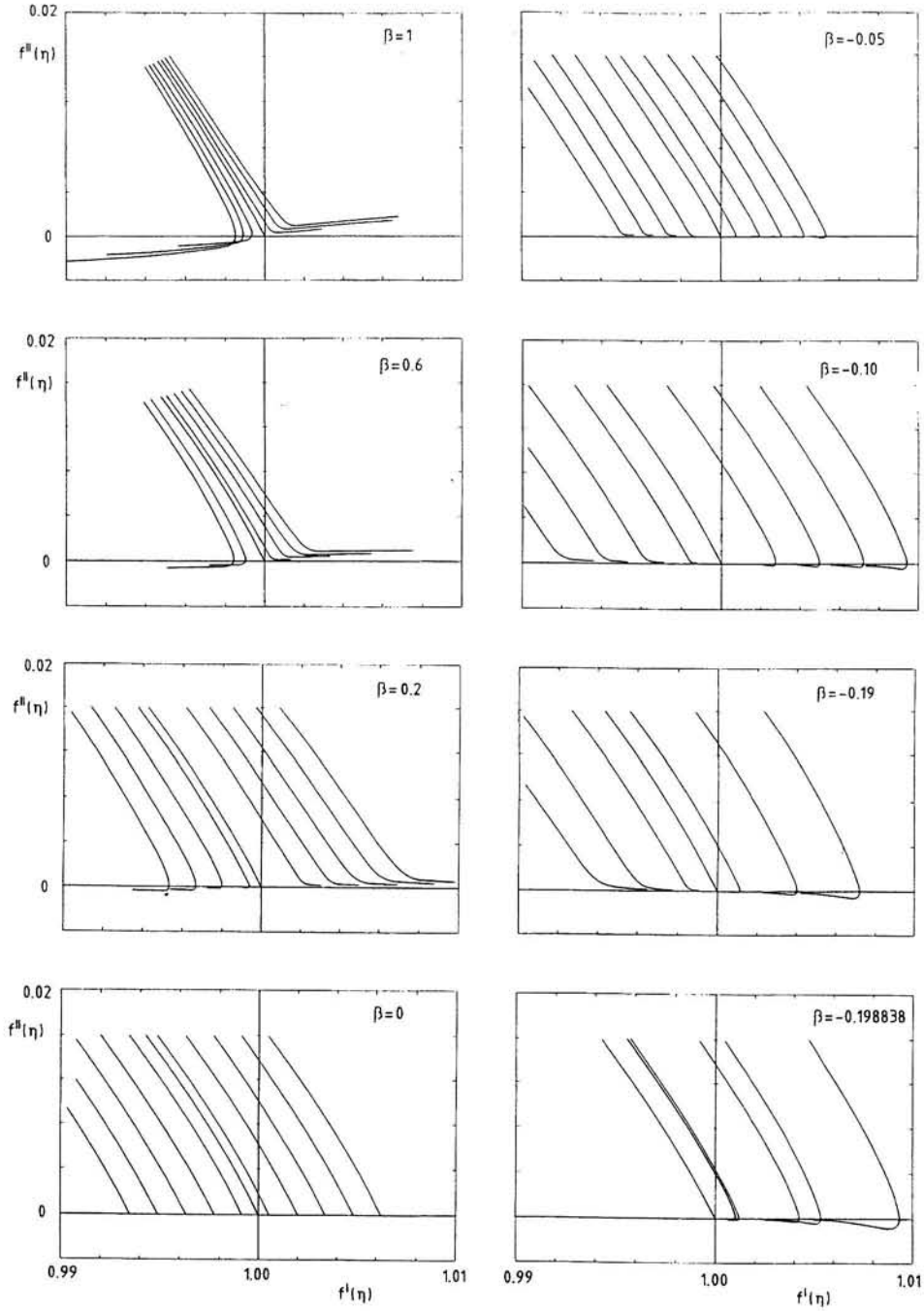

Fig. 12 Trial solutions of the Falkner-Skan equation for various values of β and f "(0). The values of f "(0) for the different curves can be found in table 1 on the next page.

Table 1: **Values of f '' (0) corresponding to the different curves in fig. 12**
For each value of β the curves should be labelled from left to right with the values of f ''(0) given in the table below

β	f''(0)
1.0	1.23246; 1.23250; 1.23254; 1.232588; 1.23262; 1.23266; 1.23270
0.6	0.99560; 0.99570; 0.995836; 0.99590; 0.99600; 0.99610; 0.99620
0.2	0.6850; 0.6855; 0.6860; 0.6865; 0.686708; 0.6875; 0.6880; 0.6885; 0.6890; 0.6895
0.0	0.465; 0.466; 0.467; 0.468; 0.469; 0.46960;, 0.470; 0.471; 0.472; 0.473; 0.474
-0.05	0.396; 0.397; 0.398; 0.399; 0.400323; 0.401; 0.402; 0.403; 0.404; 0.405
-0.10	0.3100; 0.3125; 0.3150; 0.3175; 0.319270; 0.3225; 0.3250; 0.3275; 0.3300
-0.19	0.06; 0.07; 0.08; 0.08570; 0.09; 0.10; 0.11
-0.198838	0.0; +0.025; -0.025; +0.05; -0.05; +0.075

For $\beta > 0$ it is clear that a 'saddle-point' type solution occurs; for $\beta < 0$ there is a behaviour very similar to the node-type for the case of outflow between non-parallel plane walls with suction. Note that the flat main branch is not a single curve because we have to do with the projection of 3-D curves. This flat main branch remains very near to the horizontal axis. It is clear that the Hartree condition is equal to selecting the steep main branch as the required solution; it is not difficult to pick out this solution from its neighbours.
It is tempting to use a polynomial approximation for the steep main branch. Formally this is not permitted because it was shown by Mills [11] that for the Falkner-Skan equation the solutions which satisfy the Hartree condition behave like

$$f'' = (1 - f')\sqrt{\ln(1 - f')} \tag{56}$$

near $f' = 1$.
It was shown by van de Maarel [12] that in practice the singularity (56) can be neglected and replaced by a polynomial behaviour. As a simple illustration we present in

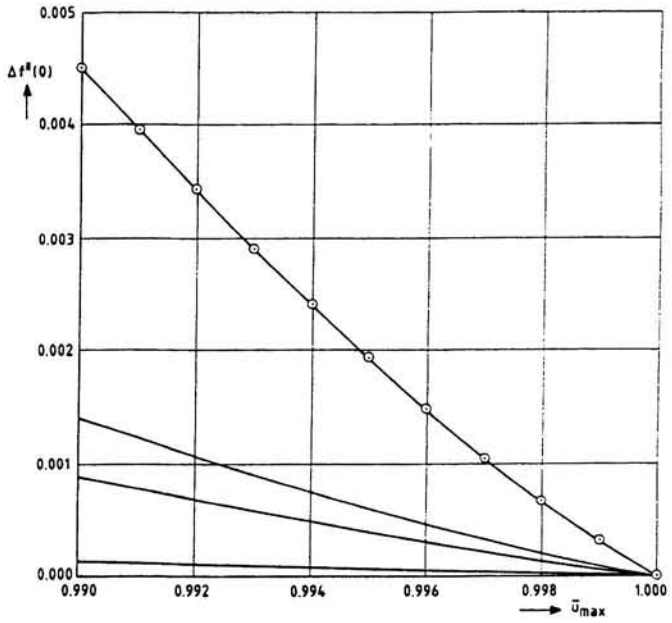

Fig. 13 Error $\Delta f''(0)$ defined as $f''(0)_{exact} - f''(0)_{approx}$ when the boundary condition at $\bar{u} = 1$ is satisfied in the phase plane by linear extrapolation of f'' from $\bar{u} = \bar{u}_{max}$ to $\bar{u} = 1$. The curves (from top to bottom) are for $\beta = -0.19; -0.10;$ 0.0 and 1.0. The exact values of $f''(0)$ for these cases are 0.08570; 0.31927; 0.46960 and 1.23259 respectively.

fig. 13 the values of $f''(0)$ which were obtained by assuming that from a certain value of f' near 1 a linear extrapolation of the $f'' - f'$ curve to (1,0) would be acceptable. Of course the final value which is obtained for $f''(0)$ depends on the value of f' from which the extrapolation starts. For all practical purposes the accuracy is sufficient; if needed this procedure can be refined by using higher order polynomials. Using the present procedure leads to a considerable reduction in computer time because the long tail of the velocity profiel in the u vs y plane does not have to be calculated.

5. On the calculation of non-similar boundary layers

Non-similar boundary layers can be calculated from a partial diferential equation which resembles the Falkner-Skan equation. The equation is, in principle equal to (10); however here we will use a transformation which was given by Görtler. First new variables ξ and η are introduced by:

$$\xi = \frac{1}{\nu} \int_0^x U(x)\, dx \tag{57}$$

$$\eta = \frac{y\,U(x)}{\sqrt{2\nu \int_0^x U(x)\,dx}} \tag{58}$$

For the streamfunction we write

$$\psi(x,y) = \nu \sqrt{2\xi}\, f(\xi, \eta) \tag{59}$$

Introducing these variables into the boundary layer equation leads to the following partial differential equation for f (primes denote differentiation w.r.t. η)

$$f''' + ff'' + \beta(\xi)\,\{1 - (f')^2\} = 2\xi\,\{f' \frac{\partial f'}{\partial \xi} - \frac{\partial f}{\partial \xi} f''\} \tag{60}$$

In (60) the factor $\beta(\xi)$ stands for:

$$\beta(\xi) = \frac{2\frac{dU}{dx}\int_o^x U dx}{U^2} = \frac{2\xi \frac{d^2\xi}{dx^2}}{(\frac{d\xi}{dx})^2} \tag{61}$$

it represents the pressure gradient in the main stream.
For the special case

$$U = u_1 x^m \tag{62}$$

where u_1 and m are constants, β is given by

$$\beta = \frac{2m}{m+1} \tag{63}$$

For this case f becomes a function of η only; the right hand side of (60) disappears and the equation reduces to the Falkner-Skan equation. From (60) it follows that for $\xi \to 0$ the solution tends to the Falkner Skan solution for β = constant = β_o at $\xi = 0$. Many authors have based numerical solutions of the boundary layer equations on Görtlers form (60) of the boundary layer equation. This form has the advantage that for $x \to 0$ the equation reduces to the Falkner-Skan equation; this means that it is exactly known how to start the solution. An example of such a method has been contributed by Fanneloep to chapter IX of the 7th edition of Schlichting's book.

In this method derivatives w.r.t both ξ and η are replaced by finite differences. After linearising the successive velocity profiles are calculated iteratively.
A different approach has been taken by Smith and Clutter [13]. They only replace the streamwise derivatives by finite differences (Hartree-Woomersley method). The derivatives in η direction are retained, leading to a procedure where the boundary layer is calculated by repeatedly applying a shooting procedure as was used for the solution of the Falkner-Skan equation. It is found that the various trial solutions always show the saddle type character, irrespective of the sign of the local value of β. It may be shown that also in this case the computation speed can be increased by using the phase plane description.

References

1 Ingen, J.L. van: Phaseplane representation of the incompressible viscous flow between non-parallel plane walls. Rept. VTH-118, Dept. Aeron. Eng. Delft, 1964.

2 Ingen, J.L. van: Theoretical and experimental investigations of incompressible laminar boundary layers with and without suction. Rept. 124, Dept. Aerospace Eng., Delft University of Technology, 1965.

3 Ingen, J.L. van: Phaseplane representation of the incompressible viscous flow between non-parallel plane walls. Journal of Applied Mathematics and Physics (ZAMP), Vol. 18, Fasc. 1 (1967), pp 120-126.

4 Schlichting, H. : Boundary layer theory (various editions).

5 Rosenhead, L.: Laminar boundary layer theory. Clarendon Press, Oxford 1963.

6 Mangler, W.: Die ähnlichen Lösungen der Prandtlschen Grenzschichtgleichungen. Z.A.M.M. 23, p. 241-251, 1943.

7 Falkner, V.M., Skan, S.W.: Some approximate solutions of the boundary layer equations. A.R.C., R. and M 1314, 1930 (see also Solutions of the boundary layer equations. Phil. Mag. 7, 12, p. 865-896, 1931).

8 Hartree, D.R.: On an equation occurring in Falkner and Skan's approximate treatment of the equations of the boundary layer. Proc. Camb. Phil. Soc. 33, p. 223-239, 1937.

9 Stewartson, K.: Further solutions of the Falkner-Skan equation. Proc. Cambr. Phil. Soc., Vol. 50, 1954, pp 454-465.

10 Stoker, J.J.: Nonlinear vibrations in mechanical and electrical systems. Inters. Publ. 1950.

11 Mills, R.D.: The steady laminar incompressible boundary layer problem as an integral equation in Crocco variables: Investigation of the similarity flows. RM 3514, 1968.

12 Maarel, H.T.M. van der: Numerical investigations on 2-D incompressible boundary layer calculations, based on the modified Crocco equation. (engineering thesis, Delft 1988)

13 Smith, A.M.O. and Clutter, D.W.: Solution of the incompressible laminar boundary layer equations. AIAA Journal, Vol. 1, nr. 9, September 1963, p 2062-2071.

An introduction to computer algebra

By A.J.M. Jansen

Faculty of Aerospace Engineering, TU Delft

1. Introduction

Having executed analytical calculations in the fields of hydrodynamics and magnetohydrodynamics for about twenty years by hand, it becomes time, speaking in computer terms, that the master looks for a slave. Nowadays excellent slaves are available in the form of computer algebra systems.
Basic designs of computer algebra systems, such as Altran, Camal, Macsyma and Reduce are based on the 1960's computing technology. In the 1980's new computer algebra systems, such as Maple and Mathematica, are developed from scratch taking advantage of the software engineering technology and experience which have become available since then. In this paper the attention will be focussed upon the possibilities of the computer algebra Maple.

2. The importance of computer algebra systems

Computer algebra systems are computer programs that are able to execute computations with variables and constants according to the rules of algebra, analysis and other fields of the mathematics, or formula manipulation involving symbols, unknows, and formal operations rather than the conventional computer data of numbers and character strings. The mean importance of computer algebra systems is determined by the fact that they have the ability of doing mathematical computations with unassigned variables; in fact it is computing character strings according to the rules of the mathematics.
Moreover most systems also provide all kinds of additional features, such as: simple numerical calculations, plotting of functions, etcetera. Nevertheless the largest advantage of algebraic manipulation is the very large profit in time gained in comparison to the execution of analytical calculations by hand.
An essential condition to be imposed upon a useful computer algebra is that it combines computation power and computation speed.
One of the most powerful and fastest of the modern computer algebra systems is Maple. The Maple project was started in 1980 by prof. K.O. Geddes and prof. G.H. Gonnet at the University of Waterloo in Canada. They formed the Symbolic Computation Group for the on-going design and implementation of the Maple computer algebra system.

Maple is designed as a symbolic and numerical calculator and it is implemented with a compact, efficient and easily applicable programming language.
The computer algebra system contains a great number of functions and packages that can be loaded separately, involving an applicability over many fields of the mathematics.
Since this algebraic manipulation program is not menu-driven, like e.g. Derive for the personal computer, the user has to know the specific Maple commands to perform a required action. To that purpose Maple is equipped with an excellent and comprehensive help and example facility.
Additional features of the Maple program are: two-dimensional and three-dimensional plotting, translation of programs written in the Maple language into C or Fortran, debugging of Maple programs, user interfaces for windows, etcetera.
If desired, one can even create his own mathematical functions with their specific properties.

Results obtained can easily be checked. It should be noticed that it is always possible, due to the complicated structures and algorithms of the computer algebra program, the nested use of operators or due to the improper use of commands or variable names by the user, that the obtained results are wrong.
Like everybody even a computer algebra can make mistakes.

At the moment, November 1991, version 5 of Maple is available for a large number of machines, e.g. DOS 386, Apollo, Convex, Cray, DEC, HP, Sun, etcetera.

The application of symbolic computation programs in the education of mathematics to students is of great importance, it does not affect, but supplements the existing instructions. Moreover àn entry to a large computer algebra package like Maple invites the user to new branches of the mathematics.

3. Description of the Maple Library

The Maple library functions, i.e. the Maple commands, can be divided into four categories:

1. Internal built-in functions of the Maple system (kernel).
2. Library functions which are automatically loaded on demand.
3. Functions that are not automatically loaded.
4. Packages of functions loaded with the 'with' command.

Basic mathematical tools for symbolic and numerical calculations, programmed in a variant of C and translated into the system code, form the kernel of Maple. The external functions 2 - 4 are written in Maple's own programming language and are available for inspection by the user.

In the following example of a Maple run, see chapter 5, a function like 'diff' for differentiation is built-in. The mathematical functions sin(x) and cos(x) are of the second category. The function 'isolate' must be explicitly loaded by the user: readlib(isolate). Whereas for the matrix calculations at the end of the run the package 'linalg' is loaded by with(linalg).

In version 5 more than 2000 Maple commands are available. This might be overwhelming, but it should be noticed that never all these commands are necessary in an normal Maple run. It is more important to know where a Maple command for a distinct operation can be found. To that purpose Maple is equipped with excellent help and example facilities.

4. Explanation of the demonstration

Since a presentation of a calculation of a hydrodynamic problem in Maple on the occasion of the retirement of prof. J.A. Steketee is beyond the scope of this paper (too extensive and complicated), we will confine ourselves here to a review of some basic mathematical manipulations to show the applicability of Maple in the fields of algebraic manipulations with expressions, analytical calculation and numerical computations.

The capability of Maple is demonstrated in an example of a Maple run to be presented in chapter 5. A file 'input' has been created of about 220 lines with Maple commands. This file is appended to Maple and redirected to the file 'output', viz.

maple < imput > output

The "output" file is shown in the next chapter.
For the sake of clearness some minor editing has been done to the "output" file as presented hereafter.

In order to clarify the demonstration, a global explanation of the appearance of the most important basic typically Maple characters will be discussed here.
Every Maple session opens with the Maple logo: the maple leaf, because it is a Canadian product.
Lines beginning with the Maple prompt ">" are command lines as these are input to the Maple system. The other lines are the output of Maple.
Input lines beginning with the sharp character "#" are for the programmer's comments and are used here as explanation to the reader. These lines are not regarded by Maple as instructions to compute anything.
During the Maple run, an escape to the host operating system is possible, by preceding the Unix command by an note of exclamation, viz. ! <Unix command>.

Every input statement to Maple after the prompt '>' must finish with a semi-colon ';'

or a colon ':'. With the semi-colon the result is displayed, while the colon suppresses the output generated by Maple. The semi-colon is very useful when entering multiple input, see section 7.2 of chapter 5.
Expressions can be labelled with ':=' for later use. For example in section 2 of the demonstration f1 is assigned to x * ln(x) and the whole expression is labelled as a2. The convenience of this method becomes clear in section 3.
Double quotes are used to refer to previously computed expressions by Maple: " to the last expression, "" to the second last expression and """ to the third last expression, see section 6.2.
Single quotes around variables unassign them, while around operators 'oper' they delay the evaluation of the expression, see sections 2., 8. and 9.
A pair of backquotes ` ` is used to form a character string, see section 6.4.
Concatenation of strings is done by the dot operator, viz. a.b result in ab. Or with the function 'cat', see sections 7.1. and 7.2.
In standard mode Maple creates subexpressions to keep the results better readable. These subexpressions are labelled by Maple with: %1 - %3, _C1 or _Z, see 12.1 and 13.5. By setting an option in the command 'interface' this action can be suppressed.
In section 14 examples of the excellent help and example facilities of Maple are presented.

To show the time Maple needed for the calculations the program starts and finishes with an escape to the host operating system to execute the Unix command 'date'.

The example was run on the CANB computer (Sun 4/280 with 64 Mb memory) of the foundation Computer Algebra Netherlands (CAN) in Amsterdam.

5. Demonstration of a Maple run

```
    |\^/|     MAPLE V
._|\|   |/|_.  Copyright (c) 1981-1990 by the University of Waterloo.
 \  MAPLE  /   All rights reserved. MAPLE is a registered trademark of
 <____ ____>   Waterloo Maple Software.
      |        Type ? for help.
               Type !qh for quick help on Maple commands.

                    TECHNICAL UNIVERSITY DELFT
                  FACULTY OF AEROSPACE ENGINEERING
                SECTION OF THEORETICAL AERODYNAMICS

> # To show the time Maple needs for this run, we start and finish with an
> # escape to the host operating system to execute the Unix command "date"
> ! date
Thu Oct 31 15:09:56 MET 1991

> # 1. Simple calculations
> 12 + 7;
                                      19

> 5^67;
          677626357803440271254658000543713569641113281 25

> Pi;
                                      Pi

> sin(Pi/2);
                                      1

> arctan(1);
                                    1/4 Pi

> ln(exp(x^sin(arcsin(x^2))));
                                      2
                                    (x )
                                   x

> sqrt(2);
                                     1/2
                                    2

> sqrt(256);
                                      16

> sqrt(-256);
                                     16 I

> # 2. Assignment and unassignment
> a1 := sin(x);
                                a1 := sin(x)

> a2 := f1 = x * ln(x);
                              a2 := f1 = x ln(x)

> a1;
```

```
                                    sin(x)

> a1 := 'a1';
                                   a1 := a1

> a1;
                                      a1

> # 3. Left and right-hand side
> lhs(a2);
                                      f1
> rhs(a2);
                                   x ln(x)

> # 4. Calculation of numerical values with "evalf" = float evaluation
> # Numerical evaluation in 10, 60 and 100 digits; \ = continuation
> a1 := arctan(1);
                                 a1 := 1/4 Pi

> evalf(a1);
                                 .7853981635

> evalf(a1,60);
        .785398163397448309615660845819875721049292349843776455243735

> evalf(Pi,100);
3.141592653589793238462643383279502884197169399375105820974944592307816406286\
0899862803482534211706 8

> evalf(sqrt(2));
                                 1.414213562

> # 5. Calculation of the first 50 and the 10000-th prime numbers
> # $ = sequence operator
> ithprime(i) $i = 1..50;
2, 3, 5, 7, 11, 13, 17, 19, 23, 29, 31, 37, 41, 43, 47, 53, 59, 61, 67, 71,

    73, 79, 83, 89, 97, 101, 103, 107, 109, 113, 127, 131, 137, 139, 149, 151,

    157, 163, 167, 173, 179, 181, 191, 193, 197, 199, 211, 223, 227, 229

> ithprime(10000);
                                    104729

> # 6. Mathematical manipulations; " = previous result from Maple
> # 6.1. Example 1. Expand an expression
> a1 := (1 + x)^4;
                                          4
                                 a1 := (1 + x)

> expand(a1);
                                       2      3    4
                           1 + 4 x + 6 x  + 4 x  + x

> # 6.2. Example 2. Some polynom manipulations
> a2 := (1 - x)^3/(x + 2 * x^2 + x^3);
                                        3
                                   (1 - x)
                          a2 := -------------
                                      2    3
                                 x + 2 x  + x
> expand(a2);
                                        2      3
                          1         x       x      x
                        ---- - 3 ---- + 3 ---- - ----
                         %1       %1      %1     %1
```

```
%1 :=                                  2    3
                                  x + 2 x  + x

> simplify(");
                                                 2    3
                                    - 1 + 3 x - 3 x  + x
                                  - --------------------
                                                   2
                                      x (1 + 2 x + x )

> # Convert to partial fraction form
> convert(",parfrac,x);
                                                 8         4
                                - 1 + 1/x - --------- + -----
                                                   2     1 + x
                                            (1 + x)

> # Extract the coefficient of the term of the order (1 + x)^(-1)
> coeff(",(1+x)^(-1));
                                             4

> # Factor the polynom; "" = second last result of Maple
> factor("");
                                                 3
                                          (x - 1)
                                        - ---------
                                                  2
                                         x (1 + x)

> # 6.3. Example 3. Collect all the coefficients with the same power of x

> a3 := (1 + 2 * x - 3 * y)^3 * (1 - z)^2;
                                                3         2
                              a3 := (1 + 2 x - 3 y)  (1 - z)

> expand(a3);
                    2  2              2    2         2              3
  1 + 6 x + 54 x y  z  - 9 y - 36 x  y z  + 12 x  - 2 z + 8 x  + 72 x y z

            2                2                    2         2           2    2
        + 72 x  y z - 108 x y  z - 36 x y + 27 y  - 36 x  y + 54 x y  + z

                          2                  2         2  2         2
        - 12 x z + 6 x z  + 18 y z - 9 y z  - 24 x  z + 12 x  z  - 54 y  z

              2  2        3          3  2        3          3  2        3           2
        + 27 y  z  - 16 x  z + 8 x  z  + 54 y  z - 27 y  z  - 27 y  - 36 x y z

> collect(a3,x);
             2  3                      2  2
 8 (1 - z)  x  + (12 - 36 y) (1 - z)  x

                                                 2          2          3         2
      + ((1 - 3 y) (4 - 12 y) + 2 (1 - 3 y) ) (1 - z)  x + (1 - 3 y)  (1 - z)

> # 6.4. Examples of manipulations with trigonometric functions
> # Note that backquoted expressions `expr` are treated as text by Maple

> `cos(2*x)` := expand(cos(2*x));
                                                  2
                                 cos(2*x) := 2 cos(x)  - 1

> `sin(7*x) + cos(3*x)` := expand(sin(7*x) + cos(3*x));
                                                      6          4
          sin(7*x) + cos(3*x) := 64 sin(x) cos(x)  - 80 sin(x) cos(x)
```

```
                                        2                      3
              + 24 sin(x) cos(x)^2 - sin(x) + 4 cos(x)^3 - 3 cos(x)

> `cos(x)^2` := combine(cos(x)^2,trig);

                          cos(x)^2 := 1/2 cos(2 x) + 1/2

> `7 * sin(x) * sin(y) - 9 * cos(x) * cos(y)` :=
> combine(7 * sin(x) * sin(y) - 9 * cos(x) * cos(y),trig);

    7 * sin(x) * sin(y) - 9 * cos(x) * cos(y) := - cos(x - y) - 8 cos(x + y)

> # 7. Solving equations with the command "solve"
> # 7.1. Solving an equation of the fifth degree

> eq1 := x^5 + 23 * x^4 - 67 * x^3 + 1234 * x^2 - 88 * x + 576 = 0;
                      5       4       3         2
               eq1 := x  + 23 x  - 67 x  + 1234 x  - 88 x + 576 = 0

> result1 := solve(eq1,x);
                                  5         4         3          2
       result1 := RootOf(_Z^5 + 23 _Z^4 - 67 _Z^3 + 1234 _Z^2 - 88 _Z + 576)

> # Evaluation of the result; " = previous result from Maple
> result1a := allvalues(");

        result1a := -27.14778261, .02321672236 + .6867154851 I,

            .02321672236 - .6867154851 I, 2.050674583 + 6.382419402 I,

            2.050674583 - 6.382419402 I
> # The third term of the list result1a
> result1a[3];
                          .02321672236 - .6867154851 I

> # Printing the solutions with a loop construction, written in the Maple
> # programming language
> for i from 1 to 5 do;
>   lprint(cat(`solution(`,i,`) =`),result1a[i]);
> od;
solution(1) =   -27.14778261
solution(2) =   Float(2321672236,-11)+.6867154851*I
solution(3) =   Float(2321672236,-11)-.6867154851*I
solution(4) =   2.050674583+6.382419402*I
solution(5) =   2.050674583-6.382419402*I

> # 7.2. Solving a system of linear equations
> # Finishing a statement with ":" suppresses the Maple output

> eq1 := 10 + 5 * x1 + 67 * x2 + 5 * x3 - 78 * x4 - 4 * x5 = 0:
> eq2 := 3 - 73 * x1 - 76 * x2 + 20 * x3 + 7 * x4 - 5 * x5 = 0:
> eq3 := 81 + 9 * x1 - 33 * x2 - 3 * x3 - 122 * x4 + 19 * x5 = 0:
> eq4 := 12 - 3 * x1 + 12 * x2 + 49 * x3 + 85 * x4 - 71 * x5 = 0:
> eq5 := 2 + 61 * x1 - 44 * x2 - 7 * x3 - 99 * x4 + 6 * x5 = 0:
> sys :=  {eq1,eq2,eq3,eq4,eq5}:
> vars := {x1,x2,x3,x4,x5}:

> sol2 := solve(sys,vars);
                      67927513          243784403          386992463
       sol2 := {x3 = - --------, x2 = - ---------, x4 = - ---------,
                       2903573          243900132          243900132

                 1038100729          1089325042
           x1 = - ----------, x5 = - ----------}
                  243900132           60975033
```

```
> # Checking the result; subs = substitution, . = concatenation of
> # eq.i to eq1 - eq5
> i := 1:
> while i < 6 do;
>    subs(sol2,eq.i);
>    i := i + 1:
> od;
```

$$0 = 0$$
$$0 = 0$$
$$0 = 0$$
$$0 = 0$$
$$0 = 0$$

```
> # This answer is encouraging

> # 8. Differentiation
> # 8.1. Ordinary differentiation

> # Note that x$3 represents the third derivative with respect to x
> # Operators placed between quotes 'oper' are not evaluated the first time
> # Evaluation takes place by ";

> f(x) := ln(5 + 3 * x^5)/sqrt(x^2 + 4);
```

$$f(x) := \frac{\ln(5 + 3\,x^5)}{(x^2 + 4)^{1/2}}$$

```
> 'diff(f(x),x)';
```

$$\frac{d}{dx} f(x)$$

```
> ";
```

$$15\,\frac{x^4}{(5 + 3\,x^5)\,(x^2 + 4)^{1/2}} - \frac{\ln(5 + 3\,x^5)\,x}{(x^2 + 4)^{3/2}}$$

```
> diff(f(x),x$2);
```

$$60\,\frac{x^3}{(5 + 3\,x^5)\,(x^2 + 4)^{1/2}} - 225\,\frac{x^8}{(5 + 3\,x^5)^2\,(x^2 + 4)^{1/2}}$$
$$- 30\,\frac{x^5}{(5 + 3\,x^5)\,(x^2 + 4)^{3/2}} + 3\,\frac{\ln(5 + 3\,x^5)\,x^5\,2}{(x^2 + 4)^{5/2}} - \frac{\ln(5 + 3\,x^5)}{(x^2 + 4)^{3/2}}$$

```
> # 8.2. Partial differentiation

> g(x,y) := 1/((x - a)^2 + (y - b)^3 + 16)^(1/2);
```

$$g(x, y) := \frac{1}{((x - a)^2 + (y - b)^3 + 16)^{1/2}}$$

```
> diff(g(x,y),x);
```

$$-1/2\,\frac{2\,x - 2\,a}{((x - a)^2 + (y - b)^3 + 16)^{3/2}}$$

```
> diff(g(x,y),y);
```

$$-3/2\,\frac{(y-b)^2}{((x-a)^2+(y-b)^3+16)^{3/2}}$$

```
> 'diff(diff(g(x,y),x),y)';
```

$$\frac{d^2}{dy\,dx}\,g(x,y)$$

```
> ";
```

$$9/4\,\frac{(2x-2a)(y-b)^2}{((x-a)^2+(y-b)^3+16)^{5/2}}$$

```
> # 9. Integration
> # 9.1. Indefinite integrals

> a1 := int(x^2,x);
```

$$a1 := 1/3\,x^3$$

```
> # Note that Maple omits the constant of integration
> a2 := 'int(x^5,x)' = int(x^5,x);
```

$$a2 := \int x^5\,dx = 1/6\,x^6$$

```
> a3 := 'int(1/(1 + sin(x) + cos(x)),x)' = int(1/(1 + sin(x) + cos(x)),x);
```

$$a3 := \int \frac{1}{1+\sin(x)+\cos(x)}\,dx = \ln(2+2\tan(1/2\,x))$$

```
> # Check of the result; rhs = right-hand side
> diff(rhs("),x);
```

$$\frac{1+\tan(1/2\,x)^2}{2+2\tan(1/2\,x)}$$

```
> expand(");
```

$$\frac{1}{\%1}+\frac{1}{\%1\,\sin(x)^2}-2\,\frac{\cos(x)}{\%1\,\sin(x)^2}+\frac{\cos(x)^2}{\%1\,\sin(x)^2}$$

$$\%1 := 2+\frac{2}{\sin(x)}-2\,\frac{\cos(x)}{\sin(x)}$$

```
> simplify(");
```

$$\frac{1}{1+\sin(x)+\cos(x)}$$

```
> # One should never trust the primary results of one's own analytical
> # calculations, neither that of a computer algebra
```

```
> # 9.2. Definite integrals

> a4 := int(exp(- x) * ln(x), x = 0..infinity);
                                  a4 := - gamma

> # When the gamma function is unknown to the user the Maple command "? gamma"
> # will provide more information about that function

> # 9.3. Numerical calculation of integrals
> # Numerical evaluation of the previous result
> a4 := evalf(");
                               a4 := -.5772156649

> # Another example; the option "x = 0..1" defines the bounds of the integral
> a5 := int(exp(arccos(x/17)), x = 0..1);

                                    1
                                   /
                                  |
                          a5 := |  exp(arccos(1/17 x)) dx
                                  |
                                 /
                                 0

> # When Maple cannot find an analytical solution no output is given
> # Therefore numerical evaluation of the integral
> evalf(a5);
                                  4.671687675

> # 10. Sums and a limit
> 'sum(p^5, p = 1..30)';
                                     30
                                   -----
                                   \      5
                                    )    p
                                   /
                                   -----
                                   p = 1

> ";
                                   133987425

> 'sum(1/(p^2+p)^3, p = 1..a)';
                                    a
                                  -----
                                  \          1
                                   )    ---------
                                  /       2     3
                                  ----- (p  + p)
                                  p = 1

> ";
                                  2
                    - 2 + 6 (a + 1)  - 3 a                                  2
                - ---------------------- + 6 Psi(1, a + 2) + 10 - Pi
                                  3
                         (a + 1)

> # And now the answer when "a" tends to infinity
> limit(", a = infinity);
                                       2
                                   10 - Pi

> # 11. A product
> 'product((n + 1)/(n + 1/a), n=1..N)' = product((n + 1)/(n + 1/a), n=1..N);
```

```
                    N
                  .---.
                  |   |      n + 1     GAMMA(N + 2) GAMMA(1 + 1/a)
                  |   |     ------- = ---------------------------
                  |   |     n + 1/a           GAMMA(N + 1 + 1/a)
                  |   |
                  '---'
                 n = 1
```

```
> # 12. Differential equations
> # 12.1. Analytical calculation with the command "dsolve"; \ = continuation

> # Example 1.
> deq1 := x * diff(y(x),x) - ln(x * y(x)) * y(x) + y(x) = 0;
                                 /  d      \
                      deq1 := x |---- y(x)| - ln(x y(x)) y(x) + y(x) = 0
                                 \ dx      /

> res1 := dsolve(deq1,y(x));

                          res1 := x = _C1 ln(x) + _C1 ln(y(x))

> # To solve the result "res1" with respect to y(x) we may enter the library
> # function "isolate", which is of the third catagory, see section 3
> # The library function is loaded with the Maple command "readlib"
> readlib(isolate);
proc(expr,x,n) ... end

> res1a := isolate(res1,y(x));
                                                  - x + _C1 ln(x)
                          res1a := y(x) = exp(- ---------------)
                                                       _C1

> # Substitution of the boundary condition y(1) = 3
> subs(x = 1,");
                                        - 1 + _C1 ln(1)
                             y(1) = exp(- ---------------)
                                              _C1
> subs(y(1) = 3,");
                                           1
                                    3 = exp(---)
                                           _C1
> isolate(",_C1);
                                           1
                                    _C1 = -----
                                          ln(3)
> subs(",res1a);
                                      /       ln(x)\
                           y(x) = exp(- |- x + -----| ln(3))
                                      \       ln(3)/
> # The final result
> simplify(");
                                           x
                                          3
                                    y(x) = ----
                                           x

> # Example 2. A more complicated one; \ = continuation of the expression
> deq2 := diff(z(x),x$3) -7 * diff(z(x),x$2) + 9 * diff(z(x),x) + 2 * z(x) = \
> 37;
                 /   3      \     /   2      \
                 |  d       |     |  d       |     /  d      \
          deq2 := |----- z(x)| - 7 |----- z(x)| + 9 |---- z(x)| + 2 z(x) = 37
                 |   3      |     |   2      |     \ dx      /
                 \ dx       /     \ dx       /

> # Solving the differential equation for the boundary conditions: z(0) = 0,
```

```
> # z'(0) = 1 and z''(0) = 2
> sol2 := dsolve({deq2,z(0)=0,D(z)(0)=1,D(D(z))(0)=2},z(x));

                                  74                                  exp(2 x)
   sol2 := z(x) = ------------------------------ - 62/7 ------------------------------
                                1/2          1/2                  1/2          1/2
                  (5 + 29    ) (- 5 + 29    )          (5 + 29    ) (- 5 + 29    )

            /323   1/2        \                    1/2
            |--- 29    - 57/7| exp(1/2 (5 + 29    ) x)
            \203              /
       + 4 ---------------------------------------------
                                1/2          1/2
                  (5 + 29    ) (- 5 + 29    )

                    1/2                          1/2
     152 (29 + 29    ) exp(- 1/2 (- 5 + 29    ) x)
   - --- ---------------------------------------------
     203                1/2          1/2 2
                  (5 + 29    ) (- 5 + 29    )

> # Checking the result with an example of nested commands: substitute the
> # solution sol2 into the differential equation deq2, simplify the answer
> # and combine the respective results

> combine(simplify(subs(sol2,deq2)));
                                     37 = 37

> # Hence the above solution of the differential equation is okay
> # 12.2. Numerical calculation of a differential equation

> deq3 := x * diff(h(x),x$2) + ln(x * h(x)) * h(x)^4 + 3 * h(x)^(3/2) = 0;
                          /   2      \
                          |  d       |                          4         3/2
                deq3 := x |----- h(x)| + ln(x h(x)) h(x)  + 3 h(x)    = 0
                          |   2      |
                          \ dx       /

> dsolve({deq3,h(1)=1,D(h)(1)=2},h(x));
>
> # When Maple returns with the prompt, it cannot find an analytical solution
> # A numerical solution of the differential equation can be determined by
> # adding the option "numeric" to the command "dsolve"

> sol3 := dsolve({deq3,h(1)=1,D(h)(1)=2},h(x),numeric);

sol3 := proc(x) `dsolve/numeric/result2`(x,1945152,[2]) end

> # Calculation of eleven values of the function h(x) between x = 1 and x = 2
> dx := 0.1:
> for i from 0 to 10 do;
>    x := 1 + i * dx:
>    sol3(x);
> od;
                                      1., 1.
                                1.100000000, 1.183428615
                                1.200000000, 1.326983578
                                1.300000000, 1.420497811
                                1.400000000, 1.456223789
                                1.500000000, 1.432018638
                                1.600000000, 1.352549760
                                1.700000000, 1.227581591
                                1.800000000, 1.068681796
                                1.900000000, .8864234006
                                    2., .6890955324
```

```
> # In the above list the first numerical value represents the value of x
> # and the second one the value of the function h(x)

> # 13. Matrix operations

> # To execute matrix calculations in Maple the package "linalg" must be
> # loaded with the command "with"
> with(linalg):

> # 13.1. Example 1. Definition of a matrix

> A1 := array([[b1,3,b2,5],[1,b3,7,b4],[b5,8,b6,6]]);

                                [ b1   3  b2   5 ]
                                [                ]
                           A1 := [  1  b3   7  b4 ]
                                [                ]
                                [ b5   8  b6   6 ]

> A1[2,4];
                                     b4

> # Changing the value of an element of the matrix

> A1[2,4] := Pi;

                                A1[2, 4] := Pi

> # Show the modified matrix A1
> print(A1);
                              [ b1   3  b2   5 ]
                              [                ]
                              [  1  b3   7  Pi ]
                              [                ]
                              [ b5   8  b6   6 ]

> # 13.2. Example 2. The determinant of a random matrix
> A2 := randmatrix(4,4);

                                [ -55  -37  -35   97 ]
                                [                    ]
                                [  50   79   56   49 ]
                           A2 := [                    ]
                                [  63   57  -59   45 ]
                                [                    ]
                                [  -8  -93   92   43 ]
> det(A2);
                                  118510712

> # 13.3. Example 3. The inverse of a matrix
> A3 := randmatrix(5,5);

                              [ -62   77   66   54   -5 ]
                              [                         ]
                              [  99  -61  -50  -12  -18 ]
                              [                         ]
                         A3 := [  31  -26  -62    1  -47 ]
                              [                         ]
                              [ -91  -47  -61   41  -58 ]
                              [                         ]
                              [ -90   53   -1   94   83 ]
```

```
> evalm(A3^(-1));
```

$$\begin{bmatrix} \frac{8554681}{1872944270} & \frac{15885721}{1872944270} & \frac{8881379}{3745888540} & -\frac{16579737}{3745888540} & \frac{1364251}{3745888540} \\ \frac{950097}{1872944270} & -\frac{28483953}{1872944270} & \frac{88939883}{3745888540} & -\frac{41793169}{3745888540} & \frac{8918667}{3745888540} \\ \frac{8123979}{936472135} & \frac{10686694}{936472135} & -\frac{19397587}{936472135} & \frac{4476641}{936472135} & -\frac{5048928}{936472135} \\ \frac{2182501}{187294427} & \frac{3261493}{187294427} & -\frac{1187719}{187294427} & \frac{882396}{187294427} & \frac{782838}{187294427} \\ -\frac{15852251}{1872944270} & -\frac{1265851}{1872944270} & -\frac{21194799}{3745888540} & -\frac{11061883}{3745888540} & \frac{22940369}{3745888540} \end{bmatrix}$$

```
> # The inverse matrix of the previous result must lead to the original matrix
> evalm("^(-1));
```

$$\begin{bmatrix} -62 & 77 & 66 & 54 & -5 \\ 99 & -61 & -50 & -12 & -18 \\ 31 & -26 & -62 & 1 & -47 \\ -91 & -47 & -61 & 41 & -58 \\ -90 & 53 & -1 & 94 & 83 \end{bmatrix}$$

```
> # Okay

> # 13.4. Example 4. Multiplication of two random matrices A4 and A5
> A4 := randmatrix(3,4);
```

$$A4 := \begin{bmatrix} -86 & 23 & -84 & 19 \\ -50 & 88 & -53 & 85 \\ 49 & 78 & 17 & 72 \end{bmatrix}$$

```
> A5 := randmatrix(4,2);
```

$$A5 := \begin{bmatrix} -99 & -85 \\ -86 & 30 \\ 80 & 72 \\ 66 & -29 \end{bmatrix}$$

```
> multiply(A4,A5);
```

$$\begin{bmatrix} 1070 & 1401 \\ -1248 & 609 \\ -5447 & -2689 \end{bmatrix}$$

```
> # 13.5. Example 5. The eigenvalues and eigenvectors of a matrix
> A6 := randmatrix(3,3);
```

$$A6 := \begin{bmatrix} -91 & -53 & -19 \\ -47 & 68 & -72 \\ -87 & 79 & 43 \end{bmatrix}$$

```
> eigenvals(A6);
                                                                  1/2
      %3 + %2 + 20/3, - 1/2 %3 - 1/2 %2 + 20/3 + 1/2 3    (%3 - %2) I,

                                                 1/2
          - 1/2 %3 - 1/2 %2 + 20/3 - 1/2 3    (%3 - %2) I

                                        1/2  1/2
%1 :=                     9962439832666    3

                         /  16557859          \1/3
%2 :=                    |- --------- - 1/9 %1|
                         \      27            /

                         /  16557859          \1/3
%3 :=                    |- --------- + 1/9 %1|
                         \      27            /

> eigenvects(A6);
 [%1, 1,

            194173    788          19     2    53     2     47        684187
     {[ 1, - ------ - ----- %1 - ------ %1 , ------ %1  - ----- %1 - -------* ]}]
            255942   42657       255942      255942       42657     255942

                                                        2     3
%1 :=            RootOf(1264654 - 5633 _Z - 20 _Z  + _Z )

> # In the above result %1 - %3, _Z are subexpressions introduced by Maple

> # 13.6. Example 6. Solving the system Ax = B
> A := randmatrix(4,4);
                                  [ -66  -53  -61  -23 ]
                                  [                    ]
                                  [ -37   31  -34  -42 ]
                             A := [                    ]
                                  [  88  -76  -65   25 ]
                                  [                    ]
                                  [  28  -61  -60   9  ]

> B := randmatrix(4,1);
                                       [  29 ]
                                       [     ]
                                       [ -66 ]
                                  B := [     ]
                                       [ -32 ]
                                       [     ]
                                       [  78 ]

> X := linsolve(A,B);
                                     [   14573057 ]
                                     [ - -------- ]
                                     [    2229019 ]
                                     [            ]
                                     [  22251367  ]
                                     [  --------  ]
                                     [   2229019  ]
                                X := [            ]
                                     [   24438495 ]
                                     [ - -------- ]
                                     [    2229019 ]
                                     [            ]
                                     [  52548085  ]
                                     [  --------  ]
                                     [   2229019  ]
```

```
> # 14. The Maple help facility

> # The command "? package" or "help(package)" shows the number of packages
> # available in the present version 5 of Maple

> ? package

HELP FOR: Index of descriptions for packages of library functions

SYNOPSIS:
- The following packages are available:

              combinat:     combinatorial functions
              difforms:     differential forms
              geom3d:       three-dimensional Euclidean geometry
              geometry:     two-dimensional Euclidean geometry
              grobner:      Grobner bases
              group:        permutation and finitely-presented groups
              liesymm:      Lie symmetries
              linalg:       linear algebra
              logic:        Boolean logic
              np:           Newman-Penrose formalism
              numtheory:    number theory
              orthopoly:    orthogonal polynomials
              plots:        graphics package
              powseries:    formal power series
              projgeom:     projective geometry
              simplex:      linear optimization
              stats:        statistics
              student:      student calculus
              totorder:     total orders on names

- For information see ?<package> where <package> is from the above list.  This
  will give a list of the functions available in the package.   To cause all
  functions in a package to be defined in the session, do: with(<package>);

- For information on a particular package function, see ?<package>,<function>

SEE ALSO:  with


> # The command "example" shows an example of a specific Maple command

> example(limit);
                                 limit          exp(x)
                                 x -> infinity

> # We finish the session with an escape to the host operating system with
> # the command "! <Unix command>, to show the time Maple needed for the
> # execution of this run
> ! date
Thu Oct 31 15:12:06 MET 1991

# Finishing of the Maple session
> quit
```

6 Final remarks

The above demonstration only presents an introduction to the applicability of Maple in mathematics.
The number of packages, shown by the on-line help command '? package', suggests that a great number of other and more complicated applications and calculations are possible. Only the packages already contain 476 library functions, of which most have also different options. Champion is the package linalg which contains 100 library functions or commands. Lists of more basic library functions are found with '? library'.
A novice to Maple may start with '?' to see the introduction to Maple and then can go down to help on other more sophisticated commands.

Finally we may conclude that execution by hand of analytical calculations and algebraic manipulations, either writing of numerical programs in a computer language, such as Fortran, in order to carry out numerical evaluation of assigned variables, to calculate numerical solutions of integrals, ordinary differential equations or to generate two-dimensional or three-dimensional plots, is no longer necessary.
These actions can be performed easier and much faster by a modern computer algebra like Maple.

A survey of theoretical and experimental ventilation modelling

By Frans de Jongh

Faculty of Aerospace Engineering TU Delft

1. Introduction

The final goal of this investigation is the establishment of a relation between ventilation efficiency and frequency. A first step in this process is the construction of a lung model. The lung model contains many material,geometrical and flow parameters. Obviously a simple model is preferred. Therefore some insight in the influence of the various material, geometrical and flow parameters in the lung model on the output quantities has to be obtained. In order to get this insight a computer-program is constructed to analyze the influence of the various parameters in a human lung. The output quantities are for instance: concentration of the different gases, pressure-drop across the bronchii, flow velocities and diffusion rates. The conditions to be analyzed are normal ventilation, maximum expiration and high frequency ventilation occurring in human beings in the range from early born infants to adults.

In the literature various lung models can be found and also different aspects of respiration are considered. In this report a survey is given of existing models for the different aspects to be studied. The applicability in the computer-program is emphasized.

Explanation of terms used

Because of the use of some terms which may not be familiar to the reader, a short explanation will be given of the ones used. See the following figure.
The air we inhale enters via the mouth and/or nose. It passes a restriction (the larynx) before it enters the first tube (the trachea). In the model used each tube splits up in two identical tubes. So the number of tubes will increase following the simple formula 2^n with n = 0,1,2 .... For n = 0 this gives one tube (the trachea) for n = 1 two tubes, for n = 2 four tubes etc. The number n is called the generation number. A normal lung of an adult human exists of 23 generations. So at the lower side of the lung the tube system ends in 2^{23} = 8.388.608 tubes. These tubes end in small sacs (the alveoli). In a lung the alveoli start to appear at generation number 16 and their

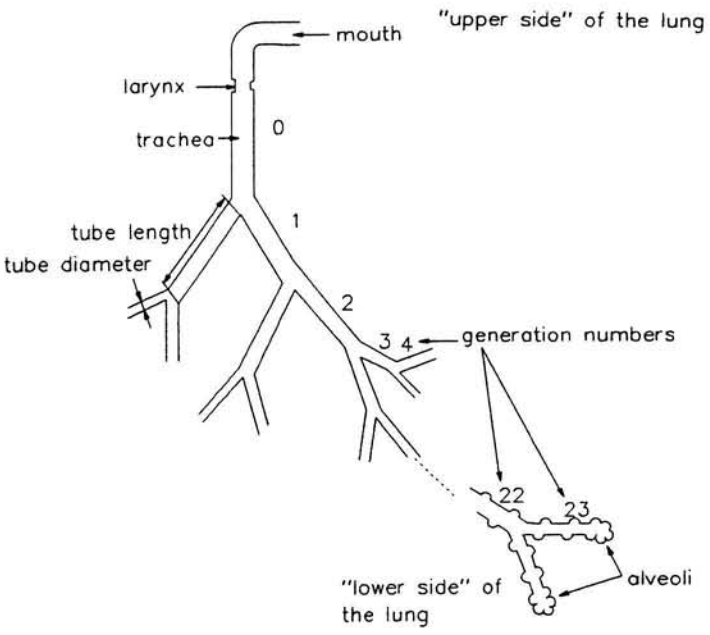

Fig. 1

number will increase till generation 23 where the tube system ends. The alveoli are lined with a fluid to release their surface tension, and which is called the surfactant. Besides terms used in lung geometry, also terms used in breathing have to be clarified. The following figure gives a typical view of the lung volume against the time.

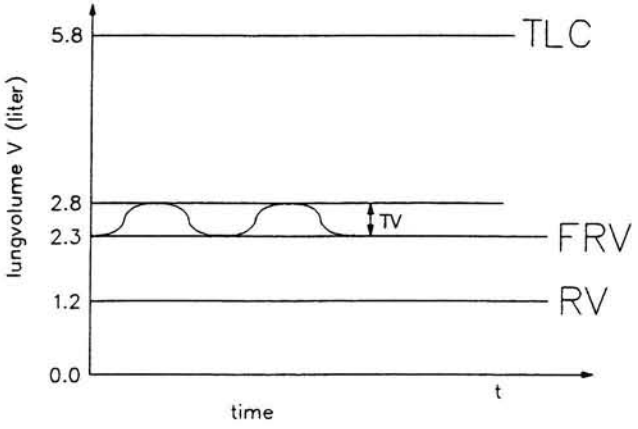

Fig. 2

(One must keep in mind that the lung considered, is the lung of an adult).

TLC = Total Lung Capacity.
The amount of air that a lung contains after the deepest inhalation.
RV = Residual Volume.
The amount of air which is still in the lung after the deepest expiration.
FRV = Functional Residual Volume.
The amount of air you normally have in your lung after a normal expiration.
TV = Tidal Volume.
The amount of air of a normal inhalation.

During inhalation the freshly inhaled air has first to fill the tube system before it reaches the alveoli. This amount of air has to be subtracted from TV if one wants to know the amount of air which effectively refreshes the alveoli where gas exchange with the blood can occur. It is called the anatomical dead space.

2. Parameters

In order to construct a flexible program first a list is made of input parameters. The input parameters are divided into three categories, geometrical quantities , material quantities and flow quantities.
For the lung model variation of the following parameters is desired.

geometrical parameters:
1 - number of generations of bronchii
2 - number of tubes per generation
3 - length and diameter of the tubes
4 - total lung volume
6 - (a-)symmetry of the lung
7 - anatomical dead space
8 - surface area

material parameters:
1 - tube elasticity (may differ per generation)
2 - surfactant

flow parameters:
1 - tidal volume
2 - flow rate
3 - ratio of inspiration and expiration time
4 - frequency

In this study especially the influence of the geometrical and material parameters on the flow parameters mentioned above will be emphasized, the final goal being the

determination of an individual optimum ratio of inspiration and expiration time and frequency.
Of course the list of parameters mentioned above is not exhaustive. The more detailed the model is made, the more parameters can be distinguished. But the chosen ones are seen as a compromise between validity of the model and the computational effort.

3. Model boundaries

The model boundaries are formed by the trachea on the upperside and the alveoli on the lower side. The influence of the first part of the ventilation system formed by mouth, nose, throat and larynx is neglected. On the lower side the gas exchange between air and blood over the alveolar membrane is modelled by means of data obtained from the literature.
Also energy consumption during ventilation in this model is not considered as a limiting constraint. During ventilation energy is consumed and exchanged between the following mechanisms:

1 Elasticity of the lungtissue, compliance work = $(\Delta p * \Delta V)/2$.
2 Lungtissue viscosity, energy dissipation by viscosity work.
3 Airway resistance, energy dissipated in the airflow.
4 Kinetic energy of the flow and the thorax wall, inertial work.

– Terms 2 and 3 form the so-called viscous pulmonary resistance.

These mechanisms need some explanation

1) Elasticity of the lungtissue is caused by the tension in the elastic fibers of the lung parenchyma, and the surface tension of the alveoli. These elastic forces tend to reduce the lung volume. Normal breathing therefore requires energy to inhale, while expiration is passive, and will be done by the elasticity of the lungtissue.

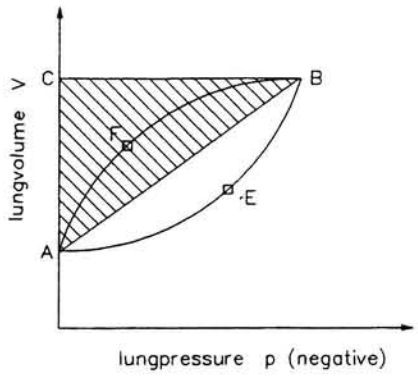

Fig. 3

In the figure above the p-V curve for only elastic effects is the line AB. A straight line, because without viscous effects the lung volume will directly change according to the pressure change. The area of the triangle ABC is defined as the compliance work.

2) Lungtissue viscosity is associated with the friction in the tissues and the non-elastic deformation of the thorax and abdomen. Normally however 80-90% of the viscous pulmonary resistance is caused by airway resistance (mechanism 3) and only 10-20% by lungtissue viscosity resistance.

3) Airway resistance is the resistance caused by the viscosity of the flow passing through the conducting airways from the mouth to the alveoli. It is due to the resistance of the laminar or turbulent boundary layer in the pipes. The viscous terms cause the line AB to deform in A loop AEBFA. For instance inspiration is achieved by lowering the pressure in the lung by increasing its volume. The lung volume achieved, by a certain pressure drop, will be less than the lung volume achieved if only elastic forces were working, due to the viscous resistance.

4) The inertial resistances are assumed to be so small compared with the elastic and viscous resistances that they may be neglected.

During natural ventilation an energy balance exists between the mechanisms mentioned above and the work done by the muscles. The participation of the various mechanisms in the balance depends on the ventilation frequency. Inversely the natural ventilation frequency range and also the optimum ventilation frequency is influenced by maintenance of the energy balance. During artificial ventilation, in which a person is ventilated by a ventilatory machine outside his natural respiration, an extra work term is induced in the balance. This source term is contributed by the external ventilation apparatus. Therefore during artificial ventilation the frequency range is no longer limited by the maintenance of the natural energy balance and hence an optimum artificial ventilation frequency is no longer influenced by the maintenance of this balance.

4. Ventilation mechanisms

During both natural and artificial ventilation in general five mechanisms may be distinguished. In the five mechanisms two physical principles are involved:

a Convection.
b Diffusion of one gas with respect to other gases.

Depending on the part of the lung considered one or more of the five ventilation mechanisms play a role. The five mechanisms, which will be explained more thoroughly later are:

1 Direct (convective) ventilation. This kind of ventilation for instance applies for the alveoli close to the mouth. It should be noted that this mechanism is not effective for a tidal volume (V_t) smaller than the anatomical dead space (V_d).

2 'Pendelluft'-mechanism. The 'pendelluft'-mechanism is a convective mechanism and it corresponds to the relaxation phenomenon occurring in the transition phase between inhalation and expiration when internal pressure differences are equalized. The pressure differences developed during inhalation because of the asymmetry in the lung geometry.

3 Effective gastransport caused by differences between the velocity profiles occurring during inhalation(inspiration) and expiration.

4 Taylor dispersion (=augmented diffusion) (ref 11). In the flow of a viscous medium with an axial concentration gradient through a (branched) tubesystem axial dispersion of species originates from convection and diffusion. If the flow is unsteady an extra contribution is added to the axial dispersion. This contribution originates from an interaction between axial convection and radial diffusion.

5 Molecular diffusion.In this process the molecules move from a place where their concentration is high to a place where it is lower, the work of displacement being supported by the kinetic energy of the molecules. If convective velocities are small diffusion becomes the dominating transport mechanism.

In the remaining part of this paragraph various aspects of the five mechanisms will be elaborated.

During artificial ventilation at higher frequencies usually the direct (convective) ventilation mechanism is assumed to be of negligible influence since in that case the tidal volume is smaller than the anatomical dead space. In the past it was assumed as a rule of thumb that overall ventilation efficiency depends only on the volume of air ventilated per unit time. Hence with a constant ventilation efficiency, an increase of the ventilation frequency corresponds to a decrease of the tidal volume.
However as soon as $V_t < V_d$ further increase in ventilation frequency should affect the efficiency since the alveoli no longer are reached directly by the small tidal volume. Hence for high frequency ventilation the direct convection mechanism is only important in the higher airways.

To clarify the process of the 'pendelluft' mechanism one is referred to figure 4. It shows a pipe splitting up into two pipes ending into two sacks. The pipes leading to the sacks may have different resistances and the sacks may have different compliances. The product of compliance times resistance gives a time constant. This time constant governs the rate of charge and discharge of a sack in the presence of a given pressure gradient. So if unit A has the smaller time constant it is observed that at the

end of an inspiration unit A is ready to empty while unit B is still filling. Air thus flows from unit A to unit B. This is called 'pendelluft'.
The importance of the 'pendelluft' mechanism depends on the lungmodel adopted. In the literature often the lungmodel of Weibel (ref 12)is used. This is a symmetrically branched model and therefore the 'pendelluft' mechanism plays no role. If however an asymmetrical model is used as suggested by Horsfield and Cummings (ref 13) the 'pendelluft' indeed is of importance.

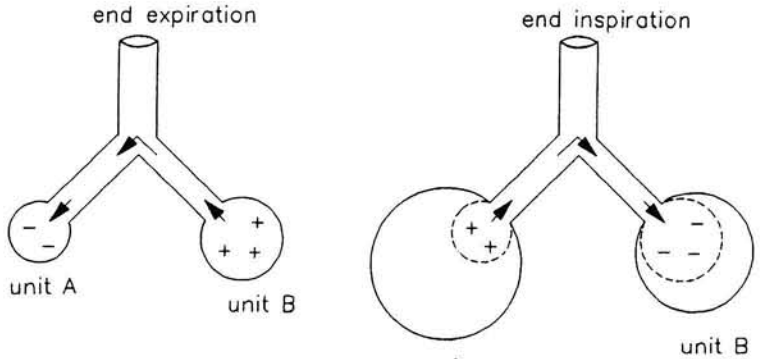

Fig. 4

Differences in velocity profiles between inhalation and expiration result in a redistribution of the time average transport over the cross-section of the lungtubes. Although the transport averaged over both the cross-section and the time is zero because of continuity, the time averaged transport in the neighbourhood of the centerline of the tube may be non-zero and is balanced by a time averaged counterflow near the wall. During high frequency ventilation this mechanism is enhanced since the generated pressure oscillations act differently on the viscous flow in the boundary layer and on the inertial flow near the centerline.

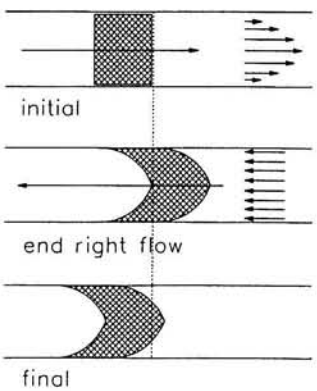

Fig. 5

The same enhancement applies for Taylor dispersion, which is supposed to be the main transport mechanism during high frequency ventilation. Because of the generated velocity profile a radial concentration gradient develops resulting in radial diffusion of species, which again results in an enhanced axial transport of species.

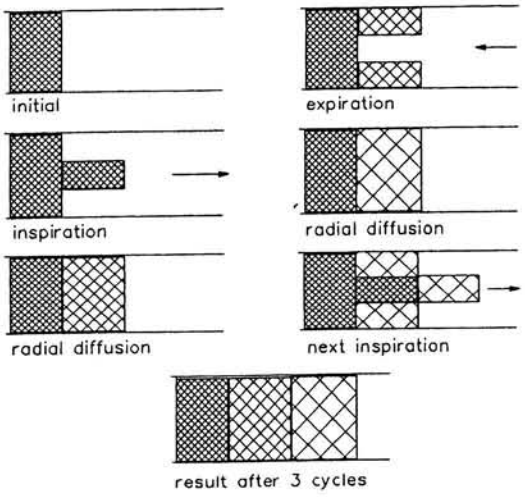

Fig. 6

Summarizing it should be noted that during high frequency ventilation descending down the airways the species transport mechanism shift from unsteady pure convection in the upper airways via a time averaged interaction between convection and diffusion to almost steady diffusion in the neighbourhood of the alveolar membranes, where convection velocities are negligible.

5. Strategy

During the construction of the computermodel the various ventilation mechanisms will be incorporated one by one and the influence of the different variables on the output parameters will be analyzed step by step.

In a first step a quasi-steady convection model is made for the inhalation and the expiration cycle. This step will mainly be based on existing literature (see for instance Pedley et al.).
In a next step the effect of the normal diffusion is considered at the deep end (the alveoli). The first two steps will be combined and Taylor-dispersion in an oscillating flow is added to the previous model. In a separate step the influence of asymmetry of the velocity-profiles is analyzed and if necessary added to the model. Next elasticity of the tubes and the alveoli(compliance) is added. In a final step geometrical asymmetry is introduced and the 'pendelluft' mechanism is analyzed.

Once the lungmodel and ventilation mechanisms have been established in a satisfactory way the influence of external disturbances like for instance cardiogenic oscillations will be analyzed and the results are used for a refinement of the model. The validity of the modelled mechanisms will be tested by comparing the calculated results with results of measurements given in literature.

If all steps are successfully performed optimum values of the various artificial ventilation parameters like frequency and time resolved tidal profile may be calculated and if possible experimentally verified.

6. Quasi-steady convection

The lungmodel used to study convection is Weibels model (ref 12). The lungmodel of Weibel consists of 23 generations of branched tubes. In one generation the number of tubes is doubled. Hence the number of tubes in the n'th generation is 2^n, the zero'th generation being the trachea. According to Weibel tube lengths and diameters are given by the following formulas:

$$0 < n < 3 \; : \quad l = l_0 \, e^{-nm} \qquad S = S_0 \, e^{-nG} \quad , \tag{6.1}$$

$$4 < n < 23 : \quad l = l'_0 \, e^{-nu} \qquad S = S'_0 \, e^{(H+nJ)n} \quad . \tag{6.2}$$

For a normal adult man, his lungs inflated till 75% TLC, this becomes (ref 12):

$$0 < n < 3 \; : \quad l = 12e^{-0.92n} \quad S = 2.54e^{-0.083n} \quad , \tag{6.3}$$

$$4 < n < 23 : \quad l = 2.5e^{-0.17n} \quad S = 1.32e^{(0.1074 + 0.0125n)n} \quad . \tag{6.4}$$

6.1. Theory and experiments

Following Pedley and based on both theoretical and experimental results an estimate for the viscous pressure drop (= the pressure drop due to the working of viscous forces in the fluid) over a branched tube system in a steady flow will be given. This branched tube system models the first five generations of lungtubes.
The energy dissipation rate per unit volume in a steady viscous flow is expressed in cylindrical coordinates by:

$$E = \mu\left[2\left(\frac{\partial u}{\partial x}\right)^2 + 2\left(\frac{\partial v}{\partial r}\right)^2 + 2\left(\frac{\partial v}{\partial r} + \frac{1}{r}\frac{\partial w}{\partial \theta}\right)^2 + \left(\frac{\partial u}{\partial r} + \frac{\partial v}{\partial x}\right)^2\right] + \mu\left[\left(\frac{1}{r}\frac{\partial u}{\partial \theta} + \frac{\partial w}{\partial x}\right)^2 + \left(\frac{1}{r}\frac{\partial v}{\partial \theta} + \frac{\partial w}{\partial r} - \frac{w}{r}\right)^2\right]. \tag{6.5}$$

In slender tubes the radial and swirl velocity components are small compared to the axial velocity. Hence from the continuity equation,

$$\frac{\partial u}{\partial x}+\frac{1}{r}\frac{\partial (rv)}{\partial r}+\frac{1}{r}\frac{\partial w}{\partial \theta}=0, \tag{6.6}$$

it follows that $\partial u/\partial x$ will be negligible also.
The expression for the dissipation rate then simplifies to ($v = w = \partial u/\partial x = 0$):

$$E=\mu\left[\left(\frac{\partial u}{\partial r}\right)^2+\frac{1}{r^2}\left(\frac{\partial u}{\partial \theta}\right)^2\right]. \tag{6.7}$$

Integration of the dissipation rate per unit of volume over the tube cross section yields the energy dissipation rate per unit of length D(x):

$$D(x)=\int_0^{2\pi}\int_0^a Erdrd\theta. \tag{6.8}$$

The total energy dissipation rate in the tube between x_1 and x_2 is:

$$F=\int_{x_1}^{x_2} D(x)dx. \tag{6.9}$$

The dissipated energy is balanced by the work done by the pressure forces. If the pressure is supposed to be constant over a cross-section (slender tubes) the work done by the pressure force is

$$W_p=\Delta p(x_1,x_2)Q. \tag{6.10}$$

So $W_p = F$,

where $\Delta p(x_1,x_2)$ is equal to the pressure difference between a cross-section at axial station x_1 and a cross-section at x_2 and Q is the volume flow. Equating the viscous energy dissipation rate and the work done by the pressure forces yields an expression for the effective viscous pressure drop $\Delta p(x_1,x_2)$. If the flow in the tube is a fully developed Poiseuille flow the energy dissipation rate per unit length is constant and given by:

with :

$$u = 2\bar{u}\left(1 - \frac{r^2}{a^2}\right) \Rightarrow \frac{\partial u}{\partial \theta} = 0 \ , \ \frac{\partial u}{\partial r} = \frac{-4r\bar{u}}{a^2},$$

$$D_p = \int_0^{2\pi} \int_0^a \mu \left[\left(\frac{-4r\bar{u}}{a^2}\right)^2 + 0\right] r dr d\theta = 8\pi\mu\bar{u}^2. \tag{6.11}$$

The amount of energy dissipated per unit time in a section between x_1 and x_2 is:

$$F_p = 8\pi\mu\bar{u}^2(x_1 - x_2) \, . \tag{6.12}$$

And hence

$$\Delta p = \frac{F_p}{Q} = \frac{F_p}{\pi a^2 \bar{u}} = 8\mu\bar{u}\left(\frac{x_2 - x_1}{a^2}\right). \tag{6.13}$$

With these results a factor Y(x) may be defined being the ratio of the actual energy dissipation rate per unit length and the energy dissipation rate in a Poiseuille flow:

$$Y = \frac{D(x)}{D_p}. \tag{6.14}$$

In the same way a factor Z may be defined being the ratio of the integrated energy dissipation rate in the actual flow and in a Poiseuille flow:

$$Z = \frac{F}{F_p} = \frac{1}{(x_1 - x_2)} \int_{x_1}^{x_2} Y(x) dx. \tag{6.15}$$

In order to calculate Y(x) or Z first D(x) has to be determined. Therefore the axial velocity u is measured as a function of radial distance r and the circumferential angle θ at a few stations in axial direction. However since in a branched tube system like the lung a completely developed Poiseuille flow never exists the factors Y(x) and Z will probably differ considerably from 1. Therefore the results of the measurements will also be compared with some simple theoretical results obtained by means of a simplified boundary layer model for an axially symmetrical configuration.
In a developing tube flow one can distinguish two domains. Near the wall a small boundary layer in which the no slip conditions must be fulfilled, and at the center a

layer in which the flow is still undisturbed. The axial velocity is supposed to vary linearly between the value U at the outer edge of the boundary layer and 0 at the wall. From boundary layer theory it is known that the boundary layer thickness on a flat plate increases proportional to the square root out of the axial distance. It is assumed that this result may also be applied to the boundary layer on the inner wall of a tube. After some calculations (ref 14) the quantities Y(x) and Z follow as:

$$Y = \frac{C}{8\sqrt{2}}\sqrt{Re\frac{d}{x}}, \tag{6.16}$$

$$Z = \frac{C}{4\sqrt{2}}\frac{\sqrt{Re}}{\left(\sqrt{\frac{x_1}{d}} + \sqrt{\frac{x_2}{d}}\right)}. \tag{6.17}$$

The proportionality constant C depends on the velocity profile at the entrance of the tube. If the flow starts with a block profile C=1. In a branched tube system each new generation starts with a velocity distribution inherited from the former generation. From the measurement (ref 4) results a mean value for C is obtained of 1.85 with a standard deviation of less than 15%. This result appeared to be independent of the Reynolds number and independent of the position in axial direction of the measuring point. During the measurements the bifurcation angle was fixed at a typical value for lungs and so was the cross-section ratio between generations of tubes.

6.2. Implementation

In the program first an effective Poiseuille viscosity is calculated by means of the formula:

$$R_{p(n)} = \frac{1}{TT(n)}\frac{128\mu L}{\pi d^4}. \tag{6.18}$$

The factor Z correcting this viscosity for entrance effects and secondary flows is given in (6.17) and takes the form :

$$Z = \frac{1.85}{4\sqrt{2}}\sqrt{Re\frac{d}{l}}. \tag{6.19}$$

The correction factor is never allowed to become smaller than one. Because if this would be the case, the viscous pressure drop would be less than the Poiseuille pres-

sure drop which is impossible. This correction is used to calculate the viscous pressure drop. In addition to the viscous pressure drop a pressure increase occurs since the flow decelerates down the lung because of the increasing cross-sectional area. An estimate for this compensating effect can be obtained by means of Bernoulli's equation, where viscous effects are neglected. Theoretically one finds for the inviscid pressure difference between trachea where $u = U_{tr}$ and the alveoli where $u = 0$:

$$\Delta p_s = -(p_{k1} - p_{k2}) = -B\rho(U_{tr})^2 . \tag{6.20}$$

Experimentally viscosity being included is found from :

$$p_{s1} + p_{k1} = p_{s2} + p_{k2} + \Delta p_v \quad \rightarrow \quad p_{s1} - p_{s2} = \Delta p_v - (p_{k1} - p_{k2}) , \tag{6.21}$$

leading to

$$\Delta p_s = \Delta p_v - B\rho(\overline{U}_1^2 - \overline{U}_2^2) , \tag{6.22}$$

(with $B = 0.85$), in which p_k is defined as

$$p_k = \frac{\iint \frac{1}{2}\rho u^3 dA}{\iint u dA} = B\rho\overline{u}^2. \tag{6.23}$$

Measurements of a complete tube system (ref. 6) showed that the value of B should be 0.85. For Poiseuille flow the value of B may also be predicted by theory yielding $B = 1$. For fully turbulent flow $B = 0.5$. In this way the pressure drop per generation can be calculated and summation over all 23 generation yields the pressure drop between trachea and alveoli.

So far the considerations applied to steady flow. During normal ventilation however the flow is unsteady.
Since normal ventilation frequencies are rather low (0.2 Hz) a quasisteady approximation seems reasonable. This implies that the pressure drop is calculated in correspondence with the instantaneous flowrate. An other complication is formed by the elasticity of the tube walls. The wall compliance introduces a change in cross-section. The wall stretch depends on the tidal volume (see figure 7).

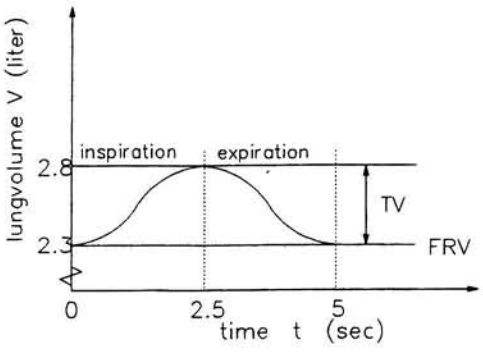

Fig. 7

The lung model of Weibel is based on ventilation at 75% of the Total Lung Capacity. Hence with respect to this unsteady aspect, again , a quasisteady approximation is chosen and an instantaneous stretch factor is introduced proportional to the amplitude of the tidal volume.Because the inhaled amount of air is directly responsible for the expansion of the lung. Based on the corrected cross-section a pressure drop is calculated.

In figures 8, 9 and 10 some calculated results are presented.

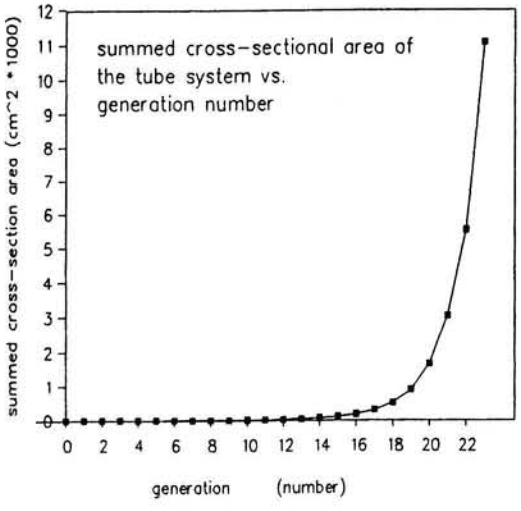

Fig. 8

It is noticed that the pressure drop is low if the flow rate is low. And the flow rate is low in the higher generations because of the large cross-sectional area. Therefore the

larger part of the pressure drop occurs in the first generations. If the flowrate is high the deviation from Poiseuille flow is large and the corresponding pressure drop is also large.
In this model different from reality expiration is treated in the same way as inhalation.

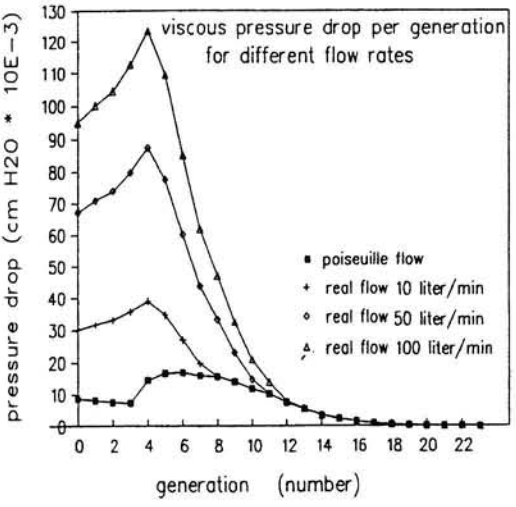

Fig. 9

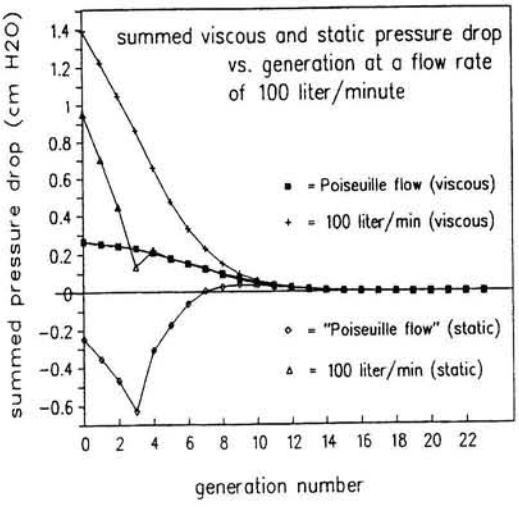

Fig. 10

References

1 T.J.Pedley,R.C.Schroter,M.F.Sudlow. Gas flows and mixing in the airways (1977) Bio-engineering aspects of the lung: 163-265.

2 T.J.Pedley. Pulmonary fluid dynamics (1977) Ann.Rev.Fluid Mech (9): 229-274.

3 R.C.Schroter,M.F.Sudlow. Flow patterns in models of the human bronchial airways (1969) Resp.Physiol.(7): 341-355.

4 T.J.Pedley,R.C.Schroter,M.F.Sudlow. Energy losses and pressure drop in models of human airways (1970) Resp.Physiol.(9): 371-386.

5 T.J.Pedley,R.C.Schroter,M.F.Sudlow. Flow and pressure drop in systems of repeatedly branching tubes (1971) J.Fluid.Mech.(46.2): 365-383.

6 T.J.Pedley,R.C.Schroter,M.F.Sudlow. The prediction of pressure drop and variation of resistance within the human bronchial airways (1970) Resp.Physiol.(9): 387-405.

7 R.W.Douglass,B.R.Munson. Viscous energy dissipation in a model of the human bronchial tree (1974) J.Biomech.(7): 551-557.

8 D.E.Olson,G.A.Dart,G.F.Filley. Pressure drop and fluid flow regime of air inspired into the human lung (1970) J.Appl.Physiol.(28) : 482-494.

9 M.Y.Jaffrin,P.Kesic. Airway resistance: a fluid mechanical approach (1974) J. Appl. Physiol.(36): 354-361.

10 A.S.Slutsky,G.G.Berdine,J.M.Drazen. Steady flow in a model of human central airways (1980) J.Appl.Physiol.(49): 417-423.

11 G.I.Taylor. Dispersion of soluble matter in solvent flowing slowly through a tube (1954) Proc.R.Soc.London Ser.A (223): 446-468

12 E.R.Weibel. Morphometry of the human lung (1963)

13 K.Horsfield,G.Cumming. Morphology of the bronchial tree in man (1968) J. Appl. Physiol.(24):373-383

14 F.H.C. de Jongh. Frequency and ventilation (1990) Report LR-625

Nomenclature

a	tube radius
B,C	correction factors for turbulent flow and entry effects
d	tube diameter
D(x)	energy dissipation rate in a tube per unit of length
E	energy dissipation rate in a tube per unit volume
F	total energy dissipation rate
FR	flow rate
l	tube length
l_0,l_0'	coefficient for calculating the tube length
n	generation number
p_k	kinetic pressure drop
p_s	static pressure drop
p_v	viscous pressure drop
Δp	pressure difference
Q	volume flow
r	radius
Re	Reynolds number according to the tube diameter
S	tube cross-sectional area
S_0,S_0'	coefficient for calculating the tube cross-sectional area
TT(n)	number of tubes in the nth generation
u	velocity component in x direction
$\bar{u}$	averaged axial velocity
$\overline{U_0}$	undisturbed axial velocity
U_{tr}	axial velocity in the trachea
v	velocity component in y direction
V	lung volume
V_d	anatomical dead space
V_t	tidal volume
w	velocity component in z direction
W_p	work done by the pressure forces
x,y,z	cartesian coordinates
x,r,θ	cylindrical coordinates
Y	ratio of the actual energy dissipation and the energy dissipation in a Poiseuille flow per unit length
Z	ratio of the length integrated energy dissipation of the actual flow and Poiseuille flow
δ	boundary layer thickness
ρ	density of air
μ	dynamic viscosity
υ	kinematic viscosity
θ	angle in cylindrical coordinates
ω	angular frequency

subscripts

p	Poiseuille flow

Staal en Stroming

By G. Klein Lebbink

Hoogovens IJmuiden

1. Inleiding

Na afronding van mijn studie vliegtuigbouw heb ik de wellicht niet zo voor de hand liggende keus gemaakt om te gaan werken voor Hoogovens te IJmuiden. Dit bedrijf heeft als belangrijkste aktiviteit de produktie van staal, zo'n 5 miljoen ton per jaar, maar kent daarnaast een aantal andere activiteiten waarvan de produktie van aluminium (ruim 175.000 ton) de belangrijkste is. Gezien de enorme omvang van het bedrijf kent Hoogovens een eigen research laboratorium van ruim 500 mensen. Naast puur produktie ondersteunende research is er tevens fundamenteel onderzoek. Momenteel ben ik werkzaam in de afdeling warmte- en stromingstechnologie, die als belangrijkste projekten energievraagstukken en stromingsonderzoek heeft.
Belangrijke warmtehuishoudingsproblemen betreffen bijvoorbeeld het opstookgedrag van procesovens en verbrandingsverschijnselen van procesgassen. Typische stromingsproblemen houden verband met de stroming van vloeibaar staal of aluminium, of met de menging van gas en vloeistof bij gasreinigingsprocessen.
Wat mij het meest heeft getroffen tijdens mijn werkzaamheden tot nu toe is dat de kennis die ik opgedaan heb in Delft zo goed inzetbaar is in een grofstoffelijke omgeving als Hoogovens. Dat men daarbij spreekt van ferrodynamica in plaats van aerodynamica doet niets af aan de benodigde basiskennis om verder te komen bij zowel procesbeheersing als kwaliteitsbeheersing. Opmerkelijk is verder het verschil in schaalgroottes waarin bij Hoogovens wordt gewerkt: dit blijkt bijvoorbeeld uit het feit dat wanneer je in een fabriek op de 3e verdieping uit de lift stapt je voorbereid moet zijn op passerende vrachtwagens van 25 ton of meer, terwijl aan de andere kant de zinklaag dikte bij het continu verzinkproces kan worden beheerst met een nauwkeurigheid in de orde van grootte van 10 μm. Om te illustreren hoe ver de stand van de techniek gevorderd is in de staalindustrie wil ik een kort overzicht geven van een tweetal projekten zoals die bij mijn afdeling zijn of worden uitgevoerd. Alvorens iets dieper in te gaan op deze vraagstukken volgt een globale beschrijving van het produktieproces bij Hoogovens.

Het produktieproces van staal uit ijzererts en kolen bestaat uit een aantal stappen die in figuur 1 schematisch zijn weergegeven. Na de voorbereidingsfase van erts in sinter en pellets en van de kolen in kooks vindt de reductie van het erts tot ruwijzer plaats in de hoogoven. Om de benodigd hoge temperaturen te kunnen bereiken wordt de hoogoven gevoed met hete lucht van temperaturen tot boven de 1000 °C. Deze

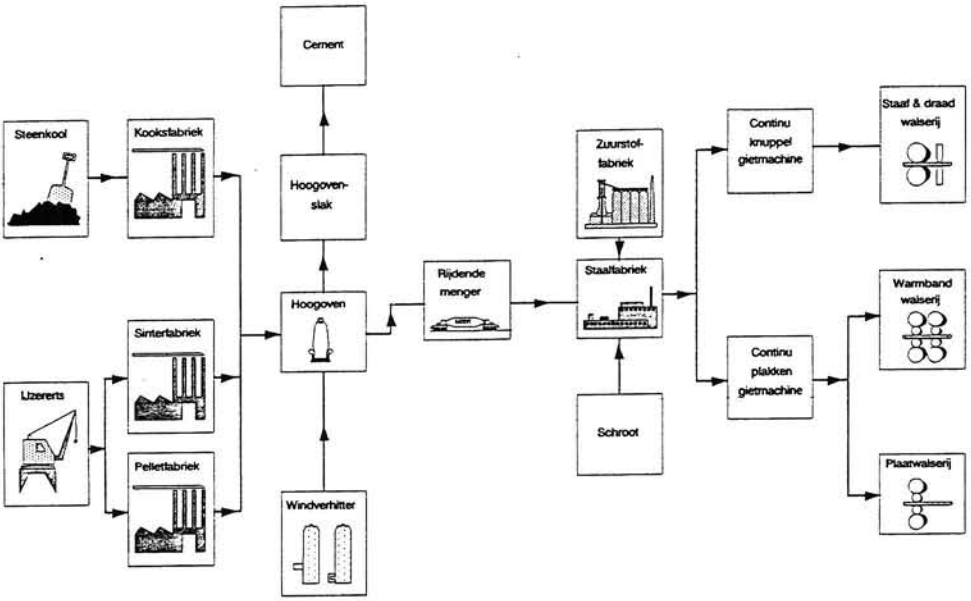

Fig. 1 Produktie proces Hoogovens

hete lucht wordt geproduceerd in zgn. windverhitters. Momenteel is de stroming en verbranding in deze windverhitters onderwerp van studie. Later zal ik hier wat uitgebreider op terug komen.
Het ruwijzer wordt vervolgens afgetapt bij de hoogoven en stroomt daarbij in een vuurvaste wagon, de rijdende menger, die zo'n 300 ton lading kan vervoeren. Middels deze rijdende menger wordt het ruwijzer in vloeibare vorm getransporteerd naar de staalfabriek, alwaar door inblazing van zuurstof in het vloeibare ijzerbad veredeling tot staal plaatsvindt. Het zo ontstane vloeibare staal wordt vervolgens verwerkt tot plakken of knuppels. De produktie van plakken en knuppels geschiedt continu, de studie naar het optredende gietproces is een projekt dat ik eveneens wat uitvoeriger zal bespreken. Na stolling van het staal worden de halfprodukten i.h.a. gewalst. De dan verkregen plaat of staaf kan vervolgens worden geleid door een vloeibaar zinkbad, waarbij zich een laag zink op het staal afzet. Ook vindt vertinning of verchroming van het staal plaats.

2. Stroming van vloeibaar staal

Zoals in de inleiding al beschreven wordt het vloeibare staal van 1600 °C deels continu gegoten tot plakken. Dit gietproces vindt plaats op de zgn. continu gietmachine. In figuur 2 is een dergelijke machine getekend. Het gesmolten staal wordt uit de staalpan via een gietpijp in een verdeelbak gegoten. (Overigens fungeert deze

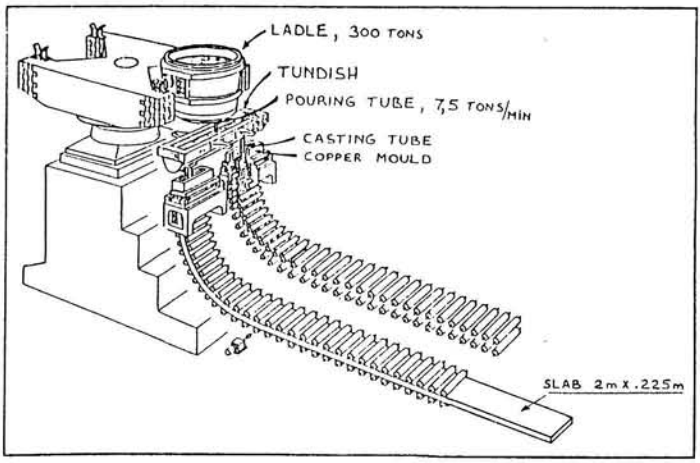

Fig. 2 Continu gietmachine

verdeelbak als buffer tijdens het wisselen van de staalpan). Via een keramische dompel pijp stroomt het staal uit in twee watergekoelde gietvormen. De dompelpijpen steken daarbij een eind in het vloeibare staal in de gietvorm, en de instroom van staal in de gietvorm geschiedt dus onder het oppervlak. Omdat het staal direct uit de staalfabriek naar de gietstand wordt getransporteerd, zal bij het vullen van de verdeelbak een deel van de in de staalpan aanwezige slak in deze bak terecht komen. Deze slak heeft een lagere dichtheid dan het staal en zal dus op het staal drijven wat als prettige bijkomstigheid heeft dat het staal wordt afgesloten van de omgevingslucht. Daarnaast wordt er om oxidatie van het staal te voorkomen, een gietpoeder toegevoegd aan het staal. Dit poeder dient tevens als smering tussen staal en gietvorm. Aangezien de dompelpijpen een beperkte levensduur hebben zal van tijd tot tijd de verdeelbak geheel leeg moeten lopen. In het verleden bleek dat er bij dit leeg lopen wervels ontstonden boven de dompelpijpen, waardoor de zich op het oppervlak bevindende slak meegezogen werd met het vloeibare staal. Tijdens het stollen ontstonden daardoor insluitsels, wat uiteindelijk afkeur van de gegoten plakken tot gevolg had. Daarnaast is het van belang te weten wat er gebeurt met de eventueel meegezogen slak deeltjes. Bij voorkeur dienen deze in de gietvorm boven te komen drijven.

Om een indruk te krijgen van het effect van de vorm van de dompelpijp op de stroming is er naast een fysisch model een numeriek model ontwikkeld om de stroming te kunnen bestuderen. Omdat staal als modelmedium is uitgesloten, is gekozen voor een watermodel. In tabel 1 zijn de eigenschappen van staal en water vergeleken.

Tabel 1

	water 15 °C	staal 1600 °C
kin. viscositeit (m^2/s)	$1.16\ 10^{-6}$	$0.93\ 10^{-6}$
dichtheid (kg/m_3)	$1\ 10^3$	$7.14\ 10^3$
oppervlakte spanning (N/m)	0.076	1.6

Voor deze stroming blijkt de gietsnelheid in de orde van 2m/s te liggen, terwijl de diameter van de dompelpijp ongeveer 10cm is. Dit leidt tot een turbulente stroming (Reynolds in de orde 10^5). Het experimentele model is daarbij dusdanig ontworpen dat het Froude getal overeenkomt met de werkelijke stroming in het staal waarbij de afmetingen gelijk zijn gehouden. Hierdoor konden de werkelijke dompelpijpen worden gebruikt, terwijl de stroming zichtbaar werd door gebruik te maken van een plexiglazen model. Voor de bepaling van de stroming is gebruik gemaakt van een videocamera en snelheidsmetingen op diverse plaatsen met anemometers.
Voor de berekening van het stromingsveld zijn met behulp van een software pakket (Fluent) de bewegingsvergelijkingen opgelost. Daarbij is het stationaire veld berekend voor een incompressibele wwn-fase stroming. Turbulentie is gemodelleerd met behulp van het k-e model. Uiteraard is daarbij gebruik gemaakt van symmetrie, waardoor het model beperkt kon worden tot een kwart van de gietvorm en dompelpijp. Het vrije oppervlak is tenslotte gemodelleerd als een wrijvingsloze vaste wand. In figuur 3 en 4 zijn enkele resultaten van de berekeningen weergegeven. De dompelpijp in figuur 3 met een uitstroomopening onder een hoek van 45 graden laat zien dat het staal vrijwel vertikaal wegstroomt. De in figuur 4 gebruikte dompelpijp, met een drempel in de uitstroom-opening laat een stromingsbeeld zien met een veel vlakker snelheidsveld. Dit leidt er toe dat meestromende deeltjes, meer tijd hebben om naar het vrije oppervlak te bewegen.
Naar aanleiding van de resultaten van dit model konden aanbevelingen worden gedaan voor wijzigingen aan de dompelpijp. Daarnaast is er een studie begonnen naar de stromingsverschijnselen in de verdeelbak.

3. Modellering van windverhitters

In de inleiding heb ik al even de windverhitter genoemd. Deze dient voor het voorverwarmen van lucht voor het hoogovens proces. In figuur 5 is een doorsnede van een windverhitter getekend. De windverhitter kent een cyclisch bedrijf: gedurende de gasfase wordt laag calorisch gas verbrand in de zgn. branderschacht, de hete rookgassen warmen in deze fase het keramische stapelwerk op. Gedurende de luchtfase stroomt koude lucht door de branderschacht. In het keramische stapelwerk wordt vervolgens de lucht opgewarmd tot de vereiste temperaturen. De kantelen brander zoals aangegeven in de figuur heeft een vermogen van tussen de 50 en 100 MW. Om een idee te krijgen van de grootte van deze branders: de breedte bedraagt 3m terwijl de lengte 6m is. De branderkroon bestaat uit een gasspleet van een paar meter lang en

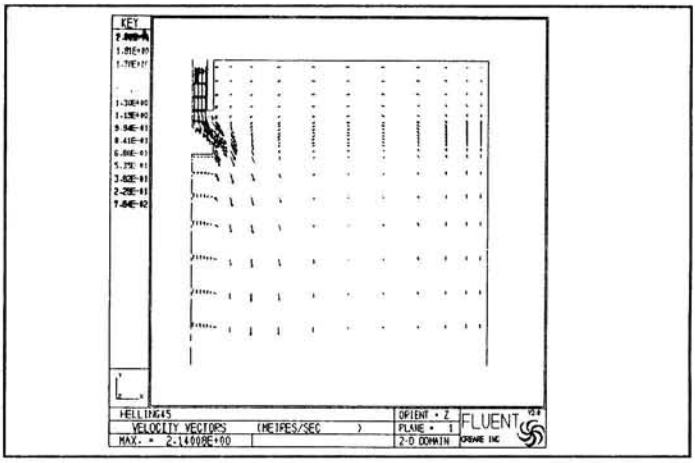

Fig. 3 Snelheidsvectoren bij 45° uitstroming

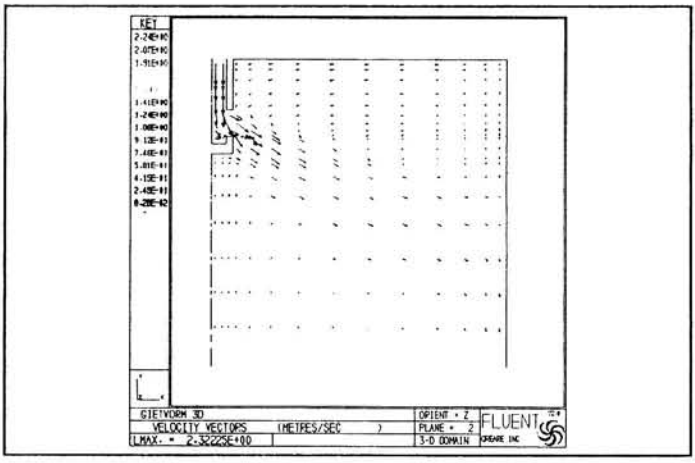

Fig. 4 Snelheidsvectoren met drempel

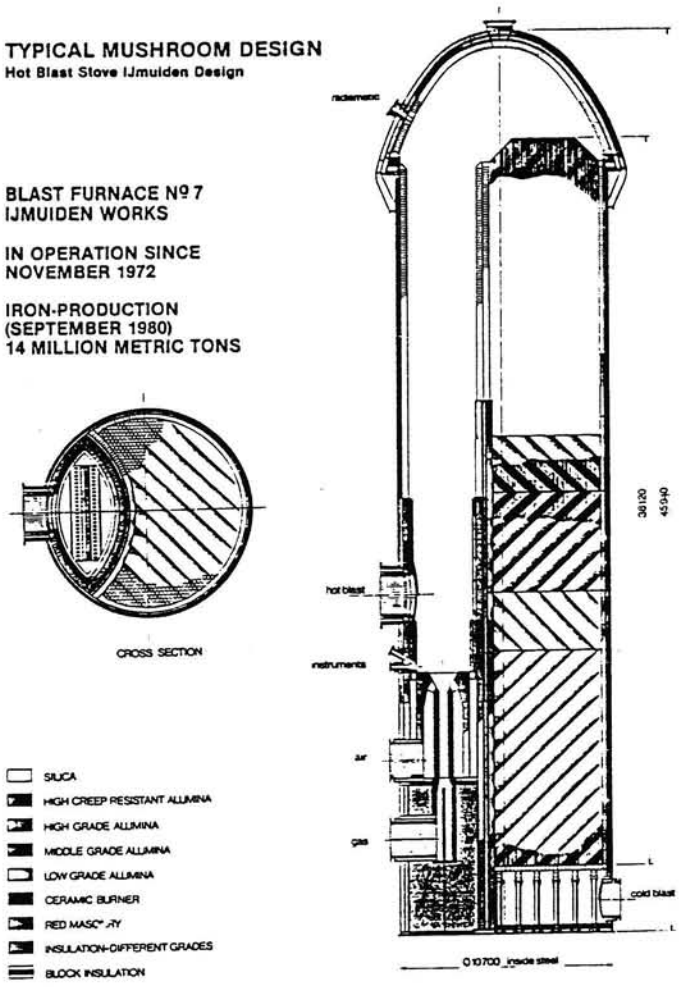

Fig. 5 Doorsnede windverhitter

een breedte van halve meter. Aan beide zijde van de gasspleet zijn een 20-tal luchtpoorten aangebracht die de verbrandingslucht onder een hoek van ongeveer 45° inblazen. De luchtpoort aan de ene zijde van de brander staat precies tussen de luchtpoorten aan de overzijde in. Om de vlam te stabiliseren zijn de luchtpoorten enigszins verzonken. Aan de zo ontstane kantelen ontleent de brander dus zijn naam. Verdere karakteristieken van deze brander zijn de grote gasvolumina, de beperkte toegestane drukval en de hoge temperaturen in de elliptische branderschacht.
Belangrijke problemen die zich kunnen voordoen bij deze branders zijn akoestische pulsaties, vlaminstabiliteit en hoge koolmonoxide concentraties in het rookgas. Met name het laatste probleem samen met de NO_x emissies van deze brander vormen een

reden om het verbrandingsproces nauwgezet te bestuderen. Daarbij is de doelstelling verlaging van de uitstoot van schadelijke stoffen. Tevens willen wij een indruk krijgen waarom sommige van dergelijke branders wel problemen geven terwijl andere overeenkomstige branders deze problemen niet kennen. Hoogovens verkeert daarbij in de gelukkige omstandigheid dat ze als leverancier van windverhitters over meetgegevens van deze branders over heel de wereld beschikt.

3.1. Model

Gedurende de afgelopen anderhalf jaar is een model van een windverhitter brander opgezet m.b.v. het software pakket FLUENT. Daarbij zijn de onderstaande vergelijkingen/ modellen uitgangspunt:

- De stroming wordt gemodelleerd met de Navier-Stokes vergelijkingen.
- De turbulentie wordt gemodelleerd met het k-e model. Een karakteristieke intreesnelheid van de lucht is 25m/s. Het getal van Reynolds ligt daarmee in de orde van grootte van 10^6.
- Voor de beschrijving van de niet voorgemengde turbulente vlam wordt uitgegaan van het zgn. eddy-break-up model. De basis van het model vormt de gedachte dat brandstof en zuurstof in gescheiden wervels voorkomen. Deze wervels hebben een beperkte levensduur, na menging op moleculaire schaal vindt de verbranding plaats. De reacties worden vooralsnog op de meest elementaire manier beschreven:

  $$\text{Brandstof} + \text{Zuurstof} \rightarrow \text{Produkt}$$

  Omdat de levensduur van de wervels van brandstof en zuurstof maatgevend is voor de verbrandingssnelheid zal deze evenredig zijn met het quotient van e/k, dus de verhouding tussen turbulente energie dissipatie en turbulente energie. Voor de verbrandingssnelheid wordt daarom het model van Magnusson en Hjertager gebruikt waarin de verbrandingssnelheid wordt beschreven door:

  $$r = A\ e/k\ rho\ Min[m_{fu}, m_o/s_{fu}, B/A\ m_{pr} / (1 + s_{fu})]$$

  De dichtheid rho geeft een indirecte drukafhankelijkheid, terwijl de minimum functie staat voor een beschikbaarheidsrelatie van brandstof, m_{fu}, en zuurstof, m_o (de term s_{fu} staat voor de stoichiometrische lucht behoefte). De laatste term met daarin de hoeveelheid produkt, m_{pr}, heeft tot gevolg dat de verbrandingssnelheid temperatuur afhankelijk is. De twee coefficienten A en B zijn constanten.

- Straling wordt beschreven met het flux model. Dit model gaat er van uit dat er alleen stralingsuitwisseling is tussen aangrenzende cellen. Voor de windverhitter, waar er geen koude wanden zijn, zal deze aanname bij benadering toelaatbaar zijn. Dit stralingsmodel heeft tot gevolg dat de straling kan worden beschreven met de transportvergelijkingen wat het model zeer flexibel maakt.

Met het FLUENT programma zijn vervolgens de resulterende vergelijkingen opgelost met de voor het probleem geldende randvoorwaarden.

3.2. Resultaten

Allereerst is de configuratie vereenvoudigd tot een 2-dimensionaal model. Daarbij is uitgegaan van symmetrie rond de hartlijn van de gasspleet (figuur 6). Om te bepalen of volstaan kon worden met een dergelijk 2-D model is het met FLUENT berekende stromingsveld vergeleken met metingen aan een proefopstelling. In deze opstelling is daarbij door de gasspleet lucht toegevoerd van 100 °C, terwijl door de luchtpoorten koude lucht van 20 °C werd toegevoerd. Na vergelijking van numerieke resultaten en metingen bleek de recirculatie zone bij B (figuur 6) redelijk te worden voorspeld, alhoewel de gemeten terugstroming de luchtpoort in, niet werd gevonden. De gemeten temperaturen bij A bleken echter aanzienlijk hoger dan de berekende temperaturen van 20 °C. In werkelijkheid vindt ten gevolge van de luchtpoorten menging plaats van koude en hete lucht (gas). Door de optredende recirculatie wordt het gas uit het centrum tot punt A gevoerd. Omdat dit effect niet werd waargenomen in het numerieke model is besloten over te gaan tot een 3-D model.

Voor het 3-dimensionale model is in eerste instantie het stromingsveld bepaald. Daarbij is een segment ter grootte van één luchtpoort gemodelleerd. In dit model is er daarbij nog steeds sprake van symmetrie: de luchtpoorten staan exact tegenover elkaar. Uit analyse van de berekende resultaten blijkt dat in dit model wel de hogere temperaturen in punt A werden gevonden. In figuur 7 zijn de berekende snelheden langs de lijn I-I' van figuur 6 getekend. Bij I blijken zeer lage snelheden op te treden, terugstroming de luchtpoort in, is echter voor geen van de doorgerekende configuraties gevonden.

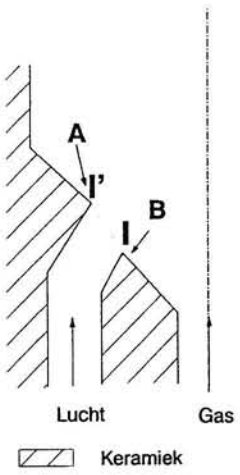

Fig. 6 Doorsnede brander

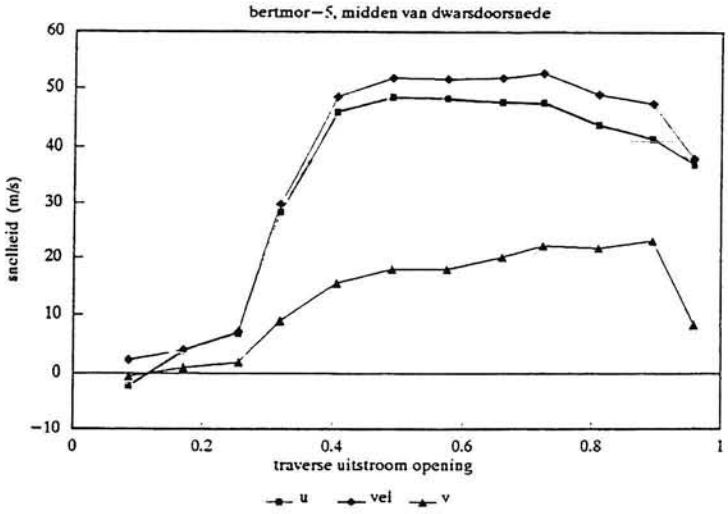

Fig. 7 Snelheden in luchtpoort

Tenslotte is er een model gemaakt waarbij verbranding wordt meegenomen. Gezien de schaal van de windverhitter is het model daarbij in twee delen gesplitst: een eerste model waarbij de branderkroon in detail wordt berekend en een tweede deel voor de branderschacht.Tevens is in dit model rekening gehouden met de verspringende luchtpoorten. De resultaten van het detailmodel zijn daarbij gebruikt als inlaat condities voor het branderschacht model. In figuur 8 is de gestippelde lijn de overgang tussen detail en globale model. De hier aangegeven lijn is het met het detailmodel berekende temperatuurprofiel net boven de branderkroon. Op dit niveau is er alleen op het grensvlak tussen gas en lucht sprake van verbranding.

Overigens wordt de inlaat van het globale model gelegd direct onder de luchtpoort. Hiermee wordt voorkomen dat deze inlaat recirculatie gebieden doorsnijdt.

In het globale model kan i.v.m. de symmetrie worden volstaan met berekening van een kwart van de schacht. Het blijkt dat de vlammen zeer lang zijn, de ontsteking van de vlammen vindt plaats op de branderkroon. Tevens blijkt dat de menging van gas en lucht slecht is: op 15m boven de branderkroon blijkt de zuurstof zich aan de lange zijde van de schacht te bevinden, terwijl de brandstof zich in het hart en in de korte zijde van de schacht bevindt. Op 30m hoogte, aan het einde van de schacht, zijn de brandstofrijke gebieden in het hart van de stroming verdwenen, de gebieden aan de korte zijde zijn echter nog aanwezig. Na dit punt gaan de gassen het keramisch stapelwerk in (ziefiguur 5), wat bestaat uit een groot aantal vertikale kanalen. Dit houdt in dat er nauwelijks verbranding meer plaatsvindt, de berekende verdeling boven in de branderschacht moet dus in principe terug te vinden zijn aan het einde van het

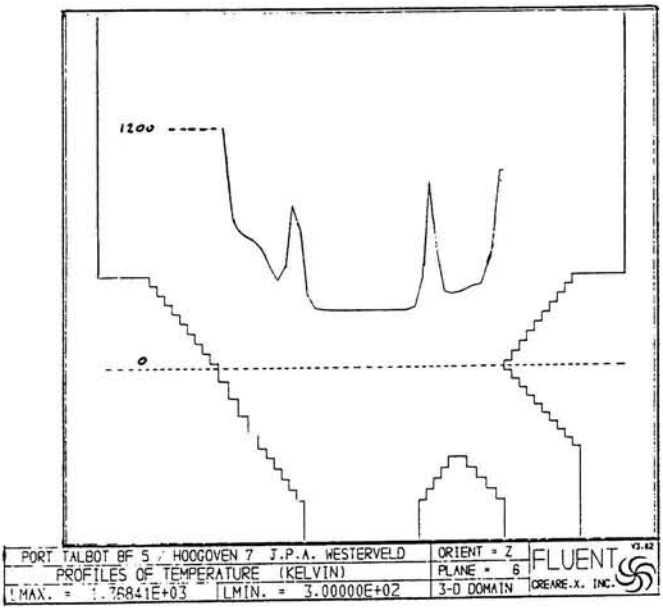

Fig. 8 Temperatuurprofiel branderkroon

stapelwerk. Uit metingen blijkt er een goede overeenkomst te zijn tussen de berekende en gemeten CO-verdeling.In de toekomst zal het bovenbeschreven model verder worden uitgewerkt. De motivering hiervoor is de te verwachten verscherping van milieu-eisen en de hiermee samenhangende garanties die door klanten worden gevraagd. De aanpak zal daarbij in eerste instantie bestaan uit het valideren van de berekeningsresultaten en daarna uit het doorrekenen van een aantal alternatieve branderconfiguraties.

4. Slotwoord

Tot zover wilde ik mijn bijdrage beperken. Daarbij hoop ik dat ik het belang heb kunnen aangeven van de stromingsleer buiten de lucht- en ruimtevaart techniek, en dat de lezer dezes zich kan vinden in de stelling dat staalproduktie en vliegtuigbouw wel degelijk overeenkomsten vertonen.

System studies of closed and open cycle, disk and linear MHD generators

By P. Massee

Group Electrical Energy Systems
Eindhoven University of Technology

Abstract

In this paper the performance of four systems is compared i.e. the disk and the linear MHD generator both for open cycle and for closed cycle conditions. The systems are considered as a topping cycle for a conventional steam cycle and are compared on the basis of the coal to busbar efficiency. It is concluded that the closed cycle disk system has a small advantage over the other three systems.

1. Introduction

A lot of information can be found in the literature on the comparison of the total plant efficiency for systems with an open cycle (OC) or a closed cycle (CC) linear MHD generator as a topping cycle. A similar situation exists for the comparison of systems with an OC or a CC disk MHD generator. It is, however, not possible to compare the performance of the four systems mentioned above on the basis of one common set of ground rules. The present paper aims at an improvement of this situation. The plant description of the OC and the CC system show the same amount of details (figures 1 and 2). Furthermore most of the efficiencies of the components surrounding the MHD generator are equal for the OC and the CC system (table I). The differences in assumed design parameters for the OC and the CC system are clearly indicated (tables II and III). The most relevant results for the different systems are presented in the form of tables and figures which show the influence of the variation of the important parameters on the efficiencies. The work that the authors had in mind has not been entirely completed, however. In the near future the influence of plant size on the efficiencies will be studied. More important yet, the cost of electricity of the four systems also has to be calculated and has to be taken into account in the comparisons.

2. Closed cycle generator performance

Generator model and assumptions

In describing the generator model it is convenient to concentrate first on the disk generator. It is assumed that only a variation in the radial direction will exist, thus leading to the usual one-dimensional description of the variation of heavy particle properties:

$$\frac{d}{dr}(\rho V_r A) = 0 \tag{1}$$

$$\rho V_r \frac{dV_r}{dr}\frac{dp}{dr} = \rho \frac{V_\theta^2}{r} + J_\theta B - C_f \frac{\rho V V_r}{z} \tag{2}$$

$$\rho V_r \frac{dV_\theta}{dr} = -\rho \frac{V_r V_\theta}{r} - J_r B - C_f \frac{\rho V V_\theta}{z} \tag{3}$$

$$\rho V_r \frac{d}{dr}(h + \frac{V_r^2 + V_\theta^2}{2}) = J_r E_r + \frac{2}{z} Q \tag{4}$$

In these equations the symbols have their usual meaning. The electrical current densities and field can be calculated from the electron gas equations. For these equations two simplifying assumptions are made:

(i) the inlet relaxation length is negligible in comparison with the generator length, and

(ii) the electron continuity and energy equation are assumed to be in equilibrium so that the first equation reduces to a Saha equation for Cs ions and a Saha equation for Ar ions and the second equation reduces to jheat = ellos.

Here ellos stands for the usual expression for the electron energy loss through elastic collisions and the internal Joule dissipation in the plasma is written as

$$jheat = \frac{J_r^2 + J_\theta^2}{\sigma_{eff}}$$

The momentum equation for the electron gas leads to

$$J_r = \frac{\alpha}{\beta_{eff}} \sigma_{eff} V_r B$$

$$J_\theta = -\sigma_{eff} V_r B(1-\alpha)$$

$$E_r = -\beta_{eff} V_r B\left[1+\frac{S}{\beta_{eff}}-\alpha-\frac{\alpha}{\beta_{eff}^2}\right] \tag{5}$$

where α is the loading parameter defined by Klepeis and Louis[3] and the swirl $S = V_\theta/V_r$

The effective values of the electrical conductivity σ and the Hall parameter ß are calculated from the quasi-linear plane wave theory of electrothermal waves in a simplified form:

$$if\ \beta < \beta_{crit}\ \ then\ \ \sigma_{eff} = \sigma,\ \ \beta_{eff} = \beta$$

$$if\ \beta \geq \beta_{crit}\ \ then\ \ \frac{\sigma_{eff}}{\langle\sigma\rangle} = \frac{\beta_{eff}}{\langle\beta\rangle},\ \beta_{eff} = \beta_{crit} \tag{6}$$

The value of the Hall parameter at the stability limit $ß_{crit}$ follows from the linearized plane wave theory and is calculated according to the expressions given by Nakamura and Riedmüller[5].

The equations describing the flow in the closed cycle linear, segmented Faraday MHD generator are strongly analogous to the above equations. In the linear generator the Coriolis forces are absent and the perpendicular velocity component vanishes. Due to the segmented Faraday configuration the longitudinal component of the electric current density is zero in the one-dimensional approximation so that Ohm's law reduces to

$$J_y = -\sigma_{eff} V B (1-k_F)$$

$$E_y = k_F V B \tag{7}$$

Here the Faraday load factor k_F can be written as

$$k_F = \frac{R_L}{(R_i + R_L)} \tag{8}$$

with R_L = external load resistance and R_i = internal resistance = $\frac{h}{\sigma_{eff} w s}$ (h = height, w = width and s = pitch of the generator segment). In the linear generator segmentation

losses have to be taken into account which is done by introducing an apparent electrical conductivity defined by

$$\sigma_{app} = \frac{\sigma_{eff}}{1 + \beta_{eff} \frac{s}{h}} \tag{9}$$

which takes into account the bending of the electric current lines in the segment.

In the way described above the effect of streamers (constricted discharges which cannot be described in principle by a quasi-linear theory) has not been taken into account. The presence of streamers, which is in general observed experimentally, may reduce the performance of the generator[6]. Neither has the fact been taken into account that the disk generator may also be operated under the condition of fully ionized seed[7]. It has not yet been shown experimentally that a disk generator with large enthalpy extraction may fulfil this condition over the entire expansion range. On the other hand it has been shown before[7] that the advantage of the fully ionized seed condition over other loading conditions is probably limited.

Plant description

The closed cycle MHD generator is included in a loop which is shown in figure 1. The system configuration of a coal burned closed cycle MHD-steam plant can be divided into three subsystems:

- an open cycle coal combustion system to heat up the argon by means of ceramic regenerative heat exchangers,
- a closed cycle argon system with the previously mentioned heat exchangers, the MHD generator and diffusers, components for heat transfer to the steam cycle and an argon compressor, and
- a steam cycle.

A disadvantage of the closed cycle MHD system is that the total heat flux has to be supplied to the argon by means of a system of ceramic regenerative heat exchangers which has a negative effect on the investments. The combustion gases which leave the regenerative heat exchangers are used to preheat the combustion air and to dry the coal. The combustor is cooled with feed water from the high temperature economizer. The argon which is heated up in the regenerative heat exchangers to a temperature of 2000 K is accelerated in the nozzle to obtain the desired Mach number and flows through the MHD duct. The flow which is still supersonic at the generator exit is decelerated in a diffuser system and the remaining heat is transferred to the steam system by means of several heaters and boilers. The argon compressor operates without intercooling and is driven by a steam turbine.
The cesium is injected in the high temperature argon before it enters the nozzle.

Removal of the cesium from the argon is accomplished by condensation of the cesium vapour. The reclaimed seed is purified, mixed with make-up seed and passed to a liquid metal pump before re-injection into the argon cycle. To keep the contamination level of the argon low, a gas cleanup system is desired.

A supercritical steam cycle of 230 bar/823 K is used as bottoming cycle. The cycle rejects heat to surface water through a 0.027 bar condenser and yields a thermodynamic efficiency of 43.2%[8]. In the performance analysis, channel cooling with low temperature feed water is assumed.

The components in the loop are specified by efficiencies which are listed in table I. The design parameters needed to specify the burner system, MHD generator and the steam bottoming plant are specified in table II. These numbers make the calculation of the performance of the argon cycle straightforward once the enthalpy extraction and the isentropic efficiency of the MHD generator plus nozzle and diffusers has been determined. The specification of the burner system is very simple since the constant stack temperature implies constant stack losses. This also implies a constant efficiency of the combustion system wich can be calculated from the relevant equations[9] and equals 0.966 for a stack temperature of 393 K.

Design constraints and optimization results

For the calculations of both types of closed cycle MHD generators, assuming supersonic flow, the following general constraints have to be fulfilled:

- the Mach number at the generator exit must be larger than 1.05 in order to avoid shock waves inside the channel, and
- the half divergence angle between the channel walls must be smaller than 5 degrees in order to avoid separation of the flow from the wall[9].

Following Retallick[2] the closed cycle disk MHD generator is designed to work in the optimum loading mode. In this mode the loading parameter α equals the optimum value α_{opt} for each value of the radius r for which purpose the channel height z is accommodated at each location. The optimum loading parameter α_{opt} is easily calculated and leads to the maximum value of the local electrical efficiency η_L[7]. Both α_{opt} and η_L depend on the value of the swirl S and on the value of the effective Hall parameter β_{eff}. It has been shown before[7] that the optimum loading mode may be preferred for an unstable plasma i.e. for a plasma which will not be in the condition of fully ionized seed over a large range of the expansion.

For the optimization of the performance of the disk generator about 200 calculations have been performed. For this the inlet parameters have been varied in the following way: Mach number M = 1.8, 2, 2.2 and 2.4; stagnation pressure p_s= 4, 6, 7 and 8 bar; seed ratio SR = 10^{-5}, 5×10^{-5}, 10^{-4}, 5×10^{-4} and 10^{-3} and inlet swirl S = 0.75, 1, 1.5 and 2. The most significant results have been collected in table IV and the influence

of the variation of parameters on efficiencies is illustrated in figure 3. The comparison which can be made from table IV is at a constant enthalpy extraction of 30% and a seed ratio of 5×10^{-5}. At a seed ratio of 10^{-5} an enthalpy extraction of 30% is only obtained in 4 situations. At a seed ratio of 10^{-4} or larger an enthalpy extraction of 30% has not been reached at all. The limiting factor in most cases is the half divergence angle becoming too large, which also leads to some empty lines in table IV. It is apparent from figure 3 that the best coal to bus bar efficiency is obtained at the lowest inlet stagnation pressure, the largest value of the magnetic induction and the highest enthalpy extraction which have been considered. The optimum Mach number appears to be 2.2 and the optimum swirl 0.75. The best operation of the disk generator has been obtained for the inlet conditions M = 2.4, p_s= 4 bar, SR = 5×10^{-5} and S = 2 (B = 5 T). At an enthalpy extraction of 35% this leads to an isentropic efficiency (of generator plus nozzle and diffusers) η_{is} of 75.5% and a coal to bus bar efficiency η_{cb} of 51.3%. Comparison with the corresponding numbers in table IV shows an increase of 3.7 percentage points in η_{is} and 1.9 percentage points in η_{cb} due to the increase in enthalpy extraction from 30 to 35%. At a magnetic induction B = 6 T the best operation of the disk generator has been obtained for M = 2.2, p_s = 4 bar, SR = 5×10^{-5}, S = 2 and η_{ent} = 35%. This leads to η_{is} = 76.8% and η_{cb} =51.6% which is only a limited gain compared to the case mentioned above. The variation in compressor power P_c is also shown in figure 3 because this can explain the variation of η_{cb}. At constant enthalpy extraction the electric power from the MHD generator and from the steam bottoming plant are both constant.

Following Geutjes and Kleyn[9] the closed cycle linear MHD generator is designed with straight channel walls under the maximum divergence angle and operates at constant Faraday load factor k_F. It has been shown in[9] that closed cycle linear MHD generators with subsonic flow do not have attractive part load behaviour so that supersonic flow has been chosen. For the optimization of the performance about 50 calculations have been performed. For this the inlet parameters have been varied in the following way: M = 1.2, 1.45, 1.7 and 2; p_s = 4, 6, 7 and 8 bar and SR = 10^{-4}, 5×10^{-4} and 10^{-3}. The most significant results have been collected in table V and the influence of the variation of parameters on efficiencies is illustrated in figure 4. The comparison which can be made from table V is at a constant enthalpy extraction of 30% and a seed ratio of 10^{-3}. The influence of the seed ratio on the isentropic efficiency and on the coal to bus bar efficiency is minute and is therefore not shown in figure 4. It has been observed from the calculations that boundary layer separation quite often prevents an enthalpy extraction of 35% to be reached at the Mach numbers 1.2 and 1.45 and at an inlet stagnation pressure larger than 4 bar. It is apparent from figure 4 that the best coal to bus bar efficiency is obtained at the lowest inlet stagnation pressure, the smallest Mach number and the largest enthalpy extraction which have been considered. The gain which can be obtained by increasing the magnetic induction from 5 to 6 T is very limited. The best operation of the linear generator is thus obtained for the inlet conditions M = 1.2, p_s = 4 bar and SR = 10^{-3} (B = 5 T). At an enthalpy extraction of 35% this leads to an isentropic efficiency (of generator

plus nozzle and diffusers) η_{is} of 73.4% and a coal to bus bar efficiency η_{cb} of 49.1%. Comparison with the corresponding numbers in table V shows an increase of 3 percentage points in η_{is} and 1.5 percentage points in η_{cb} due to the increase in enthalpy extraction from 30 to 35%.

3. Open cycle generator performance

Generator model and assumptions

Again starting with the disk generator in this case, the equations governing the behaviour of the flow are exactly identical with the equations (1) to (5). The difference with the closed cycle case is that the electron gas is now strongly coupled to the heavy particle gas so that the electrical conductivity σ and the Hall parameter ß are completely determined by the heavy particle properties. Calculations have been performed of the equilibrium composition of the combustion gas leading to values of enthalpy h , entropy s, speed of sound c, ratio of specific heats γ, electrical conductivity σ and Hall parameter ß for various conditions of the gas. For the calculation of the flow in the generator all these properties are required. They are obtained from the NASA SP-273 chemical equilibrium computer code[10] and are modeled by a least squares curve fit as function of temperature and pressure in the general form

$$\xi = \xi_0 + \xi_1 \left[\frac{p}{p_{ref}}\right]^{\xi_2} \left[\frac{T}{T_{ref}}\right]^{\xi_3} \tag{10}$$

where p_{ref} and T_{ref} are reference values of the static pressure and static temperature (p_{ref} = 1 bar, T_{ref} = 2500 K).

In the case of the open cycle linear generator segmentation losses and the effect of inhomogeneities are not explicitly taken into account. Voltage drops are assumed to be constant over the length of the channel and the relaxation length is supposed to be negligible.

For the calculation of the linear channel the Mach number is kept constant at 0.9 and the load factor is constant and is adjusted such that the stagnation pressure at the exit of the subsonic diffuser is 1.14 bar. The viscous and thermal losses are treated by semi-empirical relations governing the wall skin friction and wall heat flux. To fulfil the above mentioned conditions the square cross section of the channel is adjusted.

Plant description

The open cycle MHD generator is included in a loop which is shown in figure 2. The system configuration can be divided into two subsystems:

- an open cycle coal combustion system, MHD generator and diffuser and components for the heat transfer to the steam cycle, and
- a steam cycle.

Compared with the closed cycle system the main difference in the combustion system is the location of the combustion air preheater. In the closed cycle system it is located downstream of the high temperature ceramic regenerative heat exchangers and in the open cycle it is located downstream of the radiant boiler. The seed in the form of dry potassium carbonate is added to the combustor in an amount that the plasma will contain 1% of potassium by weight. The combustion gases are accelerated through a nozzle to the desired Mach number. In the MHD channel enthalpy is extracted in such a way that the stagnation pressure leaving the diffuser is 1.14 bar. From the diffuser the combustion gases enter the heat recovery/seed recovery system, including a steam generator, air heaters, gas clean up equipment and coal dryers.

The steam cycle is the same as for the closed cycle system. From the calculations of nozzle, generator channel and diffuser enthalpy extraction and isentropic efficiency have been determined. The heat which is carried off by cooling the burner, nozzle, channel and diffuser can be used in the steam bottoming cycle. Given the specific efficiencies of the cycle components (see table I) the coal to bus bar efficiency can be calculated.

Design constraints and optimization results

For the calculations of both types of open cycle MHD generators the coal thermal input is 1000 MWt. The burner system is a two stage combustor with high slag rejection (85%) and the combustion air is directly preheated to a temperature of 1800 K. The coal type is Illinois no. 6 with a higher heating value of 28.8 MJ/kg and a lower heating value of 26.2 MJ/kg. The coal is burned substoichiometrically to reduce NO_x formation and the seed , in the form of dry potassium carbonate, is added to the second stage of the burner to prevent partial seed loss in the slag removal after the first stage. The total heat losses in burner and nozzle are supposed to be 4.5% of the coal thermal input. For a stagnation pressure of 7.2 bar at the inlet of the generator a stagnation temperature of 2828 K is calculated. Heat losses in the generator are based on the assumption that the difference in stagnation and wall temperature is constant and equals 500 K.

Following Retallick[2] the open cycle disk generator has been designed for constant radial electric field (E_r = 12 kV/m) since this leads to the most compact configuration. In order to keep E_r at this maximum allowable value the channel height is adjusted at each location. It has been shown that variation of the value of E_r does not have

a large influence on the results. For the optimization of the performance about 80 calculations have been executed. For this the inlet parameters have been varied in the following way: M = 1.7, 1.8, 1.9 and 2; p_s = 5, 6, 7 and 8 bar and S = 0.5, 0.75, 1, 1.5 and 2. The most significant results have been collected in table VI and the influence of the variation of parameters on efficiencies is illustrated in figure 5. The comparison which can be made from table VI is at a swirl S = 1. It is apparent from figure 5 that the best coal to busbar efficiency is obtained at the lowest Mach number, the smallest inlet stagnation pressure and the largest value of the magnetic interaction which have been considered. The optimum swirl appears to be S = 1.5 but the effect of swirl is limited. The latter is connected with the fact that losses due to the inlet swirl vanes have not been taken into account[2]. The best operation of the disk generator is obtained for the inlet conditions M = 1.7, p_s = 5 bar and S = 1 (B = 5 T). At a magnetic induction B = 7 T this leads to η_{ent} = 20.8% (related to the coal thermal input), η_{is} = 69.8% and η_{cb} = 44.5%. Comparison with the corresponding numbers in table VI shows an increase of 3.5 percentage points in η_{ent}, of 7 percentage points in η_{is} and 1.7 percentage points in η_{cb} due to the increase in magnetic induction from 5 to 7 T. A further increase of the magnetic induction to 9 T leads to a maximum coal to busbar efficiency η_{cb} = 45.5% under the inlet conditions M = 1.8, p_s = 7 bar and S = 0.5. The corresponding other efficiencies in this case are η_{ent} = 24.6% and η_{is} = 67.4%. When the difference in unit size is taken into account the quoted values of efficiencies are comparable to those given by Retallick[2].

The linear channel is loaded in the segmented Faraday mode and the Mach number is kept constant at 0.9. The voltage drop is constant (150 V) and the load factor is constant for the whole generator and is adjusted such that the stagnation pressure at the exit of the subsonic diffuser is constant and equals 1.14 bar. To satisfy these conditions the square cross section of the generator is adjusted. To prevent boundary layer separation the half divergence angle between the channel walls is checked and may not exceed 5 degrees.
Due to the decrease of the plasma temperature the electrical conductivity changes under base case conditions from 7.4 mho/m at the inlet to about 2 mho/m at the exit of the channel. The maximum Hall parameter amounts 5.3 at the exit. The maximum electrical field in the axial direction is 4370 V/m and in the Faraday direction 3140 V/m.
The inlet cross section is 0.8 × 0.8 m^2, the exit cross section is 1.96 × 1.96 m^2 and the heat loss of the channel is 63 MWt. For the base case the isentropic efficiency η_{is} amounts 74.8% and the coal to bus bar efficiency η_{cb} = 49.0%.
The most significant results have been collected in table VII and the influence of the variation of parameters on efficiencies is illustrated in figure 6. Comparison of the calculations shows that an increase of the length of the channel from 16 to 24 m results in an increase of 4.8 percentage points in η_{is} and 1.0 percentage points in η_{cb}. The influence of the magnetic induction is more pronounced. An increase in B from 4 to 6 T results in an increase of 15.4 percentage points in η_{is} and 2.7 percentage points in η_{cb}.

Variation of the stagnation pressure at the inlet of the generator from 5.4 to 9.0 bar shows a decrease in η_{is} of 12.5 percentage points but the effect on η_{cb} is only 0.9 percentage points and a maximum is reached for $p_s \cong 6.5$ bar. The voltage drop is varied from 50 to 250 V which results in a decrease in η_{is} and η_{cb} of respectively 3.2 and 0.7 percentage points. The difference between the stagnation and the wall temperature is varied from 400 to 600 K. Due to the larger heat loss in the generator this results in a decrease in η_{is} and η_{cb} of respectively 1.6 and 0.4 percentage points. The heat losses in burner and nozzle are varied from 4.05 to 4.95% of the coal thermal input. The influence on the efficiencies is rather small. With increasing heat losses the decrease in η_{is} and η_{cb} is respectively 0.6 and 0.4 percentage points. For one case the air preheat temperature is decreased from 1800 to 1650 K. This results in a lower stagnation temperature (2775 K) and also a lower value for the electrical conductivity (5.8 mho/m at the inlet). This effect lowers η_{is} and η_{cb} with respectively 3.2 and 1.5 percentage points.
When the difference in unit size is taken into account the comparison of the efficiencies with the corresponding numbers of the ECAS study[11] shows a good agreement.

4. Conclusions

- For the closed cycle (CC) system the disk MHD generator leads to an advantage of 2.2 percentage points in the coal to busbar efficiency η_{cb} in comparison with the linear MHD generator (both at B = 5 T).
- For the open cycle (OC) system the linear MHD generator (at B = 6 T) leads to an advantage of 5.1 percentage points in η_{cb} in comparison with the disk MHD generator (at B = 9 T).
- Comparison of the best closed cycle system with the best open cycle system shows an advantage of 1 percentage point in η_{cb} for the CC disk MHD/steam cycle in comparison with the OC linear MHD/steam cycle (both at B = 6 T).
- In the near future the cost of electricity of the different systems will be determined. When a comparison on this basis is performed the conclusions reached above may be changed.

Acknowledgement

The work has been performed with financial support of the Netherlands Technology Foundation (STW) in cooperation with the Group Low Temperatures of the University Twente.

References

1 Alyea, F.N. et al., 'Comparative analysis of CCMHD power plants', 19th Symp. on Engineering Aspects of MHD, Tullahoma, Tenn., 1981, pp. 6.5.1-6.5.8.

2 Retallick, F.D., 'Disk MHD generator study', NASA report CR-759872, Cleveland, Ohio, 1980.

3 Klepeis, J.E. and Louis, J.F., 'The disk generator applied to open cycle power generation', 5th Intern. Conf. on MHD Electrical Power Generation, Munich, 1971, Vol. 1, pp. 649-661.

4 Solbes, A., 'Instabilities in nonequilibrium MHD plas- mas, a review', AIAA paper no. 70-40, New York, 1970.

5 Nakamura, T. and Riedmüller, W., 'Stability of non-equilibrium MHD plasma in the regime of fully ionized seed', AIAA Journal, Vol. 12, 1974, pp. 661-668.

6 Merck, W.F.H. and Rietjens, L.H.Th., 'Empirical description of discharge phenomena in A-Cs MHD genera- tors', 10th Intern. Conf. of MHD Electrical Power Generation, Tiruchirapalli, 1989.

7 Massee, P., 'Performance of closed cycle disk genera- tors operating with stable or unstable plasma', 19th Symp. on Engineering Aspects of MHD, Tullahoma, Tenn., 1981, pp. 7.1.1-7.1.7.

8 Cervenka, S. et al., 'Conceptual design study of a 600 MWe coal fired open cycle MHD plant', 20th Symp. on Engineering Aspects of MHD, Irvine, 1982, pp. 13.4.1- 13.4.10.

9 Geutjes, A.J. and Kleyn, D.J., 'A parametric study of 1000 MWe combined closed cycle MHD/steam electrical power generation plants', report Eindhoven University of Technology, nr. 78-E-91, Eindhoven, 1978.

10 Mc. Bride, B.J. and Gordon, S., 'Computer program for calculation of complex chemical equilibrium compositions, rocket performance, incident and reflected shocks and Chapman-Jouguet detonations', NASA SP-273, 1976, Rev.

11 Lewis Research Center, 'Comparative evaluation of phase I results from energy conversion alternatives study (ECAS)', Report no. NASA TM-X-71855, febr. 1976.

Table I Efficiencies of components valid for both OC and CC and for both linear and disk.

Radiative boiler	0.99
Convective apparatuses	0.99
Thermodynamic efficiency of the steam bottoming plant	0.432
Mechanical efficiencies	0.99
DC-AC converter	0.96
AC generator	0.998
Internal electricity consumption	0.03
Compressor efficiency	0.82
Isentropic efficiency of nozzle	0.99
Isentropic efficiency of subsonic diffuser	0.9
Correction factor for non ideal shock supersonic diffuser	0.9
Pressure drops per component	0.02
Heat for seed recovery	0.03*)
Heat for coal drying	0.01*)
pressure loss of combustion air system	0.10
pressure loss of burner system	0.10

*) related to coal thermal input

Table II Assumed design parameter for CC studies (both disk and linear MHD generator)

Enthalpy flux at generator entrance	1200 MWt
Coal type	Illinois no 6
Burner system	
stoichiometry	0.95
cooling power related to coal thermal power	0.03
stack temperature	393 K
efficiency of the burner system	0.966
MHD generator	
medium	Ar + Cs
magnetic induction (constant)	5 T
stagnation temperature-wall temperature	300 K
voltage drop per electrode pair (linear segmented Faraday type only)	150 V
cooling	feed water
total pressure drop argon loop	0.12

Table III Assumed design parameters for OC studies (both disk and linear MHD generator)

Coal thermal input to combustor	1000 MWt
Coal type	Illinois no 6
Air preheat system	direct
preheat temperature	1800 K
seed	dry K_2CO_3, 1 % wt K
Burner system	2 stage cyclone
stoichiometry	0.95
cooling power incl. nozzle related to coal	0.04
thermal input	0.85
slag rejection	
MHD generator	
magnetic induction (constant)	5 T
stagnation temperature-wall temperature	500 K
voltage drop per electrode pair	150 V
(linear segmented Faraday type only)	feed water
cooling	1.14 bar
downstream pressure subsonic diffuser	

Table IV Summary of most significant results for the closed cycle disk MHD generator. Seed ratio = 5×10^{-5}, B = 5 T, $T_{s,in}$ = 2000 K and inlet radius = 1.85 m. Optimum loading mode ($\alpha = \alpha_{opt}$ for each radius).

S_{in}	M_{in}	$p_{s,in}$ bar	η_{ent} %	η_{is} %	η_{cb} %	P_{MHD} MW	P_c MW	P_{st} MW	P_{net} MW
2.0	2.4	4	30.3	71.8	49.4	363	183	271	424
		6	30.3	68.5	48.6	363	198	271	409
		7	30.2	66.8	48.1	362	206	272	401
		8	30.2	65.1	47.6	363	216	271	391
	2.2	4	30.3	72.4	49.6	363	180	271	426
		6	30.1	67.7	48.4	361	200	272	406
		7	30.2	65.5	47.7	362	213	272	394
		8							
1.5	2.4	4	30.1	70.5	49.1	361	187	272	419
		6	30.3	68.5	48.6	364	199	271	409
		7	30.3	67.3	48.3	363	204	271	403
		8	30.3	66.1	47.9	363	211	271	397
	2.2	4	30.3	72.5	50.0	364	181	271	426
		6	30.3	69.2	48.8	364	195	271	412
		7	30.3	67.5	48.3	363	203	271	404
		8	30.3	65.8	47.8	363	212	2714	395

Table V Summary of most significant results for the closed cycle linear MHD generator (segmented Faraday type). Seed ratio = 10^{-3}, B = 5 T, $T_{s,\,in}$ = 2000 K, voltage drop = 150 V and Faraday load factor k_F = constant.

M_{in}	$p_{s,\,in}$ bar	k_F	η_{ent} %	η_{is} %	η_{cb} %	P_{MHD} MW	P_c MW	P_{st} MW	P_{net} MW
1.20	4	0.845	30.3	70.4	47.6	362	188	271	417
	6	0.815	30.3	67.4	46.9	363	204	270	402
	7	0.805	30.2	66.0	46.4	361	209	271	396
	8	0.790	30.1	64.8	46.0	360	215	271	389
1.45	4	0.865	30.3	68.9	47.3	362	195	271	410
	6	0.840	30.3	66.2	46.5	363	210	270	396
	7	0.825	30.8	65.7	46.4	369	219	267	390
	8	0.815	30.7	64.5	45.9	366	224	268	384
1.70	4	0.880	30.3	66.8	46.7	362	207	270	399
	6	0.855	30.1	64.2	45.8	360	219	271	386
	7	0.845	30.2	63.3	45.5	360	226	271	379
	8	0.835	30.2	62.4	45.2	360	231	271	374
2.00	4	0.890	30.3	64.5	45.9	362	220	270	386
	6	0.875	30.4	61.3	44.7	363	243	270	364
	7	0.865	30.9	61.2	44.5	369	251	267	359
	8	0.855	30.3	60.1	44.1	362	252	270	355

Table VI Summary of most significant results for the open cycle disk MHD generator. Inlet swirl S = 1, B = 5 T and electric field constant (E_r = 12 kV/m). The character M in the last column indicates that the expansion had to be stopped because a Mach number = 1.05 was reached.

M_{in}	$p_{s,\,in}$ bar	η_{ent} %	η_{is} %	η_{cb} %	P_{MHD} MW	P_c MW	P_{st} MW	P_{net} MW	
2.0	5	15.0	64.1	41.6	150	65.5	363	416	
	6	16.2	59.5	41.7	161	74.5	362	417	
	7	16.6	55.4	41.5	166	82.5	364	415	
	8	16.5	51.6	41.1	166	89.8	367	411	
1.9	5	16.4	64.1	42.3	164	65.5	357	423	
	6	17.4	59.8	42.3	175	74.5	357	423	
	7	17.9	56.6	42.2	179	82.5	358	422	
	8	17.8	53.0	41.7	178	89.8	362	417	
1.8	5	17.1	63.5	42.6	170	65.5	354	426	
	6	18.0	59.5	42.6	180	74.5	354	426	
	7	18.3	56.5	42.3	183	82.5	357	423	
	8	7.1	26.0	36.3	71	89.8	407	363	M
1.7	5	17.3	62.8	42.8	172	65.5	353	428	
	6	7.4	32.7	37.3	74	74.5	399	373	M
	7	7.1	28.3	36.7	71	82.6	404	367	M
	8	6.5	24.0	36.0	65	89.8	410	360	M

Table VII Summary of most significant results for the open cycle linear MHD generator (segmented Faraday type). Mach number = constant (M = 0.9), B = 5 T, voltage drop = 150 V and Faraday load factor k_F = constant.

$p_{s,\,in}$	l	k_F	η_{ent}	η_{is}	η_{cb}	P_{MHD}	P_c	P_{st}	P_{net}
bar	m		%	%	%	MW	MW	MW	MW
5.4	16	0.84	29.8	78.9	48.6	298	75	305	486
5.4	20	0.86	30.4	80.7	48.9	304	75	302	489
5.4	24	0.88	30.8	81.6	49.1	308	75	300	491
6.3	16	0.79	30.7	75.5	48.6	307	83	304	486
6.3	20	0.82	31.7	77.9	49.1	317	83	300	491
6.3	24	0.84	32.2	79.3	49.4	322	83	298	494
7.2	16	0.74	30.9	71.9	48.4	309	90	306	484
7.2	20	0.78	32.2	74.8	49.0	322	90	301	490
7.2	24	0.81	33.0	76.7	49.4	330	90	297	494
8.1	16	0.69	30.7	68.1	47.9	307	96	310	479
8.1	20	0.73	32.3	71.6	48.7	323	96	303	487
8.1	24	0.77	33.3	73.8	49.2	333	96	299	492
9.0	16	0.65	30.1	64.3	47.3	301	102	315	472
9.0	20	0.70	32.0	68.2	48.2	320	102	307	482
9.0	24	0.73	33.2	70.8	48.8	332	102	302	488

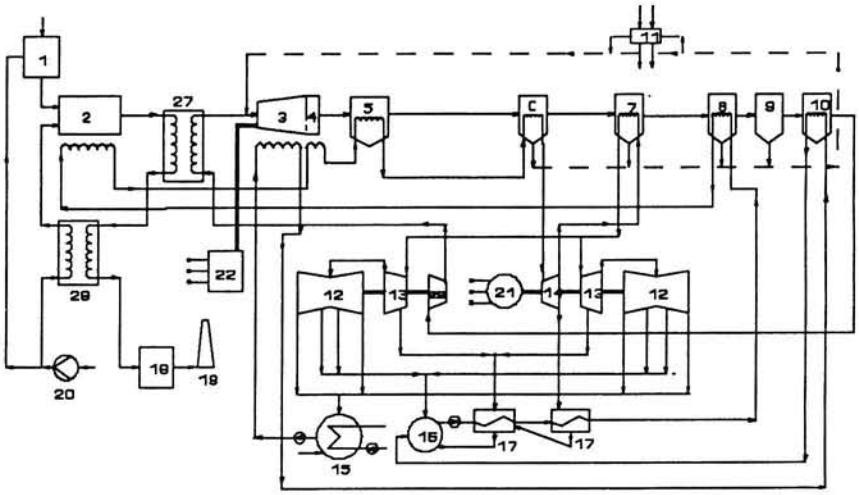

Fig. 1 Plant arrangement schematic of the closed cycle MHD/steam plant.

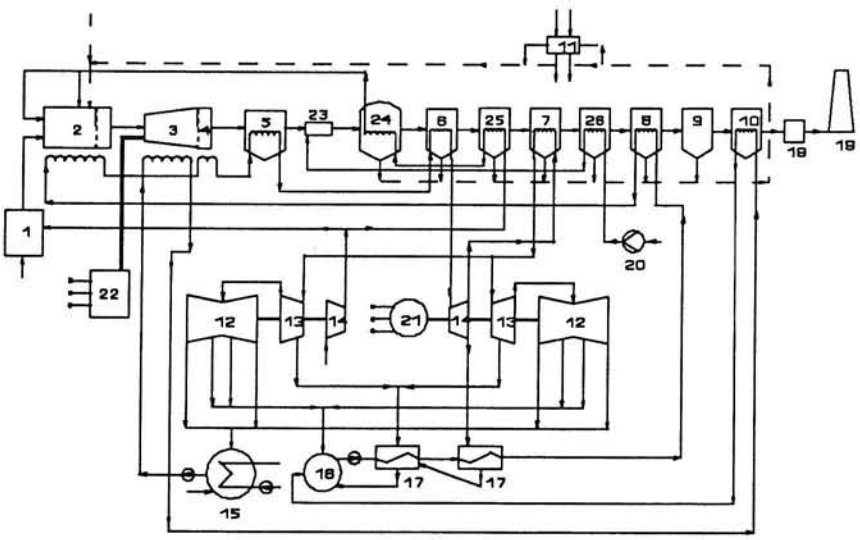

Fig. 2 Plant arrangement schematic of the open cycle MHD/steam plant.

The numbers in the figures 1 and 2 have the following significance: 1. coal treatment, 2. combustor, 3. MHD generator, 4. diffuser, 5. radiant boiler, 6. superheater, 7. reheater, 8. high temperature economizer, 9. gas cleanup equipment, 10. low temperature economizer, 11. seed treatment, 12. low pressure steam turbine, 13. medium pressure steam turbine, 14. high pressure steam turbine, 15. condenser, 16. degas equipment, 17. water preheaters, 18. coal dryer, 19. stack, 20. air compressor, 21. generator, 22. dc-ac invertor, 23. secondary combustor, 24. intermediate and high temperature air heater, 25. low temperature air heater, 26. secondary air preheater, 27. high temperature argon heater, 28. air preheater.

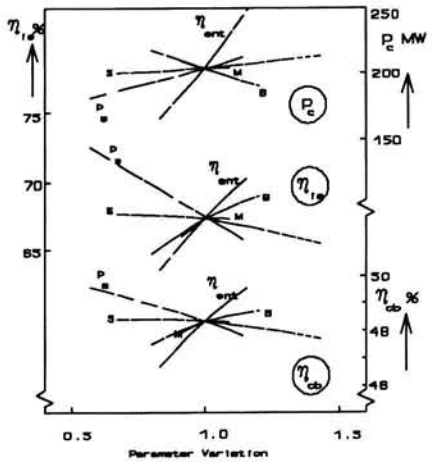

Fig.3 Effect of parametric variations on compressor power P_c , isentropic efficiency η_{is} and on the coal to bus bar efficiency η_{cb}. Closed cycle disk MHD/steam system. Base case conditions for the reference point: $p_{s,in} = 7$ bar, $M_{in} = 2.2$, $S_{in} = 1.5$, SR = 5 x 10^{-5}, B = 5 T and $\eta_{ent} = 30$ %. Under these conditions: r = 1.85 m ÷ 2.58 m, h = 0.4 ÷ 0.33 m, $ß_{eff} = 3.9 \div 5.6$, $\eta = 36 \div 45$ mho/m.

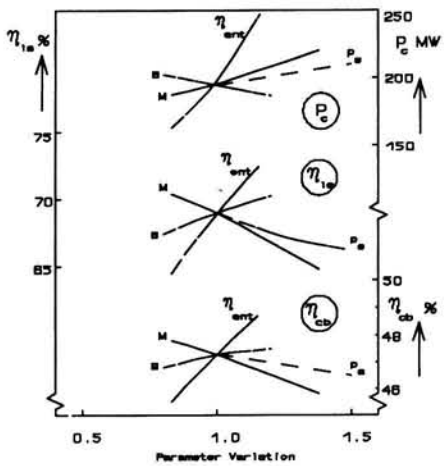

Fig. 4 Effect of parametric variations on compressor power P_c, isentropic efficiency η_{is} and on the coal to bus bar efficiency η_{cb}. Closed cycle linear MHD/steam system. Base case conditions for the reference point: $p_{s,in} = 4$ bar, $M_{in} = 1.45$, SR = 10^{-3}, B = 5 T and $\eta_{ent} = 30$ %. Under these conditions: $h_{in} = b_{in} = 1.70$ m, $h_{out} = b_{out} = 2.92$ m, l = 7 m, $ß_{eff} = ß_{crit} = 1.5$, $\sigma_{app} = 1.7 \div 3$ mho/m.

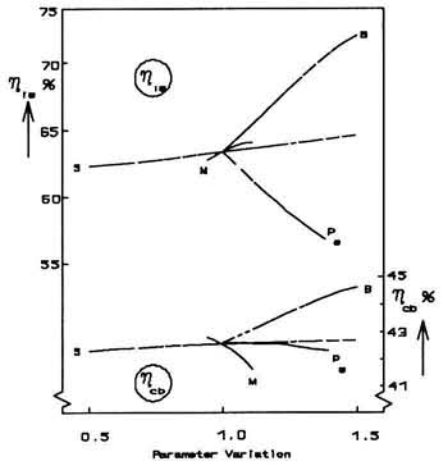

Fig. 5 Effect of parametric variations on isentropic efficiency η_{is} and on the coal to bus bar efficiency η_{cb}. Open cycle disk MHD/steam system. Base case conditions for the reference point: $p_{s,in}$ = 5 bar, M_{in} = 1.8, S_{in} = 1, and B = 5 T. Under these conditions: r = 1.3 ÷ 3.4 m, h = 0.31 ÷ 0.18 m, ß = 4.8 ÷ 8.4, σ = 3.4 ÷ 3.2 mho/m.

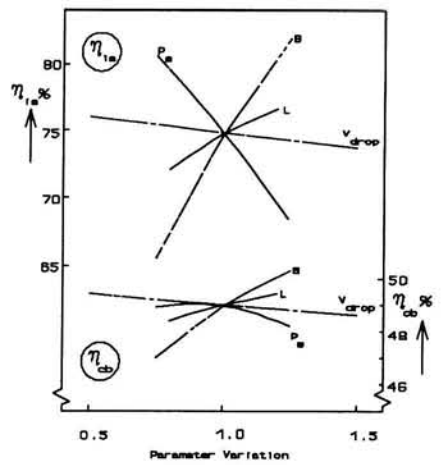

Fig. 6 Effect of parametric variations on isentropic efficiency η_{is} and on the coal to bus bar efficiency η_{cb}. Open cycle linear MHD/steam system. Base case conditions for the reference point: $p_{s,in}$ = 7.2 bar, M_{in} = 0.9, and B = 5 T. Under these conditions: $\eta_{in} = b_{in}$ = 0.8 m. $h_{out} = b_{out}$ = 1.96 m, l = 20 m, ß = 0.9 ÷ 5.3, σ = 7.4 ÷ 2.1 mho/m. H.A.L.M. de Graaf and W.J.M. Balemans

[1]) The work described in this paper was carried out i close cooperation with

H.A.L.M. de Graaf and
W.J.M. Balemans
Group Electrical Energy Systems
Eindhoven University of Technology

H. Knoopers and
H.H.J. ten Kate
Group Low Temperatures
Twente University of technology

De invloed van filtering op het twee-gebiedsmodel voor uitstervende isotrope turbulentie

By F.T.M. Nieuwstadt

Laboratorium voor Aero en Hydrodynamica Faculteit voor Werktuigbouwkunde en Maritieme Techniek TU Delft

1. Inleiding

Tijdens de korte periode dat ik medewerker was van de vakgroep theoretische aerodynamica, hoorde ik van professor Steketee de volgende anekdote. Na zijn studie ging hij naar Toronto om te gaan werken als medewerker van de plaatselijke universiteit. Direct bij zijn aankomst werd hij geconfronteerd met de mededeling: jij komt toch bij Burgers vandaan, nu dan kun jij wel de colleges homogene turbulentie geven.

Dit lijkt me een uitstekende achtergrond waartegen ik in dit boek ter gelegenheid van het emeritaat van professor Steketee een klassiek probleem uit de homogene turbulentie wil behandelen: het uitsterven van isotrope, homogene turbulentie. Een van de hoogtepunten uit de klassieke statistische turbulentie.

Dit op het eerste gezicht eenvoudige probleem is nog steeds niet volledig opgelost. Experimenten geven tegenstrijdige resultaten, die voor een gedeelte te wijten zijn aan het feit dat het verwezenlijken van volledige homogene, isotrope turbulentie in het laboratorium een vrijwel onbegonnen zaak is. Ook de theorie heeft geen uitweg geboden omdat de vergelijkingen tengevolge van het sluitingsprobleem niet rechtstreeks oplosbaar zijn.

Moderne ontwikkelingen op het gebied van computers hebben echter een nieuwe weg geopend: simulatie van turbulentie. In het kort bestaat deze techniek uit het numeriek oplossen van de Navier-Stokes vergelijkingen. Het voordeel is dat op deze manier de condities van homogene turbulentie beter nagebootst kunnen worden dan in het laboratorium. Numerieke simulatie lijkt daarmee een aantrekkelijk stuk gereedschap om homogene turbulentie en in ons geval het uitsterven van isotrope turbulentie te bestuderen. Met de resultaten kunnen dan nieuwe theoretische modellen worden getoetst.

In dit artikel zullen we ons richten op een speciale vorm van numerieke simulatie: de

zogenaamde 'large-eddy' simulatie, waarbij alleen de grote schalen van de turbulentie berekend worden. We zullen ons hier niet zozeer bezighouden met de eigenlijke numerieke simulatie en de resultaten daarvan. Daarentegen zullen we ons de vraag stellen: hoe moeten we de resultaten van een dergelijke simulatie interpreteren? Hiertoe zullen we gebruik maken van een spectraal model voor het uitsterven van isotrope turbulentie: het zogenaamde twee-gebiedsmodel. In dit artikel zullen we analyseren onder welke voorwaarden dit model met de resultaten van een 'large-eddy' simulatie vergeleken kan worden.

Als inleiding zullen we eerst een korte beschrijving geven van de belangrijkste kenmerken van uitstervende isotrope turbulentie. Vervolgens zullen we het twee-gebiedsmodel bespreken. Daarna komen de belangrijkste eigenschappen van 'large-eddy' simulatie aan de orde. We zullen het artikel afsluiten met een gedetailleerde behandeling van de modificatie van het twee-gebiedsmodel, die in het kader van een vergelijking met het 'large-eddy' simulatie nodig is.

Voordat we hieraan beginnen is het misschien terecht om ons af te vragen of een dergelijke studie relevant is. Uitstervende isotrope turbulentie is tenslotte een geïdealiseerd proces dat nauwelijks een praktische toepassing kent. Echter, de meeste turbulentie modellen die wel in de praktijk worden toegepast, maken gebruik van de resultaten voor uitstervende isotrope turbulentie om één van de empirische constanten, die in deze modellen voorkomen, vast te leggen. Om die reden is de studie van dit onderwerp meer dan alleen een oefening in homogene turbulentie.

2. Isotrope turbulentie

Isotrope turbulentie wordt gedefiniëerd als een turbulent snelheidsveld dat homogeen en bovendien invariant is voor rotaties en reflecties. Dit betekent dat alle ruimtelijke gradiënten van statistische grootheden zoals gemiddelden en varianties gelijk aan nul zijn. Tevens beperken we ons tot het geval waarin ook het gemiddelde snelheidsveld gelijk aan nul is. De vergelijking voor de turbulente kinetische energie e kan in dit geval gereduceerd worden tot de eenvoudige vorm

$$\frac{de}{dt} = -\varepsilon \tag{1}$$

waarin de ε de visceuze dissipatie voorstelt waardoor turbulentie kinetische energie omgezet wordt in warmte. De ε is altijd > 0 en noodzakelijkerwijze neemt de energie af als functie van de tijd. Deze op het eerste gezicht betrekkelijk eenvoudige vergelijking is niet exact oplosbaar omdat het verband tussen e en ε niet zonder meer voor te schrijven is.
Laten we eerst een kort overzicht geven van de experimentele resultaten. Deze zijn grotendeels gebaseerd op windtunnel-experimenten waarbij isotrope turbulentie

wordt benaderd door turbulentie geproduceerd door een rooster. De turbulentie wordt op verschillende afstanden achter het rooster gemeten. Door toepassing van de Taylor-transformatie van bevroren turbulentie kan deze variatie als functie van de afstand worden omgezet tot een variatie als functie van de tijd.

We beperken ons tot de beginperiode van het uitsterfproces, waarin het Reynoldsgetal van voldoende grootte is. We kunnen dan uitgaan van het beeld van volledig ontwikkelde turbulentie. De kinetische energie wordt in dat geval voornamelijk bepaald door de grote schalen (macrostructuur), terwijl de visceuze dissipatie plaatsvindt op de kleinste schalen (microstructuur). De energie-overdracht tussen deze twee schalingsgebieden vindt plaats in een tussengebied, dat de 'inertial subrange' wordt genoemd. Het vinden van een juiste beschrijving van deze energie-overdracht is de oorzaak van de moeilijkheden bij de oplossing van ons probleem.

De eerste experimenten, die rond de vijftiger jaren in Engeland werden uitgevoerd, lieten het volgende gedrag voor e zien

$$e = \frac{K}{t} \tag{2}$$

waarin K een constante is die samenhangt met de beginvoorwaarde. Hierbij moeten we tevens opmerken dat bovenstaande vergelijking alleen geldig is voor voldoend grote waarde van t, wanneer de inschakelverschijnselen als het ware zijn uitgedempt.

Het gedrag van e volgens (2) kon theoretisch onderbouwd worden door een veronderstelling te maken van gelijkvormigheid. Eén en ander wordt uitgebreid behandeld in het werk van Batchelor (1953) en van Monin en Yaglom (1975). Echter, deze gelijkvormigheid moet in gelijke mate gelden voor alle turbulente schalen.

Op basis van experimenten wordt echter vrij snel duidelijk dat aan deze voorwaarde niet voldaan wordt. Er bestaat geen uniforme gelijkvormigheid over alle schalen van turbulentie, en zodra men de voorwaarde van uniforme gelijkvormigheid laat vallen volgt dat de machtwet, zoals gevonden in (2) ook andere exponenten toelaat.

Deze conclusie werd bevestigd door experimenten die in de zestiger jaren in de Verenigde Staten werden uitgevoerd. Men vond hier dat het gedrag van e beschreven kan worden volgens

$$e = \frac{K}{t^n} \tag{3}$$

waarbij de exponent n variëert tussen 1.2 ~ 1.4.

3. Het twee-gebiedsmodel

De achtergrond van de variabele exponent in de machtwet (3) kan geïllustreerd worden met behulp van een eenvoudig model: het twee-gebiedsmodel.
Uitgangspunt is het energie-spectrum $E(k)$ dat gedefiniëerd is als

$$e = \int_0^\infty E(k)dk \tag{4}$$

waarin de k de absolute waarde is van het golfgetalvector $\underset{\sim}{k}$.

Formeel is E de integraal van het snelheidsspectrum $\Phi_{ij}(\underset{\sim}{k})$ over een bolschil in de $\underset{\sim}{k}$ ruimte

$$E(k) = \iint_{|\underset{\sim}{k}|} \frac{1}{2}\Phi_{ii}(\underset{\sim}{k})\, d\sigma \tag{5}$$

waarin $d\sigma$ een oppervlakte-element is van de bol met straal k.

Het snelheidsspectrum $\Phi_{ij}(\underset{\sim}{k})$ is per definitie de Fourier-transformatie van de snelheidscorrelatie $R_{ij}(\underset{\sim}{r}) = < u_i(\underset{\sim}{x}), u_j(\underset{\sim}{x}+\underset{\sim}{r})>$. Er volgt dan

$$R_{ij}(\underset{\sim}{r}) = \iiint_{-\infty}^{\infty} \Phi_{ij}(\underset{\sim}{k}) e^{i\underset{\sim}{k}\cdot\underset{\sim}{r}}\, d\underset{\sim}{r} \tag{6}$$

Laten we nu voor het spectrum E het volgende model nemen zoals geïllustreerd in figuur 1.

$$\begin{aligned} E(k) &= Ck^m \quad k < k_l \\ E(k) &= \alpha\varepsilon^{2/3}k^{-5/3} \quad k < k_l \end{aligned} \tag{7}$$

waarbij de k_l samenhangt met de karakteristieke lengteschaal van de turbulente macrostructuur.
Het spectrum is opgedeeld in twee gebieden. Voor kleine waarden van $k < k_l$, dat wil zeggen grote golflengten ofwel de grote schalen van turbulentie, heeft het spectrum de vorm van een machtwet. De exponent m is in principe willekeurig en hangt met name af van de begincondities[1].

1 In isotrope turbulentie wordt vaak de waarde $m = 4$ genomen omdat deze correspondeert met een analytisch spectrum voor $k = 0$. Willekeurige waarden van m zijn echter niet uit te sluiten.

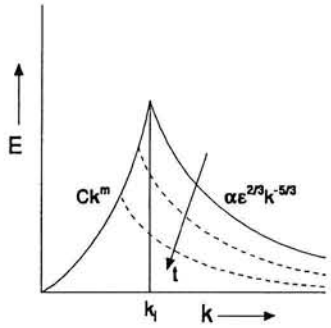

Fig. 1 Het energie spectrum volgens het twee-gebiedsmodel

Voor grote waarden van $k > k_l$ heeft het spectrum de bekende 5/3-macht voor een spectrum in de 'inertial subrange'. Deze relatie is het resultaat van de Kolmogorov schalingshypothese. Deze stelt dat in volledig ontwikkelde turbulentie de macro- en microstructuur een onafhankelijke schaling toelaat. Matching tussen beide schalingsgebieden leidt dan tot de genoemde 5/3-wet.

We stellen nu dat de vorm van het spectrum (7) behouden blijft als de turbulentie uitsterft als functie van de tijd. Hierbij wordt verondersteld dat de constante C geen functie van de tijd is. Dit wordt soms de persistentie van de grote wervels genoemd, die het laatst zullen verdwijnen. Het spectrum neemt dus af vanuit de kleine schalen (grote k). De vorm volgens de 5/3-wet blijft hierbij behouden. Dit proces is schematisch geïllustreerd in figuur 1.
Een consequentie is dat de k_l kleiner wordt als functie van de tijd. Met andere woorden de karakteristieke lengteschaal van de turbulentie ($\sim k_l^{-1}$) wordt groter. Deze conclusie wordt in het algemeen bevestigd door experimenten.
Wat is nu de consequentie van dit model voor de afname van de turbulente kinetische energie als functie van de tijd?
Uit de continuïteit van het spectrum ter plaatse k_l volgt

$$Ck_l^m = \alpha\epsilon^{2/3} k_l^{-5/3}. \tag{8}$$

Als we nu het spectrum (7) substitueren in (4) en tevens gebruik maken van de relatie (8) volgt

$$e = \frac{\alpha}{2}\frac{3m+5}{m+1}\left(\frac{\alpha}{C}\right)^{\frac{-2}{3m+5}} \varepsilon^{\frac{2m+2}{3m+5}} \tag{9}$$

oftewel we hebben naast (1) een tweede relatie gevonden tussen e en ε. We kunnen

nu de vergelijking (1) integreren met als resultaat

$$e = Kt^{-\frac{2m+2}{m+3}} \tag{10}$$

waarin K een constante is die samenhangt met de coëfficiënt voor ε in vergelijking (9) en met de beginvoorwaarde voor e. Vergelijking (10) is een vereenvoudiging van de volledige oplossing van (1) die alleen geldig is voor $t \to \infty$ omdat we het inschakelgedrag rond de begintijd $t = 0$ hebben weggelaten.

Er volgt nu dat de energie afneemt volgens een machtwet waarbij de exponent alleen afhangt van de exponent m. De vorm van het spectrum voor kleine waarden van het golfgetal bepaalt dus volledig het uitsterfproces. De verdere details van het spectrum zijn onbelangrijk.
We hebben hierboven betoogd dat deze exponent in eerste instantie samenhangt met de begincondities voor het snelheidsveld. Met andere woorden, deze beginconditie bepaalt nu hoe snel de turbulentie uitsterft. Dit is een aannemelijke verklaring voor de verschillen in de experimentele resultaten die we in de vorige sectie genoemd hebben.
Kan dit twee-gebiedsmodel, en met name de conclusie dat de beginconditie verantwoordelijk is voor het verdere uitsterfgedrag getoetst worden? Een rechtstreekse experimentele verificatie lijkt nauwelijks realiseerbaar om de volgende twee redenen. Ten eerste is de vorm van het spectrum voor kleine golfgetallen experimenteel zeer moeilijk beheersbaar. Deze vorm wordt namelijk bepaald door details en de beperkte geometrie van de experimentele opstelling. Ten tweede is de vorm van het spectrum voor $k \approx 0$ nauwelijks meetbaar.
Een andere mogelijkheid tot verificatie van het twee-gebiedsmodel is numerieke simulatie.

4. 'Large-eddy' simulatie

De rekensnelheid en geheugencapaciteit van de huidige supercomputers maken het mogelijk turbulentie te simuleren op basis van een numerieke oplossing van de volledige Navier- Stokes vergelijkingen. In sommige opzichten zijn deze berekeningen ideaal om resultaten in isotrope turbulentie te verifiëren. In numerieke experimenten kan namelijk veel gemakkelijker aan isotropie voldaan worden dan in laboratorium omstandigheden. Een bijkomend voordeel is dat in de numerieke experimenten het volledige drie-dimensionale snelheidsveld beschikbaar is, zodat alle details van de turbulentie bekend zijn.

Bij een zogenaamde directe simulatie worden alle schalen van de turbulentie expliciet opgelost. Om zowel de macro- als microstructuur te berekenen hebben we echter een groot aantal roosterpunten nodig. Dit aantal neemt zeer sterk toe als het Reynoldsgetal groter wordt. Daarom valt reeds bij betrekkelijk bescheiden waarde van

het Reynoldsgetal een directe simulatie buiten het bereik van de huidige computers. In ons twee-gebiedsmodel zijn we uitgegaan van volledig ontwikkelde turbulentie, dat wil zeggen grote Reynoldsgetallen. Om die reden is een directe simulatie dan ook niet mogelijk. We zullen ons daarom richten op een simulatie met behulp van een zogenaamd 'large-eddy' model. In dit model worden alleen de grote schalen van de turbulentie expliciet uitgerekend terwijl de kleine turbulentie schalen, die we ook wel 'subgrid' noemen, worden weggefilterd.

We hebben hierboven gezien dat ons probleem gedomineerd wordt door het spectrum bij lage waarden van k, dat wil zeggen de grote schalen van de turbulentie. Een 'large-eddy' model lijkt daarom bij uitstek geschikt om de relatie tussen het spectrum en het uitsterven van isotrope turbulentie te verifiëen.

We zullen hier niet verder ingaan op details van 'large-eddy' modellering voor wat betreft numerieke modellering. Voor een overzicht hiervan kan bijvoorbeeld worden verwezen naar het artikel van Rogallo en Moin (1984).

Daarentegen zullen we ons hier richten op een nadere analyse van het tweegebiedsmodel. De vraagstelling is: kunnen we dit model ongewijzigd toepassen bij een vergelijking met de resultaten van een 'large-eddy' simulatie? Immers in een 'large-eddy' model worden de kleine schalen weggefilterd, en we zullen zien dat de weggefilterde schalen met een eenvoudig model geparameteriseerd worden. Heeft deze filter-operatie ook consequenties voor het twee-gebiedsmodel?

5. Het twee-gebiedsmodel met een filter

In het 'large-eddy' model wordt onderscheid gemaakt tussen grote schalen ('resolved') en kleine schalen ('subgrid') op basis van een filter. We veronderstellen dat dit een scherp filter is in de Fourier-ruimte ter plaatse $k = k_f$. Er volgt dan voor de kinetische energie van de 'resolved' schalen

$$e_r = \int_0^{k_f} E(k)\, dk \tag{11}$$

terwijl de energie op de 'subgrid' schalen gegeven wordt door

$$< e_s > = \int_{k_f}^{\infty} E(k)\, dk \tag{12}$$

Hierin stellen de haken (< . . . >) een ensemble gemiddelde voor dat in het hier beschouwde geval van homogene turbulentie ook als ruimte gemiddelde geïnterpreteerd kan worden.
De vergelijkingen voor e_r en $< e_s >$ voor het geval van uitstervende isotrope

turbulentie luiden nu

$$\frac{de_r}{dt} = -< \tau_{ij} \frac{\partial \bar{u}_i}{\partial x_j} >$$

$$\frac{d< e_s >}{dt} = < \tau_{ij} \frac{\partial \bar{u}_i}{\partial x_j} > -\varepsilon . \tag{13}$$

In deze vergelijking betekent een overstreping dat een variabele gefilterd is.
De τ_{ij} in (13) is de zogenaamde subgridspanning, die als het ware het effect van de kleine 'subgrid' schalen op de grote, 'resolved' schalen voorstelt. Hiermee volgt dat de term aan de rechterzijde van de vergelijking voor e_r de energie voorstelt die de 'resolved' schalen verliezen aan de 'subgrid' energie. Het proces is hierbij de vervormingsarbeid door de subgridspanningen. We zien dat dezelfde term in de vergelijking voor $< e_s >$ voorkomt maar nu met een tegengesteld teken. Met andere woorden deze term stelt de interactie tussen de 'resolved' en de 'subgrid' energie voor. Terzijde merken we nog op dat in de vergelijking voor e_r aan de rechterkant in principe nog een term moet staan die rechtstreeks afhangt van de viscositeit. Omdat we echter uitgaan van grote waarden van het Reynoldsgetal is deze directe visceuze dissipatie van de grote schalen verwaarloosbaar.

We komen nu niet verder zonder een sluitingshypothese voor τ_{ij} te poneren. We nemen hiervoor de gebruikelijke sluiting zoals die in het kader van 'large-eddy' modellering wordt toegepast

$$\tau_{ij} = K_s \left(\frac{\partial \bar{u}_i}{\partial x_j} + \frac{\partial \bar{u}_j}{\partial x_i} \right) \tag{14}$$

waarin K_s een turbulentie viscositeit is die gedefiniëerd wordt volgens

$$K_s = c_\mu \sqrt{e_s} k_f^{-1} \tag{15}$$

Hierin is de c_μ een constante die we hier niet nader zullen specificeren. Let op: in deze vergelijking stelt e_s de lokale waarde van de 'subgrid' energie voor. Met andere woorden de K_s varieert van plaats tot plaats in het snelheidsveld.

Substitutie van (14) in de vervormingsarbeid in vergelijking (13) leidt nu tot

$$-<\tau_{ij}\frac{\partial\overline{u}_i}{\partial x_j}> = -\frac{1}{2}<K_s\,(\frac{\partial\overline{u}_i}{\partial x_j}+\frac{\partial\overline{u}_j}{\partial x_i})^2>$$

$$\approx -\frac{1}{2}<K_s><(\frac{\partial\overline{u}_i}{\partial x_j}+\frac{\partial\overline{u}_j}{\partial x_i})^2>. \tag{16}$$

Hieruit volgt inderdaad dat de vervormingsarbeid altijd negatief is. Anders gezegd, energie stroomt van de 'resolved' naar de 'subgrid' schalen. Dit lijkt fysisch gezien juist. Niettemin moeten we hier benadrukken dat het niet zonder meer duidelijk is dat dit gedrag overal in het snelheidsveld moet gelden. Bijvoorbeeld een omgekeerde richting van de energiestroom is lokaal niet uit te sluiten. Alleen gemiddeld over het gehele snelheidsveld gaat de energie van de grote naar de kleine schalen. Kortom, hoewel de sluitingshypothese (14) voor het ensemble gemiddelde het juiste resultaat oplevert, kunnen we hieruit niet zonder meer concluderen dat dit sluitingsmodel lokaal overal de juiste resultaten oplevert. Hierop zullen we later nog terugkomen.

Met behulp van de vergelijking en (4), (5) en (6) volgt nu

$$<(\frac{\partial\overline{u}_i}{\partial x_j}+\frac{\partial\overline{u}_j}{\partial x_i})^2> = 4\int_0^{k_f} k^2E(k)\,dk\,. \tag{17}$$

Daarnaast volgt op basis van vergelijking (15)

$$<K_s>\approx c_\mu\sqrt{<e_s>}\,k_f^{-1}. \tag{18}$$

Het stelsel van vergelijkingen is nu gesloten en we kunnen met behulp van het modelspectrum voor het twee-gebiedsmodel, dat we in sectie 3 geïntroduceerd hebben, de consequenties van de filter-procedure berekenen. Het probleem heeft vier onbekenden, namelijk e_r, $<e_s>$, k_l en ε. Het aantal vergelijkingen is echter gelijk aan vijf. Immers, naast de vergelijking (8) die continuïteit van het spectrum ter plaatse k_l beschrijft moeten we in dit geval voldoen aan nog vier andere vergelijkingen: (11), (12) en de beide vergelijkingen (13).

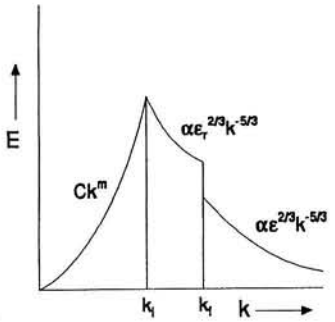

Fig. 2 Het energie spectrum volgens het twee-gebiedsmodel met filter.

Kortom ons probleem is overgedetermineerd en dus niet zonder meer oplosbaar. Wat is de oorzaak? Als hypothese stellen we dat naar alle waarschijnlijkheid de oorzaak samenhangt met onze keuze van het sluitingsmodel (14) voor de subgridspanning. Op mogelijke problemen met betrekking tot het subgrid model hebben we hierboven reeds gewezen. We verwachten dat het gekozen subgrid model niet in staat is om de vorm van het spectrum, zoals die in sectie 3 geponeerd is, tijdens het uitsterfproces te behouden.

Daarom stellen we een modificatie van het spectrum voor. Het gemodificeerde spectrum wordt geïllustreerd in figuur 2. We stellen dat tijdens het uitsterfproces het energie-spectrum een discontinuïteit ontwikkelt ter plaatse van k_f. Met andere woorden, de vorm van het energie-spectrum blijft niet behouden. Hoewel deze discontinuïteit in fysisch opzicht niet erg realistisch lijkt, is deze toch wel te verdedigen in termen van ons 'large-eddy' model. We dienen ons immers te realiseren dat in een 'large-eddy' simulatie alleen de grote schalen ($< k_f$.) expliciet opgelost worden. Voor de 'subgrid' schalen ($> k_f$.) wordt dus geen expliciet spectrum berekend. Het spectrum voor deze schalen is eigenlijk impliciet in het sluitingsmodel voor de subgridspanningen. Tenslotte merken we op dat deze vorm van het spectrum anticipeert op het resultaat dat we later zullen vinden, namelijk: de 'resolved' en de 'subgrid' energie sterven uit volgens een andere machtwet.

Door bovengenoemde modificatie van het spectrum hebben we een nieuwe onbekende geïntroduceerd: ε_r. Hiermee is ons twee-gebiedsmodel oplosbaar geworden.

De eerste stap is wederom de eis van continuïteit ter plaatse van k_l. Dit leidt tot

$$Ck_l^m = \alpha\varepsilon_r^{2/3} k_l^{-5/3}. \tag{19}$$

Met behulp van deze relatie berekenen we vervolgens de 'resolved' energie op basis van (11) als

$$e_r = \frac{C}{m+1} k_l^{m+1} + \frac{3}{2} C k_l^{\frac{3m+5}{3}} (k_f^{-2/3} - k_l^{-2/3}), \tag{19}$$

en de deformatie arbeid T als

$$T = < \tau_{ij} \frac{\partial \bar{u}_i}{\partial x_j} > \tag{20}$$

$$= 2c_\mu k_f \sqrt{< e_s >} \int_0^{k_f} k^2 E(k)\, dk \tag{21}$$

$$= 2c_\mu k_f \sqrt{< e_s >} \left(\frac{C}{m+3} k_l^{m+3} + \frac{3}{4} C k_l^{\frac{3m+5}{3}} (k_f^{4/3} - k_l^{4/3}) \right).$$

Een verdere analyse met deze uitdrukkingen leidt tot zeer gecompliceerde expressies, die verder niet bijdragen aan ons inzicht. Daarom zullen we nu enige vereenvoudigingen en veronderstellingen invoeren.
Ten eerste veronderstellen we dat $k_f \gg k_l$. Dit betekent dat we de filterlengte veel kleiner nemen dan de integraalschaal van de turbulentie. We merken op dat dit volledig consistent is met de filosofie van een 'large-eddy' model. Hiermee kan de hierbovenstaande vergelijking voor e_r gereduceerd worden tot

$$e_r = \frac{C}{2} \frac{3m+5}{m+1} k_l^{m+1} \tag{22}$$

hetgeen een verband tussen e_r en k_l vastlegt.
Vervolgens passen we dezelfde benadering ($k_f >> k_l$) toe op de uitdrukking (21) voor T, waarbij we tevens gebruik maken van (22). Er volgt dan

$$T = 4c_\mu k_f \sqrt{< e_s >} \left[\frac{C}{m+3} \left\{ \frac{2m+1}{C(m+3)} \right\}^{\frac{m+3}{m+1}} e_r^{\frac{m+3}{m+1}} + \right.$$

$$\left. \frac{3}{4} C k_f^{4/3} \left\{ \frac{2m+1}{C(m+3)} \right\}^{\frac{3m+5}{3m+3}} e_r^{\frac{3m+5}{3m+3}} \right]. \tag{23}$$

Ten tweede beperken we ons tot het geval $t \rightarrow \infty$ waarvoor we mogen verwachten dat e_r uitsterft volgens een machtwet. Er volgt dan dat de eerste term in (23) sneller tot nul nadert dan de tweede term. Daarom verwaarlozen we deze eerste term in (23).

Het resultaat van deze berekeningen en benaderingen substitueren we vervolgens in de vergelijkingen (13). Er volgt dan

$$\frac{de_r}{dt} = - A\sqrt{< e_s >}\, k_f^{4/3}\, e_r^{\frac{3m+5}{3m+3}}$$

$$\frac{d< e_s >}{dt} = A\sqrt{< e_s >}\, k_f^{4/3}\, e_r^{\frac{3m+5}{3m+3}} - (\frac{2}{3\alpha})^{3/2} < e_s >^{3/2} k_f \qquad (24)$$

Hierbij hebben we gebruik gemaakt van (12) om de ε te elimineren. In de coëficiënt A hebben we een aantal constante factoren verzameld.
In principe is het bovenstaande stelsel numeriek oplosbaar en het resultaat is e_r en $< e_s >$ als functie van de tijd. Echter, we kunnen onze benadering een stap verder voeren zodat een analytische oplossing van (24) mogelijk wordt. Hiertoe maken we de veronderstelling dat in de vergelijking voor $< e_s >$ de term $d < e_s > / dt$ verwaarloosbaar is ten opzichte van de overige termen. Anders geformuleerd, de subgrid turbulentie is quasi-stationair. Dat wil zeggen de produktie is in balans met de dissipatie. In dat geval voldoet de oplossing van (24) aan een machtwet volgens

$$e_r \sim t^{-\frac{2m+2}{m+3}}$$

$$< e_s > \sim t^{-\frac{6m+10}{3m+9}} \qquad (25)$$

Voor de 'resolved' energie e_r vinden we dus hetzelfde resultaat als we in sectie 3 hebben afgeleid voor het standaard twee-gebiedsmodel. De 'subgrid' schalen volgen een machtwet met een andere exponent met als resultaat dat de 'subgrid' energie sneller afneemt dan de 'resolved' energie. Op basis van dit resultaat voor $< e_s >$ kunnen we berekenen dat het verwaarlozen van $d < e_s > /dt$ inderdaad gerechtvaardigd is, omdat de exponent van de machtwet die deze term beschrijft kleiner is dan de exponent van de overige termen in de vergelijking voor $< e_s >$.

Laten we deze resultaten vergelijken met de simulatie-berekeningen die we hebben uitgevoerd met het 'large-eddy' model bij een resolutie van 32^3. De berekeningen zijn uitgevoerd voor een tweetal begincondities voor het snelheidsveld. Deze begincondities voldoen aan het spectrum van figuur 1 met respectievelijk $m = 2$ en $m = 4$. Voor verdere details betreffende de berekeningen wordt verwezen naar de Korte

Tabel 1: Vergelijking van de machtwet exponenten voor een berekening met het 'Large-eddy' model en met het twee-gebiedsmodel

m	$\frac{2m+2}{m+3}$	n_r	$\frac{6m+10}{3m+9}$	n_s
2	1.20	1.20	1.47	1.50
4	1.43	1.36	1.69	1.54

(1991).
We vinden dat de simulatie-berekeningen een machtwet volgen gegeven door

$$e_r \sim t^{-n_r} \qquad (26)$$

$$< e_s > \sim t^{-n_s}$$

De resultaten van deze berekeningen worden in tabel 1 vergeleken met de uitkomsten van het gemodificeerde twee-gebiedsmodel volgens (25). Gezien de vele benaderingen die we hierboven hebben gemaakt maar ook gezien het feit dat de uitkomst van de 'large-eddy' berekeningen een zekere statistische fout heeft, is de overeenkomst tussen beide resultaten uitstekend te noemen.

6. Conclusies

Om een vergelijking mogelijk te maken met simulatie-resultaten verkregen met een 'large-eddy' model hebben we de consequenties van een filter in het twee-gebiedsmodel voor uitstervende isotrope turbulentie beschouwd. De analyse leidt tot de volgende conclusies:

1. Om een gefilterd twee-gebiedsmodel te krijgen dat oplosbaar is moeten we toestaan dat het spectrum van vorm verandert tijdens het uitsterfproces. Dit duidt naar alle waarschijnlijkheid op het feit dat het gebruikte subgrid-model niet helemaal correct is.

2. Op basis van het gemodificeerde twee-gebiedsmodel vinden we, in de limiet $t \to \infty$, dat de 'subgrid' energie $< e_s >$ en de 'resolved' energie afnemen volgens een machtwet.

3. In bovengenoemde limiet voor t volgt dat de exponent in de machtwet voor e_r gelijk is aan de exponent die we gevonden hebben voor het standaard twee-gebiedsmodel. De $< e_s >$ sterft uit volgens een machtwet met een grotere exponent en $< e_s >$ daalt dus sneller dan e_r. De consequentie is dat de totale kinetische energie $e \equiv e_r + e_s$ nu niet meer voldoet aan het standaard twee-gebiedsmodel.

de vorm van het spectrum niet behouden blijft.

4. De uitkomsten van het gemodificeerde twee-gebiedsmodel zijn in goede overeenkomst met de resultaten van 'large-eddy' simulaties. Dit betekent ten eerste dat het twee-gebiedsmodel een geschikt model is om het uitsterfproces van isotrope turbulentie te beschrijven. Ten tweede wordt hiermee bevestigd dat de exponent van de machtwet van de kinetische energie afhankelijk is van de vorm van het spectrum bij $k = 0$.

Dankbetuiging

Ik ben ir. P. de Korte erkentelijk voor het gebruik van zijn resultaten en voor discussies aangaande het twee-gebiedsmodel.

Referenties

Batchelor G.K. The Theory of Homogeneous Turbulence. 1953, Cambridge University Press.

Monin A.S. and A.M. Yaglom. Statistical Fluid Mechanics II. 1975, MIT Press.

Korte P. de. Large-eddy simulation of freely decaying turbulence. An investigation on the influence of the initial conditions on the decay exponent. 1991. MEAH-Report

Rogallo R.S. and P. Moin. Numerical simulation of turbulent flow. 1984. Annual Review of Fluid Mechanics, 16, 99-137.

Hall current effects in rotating mhd flows

By L.V.K.V. Sarma

Visiting Professor TU Delft

1. Introduction

New journals sometimes with narrower specializations are coming up to accommodate increasing output of research work. Gone are the days of research marked by ingenuity of thought and sparks of landmarks. Computers have 'revolutionized' research. No more a researcher is bothered about the old ways of looking at a problem physically and mathematically and in the process dicovering new methods in the application of Mathematics or new techniques of resolving a physical problem. In the coming generations one will find a researcher depending more on a fresh generation computer. For example, the solution of a problem in Navier-Stokes equations will be exhibited on a computer in parametric space showing changes with change in the values of the parameters by the turn of a knob.

Those were the days when I was still undecided about the topic of my research work. While turning the pages of Horace Lamb's Hydrodynamics, I came across the following lines:
'The motion of a solid in a liquid endowed with vorticity is a problem of considerable interest, but is unfortunately not very tractable. The only exception is when the motion is two-dimensional, and the vorticity uniform'.
Two references one to Hill's paper in Phil.Trans (1884) 'on the motion of fluid part of which is moving rotationally and part irrotationally' and the second to Proudman's paper in Proc.Roy.Soc.A (1916) 'on the motion of solids in a liquid possessing vorticity' were given. It may be said that this inspired my work on rotating fluids.

When a symmetrical body moves steadily along the axis of an inviscid rotating liquid, the general equations of motion reduce to a single linear equation for the stream function Ψ

$$\frac{\partial^2\psi}{\partial z^2} + \frac{\partial^2\psi}{\partial r^2} - \frac{1}{r}\frac{\partial\psi}{\partial r} + K^2\psi = \frac{-K^2}{2} U r^2 \qquad (1)$$

z,r being cylindrical coordinates. $K = \frac{2\Omega}{u}$ Ω is the uniform angular velocity of the liquid about the z-axis, U is the uniform velocity of the body along the z-axis. If u, v, w are the velocity components of the fluid along r, ϕ, z directions

$$u = \frac{1}{r}\frac{\partial \psi}{\partial z}, \quad v = \frac{-K\psi}{r}, \quad w = \frac{-1}{r}\frac{\partial \psi}{\partial r} \tag{2}$$

Expressing equation (1) in spherical polar coordinates, Taylor gives the solution for (1) as

$$\psi = \frac{1}{2}UR^2 sin^2\theta + (KR)^{\frac{1}{2}}\sin\theta \sum_{n=1}^{\alpha}\left[A_n J_{n+\frac{1}{2}}(KR) + B_n J_{n-\frac{1}{2}}(KR)\right] P_n'(\cos\theta) \tag{3}$$

This solution satisfies the condition of uniform flow at infinity and uniform rotation. The condition of zero normal velocity on the body provides only one relation to determine the constants A_n and B_n. Thus the problem is indeterminate.
Taylor suggests that the other set of constants may be determined by either i) imposing the condition that the upstream waves are absent (solution (3) contains waves both upstream and downstream) or by ii) finding the force on the sphere experimentally and thereby determining the other set of constants. An ingenious idea indeed.
A preliminary report on 'Hall effects in a rotating MHD flow' the study of which was started during the visit to Luchtvaart- en Ruimtevaarttechniek and dedicated to Professor Steketee follows.

2. Hall effects in a rotating magnetohydrodynamic flow

The equations of motion w.r.t.a coordinate system rotating with a constant angular velocity Ω about the z-axis along which the unit vector is $\hat{K}$ for an electrically conducting, incompressible fluid, are

$$\rho\frac{D\vec{q}}{Dt} = -\nabla p + \mu_e \vec{j} \times \vec{H} - 2\rho\Omega\,\hat{K} \times \vec{q} - \rho\Omega^2\hat{K} \times (\hat{K} \times \vec{r}) + \mu\nabla^2\vec{q} \tag{1}$$

along with Maxwell's equations

$$\nabla \cdot \vec{q} = 0 \tag{2}$$

$$\nabla \cdot \vec{H} = 0 \tag{3}$$

$$\nabla \times \vec{H} = \vec{j} \tag{4}$$

$$\nabla \cdot \vec{E} = 0 \tag{5}$$

$$\nabla \times \vec{E} = -\mu_e \frac{\partial \vec{H}}{\partial t} \tag{6}$$

and Ohm's law (generalized)
where the two extra terms one on the left hand side and the second on the right hand side of equation (7) enter the generalized Ohm's Law due to Hall currents. The Hall parameter m = $\omega_e Y_e$ is cyclotron frequency (ω_e) times the collision time (Y_e) of electrons. p_e is electron pressure and m' is a second Hall parameter. m' = electric charge (e) times the number density (n_e) of electrons.

$$\vec{j} + \frac{m}{H_o}\vec{j} \times \vec{H} = \sigma\left(\vec{E} + \mu_e \vec{q} \times \vec{H} + \frac{1}{m^1}\nabla p_e\right) \tag{7}$$

In writing equation (7) the ionslip and thermoelectric effects are neglected and for partially ionized gases the electron pressure gradient appearing as the last term in equation (7) may also be neglected.
It may be noted that the above equations (1) to (7) form 14 equations (on omitting equation (3) for reasons well-known) for the 14 unknown $\vec{q}, \vec{j}, \vec{H}, \vec{E}$, p, p_e.
Equation (7) is taken in the form

$$\vec{j} + \frac{m}{H_o}\vec{j} \times \vec{H} = \sigma\left(\vec{E} + \mu_e \vec{q} \times \vec{H} + \frac{1}{m^1}\nabla p_e\right) \tag{8}$$

Using (8), the Induction equation becomes

$$\frac{\partial \vec{H}}{\partial t} = \eta \nabla^2 \vec{H} + (\vec{H} \cdot \nabla)\vec{q} - (\vec{q} \cdot \nabla)\vec{H} - \frac{m\eta}{H_o}(\nabla \times \vec{H}) \times \vec{H} \tag{9}$$

Equations (1) and (9) are the exact non-linear coupled equations for and $\vec{q}$ and $\vec{H}$.
In general, one effect of the Hall currents is the introduction of a cross flow leading

to an effect equivalent to that due to rotation. Because, by introducing a uniform magnetic field H_0 along the z-direction and a uniform rotation Ω about the same direction, the x-component of the equation of motion gives

$$\frac{\partial u}{\partial t} = \frac{-1}{\rho}\frac{\partial p}{\partial x} - \frac{\sigma H_o^2 \mu}{\rho} + 2\rho\left(\Omega + \frac{\sigma m H_o^2}{2\rho^2}\right)v \tag{10}$$

which shows that one effect of the Hall currents is to increase the angular velocity of rotation Ω by $\dfrac{\sigma m H_o^2}{2\rho^2}$

In order to make the above observation (which is very important because various authors in the past have sought to include Hall current in MHD rotating flows with linearized equations leading to not very significant effects) more explicit, we consider linearization of equations (1) and (9) in connection with two problems, where we make the usual assumption that the magnetic Reynolds number is small and in consequence, the induced magnetic field is negligible in comparison with the applied field.

The first problem is two-dimensional, where the fluid is bounded by an infinite rigid plate at z = 0. Both the plate and the fluid are in a state of rigid rotation with uniform angular velocity Ω about the z-axis. We consider the MHD flow induced in the fluid in the presence of a uniform magnetic field of strength H_0 normal to the plate when the plate executes harmonic oscillations in its own plane. In the absence of pressure gradient the equations of motion are

$$\frac{\partial u}{\partial t} - K^2 v = \frac{\partial^2 u}{\partial z^2} + \frac{M^2}{1+m^2}(mv - u) \tag{11}$$

$$\frac{\partial u}{\partial t} - K^2 v = \frac{\partial^2 u}{\partial z^2} + \frac{M^2}{1+m^2}(v - M)$$

where $K^2 = \dfrac{2\Omega\mu}{U^2}$, M is the Hartmann number, where $M^2 = \dfrac{\sigma\mu_e H_0^2 \mu}{\rho u^2}$ and m is the Hall parameter.

One may use Laplace Transforms to solve the above initial-value problem. Equations (11) show that the observation about the Hall current effect in a rotating MHD flow made above is correct.

The second problem is three-dimensional and the infinite disc, bounding the fluid at z = 0, performs torsional oscillations. In cylindrical polar coordinates (r, θ, z), in view of axial symmetry, the velocity components may be written as

$$u = \frac{\partial \psi}{\partial z};\ \mu = r\,v\,(z,t);\ \omega = \left(\frac{\partial \psi}{\partial r} + \frac{\psi}{r}\right).$$

With $\Psi = r\,\phi\,(z, t)$ the linearized equations take the form

$$D^2 v - 2c\frac{\partial \phi}{\partial z} = 0 \tag{12}$$

and

$$D^2\frac{\partial \phi}{\partial z^2} + 2c\frac{\partial v}{\partial z} = 0$$

with

$$D^2\frac{\partial^2}{\partial z^2} - \frac{\partial}{\partial t} - \frac{M^2}{1+m^2}, \qquad c = 1 + \frac{mM^2}{2(1+m^2)}$$

and $M^2 = \dfrac{\sigma\mu_e H_0^2}{\rho\Omega}$

Again, use of Laplace Transforms yields solution to the above problem.

Removing the assumption of negligible induced magnetic field, one may now try to solve the exact MHD equations. It appears in the context of swirling MHD flows with Hall currents, one has to necessarily take non-linearity into account to arrive at new results.

Theodorsen's ideal propeller performance with ambient pressure in the slipstream

By Gerrit Schouten

Faculty of Aerospace Engineering TU Delft of Technology

Summary

In Theodorsen's 'Theory of Propellers' [1], the static pressure in the slipstream is higher than the pressure in the ambient atmosphere. The difference amounts to the dynamic head in the slipstream. In this paper it is proposed that this overpressure be corrected for by an adaptation of the model to a fully developed homogeneous slipstream with a reduced cross-sectional area. Keeping the mass coefficient κ and the axial loss factor ε as they are defined by Theodorsen, the modification yields lower thrust and power coefficients. The expression for the optimal efficiency η, in terms of the excess velocity w in the slipstream, becomes identical to the one for the actuator disc. The propeller efficiency is smaller than that of the actuator because propeller thrust goes with a higer excess velocity w. The required power in the adapted model is equal to the product of thrust and average velocity through the propeller area, this is more realistic than in Theodorsen's model where the required power is less. The tendency of the effects of the adaptation is shown in diagrams as presented by Ribner and Foster [4], in the convenient form devised by Kramer [5].

1. Introdution and scope

Theodorsen's propeller theory [1], dating as far back as 1948 (and earlier in the NACA-REPORTS), provides a rational estimation of the highest efficiency attainable for specified operating conditions. The theory however suffers from the deficiency that it yields a static pressure in the slipstream which is too high by an amount of $O[\rho w^2/2]$. This high pressure explicitly is a consequence of Theodorsen's model, inspired by Betz's rigidly moving trailing vortex sheets providing minimum induced drag. The unrealistic notion of rigidly moving trailing vortex sheets, neglecting the rolling-up of the sheets, is very useful for the kinematical computation of the ideal propeller blade loading and the associated bound vorticity distribution. It is alloweable to neglect the rolling-up for this computation because the exact far-downstream shape of the sheets has only minor influence on the induced velocities in the propel-

ler area. As it comes to computation of the pressure in the slipstream the more realistic model incorporating the rolling-up of the sheets, as suggested in [2] in 1982, is probably more appropriate. It must be understood that the half-infinite rigid helicoidal trailing vortex sheet system is unrealistic as it is not force-free. It could only possibly survive as a bound system, capable of sustaining the edge forces. In reality the sheets start rolling up at the edges in an exponential spiral as soon as they leave the material propeller blade surface and become free trailing sheets.
As a consequence of the high pressure in the slipstream Theodorsen's theory leads to the optimistic result that the required power is less than what one would roughly expect from the product of thrust and average velocity through the propeller area. The power coefficient c_p as found by Theodorsen in [1], and reestablished recently (1990) by Ribner and Foster [4], is

$$c_p = 2\kappa\overline{w}(1+\overline{w})\,(1+\frac{\varepsilon}{\kappa}\overline{w}) \tag{1.1}$$

One would expect a power coefficient c_p^*, as estimated from the product of thrust (using Theodorsen's thrust coefficient) and average velocity at the propeller, to have minimally the magnitude

$$c_p^* = 2\kappa\overline{w}(1+\overline{w}(\frac{1}{2}+\frac{\varepsilon}{\kappa}))\,(1+\frac{\overline{w}}{2}) = c_p + \frac{\overline{w}^2}{2}(\frac{1}{2}-\frac{\varepsilon}{\kappa}) \tag{1.2}$$

The expected power coefficient c_p^* must be considered to be a minimum estimation, relating to idealised conditions with constant velocity in the propeller area, deviations from the constant average values would lead to a higher power coefficient. The difference between Theodorsen's result and the expected minimum value leads for values of λ_T above .75 to an underestimation by Theodorsen because then ε/κ becomes smaller than .5.
The remedy we propose for both the deficiencies, the high pressure in the slipstream and the low required power, is to allow the helicoidal sheets to roll up in helical vortices wrapped around a homogeneous slipstream with excess velocity w. The rolling up of the sheets induces the vortices to move with a velocity w/2, whereas the sheets by definition moved with velocity w. The $\partial\Phi/\partial t$-term, which causes the high pressure in Theodorsen's model, is halved by the reduction of the velocity of the vortices to w/2.

It is not our aim to rephrase Theodorsen's theory here, only the effects on the expressions for the thrust coefficient c_s, the power coefficient c_p and the efficiency η will be discussed in detail. For the theory we will refer to Theodorsen's book [1] and to Ribner and Foster's paper with the provocative title 'Ideal Efficiency of Propellers: Theodorsen Revisited', [4]. The latter authors do not comment on the theory, they present a computer algorithm for the computation of the ideal blade circulation

K(r/R) and the key parameters κ and ε/κ derived therefrom. Furthermore they present the results in a much more convenient format, due to Kramer [5]. It is these results, plots of power coefficient vs advance ratio at constant efficiency, that are affected by the modification presented below. The general properties of the potential flow model, i.e. the ideal blade circulation K(r/R) and the parameters κ and ε/κ, remain as they are and we will use them as presented in figs. 2 and 3, (these are the figs. 1 and 2 of Ribner and Foster [4]).

2. Momentum and energy theorems

Applying Newton's law (the momentum balance) to a large deformable volume C around the propeller we have

$$total\,force\ \bar{F} = \frac{D}{Dt}\iiint_{C(t)} m\bar{v}dV \tag{2.1}$$

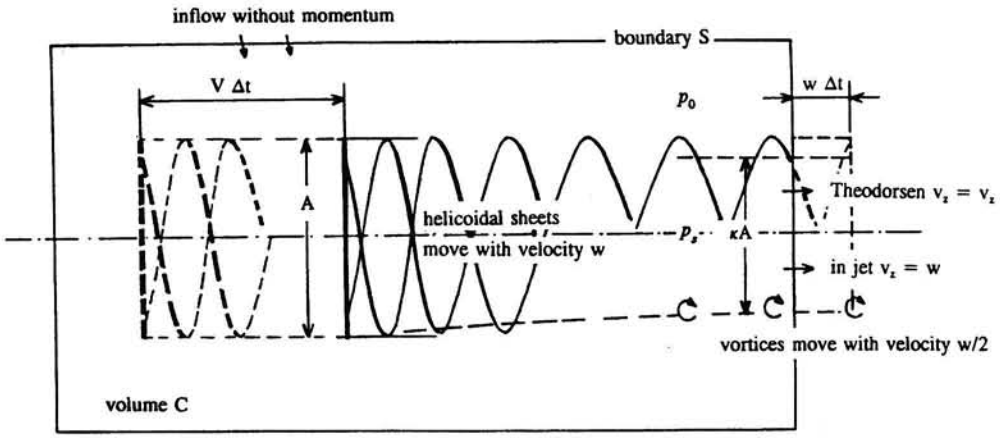

Fig. 1 The control surface C around a propeller moving with velocity V in an atmosphere at rest

Or applying (2.2), i.e. Reynolds' transport theorem (see [3]), to (2.1)

$$\frac{D}{Dt}\iiint_{C(t)} m\bar{v}dV = \iiint_{C_o} m\bar{v}dV + \iint_S m\bar{v}(\bar{v}.\bar{n})dS \tag{2.2}$$

we get the integral (2.3) for the propeller thrust T. (note that the T in (2.3) is a force on the air in positive z-direction, the thrust on the propeller is T positive in negative z-direction)

$$T + \iint (p_0 - p_s)\, dS = \rho \iint (V + v_z) v_z\, dS \tag{2.3}$$

The pressure p_s is found from the unsteady Bernoulli equation (2.4).

$$p = p_o - \rho v^2/2 - \rho \partial\phi/\partial t \tag{2.4}$$

It is the $\partial\Phi/\partial t$-term that causes the high pressure in Theodorsen's formulation. Considering the helicoidal vortex sheet system to move rigidly backwards with velocity w, (as Theodorsen does), we have $\Phi = \Phi(z\text{-}wt, r, \theta)$ and $\rho\partial\Phi/\partial t = -\rho w \partial\Phi/\partial z$. When we consider the sheets to be rolled-up the resulting vortices move with w/2 and we have $\Phi = \Phi(z\text{-}wt/2, r, \theta)$, leading to $\rho\partial\Phi/\partial t = -\rho(w/2)\partial\Phi/\partial z$.

In the following we present the formulas of Theodorsen with index T and the formulas as they result from the proposed modification next to each other. The thrust would yield

$$T = \rho \int [(V + v_z) v_z + v_z w - \frac{v^2}{2}]\, dS; \quad T = \rho \int [(V + v_z) v_z + v_z \frac{w}{2} - \frac{v^2}{2}]\, dS; \tag{2.5}$$

Note that the velocity w only enters through $\partial\Phi/\partial t$, we left v_z to keep up with Theodorsen's formulation although in the homogeneous slipstream it has the value w. The reduced cross-section of the homogeneous slipstream is also defined using v_z.

We find the power delivered by the propeller by applying the energy balance to the control volume, the general expression is

$$P = T V + \int [(p_s - p_o)\, v_z + (V + v_z) \frac{v^2}{2}]\, dS \tag{2.6}$$

leading to the different expressions for P_T and P

$$P_T = T_T V + \rho \int (v_z^2 w + V \frac{v^2}{2})\, dS \; ; \; P = TV + \rho \int (v_z^2 \frac{w}{2} + V \frac{v^2}{2})\, dS$$

$$= \rho \int (V v_z + v_z^2)(V + w)\, dS \; ; \; = \rho \int (V v_z + v_z^2)(V + \frac{w}{2})\, dS \tag{2.7}$$

The integrals involving v and v_z are evaluated in the potential flow model. Theodorsen used an electrical analogon to arrive at the value of the integrals, Ribner and Foster use a computational method. We will use the same definitions (2.8) as Theodorsen for the nondimensional parameters κ and ε, κ is the mass factor and ε is the axial loss factor.

$$\kappa \equiv \iint \frac{v_z dS}{wA} = \iint \frac{v^2 dS}{w^2 A} \; ; \; \varepsilon \equiv \iint \frac{v_z^2 dS}{w^2 A} \tag{2.8}$$

That the integral involving v^2 dS leads to the value κ has been shown by Theodorsen in [1]. The values of κ and ε/κ as a function of the advance coefficient $\lambda_T = (V+w)/\pi n D_\infty$ and the number of blades B, as computed by Ribner and Foster [4], are represented in figs. 2 and 3, copied from [4].

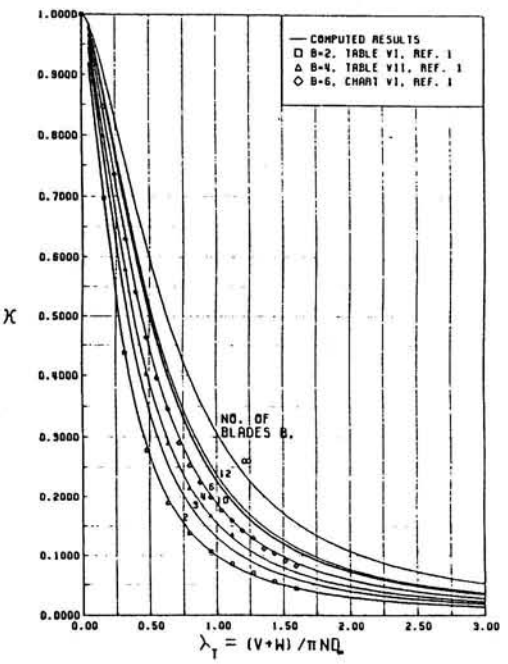

Fig. 2 Total kinetic energy loss factor κ

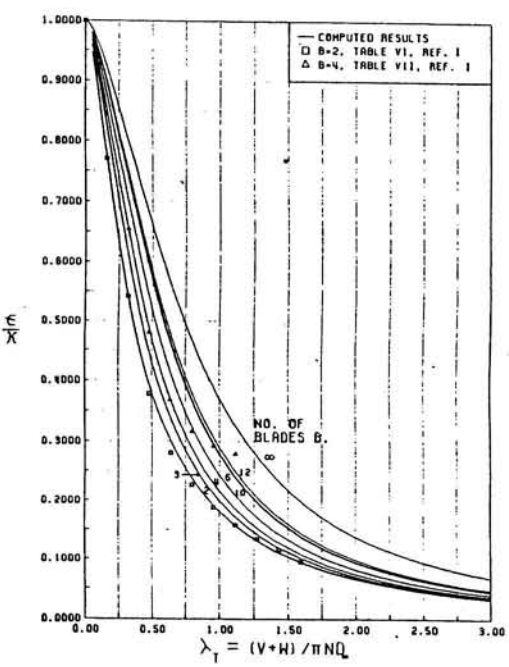

Fig. 3 Axial/total kinetic energy loss ratio ε/κ

Defining the thrust- and powercoefficients as

$$c_s = \frac{T}{\rho V^2/2\, A} \; ; \; c_p = \frac{P}{\rho V^3/2\, A} \tag{2.9}$$

we arrive at (2.10), where we introduced the notation w/V = $\overline{w}$

$$(c_s)_T = 2\kappa\overline{w}[1 + \overline{w}(\frac{1}{2} + \frac{\varepsilon}{\kappa})] \; ; \; c_s = 2\kappa\overline{w}(1 + \overline{w}(1 + \frac{\varepsilon}{\kappa}\overline{w})$$

$$(c_p)_T = 2\kappa\overline{w}(1 + \overline{w})\,(1 + \frac{\varepsilon}{\kappa}\overline{w}) \; ; \; c_p = 2\kappa\overline{w}(1 + \frac{\overline{w}}{2})\,(1 + \frac{\varepsilon}{\kappa}\overline{w}) \tag{2.10}$$

As a consequence of these expressions the efficiency η_T, and the improved efficiency η get the form

$$\eta_T = \frac{(c_s)_T}{(c_p)_T} = \frac{1 + \overline{w}(1/2 + \varepsilon/\kappa)}{(1 + \overline{w})\,(1 + \overline{w}\varepsilon/\kappa)} \; ; \; \eta = \frac{c_s}{c_p} = \frac{1}{1 + \overline{w}/2} \tag{2.11}$$

It seems unrealistic at first sight that the expression for the efficiency η in terms of w/V becomes identical to the one for the actuator surface, one must note however that the slipstream velocity w is higher for a propeller than for an actuator surface yielding the same thrust. Note that for an actuator surface $v=v_z$, so that in that case $\varepsilon = \kappa$, the value of κ then is $\kappa = (V+w/2)/(V+w)$.

3. Results

Diagrams of power coefficient at constant efficiency vs advance coefficient $\lambda = V/\pi n D_\infty$ for propellers with B=2 blades are presented by Ribner and Foster in their figs. 5 of [4]. Following Kramer [5], the same diagrams apply with shifted scale to B = 3,4,5,6,8,10,12 or ∞. The modification of the model as proposed in this paper would severely affect these diagrams. Making use of the values of κ and ε/κ, as computed by Ribner and Foster [4], figs. 2 and 3, we are able to compute the thrust and power coefficients as they would result from the proposed modified theory.
The procedure to compute the modified c_p vs λ-curves for constant efficiency η, of a propeller with B blades then is : 1) select η; 2) the value of w/V then follows from (2.11); 3) find λ_T from $\lambda_T \equiv \lambda\,(1 + w/V)$; 4) from figs. 2 and 3 then find the values of κ and ε, appropriate to w/V; 5) find c_p from (2.10).
A number of modified curves is plotted as fat lines in the graphs of Ribner and Foster as shown below in figs. 4a, 4b and 4c, (these are copies of figs. 5a, 5b and 5c of [4]).

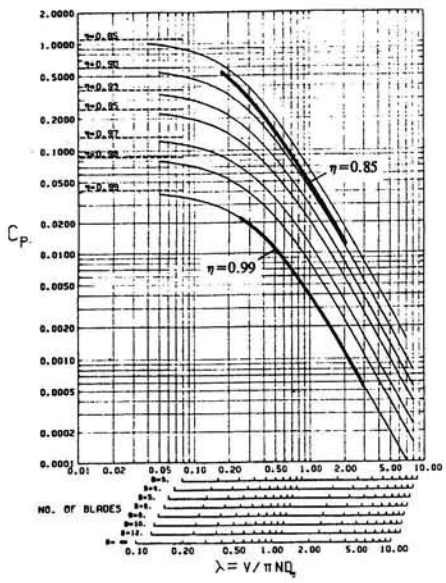

Fig. 4a Power coefficient c_p at constant efficiency η, $0.99 > \eta > 0.85$

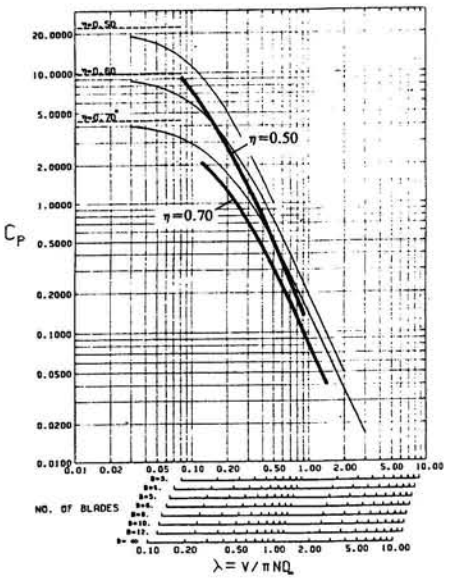

Fig. 4b Power coefficient c_p at constant efficiency η, $0.85 > \eta > 0.70$

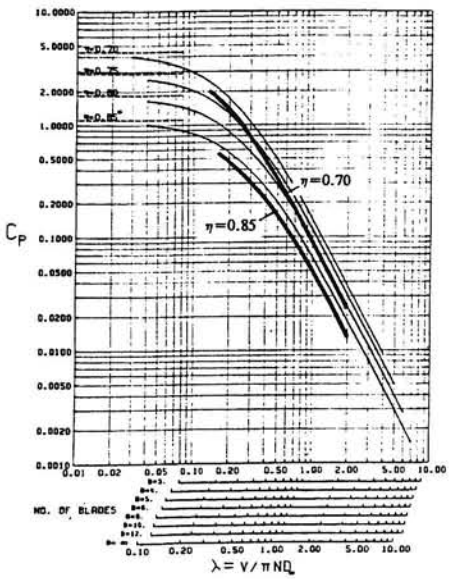

Fig. 4c Power coefficient c_p at constant efficiency η, $0.70 > \eta > 0.50$

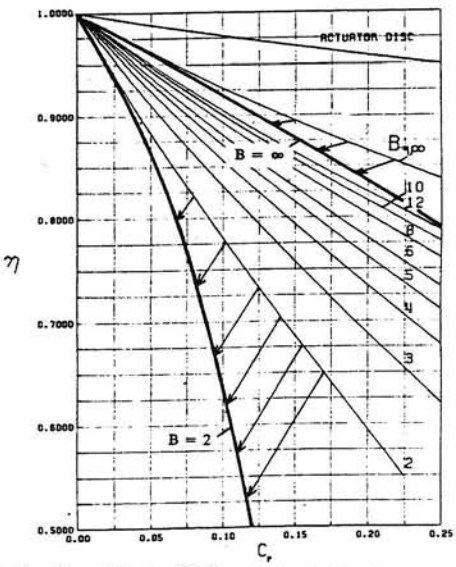

Fig. 5 Ideal efficiency η vs power coefficient c_p at constant advance coefficient $\eta = 1$; various num-

Fat lines lin figs. 4 and 5 are following the modified theory.

Diagrams of ideal efficiency η vs power coefficient c_p for various blade numbers B at constant advance coefficient $\lambda = 1$ are presented by Ribner and Foster in their fig. 6. This ideal efficiency is also reduced by the proposed modification. The procedure to compute the modified curves is: 1) select w/V; 2) find λ_T from $\lambda_T = 1 + w/V$; 3) find κ and κ/ε from figs. 2 and 3; 4) find c_p (and also $(c_p)_T$) from (2.10); 5) find η (and also η_T) from (2.11).
The modified lines for B=2 and for B=∞ are plotted as fat lines in the graph of Ribner and Foster as shown in fig. 5.

4. Conclusion

As a conclusion we state that the changes evoked by the proposed modification are substantial. The deficiencies of the rigid sheet model, i.e.

- high static pressure in the wake
- underestimated required power

are both cured, and the model is more in agreement with physical reality.
The results should therefore be incorporated in a revised Theory of Propellers.

5. References

1 Theodorsen,T., Theory of Propellers, McGraw Hill, New York, 1948.

2 Schouten,G., 'Static Pressure in the Slipstream of a Propeller', Journal of Aircraft, Vol. 19, March 1982, pp. 251-252.

3 Aris, Rutherford, Vectors, Tensors, and the Basic Equations of Fluid Mechanics, Prentice Hall inc., N.J. 1962, pp. 84-85.

4 Ribner,H.S. and Foster,S.P., 'Ideal Efficiency of Propellers: Theodorsen Revisited', Journal of Aircraft, Vol. 27, No. 9, pp. 810-819.

5 Kramer, K.N., 'The Induced Efficiency of Optimum Propellers Having a Finite Number of Blades', Luftfahrtforschung, Vol. 15, 1938, pp. 326-333, (also NACA TM 884).

Some remarks on aeroacoustics; the synthesis of aerodynamics and acoustics

By J.B.H.M. Schulten

Aeroacoustics Department National Aerospace Laboratory,
NLR, the Netherlands

Lighthill's theory for flow noise and its extension by Ffowcs Williams and Hawkings are exact descriptions of the flow and acoustic processes involved. However, practical application of these theories is hampered by the complexity of the quadrupole field, i.e. the acoustic source strength resulting from the nonlinearities in the flow. It is shown that this problem can be avoided by formulating sources on a surface enclosing the nonlinear flowfield. This approach, which avoids the laborious evaluation of the quadrupole volume sources, is to be considered as a generalization of the classical Kirchhoff-Helmholtz theorem in acoustics. Finally, it is shown how an aerodynamic lifting surface theory for arbitrarily moving bodies can be derived from an aeroacoustic formulation.

1. Introduction

Aeroacoustics is the study of sound generation by fluid flow and by the interaction of flow with solid surfaces. It is a relatively young discipline that often causes confusion among researchers in the acoustics and aerodynamics fields. For instance, the average aerodynamicist will not always be aware of the difference between a pressure fluctuation and sound. On the other hand, a traditional acoustician may have difficulty in appreciating the paramount importance of vorticity in flow processes. However, aerodynamics and acoustics are of course both branches of the very same fluid mechanics and do not contradict each other if they are properly interpreted.
Flow noise is typically radiated from a limited region of non-uniform flow into the surrounding infinite volume of air at rest. The central problem of aeroacoustics is how to relate the acoustic field, i.e. the radiated sound to the source region of non-uniform flow. The present paper discusses some of the more fundamental issues of the relation between aerodynamics and acoustics, which have not been elaborated in the author's more specific work on the aeroacoustics of fans and propellers. Reflecting much of the spirit of classical theoretical aerodynamics, they seemed to form an appropriate subject to honour Prof. J.A. Steketee on the occasion of his retirement.

2. The acoustic analogy

It may be a surprise that it was not earlier than in the 1950's that the problem of sound radiated from a region of unsteady flow was in principle solved by Lighthill [1952]. The publication of his famous article 'On Sound generated Aerodynamically' is generally considered to be the start of a new branch of fluid mechanics, nowadays known under the name of 'aeroacoustics'.
Lighthill considered a bounded region of unsteady flow embedded in a medium at rest. Solid surfaces were assumed to be absent. It is well known that any fluid flow is governed by the Navier-Stokes equations. Lighthill's approach was to rearrange the Navier-Stokes equations into the following wave equation for the pressure perturbation $\tilde{p}$:

$$\nabla^2\tilde{p} - \frac{\partial^2\tilde{p}}{\partial t^2} = -\frac{\partial^2\tilde{T}_{ij}}{\partial x_i \partial x_j} \tag{1}$$

The equation has been made dimensionless by scaling the variables on a typical length in the problem and the speed of sound and mass density at infinity. With this scaling, pressure and density perturbations become identical. The tilde symbol stands for 'in the time domain'. The right hand side of Eq.(1) acts, at least formally, as a source term that drives the acoustic field, whichs explains the term 'Acoustic Analogy' for Lighthill's modelling. The term $\tilde{T}_{ij}$ is the so-called Lighthill Stress Tensor which accounts for the *difference* between the effective stresses in the real flow and the stresses in the uniform medium at rest. It is important to note that $\tilde{T}_{ij}$ not only incorporates the generation of sound but also its convection, propagation and dissipation in the source region. Indeed Eq.(1) still contains the full complexity of the Navier-Stokes equations. For our purpose it is not necessary to write out $\tilde{T}_{ij}$ in detail here. It is sufficient to know that it is of quadratic order in the flow variables.
Acoustically, the double spatial derivative in the right hand side of Eq.(1) shows the quadrupole character of the source term. Here, a single spatial derivative would have indicated a dipole character, while the absence of a spatial derivative would have implied a monopole. In general the higher the order of the source the less acoustic energy, compared to the energy in the source region, is radiated. So a monopole is a more efficient radiator than a dipole, a dipole a more efficient one than a quadrupole, etc. The reduction of radiation efficiency with increasing order can be understood by constructing a dipole from two monopoles. Monopoles may be considered as pulsating spheres and bringing two of them of equal amplitude but in opposite phase close to each other will obviously cause a strong interference. Since this interference is destructive the radiated sound is dramatically reduced compared to the acoustic field of an isolated monopole. Similarly, quadrupoles can be considered as being composed by two dipoles in opposite phase close to each other resulting in a further reduction of radiation efficiency. Because of the high energy level in a quadrupole source region compared to the level in the surrounding acoustic field there is almost

no back-reaction from the acoustic field on the source region. As Lighthill [1952] convincingly shows, it is correct to say that the right hand side of Eq.(1) virtually drives the acoustic field and is indeed a source term in the physical sense.
The usefulness of manipulating the Navier-Stokes equations into Eq.(1) is that the fundamental solution $\widetilde{G}$ for an impulsive point source is known, not only for an infinite anechoic space, but also for a number of special configurations like an infinite, cylindrical duct. The fundamental solution, also called Green's function, satisfies

$$\nabla^2\widetilde{G} - \frac{\partial^2\widetilde{G}}{\partial t^2} = -\delta(\boldsymbol{x}-\underline{\xi})\,\delta(t-\tau) \qquad (2)$$

Thus, for a given $\widetilde{T}_{ij}$ distribution the acoustic field can formally be calculated by integration over the source region and time. However, it is not always understood that this formulation of the acoustic field is *not* a *deductive* solution of the Navier-Stokes equations, since the stress tensor $\widetilde{T}_{ij}$,i.e. the flow field, is still to be specified [Crighton,1975].
In practice it is very difficult to obtain precise data for $\widetilde{T}_{ij}$ and one usually has to rely on approximations. Lighthill applied dimensional analysis to approximate the stress tensor for turbulence in a jet. He found the quadrupole strength to vary as the fourth power of the main jet velocity U. As a result the sound power is proportional to U^8. This indicates the tremendously beneficial effect of lower jet velocities. Probably, in aeroacoustics no single theoretical result has ever had so much practical significance. Indeed, the high by-pass turbofans of today have considerable lower jet velocities and noise than the turbojets of the first generation. Admittedly, the increase of propulsive efficiency with by-pass ratio also stimulated this development. It may be noted that the U^8 result is highly approximative and should not be used to 'validate' the acoustic analogy which is an exact formulation.

As distinct from the pure flow noise in Lighthill's problem, in many practical cases it is the interaction of flow and solid surfaces that gives rise to sound. The acoustic effect of the presence of solid surfaces in a region of unsteady fluid flow was analyzed by Ffowcs Williams and Hawkings [1969]. Their approach is based on a very elegant use of generalized functions, in particular the Heaviside function H, also called the unit step function. They introduced a function $S(\boldsymbol{x},t)$ which is positive outside the body and negative inside. Then it is clear that we can make the Navier-Stokes equations formally valid throughout space by multiplying them by $H[S(\boldsymbol{x},t)]$ since outside the body the fluid medium is governed by the flow equations as before while in the body interior the equations simply become $\mathbf{0} = \mathbf{0}$. The next step is to link the Heaviside function to the flow variables by applying the chain rule of differentiation as follows :

$$\nabla [p\,\mathrm{H}(S)] = \mathrm{H}(S)\nabla p + p\,\nabla S\;\delta(S) \text{ etc.} \tag{3}$$

The interesting point here is that the differential operator automatically creates a singularity surface at the body surface, i.e. the term with $\delta(S)$. Note that $S(\boldsymbol{x},t)$ not only describes the body shape but also its motion, on which no restrictions are imposed. Carrying out the differentiations as in Eq.(3) we eventually obtain

$$[\nabla^2 - \frac{\partial^2}{\partial t^2}]\,\tilde{p}\,\mathrm{H}(S) = -\frac{\partial}{\partial t}[\tilde{Q}\,\delta(S)] + \nabla\cdot[\tilde{\boldsymbol{F}}\,\delta(S)] - \frac{\partial^2 \tilde{T}_{ij}}{\partial x_i \partial x_j} \tag{4}$$

which is called the Ffowcs Williams-Hawkings equation. In this equation two extra source terms appear in addition to Ligthill's quadrupole term. The first term, i.e. the one containing $\tilde{Q}$, has been generated in the continuity equation. It has the monopole character of a mass source distribution at the surface and can be interpreted as the displacement by the moving body of the surrounding medium. The contribution of this term to the sound is often adressed as 'thickness' noise.
The second term, which contains $\tilde{\boldsymbol{F}}$, comes from the differentiations in the momentum equation. It has the dipole character typical for a force distribution and may be associated with the stress exerted by the body surface on the adjacent fluid. Since the major component in the surface stress normally is the pressure, the contribution of this term to the sound emitted is often called 'loading noise'. The situation is depicted schematically in Fig.1 in which the shape of the source region is entirely the author's phantasy, of course. The use of the Heaviside function to obtain surface source distributions is the key in the Ffowcs Williams - Hawkings extension of Lighthill's acoustic analogy. Actually, it was Lighthill who suggested the use of generalized functions to include surface effects in the acoustic analogy [Ffowcs Williams, 1984],

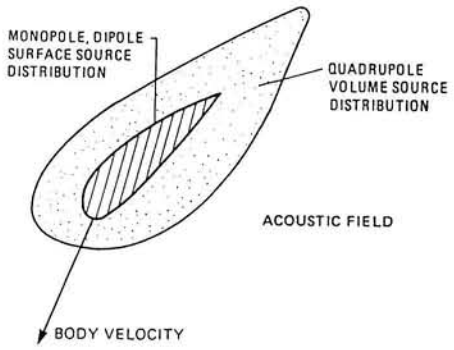

Fig. 1 Acoustic analogy for a moving body in a fluid at rest

instead of postulating singularity surfaces. It may be reitirated that also the Ffowcs Williams-Hawkings equation is not a deductive solution of the sound field; the surface conditions and the quadrupole distribution must be known before the sound field can be calculated. Its outstanding merit however is that it constitutes an exact, physically meaningful relation between the flow region and the resulting sound field.

3. The kirchoff-helmholtz alternative

In modern aeroacoustic theory it has become the standard to adopt the Ffowcs Williams-Hawkings equation as the point of departure. Whereas the acoustic analogy was clearly developed with a complex turbulent flow in mind, it is also valid for smooth, deterministic flows. Therefore, it is often used as the basis for the calculation of the noise generated by fans, propellers and helicopter rotors. Although these devices may have a turbulent boundary layer this is not an important contribution to their sound. Instead, their motion relative to a fixed observer or their interaction with an incdent field is the main source mechanism. However, there are some practical difficulties in a straightforward application of the Ffowcs Williams-Hawkings equation. Although formally exact, a direct evaluation of the quadrupole terms requires an extremely high numerical accuracy of the computed flow field because of the multiple derivatives in the quadrupole term. Apart from this, $\tilde{T}_{ij}$ itself is very complex.

Therefore, in most aeroacoustic studies the quadrupole term is simply neglected. Sometimes this is justified by making reference to Hanson and Fink [1979], who considered the relative importance of quadrupole sources for transonic propfans and helicopter rotors. However, from two-dimensional flow fields of airfoil sections they concluded that the quadrupoles in general can not be neglected. Only in the case of very thin and highly swept propfan blades at small angles of attack, the quadrupoles are less important. Hence, it is worthwhile to seek an alternative, more convenient formulation in which the influence of the quadrupole field is still correctly represented.

The first, and crucial, step to this end is to define a new surface S in such a way that it encloses all quadrupole strength adjacent to the moving body. The second step, which is more a matter of convenience, is to consider the problem in a translating frame of reference such that we have a uniform flow at infinity. This is the classic situation in aerodynamics which of course finds its origin in an aircraft in uniform, rectilinear motion. Now outside $S = 0$ the flow is governed by the linearized Euler equations for inviscid compressible flow (Fig.2). Proceeding as before we can make them formally valid throughout space by multiplying by H(S) to obtain

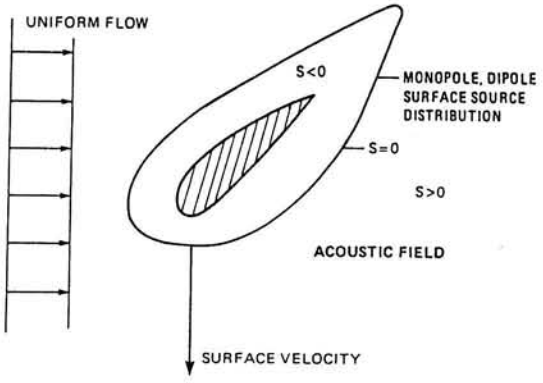

Fig. 2 Generalized Kirchhoff-Helmholtz description of the acoustic field of a body moving in a uniform flow

$$\mathrm{H}(S)\left[\frac{\mathrm{D}\tilde{p}}{\mathrm{D}t}+\nabla\cdot\tilde{\boldsymbol{v}}\right]=0 \tag{5}$$

and

$$\mathrm{H}(S)\left[\frac{\mathrm{D}\tilde{\boldsymbol{v}}}{\mathrm{D}t}+\nabla\tilde{p}\right]=\mathbf{0}. \tag{6}$$

Here the material derivative $\mathrm{D}/\mathrm{D}t = (\partial/\partial t) + M(\partial/\partial x)$ as we have chosen, without any loss of generality, the x-axis parallel to the main flow direction. Rearrangement of Eqs. (5) and (6) yields the following equations for the pressure and velocity outside $S = 0$:

$$\frac{\mathrm{D}}{\mathrm{D}t}[\tilde{p}\,\mathrm{H}(S)]+\nabla\cdot[\tilde{\boldsymbol{v}}\,\mathrm{H}(S)]=\tilde{Q}\,\delta(S) \tag{7}$$

and

$$\frac{\mathrm{D}}{\mathrm{D}t}[\tilde{\boldsymbol{v}}\,\mathrm{H}(S)]+\nabla[\tilde{p}\,\mathrm{H}(S)]=\tilde{\boldsymbol{F}}\,\delta(S), \tag{8}$$

where

$$\widetilde{Q} = \widetilde{p}\,\frac{DS}{Dt} + \left\langle \widetilde{\boldsymbol{v}} \cdot \nabla S \right\rangle \tag{9}$$

and

$$\widetilde{\boldsymbol{F}} = \widetilde{\boldsymbol{v}}\,\frac{DS}{Dt} + \widetilde{p}\,\nabla S \tag{10}$$

Elimination of $\widetilde{\boldsymbol{v}}$ H(S) from Eqs.(7) and (8) yields

$$\left[\nabla^2 - \frac{D^2}{Dt^2}\right]\widetilde{p}\,\mathrm{H}(S) = \nabla \cdot \left[\widetilde{\boldsymbol{F}}\,\delta(S)\right] - \frac{D}{Dt}\left[\widetilde{Q}\,\delta(S)\right] \tag{11}$$

which is a convected-wave equation for the (sound) pressure field outside $S = 0$. The interesting point is that the quadrupole term does not appear as a source term in Eq.(11). Only a surface source distribution is present in the right hand side. Moreover, the surface source terms written out in Eqs.(9) and (10) contain just the flow perturbation variables $\widetilde{p}$ and $\widetilde{\boldsymbol{v}}$ and not derivatives of them. So whereas the acoustic analogy requires knowledge of the flow variables throughout the volume of quadrupoles, the present formulation only requires data on the interface between the nonlinear and the linear region.

Anticipating the existence of a Green's function satisfying the convected-wave equation we can formally solve Eq.(11) to obtain [Schulten, 1987,1988]

$$\widetilde{p}\,\mathrm{H}(S) = \int_{\tau=-\infty}^{\infty} \iint_{S=0} \frac{\left\langle \nabla_0 \widetilde{G} \cdot \widetilde{\mathbf{F}} \right\rangle - \dfrac{D\widetilde{G}}{D\tau}\widetilde{Q}}{\left|\nabla_0 S\right|}\, d\underline{\xi}\, d\tau. \tag{12}$$

where τ is the source time, $\underline{\xi}$ the source coordinates and ∇_0 the gradient operator with respect to the source coordinates.

This equation is the generalization of the classical Kirchhoff-Helmholtz theorem, e.g. Pierce [1981], for the acoustic pressure of a source region in a uniform mean flow. Note that Eq.(12) has been derived without the assumption of a velocity potential. The merits of the Kirchhoff-Helmholtz formulation have also been recognized by Lyrintzis and George [1987,1989], Isom et al.[1987] and Ardavan [1991]. Likewise, the advantage of converting the volume quadrupole integrals into surface integrals is mentioned by Farassat[1987].

To compute the interaction of the sound field with another body, we need the induced velocity rather than the pressure since the boundary condition at the foreign body surface is with respect to the normal velocity. A similar elimination process as used

for the pressure again leads to a convected-wave equation; however, now with an additional, linear volume source term $[\nabla \times (\nabla \times \tilde{\boldsymbol{v}})]\mathrm{H}(S)$ next to a surface source distribution at $S = 0$. This volume source explicitly shows the coupling of vorticity and the vorticity-driven velocity field. Although much more simple than the quadrupole source distribution it still is inconvenient as the vorticity may be trailing behind the body over a very long distance.
Therefore we will follow a different approach in which the effect of the linear vorticity term is included analytically and in which it is sufficient to integrate over the surface $S = 0$ just as for the pressure.
First we define the Fourier-transformed variables as

$$\begin{bmatrix} \hat{p} \\ \hat{\boldsymbol{v}} \\ \hat{\boldsymbol{F}} \end{bmatrix} = \int_{-\infty}^{\infty}\int \exp\left[-\mathrm{i}\,(\omega t + \alpha x)\right] \begin{bmatrix} \tilde{p}\,\mathrm{H}(S) \\ \tilde{\boldsymbol{v}}\,\mathrm{H}(S) \\ \tilde{\boldsymbol{F}}\,\delta(S) \end{bmatrix} \mathrm{d}x\,\mathrm{d}t\,. \tag{13}$$

Now consider the momentum equation Eq.(8) and take Fourier transforms in time and axial direction. Then the velocity in (α,ω) space is given by

$$\hat{\boldsymbol{v}} = \frac{1}{\mathrm{i}\,(\omega + M\alpha)} \left[\hat{\boldsymbol{F}} - (\mathrm{i}\alpha \boldsymbol{i}_x + \boldsymbol{i}_y \frac{\partial}{\partial y} + \boldsymbol{i}_z \frac{\partial}{\partial z}) \ \hat{p} \right] \tag{14}$$

In Eq.(14) the velocity is exclusively in the flow quantities at the (S=0) surface; for $\hat{\boldsymbol{F}}$ this is immediately clear through the occurrence of $\delta(S)$ in its definition in Eq.(13), whereas for $\hat{p}$ this becomes evident when we consider Eq.(12). Upon evaluation of $\hat{\boldsymbol{F}}$ and $\hat{p}$ the velocity field in physical space is found by applying the appropriate inverse transform. Thus

$$\tilde{\boldsymbol{v}}\,\mathrm{H}(S) = \frac{1}{(2\pi)^2} \int_{-\infty}^{\infty}\int \exp\left[\mathrm{i}\,(\omega t + \alpha x)\right] \hat{\boldsymbol{v}}\,\mathrm{d}\alpha\,\mathrm{d}\omega\,. \tag{15}$$

Equation (15) is to be considered as the generalized Kirchhoff-Helmholtz theorem for the velocity. In general an irrotational *acoustic* velocity field as well as a divergence-free, i.e. incompressible, *vortical* velocity field is 'generated' at the surface $S = 0$.
The Green's function $\tilde{G}$, or fundamental solution, has deliberately been left unspecified. Many papers on the present subject directly adopt the Green's function for unbounded space and present their formulation of the acoustic analogy with this Green's function already substituted. Although historically understandable, this may give the wrong impression that the acoustic analogy, or the Kirchhoff-Helmholtz theorem, is limited to unbounded space. This is certainly not the case and there are several other configurations for which Green's functions have been constructed.

Among these is the fundamental solution inside a cylindrical duct, which has particular relevance for the analysis of sound generation by ducted fans [Schulten, 1982, 1983]. When dealing with propellers it is possible to include the presence of the hub in the Green's function. For these cases the ideas of the acoustic analogy and the generalized Kirchhoff-Helmholtz theorem apply equally well.

4. The route to a deductive aeroacoustic theory

As pointed out in the above sections neither the acoustic analogy nor the Kirchhoff-Helmholtz theorem are deductive theoretical models since they require knowledge of the flow variables, respectively in a limited region (the source region) or over a surface, to establish the outer field. In case this information happens to be known, for instance by detailed measurements or numerical computation, the acoustic field can be calculated straightforwardly.

However in most cases such information will not be available and one has to rely on approximate methods. The aforementioned aeroacoustic formulations offer an elegant starting point to derive such an approximate method.

To this end we will consider the problem in the light of asymptotic expansions (perturbation theory). This is a much more secure and systematic way to derive approximations than the poor practice of just dropping terms in the complete equations. A most readable text on the application of perturbation methods in fluid mechanics is Van Dyke's [1975] book. First we will restrict ourselves to high Reynolds number flows where the small parameter is $Re^{-\alpha}$, with $\alpha > 0$ [1]. Then, outside the viscous boundary layers and wakes, the flow is to leading order (in $Re^{-\alpha}$) governed by the Euler equations for inviscid flow. Secondly, it pays to be practical and to concentrate on streamlined bodies, such as propeller or fan blades. In the sequel we will talk for convenience about 'blades', but wings and helicopter rotors are tacitly included as well. In design conditions flow and blades are well aligned and consequently the flow perturbations by the blades are relatively small,i.e. $O(\varepsilon)$, where ε is the 'thickness ratio' of the blade. Here, 'thickness' should be understood in a general sense to include incidence as well. Under these circumstances the flow is to leading order (in ε) governed by the linearized Euler equations, i.e. linearized about a uniform main flow. The resulting problem is called the lifting surface approximation. Note that this does not imply an infinitely thin blade but rather an $O(\varepsilon)$ thickness of the blade. A particular useful feature of the perturbation approach is that we are able to say something about the accuracy of the solution. In the present case the absolute error of the solution will be of the order of Max (ε^2, $Re^{-\alpha}$). For Reynolds numbers and blade geometries in the range of practical interest this will turn out to be ε^2, and so the *relative* error will be $O(\varepsilon)$, which is much better than often presumed.

Now returning to the acoustic analogy we remember that the quadrupoles are of

[1]) Since the expansion for high Reynolds number is a *singular* perturbation, e.g. [Van Dyke, 1975], the value of α is to result from the asymptotic matching process. This does not affect the present discussion.

quadratic order in the flow perturbation variables, i.e. $O(\varepsilon^2)$, and so they can be neglected in a lifting surface approximation. Likewise, the $S = 0$ surface in the Kirch hoff-Helmholtz formulation 'shrinks' to the actual blade surfaces. In other words, the two methods become identical in the lifting surface approximation.
Following Crighton [1975] we will eliminate DS/Dt in the source terms $\tilde{Q}$ and $\tilde{F}$ defined by Eqs.(9) and (10). To this end a point $\boldsymbol{x}(t)$ at the moving surface $S=0$ is considered for which for all t, $S(\boldsymbol{x}(t),t) = 0$ and so

$$\frac{\mathrm{d}}{\mathrm{d}t} S\left[\boldsymbol{x}(t), t\right] = \left[\frac{\partial S}{\partial t} + \left\langle \frac{\mathrm{d}\boldsymbol{x}(t)}{\mathrm{d}t} \cdot \nabla S \right\rangle\right]_{S=0} = 0. \tag{16}$$

Now the surface velocity is by definition

$$\hat{\boldsymbol{v}}_{\text{blade}} = \frac{\mathrm{d}\boldsymbol{x}(t)}{\mathrm{d}t} \tag{17}$$

At the blade surface we have to satisfy the boundary condition (Fig.3)

$$\left\langle \nabla S \cdot \hat{\boldsymbol{v}}_{\text{blade}} \right\rangle = \left\langle \nabla S \cdot \left(\mathrm{M} i_x + \hat{\boldsymbol{w}} + \hat{\boldsymbol{v}} \right) \right\rangle \tag{18}$$

where $\tilde{\boldsymbol{w}}$ denotes an optional incident velocity not generated by the blade row but also of $O(\varepsilon)$. This velocity field can be used to calculate the interaction with another blade row.
Now substitution of Eq.(17) into Eq.(16) followed by substitution of the boundary condition Eq.(18) yields

$$\frac{\partial S}{\partial t} = -\left\langle \hat{\boldsymbol{v}}_{\text{blade}} \cdot \nabla S \right\rangle = -\left\langle \nabla \mathrm{S} \cdot \left(\mathrm{M} i_x + \hat{\boldsymbol{w}} + \hat{\boldsymbol{v}} \right) \right\rangle, \tag{19}$$

which implies

$$\frac{\mathrm{D}S}{\mathrm{D}t} = \frac{\partial S}{\partial t} + M \frac{\partial S}{\partial x} = -\left\langle \nabla \mathrm{S} \cdot \left(\mathrm{M} i_x + \hat{\boldsymbol{w}} + \hat{\boldsymbol{v}} \right) \right\rangle \tag{20}$$

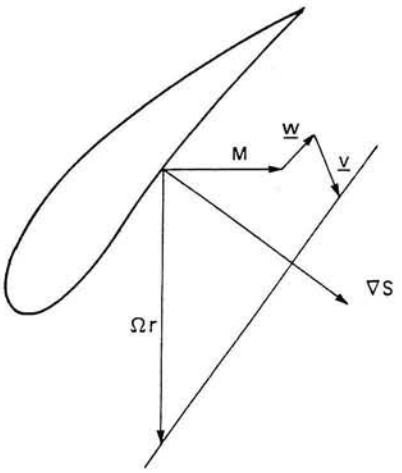

Fig. 3 Boundary condition at a rotor blade surface

Since $\tilde{w}$ and $\tilde{v}$ are $O(\varepsilon)$, Eq.(20) shows that $[DS/Dt]_{S=0}$ is also $O(\varepsilon)$. Therefore the source terms Eqs.(9) and (10) in the lifting surface approximation become

$$\tilde{Q} = \langle \tilde{v} \cdot \nabla S \rangle + O(\epsilon^2) \tag{21}$$

and

$$\tilde{F} = \tilde{p} \nabla S + O(\epsilon^2) . \tag{22}$$

Substitution of the boundary condition Eq.(18) into Eq.(21) and dropping of the higher order terms yields

$$\tilde{Q} = \left\langle \nabla S \cdot (\tilde{v}_{\text{blade}} - \mathrm{M} i_x - \tilde{w}) \right\rangle , \tag{23}$$

which shows that $\tilde{Q}$ is completely expressed in known quantities. Since $\tilde{F}$ contains the still unknown surface pressure we will distinguish between the fields of $\tilde{Q}$ and $\tilde{F}$. From Eq.(12) it is obvious what $\tilde{p}_Q \mathrm{H}(S)$ and $\tilde{p}_F \mathrm{H}(S)$ are.
The assumption of small perturbations implies that the blade can be described by

$$S(x,t) = S_0(x,t) + \varepsilon S_1(x,t) , \tag{24}$$

where $S_0(\boldsymbol{x},t) = 0$ is parallel to the undisturbed, relative flow,i.e.

$$\left\langle \nabla S_0 \cdot (\hat{\boldsymbol{v}}_{\text{blade}} - M \boldsymbol{i}_x) \right\rangle_{S_0=0} = 0. \tag{25}$$

Careful elimination of geometrically introduced higher order terms in Eq.(12) will reveal that it is rather the pressure difference between upper and lower blade surface that is the unknown distribution. Substitution of $\hat{p}_Q$ and $\hat{p}_F$ into Eq.(14) yields

$$\hat{\boldsymbol{v}}_Q = \frac{-1}{\mathrm{i}(\omega + M\alpha)} (\mathrm{i}\alpha \boldsymbol{i}_x + \boldsymbol{i}_y \frac{\partial}{\partial y} + \boldsymbol{i}_z \frac{\partial}{\partial z}) \hat{p}_Q \tag{26}$$

and

$$\hat{\boldsymbol{v}}_F = \frac{1}{\mathrm{i}(\omega + M\alpha)} \left[\hat{\boldsymbol{F}} - (\mathrm{i}\alpha \boldsymbol{i}_x + \boldsymbol{i}_y \frac{\partial}{\partial y} + \boldsymbol{i}_z \frac{\partial}{\partial z}) \hat{p}_F \right]. \tag{27}$$

The inverse transforms to the x,t domain and substitution into the boundary condition Eq.(18) ultimately lead to

$$\lim_{S \downarrow 0} \left\langle \tilde{\boldsymbol{v}}_F \mathrm{H}(S) \cdot \nabla S \right\rangle = -\lim_{S \downarrow 0} \left\langle \tilde{\boldsymbol{v}}_Q \mathrm{H}(S) \cdot \nabla S \right\rangle + \tilde{Q}. \tag{28}$$

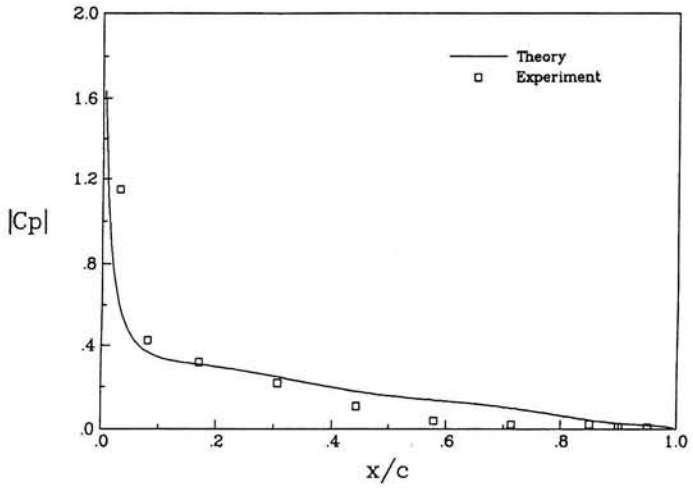

Fig. 4 Typical result of lifting surface theory: absolute value of chordwise pressure jump distribution, midspan section, 1st harmonic

Although possibly not immediately clear, Eq.(28) essentially is an integral equation for the pressure jump distribution over the blades, which is the only unknown left in the problem. Its solution for an actual configuration is still a considerable task and beyond the scope of this paper. It may be noted that Eq.(28) is a very general formulation since the motion of the blades is still arbitrary. Therefore it covers a broad range of geometries and kinematic conditions, including classical subsonic and supersonic wings.
The lifting surface approach has been successfully applied in so-called rotor-stator interaction problems in which a highly oscillatory distortion field impinges on a rotor or stator.
To conclude a typical result of this lifting surface theory will be given here. Fig. 4 shows the comparison of the computed and measured pressure jump distribution over a stator, which was exposed to an incident wake system generated by rotating rods [Schulten, 1989]. Only the first harmonic of the periodic pressure jump is shown. In view of the high disturbance level of 20 percent of the main flow velocity, the lifting surface modelling is surprisingly accurate.

5. Concluding remarks

In the past the acoustic analogy of Ligthill has been quite successfully applied to turbulent flow noise and in particular jet noise. The main reason for this success was the possibility to approximate the acoustic quadrupole source strength in terms of the global turbulence characteristics. The extension of the acoustic analogy by Ffowcs Williams and Hawkings to include solid surfaces has been equally successful in similar problems, i.e. problems where turbulence is the main source of noise. However, in cases where the motion of a body surrounded by a deterministic flow field is the main source, the quadrupole field can not simply be approximated and has to really computed. For several reasons this proves to be extremely cumbersome.
For the acoustics of the flow field about a propeller or fan blade, an attractive alternative formulation has been derived in which the sound field is expressed in flow variables on a surface that completely encloses the body and its adjacent quadrupole field. Also the outside velocity field can be expressed in terms of an integral over this surface. The formulation is to be considered as a generalization of the Kirchhoff-Helmholtz theorem in classical acoustics. If one would have to indicate an interface between aerodynamics and acoustics the Kirchhoff-Helmholtz surface would be a good choice.
Finally, it has been shown how close aeroacoustics and aerodynamics become if the flow can be linearized. In particular this is demonstrated by deriving the integral equation of the lifting surface approximation for an arbitrarily moving body from an aeroacoustic formulation. The necessity to distinguish between thickness induced velocity and loading induced velocity most naturally appears during the derivation. Whereas the aeroacoustic formulation is not a deductive theory, the incorporation of the surface boundary condition in the lifting surface approximation leads to a real solution of the problem.

6. References

Ardavan, H., 1991, 'The breakdown of the linearized theory and the role of quadrupole sources in transonic rotor acoustics', *Journal of Fluid Mechanics*, Vol.226, pp.591-624.

Crighton, D.G., 1975, ' Basic principles of aerodynamic noise generation', *Progr. Aerospace Sci.*, Vol.16, No.1, pp. 31-96.

Farrasat, F., 1987, 'Quadrupole Source in Prediction of the Noise of Rotating Blades - A New Source Description', AIAA Paper 87-2675.

Ffowcs Williams, J.E. and Hawkings, D.L., 1969, ' Sound generation by turbulence and surfaces in arbitrary motion', *Philosophical Transactions of the Royal Society of London*, Series A, Vol.264, pp. 321-341.

Ffowcs Williams, J.E., 1984, private communication.

Hanson, D.B. and Fink, M.R., 1979, ' The importance of quadrupole sources in prediction of transonic tip speed propeller noise', *Journal of Sound and Vibration*, Vol.62(1), pp.19-38.

Isom, M., Purcell,T.W., and Strawn, R.C., 1987, 'Geometrical Acoustics and Transonic Helicopter Sound ', AIAA Paper 87-2748.

Lighthill, M.J., 1952, ' On sound generated aerodynamically. I. General theory ', *Proceedings of the Royal Society of London*, Series A, Vol.221, pp. 564-587.

Lyrintzis, A.S. and George, A.R., 1987, 'Calculation of Far-Field Noise Using the Kirchhoff Method', AIAA Paper 87-2673.

Lyrintzis, A.S. and George, A.R., 1989, 'Use of the Kirchhoff Method in Acoustics', *AIAA Journal*, Vol.27, No.10, pp.1451-1453.

Pierce, A.D., 1981, *Acoustics. An Introduction to Its Physical Principles and Applications*, Series in Mechanical Engineering, McGraw-Hill, New York.

Schulten, J.B.H.M., 1982, 'Sound Generated by Rotor Wakes Interacting with a Leaned Vane Stator,' *AIAA Journal*, Vol.20, No.10, pp. 1352-1358.

Schulten, J.B.H.M., 1984, ' Vane Stagger Angle and Camber Effects in Fan Noise Generation, '*AIAA Journal*, Vol.22, No.8, pp. 1071-1079.

Schulten, J.B.H.M., 1987, 'A Spectral Method for the Computation of Propeller Acoustics', AIAA Paper 87-2674.

Schulten, J.B.H.M., 1988, 'Frequency-Domain Method for the Computation of Propeller Acoustics,'*AIAA Journal*, Vol.26, No.9, pp. 1027-1035.

Schulten, J.B.H.M., 1989, 'Experimental Validation of a Lifting Surface Model for Rotor Wake - Stator Interaction', AIAA Paper 89-1125.

Van Dyke, M., 1975, *Perturbation Methods in Fluid Mechanics*, The Parabolic Press, Stanford, Ca.

Asymptotic solution of the Boltzmann-Krook Equations for a reacting gas mixture flowing past a catalytic wall

By T. Kurotaki, O. Perot & L. Trilling

Department of Aeronautics and Astronautics
Massachusetts Institute of Technology

We examine the Rayleigh flow of a reacting mixture of gases near a catalytic wall in the presence of a small slip in velocity and temperature. In the thin Knudsen layer adjacent to the wall, the distribution functions of the gases satisfy a set of coupled Boltzmann Equations (1,2). The bulk equations of motion obtained by summing the conservation laws over velocity space satisfy averaged boundary conditions on the wall and the outer edge of the Knudsen layer.
A critical step in the analysis is the definition of small parameters which relate the gas free paths to the thickness of the bulk boundary layer. The description of the flow in the Knudsen layer is in fact given as the inner solution of a matched asymptotic expansion scheme (3) in which the continuum boundary layer provides the outer solution. One result of this analysis is the systematic definition of slip boundary conditions and of the bulk equations of motion in powers of the (small) Knudsen Numbers.
As a specific example, we consider the high energy Rayleigh flow of an atomic species (say Oxygen) past a cool flat plate on which most atoms recombine and are emitted as diatomic molecules. In the gas, atom-molecule collisions whose kinetic energy exceeds a threshold value cause dissociation of the molecule; recombination requires a triple collision and is an event so rare that we neglect its effects.
The analysis we present is based on the work of Kurotaki (4) and Perot (5) who generalized the expansion scheme developed by Trilling (6) to reacting mixtures. While the handling of the equations of motion is a fairly straightforward extension of the single species case, the wall boundary conditions require considerable care.

One issue which requires discussion is the selection of mean collision times τ_{rs} for the species in the mixture. Burgers (1) and Morse (2) assumed that the collision rate with a given species is proportional to the local density of that species; this is a

plausible model, for which, however, it has not been possible to prove a Boltzmann H theorem. An alternative studied by Perot assumed that on the average

$$\tau_{12} = \tau_{21} \tag{1}$$

This model does satisfy the H theorem in the absence of reactions (5) and when the gas reaction rate is small. It is the model chosen here. There seems to be little difference between the predictions of the two models when the densities n_1, n_2 are comparable.

Under these conditions, the distribution functions f_1, f_2 for the atomic and molecular species satisfy the equations

$$\frac{\partial f_1}{\partial t} + \eta_1 \frac{\partial f_1}{\partial y} = \frac{\Psi_{11} - f_1}{\tau_{11}} + \frac{\Psi_{12} - f_1}{\tau_{12}} + 2\frac{n_2 P}{n_1 + n_2}\frac{\Psi_{12}}{\tau_{12}} \tag{2}$$

$$\frac{\partial f_2}{\partial t} + \eta_2 \frac{\partial f_2}{\partial y} = \frac{\Psi_{21} - f_2}{\tau_{21}} + \frac{\Psi_{22} - f_2}{\tau_{22}} - \frac{n_1 P}{n_1 + n_2}\frac{\Psi_{21}}{\tau_{21}} \tag{3}$$

where $(\xi,\eta,\zeta)_{1,2}$ are the molecular velocities of species $(\,)_1$ and $(\,)_2$. Ψ_{rs} are reference distributions given by

$$\Psi_{sr} = \rho_s \left(\frac{m_s}{2\pi k T_{sr}}\right)^{3/2} e^{\frac{m_s}{2kT_{sr}}\left(\vec{\xi}_s - \vec{u}_{sr}\right)^2} \tag{4}$$

$\vec{u}_{sr}$ is the bulk diffusion velocity of one species into the other.
T_{sr} is a reference temperature given by

$$T_{sr} = \frac{1}{3kn_s}\iiint \left|\vec{\xi} - \vec{u}_s\right|^2 f_2 d\vec{\xi}_s = T_s - \frac{m_s \rho_r^2}{3k\rho^2}\left|\vec{u} - \vec{u}_s\right|^2 \tag{5}$$

In particular Kurotaki (4) shows that a good approximation when $P << 1$ is:

$$T_{12} = T\frac{n^2 - \frac{2}{3}n_1 n_2 P(E/kT)}{n^2 + n_1 n_2 P} \tag{6}$$

This last temperature reflects the dissociation energy (E/kT) removed from translational degrees of freedom by reacting collisions (of which the fraction is P). The distribution functions themselves are related to the bulk properties in the conventional way

$$\rho_s = \int f_s d\vec{\xi} \; ; \quad \rho = \sum_s \rho_s \; ; \quad n_s = \frac{P_s}{m_s} \tag{7a}$$

$$\rho_s \vec{v}_s = \int \vec{\xi} f_s d\vec{\xi} \; ; \quad \rho \vec{v} = \sum_s \rho_s \vec{v}_s \; ; \quad \vec{V}_s = \vec{v}_s - \vec{v} \tag{7b}$$

$$(P_s)_{ij} = \frac{1}{2}\int (\xi_s - v)_i (\xi_s - v)_j f_s d\vec{\xi} \; ; \quad P_{ij} = \sum_s (P_s)_{ij} \tag{7c}$$

$$\frac{3}{2} n_s k T_s = \frac{1}{2}\int \left(\vec{\xi}_s - \vec{v}\right)^2 f_s d\vec{\xi} \; ; \quad \frac{3}{2} nkT = \sum_s \frac{3}{2} n_s k T_s \tag{7d}$$

$$\vec{q}_s = \frac{1}{2}\int \left(\vec{\xi}_s - \vec{v}\right) |\xi_s v|^2 f_s d\vec{\xi} \; ; \quad \vec{q} = \sum_s \vec{q}_s \tag{7e}$$

The equations (2,3) state that the rate of change of the mass per unit volume of particles $(\,)_1$, $(\,)_2$ in the velocity element $(\vec{\xi}, d\vec{\xi})$ is the sum of addition rates due to collisions with both species minus depletion rates tue to collisions with both species plus $(\,)_1$ or minus $(\,)_2$ the dissociation rate due to energetic collisions.

The detailed derivation of these equations is given in Ref. (4,5). In terms of the quantities defined by (7), we can write the laws of conservation of mass, momentum and energy as follows

$$\frac{\partial \rho_1}{\partial t} + \frac{\partial (\rho_1 v_1)}{\partial y} = \dot{w} \tag{8a}$$

$$\frac{\partial \rho_2}{\partial t} + \frac{\partial (\rho_2 v_2)}{\partial y} = -\dot{w} \tag{8b}$$

$$\rho\left(\frac{\partial u}{\partial t} + v\frac{\partial u}{\partial y}\right) + \frac{\partial P_{xy}}{\partial y} = 0 \tag{8c}$$

$$\rho\left(\frac{\partial v}{\partial t} + v\frac{\partial v}{\partial y}\right) + \frac{\partial P_{yy}}{\partial y} = 0 \tag{8d}$$

$$\frac{3}{2}nk\left(\frac{\partial P}{\partial t} + v\frac{\partial T}{\partial y}\right) + \frac{\partial q_y}{\partial y} + P_{xy}\frac{\partial u}{\partial y} + P_{yy}\frac{\partial v}{\partial y} + \frac{\dot{w}}{m_2}\left(E + \frac{3}{2}kT\right) = \frac{3}{2}kT\frac{\partial}{\partial y}\left(\sum n_s V_s\right) \tag{8e}$$

$$\dot{w} = \frac{\rho_2 n_1}{n_1 + n_2}\frac{P}{\tau_{12}} \tag{8f}$$

The boundary conditions at the wall must be specified for normal and tangential components of velocity and either for the wall temperature or the rate of heat transfer.

They take the following form:

No fluid crosses the wall, so that

$$\rho v\,(0) = 0 \tag{9a}$$

The net flux of species $(\,)_1$ at the wall is balanced by the rate at which $(\,)_1$ recombine on the surface to form species $(\,)_2$

$$\rho_1 v_1\,(0) = -\,kw\rho_1\,(0) = \gamma\iiint \eta_1 f_1\,(-\eta_1\tau_1, t - \tau_1)\,d\vec{\xi}_1 \tag{9b}$$

where k_w is a catalytic reaction rate and γ is the fraction (of order unity) of incoming $(\,)_1$ atoms which recombine on the surface. Note that the distribution function in (9b) is evaluated one free path from the wall where it acquired the value it still has at the wall.

A fraction of the incoming $(\,)_1$ flux $(1 - \theta_1)\,(\rho_1 v_1)_{in}$ is reflected specularly; a fraction $(\theta_1 - \gamma)$ is reflected diffusely as $(\,)_1$ and a fraction γ is reflected diffusely as $(\,)_2$; The flux $(\rho_2 u_2)_{in}$ is re-emitted in part $(1 - \theta_2)$ specularly and in part θ_2 diffusely. All incoming fluxes are evaluated one free path from the wall.

The tangential velocity boundary condition in a reference frame at rest with the wall then becomes

$$\rho u\,(0) = \rho_1 u_1 + \rho_2 u_2 = \frac{2-\theta_1}{2-\gamma}\,(\rho_1 u_1)_{in} + \rho_2(0)\,\frac{(2-\theta_1)\,u_{2_{in}}}{2+\gamma\left(\dfrac{\rho_1 v_1}{\rho_2 v_2}\right)_{in}} \tag{9c}$$

where

$$(\rho_s v_s)_{in} = \int_{-\infty}^{\infty}\int_{-\infty}^{0}\int_{-\infty}^{\infty} \eta_s f_s\,(-\eta_s\tau,\, t-\tau)\,d\vec{\xi}_s \tag{9d}$$

and similarly for a specified wall temperature T_w, the slip is given by

$$nT(0) = \frac{2-\theta_1}{2-\gamma}\,n_1(0)T_{1_{in}} + \frac{\theta_1-\gamma}{2-\gamma}\,n_1(0)T_w \tag{9e}$$

$$+\; n_2\,\frac{(2-\theta_2)T_{2_{in}} + \theta_2 T_w + \dfrac{\gamma}{2}\dfrac{(n_1v_1)_{in}}{(n_2v_2)_{in}}}{2+\dfrac{\gamma}{2}\dfrac{(n_1v_1)_{in}}{(n_2v_2)_{in}}}$$

where

$$(T_s)_{in} = \frac{1}{3kn_s}\int_{-\infty}^{\infty}\int_{-\infty}^{0}\int_{-\infty}^{\infty}\left(\xi_s^2, \eta_s^2, \zeta_s^2\right) f_s\left(-\eta_s\tau,\, t-\tau\right) d\vec{\xi}_s \tag{9f}$$

At the outer edge of the Knudsen layer, we require that the bulk velocity be $(U_\infty,0)$ and the temperature T_∞; we also require that the density n_2 vanish.

The coupled Boltzmann-Krook equations (2,3) depend on the bulk properties which satisfy the bulk conservation laws (8) and boundary conditions (9); these in turn are weighted averages of the distribution functions.

To disentangle this problem, we use a strategy originally developed by Chapman and Enskog (7) which relies on the notion that molecular properties do not change between collisions and the time rates of change of the distribution functions at the macroscopic scale are the result solely of time rates of change of the bulk properties. This implies the existence of a small parameter, intrinsic in Chapman's analysis, but

defined by the geometry of the problem here, to relate molecular motion to bulk motion.

One such parameter is the ratio of free path to boundary layer thickness $\varepsilon = \lambda/\delta$ and therefore depends on the particular problem chosen. Indeed, that parameter is proportional to the slip velocity at the wall since

$$u(0) - u(w) \sim \lambda \frac{du}{dy} \sim \lambda u/\delta \sim u(\lambda/\delta) \sim u\varepsilon \tag{10}$$

so that the choice of this small parameter is consistent with small slip at the wall.

We must also consider the relation between the collision times (τ_{11}, τ_{22}, τ_{12}) in our configuration. If the wall is highly catalytic, then near the wall, the $(\,)_1$ particles will largely move toward the wall and the $(\,)_2$ particles away from the wall. As long as (n_1, n_2) are of the same order, it follows that

$$\tau_{11}, \tau_{22} >> \tau_{12}, \tau_{21} \tag{11}$$

and the ratio τ_{12}/τ_{11} is a parameter of the problem. Now the $()_2$ particles, after one collision, will have a normal persistence velocity of (0.432) c_0 (8) and after a large number m of collisions a velocity $(0.432)^m c_0$. If the time between collisions, which depends on the $()_1$ flux, does not change much, then the molecules will travel an average distance of order

$$L_2 \equiv \lambda \sum_0 (0.432)^m \cong 1.73\lambda_{12} \tag{12}$$

so that the $()_2$ molecules remain largely confined to a sublayer whose thickness is of order λ_{12}. Since the $()_1$ particles occupy a layer of thickness δ and since at the wall the flux of $()_1$ and $()_2$ must be comparable, the densities and collision frequencies must be:

$$\frac{n_2}{n_1} \sim \frac{\tau_{12}}{\tau_{11}} \sim \delta/\lambda \tag{13}$$

Thus, the consequence of high catalycity of the wall is that the recombines species $()_2$ is confined to a relatively dense thin sublayer near the wall.

We must finally make some assessment of the dissociation probability P. That parameter depends on the ratio E/kT where E is the dissociation energy and T is the local gas temperature. That parameter is physically independent of (λ/δ) and varies with the choice of characteristic temperatures.

At this point, two choices are possible for the needed small parameter ε, depending on the nature of the physical problem, or the domain of the field we choose to focus our magnifying glass on.

If the reaction rate is high ($P \sim 0(1)$) and most heterogeneous collisions produce dissociation or if we focus our attention on a small enough scale then for the mass conservation equation (8a,b) to connect chemical and convective mass fluxes, we must choose the variable:

$$\tilde{t} = \frac{t}{\tau_{12}}; \quad \tilde{\varepsilon} = \frac{c\tau_{12}}{L} \tag{14}$$

Since chemical changes occur over times of the order of the time between collisions, a characteristic time of that order is needed to organize the flow. If the geometry of the motion eventually involves lengths of many free paths, the motion with $P = 0(1)$ describes an initial phase, or a sublayer of the Knudsen layer; spatial variations only affect higher order terms than the second in this description.

For such a flow, the conservation of mass equation yields

$$\frac{\partial n_1^{(0)}}{\partial \tilde{t}} = \frac{2n_1^{(0)} n_2^{(0)}}{n_1^{(0)} n_2^{(0)}} P; \quad \frac{\partial n_2^{(0)}}{\partial \tilde{t}} = \frac{n_1^{(0)} n_2^{(0)}}{n_1^{(0)} n_2^{(0)}} P \tag{15}$$

with the condition $n_1^{(0)} + 2n_2^{(0)} = N$ to denote the conservation of number of particles. Then with the notation $x = \frac{n_1^{(0)}}{N}$ equation (15) becomes

$$2P d\tilde{t} = \frac{(1 + x)\, dx}{x(1 - x)} \tag{16}$$

which is integrated to give

$$x = 1 + \frac{e^{-2P\tilde{t}}}{2} - \sqrt{e^{-2P\tilde{t}}\left(1 + \frac{e^{-2P\tilde{t}}}{4}\right)} \tag{17}$$

It is easily verified that $\lim_{\tilde{t} \to -\infty} x = 0$ and $\lim_{\tilde{t} \to -\infty} x = 1$ so that the process describes the increase in the number of atoms which results from their dissociating molecules irreversibly; this is what happens for example if one follows a fluid element as it leaves the surface.

The energy equation takes the form

$$\left(n_1^{(0)} + n_2^{(0)}\right)\frac{\partial E^{(0)}}{\partial t} + \frac{n_1^{(0)} n_2^{(0)}}{n_1^{(0)} + n_2^{(0)}} E^{(0)} = 0 \tag{18}$$

where $E^{(0)} = \frac{3}{2} kT^{(0)} + E_{dissoc}$

This is integrated in terms of the variable $\left(x = \frac{n_1}{N}\right)$ defined above to give

$$\frac{T^{(0)}}{T_0} = \frac{1 - x(x + 2)\bar{E}}{(1 + x)^2} \text{ with } \bar{E} = \frac{E_{dissoc}}{\frac{3}{2}kT_0} \tag{19}$$

where the reference temperature T_0 defines the gas when $x = 0$, that is, before the dissociation process begins. This is the equivalent of Eq. 6 for high reaction rate.

Returning to the distribution function itself, when the scaling (14) is applied to Equation (2) it becomes

$$\frac{\partial f_1^{(0)}}{\partial \tilde{t}} = \Psi_{12}^{(0)}\left(1 + \frac{2n_2^{(0)} P}{n_1^{(0)} + n_2^{(0)}}\right) - f_1^{(0)} \tag{20}$$

where the number densities are given by (17) and the temperatures by (19). The solution is

$$f_1^{(0)} = e^{-\tilde{t}}\left[\Psi_{12}^{(0)}(0) + \int_o^t e^{\tau}\Psi_{12}^{(0)}(\tau)\left(1 + \frac{2n_2^{(0)}P}{n_1^{(0)} + n_2^{(0)}}\right)d\tau\right] \tag{21}$$

where $\Psi_{12}^{(0)}$ is the initial zero order distribution of species $()_1$.

Over most of the sublayer, we require that bulk reaction rates be comparable to bulk fluid properties is carried out in powers of $\varepsilon = \lambda/\delta$. This yields a hierarchy of equations and boundary conditions for our problem. We introduce the variables.

$$\bar{t} = \frac{tc_\infty}{L}; \quad \bar{y} = \frac{y}{\varepsilon L}; \quad c_\infty = \sqrt{\frac{2n_\infty kT_\infty}{\rho_\infty}}$$

$$\bar{\rho} = \frac{\rho}{\rho_\infty}; \quad \bar{T} = \frac{T}{T_\infty}; \quad \bar{u} = \frac{u}{c_\infty}; \quad \vec{\bar{\xi}} = \frac{\vec{\xi}}{c_\infty} \tag{22}$$

$$\bar{f}_{s_1}\bar{\Psi}_{sr} = \frac{f_{s_1}\Psi_{sr}c_\infty^3}{\rho_\infty}; \quad \bar{P}_{yy} = \frac{P_{yy}}{\rho_\infty c_\infty^2}$$

$$\bar{v} = \frac{v}{\varepsilon c_\infty}; \quad \bar{P}_{xy} = \frac{P_{xy}}{\varepsilon\rho_\infty c_\infty^2}; \quad \bar{q}_y = \frac{q_y}{\varepsilon\rho_\infty c_\infty^3}$$

where the (normal) y coordinate and the normal fluxes (v, P_{xy}, q_y) are stretched in the usual way (3). In particular, the slip velocity near the wall is of order

$$u(0) \cong \lambda\frac{\partial u}{\partial y} \cong \frac{\lambda}{\varepsilon L}\frac{\partial u}{\partial \bar{y}} \cong \frac{\lambda}{\varepsilon\delta}\frac{\delta}{L}\frac{\partial u}{\partial \bar{y}} \tag{23}$$

so that if u(0) is to be of order ε, then $\varepsilon \sim \frac{\lambda}{\delta} \sim \frac{\delta}{L} \sim \sqrt{\frac{\lambda}{L}}$ where L is a length characteristic of streamwise direction features.

It follows by substitution of the expansions

$$\bar{f}_s = \sum_0^\infty \bar{f}_s^{(n)} \varepsilon^n \quad \overline{\Psi}_{sr} = \sum_0^\infty \overline{\Psi}_{sr}^{(n)} \varepsilon^n \tag{24}$$

into the Boltzmann Krook equations that, dropping the bars for convenience

$$f_1^{(0)} = \Psi_{12}^{(0)}$$

$$f_1^{(0)} = \Psi_{11}^{(0)} - f_1^{(0)} + \Psi_{12}^{(1)} - \eta_1 \frac{\partial f_1^{(0)}}{\partial y}$$

$$f_1^{(2)} = \Psi_{11}^{(1)} - f_1^{(1)} + \Psi_{12}^{(2)} - \eta \frac{\partial f_1^{(1)}}{\partial y} - \frac{\partial f_1^{(0)}}{\partial t} + \frac{2n_2^{(0)}}{n^{(0)}} \alpha \Psi_{12}^{(0)}$$

$$f_1^{(n)} = \Psi_{11}^{(n-1)} - f_1^{(n-1)} + \Psi_{12}^{(n)} - \eta_1 \frac{\partial f_1^{(n-1)}}{\partial y} - \frac{2f^{(n-2)}}{\partial t} \tag{25}$$

$$+ \text{(terms involving bulk properties)}$$

and similarly

$$f_2^{(0)} = \Psi_{21}^{(0)}$$

$$f_2^{(1)} = \Psi_{22}^{(0)} - f_2^{(0)} + \Psi_{21}^{(1)} - \eta_2 \frac{\partial f_2^{(0)}}{\partial y}$$

$$f_2^{(2)} = \Psi_{22}^{(1)} - f_2^{(1)} + \Psi_{21}^{(2)} - \eta_2 \frac{\partial f_2^{(1)}}{\partial y} - \frac{\partial f_2^{(0)}}{\partial t} - \frac{n_1^{(0)}}{n^{(0)}} \alpha \Psi_{21}^{(0)}$$

$$f_2^{(n)} = \Psi_{22}^{(n-1)} - f_2^{(n-1)} + \Psi_{21}^{(n)} - \eta_2 \frac{\partial f_2^{(n-1)}}{\partial y} - \frac{2f_2^{(n-2)}}{\partial t} + \qquad (26)$$

(terms involving bulk properties)

with the notation $\alpha = \varepsilon^2 Pe^{-E/kT_{12}^{(0)}}$. In all of these expressions, the bulk properties are expanded in powers of ε and at each level of approximation (n), the *n*th estimate of the bulk properties is used; that estimate in turn is obtained by solving the *n*th set of bulk equations. In particular:

$$f_1^{(0)} = \frac{\rho_1^{(0)}}{\left[2\pi R_1 T^{(0)}\right]^{3/2}} e^{-\frac{\left(\xi_1 - u^{(0)}\right)^2 + \eta_1^2 + \xi_1^2}{2R_1 T}}; \quad R_1 = \frac{\rho_\infty}{2n_\infty m_1}$$

$$f_2^{(0)} = \frac{\rho_2^{(0)}}{\left[2\pi R_2 T^{(0)}\right]^{3/2}} e^{-\frac{\left(\xi_2 - u^{(0)}\right)^2 + \eta_2^2 + \xi_2^2}{2R_2 T}}; \quad R_2 = \frac{\rho_\infty}{2n_\infty m_2} \qquad (27)$$

It folows by symmetry from (7) that $P_{xy}^{(0)} = q_y^{(0)} = \left(\rho v\right)^{(0)} = 0$ and that $P_{yy}^{(0)} = \frac{1}{2}$ and $n^{(0)}\, T^{(0)} = 1$ so that the zero order approximation yields a mixture of ideal gases in uniform motion as one would expect for a Rayleigh problem.

Substitution into the second of equations (25,26) yields

$$f_2^{(1)} = \Psi_{s\tau}^{(1)} - \eta_s \frac{\partial f_s^{(0)}}{\partial y} = f_s^{(0)} \left\{ \frac{\rho_s^{(1)}}{\rho_s^{(0)}} + \left(W_{s_1}^2 - \frac{3}{2} \right) \frac{T^{(1)}}{T^{(0)}} + W_{s_2}^2 \right\}$$

$$- \left\{ \eta_s \left[\frac{1}{\rho^{(0)}} \frac{\partial \rho_s^{(0)}}{\partial y} + \left(W_{s_1}^2 - \frac{3}{2} \right) \frac{1}{T^{(0)}} \frac{\partial T^{(0)}}{\partial y} + \frac{\xi_s - u^{(0)}}{R_s T^{(0)}} \frac{\partial u^{(0)}}{\partial y} \right] \right\} \qquad (28a)$$

with

$$W_{s_1}^2 = \frac{\left(\xi_s - u^{(0)}\right)^2 + \eta_s^2 + \zeta_s^2}{2R_s T^{(0)}}; \quad W_{s_2}^2 = \frac{\left(\xi_s - u^{(0)}\right)u^{(1)} + \eta_s v^{(0)}}{2R_s T^{(0)}} \tag{28b}$$

so that

$$\rho_s^{(0)} v_s^{(1)} = \rho_s^{(0)} v^{(1)} - \frac{1}{2}\frac{\partial (n_s T)^{(0)}}{\partial y} \tag{29a}$$

$$P_{s_{xy}}^{(1)} = -\frac{1}{2} n_s^{(0)} T^{(0)} \frac{\partial u^{(0)}}{\partial y} \tag{29b}$$

$$q_{s_y}^{(1)} = -\frac{5}{4}\frac{\partial}{\partial y}\left[n_1^{(0)} R_s \left(T^{(0)}\right)^2\right] \tag{29c}$$

Substitution of (29) into the equations of motion gives the following first order set of approximations

$$\frac{\partial n_1}{\partial t} + \frac{\partial (n_1 v)}{\partial y} = \frac{\partial^2 (n_1 R_1 T)}{\partial y^2} + 4\frac{n_1 n_2}{n}\alpha \tag{30a}$$

$$\frac{\partial n_2}{\partial t} + \frac{\partial (n_2 v)}{\partial y} = \frac{\partial^2 (n_2 R_2 T)}{\partial y^2} - 2\frac{n_1 n_2}{n}\alpha \tag{30b}$$

$$nT = 1 \tag{30c}$$

$$\rho\left(\frac{\partial u}{\partial t} + v\frac{\partial u}{\partial y}\right) = \frac{1}{2}\frac{\partial^2 u}{\partial y^2} \tag{30d}$$

$$\frac{5}{4}\frac{\partial v}{\partial y} - \frac{1}{2}\left(\frac{\partial u}{\partial y}\right)^2 - \frac{5}{4}\frac{\partial^2}{\partial y^2}[(n_1 R_1 + n_2 R_2)T^2] + \frac{n_1 n_2}{n}\alpha E = 0 \tag{30e}$$

These are the generalized Navier Stokes equations for a mixture of ideal compressible gases of constant viscosity and heat conduction; the convection conduction and

energy diffusion terms have been combined with use of continuity to produce (30e).

The next approximation of the distribution functions obtained by Kurotaki (4) after considerable labor has been the form:

$$\frac{f_2^{(2)}}{f_2^{(0)}} = \frac{\rho_2^{(2)}}{\rho_2^{(0)}} + \left(W_{s1}^2 - \frac{3}{2}\right)\frac{T_{12}^{(2)}}{T_2^{(0)}}$$

$$+ \left[\left(\frac{1}{2}W_{s2}^4 - \frac{5}{2}W_{s1}^2 + \frac{15}{8}\right)\frac{T^{(1)}}{T^{(0)}} + \left(W_{s1}^2 - \frac{3}{2}\right)\frac{\rho_2^{(1)}}{\rho_2^{(0)}} + \left(W_{s1}^2 - \frac{5}{2}\right)W_{s2}^2\right]\frac{T^{(1)}}{T^{(0)}}$$

$$+ W_{s2}^2\frac{\rho_s^{(1)}}{\rho_s^{(0)}} + \frac{1}{2}W_{s2}^4 - W_{s3}^2$$

$$- \left[\frac{1}{\rho^{(0)}}\frac{\partial\rho_s^{(0)}}{\partial t} + \left(W_{s1}^2 - \frac{3}{2}\right)\frac{1}{T^{(0)}}\frac{\partial T^{(0)}}{\partial t} + \frac{\xi_s - u^{(0)}}{R_s T^{(0)}}\frac{\partial u^{(0)}}{\partial y}\right]$$

$$+ \eta_s\left[\left(W_{s1}^2 - \frac{5}{2}\right)\frac{1}{T^{(0)}}\frac{\partial T^{(0)}}{\partial y} + \frac{\xi_s - u^{(0)}}{R_s T^{(0)}}\frac{\partial u^{(0)}}{\partial t}\right]$$

$$- \eta_s\frac{\partial}{\partial y}\left[\frac{\rho_s^{(1)}}{\rho_s^{(0)}} + \left(W_{s1}^2 - \frac{3}{2}\right)\frac{T^{(1)}}{T^{(0)}} + W_{s2}^2\right]$$

$$+ \eta_s^2\frac{\partial}{\partial y}\left[\frac{1}{\rho^{(0)}}\frac{\partial\rho_s^{(0)}}{\partial y} + \left(W_{s1}^2 - \frac{3}{2}\right)\frac{1}{T^{(0)}}\frac{\partial T^{(0)}}{\partial y} + \frac{\xi_s - u^{(0)}}{R_s T^{(0)}}\frac{\partial u^{(0)}}{\partial y}\right]$$

$$- \eta_s\left[\frac{\rho_s^{(1)}}{\rho_s^{(0)}} + \left(W_{s1}^2 - \frac{3}{2}\right)\frac{T^{(1)}}{T^{(0)}} + W_{s2}^2\right]$$

$$\left[\frac{1}{\rho^{(0)}}\frac{\partial \rho_s^{(0)}}{\partial y}+\left(W_{s1}^2-\frac{3}{2}\right)\frac{1}{T^{(0)}}\frac{\partial T^{(0)}}{\partial y}+\frac{\xi_s-u^{(0)}}{R_s T^{(0)}}\frac{\partial u^{(0)}}{\partial y}\right]$$

$$+\eta_s^2\left[\frac{1}{\rho^{(0)}}\frac{\partial \rho_s^{(0)}}{\partial y}+\left(W_{s1}^2-\frac{3}{2}\right)\frac{1}{T^{(0)}}\frac{\partial T^{(0)}}{\partial y}+\frac{\xi_s-u^{(0)}}{R_s T^{(0)}}\frac{\partial u^{(0)}}{\partial y}\right]^2 \tag{31a}$$

$$+F_R$$

where

$$F_R = +4\frac{n^{(2)}}{n^{(0)}}\alpha \quad (\text{for } s=1)$$

$$F_R = -2\frac{n^{(1)}}{n^{(0)}}\alpha \quad (\text{for } s=2) \tag{31b}$$

and the resulting second approximation equations have the form

$$\frac{\partial n_1^{(1)}}{\partial t}+\frac{\partial (n_1 v)^{(1)}}{\partial y}=\frac{\partial^2 (n_1 R_1 T)^{(1)}}{\partial y^2}+4\frac{(n_1 n_2)^{(1)}}{n^{(0)}}\alpha \tag{32a}$$

$$\frac{\partial n_2^{(1)}}{\partial t}+\frac{\partial (n_2 v)^{(1)}}{\partial y}=\frac{\partial^2 (n_2 R_2 T)^{(1)}}{\partial y^2}-2\frac{(n_1 n_2)^{(1)}}{n^{(0)}}\alpha \tag{32b}$$

$$\rho^{(0)}\left(\frac{\partial u^{(1)}}{\partial t}+v^{(0)}\frac{\partial u^{(1)}}{\partial y}\right)-\frac{1}{2}\frac{\partial^2 u^{(1)}}{\partial y^2}=-\rho^{(0)}v^{(1)}\frac{\partial u^{(0)}}{\partial y}-\frac{1}{2}\left(1+\frac{\rho^{(1)}}{\rho^{(0)}}\right)\frac{\partial^2 u^{(0)}}{\partial y^2} \tag{32c}$$

$$\frac{n^{(1)}}{n^{(0)}}+\frac{T^{(1)}}{T^{(0)}}=0 \tag{32d}$$

$$\frac{5}{4}\frac{\partial v^{(1)}}{\partial y} - \frac{\partial u^{(0)}}{\partial y}\frac{\partial u^{(1)}}{\partial y} - \frac{5}{4}\frac{\partial^2\left(\tilde{n}T^2\right)^{(1)}}{\partial y^2}$$

$$= -\frac{1}{2}\left(\frac{\partial u^{(0)}}{\partial y}\right)^2 - \frac{5}{4}\frac{\partial}{\partial y}\left(\tilde{n}T\frac{\partial T}{\partial y}\right)^{(0)} - \frac{(n_1 n_2)^{(1)}}{n^{(0)}}\alpha E - \frac{3}{2}\frac{n_1^{(0)} n_2^{(0)}}{n^{(0)}}T^{(1)}\alpha \qquad (32e)$$

To define the boundary conditions satisfied by the flowing reacting mixture to a consistent level of approximation, we expand the boundary conditions (9) in powers of ε .

To all degrees of approximation

$$v^{(0)} = v^{(1)} = \ldots = 0 \qquad (33a)$$

The boundary condition which defines the catalytic behavior of the surface gives

$$[\rho_1 v_1(())] = -k_w \rho_1(0) = -\rho_2 v_2(0) \qquad (33b)$$

where

$$\rho_1(()) k_w = -\gamma\int_{-\infty}^{\infty}\int_{-\infty}^{0}\int_{-\infty}^{\infty}\eta_1 f_1\left(-\eta_1\varepsilon^2, t-\varepsilon^2\right)d\vec{\xi}_1 \qquad (33c)$$

and $\tau_{12} = \varepsilon^2$ was applied. Condition (31b,c) states that a fraction γ of the incoming flux of $()_1$ react on the surface to form $()_2$. Now in analyzing (33b), we note that at the wall, the velocity V_1 is of order of the speed of sound because for $\gamma = 0(1)$ very few $()_1$ molecules are re-emitted by the wall, so their distribution is close to a one-sided Maxwellian. But some $()_2$ molecules leave the wall and some approach the wall after collisions with other $()_2$ molecules or $()_1$ molecules most of which fail to reach the wall; therefore the bulk velocity of $()_2$ molecules is of order ε. It follows (33b) that $v_2 = 0(\varepsilon)$; $\rho_1 = 0(\varepsilon)$.

Substituting this result into (28a) and carrying out the integrations, we obtain

$$k_w^{(0)} = \gamma\sqrt{\frac{R_1 T^{(0)}}{2\pi}} + \frac{\gamma}{2}R_1 T^{(0)}\frac{1}{\rho_1^{(1)}(0)}\left(\frac{\partial\rho_1^{(0)}}{\partial y}\right)_0 \qquad (33d)$$

$$\rho_1^{(1)} = \frac{2-\gamma}{4\gamma}\sqrt{\frac{2\pi T^{(0)}}{R_1}}\left(\frac{\partial n_1^{(0)}}{\partial y}\right)_0 \tag{33e}$$

so that the second order density of the $()_1$ species is proportional to the finite $()_1$ density gradient at the wall.

The first order slip conditions obtained from (9) are then

$$u^{(0)}(0) = u_2^{(0)}(0) = 0 \tag{33f}$$

$$T^{(0)} = T_w \tag{33g}$$

while substitution of (28) into the boundary conditions yields

$$u^{(1)}(0) = \frac{2-\theta_2}{\theta_2}\frac{\partial u^{(0)}}{\partial y} \tag{33h}$$

$$T^{(1)}(0) = \frac{2-\theta_2}{\theta_2}\frac{\partial T^{(0)}}{\partial y} \tag{33i}$$

This analysis leads us to two sets of conclusions. The first deals with structure of the equations and the boundary conditions. We show that for small slip, the conclusions of (6) are extended from a single species to a reacting binary mixture – the basic first order solution is the appropriately generalized Navier Stokes solution for no slip. The next approximation satisfies a linear partial differential equation set of the same structure as the Navier Stokes equation, with first order slip boundary conditions. Any higher order differential terms bear on quantities known from the preceding integration, so that the number and kind of boundary conditions remains matched on the equations at every order.

The other set of conclusions is the finding that if the wall is catalytic, then the recombined species forms a narrow relatively dense layer adjacent to the wall; the density of the original species becomes small (second order) at the wall.

References

1 J.M. Burgers: Flow Equations for composite gases - Academic Press, NY, 1969.

2 T.F. Morse: Kinetic model equations for a gas mixture, Phys. of Fluids, Vol. 7, pp. 2012-2013, 1964.

3 M. Van Dyke: Perturbation methods in fluid mechanics, Academic Press, NY, 1964.

4 T. Kurotaki: Asymptotic solution of the Boltzmann Krook equation for the Rayleigh flow, SM Thesis, MIT, January 1991.

5 O. Perot: Asymptotic solution of the Boltzmann Krook equation for a reacting mixture of gases, SM Thesis, MIT, June 1989.

6 L. Trilling: Asymptotic solution of the Boltzmann Krook equation for the Rayleigh shear flow problem, Phys. of Fluids, Vol. 7, pp. 1681-1691, 1964.

7 S. Chapman & T.G. Cowling: The mathematical theory of non-uniform gases, Cambridge U Press, 1970.

8 J. Jeans: An introduction to the kinetic theory of gases, Cambridge U Press, 1940.

Inviscid Hypersonic Flow Simulations including Air Dissociation

By J.B. Vos

Hydraulic Machines and Fluid Mechanics Institute (IMHEF)
Swiss Federal Institute of Technology – Lausanne
1015 Lausanne, Switserland

Abstract

A 2D and a 3D Euler solver which both incorporate the effects of equilibrium and non-equilibrium air chemistry have been developed. Both solvers employ the same numerical method, in which the Euler equations are solved using a space centered, explicit time marching scheme augmented by artificial dissipation terms. Non-equilibrium chemistry has been implemented *without* altering the simple and efficient numerical scheme. Calculation results for 2D flows around a sphere, and for 3D flows around the HERMES space shuttle are presented.

1. Introduction

Since the mid 1980's, a renewed interest in hypersonic flows appeared owing to various ambitious projects to build vehicles flying at hypersonic speeds. Examples of such projects are in Europe the space shuttle HERMES and the German space plane Sänger, and in the USA the NASP (National Aero-Space Plane), AOTV (Aeroassist Orbiter Transfer Vehicle) and AFE (Aeroassist Flight Experiment).

An exact definition of hypersonic flows does not exist, but in general these flows can be described as high speed flows in which physical processes, as for instance air dissociation or radiative heat transfer, are important [1]. These processes are initiated by strong shock waves present in flow fields around vehicles flying at hypersonic speeds. In some cases they are found in flows with a freestream Mach number of 3, but in other situations they may appear only when the freestream Mach number is larger than 8. Correct modelling of these physical processes is of major importance in the design of hypersonic vehicles. As an example, consider the stagnation temperature at a vehicle flying with free stream Mach number of 25, in air with free stream temperature of 230 K. According to supersonic flow theory, which assumes that the

air can be treated as a caloric perfect gas, the stagnation temperature at the nose of the body will be around 28,000 K. In reality, the stagnation temperature will be between 6,000 and 9,000 K, depending on the value of the free stream pressure. This strong reduction in temperature is caused by the dissociation of air, a process which costs energy and hence reduces temperatures.

Figure 1 shows the different thermodynamic phenomena as function of the velocity and altitude [2]. At high altitudes, typically above 80 km, the continuum approximation does not hold, and the Boltzmann equations, describing the flow from a molecular point of view, must be used. At lower altitudes the pressure is sufficiently high to permit a macroscopic description of the flow, and the flow phenomena can be correctly described by the Navier Stokes equations. For altitudes between 30 and 80 km, and at high velocities, chemical non-equilibrium effects are important. The maximum heat flux to the wall of a reentry vehicle will occur in this phase. Above 50 km, the flow is in general laminar, due to the very low densities in this regime. At lower altitudes, transition to turbulence will occur which will lead to an increase in wall heat flux. However, the total heat flux will remain smaller than the heat flux encountered at an altitude of 80 km since the shock wave is much weaker.

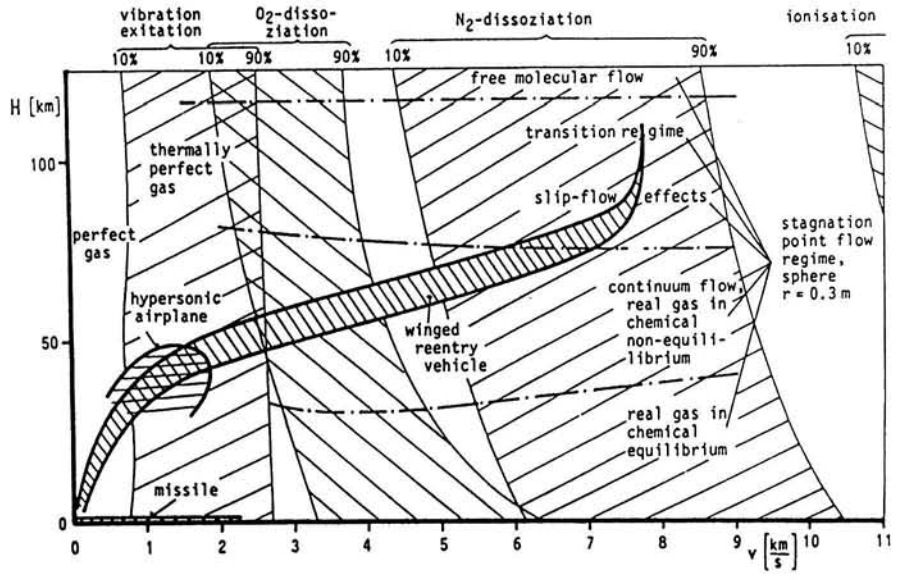

Fig. 1 Thermodynamic phenomena for typical reentry flight regions and trajectories.

Experimental simulation of hypersonic flows over the whole range of possible flight conditions is impossible, since no experimental facilities exist in which *at the same time* a high Mach number and a high enthalpy flow can be simulated [3]. Cryogenic windtunnel are used to simulate high Mach number flows by reducing the speed of sound; hence the effects of air dissociation are not accounted for. The design of the American Space Shuttle was mainly based on the results of these type of experiments, and empirical correlations were used to account for the incomplete simulations. Although the drag and lift of the shuttle were predicted correctly, the flight data showed a large discrepancy in the pitch-up moment, especially at high Mach numbers [4]. This and other experiences with the American Space shuttle showed that there is a lack of understanding of the physical processes occurring in hypersonic flows.

Since the completion of the design of the American Space Shuttle by the end of the 1960's, the field of Computational Fluid Dynamics (CFD) has experienced a rapid growth. At present, CFD is complementing experimental and analytical methods in fluid dynamics. This can be seen, for instance, from the development program of the HERMES space shuttle, where numerical simulation will be used to simulate flow conditions which cannot be simulated experimentally. The final design of HERMES will therefore be based on both experimental and numerical simulation.

Numerical simulation, however, also has its limitations. Solution of the complete 3D Navier Stokes equations including finite rate chemistry describing the air dissociation is beyond the reach of the present generation of computers. At present, 3D Euler simulations assuming equilibrium chemistry is the maximum feasible for design purposes. A second limitation is the uncertainty in the values of physical properties as, among others, the chemical reaction rates and the transport coefficients (viscosity, thermal conductivity and diffusion velocities). Great care must be taken in interpreting the calculated results, and sensitivity studies should be made to reveal the influence of these properties on the numerical solution. A third limitation is the accuracy of the numerical method. Numerical methods in common use are at maximum second order accurate in space, and very often this is valid for orthogonal cartesian coordinate systems only. Grid refinement studies should be carried out to prove that the calculated solution is independent of the number of grid points used. Finally, assumptions are often made to simplify the problem to be solved, introducing other inaccuracies in the solution. For example, if the flow is turbulent it is often assumed that the turbulent field can be described using simple empirical laws. Although this gives satisfactory results for some simple flow problems, it is doubtful that this should yield reliable results for complex flows. Extensive validation work has to be done to compare numerical solutions with experimental results and/or results obtained using different numerical methods. Only in this way it is possible to define an error margin for results obtained by numerical simulations and to use CFD as a design tool.

The work described in this paper is the result of a joint research project between KTH and FFA in Stockholm, and IMHEF in Lausanne. The aim of this project is to simulate high Reynolds number hypersonic flows. For these flows the Compressible Navier Stokes equations can be reduced to the Euler equations; solution of these equations is sufficient for the prediction of the aerodynamic coefficients. However it does not provide any information about, for example, heating rates, since this is a viscous effect. The Euler equations are discretized using a space centered finite volume scheme. These type of schemes are simple and easy to extend to account for the effects of air dissociation, this compared to the mathematically more complicated upwind methods. After a description of the governing equations and the numerical scheme, the implementation of chemistry in the solvers is briefly addressed. Several results of calculations are presented.

2. Governing Equations and Numerical Method

In 3D and for a cartesian coordinate system, the Euler equations for chemical non-equilibrium flows state

$$\frac{\partial}{\partial t}\mathbf{w} + \frac{\partial}{\partial x}\mathbf{F}(\mathbf{w}) + \frac{\partial}{\partial y}\mathbf{G}(\mathbf{w}) + \frac{\partial}{\partial z}\mathbf{H}(\mathbf{w}) = \mathbf{S}(\mathbf{w}) \tag{1}$$

where

$$\mathbf{w} = \begin{pmatrix} \rho \\ \rho u \\ \rho v \\ \rho w \\ \rho E \\ \rho_s \end{pmatrix}, \mathbf{F}(\mathbf{w}) = \begin{pmatrix} \rho u \\ \rho u^2 + p \\ \rho uv \\ \rho uw \\ u(\rho E + p) \\ \rho_s u \end{pmatrix}, \mathbf{G}(\mathbf{w}) = \begin{pmatrix} \rho v \\ \rho uv \\ \rho v^2 + p \\ \rho vw \\ v(\rho E + p) \\ \rho_s v \end{pmatrix},$$

$$\mathbf{H}(\mathbf{w}) = \begin{pmatrix} \rho w \\ \rho uw \\ \rho vw \\ \rho w^2 + p \\ w(\rho E + p) \\ \rho_s w \end{pmatrix}, \mathbf{S}(\mathbf{w}) = \begin{pmatrix} 0 \\ 0 \\ 0 \\ 0 \\ 0 \\ \dot{\omega}_s \end{pmatrix} \tag{2}$$

ρ equals the density, u, v and w the cartesian velocity components, p the pressure and E the total energy. The equations for partial densities, ρ_s, are only solved for chemical non-equilibrium flows, and the source term $\dot{\omega}_s$ in these equations denotes the net

production rate of a chemical species by chemical reactions. The internal energy is related to the total energy by

$$e = E - \frac{1}{2}\left(u^2 + v^2 + w^2\right). \tag{3}$$

The system of equations is closed by the equation of state, which relates the pressure to the density, temperature and chemical composition,

$$p = R^{\circ} T \sum_s \frac{\rho_s}{M_s}, \tag{4}$$

where R° is the universal gas constant, T the temperature and M the molar mass. Equation (1) is discretized in space using the finite volume method, yielding the following system of ordinary differential equations,

$$\frac{d}{dt}\left(V_{i,j,k}\,\mathbf{w}_{i,j,k}\right) + \mathbf{Q}_{i,j,k} - \mathbf{S}_{i,j,k} = 0, \tag{5}$$

where $V_{i,j,k}$ is the volume of the cell (i,j,k), and $\mathbf{w}_{i,j,k}$ and $\mathbf{S}_{i,j,k}$ are approximations of respectively $\mathbf{w}$ and $\mathbf{S}$ in this cell. $\mathbf{Q}_{i,j,k}$ represents the net convective flux leaving or entering the cell, which can be calculated from

$$\begin{aligned} Q_{i,j,k} = {} & h_{i+1/2,\,j,k} + h_{i-1/2,\,j,k} + h_{i,\,j+1/2,k} + h_{i,\,j-1/2,k} + h_{i,\,j,k+1/2} \\ & + h_{i,\,j,k-1/2} \end{aligned} \tag{6}$$

where

$$h_{i-1/2j,k} = \int_{i-1/2j,k} \hat{\mathbf{H}} \cdot n \, dS = \hat{\mathbf{H}}_{i-1/2j,k} \cdot \int_{i-1/2j,k} n \, dS \tag{7}$$

In this equation, n is the surface normal, and $\hat{\mathbf{H}}$, is the convective flux tensor $\hat{\mathbf{H}} = (\mathbf{F},\mathbf{G},\mathbf{H})$. The value of this tensor at the surface i-1/2,j,k is calculated from Eq. (2) using the average of the state vectors having this surface in common. On a cartesian grid this results in a centered scheme which is second order accurate in space.

In order to capture shock waves present in hypersonic flows oscillation free, an artificial dissipation term based on a second order difference is added near discontinuities [5], making the scheme locally first order in these regions. This second order difference is blended with a fourth order dissipation term to prevent odd/even oscil-

lations which are undamped by centered schemes. Equation (5) can now be written as

$$\frac{d}{dt}(V_{i,j,k}\, \mathbf{w}_{i,j,k}) + \mathbf{Q}_{i,j,k} - \mathbf{D}_{i,j,k} - \mathbf{S}_{i,j,k} = 0 \qquad (8)$$

where $\mathbf{D}_{i,j,k}$ is the net dissipative flux in cell (i,j,k). Equation (8) is integrated in time using the explicit Runge Kutta scheme [5]. This type of schemes is normally used for their high accuracy in time, but here properties as stability and damping are of greater interest.
Boundary conditions have to be prescribed at all the sides of the calculation domain. At solid walls, the tangency condition is imposed, and the pressure at the wall is obtained by linear extrapolation from the interior field to the wall. Outflow boundaries are assumed to be supersonic, and the state vector **w** is extrapolated. At the far-field boundary, the state vector is set to the free stream conditions. For the 3D calculations, only half the geometry is calculated, which means that there is a symmetry boundary condition. In the 2D solver the computational domain is bounded by the bow shock owing to the use of a shock fitting procedure [6], where the Rankine Hugoniot conditions for a moving shock wave are applied.

3. Implementation of Chemistry

For flows in chemical equilibrium, no partial differential equations for the partial densities need to be solved, and Eq. (1) reduces to the Euler equations for a caloric perfect gas flow. The effects of equilibrium chemistry appear only in the equation of state, Eq. (4), which relates the pressure to the temperature, density and composition. Figure 2 shows the composition of air at chemical equilibrium as function of the temperature. As can be seen from this figure, air dissociation is not important until about 2,000 K, at which temperature the Oxygen molecules start to dissociate. Some NO is formed for temperatures between 2,500 and 4,000 K, reaching a maximum at 3,500 K. At temperatures above 4,000 K the Oxygen molecules are completely dissociated, while the Nitrogen molecules start to dissociate.

Equilibrium air chemistry is in general described by considering five chemical species, respectively N2, O2, NO, N and O. This assumption is valid for temperatures below 9,000 K, where ionization processes have not become important yet. Of these five species, two are elements which are conserved under chemical reactions, which means that only three equilibrium reaction equations need to be considered. These equations, often called the 'laws of mass action' [7], are the reactions in which a species (NO, O and N) is formed from its elements,

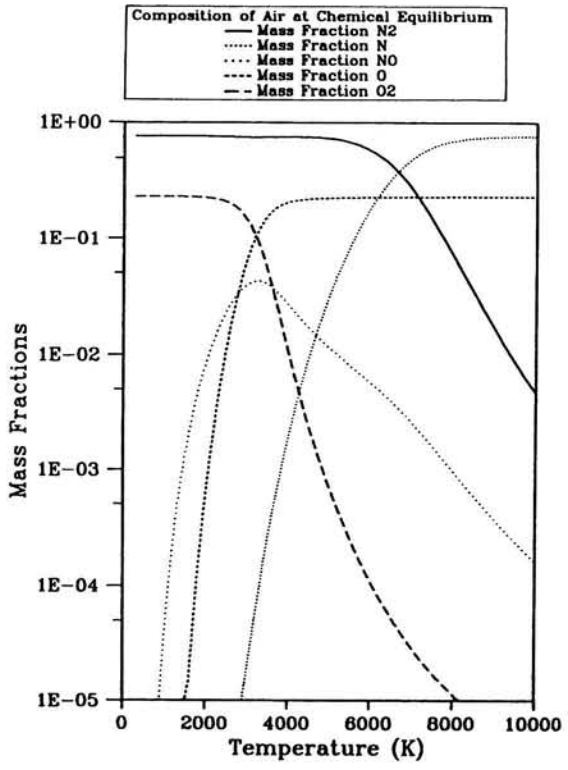

Fig. 2 The composition of Air at chemical equilibrium, p =10 Pa.

$$\frac{1}{2}O_2 \leftrightarrow O \;:\qquad \rho^{1/2}\left(\frac{Y_O}{M_O}\right)\left(\frac{Y_{O_2}}{M_{O_2}}\right)^{-\frac{1}{2}} = K_{C,1}\,,$$

$$\frac{1}{2}N_2 \leftrightarrow N \;:\qquad \rho^{1/2}\left(\frac{Y_N}{M_N}\right)\left(\frac{Y_{N_2}}{M_{N_2}}\right)^{-\frac{1}{2}} = K_{C,2} \qquad (9)$$

$$\frac{1}{2}O_2 + \frac{1}{2}N_2 \leftrightarrow NO \;:\qquad \left(\frac{Y_{NO}}{M_{NO}}\right)\left(\frac{Y_{O_2}}{M_{O_2}}\right)^{-\frac{1}{2}}\left(\frac{Y_{N_2}}{M_{N_2}}\right)^{-\frac{1}{2}} = K_{C,3}\,.$$

In these equations Y is the mass fraction and K_C the equilibrium constant based on the concentrations which is in general a function of the temperature. These constants are calculated using the model of Park [8]. The equations for the conservation of the elements O_2 and N_2 state:

$$\begin{aligned} O_2 : \quad & Y_{O_2} + Y_O + \frac{1}{2}\frac{M_{O_2}}{M_{NO}} Y_{NO} = Z_{O_2} \\ N_2 : \quad & Y_{N_2} + Y_N + \frac{1}{2}\frac{M_{N_2}}{M_{NO}} Y_{NO} = Z_{N_2} \end{aligned} \tag{10}$$

where Z is the elemental mass fraction. For inviscid flows Z is a constant and equal to its freestream value. The system of equations (9) and (10) can be solved by iteration for the equilibrium composition.
The specific enthalpy of the mixture is calculated as the sum of the contributions of the translational and rotational energy modes, the vibrational energy modes and the heat of formation,

$$h = \sum_s Y_s c_{p,s} T + \sum_{s=O_2,N_2,NO} Y_s e_s^{vib} + \sum_{s=O,N,NO} Y_s h_{f,s}^0 \tag{11}$$

where the specific heat c_p equals 2.5 R°/M for the atoms, and 3.5 R°/M for the molecules. The vibrational energies e^{vib} are given by their equilibrium value [1]. Once the composition is known, the temperature can be solved from Eq. (11). However, due to the strong dependence of the equilibrium constants on the temperature, Eqs. (9), (10) and (11) are in general solved simultaneously.
Non-equilibrium air chemistry has been described by the five species and seventeen reaction model of Park [8]. The partial densities of the species N, O and NO are found by solving Eq. (1), while the partial densities of N2 and O2 are found from the conservation of elements, Eq. (10). The chemical source term, $\dot{\omega}_s$, is calculated as follows: for the general system of reversible chemical reactions

$$\sum_s \nu_{s,k}^a A_s \underset{k_{f,k}}{\overset{k_{b,k}}{\leftrightarrow}} \sum_s \nu_{s,k}^b A_s \qquad k = 1,\ldots,m \tag{12}$$

with $k_{f,k}$ and $k_{b,k}$ respectively the forward and backward reaction rates, A_s the chemical symbol for the species s, and $\nu_{s,k}^a$ and $\nu_{s,k}^b$ the stoichiometric coefficients, the chemical source term $\dot{\omega}_s$ is calculated from

$$\dot{\omega}_s = M_s \sum_{k=1}^{m} (\nu^b_{s,k} - \nu^a_{s,k})\, J_k ,$$

$$J_k = k_{f,k} \prod_r \left[\frac{\rho_r}{M_r}\right]^{\nu^a_{r,k}} - k_{b,k} \prod_r \left[\frac{\rho_r}{M_r}\right]^{\nu^b_{r,k}}, \qquad (13)$$

$$\rho_s \equiv \rho Y_s . \qquad (15)$$

No special numerical procedures were used when implementing non-equilibrium air-chemistry in the Euler solvers. The chemical source term, $\dot{\omega}_s$ in Eq. (13), is calculated using the partial densities and the temperature of the previous Runge Kutta stage. The time step in the Runge Kutta time integration procedure has been taken as the minimum of the fluid dynamics and the chemical time step, the latter being defined as

$$\Delta t_{chem} = \min \left[\frac{\partial \dot{\omega}_s}{\partial \rho_s}\right]^{-1} \qquad s = 1,...,5$$

For most of the calculations presented here, it was found that the fluid dynamic time step was the smallest during the time integration process.

4. Calculation Results flow over a sphere

To show some important features of hypersonic flows, two sets of calculations for the flow over a sphere were carried out. In the first set, a sphere with a radius of 1 m. was considered, and calculations were made assuming respectively a caloric perfect gas, a thermal perfect gas, air at chemical equilibrium, and non-equilibrium air. A 40 × 30 grid was used in all calculations except for the non-equilibrium calculation, in which a 40 × 50 grid with grid point clustering close to the shock wave was employed in order to improve the resolution of the high temperature gradients.
Figure 3 shows the calculated temperatures along the symmetry line and the body for the four calculations made. As to be expected, the caloric perfect gas calculation yields the highest temperatures since this model does not take into account chemistry nor the variation of the specific heats with the temperature. Assuming with temperature varying specific heats reduces maximum temperatures with about 5,000 K (thermal perfect gas) since energy is stored in the vibrational energy modes of the N2 and O2 molecules, but temperatures between shock and body temperatures remain high since chemistry is not accounted for. The lowest temperatures are found for the

equilibrium air calculation, since here it is assumed that the chemistry is in chemical equilibrium everywhere. Since air dissociation costs energy, temperatures are considerably lower compared to the perfect gas results. For the non-equilibrium calculation, the temperature is high close to the shock, since it has been assumed that the flow is frozen across the shock. However, the temperature directly behind the shock is not equal to the thermal perfect gas temperature here because, even with 50 grid points between body and shock, the grid is not sufficiently fine to resolve properly the large temperature gradients between shock and body.
At the stagnation point, the chemical non-equilibrium temperature is almost equal to the equilibrium temperature, but along the body, the chemical non-equilibrium temperature is much lower than the chemical equilibrium one. This is due to the fact that N-atoms were formed close to the shock which did not have had the time to recombine yet; the flow is frozen in this region. Since the dissociation of N2 costs energy, much energy is stored in these N-atoms, which explains the low temperature along the body.
Table 1 gives the temperatures directly behind the shock, at the stagnation point and at the outflow for the four calculations made. For all calculations except the chemical non-equilibrium, temperature variations between body and shock are small and maximum temperatures are found at the stagnation point. The influence of the thermodynamic model on the stagnation pressure is small, as can be seen from Table 1. From Fig. 3, it can be seen that the shock stand off distance is the largest for the caloric perfect gas calculation, and the smallest for the equilibrium simulation. The shock stand off distance is inversely proportional to the density ratio across the shock wave [9], and since the pressure is hardly affected by the thermodynamic model used, it follows from the equation of state (Eq. (4)) that the shock stand off distance is proportional to the temperature ratio across the shock. This ratio is the largest for a caloric perfect gas, and the smallest for equilibrium air.

Table 1. Calculated results flow over a sphere for different thermodynamic approximations of the air.

Thermodynamic model	CFL	# time steps	p_{st} (Pa)	T_{shock} (K)	T_{st} (K)	T_{out} (K)	CPU (sec)†
Caloric perfect gas	2.0	710	$8.031\ 10^3$	24512	25036	10013	4.7
Thermal perfect gas	2.0	750	$8.194\ 10^3$	19608	19782	9795	5.0
Equilibrium air	1.0	2390	$8.486\ 10^3$	6070	6063	4888	16.4
Non-equilibrium air[1]	0.5	10970	$8.373\ 10^3$	16961	6166	1898	524.5

[1] 40 × 50 grid with clustering close to the shock † Cray YMP of ETH Zürich

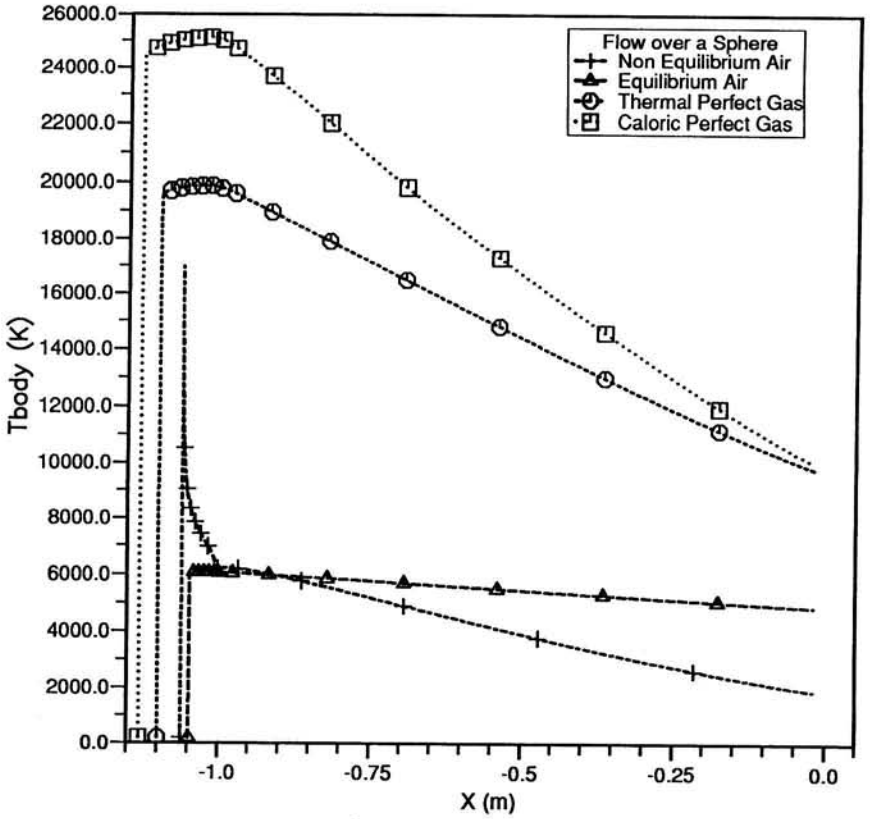

Fig. 3 Temperature profiles along the symmetry line and along the body for the flow around a sphere. $M_\infty = 25$, p_∞=10 Pa, $T_\infty = 200$ K,

The CPU times listed in Table 1 show that the chemical non-equilibrium calculation is the most expensive, partly due to the finer grid system used. The equilibrium calculation takes about three times as much time steps to converge than the perfect gas calculations due to the fact that the shock is much closer to the body, giving smaller time steps. Moreover the CFL parameter had to be decreased to get a converging time stepping process. The CPU cost per time step, however, is only slightly higher than those of the perfect gas calculations.

In the second set of calculations, chemical non-equilibrium calculations were carried out for the flow over a sphere with a radius of 10, 1, 0.1 and 0.01 m respectively. The results are compared with a chemical equilibrium calculation.

The size of the body is only important for flows in chemical non-equilibrium, as can be explained as follows. Chemistry is a process of collisions between particles in which new particles may be formed. Non-equilibrium processes take a certain time to have an influence on the flow variables, and during this time the particles have travelled a certain distance. For small bodies, it may happen that the effects of the che-

mistry will appear behind the body; the flow is said to be frozen. For very large bodies non-equilibrium chemistry effects will appear only close to the shock wave, and in the remainder of the flow field the flow is in chemical equilibrium. Remark that the assumption of chemical equilibrium means that the chemical processes proceed infinitely fast, and for inviscid flows the size of the body is not important.
Table 2 summarizes the calculated results, and Fig. 4 shows the temperature along the stagnation line and body. As can be seen from this figure, decreasing the body size increases temperatures behind body and shock, due to the fact that the influence of the chemistry will start further from the shock. Note that the temperature behind the shock for the sphere with radius of 0.01 m is very close to the thermal perfect gas temperature behind the shock listed in Table 1. Increasing the radius of the sphere decreases temperatures between body and shock, and the results for the sphere of 10 m compare along the stagnation line very well with the equilibrium chemistry result except for the region close to the shock (see inlay figure). At the stagnation point, the stagnation temperature for the equilibrium and for the 10 m non-equilibrium calculation are almost equal. Note that for the other body sizes, the stagnation temperature differs considerably from the equilibrium stagnation temperature.
As can be seen from Fig. 4, the temperature gradients along the body for the non-equilibrium calculations differ considerably from that of the equilibrium calculation. In all non-equilibrium calculations it was found that the flow along the body was frozen.

Table 2 Calculated results flow over a sphere for different body radius.

Radius	# time steps	p_{st} (Pa)	T_{shock} (K)	T_{st} (K)	T_{out} (K)	CPU (sec)†
Equilibrium	7500	$8.488\ 10^3$	6068	5948	4794	256
R = 0.01 m	4050	$8.200\ 10^3$	19434	9245	3634	195
R = 0.1 m	4950	$8.284\ 10^3$	18568	7174	2409	239
R = 1.0 m	5960	$8.380\ 10^3$	15420	6133	1834	286
R = 10.0 m	22500	$8.373\ 10^3$	11391	5885	1950	1081

† Cray YMP of ETH Zürich

The amount of frozen N-atoms differed considerably, which explains the difference in temperatures. However, the gradients were almost equal.
Table 2 also summarizes the computational costs of the calculations made. For the 10 m body, it was found that the chemistry time step was smaller than the fluid dynamics time step, and the large number of time steps required for this calculation is necessary to resolve the chemistry.

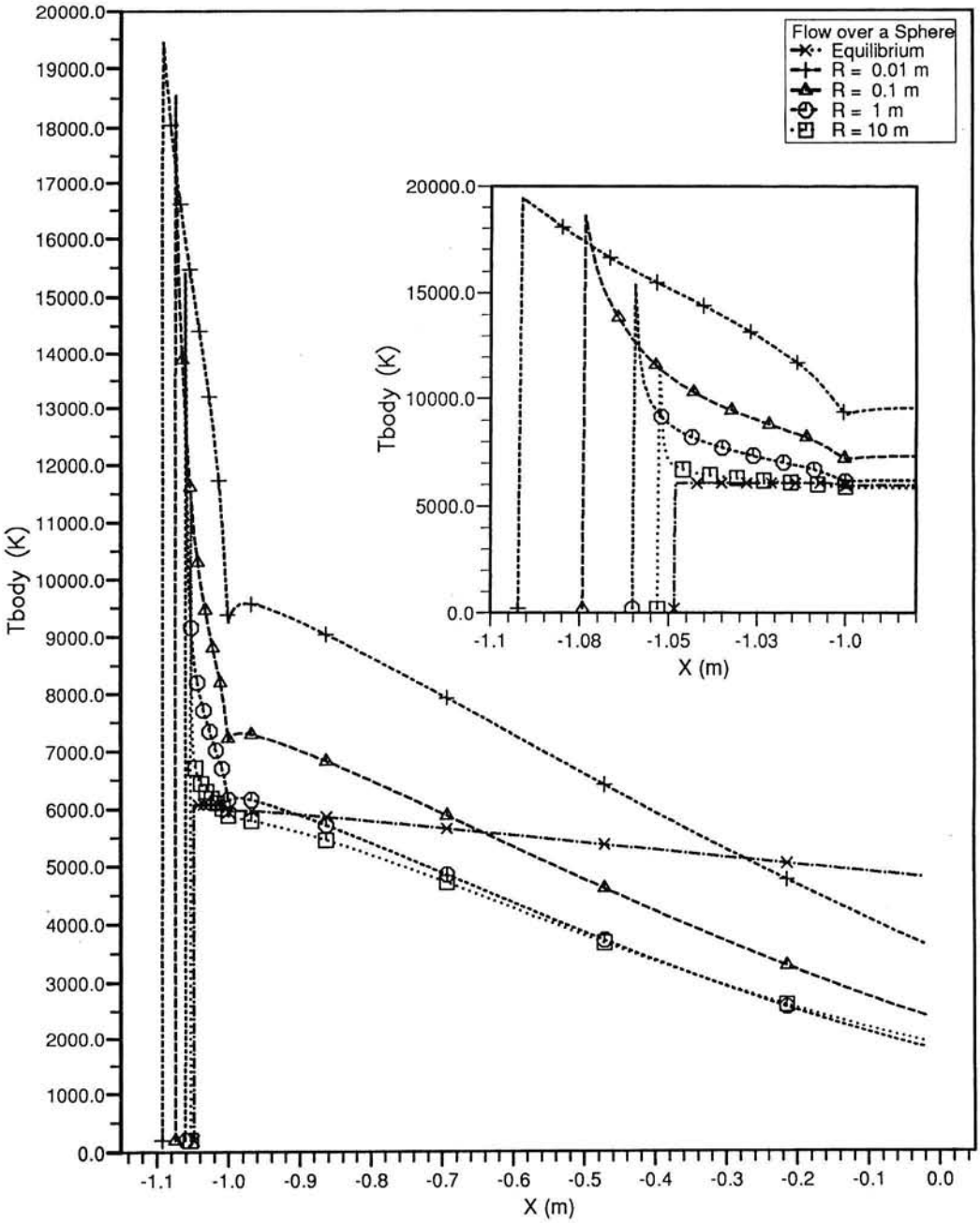

Fig. 4 Temperature profiles along stagnation streamline and along the body for the flow around a sphere. $M_\infty = 25$, $p_\infty = 10$ Pa, $T_\infty = 200$ K, Smaller and larger bodies have been rescaled. Inlay figure shows the region between shock and stagnation point.

5. Calculation Results for the flow over the HERMES Space Shuttle

The 3D Multi Block Euler solver EULMB [10] was used to calculate the flow over the HERMES space shuttle with 12° body flap at 76 km altitude. A single block mesh was used, and calculations were carried out for a caloric perfect gas, for air at chemical equilibrium, and for air at chemical non-equilibrium. Three different grid systems were employed, and Fig. 5 shows the calculated temperature along the body in the symmetry plane

for the chemical non-equilibrium calculation. At the windward side of the body, the results for the three grids are almost equal, except at the body flap where the temperature is smeared out on the coarse grid. At the leeward side the results between the coarse grid and the other two grids differ considerably, especially at and after the canopy shock. It is therefore concluded that the medium grid is sufficiently fine.
Figure 6 shows the convergence history for the chemical non-equilibrium calculation on the $91 \times 75 \times 71$ grid. The solution of the 61x49x71 grid was used to initialize this calculation. As can be seen in Fig. 4, the calculation converges rapidly until after 1,500 time steps a plateau value of 10^{-3} is reached. Note that the L2-residu is normalized with its value at the first time step, which means that its value has decreased 3 orders of magnitude. The maximum residu only decreased 1.5 order of magnitude, after which it starts to oscillate. The maximum values of the residu were found close to the body in the outflow plane. Comparing the solution after 1,600 time steps with that after 2,000 steps showed no differences in results, and it was concluded that the calculation was converged.
Figures 7 and 8 show the temperature iso lines in the symmetry plane for the equilibrium and non-equilibrium calculation respectively. The maximum temperature for the equilibrium calculation was equal to 5,729 K, compared to 13,832 K for the non-equilibrium calculation. This indicates that non-equilibrium chemistry effects are important. Comparing these figures shows that the bow shock for the equilibrium calculation is closer to the body for the reasons explained in the previous Section. At the leeward side of the body, there is a region with high temperature gradients visible for the equilibrium calculation. This region corresponds to the region where the O2 molecules are completely dissociated, but temperatures are still too low to start the N2 dissociation.
For the non-equilibrium calculation, the largest temperature gradients are found near the bow shock. This is a typical non-equilibrium effect, as is explained in the previous Section. The flow is frozen across the shock, and as soon as an sufficient amount of atoms have been formed, the temperature decreases rapidly. Temperature gradients at the canopy shock are much higher for the chemical non-equilibrium calculation due to the recombination of N-atoms. Much N-atoms have been formed at the bow shock where temperatures are high. Close to the wall temperatures are lower, but the N-atoms have not had the time to recombine yet. The increase in potential energy at the canopy shock forces the N-atoms to recombine, liberating their energy and increasing the temperature, see also Fig. 6. For the chemical equilibrium

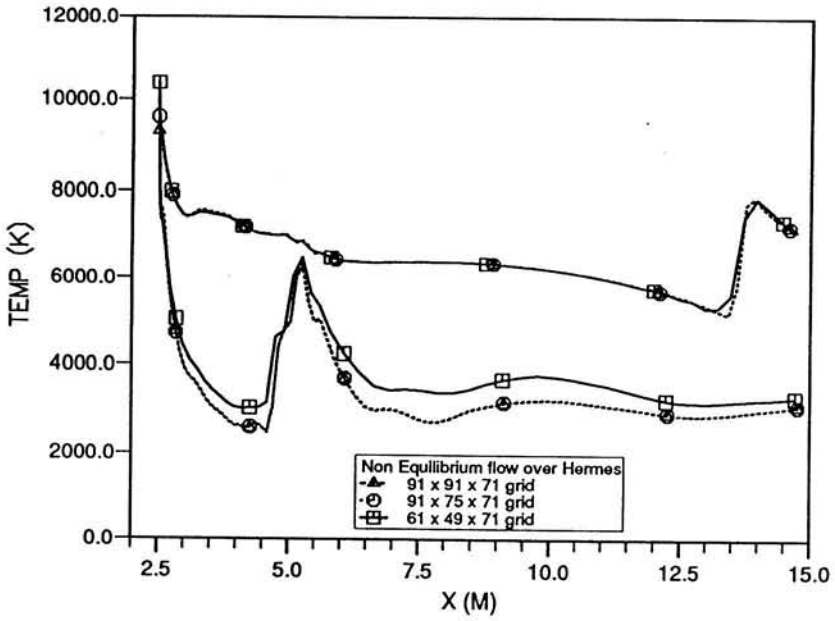

Fig. 5 Temperature contours along the body in the symmetry plane of the HERMES space shuttle. $M_\infty = 25$, $\alpha = 30°$, 76 km altitude.

calculation, the opposite process occurs: the increase in potential energy at the canopy shock leads to the dissociation of N2, and there is hardly a jump in temperature visible. For both the equilibrium and non-equilibrium calculation, the canopy shock is almost attached to the body.
Table 3 lists the aerodynamic coefficients for the calculations using the 91 × 91 × 71 grid, together with the computational costs.

Table 3 Aerodynamic coefficients for the calculations using the 91x91x71 grid.

thermodynamic model	CD	CL	CM	CPU sec / timestep †
caloric perfect gas	0.381	0.468	-0.0154	8.22
equilibrium air	0.400	0.480	-0.0261	8.27
non-equilibrium air	0.396	0.478	-0.0232	36.19

† Cray 2 of EPF-Lausanne

As can be seen from this Table, the effects of chemistry on the drag and lift is small, in the order of 5% for the drag, and about 2.5% for the lift. However, the chemistry has a much larger influence on the CM (pitch up moment), and the difference in CM between the caloric perfect gas and the equilibrium air calculation is 69%. The values of the coefficients for the non-equilibrium calculation are in between those of the caloric perfect gas and equilibrium calculation.

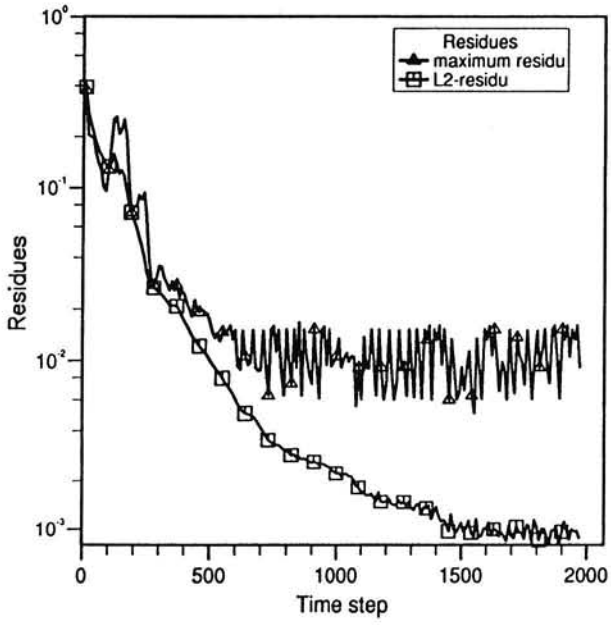

Fig. 6 Residu plot chemical non-equilibrium calculation around the HERMES space shuttle. $M_\infty = 25$, $\alpha = 30°$, 76 km altitude, $91 \times 75 \times 71$ grid.

Comparing the computational costs show that the cost per time step for the equilibrium and caloric perfect gas calculation are comparable. However, about twice as much time steps are required for the equilibrium calculation to converge. The costs per time step for the non-equilibrium calculation is 4.4 times higher than for the caloric perfect gas calculation.

6. Conclusions

2D and 3D explicit Euler solvers for hypersonic flows which incorporate the effects equilibrium and non-equilibrium air chemistry have been presented.

It has been shown that space centered schemes with added artificial dissipation can be used to simulate high Mach number flows including non-equilibrium air chemistry. Implementation of chemistry in this type of numerical scheme has been briefly addressed, and appeared to be straightforward and simple.

In the 2D solver, a shock fitting procedure for the bow shock is employed resulting in sharp and oscillation free shock waves. This technique is also employed for chemical equilibrium and non-equilibrium flows.

For the flow over a sphere calculations were carried out to show some important features of hypersonic flows. The shock stand off distance is the smallest for flows in chemical equilibrium, and the largest for caloric perfect gas flows. For flows in chemical non-equilibrium, temperature gradients are high close to the shock. It was

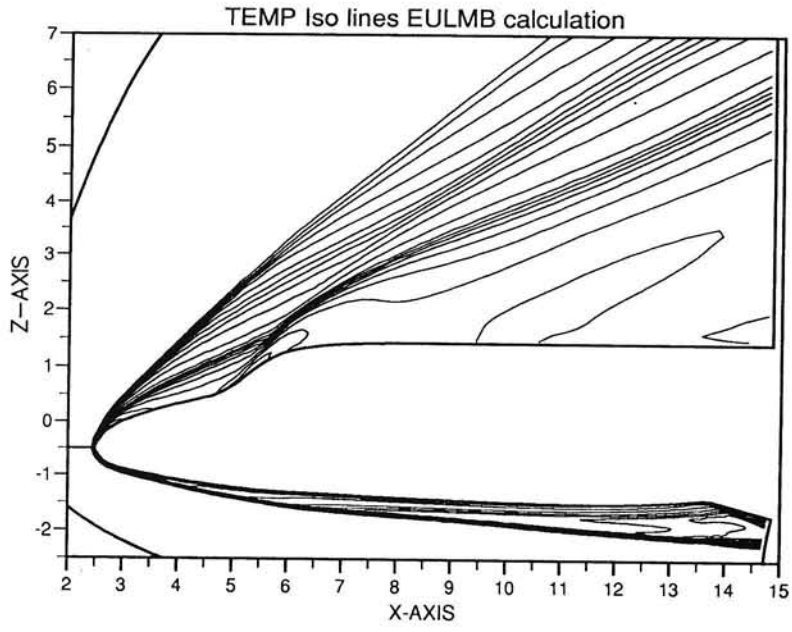

Fig. 7 Temperature iso lines chemical equilibrium flow over the HERMES space shuttle, $M_\infty = 25$, $\alpha = 30°$, 76 km altitude, 91 × 91 × 71 grid.

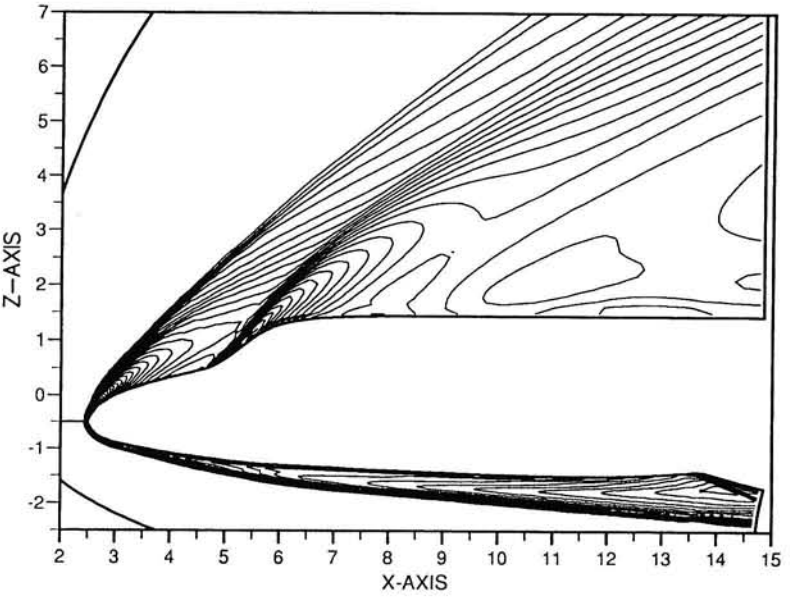

Fig. 8. Temperature iso lines chemical non-equilibrium flow over the HERMES space shuttle, $M_\infty = 25$, $\alpha = 30°$, 76 km altitude, 91x91x71 grid.

found that the chemistry has hardly any influence on the stagnation pressure. Non-equilibrium calculations made in which the size of the body was varied showed that for large bodies, the temperature along the stagnation line was almost equal to the equilibrium temperature. However, temperature along the body differed considerably. For small bodies it was found that the flow was for a great part frozen.
Calculations for the flow around the HERMES space shuttle showed that the air dissociation has a large influence on the aerodynamic coefficients, especially on the pitch up moment. If one is only interested in the aerodynamic coefficients, equilibrium air chemistry calculations are sufficient and it is not necessary to account for chemical non-equilibrium effects . However, if the determination of the heat load to the body is important, non-equilibrium chemistry effects should be taken accounted for since the temperature and chemical composition profiles along the body differed considerably between the equilibrium and non-equilibrium calculation.

7. Acknowledgements

The research at the Swiss Federal Institute of Technology was performed under contract from Avions Marcel Dassault - Breguet Aviation, with financial support by the Commission Suisse d'Encouragement des Recherches Scientifiques.

8. References

[1] Anderson Jr., J.D., 'Hypersonic and High Temperature Gas Dynamics.' McGraw-Hill, New York, 1989

[2] Hirschel, E.H., 'Equilibrium and Non-Equilibrium Viscous Flow.' CERFACS Training Cycle on Computational Fluid Dynamics, Toulouse, 1989.

[3] Wittliff, C.E., 'A Survey of Existing Hypersonic Ground Test Facilities in North America', AGARD CP-428, 1987

[4] Arrington, J.D. and Jones, J.J., 'Shuttle Performance: Lessons Learned' NASA CP 2283, 1983.

[5] Jameson, A., 'Numerical Solution of the Euler Equations for Compressible Inviscid Fluids', In: 'Numerical Methods for the Euler Equations of Fluid Dynamics', Ed.: Angrand, F., Dervieux, A., Desideri, J.A. and Glowinski, R., SIAM, Philidelphia 1985

[6] Vos, J.B., Bergman, C.M. and Petersson, N.A., 'An efficient Euler solver for Real gas flows', Report IMHEF T-89-1, CERFACS RF/89/1

[7] Vincenti, W.G., and Kruger, C.H., 'Introduction to Physical Gas Dynamics.' John Wiley & Sons, New York 1965

[8] Park, C., 'On Convergence of Chemical Reacting Flows.' AIAA 85 - 0427

[9] Hayes, W.D. and Probstein, R.F., 'Hypersonic Flow Theory.' Academic Press, New York, 1959

[10] Vos, J.B. and Bergman, C.M., 'EULMB: A Multi Block Euler Solver for 3D Compressible and Chemical Equilibrium Flows. EULMB Handbook Version 1.0', IMHEF Report 1991

The Two-wave Structure in the Wake of an Oscillating Airfoil

By Zeguang Wang

Faculty of Aerospace Engineering
TU Delft

1. Introduction and Formulation

The classical problem of an airfoil oscillating in an uniform incompressible potential flow was solved by Theodorsen and others in the 30's, by assuming small perturbation, potential theory, and a Kutta condition at the sharp trailing edge of the airfoil. Within this framework, it is consistent to assume that the shed vorticity is transported with the main stream velocity U, satisfying Kelvin's law in the form

$$\frac{\partial \gamma}{\partial t} + U\frac{\partial \gamma}{\partial x} = 0, \tag{1.1}$$

where $\gamma = \gamma(x,t)$ is the measure of the vorticity strength along the wake. Integration of equation (1.1) indicates that, in the wake one would observe a vortex wave with wave length $\gamma = UT$, where T is the period of the oscillation, stretching from the trailing edge down stream.
The amplitude of the vortex wave is $\hat{\Gamma}(c)/U$, where $\hat{\Gamma}(c)$ is the amplitude of the shed vorticity determined by enforcing the Kutta condition, in order to remove the velocity singularity at the trailing edge. In the case of zero mean angle of incidence, this is then the amplitude of the bound circulation. The bound vorticity on the airfoil and the shed vorticity in the wake perturb the upwash field such that the integral equation,

$$\hat{v}(x) = -\frac{1}{2\pi}\int_0^c \frac{\hat{\gamma}(\xi)}{x-\xi}\,d\xi + \frac{i\omega}{2\pi}\frac{\hat{\Gamma}(c)}{U}\int_0^\infty \frac{\exp(\omega(\xi - c)/U)}{x-\xi}\,d\xi, \tag{1.2}$$

is established for the boundary value problem over the chord $0 \le x \le c$, if the oscillation has gone on infinitely long. In equation (2.2), v(x) is the non-penetration condition specified according to the oscillation of the airfoil, ω is the angular frequency of the oscillation.

The scale used in potential theory is of order 1 (l is a characteristic length in the problem, for the present case it is the chord length of the airfoil). With this scale, the boundary layer, of scale $l/Re^{1/2}$, cannot be perceived. Despite its being small in dimension, it is of crucial importance for the study of flow past airfoils, since the circulation mentioned above is related to the vorticity that is solely contained in this viscous region. Boundary layers on the two sides of the airfoil contain vorticity of different sense of rotation. The location of the rear stagnation point (or the separation point, in boundary layer terminology) determines the circulation bound to the airfoil. Potential theory itself is incapable of settling this problem to yield an unique, and physically realistic solution. This difficulty is resolved by the Kutta condition which represents the property of the boundary layer flow (while ingeniously avoids bothering about its more complicated structure) consistently with the potential flow language.

If the problem is viewed with a still finer scale, say, instead of $l/Re^{1/2}$, take $l/Re^{5/8}$, a layered structure is found to exist in the neighbourhood of the separation point, i.e. the trailing edge in the present case. The extent of this structure in both of the two directions is of order $l/Re^{3/8}$. This structure is named the triple deck, since it can be distinguished into three layers.
This structure arises because, upon joining the wake, the viscous flow, which was formerly constrained by the wall, is abruptly released, resulting in a infinite acceleration at that particular point. Mathematically this is reflected as the singularity in the gradient of the centerline velocity at the trailing edge in the Goldstein near wake solution. To accommodate the acceleration of the fluid, the triple deck structure is established naturally, producing an appropriate pressure gradient down stream.

Besides the effect of accelerating the flow, the pressure perturbation due to the triple deck structure is also favourable for the flow tending to go around the trailing edge. The balance of this favourable pressure gradient and the unfavourable gradient, arises from the non-circulatory solution of the airfoil problem, makes the boundary layer flow able to go around the trailing edge and separate a little distance upstream of the trailing edge. In line of this, correction to the bound circulation can be made with respect to the one determined by the usual Kutta condition that the flow must separate at just the sharp trailing edge.

Efforts in this context were made a number of years ago by, for instance, Stewartson, Brown, and Daniels, to name a few. The present study was inspired by considering the different properties of flow in the layered structure in the neighbourhood of the trailing edge.
Shown in figure 1.1 is a sketch of the flow regime for unsteady motion of a flat plate, adapted from Crighton. In the front part of the boundary layer, vorticity is generated on the surface and diffuses outwards due to the viscosity. It is convected along the streamlines down stream. It is remarkable to note that formal analysis of the flow in the triple deck region reveals that due to the shortening of the x-scale the flow is

inviscid in the main deck (4b), which is of the scale of the boundary layer laterally. It is rotational, of course, since vorticity is convected here from upstream.

In the lower deck (4c), the flow is found to be still viscous, obeying the boundary layer equations. Vorticity can still be generated in this region, the source being the counterbalance between the inertia force and the viscous shear force. Laterally it must remain in this region, since diffusion cannot penetrate the inviscid main deck.

With this understanding of the flow structure, it is reasonable to infer that the vorticity shed into the wake consists of two parts. Of these, one coming from the upper stream boundary layer is at the outer edge of the viscous region; while the other being generated locally at the lower deck, for unsteady motion of an airfoil, is at the centerline of the wake.

Vortices move with material particles, let alone the diffusion in a viscous flow. Therefore, it is justified to argue that for unsteady motion of an airfoil in a viscous flow, the convection of the shed vorticity is conceived in a layered structure, at least initially in the near wake, before diffusion smears them out.

For the periodical oscillation of an airfoil, one would observe more waves now. A wave at the centre of the wake has its wave length initially shorter and lately extended, because the centerline velocity of a wake is initially lower than what it will asymptotically approach when the distance from the body becomes large. The other waves are at the two outer edges of the wake. For simplicity, they can be regarded as one due to the anti-symmetry on the two sides. Because the velocity defect is small there, it behaves quite like that in the potential flow.

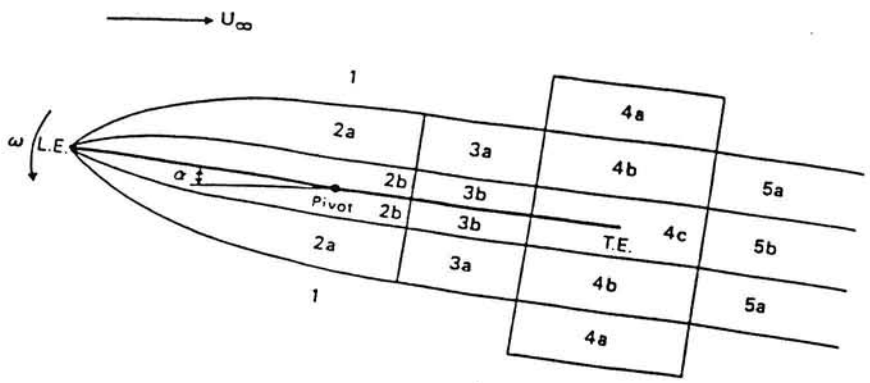

Fig. 1.1 Multilayer structure in the neighbourhood of a flat plate, oscillating about a pivot with angular frequency ω and incidence amplitude α in a uniform stream. 1. potential flow; 2. perturbed Blasius boundary layer and inner Stokes layer; 3. foredeck; 4. triple deck; 5. modified Goldstein wake.

Should this be the case, the memory pattern in the wake would no longer be that of 1-C(k), where C(k) is the Theodorsen function in the classical theory, derived in line with equation (2). Kelvin's law should now be more appropriately written as

$$\frac{\partial \gamma}{\partial t} + \frac{\partial (V\gamma)}{\partial x} = 0, \tag{1.3}$$

if diffusion of vorticity is neglected. In equation (1.3), V is the velocity with which vorticity is transported. Instead of equation (1.2), the integral equation should now take the form

$$\hat{v}(x) = -\frac{1}{2\pi}\int_0^c \frac{\hat{\gamma}(\xi)\,d\xi}{x-\xi} + \frac{i\omega\hat{\Gamma}(c)}{2\pi}\int_c^\infty \frac{\frac{1}{v(\xi)}\exp\left(i\omega\int_c^\xi \frac{d\zeta}{v(\zeta)}\right)}{x-\xi}\,d\xi. \tag{1.4}$$

In order to verify the conjecture posed above, an experiment was conducted in the M-tunnel, in the Low Speed Laboratory of the Aerospace Engineering Department, Delft University of Technology.

2. The Experiment

The cross section of the wind tunnel is 40*40 cm. A NACA 0012 airfoil was used. The chord length of the airfoil is 15 cm, the span is 60 cm.

In order to avoid the shift of the transition point and create a fully developed turbulent boundary layer, the airfoil was tripped at a distance 2 cm from the leading edge. The airfoil was made to pitch about the trailing edge with zero mean angle of attack. The principle of the experimental arrangement is shown in figure 2.1.

The acceleration signal of the pitching airfoil and the velocity signal of the flow were registered. The streamwise velocity was measured with a single-wire anemometer, just outside the wake, and above the trailing part of the airfoil. The probe is traversed in the flow direction.
The driving frequency of the airfoil oscillation ranged from 20 to 180 Hz. The Reynolds number based on the airfoil chord was in the range $7*10^4 \leq Re \leq 2*10^5$.

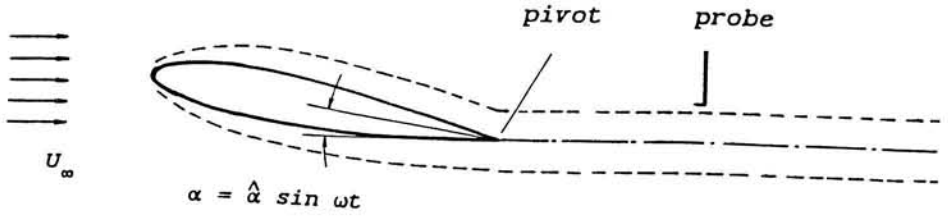

Fig. 2.1 The principle of the experimental arrangement.The broken line indicates the boundary of the viscous region.

3. Results and Discussion

The airfoil is oscillating with frequency f in a uniform flow with velocity U. Upon these the reduced frequency is defined as

$$k = \frac{\pi f c}{U}, \tag{3.1}$$

A linear wave length is estimated with

$$\lambda = \frac{U}{f}, \tag{3.2}$$

3.1. The Harmonic Composition of the Signal

In order to gain an insight of the process of the vortex shedding, it is necessary to study the harmonic composition of the excitation and response. The frequency analysis is also crucial for the data reduction and interpretation to which we shall come back later.

Figure 3.1 shows a typical amplitude spectrum of the fluctuating part of the velocity measured just outside of the near wake. It is clear, that corresponding to an excitation of specific frequency there is a distinctive response in the first harmonic. Higher harmonics, if there is any, cannot be distinguished from the ambient turbulence noise in this region. This would suggest that the process is essentially a linear one, or, at most a very weakly nonlinear one, if one prefers.

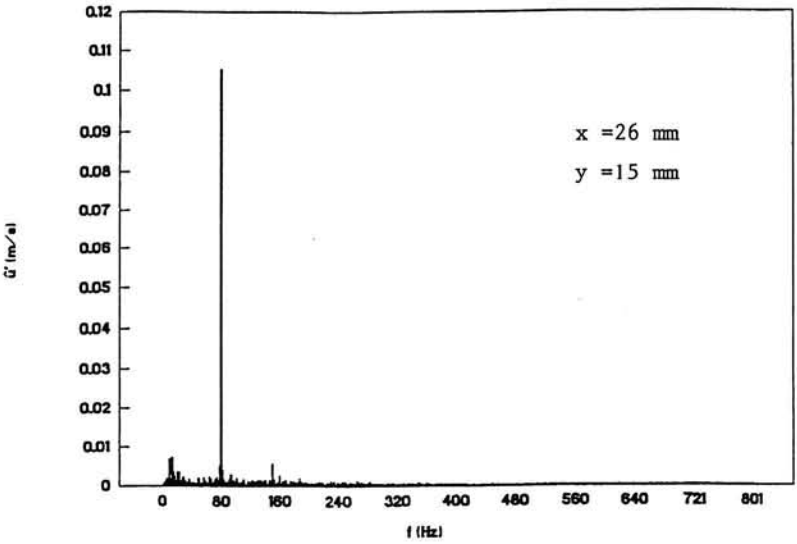

Fig. 3.1 A typical spectrum of the velocity signal. Corresponding to this velocity signal the excitation is 80 Hz.

3.2 . The Vortex Wave

The first harmonic of the velocity perturbation is in fact the measure of the shed vorticity due to the airfoil oscillation. In the case where the wake is approximated as a vortex sheet of infinitesimal thickness, measuring adjacent to the sheet one obtains $u(x_0) = \gamma(x_0)/2$. Traversing in the flow direction, one could therefore deduce the vorticity distribution in the wake as a function of streamwise distance x: $\gamma(x) = 2u(x)$.

Shown in Figure 3.2 are the results of traverses made 15 mm above the centerline of the wake. This is a distance well outside the wake, yet not too far from it in the range of traverse. In these graphs the abscissa, representing the distance measured in flow direction, is scaled with the half-wave-length, $\lambda/2$, estimated with equation (3.2). The ordinate, being the amplitude of the first harmonic perturbation, is scaled with its value at the trailing edge.

It is remarkable to observe that in both of the graphs, and all the others unshown, the curves show a consistent general trend. On the trailing part of the airfoil, the amplitude of the perturbation velocity increases until at the trailing edge, a maximum is reached. It then decreases, reaching a minimum somewhere behind the airfoil. A more careful examination reveals surprisingly that all the minima occur at a distance that is about half a wave length down stream the trailing edge irrespective of the differences in the operating parameters, e.g. the reduced frequency, k, and the Reynolds number, Re.

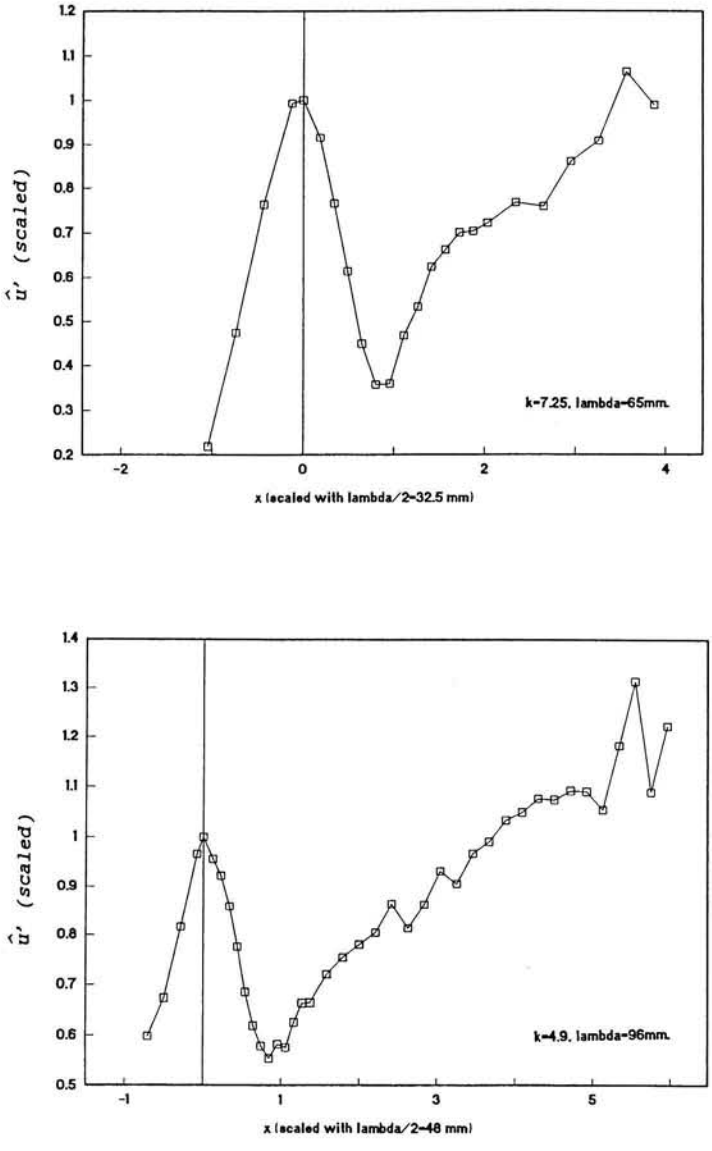

Fig.3.2 Perturbation amplitude vs distance. The abscissa is scaled with $\lambda/2$, the ordinate with the amplitude at the trailing edge

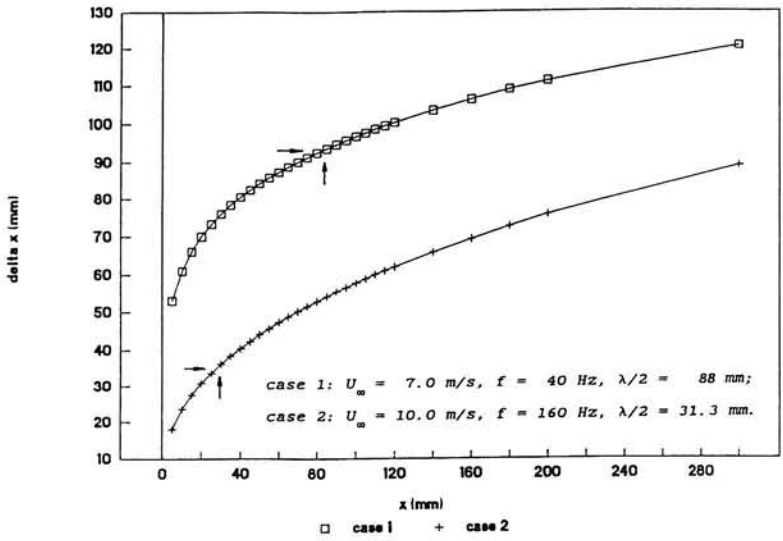

Fig. 3.3 The overrun curves. The abscissa represents the distance from the trailing edge, the ordinate represents the distance by which the outer particle overtakes the centerline particle

Vorticity is persistent. We conject that these minima are the consequences of the interference of two waves with the same frequency--while in counter-phase they result in a partial destruction, like the dark-spot one sees in optics. The uniqueness of this interpretation is supported by the results from the measurement of the mean velocity profile in the wake. There, it is found that a particle with the centerline velocity of the wake takes about twice the time to reach the half-wave-length point than does a particle with the outer flow velocity. This fact is shown in figure 3.3, in which the abscissa denotes the distance from the trailing edge, while the ordinate represents the distance by which the outer particle overtakes the centerline particle. It is clear that at the $\lambda/2$ points, which are 31 mm and 88 mm respectively, the overtake distances are approximately the two corresponding half-wave-lengths.

This implies that when the two waves are in phase at the trailing edge (as is manifested by the maxima there) they run into counter-phase at about half-wave-length point. A physical reason we could imagine why the two waves should be in phase at the trailing edge is that the outer vorticity wave alone is not sufficient to counteract the tendency of flow going around the sharp edge (facilitated with the favourable pressure gradient induced by the triple deck structure), so that the inner vorticity wave would have to come into aid.
The depth of the dip, or, the amount of the reduction, in the amplitude curve would be a reflection of the relative magnitude of the two waves. Shown in figure 3.4 is a plot of the depth of the dip as a function of the reduced frequency.

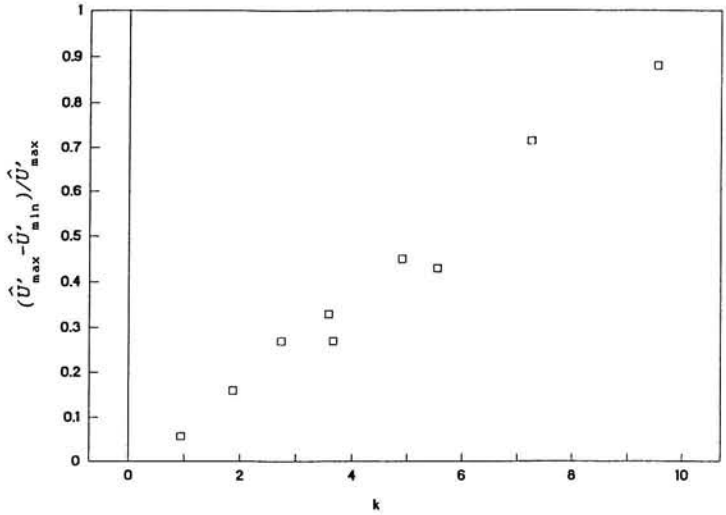

Fig. 3.4 The reduction of the perturbation amplitude. The abscissa represents the reduced frequency.
The ordinate stands for the amplitude reduction, scaled with the corresponding value at the trailing edge.

It is clear from this graph that at low reduced frequency the amplitude reduction is small, extrapolating to zero. The reduction increases with the reduced frequency systematically, indicating that the magnitudes of the two waves is becoming closer. This behaviour is physically quite plausible. Because at low reduced frequency time derivative $\partial u/\partial t$ is small, the inertia force in the lower deck is also small. The corresponding viscous shear force is therefore small, implying a smaller production of vorticity. On the other hand, in the leading part of the boundary layer, since the period is long, the diffusion of vorticity generated on the solid surface is more efficient (this can be expressed in terms of the penetration depth--a function of ν/ω, where ν is the dynamic viscosity, and ω is the angular frequency of the oscillation), so that the outer wave should be stronger. While at high reduced frequency the situation is reversed.

From the definition of the reduced frequency, equation (3.1), we see that it in fact represents the unsteadiness with respect to the mean flow. A wave structure should depend on this, as can indeed be seen in figure 3.5--the reduced frequency uniquely determines the wave structure.

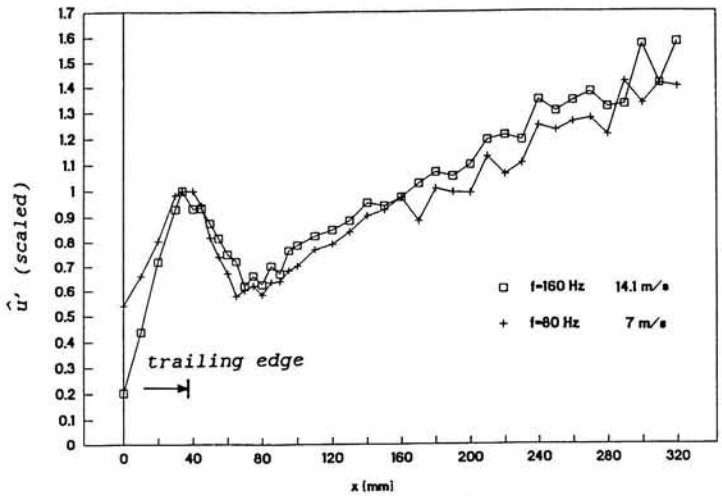

Fig. 3.5 The reduced frequency determines the wave structure. The perturbation amplitude is here scaled with its value at the trailing edge.

Vorticity generation is found to be linearly dependent on the strength of the excitation as can be seen in figure 3.6

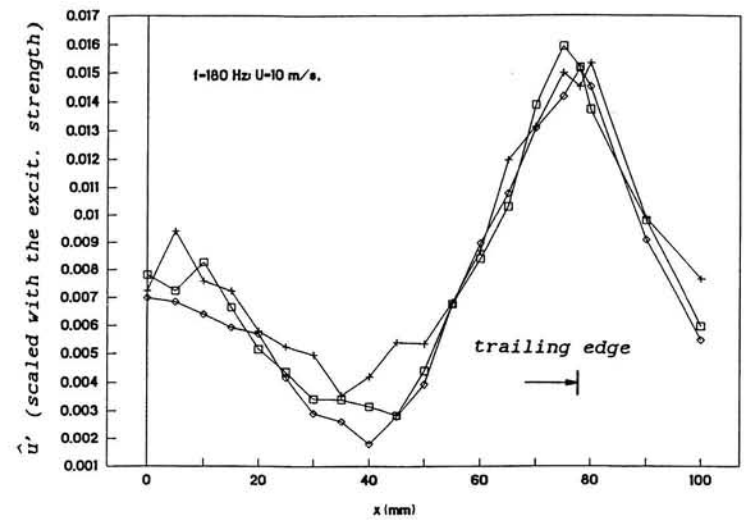

Fig. 3.6 The linear dependence of perturbation amplitude on the strength of the excitation. The velocity amplitudes are scaled with the amplitudes of the corresponding excitation

4. Conclusions

Based on the triple deck theory, it is argued that convection of shed vorticity due to an oscillating airfoil is conceived in a two-wave structure. Experimental study confirms this conjecture.

The experimental results also provide an indirect evidence of the existence of the triple deck structure which was formally derived for laminar flow with limiting Reynolds number.

The velocity perturbations are found to be linear with respect to the excitation.

References

Ashley, H. & Landahl, M. 1965, aerodynamics of wings and bodies. Addison-Wesley, Reading, Massachusetts.

Brown, S.N. & Stewartson, K. 1970, trailing edge stall. JFM. vol.42.

Brown, S.N. & Daniels, P.G. 1975, on the viscous flow about the trailing edge of a rapidly oscillating plate. JFM. vol.67.

Brown, S.N. & Cheng, H.K. 1981, correlated unsteady and steady laminar trailing edge flows. JFM. vol.108.

Crighton, D.G. 1985, the Kutta condition in unsteady flow. Ann.Rev.Fluid Mech., vol.17.

Daniels, P.G. 1978, on the unsteady Kutta condition. Q.J.Mech.Appl.Math. vol.31.

Goldstein, S. 1930, concerning some solutions of boundary layer equations in hydrodynamics, Proc.Cambridge Phil.Soc. vol.26.

Messiter, A.F. 1983, boundary-layer interaction theory, J.Appl.Mech., Trans.ASME. vol.50.

Meyer, R.E. 1983, a view of the triple deck, SIAM J.Appl.Math. vol.43.

Riley, N. & Stewartson, K. 1969, trailing edge flows, JFM, vol.39.

Stewartson, K. 1968, on the flow near the trailing edge of a flat plate, Proc.Roy.Soc. ser.A, vol.306.

Stewartson, K. 1969, on the flow near the trailing edge of a flat plate II, Mathematika, vol.16.

Stewartson, K. 1974, multistructured boundary layers on flat plates and related bodies, Advances in Applied Mechanics, ed. C.-S.Yih, vol.14. New York: Academic.

Wang, Z. & Coene, R. 1991, the two-wave structure in the wake of an oscillating airfoil, The First European Fluid Mechanics Conference, Cambridge.

Computers and fluid dynamics

By P. Wesseling

Faculty of Technical Mathematics and Informatics
TU Delft

One may try to solve the equations of mathematical physics in one of two ways: analytically or numerically. Perhaps the nicest and certainly fora long time the only way to solve is the analytical approach. Professor Steketee is a master and inspiring teacher of this art. Analytic solutions often enhance physical insight and the inaccuracies inherent in numerical approximation and the uncertainties due to the possible (even likely) occurrence of programming errors are avoided. Analytical work is often of great elegance and beauty, and getting acquainted with this field as a student of aerospace engineering has led me to devote my career to applied mathematics. However, at an early stage I found out that computers are hard to avoid. Solving, under the guidance of professor Steketee, the problem of the magnetohydrodynamic flow around an impulsively started flat plate in terms of an infinite series of Bessel functions gave me great satisfaction, but when approximating this sum numerically in order to get hard numbers the computer was needed. To my chagrin the results did not look too good for certain parameter values.This was due to slow convergence of the series, cancellation of significant digits and inaccurate approximation of the Bessel functions. Given, furthermore, the many thorns on the path of the analyst grappling with nonlinear problems, the insistence of the National Aerospace Laboratory that work be done on certain problems that did not invite ananalytical approach, and jobmarket opportunities, the present author may perhaps be excused for straying away from analysis and into numerical computing later in life; not abandoning fluid dynamics, however.

I will present some thoughts on the relation between computing and fluid mechanics. Fluid dynamics is a classical discipline. The physical principles underlying the flow of simple fluids such as water and air have been understood since the times of Newton (although the master made a small error in his derivation of the velocity field between two rotating concentric cylinders) and the mathematical formulation has been complete for a century and a half. The governing equations are called the Navier-Stokes equations. If the velocity of the flow is small compared with the speed of sound ($\cong$ 300 m/s for air at sea-level) the fluid may be regarded as incompressible, and for a given geometry the flow depends on only one dimensionless parameter, the Reynolds number Re. It is a notable fact that $Re >> 1$ for most industrial flows. For

example, $Re \equiv 7 \cdot 10^4$ for flow of air at 1 *m/s* along a flat plate 1 *m* long under room conditions.
One of the most surprising and delightful features of fluid dynamics is the phenomenon that a rich variety of solutions of the Navier-Stokes equations evolves as $Re \rightarrow \infty$. The intricate and intriguing flow patterns accurately rendered in masterful drawings by Leonardo da Vinci, or photographically recorded in Van Dyke (1982) [13] are surprising, because the physics underlying the Navier-Stokes equations is just a simple mass and momentum balance. A "route to chaos" develops as $Re \rightarrow \infty$, resulting in turbulence.
Ideally, one would like to simulate turbulent flows directly on the computer, choosing the computational grid fine enough to resolve the smallest scales of fluid motion that occur. The ratio of the length scales η and L of the smallest and largest turbulent eddies satisfies $\eta/L = O(Re^{-3/4})$ (Tennekes and Lumley (1972) [11]) with Re based on L. The size of the flow domain is larger than L, where as the mesh-size of the computational grid needs to be smaller than η, so that the number of cells required in the grid is at least $(L/\eta)^3 = O(Re^{9/4})$. With $Re \equiv 10^7$(as for a large aircraft) we have $Re^{9/4} \equiv 5 \cdot 10^{15}$. Bearing in mind that for the most powerful computers that exist today memory size is measured in megawords and speed in giga (= 10^9) operations/*s* (the NEC SX-3/12 of NLR has a top speed of 2.75gigaop/*s*) we see that direct simulation of turbulent flows is out of the question. Hence, simplified mathematical models must be used.

With large eddy simulation only in regions where viscous effects are significant and inviscid modeling elsewhere for the flow around a large aircraft, Chapman (1979) [2] has estimated a requirement of $8 \cdot 10^8$ grid cells and 10^4 megawords storage. Although strict estimates of computational complexity are out of the question in the present context, it is reasonable to expect that algorithms requiring fewer than roughly 100 operations per cell and per time-step will never be found. Postulating a requirement of 100 time steps we arrive at a lower bound for the computational cost of $8 \cdot 10^3$ giga-operations; 10^6 seems more representative for algorithms available at present. What is needed then for a numerical windtunnel is a teraflop (10^3 giga-operations/*s*) machine with gigaword storage; such machines may appear in this decade.
This gives a prospect of physical windtunnels being (partly) put out of business by numerical windtunnels. Also, the numerical analyst may put himself out of business. After all, when the optimal algorithm has been found there is no need for further numerical research. The concept of optimality cannot be defined precisely for the complicated problems under discussion. But, following Brandt (1977) [1], one may say that an algorithm is optimal if it finds the solution within discretization accuracy in just a few work units. A reasonable definition of a work unit (WU) is: the number of grid cells times the number of unknowns per cell times the number of arithmetic operations required to formulate the discrete equations for a cell. How far are we from reaching the goal of solving in a few WU? Table 1 (from Gentzsch et al. (1988) [3]) gives estimates of the required number of floating point operations (flop) for certain codes (by Jameson c.s.) to compute steady compressible inviscid flows in two

and three dimensions, using a number of iterative cycles to converge to engineering accuracy.
How much could these results still be improved by use of more efficient algorithms? Taking as a very rough guess 1 WU = 500 N with N the number of cells and assuming the work required to be 10 WU, we obtain table 2. Comparison of tables 1 and 2 gives an indication that much is still to be gained from algorithmic improvements. Once the targets of table 2 have been reached it would seem that numerical analysts will have to look for other work.

Table 1: Computing work for compressible inviscid flow computation.

Model	Flop/cell /cycle	No. of cells	No. of cycles	Total gigaflop
Potential, 3D	500	10^4	100 – 200	5 – 10
Euler, 2D	400	$5 \cdot 10^3$	500 – 1000	1 – 2
Euler, 3D	950	10^5	200 – 500	20 – 50

Table 2: Estimate of lower bound for computing work.

Model	No. of cells	10 WU gigaflop
Potential, 3D	10^4	0.050
Euler, 2D	$5 \cdot 10^3$	0.025
Euler, 3D	10^5	0.500

Reducing computational cost to just a few WU has become possible in principle thanks to the appearance of multigrid methods on the scene. For introductions to these methods, see for example [1], [4] or [14]. The basic multigrid principle is easily explained. Let the nonlinear system of discrete equations on grid G (approximating for example partial differential equations from fluid dynamics) to be solved be denoted by $N(\boldsymbol{u}) = \boldsymbol{b}$, and let application of a simple iterative method be denoted by $S(\boldsymbol{u}, \boldsymbol{b})$. Usually, S converges slowly and the computing work required is $O(N^\alpha)$ with $\alpha > 1$ (often, $\alpha = 3/2$). Multigrid makes it possible to have $\alpha = 1$. It suffices to explain the basic two-grid algorithm. Let $\bar{G}$ be a coarse grid (obtained for example by doubling the mesh-size of G) and let the discrete approximation of our system of differential equations on $\bar{G}$ be denoted by $\bar{N}(\bar{\boldsymbol{u}}) = \bar{\boldsymbol{b}}$; coarse grid quantities will be denoted by an overbar. Furthermore, let P be an (interpolating) prolongation operator from $\bar{G}$ to G, and let R be a restriction operator from G to $\bar{G}$. Then the basic nonlinear two-grid algorithm is given by

$$
\begin{gathered}
S(\boldsymbol{u},\boldsymbol{b}) \\
\text{Choose } \bar{\boldsymbol{v}} \\
\bar{\boldsymbol{b}} = \bar{N}(\bar{\boldsymbol{v}}) + sR(\boldsymbol{b} - N(\boldsymbol{u})) \\
\text{Solve } \bar{N}(\bar{\boldsymbol{u}}) = \bar{\boldsymbol{b}} \\
\boldsymbol{u} = \boldsymbol{u} + P(\bar{\boldsymbol{u}} - \bar{\boldsymbol{v}})/s \\
\mathrm{S}(\boldsymbol{u},\boldsymbol{b})
\end{gathered}
$$

Here s is a real parameter that may be chosen to ensure that $\bar{\boldsymbol{b}}$ is in the range of $\bar{N}(\bar{\boldsymbol{u}})$ in the vicinity of the solution that is sought. A possible choice of $\bar{\boldsymbol{v}}$ is $\bar{\boldsymbol{v}} = R\boldsymbol{u}$. The main idea is to choose S such that the error is made smooth rapidly, which is usually not difficult. The smooth error (here approximated by $\boldsymbol{u} - \boldsymbol{v}$ is then approximated on the coarse grid. Solving $\bar{N}(\bar{\boldsymbol{u}}) = \bar{\boldsymbol{b}}$ is still expensive, of course; therefore this is done approximately in the same way, by introducing a still coarser grid, etc. Recursive application of the twogrid method gives us multigrid. For a recent survey of applications of multigrid in computational fluid dynamics, see [16], [15].

We will now discuss a particular mathematical flow model in more detail, namely the full potential equation for transonic flow. The history of research on this equation shows an interesting interplay between analysis, numerics and physical experiment. As flight speeds increased there arose a need to model compressibility effects more exactly than was possible with the linear potenial equation. In the transonic regime a suitable model is the full potential equation:

$$\operatorname{div}(\rho \operatorname{grad} \phi) = 0, \tag{1}$$

$$\rho = \rho_\infty \{1 + \frac{\gamma - 1}{2} M_\infty^2 (1 - q^2/q_\infty^2)\}^{1/(\gamma - 1)}, \; q = |grad\, \phi| \tag{2}$$

in a notation that is familiar to aerodynamicists. Equation (1) is locally elliptic where the flow is subsonic, and hyperbolic where the flow is supersonic. This highly nonlinear equation played an important role in the 'transonic controversy' concerning thestable existence of shock-free transonic airfoil flows, which was resolved in the sixties. In pure mathematics, 'controversies' are usually settled one way or another by hard analysis. Not so in applied mathematics. In fact, the deepest analytical result available about (1), (2) points in the wrong direction. The theory of [6] shows that if there exists a shock-free transonic potential flow around an airfoil, then such a solution does not exist when the airfoil contour is infinitesimally perturbed. Quite naturally, this led many to believe that equations (1), (2) with boundary conditions for a given airfoil would be ill-posed and hence not amenable for direct numerical solution. Fortunately, this is not so, as will be seen shortly. It was also thought that in practice shock-free transonic flow would be unstable. On the other hand, mathematical analysis also helped a great deal in resolving the matter by providing exact shock-

free solutions of (1), (2). More or less shock-free flows in windtunnels were obtained by Pearcy [9], who designed his airfoil shapes in an intuitive way. But, using a hodograph method Nieuwland [8] constructed shock-free airfoil solutions of (1), (2) in a systematic way. This is a prime example of how far one may go in constructing analytical solutions of difficult nonlinear equations; not without the use of computers, however. Spee demonstrated the stability of these flows experimentally by subjecting them systematically to disturbances, investigations which were the subject of his Ph.D. thesis [10], for which professor Steketee was the advisor.

So much for the role of analysis and experiment in the 'transonic controversy'. Numerical computation also played its role. Nieuwland's approach, being based on the hodograph method, does not allow the solution of (1), (2) around a given airfoil, but with a direct numerical method this is possible. Furthermore, solutions with shocks can be computed. The fact that good results could be obtained by numerical means [5] despite the unavoidable presence of numerical inaccuracies lent further credence to the existence of stable shock-free solutions. This work has no direct bearing on (1), (2), because Magnus and Yoshihara solved the Euler equations. Furthermore, their method was impractical due to its inefficiency. A great step forward was the method of Murman and Cole [7]; the basic principles of this method are still shared by all modern methods for solving the small perturbation version of (1), (2) numerically. Supercritical solutions with and without shocks could be obtained numerically in a stable manner with satisfactory accuracy. I think the numerical approach gets around Morawetz's theorem because of the discretization error, which, as we will see shortly, has to be designed to be of a certain nature (providing the right kind of irreversibility), and plays a positive role for a change.

We will now discuss numerical methods for (1), (2) in some more detail. For simplicity it is assumed that solution takes place in two dimensions and Cartesian coordinates (x, y). In practical applications general body-fitted curvilinear coordinates are used, but the basic principles remain the same. A computational grid G is chosen as follows:

$$G = \{ (x,y) : x = x_j = j\Delta x,\ y = y_k = k\Delta y,\ j = 0,1,2 \ldots, J,\ k = 0,1,2 \ldots K \} \quad (3)$$

Figure 1 shows part of the grid, with some arbitrary grid point numbering.

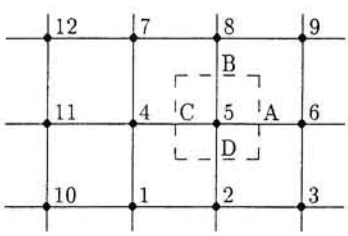

Fig. 1 Part of computational grid

The potential ϕ is approximated in the grid points. Discretization takes place by the finite volume method. Equation (1) is integrated over finite volumes (indicated by dashed lines in figure 1) surrounding the grid points. This gives

$$0 = \iint_{\Omega} div(\rho\, grad\, \phi)\, d\Omega = \oint_{\partial\Omega} \rho \frac{\partial \varphi}{\partial n} ds \equiv \rho \frac{\partial \varphi}{\partial x} \Big|_C^A \Delta y + \rho \frac{\partial \varphi}{\partial y} \Big|_D^B \Delta x$$

$$\equiv \{\rho_A (\varphi_6 - \varphi_5) - \rho_C (\varphi_5 - \varphi_4)\} \frac{\Delta y}{\Delta x} + \{\rho_B (\varphi_8 - \varphi_5) - \rho_D (\varphi_5 - \varphi_2)\} \frac{\Delta x}{\Delta y} \qquad (4)$$

This is a good discretization in elliptic regions (subsonic flow), but it is unstable in hyperbolic regions (supersonic flow). An important insight of Murman and Cole was that they realized this, and switched to another, stable, discretization in supersonic flows. Assuming for simplicity that the flow is mainly in the positive x-direction, the hyperbolic scheme of Murman and Cole is obtained by biasing $\partial\varphi/\partial x$ in the upwind direction, for example

$$\frac{\partial \varphi}{\partial x} \Big|_A \equiv (\varphi_5 - \varphi_4)/\Delta x \qquad (5)$$

A more modern and more accurate way to stabilize the scheme in supersonic zones is to bias the density evaluation, for example (cf.(2))

$$\rho_A \equiv \rho(|\, grad\, \varphi|_C) \qquad (6)$$

That some upwind bias has to be built in also follows from the following physical consideration.

The potential flow model is completely reversible (free from dissipation). As a consequence it allows not only (isentropic approximations of) compression shocks, but also expansion shocks, which are unphysical. To avoid this some irreversibility must be built in.This is done by upwind biasing as just described.

We will not discuss the implementation of boundary conditions, but turn our attention to the solution of the discrete system. In order to gain some insight we study the small disturbance limit of (1),(2). Let $\boldsymbol{u} = (1 + u, v)$ with $|u|, |v| << 1$. From (2) it follows that

$$\rho \cong \rho_\infty (1 - M_\infty^2 \partial\varphi / \partial x) \tag{7}$$

with ϕ now the disturbance potential, the equation for which follows from (4):

$$\{ \rho (1 + \frac{\partial \varphi}{\partial x}) \} \Big|_C^A \Delta y + (\rho \frac{\partial \varphi}{\partial y}) \Big|_D^B \Delta x = 0 \tag{8}$$

Equations (7), (8) are the finite volume version of the transonic small disturbance equation. In our choice of solution methods we will be guided by the requirement that the method should at least work for simple-to-analyze simplifications of (7), (8). If $M_\infty^2 < 1$ then ρ is not upwind biased,and is evaluated in the same points as $\partial\varphi/\partial x$. Equation (8) is further simplified by neglecting the non linear term (which is of course physically inaccurate in the transonic case $| M_\infty^2 - 1 | << 1$) , which gives

$$(1 - M_\infty^2) \frac{\partial \varphi}{\partial x} \Big|_C^A \Delta y + \frac{\partial \varphi}{\partial y} \Big|_D^B \Delta x = 0 \tag{9}$$

If $M_\infty^2 > 1$ then ρ is evaluated at a location shifted Δx to the left. Defining the shift operator T_x by $T_x \phi_{kj} = \phi_{k-1,j}$ we obtain, again neglecting the nonlinear term

$$(1 - M_\infty^2 T_x) \frac{\partial \varphi}{\partial x} \Big|_C^A \Delta y + (\frac{\partial \varphi}{\partial y}) \Big|_D^B \Delta x = 0 \tag{10}$$

The derivatives in (9) and (10) are approximated by central differences. For (3), (9) and (10) the system of discrete equations can be denoted by

$$\sum_{\alpha=-2}^{1} \sum_{\beta=-1}^{1} \alpha_{\alpha\beta} \phi_{j+\alpha,k+\beta} = 0 \tag{11}$$

The coefficients $\alpha_{\alpha\beta}$ (nonlinear in the case of(4)) are easily determined by the reader. Next, an iterative solution method has to be chosen for (11). We require this method to work both for (9) and (10); experience shows that it then also works for (4) (letting the (in this case nonlinear) coefficients $\alpha_{\alpha\beta}$ lag one iteration behind). Murman and Cole [7] propose to use the forward vertical line Gauss-Seidel method, given by

$$\sum_{\alpha=-2}^{0} \sum_{\beta=-1}^{1} \alpha_{\alpha\beta} \phi_{j+\alpha,k+\beta}^{(n+1)} = - \sum_{\beta=-1}^{1} \alpha_{1\beta} \phi_{j+1,k+\beta}^{(n)} \tag{12}$$

where n denotes the iteration number. Because in the case of (9) and (10) $\alpha_{\alpha\beta}$ is constant Fourier analysis is applicable to the study of convergence of (12). On $G$the grid function $\phi_{j\,k}^{(n)}$can be developed in the following Fourier series (assuming periodic boundary conditions):

$$\phi_{j\,k}^{(n)} = \sum_{\Theta} c^{(n)}(\theta_1,\theta_2)\exp\{i\ (j\,\theta_1 + k\,\theta_2)\} \tag{13}$$

with

$$\Theta = \{\ (\theta_1,\theta_2)\ :\ \theta_1 = 2\pi m_1/J, m_1 = -\tilde{J},-\tilde{J}+1,\ldots,\tilde{J},\ \tilde{J} = (J-1)/2,$$

$$\theta_2 = 2\pi m_2/K,\ m_2 = -\tilde{K},-\tilde{K}+1,\ldots,\tilde{K},\ \tilde{K} = (K-1)/2\} \tag{14}$$

(assuming J,K to be odd). One easily finds

$$c^{(n+1)}(\theta_1,\theta_2) = g(\theta_1,\theta_2)\,c^{(n)}(\theta_1,\theta_2) \tag{15}$$

with the amplification factor g given by

$$g(\theta_1,\theta_2) = -\frac{\sum_{\beta=-1}^{1}\alpha_{1\beta}e^{i(\theta_1+\beta\theta_2)}}{\sum_{\alpha=-2}^{0}\sum_{\beta=-1}^{1}\alpha_{\alpha\beta}e^{i(\alpha\theta_1+\beta\theta_2)}} \tag{16}$$

The rate op convergence is determined by

$$\rho = \max\{|g(\theta_1,\theta_2)| : (\theta_1,\theta_2)\in\Theta\backslash(0,0)\} \tag{17}$$

where we have encluded $\theta_1 = \theta_2 = 0$ because ϕ is determined only up to a constant. The number of iterations required is proportional to $-1/\log\rho$.

What conclusions can be drawn from (16), (17) about the rate of convergence? In the case of (9) one finds

$$|g(\theta_1,\theta_2)| = \mu/|2(1-\cos\theta_2) + 2\mu - \mu e^{-i\theta_1}| \tag{18}$$

with $\mu = (1 - M_\infty^2)(\Delta y/\Delta x)^2$. Choosing $J = K$ (for simplicity) and $\theta_1 = \theta_2 = \theta = 2\pi/J$ we find for $J >> 1$:

$$|g(\theta,\theta)| \cong \{1 + \theta^2(1 + 2/\mu)\}^{-1} \tag{19}$$

Since $\rho \geq |g(\theta,\theta)|$ we have

$$-1/\log\rho \gtrsim \{\theta^2(1 + 2/\mu)\}^{-1} \tag{20}$$

so that the required number of iterations is $O(J^2) = O(N)$ with N the number of unknowns. Hence, for $N >> 1$ convergence will be slow, and since the work of one iteration is $O(N)$ total work will be $O(N^2)$, which is far removed from our optimum goal of just a few *WU*. Since (11) involves a total of 23 operations (multiplications and additions) for given $\alpha_{\alpha\beta}$ (in general coordinates all $\alpha_{\alpha\beta} \neq 0$ and evaluation of $\alpha_{\alpha\beta}$ requires an additional number of operations, a reasonable definition of the work unit for the present problem would be

$$1\ WU = 50\ N\ flop \tag{21}$$

and an optimal algorithm would solve the problem to engineering accuracy in $5WU$, say, one may be content with an algorithm requiring 250 *N flop*. We see that the method of Murman and Cole, although a breaktrough in its day, was still far from optimal.

Multigrid algorithms bring optimal algorithms within reach. Used as a smoother in a multigrid method, the Gauss-Seidel method does not have to be iterated till the required precision is reached, but it suffices to make the error smooth. The smoothing performance may be analyzed with Fourier analysis. A suitable definition of non-smooth Fourier wave numbers is (cf. (14))

$$\tilde{\Theta} = \Theta \setminus (-\pi/2, \pi/2) \times (-\pi/2, \pi/2) \tag{22}$$

and a smoothing factor $\bar{\rho}$ may be defined as (cf. (17)):

$$\bar{\rho} = \max\{|g(\theta_1, \theta_2)| : (\theta_1, \theta_2) \in \tilde{\Theta}\} \tag{23}$$

For equation (10) (the supersonic case) one finds the folowing smoothing factors [17]:

Table 3 Fourier smoothing factor $\bar{\rho}$ for equation (10). Forward vertical line Gauss-Seidel smoothing; $J = K = 64$

M_∞	1.0	1.1	1.3	1.7
$\bar{\rho}$	0.34	0.34	0.35	0.38

One finds that $\bar{\rho}$ does not increase with J, K. It suffices to apply only one smoothing iteration on each grid, and one finds an error reduction factor of about 0.4 per multigrid cycle, at a cost of about 2 *WU* per cycle, so that our algorithm is fairly optimal. Using so-called nested iteration [4], [14] the discrete problem can be solved within truncation error in about 10 *WU*.

This type of method has been generalized to three dimensions and further developed (notably by introducing a more sophisticated smoothing method) in [12]. It now forms the basis of the MATRICS program package, in daily use at NLR for the aerodynamic analysis of transonic potential flow around wing-body combinations.

This brief survey of transonic potential flow is illustrative of the present situation in fluid dynamics, with experiment, theoretical analysis and large scale numerical computing providing increasing insight and predictive capability for practical flows, in mutual interaction and dependence.

October 25, 1991.

References

1 A. Brandt. Multi-level adaptive solutions to boundary value problems. *Math. Comp.*, 31:333-390, 1977.

2 D. R. Chapman. Computational aerodynamics development and outlook. *AIAA J.*, 17:1293 - 1313, 1979.

3 W. Gentzsch, K.W. Neves, and H. Yoshihara. *Computational Fluid Dynamics: Algorithms and Supercomputers. AGARDograph No. 311, AGARD, Neuilly-sur-Seine, France,* 1988.

4 W. Hackbusch. *Multi-grid methods and applications.* Springer-Verlag, Berlin, 1985

5 R. Magnus and H. Yoshihara. *Inviscid transonic flow over airfoils.* AIAA Paper 70-47, 1970.

6 C.S. Morawetz. On the non-existence of continuous transonic flows past profiles. *Comm. Pure Appl. Math.*, 9:45-68, 1956

7 E.M. Murman and J.D. Cole. Calculation of plane steady transonic flows. *AIAA Journal,* 9:114-121, 1971

8 G.Y. Nieuwland. *Transonic potential flow around a family of quasi-elliptical aerofoil sections.* PhD thesis, University of Groningen, 1967.

9 H.H. Pearcy. The aerodynamic design of section shapes for swept wings. In *Advances in Aeronautical Sciences*, pages 277-322, Pergamon Press, London, 1962.

10 B.M. Spee. *Investigations on the transonic flow around aerofoils*. PhD thesis, Delft University of Technology, 1969.

11 H. Tennekes and J.L. Lumley. *A First Course in Turbulence*. MIT Press, Cambridge, Massachussets, 1972.

12 A.J. Van der Wees. *A nonlinear multigrid method for three-dimensional transonic potential flow*. PhD thesis, Delft University of Technology, 1988.

13 M. Van Dyke. *An Album of Fluid Motion*. The Parabolic Press, Stanford, 1982.

14 P. Wesseling. *An introduction to multigrid methods*. John Wiley, Chichester, 1991.

15 P. Wesseling. Large scale modeling in computational fluid dynamics. In E.F. Deprettere and A.J. van der Veen, editors, *Algorithms and parallel VLSI architectures*, pages 277-306, Elsevier, Amsterdam, 1991. Volume A: Tutorials.

16 P. Wesseling. Multigrid methods in computational fluid dynamics. *Z. angew. Math. Mech.*, 70:T337-T348, 1990

17 P. Wesseling. A survey of Fourier smoothing analysis results. In W. Hackbusch and U. Trottenberg, editors, *Multigrid Methods III*, pages 105-127, Birkhäuser, Basel, 1991. Proc., Third Int. Conf. on Multigrid Methods. International Series of Numerical Mathematics Vol. 98.

Part II

Personal memories and reflections

Dear Jaap

This is a short note with some recollections from sabbatical leaves, both yours and ours.

We remember your visit to Ann Arbor back in 1970 and 1971. You and your family's enjoyment of all this university city had to offer was most satisfying to us all. I particularly recall your intensive efforts in swimming, including some hair raising exploits in water polo. This was all entwined with our long discussions on things fluid mechanical, of course. You and Ruth and the boys were a joy to everyone.

I also recall the gracious manner in which you and Ruth arranged for my seminar visit and later for Sue's and my visit as part of an AGARD lecture tour during my sabbatical in 1978. At one and the same time you managed to arrange for technical tours and seminars for me, sightseeing tours for my wife, wonderful dinners, and beyond all, to make us feel relaxed after a hectic trip to Delft. Yours is a great talent!

So, Jaap, Sue joins me in sending to you and to Ruth, our fondest and warmest congratulations on your retirement. We hope you'll see fit to visit us now that you should have at least a bit more time for such things.

Best regards.

Sincerely yours,

Thomas C. Adamson, Jr.
professor and chairman

Barkey Wolf

Achter de horizon

Weldra gaat professor Steketee met emeritaat. Ik kan me hem als emeritus eigenlijk niet goed voorstellen. Hoe gaat hij zijn dagen doorbrengen? In de tuin aan de Rotterdamseweg de post doornemen? Elke dag het orgel van de Nieuwe Kerk bespelen? Ik denk het niet. Velen van ons dromen overigens nu al van zo'n dagindeling: weg vergaderingen, weg spanningen, back to the basics.

Na een mooie loopbaan rustig aandoen. Machtig.

Zo niet voor de jubilaris. Zijn werk deed hij met veel enthousiasme. Dat merkte je al wanneer je de 10^e verdieping binnenliep. Van alle zijden keken grote voorgangers je aan, gestreng en geleerd en een enkeling met pretoogjes. Dit was een vakgroep met traditie, dat voelde je. Hier ontsteeg men de vliegtuig industrie. Hier richtten ogen zich naar onderwerpen ver achter de horizon van de alledaagse techniek. Voortstuwing van vissen, ingewikkelde schokbuis stromingen en complexe verbrandings modellen. En dat waren nog maar afstudeeropdrachten...

Was de jubilaris niet op zijn kamer dan bromde hij wel ergens: 'Jongen, wat heb jij lekkere koffie gezet, jij verdient een medaille'; en was hij dus in de koffiekamer te vinden. Daarna kon hij enthousiast vertellen over Canadese collega's en Poolse conferenties. Immer vol respect sprak hij over professor Burgers, een inspirerend leermeester met een brede interesse.

Om computers gaf professor Steketee niet veel. Gebruik van computers leek inderdaad dieper inzicht in de materie te verdoezelen. Het nut van analytische oplossingen sprak hem meer aan. Veel problemen in de stromingsleer waren immers al in de vorige eeuw tot in de kiem geanalyseerd zonder enige electronica. Meer ervaren studenten merkten dan ook al snel dat Lamb's 'Hydrodynamics' (1879!) een effectieve gespreksopener was.

Begrijpelijk dat zo'n plezier in het werk niet plotseling ophoudt op het moment van emeritaat. Pas repte hij over een kamertje in de kelder van het gebouw. Daar zou verder werken in alle rust zeer goed mogelijk zijn. Ik hoop dat het hem lukt dat kamertje te krijgen. Voor de vakgroep en de afdeling zou het zonde zijn zijn ervaring te missen.

Zelf heb ik een fijne tijd in de vakgroep gehad. De sfeer was er open en plezierig. De discussies levendig. Onderwerpen varieerden van russische klassieken tot computers. Iedereen was bereid te helpen bij problemen in het werk. Bovendien heeft professor

Steketee mij enorm geholpen een promotieplaats in Cambridge te krijgen. Een kans die ik met beide handen aangreep en waar ik geen ogenblik spijt van heb gehad. Het onderzoek betrof turbulente loslaatblazen onder een pijlhoek. Het was een uitgelezen mogelijkheid om juist dáár wetenschappelijk onderzoek te doen. Terug in Nederland werk ik nu in de olie- en margarine-industrie. Een sprekend voorbeeld waartoe een goede opleiding en een veelzijdige vakgroep kan leiden!

Van harte wens ik professor Steketee en zijn vrouw nog een gelukkige tijd toe.

Barkey Wolf
oktober 1991

Een Pythagoreeër

In mijn middelbare schooltijd werden de lessen klassieke talen nu en dan verlevendigd met een anecdote. Zo herinner ik mij nog erg goed het volgende min of meer historische verhaal.
Ongeveer twee en half duizend jaar geleden bezocht Euclides, een van de Pythagoreeërs afkomstig van Samos, Alexandrië, een welvarende stad aan de monding van de Nijl. In Alexandrië hield hij verschillende lezingen over zijn stelsel van wiskundige stellingen. Wanneer een toehoorder hem vroeg naar het praktische nut van van een of andere stelling zei Euclides minachtend tegen een van zijn slaven: 'Hij wil profijt trekken uit de wetenschap – geef hem een muntstuk'. Dit was indachtig één van de motto's der Pythagoreeërs: 'Een diagram en een schrede (voorwaarts), geen diagram en een muntstuk'.

In de tijd dat ik als student aan de TH-Delft met professor Steketee kennis maakte was dit motto aan universiteiten en hogescholen in Nederland in brede kring geaccepteerd. Ook de theoretische aerodynamica groep hanteerde dit beginsel. Later werd dit principe op bestuurlijk niveau als luxe beschouwd en is het verdrongen door 'maatschappelijke relevantie' wat op zijn beurt nog weer is verengd tot 'commerciele relevantie' in de vorm van voorwaardelijke financiering en derde geldstroom. Toch is Prof. Steketee ook in dit minder vriendelijke klimaat er in geslaagd het Pythagorese beginsel te handhaven als leidraad bij het onderzoek in onze groep. Hierbij is hij mogelijk heen-en-weer geslingerd tussen de Zeeuwse soberheid en standvastigheid. Echter noch in de periode van 'schijnbaar onbegrensde' groei noch tijdens de operatie 'krimp en concentratie' heeft hij zijn standpunt laten beinvloeden door uitwendige omstandigheden.

Bij de werkbesprekingen die wij hielden tijdens mijn promotie onderzoek heeft hij mij diverse malen ervan doordrongen bij de keuze van de onderwerpen van onderzoek niet de waan van de dag te volgen. Hierbij kwam ook dikwijls zijn in een andere context fameuze 'autobusmodel' ter sprake.

In dezelfde 'Griekse' traditie (hoewel meer Sokrates) pasten de lunches van de sectie theoretische aerodynamica. Daarbij slaagden wij er tot ons genoegen onder leiding van prof. Steketee altijd in binnen een tijdsbestek van drie kwartier alle actuele technisch-wetenschappelijke maar vooral profane (wereld)problemen te analyseren, te ordenen en indien nodig theoretisch op te lossen. Daarbij toonde hij telkens weer een groot historisch besef.

Luctor et Emergo

Voor ik prof. Steketee in 1961 in levenden lijve ontmoette wist ik al van zijn bestaan. Als oud-lid van de Delftse Studenten Vereniging Sint Jansbrug kwam hij voor in diverse anecdotes en sterke verhalen die oude heren doorgaven aan jonge heren. Zo was er een zekere Steketee, een goede Zeeuw uit Middelburg, die Bach kon spelen op de piano, uit z'n hoofd! Diezelfde Steketee was ook oprichter en voorzitter geweest van de 'Vereniging tot het hakken van wakken', zo verluidde het. Er was enige onzekerheid of dit laatste was bedoeld voor de vogels of voor de vissen. Later bleek mij dat het voornamelijk om de vogels ging. De vissen koelen af met het water, hun metabolisme wordt heel traag, you know, that has been taken care of.

Ik had in 1960-'61 Voortgezette Stromingsleer gelopen bij prof. Broer maar het vak werd toen overgenomen door prof. Steketee en ik deed dus mondeling examen bij hem. Ik ben er zeker van dat ik meer van hem onder de indruk was dan hij van mij. Met een zekere schroom besloot ik hem voor te stellen bij hem af te studeren. Dat kon wel. Probably a good idea .... Reken dit supersone draagvlak met subsone voorranden maar eens uit. Het ging om een elliptisch probleem in een hyperbolische context dat in de literatuur over elementaire homogene velden niet behandeld werd. Ik moest nogal wat literatuur doorwerken, Stewart, Robinson, Roper, Germain, Fenain, Dorfner, Mikhlin, Heaslet en Lomax.
Ik herinner me dat ik een keer vastliep in een argumentatie van Germain. Ik stapte naar prof. Steketee toe en zei zoiets van: 'Dit gedeelte kan ik niet begrijpen. Het is te moeilijk'. Toen had ik iets verkeerds gezegd. 'Nou moet je eens goed naar me luisteren. Dit vak moet in Nederland op het hoogste niveau worden beoefend. Als ze dit soort dingen in het buitenland wel kunnen en wij vinden het te moeilijk dan kunnen we de tent hier wel sluiten. Ik zou het nog maar eens bekijken'. Ik droop af, met de staart tussen de benen en een opgerolde vlag onder de arm. Een jaar later leverde ik een verslag in met een oplossing. 'Kom volgende week maar langs voor een bespreking'. Na de bespreking zei hij: 'je bent wel geslaagd, gefeliciteerd'. Ik had blijkbaar examen zitten doen. Toen kwam de vraag of ik wetenschappelijk medewerker bij hem wilde worden. Ik heb meteen ja gezegd. Er was wel een probleem. Ik moest mijn ontslag nemen bij het N.I.V. waar ik sinds twee jaar adjunct-ingenieur was en prof. Van der Maas had andere plannen met me.
Ik heb nooit precies geweten welke plannen en ik had natuurlijk al ja gezegd tegen prof. Steketee. Het ijs onder mijn voeten kraakte en het plafond kwam bijna naar beneden. In één dag was echter alles geregeld, voor zo'n vijf en twintig jaar.

Het klimaat was goed, maar niet onbedreigd, met af en toe een bui, die meestal uit een bruine envelop tot ons kwam. Die buien kostten veel tijd en concentratie. De

Het is zijn grote verdienste dat hij door eerder genoemde kenmerken voor ons als medewerkers in de afgelopen jaren een omgeving heeft weten te handhaven, die voor het doen van onderzoek uitstekend geschikt is. We zullen trachten ook na het emeritaat van prof. Steketee deze atmosfeer te continueren.

Hans Bos

WUB, de twee fasenstructuur, 'bezuinigingen', formatieplannen, jaarverslagen (soms per cursusjaar, per kalenderjaar en een verkorte versie voor geïnteresseerden op een hoger abstractieniveau dan in de normale publikaties werden bereikt), voorwaardelijke financiering, diverse geldstromen, etc. etc. Het intrinsiek goede humeur van prof. Steketee is echter een belangrijke natuurconstante gebleken en uiteindelijk ging het altijd om de luchtvaartaerodynamica.

Als Leitmotiv in het onderzoek en het onderwijs speelde altijd Stefan Boltzmann's adagium: 'Es gibt nichts Praktischeres als eine gute Theorie'. De publikaties op het gebied van de breukmechanica, de gasdynamica, de MHD en de glasheldere colleges getuigen hiervan.
Met grote inzet en vasthoudendheid heeft prof. Steketee gestaan voor ideeën die de kern van de taak van een technische universiteit uitmaken.
Hij is een personificatie van de Zeeuwsche wapenspreuk 'Luctor et emergo' (ik strijd en ontzwem) en als ik nog eens een wak zoek weet ik precies bij welke vriend ik het zal vinden. And Ruth will be there too.

René Coene

Het graf van Gauss

Ik denk terug aan 1960 waar ik op de zolder boven de modellenverzameling als eerstejaars student druk bezig was met de constructie van een lijnenplan van een waar vliegtuig. De vloeiende vormen van de aerodynamica werden toen nog gedicteerd door de kromming van de met gewichten verzwaarde strooklatten. Dat deze kromming samenhing met drukverschillen en dat je dat kon uitrekenen, werd me pas geopenbaard bij het college Aero 1 van prof. Steketee, het eerste in een reeks van (toen nog) 4 colleges. Mijn oude diktaten van die colleges pak ik nog wel eens uit de kast. Geen ander college beschreef zo helder de essentie van de fysische wereld waar we in de toekomst mee aan de slag moesten. Maar wel een volledig abstracte, wiskundige beschrijving. Vliegtuig of vleugelvorm hoefde je niet te zoeken in dit college. Daarvoor moest je terecht bij Dobbinga waar lucht nog bestond uit laminair of turbulent bewegende partikeltjes die door Dobbinga met de hand beschreven stroomlijnen volgden. Ik denk dat de door Steketee beschreven essentie van de aerodynamica samen met de meer experimenteel gerichte uitwerking daarvan door Dobbinga de basis hebben gevormd voor mijn nog altijd voortdurende interesse in dit vak.

Het eerste persoonlijke contact met prof. Steketee, afgezien van het bijwonen van zijn colleges, had minder met aerodynamica te maken. In 1963 meldde ik mij bij hem (in zijn functie als studie begeleider) met het verzoek of er bezwaar tegen was dat ik, als beursstudent, een jaar van mijn studie opofferde aan een baantje in de studentenwereld. prof. Steketee reageerde nogal kritisch en met onbegrip. Zo'n boeiend vak had toch recht op 100 % aandacht. De toekomst was vol verwachting! Nog onlangs had hij gehoord dat men bij het NLR ontdekt had dat supersone stroming tot subsone snelheden kon worden vertraagd zonder dat dit uit oogpunt van weerstandsverhoging nadelige schokvorming tot gevolg had. Het argument heeft weinig indruk op me gemaakt. Pas later begreep ik dat het hier het werk van prof. Nieuwland betrof m.b.t. schokvrije transsone profielen dat in de '70-iger jaren zijn praktische uitwerking vond in het SKV ('Super Kritieke Vleugel') project met Fokker en het NIVR. Meer dan 10 jaar later raakte ik bij dit project betrokken; een zeer stimulerende ervaring.

Een student leeft niet bij colleges alleen. prof. Steketee was uiterst bereidwillig om, op mijn verzoek, het 2e deel van de zgn. voorontwerpoefening in te ruilen voor een theoretisch aerodynamische opgave. En hij was evenzeer bereid te bemiddelen bij prof. Erdmann, opdat ik mijn afstudeerwerk bij het NLR zou kunnen uitvoeren. En zo kwam ik dus bij het NLR terecht.

Nog verder dan Amsterdam lag Amerika, waar het toen naar ons gevoel echt gebeurde. Via contacten van prof. van der Maas waren er mogelijkheden om als

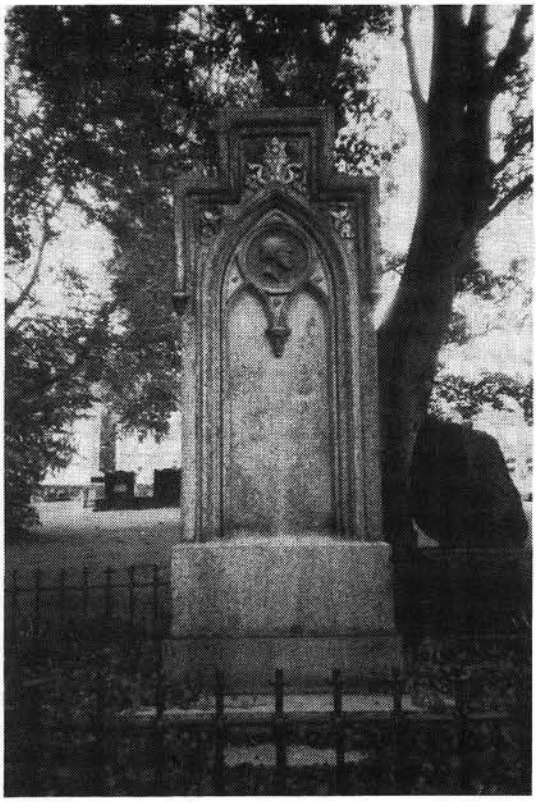

student enige jaren aan Princeton of Caltec te studeren. Ik maakte daarvoor een kans, maar het geheel sprong af op enige voor mij minder aantrekkelijke voorwaarden die door prof. van der Maas aan een dergelijk verblijf waren verbonden. Enigzins teleurgesteld luchtte ik mijn hart bij prof. Steketee, waarna hij onmiddelijk aanbood zijn contacten aan te wenden voor een verblijf aan het 'Institute for Aerospace Studies' in Toronto. En zo geschiedde. Toen ik mij in 1967 meldde, bleek al gauw dat Jaap Steketee daar een zodanige reputatie had opgebouwd dat ik mij al zeer snel deel van een familie voelde. Mijn belangrijkste negatieve punt was dat ik niet Jaap heette, zoals Steketee en de Leeuw. Ik deelde dit trouwens met 'Bill Kebinge', het hoofd van de werkplaats die bij nader onderzoek Wim Kubinga bleek te heten. Zonder overdrijving kan ik zeggen dat het verblijf in Canada, voor mij zowel als voor mijn vrouw Trudy een uiterst belangrijke ervaring is geweest waar we zeer goede vrienden aan hebben overgehouden.

In 1969 keerden wij terug in Nederland. Bij het NLR mocht ik gaan werken aan driedimensionale grenslagen, een voor Nederland klassiek onderwerp waar prof. Timman en prof. Zaat reeds vlak na de oorlog aan hadden gewerkt. Veel had ik van

prof. Steketee niet geleerd over grenslagen. Tijdens zijn promotie onderzoek is hij tussen de laminaire en turbulente grenslagen bij de 'turbulent spots' blijven steken. De studie van turbulente grenslagen bracht dan ook geen nieuwe contacten met zich mee totdat ik in 1973 op een AGARD conferentie in Göttingen mijn eerste 'paper' mocht presenteren. Het was op die conferentie dat prof. Steketee in het schemerdonker van de conferentie zaal tijdens een wat saaie middag tegen mij zei: Elsenaar, ga je mee naar het graf van Gauss? En zo wandelden wij naar dat kleine parkje achter de oude stadsmuur van Göttingen waar Gauss zich, temidden van moeders met kinderen en honden, staande hield.

Het werd niet mijn laatste wandeling met Jaap in AGARD verband. Waar het FDP vergaderde waren Jaap en Ruth te vinden en zo kwamen wij elkaar regelmatig tegen. Çesme, Toronto, Göttingen, Londen, Napels. En toen ik in 1987 in Lissabon zelf FDP lid werd kon ik met enige trots naar dat andere FDP-lid Jaap Steketee als mijn leermeester wijzen. En met niet minder genoegen beraamden Jaap en ik samen het plan om tijdens het FDP symposium in Scheveningen in 1990 Mevr. Bowes, prof. Bernard en Jaap zelf een orgelconcert te laten geven in de Lutherse kerk ter opluistering van het congres.

Na al die jaren is 'Het graf van Gauss' voor mij nog altijd synoniem met een zekere mate van relativering, nodig om je vak op plezierige wijze te beoefenen. Het kan geen kwaad af en toe weg te lopen van de actualiteit van de conferentiezaal om even stil te staan bij de groten der aarde op wetenschappelijk gebied. Een stukje van die wetenschappelijke traditie heeft Jaap Steketee op een plezierige en overtuigende wijze doorgegeven.

Bram Elsenaar
Amsterdam, september 1991

Dear prof. Steketee,

Iets te schrijven in dit boek vind ik een hele eer,
Maar op wèlke wijze geef je het beste iets weer ....
Ik heb gekozen voor de vorm van een gedicht,
Voorzien van woorden, waarin ik me tot u richt.
Ja, ik herinner het me nog, ik haal het me zo weer voor de geest,
Hoe bijna vier jaar geleden het 'sollicitatiegesprek' is geweest.
In uw kamer, met Joop Vonk erbij,
Wilde u het een en ander bespreken met mij.
Die ochtend hoorde ik dat ik als sekretaresse was aangenomen,
Dat ik bij de vakgroep a1, tiende verdieping kon komen.
'Sektie Theoretische Aerodynamica' werd voortaan mijn werkterrein,
Waarbij ik op administratief gebied anderen behulpzaam wilde zijn.
Uw takt en belangstelling in velerlei zaken,
Gaven mij plezier bij het uitvoeren van taken.
De sfeer onderling was altijd geweldig fijn,
Ik vond het heel prettig bij u sekretaresse te zijn!
Uw interesse voor 'theoretische problemen' zal beslist niet verminderen,
Waarbij 'Delftse aangelegenheden' u niet meer zo zullen hinderen.
Ik wens u en uw vrouw een goede gezondheid ten leste,
En hoop voor u in de toekomst het aller-, allerbeste!

Marion Emons- van Gelderen

A jolly good fellow

Als bewoners van de kamer tegenover die van professor Steketee hebben wij hem de laatste drie jaar van nabij meegemaakt. Daarbij kwam hij naar voren als een theoreticus van het zuiverste water. Hoewel er een keer een experiment door hem werd gedaan. Dat was die keer dat de sterkte van een ingenieuze vouwfiets beproefd moest worden door een paar rondjes over de gang te rijden. Zoals het een echte theoreticus betaamt hebben we hem ook nooit kunnen betrappen achter het toetsenbord van een computer. De enige band die hij met de nieuwe computer technologie heeft is het printer papier, waarvan hij graag de achterzijde gebruikt om er 'echte' wetenschap op neer te schrijven. professor Steketee bespeelt liever een ander soort toetsen, namelijk die van een kerkorgel, een voorliefde die hij eens met ons deelde door via een draagbare radio de klanken van een orgelconcert over de gang te verspreiden.
Een object on(lo)smakelijk verbonden met professor Steketee is de sigaar, die dan ook in ruime hoeveelheden gerookt wordt. Deze hobby wordt overigens gedeeld met een groot aantal anderen op de verdieping. Daarbij komt het regelmatig voor dat allen elkaar op hetzelfde moment een sigaar willen aanbieden, die dan van harte wordt geaccepteerd, met als gevolg dat ieder met vier of vijf sigaren in de hand (of mond) staat. Ongeveer een jaar geleden werd er echter een serieuze aanval gedaan op deze hobby. Dit door het verbieden te roken in de lift en andere openbare gedeelten van het gebouw. Hierdoor kwam het regelmatig voor dat hij met wat toeren, die een beroepsgoochelaar niet zouden misstaan, de sigaar in de palm van zijn hand moest verbergen. En zich maar afvragen waar die rooklucht vandaan zou kunnen komen.
Maar deze ongezonde hobby wordt ruimschoots gecompenseerd door een gezonde hobby.
Zodra het weer het toelaat fietst hij, getooid met baseball cap, aan het eind van de dag richting zwembad om daar de dagelijkse baantjes te trekken.
Dat zijn kennis zich niet beperkt tot de stromingsleer blijkt regelmatig op de diploma uitreikingen. Bij elke student weet hij dan wel een historische gebeurtenis te vertellen over zijn of haar geboorteplaats. Wie er graaf of hertog geweest is, of wat er in de oorlog met de plaats gebeurd is, hij weet het zo te vertellen.
Maar ook zijn zangkwaliteiten mogen niet ongenoemd blijven. Deze worden gedemonstreerd bij feestelijke aangelegenheden zoals verjaardagen of afstuderen. Daarbij galmt het 'for he's a jolly good fellow' of 'happy birthday' in E-flat door de koffiekamer.
Dit alles zullen we straks erg missen, en met recht kunnen we stellen: he's a jolly good fellow.

Andy van Esch & Frans de Jongh

Beste professor Steketee,

Na in 1980 met de studie Lucht- en Ruimtevaarttechniek te zijn begonnen kwam ik in augustus 1984 bij de afdeling Theoretische Aerodynamica terecht om af te studeren. In oktober 1986 ben ik afgestudeerd op een afstudeerwerk met de titel 'Een gemodificeerd Prandtl model en een numeriek model voor de beschrijving van een zich oprollend wervelvlak'. Dit afstudeerwerk bestaat uit twee delen. In deel een wordt een poging beschreven om de vorm van een twee-dimensionaal instationair wervelvlak, zoals gepubliceerd door Prandtl, om te zetten in een drie-dimensionale stationaire 'vortex sheet'. In deel twee wordt een numeriek model ontwikkeld om de evolutie van twee-dimensionale instationaire 'vortex sheets' te berekenen. Deze methode is gebaseerd op een methode zoals gepubliceerd door Hoeijmakers en Vaatstra.

Na het afstuderen volgde een dienstverband van drie en een half jaar bij het Nationaal Lucht- en Ruimtevaartlaboratorium. Het belangrijkste onderwerp waaraan ik tijdens dexe periode heb meegwerkt was de numerieke simulatie van de compressibele stroming om scherprandige delta vleugels wat mede heeft geleid tot het mede-auteurschap van een aantal artikelen.

In april 1990 ben ik in dienst getreden bij Shell Internationale Petroleum Maatschappij. Na een trainings periode van drie maanden volgde een eerste posting bij de Nederlandse Aardolie Maatschappij (NAM) als reservoir engineer voor de business unit Groningen. Deze business unit heeft als belangrijkste veld het Groningen gasveld onder zijn beheer. De reservoir engineer is o.a. verantwoordelijk voor het bepalen van de grootte en de inhoud van koolwaterstof reservoirs, voor het vaststellen van de hoeveelheid koolwaterstoffen die economisch winbaar zijn uit een reservoir met gebruikmaking van de energie die reeds aanwezig is in het reservoir, het voorspellen van produktie profielen en het eventueel ontwikkelen van methoden om extra koolwaterstoffen uit een reservoir te winnen door energie toe te voegen.
Gedurende mijn periode op het NLR heb ik altijd goed gebruik kunnen maken van de kennis opgedaan op de TH bij de sectie Theoretische Aerodynamica, maar ook bij mijn huidige baan is deze opleiding een waardevolle theoretische ondergrond gebleken waarop goed voortgebouwd kan worden.

Met dank voor de aangename periode die ik op Uw afdeling heb mogen doorbrengen en het enthousiasme waarmee U het vak aerodynamica aan Uw studenten heeft weten over te brengen wens ik U een hele goede tijd toe tijdens Uw emeritaat,

Jan Willem Jacobs

Een blik in de achteruitkijkspiegel

Mijn eerste kontakten met prof. Steketee dateren uit het najaar van 1967. Ik werkte toen als student-assistent bij prof. De Hoop van de vakgroep Theoretische Elektriciteitsleer op de afdeling Elektrotechniek van, wat toen nog heette de Technische Hogeschool te Delft en was bezig met het eerste deel van mijn ingenieursexamen.
Op een dag hing in de gang een papier met de aankondiging dat prof. Steketee van de afdeling Vliegtuigbouwkunde een college ging geven met als titel: Inleiding Magnetogasdynamica en de mededeling dat elektro-studenten dit vak als keuzevak konden kiezen.
De bijgevoegde beschrijving van het college intrigeerde me zo dat ik besloot om het college te gaan lopen. Het college beviel mij zo goed dat ik het daarna nogmaals heb gelopen en er tentamen in gedaan heb.
Wat was het bijzondere aan dit college? Het speciale is de manier waarop prof. Steketee college geeft.
Zoals iedereen weet behandelt het college Inleiding Magnetogasdynamica, of Aero V zoals het later is gaan heten, het menggebied van de stromingsleer en de theorie van het elektromagnetische veld. Het gevolg is dat de basisvergelijkingen nog meer wiskundige termen bevatten. Prof. Steketee bezit de uitzonderlijke eigenschap om deze uitgebreide vergelijkingen te verduidelijken door o.a. de invloed van elke term te benoemen en tijdens het college elke substitutie uit te voeren. Ik heb tijdens mijn studie in Delft geen hoogleraar meegemaakt die dat beter kon dan hij.

Na mijn afstuderen bij prof. de Hoop in 1970 kon ik bij prof. Steketee gaan werken als wetenschappelijk medewerker om onderzoek te verrichten op het gebied van de hydrodynamica met als belangrijkste onderzoeksgebied de magnetohydrodynamica. Aanvankelijk ben ik aangenomen op tijdelijke basis voor onbepaalde tijd, later toen begin zeventiger jaren de WUB ingevoerd werd, is dat omgezet in een vaste aanstelling.
Uit die tijd kan ik me nog herinnneren dat prof. Steketee ontzettend boos was op de invoering van deze wet. Hij heeft toen zelfs nog een stukje geschreven over een autobus met vier onafhankelijk bestuurde wielen. Later is door de politiek ook de WUB weer afgeschaft en hebben wij een groot aantal andere veranderingen, meestal verslechteringen, over ons heen gekregen.

Ik heb met prof. Steketee de afgelopen jaren prettig kunnen samenwerken. In het bijzonder herinner ik me de vele werkbesprekingen die we over het vakgebied en mijn onderzoek hebben gehad. Al vrij snel na mijn aanstelling concentreerde ik mij op een fundamenteel probleem uit de magnetohydrodynamica.
Het betrof de excitatie van een elektrisch geleidende vloeistofstroming ten gevolge

van een elektrische stroom en zijn eigen magnetische veld. Dit probleem is de magnetohydrodynamische equivalent van de Landau-Squire jet uit de hydrodynamica. Terwijl de hydrodynamische oplossing analytisch te bepalen is, stuit men bij het oplossen van het probleem van de magnetohydrodynamische jet op een groot aantal moeilijkheden ten gevolge van het grotere aantal vergelijkingen en termen in de magnetohydrodynamica. Bovendien bestaat er in de magnetohydrodynamica geen tweedimensionale analogie van dit probleem. Het is per definitie altijd drie-dimensionaal. Het belang van dit onderzoek was dat het meer inzicht geeft in de werking van de MPD-thruster ionenraketmoter.
Dit onderzoek resulteerde in 1986 in een promotie.

Als ik terugdenk aan de afgelopen 22 jaar dan herinner ik me vooral het groot aantal verhalen en anekdotes die Steketee verteld heeft, zoals over:

- Het voltooien van zijn middelbare schoolopleiding in Zeeland, het beginnen met zijn studie Werktuigbouwkunde aan de Technische Hogeschool Delft, in Eindhoven omdat toen alleen Zuid-Nederland nog bevrijd was, en later de voortzetting van zijn studie in Delft.
- Zijn studententijd. Bijvoorbeeld: Een student die in een Japans gevangenkamp had gezeten, had als oorlogstrofee een Samurai-zwaard meegenomen. Deze student voerde eens een zwaarddans uit waarbij hij als apotheose het zwaard dwars door de nogal dunne muur van de studentenzaal stak. Hierop klonk een ijselijke kreet. Aan de andere kant van de muur zat een student rustig op de wc en ineens stak een lemmet van een meter vlak
  naast hem uit de muur.
- Zijn assistentschap bij prof. Burgers waar hij zijn aversie tegen het meten van stromingen in de windtunnel heeft ontwikkeld.
- Zijn vertrek, na zijn studie in Delft, rond 1950 naar Canada in een gammele Constallation met een tussenlanding in Shannon en een urenlange overtocht.
- Zijn wetenschappelijke werkzaamheden aan de Universiteit van Toronto voor verschillende vakgroepen o.a. op het gebied van de stromingsleer, elasticiteitstheorie, aardwetenschappen en magnetohydrodynamica. In het bijzonder zijn onderzoek van de afleiding van de energievergelijking in de magnetohydrodynamica, waarop hij pionierswerk verricht heeft.
  Dit heeft later in Delft geleid tot een groot aantal diverse colleges op verschillende vakgebieden.
- Zijn promotieonderzoek in Toronto aan turbulent spots, dat zijn aversie tegen metingen alleen nog maar versterkt heeft.

- Zijn eerste auto's in Canada en hun specifieke eigenaardigheden.
- Zijn grote voorliefde voor de Besselfunktie boven andere bijzondere funkties.
- Het bespelen van het orgel tijdens de zondagsdienst van de Engelse kerk te Rotterdam en de problemen die soms optraden om het orgelspel en het gezang van de gelovigen gelijk te laten lopen, ten gevolge van de beperkingen van de geluidssnelheid.
- De eerste wereldoorlog en vooral de slachting in Belgie. Op vakanties bezochten hij en zijn vrouw vaak de begraafplaatsen en monumenten die aan deze verschrikking herinnnerden.

Dat prof. Steketee het niet altijd eens was met de gevestigde orde bleek al in zijn studententijd. Hij was lid van een gezelligheidsvereniging en in een winter toen het erg hard vroor en iedereen ging schaatsen richtte hij een werkgroep op 'tot het hakken van wakken'.
Na de invoering van de WUB was hij een van de medeoprichters van de Docentenraad, die tot op heden nog bestaat, zover als ik weet.
Hoe zijn lidmaatschap van 'het Bataafs genootschap tot proefondervindelijke wijsbegeerte' valt te rijmen met zijn afkeer van het uitvoeren van windtunnelproeven zal altijd wel een mysterie blijven.

Tot slot wil ik prof. Steketee bedanken voor de goede samenwerking al die jaren. Ik wens hem en zijn vrouw een goede gezondheid en een lange levensavond.

Hij heeft mij jaren geleden eens verteld dat hij na het behalen van het HBS-diploma moest kiezen tussen techniek en geschiedenis. Ik ben vergeten waarom hij uiteindelijk voor techniek heeft gekozen, maar ik hoop dat hij vanaf nu wat meer tijd heeft voor zijn andere grote hobby: geschiedenis. Of voor iets dat misschien nog interessanter is: de computer en zijn toepassingen in de stromingsleer, zowel analytisch als numeriek.

Guus Jansen

Een zekere gedrevenheid

Als äerodynamicus afgestudeerd, als fluid dynamicus begonnen en nu als dynamicus werkzaam zou een korte beschrijving kunnen zijn van mijn loopbaan.

Na het afstuderen bij de vakgroep van prof. dr. ir. J.A. Steketee ben ik in 1985 bij Ultra Centrifuge Nederland te Almelo als wetenschappelijk medewerker begonnen. Bijna gelijktijdig met R.A.M.Smit een oud student van de vakgroep.

Daar heb ik me voornamelijk bezig gehouden met de optimalisatie van het scheidingsgedrag en het theoretisch onderzoek naar de roterende compressibele gasstroming in een Ultra Centrifuge.

Stromingstechnisch is een ultra centrifuge door de diversiviteit in snelheidsgebieden variërend van nul tot ver supersoon, in dichtheden en drukken met bijna vacuüm en moleculaire stroming in de kern tot compressibele, supersone en subsone grenslaag stromingen bij de wand zeer interessant.

In 1989 werd ik hoofd van de scheidingsgroep en was ik verantwoordelijk voor al het theoretisch en experimenteel stromingstechnisch onderzoek op het gebied van de scheiding van isotopen van gassen m.b.v. centrifuges.

Sinds begin 1991 vervul ik de functie van sector manager dynamics en in die functie ben ik verantwoordelijk voor het onderzoek naar de dynamica van roterende systemen.
Daar heb ik o.a. te maken met flow induced vibrations en vloeistofdempers om aan te geven dat ik, zij het gedeeltelijk, mijn vakgebied niet heb verlaten.

Al vanaf het begin van mijn studie in Delft had ik een voorliefde voor de stromingsleer en lag het voor mij vast, dat ik zou kiezen voor de vakgroep aërodynamica.

De uiteindelijk keuze tussen de vakgroepen supersone aërodynamica, de lage snelheids windtunnel en theoretische aërodynamica was voor mij op dat moment nog erg moeilijk.
Een gesprek met prof. dr. ir. J.A. Steketee over het voor-afstudeerwerk heeft de doorslag gegeven. De manier waarop hij het probleem voorlegde straalde vakkennis uit, de duidelijkheid, met name het enthousiasme en een zekere gedrevenheid waren voor mij doorslaggevend. Van mijn keuze heb ik nooit spijt gehad.

Nog altijd denk ik met veel plezier terug aan de periode bij de vakgroep en zeker aan

het laatste jaar tijdens het afstuderen, waarbij ik dagelijks contact had met mijn mede afstudeerstudenten, de medewerkers van de vakgroep en prof. dr. ir. J.A. Steketee.

Typische details die mij altijd zullen bijblijven zijn het informele karakter, de gezamenlijke koffie pauzes, de gele enigszins agressieve kanarie, het veelvuldig gebruik van klad papier en bord en natuurlijk niet te vergeten de vele formules.

Op deze wijze wil ik U mijn dank uiten voor de begeleiding en ondersteuning tijdens en na mijn studie bij de vakgroep en ik zou U veel geluk en voorspoed willen wensen in de komende jaren.

R.F. Ketting Olivier

Strategie en krijgsgeschiedenis

Na VWO en KMA-vliegtuigbouw en vijf en een half jaar bij de Koninklijke Luchtmacht te hebben gewerkt mocht ik in 1988 voor de KLu Luchtvaart- en Ruimtevaarttechniek gaan studeren in Delft. In de Nederlandse luchtmacht wordt niet aan onderzoek en ontwikkeling van vliegtuigen gedaan, maar heerst toch de behoefte om mensen uit de organisatie een wetenschappelijke opleiding te geven. De keuze van afstudeerrichting wordt in principe aan de student overgelaten. Na een aantal jaartjes in de praktijk van het onderhoud en de inzet van vliegtuigen gaf ik er de voorkeur aan om eens wat dieper op wat fundamentelere zaken van het vliegen in te gaan. Omdat de aerodynamica nu eenmaal de basis is viel de keuze hierop en wel op de theoretische aerodynamica omdat hier de meeste nadruk ligt op het streven de fundamenten analytisch te doorgronden. Met name de combinatie van een gedegen kennis van analytische wiskunde en een aantal pc's met de nodige software bleek een zeer geschikte combinatie om leuk en redelijk diepgaand afstudeerwerk te doen. Zo'n eenvoudige pc stelt je in staat om ingewikkelde analytisch berekende oplossingen grafisch weer te geven waardoor de meest gecompliceerde resultaten op een eenvoudige manier te interpreteren zijn.

Bij de lunch hadden we meer moeite met het voorspellen van de bokkesprongen die Saddam Hoessein steeds weer ging maken en was het zeer opmerkelijk dat prof. Steketee meer wist van strategie en krijgsgeschiedenis dan ik me kon herinneren van de KMA-lessen, waardoor ik dat nog een beetje kon bijspijkeren. Het beste was volgens bepaalde veldheren een generaal die slim en lui is, aan een student worden echter hogere eisen gesteld want die mag het laatste niet zijn.

Inmiddels werk ik bij de KLu, afdeling wetenschappelijke ondersteuning. Hoewel de naam suggereert dat er iets aan wetenschappelijk onderzoek wordt gedaan, is dit toch echt niet het geval. Alle aanwezige behoefte aan wetenschappelijk onderzoek wordt uitbesteed aan het NLR en de TNO-defensie-instituten. Maar we hebben wel de 'verantwoordelijke' taak van het coördineren en het op waarde schatten van het onderzoek voor defensie. De beleidmakende vliegers zijn er echter van overtuigd dat de amerikanen het toch allemaal al uitgezocht hebben en dat je alles wat je nodig hebt daar zo kunt kopen. De enige overeenkomst met mijn afstudeerperiode is dat de lunchpauze om kwart over twaalf begint. Desalniettemin is het werk zeker boeiend genoeg om niet 's-middags in slaap te vallen, hetgeen U gelukkig ook niet deed tijdens mijn afstudeervoordracht.

Breda, september 1991
T.W.G. de Laat

12½ jaar docentenraad

Na vijf jaar TH-ervaring op het Hoofdgebouw
Kwam ik in mei '79 naar Vliegtuigbouw
Als medewerkster van het faculteitssekretariaat
En daarmee tevens notuliste van de Docentenraad

Al gauw werd ik gerustgesteld
Toen bekend was hoe de Docentenraad was samengesteld
Letterlijk en figuurlijk bleek de hoogleraarspersoon
Bijzonder gewoon tot gewoon buitengewoon

De voorzitter in dit maandelijks docentensamenzijn
Bleek al sinds vele jaren professor Steketee te zijn
En ook de afgelopen twaalfenhalf jaar
Zaten hij, als voorzitter, en ik, als notuliste, naast elkaar

Dekanen kwamen en gingen weer
De een ging wat harder dan de ander te keer
De voorzitter paste zich daar perfekt bij aan
En greep tijdig in, uiterst vakbekwaam

Normaal gesproken was Steketee altijd paraat
Als hoogleraar én als voorzitter Docentenraad
Een enkele keer was 't Schijve die hem verving
Dat had dan te maken met een AGARD-meeting

Naast het jaarlijks terugkerend docentendiner
Werd enthousiast ingestemd met een ander 'eetidee'
Door de deelnemers wordt het ten zeerste gewaardeerd
Nu elke maand een docentenlunch wordt georganiseerd

Onze samenwerking verliep immer optimaal
Vanaf kamer 1013 tot in de vergaderzaal
Een voorkeur had ik persoonlijk voor de 10e als trefpunt
Om even bij te praten én om de frisse pepermunt

Ik vind 't echt jammer dat hij nu gaat
En zal 'm missen als voorzitter van de Docentenraad
Als afsluiting wens ik hem en zijn vrouw Ruth
Een hele fijne tijd, **het ga u beiden goed!**

Pauli Paap

Zes

Getallen spelen traditioneel een belangrijke rol in het (arbeids)leven van een ingenieur. Daarbij gaat het doorgaans om tamelijk 'aardse' zaken, zoals sterkteberekeningen en (niet alleen voor ingenieurs!) het invullen van belastingformulieren. Voor mensen die zich met minder aardse dingen bezighouden heeft het getal zeven een bijzondere betekenis. Bij mijn weten is echter nog niemand op het idee gekomen eens wat meer aandacht te besteden aan de invloed van het getal zes op iemands leven. U zult nu misschien zeggen: 'Onzin!' en 'Waarschijnlijk toeval!', maar daarbij moet niet over het hoofd gezien worden dat het getal zes tenminste in mijn leven een tamelijk grote rol lijkt te spelen en dus als zodanig een mooi aanknopingspunt vormt voor een korte beschrijving van mijn levensloop/loopbaan.

Het getal zes dus. Ik werd geboren in '54 (6 x een omgekeerde zes (9 dus) = 54). Op 6-jarige leeftijd (zoals vrijwel iedereen in de tijd vóór kleuter- en basisschool samengevoegd werden) naar de 'grote' school (in '6-tig), waar je gewoonlijk zo'n 6 jaar over doet. Hier dreigde echter in mijn nog jonge leven al iets fout te gaan: Na vijf jaar mocht ik namelijk de lagere school verlaten, omdat ik 'alle lesboekjes uit had'. Vervolgens naar de MULO, in die tijd in de buurt waar ik woonde beschouwd als het hoogst bereikbare. Na één jaar MULO werd mij echter aangeraden mijn (school)geluk op een ander, wat hoger niveau te zoeken, waarmee wat het basisonderwijs betreft de periode van 6 jaar weer rond was.
Mijn ouders stuurden mij (in '66) naar het lyceum, waar in de eerste klas op HBS-niveau begonnen werd en na één jaar tussen verder gaan als HBS-er of als gymnasiast gekozen diende te worden. Dat stelde me dus in staat de vijf jaren die voor de HBS stonden te vermijden en te kiezen voor de 6 jaar die het gymnasium duren zou. Alles weer in orde, dus!
Ondanks de klassiek-kulturele vorming door het gymnasium werd mij toch wel duidelijk dat mijn interesses voor een daarna volgende studie op het technische vlak lagen: Ik wilde ingenieur worden. De keuze voor (toen nog) vliegtuigbouwkunde werd voornamelijk door de overweging bepaald, dat ik weliswaar iets werktuigbouwkundigs wilde studeren, maar geen werktuigbouw! Een duidelijk ander besluitvormingsproces dan de meeste van mijn studiegenoten, over het algemeen enthousiaste vliegtuigjes-bouwers en vliegtuig-'spotters' hadden doorgemaakt. Mijn uiteindelijke keuze voor de afstudeerrichting theoretische aerodynamica is wellicht mede door mijn betrekkelijke afstandelijkheid ten opzichte van 'het vliegtuig' bepaald, waarbij gesteld moet worden dat de neiging om dát te kiezen wat als het moeilijkst bekend staat om eens te zien 'of ik dat ook kan' tevens een rol bij deze keuze gespeeld heeft (naast natuurlijk de aanwezige interesse voor aerodynamica in het algemeen). Wellicht onnodig te zeggen dat mijn tijd in Delft in alle opzichten vrijwel altijd zeer

plezierig was en (bijna) 6(!) jaar geduurd heeft. Voordat mijn loopbaan werkelijk kon beginnen moest eerst nog de militaire dienst afgewerkt worden. De enige manier om deze periode 6 jaar te laten duren was door te tekenen als kortverband-vrijwilliger, iets wat ik, ondanks mijn voorliefde voor het getal 6, heb vermeden: Zeventien maanden leken me ruimschoots genoeg! Daarna de werkelijke start van mijn loopbaan. Daarbij moet allereerst opgemerkt worden, dat ik nooit een baan in de lucht- en ruimtevaarttechniek heb gehad, ondanks dat de mogelijkheden daarvoor er geweest zijn. Voor mijn eerste baan wilde ik liever iets vinden waarbij ik wel iets met aero-(of hydro-)dynamica kon doen, maar niet noodzakelijkerwijs in vliegtuigen en/of raketten. Zo kwam ik uiteindelijk terecht bij Shell, met als eerste 'posting' het lab in Rijswijk, waar ik aan 'offshore research' gedaan heb. Dat was niet alleen nieuw en interessant, had echter ook, omdat ik aan stabiliteit van (en dus stromingen rond) vaste en drijvende booreilanden werkte, voldoende hydrodynamische aspekten. Mijn tweede posting bij Shell, in 'pipelines', was echter minder interessant. Hoewel door pijpleidingen natuurlijk ook wel het een en ander stroomt, bleek ik voornamelijk pijpleidingprojekten te moeten 'managen', in die zin dat 'deadlines' door bedrijven over de hele wereld die onderdelen leverden voor projekten elders over de hele wereld ook aangehouden werden, dit alles vanuit een bureau in Den Haag. Deze posting, de te verwachten toekomst binnen Shell èn een toevallige aanbieding leidden er uiteindelijk toe dat ik Shell na 6(!) jaar de rug toegekeerd heb en mijn geluk in een geheel ander gebied van de techniek ben gaan beproeven: In patenten (of, in korrekt Nederlands, octrooien) bij het European Patent Office (EPO) in München, als 'patent examiner'. De overgang naar het EPO was een stap die ik tot nu toe nooit heb betreurd. Echter, de lucht- en ruimtevaarttechniek is zo langzamerhand wel kompleet uit mijn leven verdwenen. Niet alleen omdat aan patenten, naast hun technische inhoud, een semi-juridische wereld ten grondslag ligt, maar ook omdat ik (door toeval) in de civiele richting ben terechtgekomen. Het enige wat daar nog min of meer 'stroomt' is beton bij het storten! Mijn enige professionele aanrakingspunten met de wereld van het vliegtuig zijn beton-asfaltmengsels voor startbanen en machines die geschikt zijn om deze startbanen aan te leggen, op te breken en eventueel schoon te maken (sneeuwschuivers e.d.). In patenten blijkt het echter zo te zijn, dat het eigenlijke onderwerp van ondergeschikt belang is. Van meer belang zijn de juridische en formuleringsaspekten van een patentspecifikatie. Deze maken mijn huidige baan tot een zeer interessante. En hoe nu verder? Waar blijft het getal 6? Wij (we zijn inmiddels een gezin geworden; nee, geen 6 kinderen, twee lijkt ons voorlopig genoeg!) wonen hier bij München weliswaar in een huis met 6 kamers, maar hebben bijvoorbeeld geen auto met 6 cylinders (wel één met 6-tien kleppen!). We zijn echter inmiddels wel vijf jaar hier, dus volgend jaar moet er eigenlijk weer eens iets gebeuren:

Misschien wel een baan in de lucht- en ruimtevaarttechniek? Of misschien blijven we wel gewoon hier, het bevalt ons uitstekend. In dat geval verwacht ik wel op 6-tig jarige leeftijd met pensioen te gaan en daar, door zeker 96 (een omgekeerde 6 en een 6) jaar oud te worden, minstens 36 (6 x 6) jaar van te genieten!

Steef Polderdijk
september 1991

Beste Jaap,

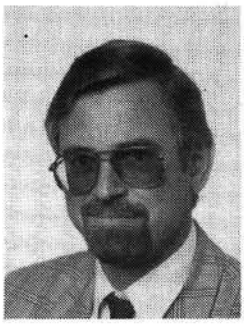

Toen ik in 1959 in Delft kwam studeren was mijn keuze voor vliegtuigbouwkunde geen vanzelfsprekende. Ik moest in die tijd kiezen tussen scheikunde en vliegtuigbouw. Scheikunde was mijn favoriete vak op de middelbare school geweest en vliegtuigen vormden mijn hobby. Uiteindelijk is het vliegtuigbouw geworden, ook al omdat de vooruitzichten van de chemie toen niet erg rooskleurig waren. Achteraf moet ik zeggen nooit spijt gehad te hebben van die keuze en ik denk dat dit mede te danken is aan het feit dat onze paden elkaar hebben gekruist.

Mijn eerste kennismaking met professor Steketee was toen ik het college Aero 1 ging volgen. Het boeide mij vrij snel en ik vermoed dat dit kwam door je systematische manier van uitleg. Stap voor stap werden de vergelijkingen vereenvoudigd tot ze oplosbaar waren met de beperkte kennis die wij als studenten toen hadden. Soms was die kennis nog te beperkt en dan werden wij ook daarin bijgespijkerd. De analytisch wiskundige oplossingen met behulp van bronnen, putten en wervels staan mij nog levendig voor de geest.

Toen ik mijn afstudeerrichting moest kiezen, had ik het weer niet eenvoudig. Aërodynamica trok mij aan, maar tenslotte waren vliegtuigen mijn hobby, zodat vakken als vliegmechanica en in mindere mate vliegeigenschappen mij ook boeiden. Mijn keuze werd nog moeilijker toen een andere hoogleraar mij een jaartje Cranfield in het vooruitzicht stelde. Ik kan mij nog goed herinneren dat jij mij dit toen afraadde en zei dat ik beter eerst mijn studie in Delft kon afmaken, om daarna naar het buitenland, bijvoorbeeld de VS, te gaan. Jouw eigen ervaringen zullen daarbij ongetwijfeld een rol gespeeld hebben. Op een of andere manier geloofde ik in die opzet en achteraf is het ook zo gelopen.

Ik had dus gekozen voor aërodynamica als afstudeerrichting, maar wie schetst mijn verbazing toen ik jouw voorstel voor een afstudeeronderwerp te horen kreeg: magneto-hydrodynamica! Stroming onder invloed van magnetische velden, daar had ik nog nooit van gehoord. Maar toch boeide dat meteen, want deze nieuwe kracht betekende immers een extra term in de vergelijkingen en een hele nieuwe wereld van analytische oplossingen. Ik moest maar eens kijken naar het MHD Rayleigh probleem. Piet Wesseling had dat ook al gedaan, maar die was na het schrijven van zijn afstudeerverslag onmiddellijk vertrokken naar, je raad het al, de Verenigde Staten. Toen bleek dat hij om verkeerde redenen een term in de vergelijkingen had verwaarloosd, was het te laat om hem daarvoor terug te roepen. Ik moest het nog maar eens over doen.

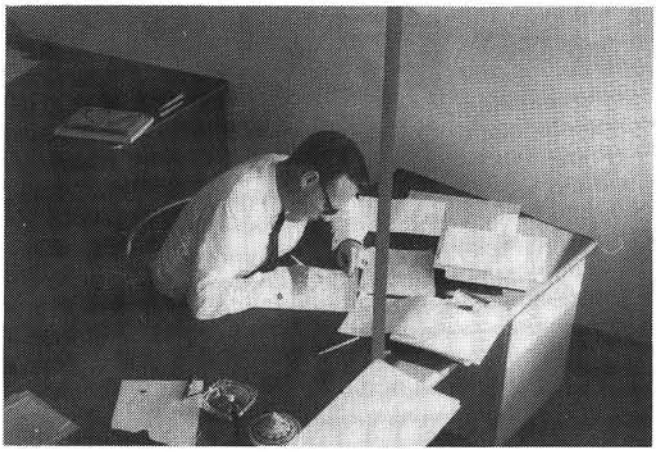

Peter Massee stond bekend als een noeste werker en bovenstaande foto illustreert dit overduidelijk. René Coene had veel meer aspiraties tot geleerde boekenwurm, zoals onderstaand blijkt.

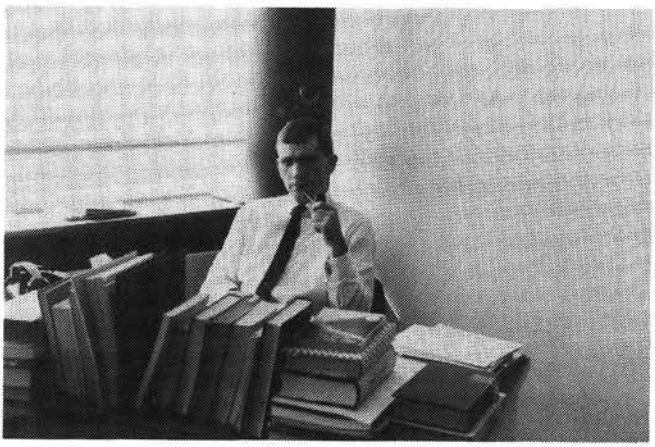

Hoewel ik een 'analytische' oplossing produceerde, ben ik vermoedelijk je eerste afstudeerder geweest, die daarbij ook het grote rekentuig, de computer, gebruikte. Dit alles speelde zich af in het oude gebouw aan de Kanaalstraat. Ik werd student-assistent en kreeg een werkkamer in het gebouw van de lage snelheid windtunnel, samen met Wim de Wolf. Maar in 1965 kwam dan eindelijk de grote overstap naar de tiende verdieping in het nieuwe gebouw aan de Kluyverweg. Wat een luxe! Met zes of zeven man bevolkten wij een hele verdieping. Namen als Tennekes, Massee, Coene en Arora komen dan boven drijven en niet te vergeten Gerrit Schouten.

Er hing altijd een gezellige sfeer. Foto's uit de lente van 1966 geven hiervan een duidelijk beeld. Bovendien blonk Gekke Gerrit vaak uit als verdiepings-nar. Ondanks

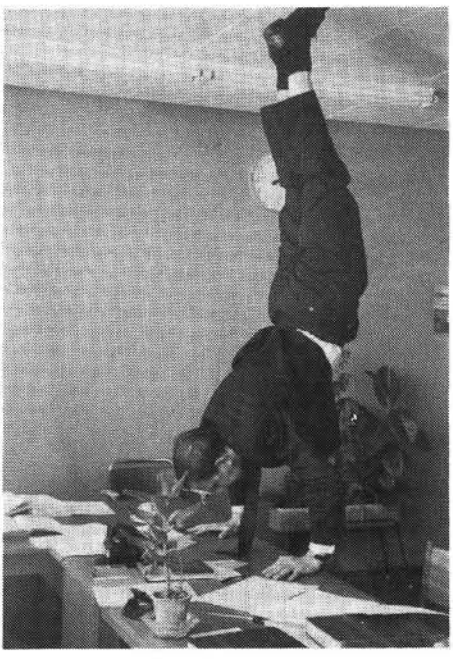

deze gezelligheid werd er toch ook serieus gewerkt. Zo zelfs dat ik medio 1966 kon afstuderen.

Inmiddels was Paul Lykoudis op bezoek geweest. Ik had hem niet ontmoet, want ik had het in die tijd nogal druk met basketbal. Van jou hoorde ik dat hij op Purdue University een plaats beschikbaar had als research-assistent met mogelijkheden om een Masters te halen. De beslissing was snel genomen, want dit was mijn kans. Met mijn vertrek naar de VS verloor je collega Van der Neut zijn secretaresse, Ank, maar als

tegenprestatie beloofde ik Van der Maas terug te komen naar Nederland. Tenslotte moest een vliegtuigbouwkundig ingenieur zijn talenten in dienst stellen van de Nederlandse vliegtuigindustrie.

Ons verblijf in de VS heeft langer geduurd dan een jaar, want al snel vroeg Paul mij te blijven voor een Ph D. De beslissing daarover heeft wat meer tijd gevergd. Na één jaar Amerika was ik nog onvoldoende gewend of vergroeit met het denken en leven daar. Uiteindelijk heb jij mij overtuigd door te wijzen op deze eenmalige kans. Jij hebt ook nog gezorgd voor verder uitstel van militaire dienst. Wat een service, alsnog dank daarvoor.

Terwijl een promotie in Nederland meestal een diepte studie behelst, vereist een Ph.D. in de VS tegelijkertijd een verbreding van het kennisgebied. Plotseling werd ik geconfronteerd met zaken als plasma physics, quantum mechanics, radiation energy transfer, stochastics, reology en biomechanics. Weliswaar is hierbij sprake van 'weinig kennis over veel onderwerpen', maar ik kan nu zeggen in mijn latere werk veel plezier van die kennisverbreding te hebben gehad. Mijn thesis betrof een 'analytische' oplossing van de peristaltische stroming in de ureter, de verbinding tussen nier en blaas. De contacten met urologen gaven hieraan een speciale dimensie.

In 1970, na vier jaar, kwamen wij terug naar Nederland en vond ik onmiddellijk werk op het NLR in de instationaire aërodynamica. Een nieuw onderwerp en dus een uitdaging. Op het NLR heb ik tien jaar lang met plezier gewerkt, zowel theoretisch als experimenteel, maar na verloop van tijd kreeg ik behoefte aan meer variatie, een nieuwe uitdaging. Die vond ik bij het NIVR, waar ik mijn oude hobby, de vliegtuigen, weer kan beoefenen. De brede opleiding en ervaring, die ik mocht genieten, komt daar goed van pas.

Uit bovenstaand verhaal blijkt dat prof. Steketee, wellicht zonder zich dat te realiseren, enkele malen een grote invloed heeft gehad op belangrijke beslissingen in mijn leven. Achteraf beoordeeld is dat een positieve invloed geweest en daar ben ik je erkentelijk voor. Het leek mij goed dat ter gelegenheid van je afscheid als hoogleraar nog eens vast te leggen.

Jaap, bedankt!

Ruud Roos

A musing von 'Elveeyes'

When we think of a philosophy of Man's life, there seem to be at least two ways one can look at it. The sages in the past, in their search for truth about life, have enunciated a theory that Man's life is ordained by God and proceeds from beginning to end as in a movie and there is nothing in the hands of Man to change it. And the joys and sorrows one experiences in this life are determined by his actions in the previous life. It is this theory that is enunciated in the great epic Mahabharat. The essence of this philosophy is abstracted in Bhagavad Gita as told by Lord himself. Every act of Man is connected to a distant past and future. As one brought up with a belief in the Hindu philosophy from childhood, I tend to look at every event as evolved from a past with seeds for the future.
Since ancient times thinkers were asking the question 'what is the meaning of life?' Religions are only faiths and do not carry us anywhere towards the answer to this question. Nevertheless, different religions have shown ways of looking at life.

Another way of looking at life is to consider all events as random, just like the growth and decay of trees in a forest or other species on the globe. For example, no reason can be attached for two persons to come together or for a dictator to take into his head to lead nations to war or for new discoveries to emerge. Just as all these are random events, the events in Man's life are also random. Why is one becoming a scientist, philosopher or politician? If someone tries to ascribe a reason, it can only be artificial and cannot remove the random nature. Scientific thinking cannot provide any theory but only strengthens the belief in the random nature of life.

It is amusing to think of the event of my first meeting with Dr. Steketee and Dr. Coene on that Monday morning at Schiphol airport. To me, the event has evolved from past and as regards the future only time will tell.

L.V.S.

De medewerker

In het jaar 1960 werd professor Steketee benoemd, ik studeerde af en werd als 'wetenschappelijk medewerker' aan de nieuwe hoogleraar toegevoegd. Medewerken klinkt mooi maar daarvan was in het begin natuurlijk geen sprake, ik had er weinig benul van wat ik met mijn vergaarde kennis kon doen of zou moeten kunnen. Ik had geleerd voorgeformuleerde vragen te beantwoorden. Het oplossen van mijn eigen bewust naief geformuleerde problemen bleek veel moeilijker. Ik vond, en vind nog steeds, dat een aankomende wijze ook vragen van een gek moet willen beantwoorden, in begrijpelijke vorm. Dat is een uitdaging, die vragen met behulp van de kennis van het beschikbare kennispakket daarin te passen. Het is hier dat de medewerking van een hooggeleerde vruchten kan afwerpen, dat is iemand die weet waar hij het over heeft, die weet waar hij wèl en haast nog beter waar hij niet een antwoord op heeft (al zal hij dat met het oog op zijn status niet altijd willen zeggen en daarom het antwoord op assertieve wijze inbedden in een verbloemend betoog waaruit in ieder geval blijkt dat de beantwoording niet zo eenvoudig is als de simpele ziel wel denkt).

Een van de eerste hoopgevende gedachten die ik hoorde uit de mond van de met mij meewerkende hooggeleerde was dat het verstandig zou zijn om de idee te laten varen dat je als ingenieur nu alle technische problemen, met de duimen in de armsgaten van je vestje gestoken, zou moeten kunnen (laten) oplossen. Dat gaf al wat rust om vragen te inventariseren. Dat legde de kiem voor waardering voor de zo schematisch en modelmatig in de colleges gepresenteerde problemen met de daarbij mogelijke antwoorden. In mijn argeloosheid had ik het kitscherige idee gekoesterd dat er veel meer was en zou moeten kunnen, maar dat professoren door tijdsbeperking ertoe werden gebracht de zaken eenvoudig voor te stellen. Ik kwam tot de ontdekking dat het vakmanschap en het meesterschap vooral daarin bestaan dat vragen zodanig worden geformuleerd dat het mogelijk is er een ter zake doend antwoord op te geven. De materie wordt daardoor hanteerbaar terwijl als prettige bijkomstigheid de omgang ermee aan aesthetische wensen en gevoelens blijkt tegemoet te komen. Dat laatste wordt gecultiveerd door resultaten uitdagend, mooi te formuleren en te presenteren, een kunst die Steketee op inspirerende wijze uitdraagt. Ik denk dan bijvoorbeeld aan de fraaie vormen van de Cauchy-Riemann relaties, de Maxwell vergelijkingen, de Quaternions van Hamilton, de Hamiltonian en de Lagrangian, Clebsch potentialen, de Lorentz transformatie, vectornotatie, Christoffelsymbolen enz. enz. Het nuttige verenigd met het aangename, zo openen zich de mogelijkheden om op veelomvattende wijze greep te krijgen op de grofstoffelijke werkelijkheid. Maar hoe ver moet je daarin gaan?
In hoeverre is onze greep op de werkelijkheid realistisch? Is voortgezette detaillering een doel? Wij leven in een met kitsch geïnfecteerde maatschappij; dat bedoel ik op

een manier die mij is aangegeven door Louis Ferron[1] , die kitsch kenmerkt als een illusoire verbeelding welke de suggestie wekt dat die verbeelding werkelijkheid zou kunnen worden.
Wetenschap houdt zich bezig met het modelleren van de werkelijkheid. De modellen moeten cohaerent zijn en niet leiden tot tegenstrijduige uitspraken. In de ingenieurspraktijk wordt van oudsher gewerkt met vuistregels. Ambachtelijk werken met vuistregels is noodzakelijk, het brengt ervaring in een makkelijk hanteerbare vorm. Maar het leidt niet tot vooruitgang. Slechts met experimenten en wilde, dat betekent vaak irrationele, ideeën worden nieuwe wegen geopend. Het kitscherige in onze maatschappij wordt gevormd door die elementen die streven naar een zo realistisch mogelijke weergave van de werkelijkheid, met de droom in het achterhoofd dat daarmee onze technische problemen worden opgelost. De echte IngenieursKunst bestaat echter veel meer daarin dat de werkelijkheid wordt ontdaan van zijn fel realistische, verdoezelende franje waardoor de essentiele structuur wordt blootgelegd. Het in model brengen en formuleren levert dan het plezier van de wetenschapsbeoefening. Het resultaat blijft abstract, in ieder geval in de formulering.
Competente ingenieurs kunnen met die abstracte resultaten omgaan, bij een universiteit wordt dat uitgedragen.

Met de komst van Steketee als hoogleraar werd op de onderafdeling der vliegtuigbouwkunde voor mij een venster geopend dat uitzicht gaf op die abstracte, wetenschappelijk georienteerde wereld waarin onze gedachtenspinsels zichtbaar worden voor diegenen die het willen zien. Hij keek zelf ook door dat venster, naar buiten, maar ook van buiten naar binnen (door het venster te verplaatsen natuurlijk). Ik herinner mij dat eens het uitzicht sterk werd belemmerd door een gigantische stofwolk, losgewerkt en opgeworpen door een voorbijrijdende bus met onafhankelijk gestuurde wielen. De situatie leek direct gevaar op te leveren voor een gedachtenexperiment, met een explosieve door L, M en S bedachte entropieverdeling, dat een eindje verder door Steketee werd voorbereid. Het gevaar werd efficient bedwongen door met een

---

[1] 'Kunst en kitsch, waarin verschillen ze, waarin komen ze overeen? Beide proberen een droom gestalte te geven. In het geval van de meest diepgezonken kitsch – en dus de hoogste, die welke als norm dient – wordt de suggestie gewekt dat de droom bereikbaar is. In de kunst blijft de droom altijd op afstand. Dat is het verschil.
De overeenkomsten mogen er ook wezen. Kunst en kitsch onttrekken zich beide aan de werkelijkheid. En beide zijn pas echt geslaagd als de werkelijkheid zich naar hen voegt, in plaats van omgekeerd.'
Louis Ferron, Parelmoeren vergezichten, NRC-Handelsblad 4-10-1977.

eenvoudige singuliere transformatie het stof inclusief de bus in een punt te concentreren. Het experiment werd echter danig verstoord en is tot op heden niet tot een bevredigende virtuele uitvoering gekomen. Wij herkregen echter het zicht op onze vliegtuigen, die met hun hoefijzerwervelsystemen door de oppervlakkige beschouwer voor paarden gehouden zouden kunnen worden. Het ontbreken van bolsymmetrie maakt de behandeling van dat soort contrapties interessanter, maar niet eenvoudiger. Het leven op de zo boeiende grens van theorie en werkelijkheid is kwetsbaar en zou dagelijks uit balans kunnen geraken bv door de onderbreking voor de lunch. Om de continuiteit te garanderen worden dan echter, eventueel met volle mond, alle voorstelbare en experimenteel ook onvoorstelbare technieken vrijelijk toegepast op het leven van alle dag maar bij voorkeur op de politiek daarvan, en met succes. Er blijven evenwel raadsels. Hoewel het niet realistisch is om dat te denken lijkt het er toch op dat Steketee een truc kent om zijn eigen tijd trager, dan wel die van zijn omgeving sneller te laten verlopen (tracht hij Einstein naar de kroon te steken?). Hoe het ook zij, voor iemand als ik, die 32 jaar in zijn omgeving heeft gezeten, zijn die jaren omgevlogen, hij lijkt nauwelijks ouder te zijn geworden. Die truc heeft hij nog niet willen verklappen hoewel zijn vrouw Ruth, met al haar liefde en geduld(?), en zijn kinderen met hun toch wilde fantasieen, en in veel mindere mate de medemensen en de studenten van de 10e verdieping het hem hierin niet eenvoudig hebben gemaakt. Maar hij laat wel sporen genoeg achter om te volgen, de zaak ziet er niet hopeloos uit. En gelukkig kunnen we altijd nog inspiratie putten uit de (genummerde) verhalen, of misschien zelfs de niet gepubliceerde geschriften uit de la.

Gerrit Schouten
november 1991

'Nature is not malicious, but it punishes the incompetent.' Albert Einstein.
'Es gibt nichts Praktischeres als eine gute Theorie.' L. Boltzmann.
'le Savant doit ordonner;
on fait la science avec des faits
comme une maison avec des pierres;
mais une accumulation de faits
n'est pas plus une science
qu'un tas de pierres n'est une maison.' Henri Poincaré
'Whoever, in the pursuit of science, seeks after immediate practical utility, may generally rest assured that he will seek in vain.' Hermann von Helmholtz

Some recollections on the occasion of Jaap Steketee's retirement

It all started with the six day war in 1967. Our original plan for my first sabbatical in the fall was to go to the Technion in Israel. But the air fare for the five of us, Anne, David (12), Peter (9), Daniel (6) and me would have been immense and so with the war we decided to change our plans. Rudi Ong, with whom I shared an office, spent his last sabbatical in Leiden and he mentioned a professor Steketee who was working on Magnetohydrodynamics in Delft and might be willing to be our host. After some preliminary contact Jaap (I will use that name from now on) very graciously agreed to have us on very short notice, and with that there started a very delightful four months in our lives. This was also the time I started keeping a daily journal so much of what follows will be quoted from that.
So on Friday, 4 August we left for Delft and after a week and a half in Copenhagen visited Delft for the first time on 8/15. 'Prof. Steketee and his wife are very nice, extremely anxious to help. Delft seems a lovely place. Interesting train ride through Haarlem, Leiden and The Hague'. [As I remember it, it was at that time that Jaap explained how one can distinguish someone who has learned Dutch. They should be able to pronounce 'Breune Leuse Kreupen ober meine Heut' or something like that. At the time Jaap, Ruth and the kids still lived on Insulindeweg.]

On 8/16 we came to Delft to get settled:
'got settled in professor Van Leeuwen's house – can stay until Sept. 9. Prof. and Mrs Steketee visited. Mrs Steketee took Anne shopping. I went to the Bank. Also have lovely office. On tenth floor overlooking polders, cows, with the spires and skyscrapers of Rotterdam in the distance'. [We finally were able to rent the Lekkerkerker house for the rest of our stay on Willem de Merodestraat 7. The office is probably the nicest I have ever had.]

'Dinner at the Prinsenkelder. Appetizer soup, then chicken with french fries, ice cream, beverage. Practically more than we could finish. For four servings *f*.40 or about $11.00'. [In 1967 the rates of exchange were *f*.3.50 and DM 4.00 for one dollar! At the time the Prinsenkelder had an amazing waiter who could make his bow tie bob up and down by moving his adams apple. The kids were ecstatic every time we went.]

22 August, Tuesday – had an opportunity to hear Jaap perform.
'Organ practice by prof. Steketee in French Church next to the Prinsenhof. A beautiful spot and lovely old church. prof. Steketee an accomplished player'.

23 August
'Dinner at the Prinsenkelder where we met the Steketees and Clark and Betty Mangelsdorf .... Went to the Steketees and had some wine together with the Mangelsdorfs. Ruth Steketee's birthday'.

29 August
'Met Mr. Dobbinga, prof. Gerlach – showed me flight simulator and flight dynamics lab. prof. Wittenberg – who spent some time with Arnie Kuethe in Ann Arbor'. [Was intrigued by Dobbinga's interest in old castles and cathedrals.]

1 September, Friday
'39th birthday [Ha! It was the real 39th.], Reception for Van Ingen in honour of his becoming a lecturer'.

7 September, Thursday
'Had Steketees and Houtman for dessert and coffee. A very pleasant evening'.

12 September, Tuesday
'To Leiden with Bram van Leer. Talked about extragalactic clouds – collision with galactic gas .... Talked with van de Hulst after lunch'.
[This contact with van Leer also led to the famous stolen AIAA Journal incident. I borrowed this from the Aero Dept. library, and Bram's forgotten briefcase, left near the entrance of the building as he was leaving, was found by one of the guards with the illegally borrowed journal inside. Well!!! Poor Jaap almost had to explain it to the Queen. In the meantime Bram has become a distinguished member of the Aerospace Engineering Faculty at the University of Michigan, and in part this is a consequence of this very early contact.]

11 November, Saturday
'Dinner party at the Steketees – wonderful dinner, tons of rice. Arora drove us there and back. Interesting discussion about the Dutch political system'. [Ruth must have made 20 liters of rice or so, and for all I know some of it may be left over still. But it was a very nice party with some of Jaap's students. We didn't have a car during our stay in Delft and so were pleased to get a ride. Have kept some contact with Arora, and one of his students is currently in our graduate program.]

6 December, Wednesday
Jaap took me to a promotie at the Aula in the afternoon. It was very impressive. '.... After one hour of what appears as carefully prepared questioning, Bedel returns, pounds staff on floor and says 'Het uur is gestrecken' The professors (opponenten) file out to reach a decision (Jaap says that they really have some coffee). ....Visited by the Schoutens and the Coenes in the Evening and had a very pleasant time'.

Well, after a wonderful stay in Delft, Ruth and Leo Beckmann, our neighbour, drove us to Schiphol on 16 Dec. for our return to Ann Arbor. I saw Jaap next at the AGARD Transonic meeting in September 1968.

18 September 1968, Wednesday, Paris
'Lunch with Jaap Steketee'. [This, as I remember it was a lovely fall day, and we sat outside. We made the remarkable discovery that on a day like that in Paris two men can easily go through a complete bottle of French wine without any effort whatsoever.]

20 September
'Meeting in morning. Lunch with Jaap, Spee, and Nieuwland. Had couscous which was very good. Interesting panel discussion in the afternoon. Visited tomb of Napoleon. Then went to Mont Martre with Jaap and Dobbinga. Dinner near Place Pigalle. Then walked down to Place Concorde via the Opera'. [And no, we did not go into any of the interesting night clubs although we were tempted.]

Jaap applied for the Dutch Professorship at The University of Michigan and so he, Ruth, Frank, and Adrian spent the '69-'70 academic year at The University of Michigan. Michigan has a strong Dutch tradition for many Dutch immigrants settled in western Michigan and they provided funding for what has become a distinguished visiting chair for someone from The Netherlands. There is even a Steketee Department Store in Grand Rapids, and Holland Michigan is famous for its annual spring tulip festival. Jaap and Ruth rented a house from the Plants on Woodside Avenue in a pleasant area called Burns Park which is also the neighbourhood where we live.

Jaap did much significant research during that year; but, even more important was his enthusiastic participation in and contribution to The Flounders, the faculty water polo team. Ralph Loomis, a member of the team from engineering still remembers Jaap's great exploits in the pool. I always wondered whether the team was named after the wonderful fish or because they did a lot of floundering about. After one of their

sessions Jaap would return to the Department pretty well 'wrung out'.

Well, time to sign off. All of us here, members of the Aero Department, and Anne and I wish Jaap a happy, productive retirement, and hope that in some of his travels he will stop by in Ann Arbor. The swimming pool is waiting.

Martin Sichel
Department of Aerospace Engineering
The University of Michigan
Ann Arbor, Michigan, USA.

Prof./Jaap Steketee, leermeester en adviseur, collega en vriend

Beste Jaap,

Toen ik de vraag kreeg of ik een bijdrage wilde leveren aan een soort gedenkboek dat bij de gelegenheid van je pensionering aan jou overhandigd zou worden heb ik geen ogenblik geaarzeld.
Ik heb ook geen moment geaarzeld toen ik de keuze kreeg tussen een wetenschappelijk getint, aan jou opgedragen artikel of een stukje aan (en over) de mens Jaap Steketee. Ik had en heb daar verschillende redenen voor.
In de eerste plaats beschouw ik jou als een volbloed academicus waar alleen wetenschappelijke artikelen van voldoende academisch niveau aan mogen worden opgedragen. Daarmee was, wat mij betreft, deze optie vervallen.
Bovendien realiseer ik me dat ik ten opzichte van jou in de waarschijnlijk unieke positie verkeer je te kennen als leermeester, als adviseur en criticus en als collega en vriend. Ik acht mezelf daarom uitstekend gekwalificeerd om vanuit die gezichtspunten een perspectivische schets van jouw persoon te geven.
Daar gaat-ie dan.

Toen ik je ca. dertig jaar geleden voor het eerst ontmoette waren we beide 'broekies', jij als beginnend hoogleraar en ik als student. Niettemin, of misschien wel juist daardoor, maakte je onmiddellijk een haast verpletterende indruk op mij. Dat had meerdere oorzaken.
Eén daarvan was dat je op een ogenschijnlijk verbijsterend-luchthartige manier college gaf over voor mij haast ontmoedigend-gecompliceerde onderwerpen. Dat ik desondanks een paar keer met goed gevolg tentamen bij je gedaan heb snap ik nog steeds niet en is alleen maar te verklaren uit het feit dat je een zeer ruimhartig mens bent.
Een andere oorzaak was dat je uit 'Amerika' kwam (wat later Canada bleek te zijn) en een 'Canadese' vrouw had (die later Engelse bleek te zijn). In die tijd was alles dat uit Amerika kwam per definitie geweldig en bovendien sprak je (en spreek je nog steeds) half-Nederlands/half-Engels wat, ofcourse, even more interesting was. De grootste schok kreeg ik echter toen tijdens jouw college prof. Van der Neut eens een keer zijn hoofd om de hoek van de deur stak met de kennelijke bedoeling om je iets te vragen. Het duurde even voordat je in de gaten kreeg dat je gehoor ergens door werd afgeleid. Maar toen volgde er onmiddellijk, met een joviaal gebaar: 'Ha die Arie!'
Heden ten dage is er ongetwijfeld niemand die begrijpt wat daar nu voor schokkends aan is. Ik moet er dan ook ter verklaring bij vermelden dat in die tijd Delftse studenten

en gewone Nederlandse mensen nog geen voornamen hadden. Laat staan hoogleraren!

Ik denk dat onze wegen zich na mijn studententijd een aantal jaren niet gekruist hebben en dat de eerste 'confrontatie' daarna heeft plaats gehad in de sub-commissie voor aërodynamica van de wetenschappelijke commissie NIVR-NLR. Je rol van leermeester zette zich daar voort in de zin dat je de rapporten en publikaties die ik, en met mij vele anderen, bij het NLR produceerde, van commentaar werd geacht te voorzien. Dat commentaar was er (bijna) altijd, in ieder geval op het veelal klunzige Engels (we mochten jouw gecorrigeerde exemplaar meestal in ontvangst nemen). Maar het was ook vrijwel altijd mild en waar maar enigszins mogelijk ook lovend. Ik geloof niet dat er ook maar één NLR-medewerker is geweest die zich door jouw commentaar beledigd heeft gevoeld.
Het moet overigens voor een rechtgeaarde theoreticus niet altijd eenvoudig zijn geweest. Dit met name doordat het numerieke geweld onweerstaanbaar verder oprukte en de stijl van schrijven, volgens jou, ook steeds meer op FORTRAN ging lijken. Later werd je voorzitter van de sub-commissie voor aërodynamica (dat ben je overigens nog steeds) en ik werd verantwoordelijk voor een stukje van het werkplan van het NLR. Dat werkplan wordt jaarlijks door de sub-commissie van commentaar voorzien en het NLR en NIVR daarmede van advies. Bezien vanuit mijn perspectief ging je rol van leermeester daarmede geleidelijk over in die van adviseur.
Het voorzitterschap van de sub-commissie heb je altijd op een ontwapenende maar tevens verrassend-efficiënte manier bekleed; ik kan me niet herinneren dat het ooit echt laat is geworden.

Als collega heb ik je in twee verschillende rollen mogen meemaken. Ten eerste als medelid van het Fluid Dynamics Panel van AGARD. Daar ben je al sinds de zestiger jaren een zeer gewaardeerd lid van. Dat niet in de laatste plaats vanwege je sociale inbreng. In dat verband moet ik denken aan het orgel recital in Scheveningen maar ook aan een gevleugelde uitspraak van Bob Rollins, één van de FDP executives. Toen deze afscheid nam van het Panel liet hij bij zijn tafelrede tijdens het panel dinner alle panelleden kort en karakteriserend, in één zin, de revue passeren. Toen hij bij jou was aangeland zei hij: 'Jaap Steketee: thank you for bringing Ruth!', waarmee meteen duidelijk is dat Ruth haar inbreng in (de sociale activiteiten van) het Panel minstens zo belangrijk is als die van jou.
Mocht daarmee de indruk zijn gewekt dat het FDP voor jou een hoofdzakelijk recreatieve functie vervulde dan haast ik mij dat te corrigeren: Je hebt zitting gehad in vele 'program committees' en bent lid van een aantal 'standing committees', waar-

AGARD, Recreational Fluid Dynamics Panel
Van links naar rechts Jaap Steketee, Keith Kushman, Bram Elsenaar,
Lars Ohman en Joop Slooff

onder het 'publications committee'. Van dat laatste nam je vorig jaar het voorzitterschap over van je goede, misschien wel beste (ex-)FDP vriend Alec Young.

Ja, en dan werd je op een gegeven moment ook nog collega-hoogleraar. Dat was helemaal gek. Maar je hebt me er snel aan doen wennen.
Hoewel we elkaar in dat verband wekelijks ontmoeten is mijn beeld van jou als collega-hoogleraar misschien wel het minst scherp. Dat komt, denk ik, doordat we beiden bijna altijd 'bezig' zijn en tijdens onze gezamenlijke lunches betrekkelijk weinig over 'het werk' praten.
Er zijn me niettemin een paar dingen opgevallen..

- Je hebt een grondige hekel aan bestuurlijke 'fratsen' en papieren rompslomp.
- Het voorzitterschap van de docentenraad bekleed je op net zo'n ontwapenende manier als het voorzitterschap van de sub-commissie voor aërodynamica van het NLR.

– Dat het docentendiner jaarlijks een groot succes is, is voor een belangrijk deel te danken aan de soepele en amusante manier waarop jij een en ander in goede banen leidt.

Beste Jaap,
Ik weet niet of je jezelf in deze schets van jouw persoon zult kunnen herkennen. Ik hoop in ieder geval dat het in voldoende mate doorklinkt dat ik het als een voorrecht beschouw jou èn als leermeester en adviseur èn als collega heb mogen leren kennen. Ik hoop tevens dat de vriendschap die daaruit is voortgekomen ook na je pensionering zal voortduren.

Joop Slooff

Mijn prototype prof!

Beste Jaap,

Hoewel mij niets is gevraagd heb ik toch de vrijheid genomen een bijdrage te leveren aan dit gedenkboek ter ere van je afscheid als hoogleraar aan de TU in Delft.
Misschien is de emancipatie nog niet tot Delft doorgedrongen, misschien ook heeft men gedacht, dat ik als 'jonkie', (omdat ik er als een van de laatsten ben bijgekomen) niet veel te vertellen zou hebben. Dat is ook zo, maar hier gaat kwaliteit boven kwantiteit.
Van mij geen wapenfeiten, maar gewoon een uit het hart gegrepen informele babbel.

Uit de tijd, dat ik met Joop verloofd was en hij in Delft studeerde, zijn me drie namen bijgebleven. Prof. van der Maas, hij was de God van Vliegtuigbouw, Van Ingen, bij wie Joop z'n afstudeerwerk deed en prof. Steketee. Ook in die tijd kwamen de hoogleraren over tafel, alleen op een andere manier dan tegenwoordig. Toen was een hoogleraar nog 'Hoogedelgeleerd', tegenwoordig wil men hem nog wel eens anders betitelen.
Het enige, wat ik me over jou herinner is, dat je met een Canadese was getrouwd. Later bleek, dat ik verkeerd was ingelicht.

De eerste keer, dat ik je in levende lijve ontmoette, was in Toronto in 1984 tijdens een AGARD meeting. Je was voor mij het proto-type van een professor: klein, een buikje, ietwat kalend en je rookte sigaren. Daarbij kwam nog, dat je voertaal, als Nederlander, Engels was. Very interesting, you know! Maar toen kende ik je nog niet. Tijdens deze reis maakte ik ook kennis met Ruth, je vrouw. Ik vond haar meteen ontzettend aardig en tot mijn stomme verbazing sprak zij Nederlands en hoe!

In de jaren hierna ontmoetten we elkaar nog wel eens op een AGARD meeting, maar het kontakt ging niet verder dan even een vluchtig goedendag zeggen.

Hierin kwam verandering toen Joop in 1986 als buitengewoon hoogleraar zijn intrede deed in het korps van docenten, ter gelegenheid waarvan op 23 april een receptie werd gegeven. Ik was naar de TU gekomen en het eerste wat ik zag toen ik op de 10e verdieping uit de lift stapte, was mijn 'proto-type van een hoogleraar', die, al fluitend, in opgerolde hemdsmouwen door de gangen liep te draven op zoek naar z'n vogeltje. En deze man kon nog lekker koffie zetten ook!
Joop moest college geven (het laatste gedeelte heb ik zelf bijgewoond) en ik werd in zijn kamer geïnstalleerd. Op een gegeven moment kwam jij binnen en vroeg me of ik interesse had in een rondgang door het gebouw. Dat had ik zeker en dit werd voor mij

een fijn begin van een onvergetelijke middag. Jij kon bij mij niet meer stuk! Ik mocht Jaap tegen je zeggen, waar ik enorm veel moeite mee had, omdat ik in jou nog steeds Joop z'n hoogleraar van vroeger zag. Ik zag en leerde toen niet alleen een hoop van de praktikumhal, maar ook, dat jij nog steeds tot de kategorie van 'Hoogedelgeleerde Heer' behoort.

In de loop der jaren groeide het kontakt, niet alleen met jou, maar ook met Ruth. Ook aan haar heb ik heel fijne herinneringen o.a. aan ons verblijf in Friedrichshafen en de prettige samenwerking tijdens de voorbereidingen voor het Ladies programm in oktober 1990.

Hiermee ben ik gekomen aan het eind van mijn ontboezemingen. Ik weet niet wat jullie plannen zijn, maar ik hoop van harte, dat het jullie gegund is samen nog van een heleboel dingen te mogen genieten. Ik hoop ook, dat een afscheid van de TU niet betekent een afscheid van Jaap en Ruth!

Lia Slooff

Niet de eerste de beste

Er gaat toch wel een lichte schokgolf door je heen, wanneer 22 jaren nadat je voor het laatst je bezig gehouden hebt met de aerodynamica, je plotseling een brief krijgt, waarin je als 'geachte collega aerodynamicus' wordt aangesproken. Graag wil ik natuurlijk in dit 'Akademische Festschrift' opgedragen aan prof. Steketee iets schrijven over mijn inmiddels enigszins getordeerde herinneringen aan hem.

Prof. Steketee kwam tot ons in die dagen, dat prof. Van der Maas nog het bewind over de onderafdeling Vliegtuigbouwkunde voerde. Het zal altijd wel een raadsel blijven, hoe deze door de 'filosofie van de wetsidee' gedetermineerde calvinist zo'n liberale en onconventionele vogel uit Canada wist te strikken: de mens wikt God beschikt; zo zag althans Van der Maas het, en wij (studenten en staf) eigenlijk ook. Prof. Steketee kwam pijprokend in een met 'UK-license plate' uitgeruste Morris/Austin Oldtimer naar Delft. Toch was hij geen Bommel. Want hij was geen Heer. Hij sprak een Nederlands, dat me toen meer aan dat van Bob Evers deed denken, die jongensboekenheld van toen voor pubers in nood. Ik was net bezig om voor m'n C2 te slagen en had een flexibele afstudeerhoogleraar nodig, liefst met een vakgebied, dat zo onbekend was, dat ik in het land der blinden ..... Dat was de Magnetohydrodynamica.

Ik was de eerste vliegtuigbouwer, die volledig bij prof. Steketee afstudeerde en werd (student-)assistent bij hem. Daarvoor hoefde ik niets te doen: geen ordinair praktikum, ook geen nakijkwerk, want sommen zijn voor de dommen. Ik was dan ook aan een daalvlucht richting theoretische fysica begonnen. Ik deed 'Kronig 1 en 2' en kreeg van prof. Steketee een boek over electrodynamica, dat er zo oud uitzag als uit de dagen van Abraham – die dan ook de schrijver bleek te zijn van deze klassieker. Ohm maakte zo plaats voor Maxwell, hetgeen een verademing was: de voorbijgaande illusie van het exact beschrijfbare. Ik kreeg (samen met Tijdeman en later Van de Hoek) de bovenste helft van één van die oude kamers in de vliegtuigbouwvleugel van het hoofdgebouw en een afstudeeronderwerp: een vlakke plaat met twee op elkaar gestapelde vloeistoffen van ongelijke electrische geleidbaarheid swingend in een loodrecht daarop gericht uniform magnetisch veld. Prof. Steketee had in Toronto hier zelf reeds een uitvoerig rapport over geschreven, wat hielp: Mijn handgeschreven blaadjes werden noch nagekeken noch met een cijfer gehonoreerd en ik was ingenieur. Inmiddels had prof. Van der Maas besloten, dat ik ter verdere wetenschappelijke rijping naar Amerika moest. prof. Steketee regelde een NASA-Fellowship voor mij. Ik bracht die door bij prof. Burgers in Maryland. Delft was deze unieke man, die op 23-jarige leeftijd nog net voor z'n promotie hoogleraar werd aan de TH, kwijtgeraakt. Prof. Burgers hokte in een klein universiteitskamertje, woonde in een simpel

appartement bij de campus van College Park, verplaatste zich uitsluitend per Greyhound en tekende de landschappen die hij op zijn wandelingen zag, in plaats van ze te fotograferen. Herinneringen die je bijblijven en waardevoller zijn dan dat beetje fysica dat ik opdeed. Ik ben hier prof. Steketee erg dankbaar voor. Hoewel ik voor het systematische spitwerk van de wetenschapper niet erg geschikt was, had ik nog net voldoende adem om bij het ESRIN in Frascati een proefschrift te schrijven. Het werd een kort en simpel werkje over stromingsleer toegepast op de zonnewind en gebaseerd op een concept, dat ik me van een tweedejaars college theoretische aero herinnerde. Reden voor promotor Van de Hulst in Leiden en mij om prof. Steketee als medebeoordelaar uit te nodigen. Overigens verscheen nadat de promotieplechtigheid reeds begonnen was onuitgenodigd (althans niet door mij) ook prof. Van der Maas. Hij streek neer achter de opponententafel en loste zich na afloop weer even geluidloos op. Nadat het mij tijdens de verdediging gelukt was met gebrekkige antwoorden verdere vragen van een opponent te voorkomen, was het de beurt aan prof. Steketee. Hiermee wordt dit essay toch nog een bijdrage tot de aerodynamica, wat mij volgens René (nee niet De Vicq, maar Coene) het recht geeft i.p.v. 2, 15 A-4's vol te schrijven. Maar ik zal daar geen gebruik van maken.

Welnu, op pag.25 van genoemd geschrift haal ik de zgn. Paradox van d'Alembert aan en zeg, dat deze inhoudt, dat in een stationaire potentiaalstroming de weerstand nul is. Steketee verklaarde dat dat onjuist was. Ik ging door de grond. Ik had dat inderdaad niet gechecked, dacht ach Steketee kijkt het toch niet na en vond dat die naam d'Alembert het wel goed moest doen in Leiden. Ik kon de kritiek slechts ter kennisname accepteren. Zo verliep mijn laatste contact met de aerodynamica. Neen ik was niet prof. Steketee's beste student! Totdat, verdomme, een paar maanden geleden die brief van Coene et.al. door mijn brievenbus gleed. Ik herinnerde mij direct weer aan het trauma van d'Alembert, en begon nieuwsgierig en stiekum die naam in de registers van mijn vergeelde aero boeken op te zoeken. Landau & Lifshitz vonden het kennelijk niet de moeite waard, maar Theodore von Kàrmàn dacht daar anders over. Deze, commercieel meer begaafde, collega van prof. Burgers (ze schreven samen een boek) gaat in zijn in 1956 in Genève uitgegeven werk 'Aerodynamik-Ausgewählte im Lichte der Historischen Entwicklung' in op d'Alembert. En zie hier de ontknoping. Daarom wend ik mij nu tot U hooggeleerde Steketee – en wel met opgeheven hoofd. Want op pag.29 (a.a.o.) schrijft Von Kàrmàn: 'Das erste Ergebnis dieser Theorie war das Paradoxen von d'Alembert (opgelet nu komt het), wonach der Widerstand eines gleichförmig bewegten Körpers in einer reibungslosen Flüssigkeit gleich null ist, wenn sich die Strömung hinter dem Körper wieder schliesst'. Aristoteles verklaarde, dat het aanzien van een spreker of schrijver beslissend is voor het waarheidsgehalte

van diens uitspraken. Hiermede is dus pag. 25 (Smit op.cit) bewezen. Zo, dat is dat. Het bijzondere aan U, prof. Steketee was, dat U zo duidelijk de relativiteit van alle dag aangaf te begrijpen. Daarom is het eigenlijk bevreemdend, dat U vooral als mathemaat de aerodynamica bedreef. Want wat is er gedetermineerder dan mathematische fysica? Maar na Bach komt Mozart. En met de TH houdt U nu misschien ook het gedetermineerde wel voor gezien. Het ongedetermineerde, plotselinge, dat wat altijd weer anders is, is immers veel wezenlijker in dit leven. Het interessante van de aerodynamica is overigens, dat het ook aanzetten tot die niet meer direkt klassiek te vatten verschijnselen bevat. De omslag van een laminaire in een turbulente stroming is een aanzet tot het ontstaan van makrostructuren ver van thermodynamisch evenwicht. Het zijn eerst de met de 2e hoofdwet van de thermodynamica strijdig schijnende phenomenen, die ons leven mogelijk en ook zo ongrijpbaar maken (en die 2e hoofdwet zelf is immers al niet meer met de klassieke tijdinvariante mechanica verenigbaar). De Delftse omgeving verwijdert zich waarschijnlijk te weinig van Newton om aldaar vruchtbaar aandacht aan dit soort dingen te geven. Maar ook Uw leermeester prof. Burgers wijdde vooral zijn pensioenjaren hieraan (het leidde o.a. tot zijn boek over Whitehead 'Experience and Conceptual Activity'). Naast vele andere goede dingen wens ik U toe, dat Uw pensioenjaren op Uw wijze even verrijkend mogen zijn.

G.R. Smit

Mijn eerste ontmoeting met professor Steketee

Ik was in 1961 in Delft als jong eerstejaars student, als zodanig duidelijk herkenbaar, nauwelijks bekend met wie er bij de staf van de onderafdeling Vliegtuigbouwkunde waren aangesteld. Ook de ouderejaars studenten waren onbekenden. De colleges en de practica vonden niet in het gebouw voor Vliegtuigbouwkunde aan de Michiel de Ruyterweg plaats, zodat het niet vreemd was, dat de stafleden grotendeels onbekend voor mij waren. De meeste colleges werden in het gebouw voor Werktuigbouw- en Scheepsbouwkunde gegeven. Daar was ook de kantine waar door velen de lunch werd genuttigd. De overgrote meerderheid daarvan had niets met Vliegtuigbouwkunde van doen.

Zo was er op een middag in oktober de kantine vrijwel vol. Plotseling viel mijn oog op een tafeltje waar een ouderejaars student alleen zat. Mijn vraag of ik mocht aanschuiven werd positief beantwoord. Na de gebruikelijke kennismaking, waarbij wederzijds geen herkenning van de naam plaatsvond, werd ik zoals gebruikelijk ondervraagd naar mijn studierichting. Het antwoord 'Vliegtuigbouwkunde' leidde tot een voor mij onverwachte reactie: 'Dan zou ik je eigenlijk moeten kennen'. Mijn kennelijk verbaasde gelaatsuitdrukking werd door mijn tafelgenoot, die ondertussen aanstalten maakte om te vertrekken, beantwoord met: 'Maar dat komt wel in het derde jaar'.

Pas later kwam ik er achter dat deze ouderejaars student, de nogal jeugdig uitziende hoogleraar Steketee was. Zijn voorspelling omtrent het derde jaar kwam uit, terwijl de relatie in het vierde en vijde jaar werd voortgezet.

Hoewel ik niet op een echt aerodynamisch onderwerp ben afgestudeerd, en evenmin een werkkring in de aerodynamica aanvaardde, bleef professor Steketee kennelijk volgen wat ik deed. Zes of zeven jaar na mijn afstuderen bleek tijdens een korte ontmoeting weer in een kantine, thans in het gebouw voor Vliegtuigbouwkunde aan de Kluyverweg, dat professor Steketee precies wist dat ik mij bezighield met vliegwielen en hun toepassing in de standregeling van satellieten.

Ik blijf met plezier aan professor Steketee terugdenken, niet alleen vanwege de hierboven gememoreerde ontmoetingen.

ir. F.J. Sonnenschein

25 jaar samenwerken met Jaap Steketee

'Investigations on the transonic flow around airfoils' heette mijn proefschrift en Jaap Steketee was mijn promotor.
Ik had bij het NLR gedurende een aantal jaren experimenteel onderzoek gedaan aan tweedimensionale transsone stromingen. Dat was in de jaren '60. Gerke Nieuwland, later hoogleraar Wiskunde aan de V.U. in Amsterdam, had zijn hodograaf-methode voor het ontwerpen van schokvrije tweedimensionale profielen ontwikkeld. We hielden rekening met de mogelijkheid dat deze schokvrije profielstromingen niet stabiel zouden zijn. Immers schokvrije profielstromingen waren tot dan toe in de werkelijkheid nooit opgetreden. De lokaal supersone snelheidsgebieden werden altijd afgesloten door een relatief sterke schokgolf. Er waren door anderen ook theorieën ontwikkeld die moesten aantonen dat schokvrije stromingen instabiel waren. Het experimenteel onderzoek was fascinerend. Het bleek dat de schokvrije profielstromingen wel degelijk in de windtunnel konden worden gerealiseerd en dus physische betekenis hadden. Er werd van alles gedaan om de stabiliteit ervan op de proef te stellen. De schokvrije profielstromingen werden met sterke geluidsgolven gebombardeerd, maar ook daar bleken ze tegen bestand te zijn. We probeerden te begrijpen waarom de stromingen stabiel waren en wat er mis was met de theorieën die het tegendeel bewezen.

In die fase van het onderzoek dacht ik voor het eerst aan het schrijven van een proefschrift. Er was tenslotte heel veel interessant materiaal verzameld.
Gerke Nieuwland suggereerde om Jaap Steketee te vragen als promotor op te treden. Ik was er niet zo zeker van dat Jaap het een goed idee zou vinden, omdat het onderzoek voornamelijk een experimenteel karakter had en de inmiddels ontwikkelde stabiliteitsbeschouwingen te weinig mathematische diepgang hadden voor iemand als Jaap met een groot gevoel en belangstelling voor de wiskunde. Ik vergiste me, Jaap was zeer geïnteresseerd, zelfs in de experimenten. Jaap vond het belangrijk dat er originele ideeën in een proefschrift zaten. Dat was wat hem betreft meer waard dan een perfecte mathematische behandeling.

De daarop volgende periode van samenwerking met Jaap was uiterst plezierig en leerzaam.
Er werd hard gewerkt. Jaap stoorde zich wel eens een beetje aan mijn gebrek aan geduld. Als hij commentaar leverde op een bepaald gedeelte en vond dat ik wat zorgvuldiger moest formuleren – en dat gebeurde nogal eens – dacht hij dat hij een tijdje van mij af was en vond het maar vreemd dat ik mij binnen de kortste keren weer

meldde met een nieuwe tekst. Jaap vond dat ongeduld niet zo goed, het was hem zelf volkomen vreemd. Maar Jaap zou Jaap niet zijn als hij me niet accepteerde zoals ik was. Ik weet zeker dat Jaap uiteindelijk vond dat er hier en daar aan het proefschrift nog het een en ander te verbeteren viel, maar ook dat accepteerde hij. Hij wilde wel wat ombuigen en toevoegen, maar hij vond dat het mijn proefschrift moest blijven en dat hij er niet te veel zijn eigen stempel op moest drukken. Ik was en ben hem daar nog zeer dankbaar voor.

Na die promotieperiode zijn de contacten gebleven in het AGARD-FDP, in de Wetenschappelijke Commissie en in de Subcommissie voor Aërodynamica. Ook later toen ik in de NLR-directie zat was Jaap een belangrijke leverancier van intelligente, voor het NLR-werk geschikte onderzoekers. Hij leverde altijd kwaliteit, dat wisten we. Als Jaap iemand 'aanbood' konden we dat ongezien accepteren. Hij is voor mij altijd een geweldenaar geweest: intelligent, humoristisch, integer. Een persoonlijkheid zoals er heel weinig te vinden zijn. Zijn vertrek zal een groot verlies zijn voor de Faculteit der Luchtvaart- en Ruimtevaarttechniek van de TU-Delft. Hopelijk zal hij nog lang een bijdrage leveren aan het NLR.

B.M. Spee

In and out of the cuckoo's nest

Gelukkig kan ik er met steeds minder weerzin naar kijken. De interne logica van wetenschappelijke organisaties wordt in belangrijke mate op zelfverzonnen, uit de lucht gegrepen criteria gebaseerd. Toetsing aan opvattingen die in de buitenwereld leven wordt uit de weg gegaan. Kennelijk is het heel beangstigend om de willekeur van de eigen conventies onder ogen te moeten zien. Het intellectuele niveau van het groepsdenken komt dikwijls niet verder dan het niveau van de constatering dat 'ze' (dwz niet-wij) in Engeland aan de 'verkeerde' kant van de weg rijden. De verschillen tussen interne en externe normen en waarden zouden juist in academische kringen-aanleiding moeten zijn voor contemplatie; daar komt in de praktijk echter bitter weinig van terecht.

Vanuit dit perspectief gezien is de dag waarop professor Van der Maas (VTH, NLL, NIV, GROC, AGARD. etc, etc) besloot Jaap Steketee uit Toronto te halen, een keerpunt in de geschiedenis van de Delftse vliegtuigbouwkunde. De benoeming van Steketee doorbrak immers alle ongeschreven wetten: hij was veel te jong (33 jaar, als ik het goed heb), zijn komst verstoorde de ancienniteitsverhoudingen in het docentenkorps, hij had tien jaar aan de 'verkeerde' kant van de Atlantische Oceaan gewerkt en moest dus wel besmet zijn met buitenissige ideeën, hij was geen vliegtuigbouwer, hij was een pure theoreticus die het vertikte om experimenteel werk te doen en hij was, godbetert, gepromoveerd.

Gepromoveerd? In het Delft van 1960 was dat praktisch een scheldwoord, vergelijkbaar met 'studeerkamergeleerde'. Een ingenieur met hart voor de techniek had wel wat beters te doen dan artikeltjes schrijven. Als je gepromoveerd was, had je je prioriteiten kennelijk niet op een rijtje. Dus hoorde je er niet bij. Jaap heeft dat geweten: hij was voor zijn collega's de belichaming van externe criteria, en is voor hen dus altijd een buitenstaander gebleven.

Ik verbeeld me dat ik daarover mag meepraten. In het studiejaar 1958-59 had ik in Baltimore kennisgemaakt met de Amerikaanse variant van de Angelsaksische academische traditie. Ik kon me daarin zo goed vinden dat ik al snel in de gaten had dat ik een doctorsbul moest halen om verder te komen in de wereld. Een ingenieursdiploma stelt niets voor als je dromen verder reiken dan Kanaalstraat of Kluyverweg. In de botte beeldspraak van m'n Amerikaanse vrienden: 'a PhD is a union card; without it you are unemployable'.

Het zal niemand verbazen dat ik binnen de kortste keren bij Steketee op de stoep stond om te vragen of hij m'n promotor wilde zijn. Ik had er geen flauw benul van

dat ik hem daarmee in de rol van bemiddelaar plaatste. Zelf een buitenstaander, die zich dus prima kon inleven in wat mij bewoog, moest hij bij de gevestige orde gaan onderhandelen over de pretenties van een pas afgestudeerde vlegel. Ik ben nooit te weten gekomen wat zich daar binnenskamers heeft afgespeeld, maar het moet danig gestormd hebben. 'Wat verbeeldt die Tennekes zich wel dat hij meent zelf te kunnen bepalen bij wie hij promoveert? Heeft-ie dan geen gevoel voor proporties? Waarom wacht hij zijn tijd niet af?' Zulke dingen moeten er gezegd zijn, maar Jaap heeft het allemaal zonder morren opgevangen, zonder zelfbeklag. De buitenstaander als bemiddelaar: een ondankbare rol omdat je voortdurend in de clinch moet met je collega's, een zware rol omdat je naar buiten toe niets mag laten merken.
Het tekent Steketee dat hij pas veel later een tipje van de sluier rondom mijn promotie heeft opgelicht. Een tipje, meer ook niet. Jaap zou het uitermate ongepast vinden om er pathetisch over te doen. Elke vorm van dramatiek, van zelfverheffing is Steketee vreemd. Wat hij doet, doet-ie in stilte. Je zult hem niet horen mopperen als de behartiging van andermans belangen voor de zoveelste keer voorrang krijgt boven de dingen die voor hemzelf belangrijk zijn. Je hoort hem niet vloeken wanneer hij voor de zoveelste keer moet uitleggen wat er aan de Delftse conventies mankeert. De buitenstaander als bemiddelaar: niet velen kunnen zo'n zware last dertig jaar dragen.

I consider it a very special privilege that I can use this occasion to write a few words about the woman in Jaap's life. I am doing this in English, not because it is Ruth's mother tongue, but because the language in which one is forced to write gibberish of the type: 'met betrekking tot de inhoudelijke aspecten van de onderhavige problematiek wil ik u thans in overweging geven dat ....' has disqualified itself as a tool for expressing sentiments too fragile for bloated words. All of us owe Ruth Steketee a huge debt of gratitude. Having to live as a perennial outsider in a town devoid of grace and woefully short on sophistication, among men renowned the world over for their lack of subtlety, requires a strength of character and a power of endurance most of us cannot begin to fathom. Ruth has made more sacrifices than Delft would dare te extract from anybody else. A powerful spirit in a frail body, she has got wat it takes to be a lady.

H. Tennekes

Hoe is het mogelijk dat professor Steketee nu al met emeritaat gaat?

Steeds als ik hem weer eens ontmoet valt het mij op dat hij zo weinig verandert in optreden en verschijning: jeugdig en opgewekt!
Toch is er nu dus aanleiding om enkele persoonlijke herinneringen op te schrijven.

Ik ben in 1964 bij prof. Steketee afgestudeerd, dit was verreweg de prettigste periode van mijn studie. Na militaire dienst en een aantal jaren bij de lage-snelheids windtunnels van het NLR ben ik HTS-docent geworden: eerst drie jaar in het toen nogal roerige Amsterdam, daarna en tot op heden bij Vliegtuigbouwkunde in het keurige Haarlem. In het begin heb ik daar zo'n beetje alle denkbare vakken in alle studiejaren gegeven. Nu houd ik mij nog uitsluitend met aerodynamica en theoretische mechanica bezig, naast allerlei organisatorische activiteiten waar je blijkbaar niet aan kunt ontkomen.

De komst van prof. Steketee naar Delft was in menig opzicht bijzonder. Tussen allerlei hele en halve godheden waar je als student in die tijd mee te maken had bleek prof. Steketee een gewoon mens te zijn die op de gang vriendelijk goedendag zei, zelfs tegen studenten!
In mijn studentenvereniging Sint Jansbrug heerste vreugde: voor het eerst konden wij een hoogleraar als oud-lid in de sociëteit begroeten. Dat gaf eindelijk eens een mogelijkheid om met zo'n prof in zijn gewone doen te praten.

Ook voor het vak aerodynamica betekende de komst van prof. Steketee iets nieuws: tot die tijd lag de nadruk in de opleiding sterk op de toegepaste aerodynamica. Nu werden wij geconfronteerd met een theoreticus pur sang, die er op hamerde dat je de grondslagen moest beheersen. Bij mondelinge tentamens die daar helemaal niet over gingen vroeg hij je onverhoeds om maar eens een paar fundamentele vergelijkingen af te leiden. Bij zijn colleges werden wij verbluft door het vanzelfsprekend gemak waarmee hij met de wiskunde omsprong. Dat bracht mij er onder andere toe om de briljante colleges functietheorie van prof. Van Veen te gaan volgen: een openbaring, wiskunde was dus toch leuk en interessant!
Soms werd het allemaal wel eens erg theoretisch, ik herinner mij een paar opmerkingen van prof. Steketee uit die tijd:

- Bij het behandelen van een praktijkvoorbeeld waar hij niet zo goed uitkwam: 'Zodra ik me met de werkelijkheid ga bezighouden, loopt er iets mis'.
- Bij de bespreking van een supersoon vleugeltype dat eigenlijk nergens werd toegepast: 'Maar je kunt er zo lekker aan rekenen'.

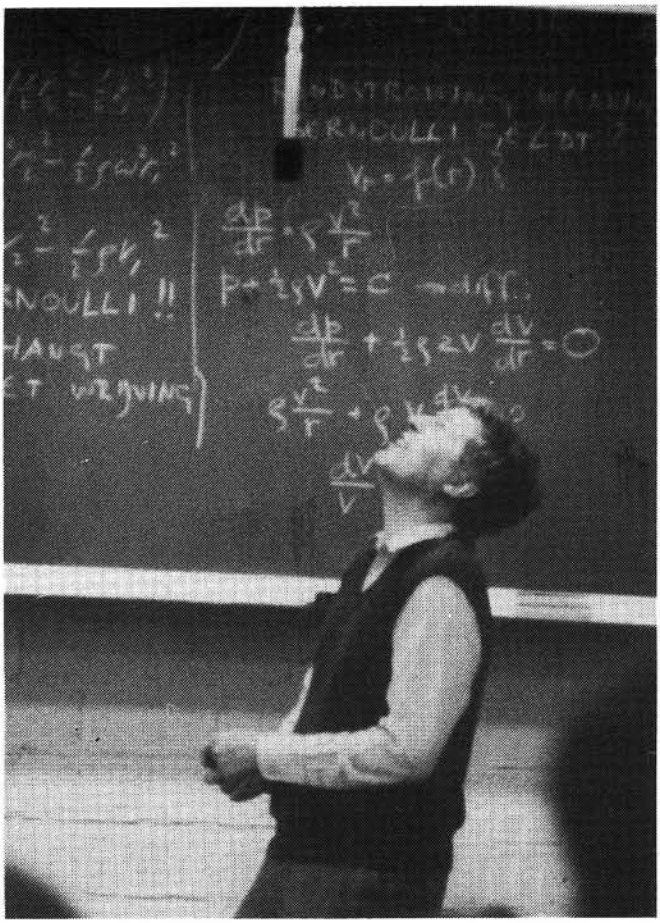

- Op de vraag hoe hij zich destijds in Canada redde met die lastige Engelse eenheden: 'Ik gebruik nooit eenheden'.
- En ook nog, tijdens een college waar uitsluitend vliegtuigbouwstudenten zaten: 'Hier ga ik maar niet verder op in, dit is meer iets voor vliegtuigbouwers'.

Wij studenten verdachten prof. Steketee er echter van dat hij op het gebied van de toegepaste aerodynamica veel meer wist dan hij wilde toegeven: niet voor niets had hij zoveel contact met de toenmalige wetenschappelijk ambtenaar Van Ingen.

Mijn afstudeerwerk bestond uit twee delen: windtunnelmetingen en grenslaagberekeningen aan een rompmodel, onder leiding van Van Ingen en Dobbinga, gevolgd door een theoretische studie over schokbuizen met variabele doorsnede onder de hoede van prof. Steketee. Toen het aan het eind van de rit eigenlijk niet gelukt was om een analytische oplossing van het probleem te vinden, sprak hij met duidelijke tegenzin: 'Als we dat van tevoren hadden geweten, hadden we het misschien toch maar eens

numeriek moeten proberen'. De computer stond nog in de kinderschoenen en werd door prof. Steketee met gezond wantrouwen en een zekere minachting bekeken.

Mijn lessen op de HTS dienen in hoofdzaak op practische toepassing gericht te zijn. Door de snelle ontwikkelingen in de vliegtuigbouwkunde dreigt echter het gevaar dat het leerplan te sterk wordt beïnvloed door de waan van de dag. Het is daarom ook voor de HTS noodzakelijk om een degelijk theoretisch fundament te leggen waarop een technicus gedurende zijn gehele loopbaan kan bouwen. De theoretische grondslagen van de aerodynamica spelen daarom in mijn werk een zeer belangrijke rol, en in die zin kan ik zeggen dat prof. Steketee tijdens mijn lessen steeds achter mij staat.

Bij zijn afscheid wil ik hem bedanken voor het vele dat ik van hem heb geleerd en voor de plezierige ontmoetingen die wij ook na mijn afstuderen nog geregeld hadden. Ik kan mij niet indenken dat hij zijn bijdragen aan de Faculteit der Lucht- en Ruimtevaarttechniek nu reeds geheel zou beëindigen. In ieder geval wens ik hem nog vele gelukkige jaren als hoogleraar 'in ruste'.

Daan de Vos

Mijmeringen over professor Steketee

Mijn eerste ontmoeting met prof. Steketee vond plaats in de lente van 1978. Na twee jaar studie Luchtvaart en Ruimtevaarttechniek was ik tot de conclusie gekomen dat Ontwerpen van Vliegtuigen niets voor mij was, en ik had besloten van de T-optie gebruik te maken. De namen van drie hoogleraren waren mij verstrekt door de studenten administratie, en prof. Steketee was de tweede op mijn lijst die ik zou bezoeken. Het bezoek met de eerste hoogleraar was geen groot succes, en gedemoraliseerd kwam ik bij prof. Steketee aan, die mij als een vader figuur met open armen ontving en verheugd was weer een T-student te mogen begroeten. Sinds die tijd kwam ik dan ook met een zekere regelmaat de rust op de tiende verdieping verstoren.

Voor prof. Steketee was ik, denk ik, een lastig geval. Ik was meer geinteresseerd in numerieke stromingsleer en grootschalige berekeningen dan het zoeken naar analytische oplossingen. Ik studeerde af bij de vakgroep a1, maar deed mijn vierde jaarswerk aan de TH-Eindhoven, en mijn afstudeerwerk werd gedaan bij het NLR. Ondanks dit alles steunde prof. Steketee mij bij al mijn projecten en ideeen, en gaf me alle vrijheid om de wetenschappelijke wereld te ontdekken. Ik kan me nog herinneren dat ik voorstelde om vakken als Atoomfysica en Theoretische Natuurkunde op mijn vierdejaarslijst te zetten, en ik dacht bij mezelf dit zal niet geaccepteerd worden. Ik had me vergist, prof. Steketee was enthousiast dat ik deze colleges wilde volgen, mede omdat hij dat vroeger ook gedaan had. Ook kon ik altijd langs komen om met prof. Steketee mijn werk te bediscussieren, en altijd kreeg ik weer een lijst van referenties mee die ik kon raadplegen. Vaak bediscussieerden we de vakgroep, en ik kan me nog herinneren dat prof. Steketee zich beklaagde dat hij geen experimentele faciliteiten had, en hij vond eigenlijk dat een orgel op de 10^{de} wel een goed idee was. Orgels en orgel spelen was dan ook een grote hobby van prof. Steketee, en ik kan me levendig voorstellen hoe hij in de St. Pauls Cathedral in London door alle mogelijk stoffige gangen en hoeken gekropen is om het orgel te bekijken.
Prof. Steketee was ook mijn promotor, en ik herinner me nog levendig dat de eerste versie van mijn proefschrift tot de bodem toe afgekraakt werd. Een uur nadat ik bij prof. Steketee vertrokken was kwam de secretaresse langs om te kijken hoe het met me ging. Ze was door prof. Steketee gevraagd even polshoogte te nemen. Deze vaderlijke bezorgdheid voor zijn studenten heb ik vaker gezien, en ik heb het ook erg gewaardeerd. Aan de ene kant had prof. Steketee zijn wetenschappelijk geweten, die hem vertelde dat mijn eerste versie van het proefschrift slecht was, aan de andere kant was daar zijn menselijke geweten, die wist dat het niet eenvoudig is om kritiek te ontvangen.
Na mijn vertrek uit Nederland heb ik nog steeds kontakt gehouden, en enige maanden geleden kreeg ik een telefoontje uit Nederland, en prof. Steketee stond mij in vloei-

end Frans te woord. Ik was verbaasd en onder de indruk, want de Franse taal is niet eenvoudig om bij te houden.

Een bijdrage als deze is fragmentarisch, maar ik hoop dat ik een indruk van de mens en wetenschapper die prof. Steketee was gegeven heb. Ik ben hem dankbaar dat hij me ingewijd heeft in het wetenschappelijk onderzoek, en voor alle dingen die hij me geleerd heeft.

Ik wens prof. Steketee en zijn vrouw Ruth een voorspoedige toekomst toe, en ik zie het nog wel gebeuren dat in de toekomst prof. Steketee de computer van zijn vrouw zal gebruiken.

Jan Vos
Lausanne, 30 september 1991

An impression on a professor

I got to know professor Steketee when I joined the theoretical aerodynamics group on August of 1987.

As I got absorbed in it, I soon found that this was a group with congenial atmosphere. I think this should largely be attributed to its chief, who often has in mind that as the supervisor of the group he has to keep everybody alive – a statement I once heard when he was summoning us for lunch as his usual routine.

There is a kind of pleasant atmosphere around him, besides the flavorous clouds of a cigar. It is like sitting under the rich, golden rays in a fine autumn afternoon, though not much experienced here in the Netherlands. In my mind, I always associate the autumn with something rich, and vast that could contain everything. In it, I feel light, free, like the fume that spirals up.

The chief himself does gas dynamics study analytically, showing quite modest interest in a 'rekentuig'. Nevertheless, on my observation, he shows no contempt at the computational stuff. For instance, he could tolerate people playing with computers, sometimes with serious scientific research, sometimes with little games, to be honest, in the room opposite to his'. As a matter of fact, he quite cares about the fate of the computers. I could recall when, late in the afternoon, before he left for home, he often remembered to check the machines in case someone may forget to switch them off occasionally. To show the intimacy, he sometimes uses the computer paper as his scratch paper.

Expertised in fluid mechanics, he seems really to be occupied with the subject constantly. I remember once, when I was busy with pursuing my girl friend, now my wife, I consulted him about the difference between eau de toilette and parfum. With little hesitation, he replied 'well, it is like beer and whisky, you see.' Lately, I realized that Dr. Bos of our group was then doing a numerical study which had some affiliation with the overflow of a beer. Whether our professor had that in mind I cannot tell.

Zeguang Wang

Lijst van promoties waarbij prof. dr. ir. J.A. Steketee als promotor optrad

jaar	*naam*	*titel*
1964	Tennekes, H.	Similarity laws for turbulent boundary layers with suction and injection. TH Delft.
1965	Ingen, J.L. van	Theoretical and Experimental investigations of incompressible laminar boundary layers with and without suction (met prof. H.J. v.d. Maas). TH Delft.
1969	Arora, N.L.	A unified theory for linearized shock-on-shock interaction problems. TH Delft.
1969	Smit, G.R.	The oscillatory motion of the magnetopause and the earth's bow shock (met prof. H.C. v.d. Hulst). RU Leiden.
1969	Spee, B.M.	Investigations on the transonic flow around aerofoils. TH Delft.
1973	Coene, R.	Quasi-homogeneous approximations for the calculation of wings with curved subsonic leading edges flying at supersonic speeds. TH Delft.
1976	Polman, R.W.	Vortex flow in a torus. A method for arc Stabilization (met prof. C.M. Braams). RU Utrecht.
1981	Nieuwstadt, F.Th.M.	The nocturnal boundary layer (met prof. H. Tennekes en prof. J.T.F. Zimmerman). VU Amsterdam.
1982	Berg, M.S. van den	Theory on a partially ionized gascentrifuge (met prof. J. Kistemaker). TH Delft.
1983	Massee, P.	Gasdynamic performance in relation to the power extraction of an MHD-generator (met prof. L.H.Th. Rietjens en prof. J.H. Blom). TH Eindhoven.
1984	Bos, H.J.	On the aerodynamic optimization of supersonic wings. TH Delft.
1986	Jansen, A.J.M.	Fluid motions generated by the injection of an electric current. TU Delft.
1987	Vos, J.B.	The calculation of turbulent reacting flows with a combustion model based on finite chemical kinetics (met prof. A.E.P. Veldman)

Lijst van afgestudeerden van prof. dr. ir. J.A. Steketee

naam	*titel afstudeerverslag*
Aarts, W.J.A.M.	De stroming door een slank glad kanaal met een constante instroming door de wand (1991).
Alamel, C.P.F.	Dissociation-recombination phenomena behind a hypersonic shock-wave (1991).
Bakker, R.J.J.	Incorporation of Vibrational Non Equilibrium in a Two-Dimensional Euler Solver (1991).
Bannink, W.J.	Enkele berekeningen en conclusies betreffende draagvlakken in supersone stroming (1961).
Barkey Wolf, F.D.	A tandem biplane in a sinusoidal gust (1983).
Beek, C.M. van	Het zwemmen van slanke vissen in golven (1980).
Berg, M.S. v.d.	Enkele stromingen uit de magneto-hydrodynamica in de omgeving van qua geleidbaarheid geïdealiseerde wanden (1973).
Boerstoel, J.W.	De vergelijking van exacte resultaten en resultaten volgens de profieltheorie bij de berekening van de onsamendrukbare stroming om een ellips en de berekening van de stroming om een quasi-ellips (1962).
Bos, H.J.	Het geluid van gasstralen (1970).
Broek, G.J. van den	Verdunningseffekten in de vlakke Couettestroming (1967).
Bruggeman, J.C.	Toepassing van de groep van gegeneraliseerde Staniukovic transformaties op enkele eenvoudige rechtlijnige stromingen (1983).
Buijk, A.	Over de uitbreiding van een 2-D Euler code naar axiale symmetrie d.m.v. een defect correctie methode, voor supersone stromingen (1988).
Chaabane, M.	Virtual mass and concentration wave velocity in a homogeneous flow of two compressible phases (1988).
Coene, R.	Drukverdeling over een gewelfde delta-vleugel (1963).

Cornelissen, M.	A Stability Investigation of the burning of a fluid rocket-propellant (1982).
Dam, R.F. van den	De expansie van een Martin-Ludford gas in een gravitatieveld (1976).
Duivenbode, E. van	Numerieke oplossingen van stromingen rond twee-dimensionale trillende profielen (1988).
Dijk, J.H. van	Krachten en momenten op lichaam in potentiaalstroming (1980).
Eek, G.M. van	De aerodynamische krachten en momenten op een trillend draagvlak met roer en hulproer tussen twee evenwijdige wanden (1962).
Elsenaar, A.	Het verband tussen wrijving en warmteoverdracht in de turbulente grenslaag (1967).
Enschede, J.J.	Circulatiebepaling om roterende vleugelprofielen in een cyclogyro (1986).
Enthoven, M.E.E.	Overwegingen bij de keuze van een beproevingsinstallatie voor hypersone stromingen t.b.v. het HSL van de Onderafd. Vliegtuigbouwkunde van de TH Delft (1967).
Esch, A.J.P.M. van	Vloeistofstromingen geïnduceerd door het injecteren van een electrische stroom; het geval met geïsoleerde symmetrieas (1989).
Florie, C.J.L.	Een door Lorentz-krachten aangedreven vloeistofstroming in een rechte tunnel en een cirkelcylindrische buis (1976).
Gadiot, G.M.H.J.L.	A new Helmholtz Resonator-burner: Design, Analysis and Experiments (1982).
Gerritsen, E.W.	Optimale voorrand van vlakke plaat met rechte achterrand in supersone stroming (1976).
Griens, F.	Een door een verhoging van oppervlaktetemperatuur geïnitieerde ontbranding van een hoeveelheid vaste brandstof (1984).
Hagmeyer, R.	Een gediscretiseerd wervelvlakmodel voor de beschrijving van het zog van een cyclogyro vleugelsysteem (1987).
Hamerling, R.	Ontwikkeling van een rekenmethode ter bepaling van de weerstand van vliegtuigen in vluchtomstandigheden uit metingen in windtunnels bij lagere getallen van Reynolds (1968).

Harting, A.	NLR rapport A1585. Experimental investigations of incompressible, two-dimensional curved wall jets in still air, flowing along circular cylinders because of the Coanda-effects (1964).
Heerema, F.J.	De berekening van een klasse vleugels met ideale invalshoek, waarbij de stoorsnelheids potentiaal homogeen is van de graad twee. Het liftgeval (1969).
Heijden, J.C. van der	Laminaire diffusie vlam oplossingen voor gebruik in een vlamlaag model voor turbulente verbranding (1990).
Heijman, M.	Magnetohydrodynamische voortstuwing van schepen (1967).
Hoeijmakers, H.W.M.	Enige berekeningen aan supersone draagvlakken met subsone voorranden (1971).
Hounjet, M.H.L.	De golfweerstand van een deltavleugel (1975).
Houwelingen, F. van	Model van een supersone versnellende bron als oplossing van de scalaire 3-dimensionale golfvergelijking (1970).
Irausquin, L.D.	Fluent Calculations of the SCGP-Gasifier (1991).
Jacobs, J.M.J.W.	Een gemodificeerd Prandtl en een numeriek model voor de beschrijving van een zich oprollend wervelvlak (1986).
Jellema, K.	Opgave theoretische aerodynamica (1968).
Jongh, F.H.C. de	Drift in potentiaalstromingen met circulatie (1987).
Ketting Olivier, R.F.	Enkele studies m.b.t. de niet-stationaire rechtlijnige stroming van een ideaal gas (1984).
Keuss, A.T.J.	Invloed van de eindige spanwijdte op het aerodynamisch gedrag van een cyclogyro-vleugelsysteem in een uniforme parallelstroming (1984).
Khalaf, M.S. Abu	Inference studies on the configuration on a delta wing and a circular cone 'fuselage' by means of slender-body theory (1973).
Klein Lebbink, G.C.	Theoretical analysis of laminar incompressible flow in slender channels (1987).
Kloet, J.J.	Enige beschouwingen over het warmte overdrachtsprobleem in potentiaalstromingen (1972).

Knoppe, J.A.	Enige berekeningen aan dunne symmetrische deltavleugels met subsone voorranden (1971).
Kokkeel, R.	De berekening van een twee-dimensionaal temperatuurveld van een vlakke Couette-stroming (1970).
Kox, P.M.J.	Theoretische methoden voor het bepalen van de Thermoforetische Kracht (1989).
Kramer, H.	Verschillende rapporten (1966).
Krijger, G.J.	Expansie van een gas achter een zuiger met een willekeurig voorgeschreven baan (1974).
Kuik, G.A.M. van	De stroming om vleugelprofielen met constante circulatie (1976).
Kuipers, W.	Een overzicht van de theorie der Lamé-functies en enige toepassingen (1964).
Laan, H. van der	Druk, temperatuur en stromingspatroon aan de basis van een raketmodel met hete straalsimulatie d.m.v. H_2O_2 in een supersone stroming (1967).
Laat, T.W.G. de	Vrije wervels bij Tweedimensionale Vliegtuigcontouren (1991).
Labrujère, Th. E.	Determination of the stability derivatives of an oscillating axi-symmetric fuselage in supersonic flow (1960).
Langedijk, C.J.A.	Het magnetohydrodynamisch Rayleigh probleem (1974).
Leussink, M.A.C.	Ervaringen met het numeriek oplossen van de Eulervergelijkingen voor kanaalstromingen m.b.v. het Osher-schema (1988).
Lindijer, G.J.H.	Studie over de interferentie van een schokgolf en een expansiegolf in een één-dimensionaal, instationaire stroming (1973).
Lutterveld, H. van	Studie van de passage van een wervel door een schokgolf in een 2-dim. stroming (1969).
Maarsingh, R.A.	Een tweetal berekeningen van het stromingsveld opgewekt door een enkele straal, stromend tegen een vaste wand, volgens de twee-dimensionale potentiaaltheorie (1962).
Martens, J.A.J.H.	Over de methodes van Glimm en Godunov voor het beschrijven van één-dimensionale, niet stationaire stromingen (1985).

Massee, P.	De dynamica en thermodynamica van een Van der Waals gas (1965).
Metselaar, L.C.	Studie over de één-dim. niet-stationaire gasbeweging, en de quasi-één-dim. stroming waarbij de polytrope relatie wordt gebruikt (1971).
Molendijk, F.	Bepaling van de wervelbeleggingen op een vlakke deltavleugel met subsone voorranden bij M=1,5 en supersone voorranden bij M=5 (1966).
Montemayor, E.M.	Description of the flow around a supersonic flat plate aerofoil (1967).
Muilman, T.	De benaderingsmethode van Whitham toegepast op de interferentie van een schokgolf en een gecentreerde expansiegolf (1975).
Mulder, H.C.	De Schwarz-Christoffel transformatie en de toepassing ervan op stromingsproblemen (1972).
Mulder, P.	Verticale Turbulente Diffusie in een homogene gelaagde vloeistof (1985).
Nebbeling, C.	Theoretische en gemeten drukverdeling bij een getal van Mach van 2.94 langs het oppervlak van een ogive omwentelings lichaam met een lengte-diameter verhouding gelijk aan 6 (1968).
Nieuwstadt, F.Th.M.	Asymptotische methoden in de stromingsleer met toepassingen op enige verschijningsvormen van de Couette stroming (1969).
Pellinkhof, G.P.	Gelineariseerde theorie voor trillende draagvlakken in een supersone parallelstroming (1968).
Poland, P.Y.C.M.	Geluid-wervel interactie in een 2-dimensionale ramjet configuratie (1989).
Polderdijk, S.H.	The optimized lifting wing with slightly curved leading edges in supersonic flow (1978).
Pröpper, J.P.	Hypersonic Shock Layer Calculations using equilibrium ideal dissociating gas approximations (1989).
Raayman, A.J.J.	Het Transport van Energie en Impuls door middel van oppervlaktegolven in water (1989).
Risseeuw, A.	Snelheid, elektrische stroomdichtheid en temperatuur rond een elektrode in een MHD-kanaal (1982).

Roos, R.	Oplossing van de vergelijkingen voor het Rayleigh-probleem met eenvoudige randvoorwaarden in de Magneto-hydrodynamica (1966).
Schermers, J,G.	Laboratoriumonderzoek naar het gedrag van niet stationaire gasstromen in pijpen, opgewekt door een pulsator met een roterende cilinder voorzien van een sleufopening, 3 rapporten (1966).
Schippers, K.A.	Toepassing van de methode met singulariteiten uit de gelineariseerde supersone theorie op een rechthoekige vleugel met variabele slankheid (1962).
Schulten, J.B.H.M.	Experimenteel onderzoek aan laminaire loslatingsblazen (1967).
Schutte, H.	Coanda-ejecteurs betreffende de wrijvingsverliezen op de buitenwand van het primair gedeelte van de zgn. 'Cylinderejecteurs' (1969).
Sijtsma, H.A.	Theoretische berekening van de weerstands coëfficiënt van een vlakke cirkelvormige plaat (1970).
Simons, Th.J.	Half-Oneindig Vast Lichaam met een Oneindig Uitgestrekte Vlakke Wand in een Samendrukbaar, Visceus, Medium (1964). Het Aequivalentie Principe voor Hypersone Stroming rond een slanke wig (1963).
Smeulders, D.M.J.	Eén dimensionale stromingen in een ideaal gas. Een studie over de frontale botsing van een schokgolf met een expansiewaaier (1987).
Smit, G.R.	De oscillerende plaat in de magnetohydrodynamica met al of niet electr. geleidende grenslaag (1963).
Smit, R.A.M.	Een analytische beschouwing van de tweedimensionale MHD-stroming door een kanaal met konstante hoogte waarvan de wanden gedeeltelijk geïsoleerd zijn en gedeeltelijk ideaal geleidend (1980).
Snel, H.	De moleculaire achtergronden van de vergelijkingen van Navier Stokes (1967).
Sonnenschein, F.J.	Electrische voortstuwing in de Ruimtevaart (1968).
Stolz, J.	Berekening van de verstoring door de aanwezigheid van stijlen van het stromingsveld om

	een axiaal symmetrische ringvleugel met romp (1961).
Sudmeijer, K.J.	'Not-so-slender' wing theorie (1973).
Sukmawanto, D.	Een model oplossing voor het stromingsveld van een laminaire diffusievlam met CH_4 als brandstof en lucht in de vrije atmosfeer als oxydator (1988).
Tambach, Th.J.J.	Enige berekeningen aan homogene stromingen om dunne deltavleugels (1970).
Tjandra, A.M.	Het effekt van de opwaartse druk en van wervels op een 2-dimensionaal laminair diffusie vlam model (1990).
Trompert, R.A.	Optimalisatie van een supersoon draagvlak (1986).
Uylenhoet, R.	Metingen van stromingsfluctuaties in de pilottunnel van het NLR m.b.v. gloeidraden (1966).
Venema, F.J.W.	Onderzoek naar uitdrukkingen voor de Reynoldsspanningen af te leiden aan de hand van de Newtonse vloeistof afwijkende van de niet-Newtonse vloeistof en een turbulente stroming door dezelfde rechte pijp met een vierkante dwarsdoorsnede (1977).
Venis, A.C.J.	An experimental and theoretical investigation of the flow on a flat delta wing with or without yaw in a supersonic uniform flow (1988).
Verbeek, P.H.J.	Een cyclo-gyro in een niet-uniforme parallelstroming met grondeffect en vrij wervelveld (1978).
Verheijden, A.J.H.	Resultaten van de voortzetting van een experimenteel onderzoek naar het gedrag van instationaire verstoringen in het transsone gebied. Laboratory report Electronics (1964).
Visser, L.	The calculation of the pressure distribution due to thickness for thin wings with arbitrary planform at supersonic speeds (1967).
Voogt, N.	Oplossing van het ballistisch probleem van Lagrange met behulp van een differentiemethode (1969).
Vos, D.M. de	Niet-stationaire stroming in een rechte buis met al of niet-constante doorsnede (1964).

Vos, J.B.	De ontwikkeling van een rekenmodel voor de 1-dimensionale instationaire MHD-stroming (1982).
Vossen, G.W.	De verandering van de Poiseuillestroming in een electrisch geleidend, visceus, incompressibel medium, door een op een willekeurig tijdstip opgelegd, magnetisch veld (1971).
Vreeburg, J.P.B.	De invloed van een magnetisch veld op een expansiestroming van een medium met kleine geleidbaarheid (1966).
Waart, E. van	De interactie van een schokgolf en een gecentreerde expansiegolf door de plotseling stoppende zuiger in de één-dimensionale instationaire beweging van een gas (1976).
Walsteijn, F.H.	Robuuste generatie van grids over enkelvoudig samenhangende 2D-gebieden (1987).
Wesseling, P.	Het MHD Stokes probleem (1964).
Wichers Schreur, B.	Second order effects in a theory of a cyclogyro wing system in a parallel flow (1985).
Woerkom, P.Th. van	Mathematical Analysis of Quasi-One-Dimensional Magneto-Gas-Dynamic Channel Flow (1969).
Wolfs, M.J.M.	Een gelineariseerde theorie voor een bolvormige windturbine met concentrator effect onder verschillende aanstroomrichtingen (1984).